

**OPTIMISATION OF THE GASEOUS
DISCHARGE AND OPTICAL COUPLING OF
A PULSED CO₂ LASER**

by

Ian Alistair Watson BSc. (Hons)

**Thesis presented for the
Degree of Doctor of Philosophy
under general regulations**

**Department of Mechanical Engineering
Faculty of Engineering
University of Glasgow**

June, 1993

ProQuest Number: 13818427

All rights reserved

INFORMATION TO ALL USERS

The quality of this reproduction is dependent upon the quality of the copy submitted.

In the unlikely event that the author did not send a complete manuscript and there are missing pages, these will be noted. Also, if material had to be removed, a note will indicate the deletion.



ProQuest 13818427

Published by ProQuest LLC (2018). Copyright of the Dissertation is held by the Author.

All rights reserved.

This work is protected against unauthorized copying under Title 17, United States Code
Microform Edition © ProQuest LLC.

ProQuest LLC.
789 East Eisenhower Parkway
P.O. Box 1346
Ann Arbor, MI 48106 – 1346

*Thesis
9617
copy 1*

GLASGOW
UNIVERSITY
LIBRARY

SYNOPSIS

Pulsed, high frequency lasers offer enhanced material processing capabilities when compared to continuous wave sources. To achieve high quality machining at the workpiece, a CO₂ laser is developed which can operate at 10 kHz with laser pulse lengths of approximately 6 μ s. The device is specifically designed to deliver the optimum laser pulse for the material workpiece interaction process, and in particular, for highly reflective and/or refractory materials.

The available laser power from CO₂, N₂ and He gas discharges is critically dependent on the gas pressure, gas composition, pumping power and the extraction efficiency of the resonator. The stability of the discharge during the pumping pulse is of paramount importance to ensure that laser output is maintained. Moreover, arcing can damage circuit components and seriously degrade the electrodes through spark erosion and sputtering processes. These factors are considered in the development of the laser.

To create laser pulses for enhanced material processing a novel, large volume, low energy density, transverse gas discharge system is developed which uses the conventional double discharge preionisation technique. The auxiliary discharge is capacitively coupled to the discharge anode - brass planar electrodes are used. Two Roots blowers operate in parallel and yield maximum gas velocities of 100 ms⁻¹ within the electrode region. A multi-pass, stable, half-symmetric resonator is used to extract the laser power.

The criteria for obtaining stable, uniform, glow discharges over a range of gas mixtures and pressures of up to 200 torr are critically assessed. The effects of preionisation and the applied discharge overvoltage on the discharge stability are examined for the operating regime of the laser. The discharge stability and the laser output is quantified for a range of pumping circuit configurations. A high voltage, low inductance, preionising circuit is fabricated and tested as an alternative method of preionisation.

The uniformity of the gas velocity between the electrodes is examined in two dimensions by using a computer controlled, Pitot-static tube and stepper motor assembly. The maximum discharge power ratings, prior to the onset of arcing, are determined for different flow-shaping geometries. Clearing ratios of less than unity are observed for low discharge energy densities. However, for higher values, the clearing ratio is above two. It is concluded that the non-uniformity of the gas flow is a major factor limiting the performance, of the planar electrode discharge

geometry, to frequencies of about 1.5 kHz.

Two ballasted electrodes with total resistances of 0.8 Ω and 8.0 Ω were fabricated and tested. They offered substantial improvement in the maximum discharge power loading and operating frequencies prior to the development of discharge instabilities. Typically, 11 kW mean power was deposited into the discharge, with frequencies above 5 kHz.

The extraction efficiency for different resonator configurations is investigated for all electrode geometries for a high inductance pumping circuit. A 5 pass, half-symmetric, stable resonator yielded the maximum laser power from the ballasted electrode system with pulse energies of 0.13 J, and plateau powers in excess of 17 kW. This delivered the laser pulse characteristics that are suitable for achieving the non-conduction limited material interaction process.

It is shown that the laser output power is substantially increased by reducing the circuit inductance and increasing the gas pressure so that the network and discharge impedances are nearly matched. Laser pulse energies of over 0.1 J are observed for a single pass resonator.

The non-conduction limited interaction process has been demonstrated by cutting and drilling holes in aluminium.

In conclusion, future work is proposed in order to fully extend the operating regime of the laser so that it is capable of a performance that would be attractive to industry.

DEDICATION

This work, and all the effort that it entailed, could not have been produced without the help and support of Sandra, to whom I dedicate this thesis and promise to spend a little bit more time with once it is complete.

ACKNOWLEDGEMENTS

I would like to thank Professor B. Scott and Dr. C. Chatwin for the many fruitful discussions on this research project and potential applications of the laser. In particular, I would like to thank Chris for taking the time and trouble to read this thesis and making useful suggestions. Thanks are also due to Dr D. McDonald for many of the worthwhile consultation periods over the power supply and the development of the H.V. preioniser.

Particular thanks are due to John Davidson, Bernard Hoey, Brian Macadam and John Dunning, who at one time and another were all there to help me in a diverse range of activities, ranging from fabricating components to aiding with the experiments.

I would like to express my gratitude to Isabelle Lawson for preparing the drawings that pervade throughout this thesis.

Finally, I appreciate the endless suffering endured by Barbara MacLeod which was caused by my continuous interruptions to use her printer.

CONTENTS

LIST OF FIGURES	xii
LIST OF TABLES	xviii
NOMENCLATURE	ixx
CHAPTER ONE INTRODUCTION	1
1.1 WORKPIECE INTERACTION MECHANISMS	1
1.2 LASER SYSTEMS REVIEW	2
1.3 SCOPE OF THE PRESENT WORK	4
CHAPTER TWO LASER SYSTEM	11
INTRODUCTION	11
2.1 DC CHARGING SUPPLY	12
2.1.1 Transformer	12
2.1.2 Rectification	12
2.1.3 Smoothing and Voltage Monitoring	13
2.2 PULSER	13
2.2.1 Pulse Forming Network (PFN)	14
2.2.2 Resonant Circuits and the PFN Charging Cycle	17
2.2.3 Thyratrons	19
2.2.4 Thyratron Trigger Units	20
2.2.5 Pulser Control Unit	21
2.3 LASER CAVITY	21
2.3.1 Anode and Cathode	21
2.3.2 Trigger Wires	23
2.3.3 Cavity Flow Shaping	23
2.3.4 Resonator	24
2.3.5 Resonator Alignment	25
2.4 GAS RECIRCULATOR	25
2.4.1 Roots Blowers and ducting	26

2.4.2	Heat Exchangers	26
2.4.3	Gas Control System	27
2.4.4	Gas Recirculator Control Unit	27
2.4.5	Gas Recirculator Instrumentation	28
2.5	FORE-OPTICS AND WORKPIECE HANDLING	28
2.5.1	Fore-Optics	28
2.5.2	Workpiece Handling	30
2.5.3	Water and Air Optical Cooling Circuit	30
2.5.4	Fore-optics Control Unit (FOC)	30
2.5.5	Flow Meters	31
2.5.6	Cone Calorimeter and Mean Power Indicator	31
CHAPTER THREE	DISCHARGE PARAMETERS, INITIATION AND PREIONISATION	54
	INTRODUCTION	54
3.1	E/N MEASUREMENTS	55
3.1.1	Measurement of E/N with Different Partial Pressures of He and N ₂	56
3.1.2	Measurement of E/N With Additions of CO	57
3.2	DISCHARGE EXPERIMENTAL RESULTS	57
3.2.1	Single Shot Stability Limits	58
3.2.2	System Modifications	59
3.2.3	Voltage and Current Waveforms of the Main Gap	61
3.2.4	Trigger Wire Characteristics and Modelling	63
3.2.5	Preionisation: A Threshold Process	66
3.2.6	Affect of the Trigger Wire Gap, Coupling Capacitance, Peaking Capacitor and Low Ionisation Potential Seedant on Discharge Performance	67
3.2.7	Gap Voltage Prior to the Discharge Thyatron, T2, Triggering	70
3.2.8	Patterns Formed on the Anode and Cathode	71

3.3	DISCHARGE INITIATION THEORY	73
3.3.1	Discharge Breakdown Mechanisms	73
3.3.2	Streamer Breakdown	76
3.3.3	Requirements for Efficient Preionisation	79
3.3.4	Formative Time Lag Calculations	83
3.4	PULSED DISCHARGE SIMULATION USING PSPICE	84
3.4.1	Model of the CO ₂ Gas Laser Discharge	84
3.4.2	Evaluation of the Simulation Validity	86
3.4.3	Affect of Gas Pressure on the Discharge Performance for a 1:1:8 Gas Mixture	87
3.4.4	Affect of the Network Voltage	88
3.4.5	Affect of Peaking Capacitance	88
3.4.6	Affect of the Discharge Thyatron Anode Inductance	89
3.4.7	Affect of Initial Preionisation Electron Density	89
3.5	INDEPENDENT PREIONISER	89
3.5.1	The Preioniser Design	90
3.5.2	Delay Time Calibration	92
3.5.3	Testing into the Trigger Wires: Single Shot and Burst Mode	93
3.5.4	Laser Output Results	95
3.6	REPOSITIONING OF T2 AND THE LAST PFN MESH	96
3.6.1	Results with Capacitive Coupling Preionisation: Single Shot Mode	98
3.7	REDESIGNING THE ELECTRODE CONFIGURATION	100
CHAPTER FOUR	GAS FLOW AND DISCHARGE STABILITY	148
	INTRODUCTION	148
4.1	AFFECT OF FLOW SHAPING AND MESH ON DISCHARGE STABILITY	150
4.1.1	Affect of Longitudinal Flow-shaping on Discharge Stability	150
4.1.2	Affect of Edge Flow-shaping on Discharge Stability	152
4.1.3	Affect of Turbulance on Discharge Stability	153

4.2	MEASUREMENT OF THE GAS VELOCITY PROFILES	153
4.2.1	Experimental Arrangement	154
4.2.2	Gas Velocity Measurements as a Function of Time	157
4.2.3	Gas Velocity Profiles Without Flow-shaping	158
4.2.4	Gas Velocity Profiles With Upstream Flow-shaping	160
4.2.5	Transverse Velocity Profiles	161
4.2.6	Gas Velocity profiles with Flow-shaping Around the Support Structures	161
4.2.7	Gas Velocity as a Function of Pressure	162
4.2.8	Summary of the Gas Velocity Measurements and the Clearing Ratios	162
4.3	BALLASTED ELECTRODE	163
4.3.1	Ballasted Electrode Design Equations	165
4.3.2	Power Transfer Efficiency	167
4.3.3	Ratio of Discharge Power to Power Developed in the Ballast Resistance	168
4.3.4	Ballasted Electrode Discharge Energy Measurements	168
4.3.5	Fault Current Analysis	169
4.4	PROTOTYPE BALLASTED ELECTRODE DESIGN	170
4.4.1	Ballast Resistance Selection	171
4.4.2	Discharge Initiation	173
4.4.3	Experimental Procedure for the Prototype Ballasted Electrode	173
4.4.4	Calibration of the Frequency Control Potentiometer	174
4.4.5	0.8 Ω Ballasted Electrode Performance	175
4.4.6	8.0 Ω Ballasted Electrode Performance	178
CHAPTER FIVE	LASER OUTPUT CHARACTERISTICS	212
		212
	INTRODUCTION	
5.1	DETECTION AND MONITORING SYSTEMS	213
5.1.1	Cone Calorimeter	213
5.1.2	Photon Drag Monitor (PDM)	214
5.1.3	Cadmium Mercury Telluride (CMT) Detector	216
5.1.4	Beam Sampling Wedge	216

5.1.5	Beam Attenuators	217
5.2	LASER OUTPUT CHARACTERISTICS: PLANE ELECTRODE GEOMETRY	218
5.2.1	Single Pass Resonator	219
5.2.2	Three Pass Resonator: With the Aperture	222
5.2.3	Three Pass Resonator: Without the Aperture	225
5.2.4	Five Pass Resonator: 10 μ s Pulse Length	226
5.2.5	Five Pass Resonator: 7 μ s Pulse Length	227
5.2.6	Summary of the Laser Output Efficiencies	228
5.2.7	Affect of the Number of Passes on the Delay Time	229
5.2.8	Affect of the Number of Passes on the Plateau Power	229
5.3	LASER OUTPUT CHARACTERISTICS: BALLASTED ELECTRODE DESIGN	229
5.3.1	Five Pass Resonator: 10 μ s Pulse Length	230
5.4	MODELLING STABLE RESONATORS	232
5.4.1	TEM ₀₀ and TEM ₀₁ Propagation, Diffraction Losses and Mode Volume Calculations for Different Resonator Designs	234
5.4.2	Single, Three and Five Pass Resonator Configurations	236
5.4.3	Eleven Pass Resonator Configuration	238
5.4.4	Concave-convex Resonator Configuration	240
5.5	RESONATOR DEVELOPMENTS	241
CHAPTER SIX	CONCLUSIONS AND FUTURE WORK	264
6.1	CONCLUSIONS	264
6.2	FUTURE WORK	269
PLATES		271
PLATE		
1	Laser System Control Units	273

2	Gas Discharge	273
3	Pitot-static tube and Mount	274
4	Ballasted Electrode	274
5	Ballasted Electrode	275
6	Trigger Wires	275
7	5 Pass Resonator, Rear Optics	276
8	5 Pass Resonator, Front Fold Optics	276
APPENDICES		
APPENDIX A		
A1	Power Supply/Laser Intialisation Process	277
A2	CX1528 Thyatron Specification	277
A3	Spot Knocking	278
A4	Roots Blowers Specification	279
A5	Instrumentation	280
A6	Data Aquisition System (DAS)	281
A7	V-I, P-I and PFN Waveforms	294
APPENDIX B		
B1	Modelling Quasi-steady Discharge Characteristics	299
B2	Townsend and Streamer Breakdown Voltages	304
B3	Preionisation Electron Densities and Critical Distances	308
APPENDIX C		
C1	Resistor Power Rating Requirements	309
C2	Transfer Efficiency for Ballasted Electrodes	309
C3	Fault Current Analysis	311
APPENDIX D		
D1	Pulse Characteristics	313
D2	Detector Specifications	314
D3	Uncoated Wedge	316
D4	Gaussian Propagation	318
D5	Ray Matrix Theory: Development of the Code	318
D6	Diffraction Losses: A Simple Estimate	323
D7	Comparison of Diffraction Losses with Numerical results	324
APPENDIX E		
E1	Workpiece Interactions	326

LIST OF FIGURES

FIGURES FROM CHAPTER ONE:

1.1	Response of aluminium to pulsed CO ₂ laser heating	8
1.2	Steady state surface temperature response	9
1.3	Time to reach steady state related to power intensity	10

FIGURES FROM CHAPTER TWO:

2.1	Basic components of the laser system	34
2.2	3-D model of the gas recirculator	34
2.3	Schematic of the DC charging supply	35
2.4	AR64 excitron tube	35
2.5	Basic components of the line type pulser	36
2.6	Line type pulser circuit details	36
2.7	Spalls 14 section 100 Ω pulse forming network	36
2.8	Lossless transmission line	37
2.9	Voltage and current characteristics of a lossless transmission line with constant load resistance	37
2.10	Simplified equivalent charging circuit of the pulser	38
2.11	Charging current and voltage waveforms	38
2.12	Network voltage and relative firing times of the thyratrons	39
2.13	High voltage connector	39
2.14	Schematic of the electrical connections and laser cavity	40
2.15	Electrode design	41
2.16	Laser cavity assembly with flow-shaping	41
2.17	Cathode pivot support	42
2.18	Trigger wire assembly	42
2.19	Trigger wire assembly showing trigger wire gap	42
2.20	Schematic of the stable z resonator	43
2.21	Output window mount	43
2.22a	Schematic of the alignment procedure	44
2.22b	Alignment of the front and rear mirror	44
2.23	Gas recirculator construction	45
2.24	Inlet diffuser	46
2.25	Inlet and outlet orifices	47
2.26	Cooling water circuit	48
2.27	Laser gas control system	48
2.28	Instrumentation points around the gas recirculator	49

2.29	Fore-optic assembly	50
2.30	Focusing lens assembly	50
2.31	Optical water cooling circuit	51
2.32	Flow sensor circuitry	52
2.33	Temperature subtracting and amplification circuit	53

FIGURES FROM CHAPTER THREE:

3.1	E/N vs gas pressure	106
3.2	E/N vs discharge current	106
3.3	E/N vs CO ₂ content	107
3.4	E/N vs He content	108
3.5	Theoretical E/N values vs CO content	109
3.6	Schematic of gas discharge circuit	111
3.7	Modified electrode profile	111
3.8	Electrode edge and trigger wires	111
3.9a	Breakdown in anode leadthroughs	112
3.9b	Modified anode leadthrough	112
3.10	Insulated EFT10 and cavity assembly	113
3.11	Discharge voltage and current: monitored at A	114
3.12	Discharge voltage and current: monitored at C	114
3.13	Trigger wire voltage and current	115
3.14	Trigger wire voltage and current	115
3.15	Trigger wire and anode voltages	116
3.16	Trigger wire voltage and current	116
3.17	Trigger wire voltage and current	117
3.18	Affect of peaking capacitor	117
3.19	LIPS gas supply system	118
3.20	Discharge and PFN voltage	118
3.21	Equivalent laser circuit	119
3.22	Discharge spatial development	119
3.23	Discharge breakdown voltage vs gas pressure	120
3.24	Breakdown voltage vs secondary ionisation coefficient	120
3.25	Initial preionisation electron density vs E/N	121
3.26	z_c vs E/N	121
3.27	Formative time lag vs E/N	122
3.28	PSPICE circuit discharge model	122
3.29	Klines discharge circuit	122
3.30	Discharge voltage and current characteristics	123
3.31	Thyratron equivalent circuit model	124

3.32	Spice model of PFN discharge circuit	124
3.33	V-I characteristics for 1:1:8 gas mixture	125
3.34	Discharge voltage	126
3.35	Discharge current	126
3.36	Discharge voltage on expanded time base	127
3.37	Discharge current on expanded time base	127
3.38	Rate of change of voltage	128
3.39	Rate of change of current	128
3.40	Discharge voltage for different network voltages	129
3.41	Discharge current for different network voltages	129
3.42	Rate of change of voltage for different V_N	130
3.43	Rate of change of current for different V_N	130
3.44	Discharge voltage: affect of peaking capacitance	131
3.45	Discharge current: affect of peaking capacitance	131
3.46	Rate of change of voltage: affect of C_p	132
3.47	Rate of change of current: affect of C_p	132
3.48	Discharge voltage: affect of inductance	133
3.49	Discharge current: affect of inductance	133
3.50	Rate of change of voltage: affect of inductance	134
3.51	Rate of change of current: affect of inductance	134
3.52	Discharge voltage: affect of n_0	135
3.53	Discharge current: affect of n_0	135
3.54	Rate of change of voltage: affect of n_0	136
3.55	Rate of change of current: affect of n_0	136
3.56	High voltage preioniser circuit	137
3.57	Rectified preioniser voltage	137
3.58	Schematic of TP and T2 trigger pulses	138
3.59	TP and T2 trigger pulses	138
3.60	TP and T2 trigger pulses	139
3.61	Calibration curve: τ_1 vs τ_2	139
3.62	Trigger wire voltage and current: 1 st pulse	140
3.63	Trigger wire voltage and current: 2 nd pulse	140
3.64	Trigger wire voltage	141
3.65	Trigger wire current	141
3.66	Laser output energy with independent preioniser	142
3.67	Modified pumping circuit	142
3.68	Laser output with discharge arcing	143
3.69	Laser output pulses	144
3.70	Discharge voltage and current: $L_a = 36 \mu\text{H}$	144
3.71	Discharge voltage and current: $L_a = 9 \mu\text{H}$	145

3.72	Laser output energy vs discharge energy	146
3.73	Laser efficiency vs discharge energy	146
3.74	Delay vs discharge energy	147
3.75	Peak power vs discharge energy	147
3.76	Plateau power vs discharge energy	147

FIGURES FROM CHAPTER FOUR:

4.1	f_1 as a function of gas pressure	183
4.2	Maximum discharge power as a function of gas pressure	183
4.3	Ratio of the discharge power with and without flow-shaping	184
4.4	Positioning of the edge flow-shaping	184
4.5	f_1 vs discharge energy with edge and longitudinal flow-shaping	185
4.6	Affect of edge flow-shaping on the maximum discharge power	185
4.7	Gas velocity experimental arrangement	186
4.8	Stuffing box	186
4.9	Stepper motor control board	187
4.10	Paths of the pitot-static tube to collect the velocity profiles	187
4.11	Gas temperature and density as a function of time	188
4.12	Velocity and temperature corrected velocity vs time	189
4.13	Velocity error due to temperature change	189
4.14	Velocity and leak rate corrected velocity as a function of time	190
4.15	Velocity error due to system leaking	190
4.16	Longitudinal velocity and position of support structures	191
4.17	Longitudinal velocity profile and the SEM	192
4.18	Longitudinal velocity profile and the SEM	193
4.19	Longitudinal velocity profile and the SEM	194
4.20	Longitudinal velocity profile and the SEM	195
4.21	Transverse velocity profile at point M	196
4.22	Transverse velocity profile at point M	196
4.23	Transverse velocity profile at point M	197
4.24	Aerofoil around support structure and theoretical flow profile	197
4.25	Longitudinal velocity profile with aerofoils positioned	198

4.26	Gas velocity as a function of the gas pressure	199
4.27	Clearing ratio as a function of discharge energy	199
4.28	Static gas discharge characteristics	200
4.29	Equivalent circuit of the ballasted cathode and pulser	200
4.30	Discharge current vs ballast resistance	201
4.31	Transfer efficiency vs ballast resistance	201
4.32	η_b vs ballast resistance	201
4.33	Prototype ballasted cathode design	202
4.34	Gas mixture thermal conductivity as a function of temperature	203
4.35	Discharge energy as a function of frequency	203
4.36	Calibration of frequency control potentiometer	204
4.37	Discharge current and voltage with partial discharge breakdown	205
4.38	Discharge current, voltage and energy with partial discharge breakdown	205
4.39	m and n vs discharge power	206
4.40	Fractional discharge breakdown vs discharge power	206
4.41	PFN voltage at 3.125 kHz	207
4.42	PFN voltage at 5.2 kHz	207
4.43	f_1 vs discharge energy - $\tau_p = 10 \mu s$	208
4.44	Discharge power vs discharge energy - $\tau_p = 10 \mu s$	208
4.45	f_1 vs discharge energy - $\tau_p = 7 \mu s$	209
4.46	Discharge power vs discharge energy - $\tau_p = 7 \mu s$	209
4.47	Best fit curves for 8Ω ballasted electrode discharge power vs discharge energy	210
4.48	f_1 vs total gas pressure	211
4.49	Discharge power vs total gas pressure	211

FIGURES FROM CHAPTER FIVE:

5.1	Cone calorimeter temporal temperature response	247
5.2	AR/AR ZnSe reflection coefficients	247
5.3	Cadmium-mercury-telluride detection system	248
5.4	Laser output pulse and discharge current	248
5.5	Active and dead space regions for single pass resonator	249
5.6	η_T vs specific discharge energy density	249
5.7	Laser output pulse	250
5.8	5 pass resonator design	250
5.9	Laser output energy as a function of discharge energy	251

5.10	Laser efficiency as a function of discharge energy	251
5.11	Delay time vs discharge energy	252
5.12	Plateau power vs discharge energy	252
5.13	Laser output pulse and discharge current	253
5.14	Laser output energy vs discharge energy	254
5.15	Laser efficiency vs discharge energy	254
5.16	Plateau power vs discharge energy	255
5.17	Delay time vs discharge energy	255
5.18	Beam radius of the TEM_{00} mode for the single pass resonator	256
5.19	Beam radius of the TEM_{00} mode for the 3 pass resonator	256
5.20	Diffraction losses of the TEM_{00} mode for 1, 3 and 5 passes	257
5.21	Diffraction losses of the TEM_{01} mode for 1, 3 and 5 passes	257
5.22	Diffraction losses as a function of R_C	258
5.23	Mode volume of the 3 pass resonator	258
5.24	3 pass resonator diffraction losses vs aperture diameter	259
5.25	Schematic of the 11 pass resonator	259
5.26	Beam radius of the TEM_{00} mode for the 11 pass resonator	260
5.27	Affect of the internal focusing optic	260
5.28	Affect of internal focusing optic at different positions	261
5.29	Beam radius of the TEM_{00} mode for 11 pass, symmetric resonator	261
5.30	Affect of the internal focusing optic	262
5.31	Affect of the internal focusing optic at different positions	262
5.32	Beam radius of TEM_{00} mode for 3 pass, concave-convex resonator	263
5.33	Beam radius of TEM_{00} mode for 3 pass, concave-convex resonator	263

FIGURES FROM CHAPTER SIX:

6.1	Uniform field electrode preionisation geometry	272
6.2	Optimum 3 pass resonator design	272

LIST OF TABLES

TABLE

2.1	PFN design characteristics	15
3.1	Experimental and theoretical values of E/N	110
3.2	Experimental values of E/N	110
3.3	Kharha's single shot stability limits	58
3.4	Single shot discharge stability limits	59
3.5	Trigger wire geometry	64
3.6	Affect of peaking capacitor on discharge characteristics	69
3.7	System characteristics for preioniser testing	93
3.8	Resonator and detector geometry	97
3.9	System parameters	98
4.1	Continuous discharge stability limits with longitudinal flow shaping	152
4.2	Summary of the gas velocities	163
Tables 5.1 - 5.7 laser output characteristics		
5.1	1:1:4 gas mixture at 156 mb, single pass resonator with aperture	220
5.2	1:1:4 gas mixture at 156 mb, "Z" resonator with aperture	223
5.3	1:1:0 gas mixture at 60 mb, "Z" resonator with aperture	225
5.4	1:1:0 gas mixture at 60 mb, "Z" resonator, no aperture	225
5.5	1:1:0 gas mixture at 60 mb, 5 pass resonator, no aperture	227
5.6	1:1:0 gas mixture at 60 mb, 5 pass resonator, no aperture, 7 μ s pumping pulse length	228
5.7	1:1:0 gas mixture at 60 mb, 5 pass resonator, no aperture, ballasted electrode	230

NOMENCLATURE

		UNITS
a_i	radius of mirror i	mm
A	electrode area	cm^2
C_a	URm74 Cable capacitance	nF
C_c	Trigger wire coupling capacitance	nF
C_d	Capacitance across anode/cathode gap	nF
C_{dc}	Main supply smoothing capacitance	nF
C_{dcp}	Preioniser smoothing capacitance	nF
C_e	Trigger wire effective capacitance	nF
C_{eff}	Effective capacitance	nF
C_N	Network capacitance	nF
C_{tw}	Trigger wire stray capacitance	nF
C_p	Peaking capacitance	nF
C_{st2}	Stray capacitance across T2	nF
CR	Clearing ratio	
C_{1p}	Preioniser capacitance	nF
d	Electrode gap	cm
d_a	Average molecular diameter	cm
d_{tw}	Trigger wire - cathode gap	mm
D	Water cooled aperture diameter	mm
D_p	Preioniser charging diode	
E	Electric field between electrodes	Vcm^{-1}
E_d	Discharge energy	J
E_{dm}	Single shot, maximum discharge energy	J
E_N	Energy stored on network	J
E_o	Laser output energy	mJ
E/N	Electric field divided by neutral particle density	Vcm^2
E/p	Electric field divided by the gas pressure	$\text{Vcm}^{-1}\text{torr}^{-1}$
E_s	Specific discharge energy density	Jcm^{-3}
f	Operating discharge, or laser, frequency	Hz
f_1	Maximum frequency where faint, filamentary arcs observed	Hz
f_m	Maximum system frequency, strong, bright arcs observed	Hz
F_m	Maximum frequency, due to ballast resistance power rating	Hz
F_s	Maximum frequency, due to charging cycle	Hz

FOC Fore-optics control Unit

I	Pre-breakdown current	A
I_d	Discharge current	A
I_{dm}	Measured discharge current through ballasted electrode	A
$I(t)$	Current as a function of time	A
I_{tw}	Trigger wire current	A
I_p	Peak discharge current	A
I_o	Photoelectric current	A
k	Relationship between pulsed and steady-state breakdown voltage	
L	Total resonator length	m
L_a	Anode inductance on T2	μH
L_g	Length of one cycle of gas recirculator	m
L_1	Anode inductance on T2 for PSPICE circuit model	μH
L_{ca}	URm74 cable inductance	μH
L_{sa}	Stray inductance on anode side	μH
L_{sc}	Stray inductance on cathode side	μH
L_{tw}	Effective trigger wire inductance	μH
L_T	Total inductance	μH
m	Number of segments passing fault current	
mb	milli-bar	mb
M_i	Mirror i	
M	Mach number	
M_r	Molecular mass, species r	kg
M_1	Mutual inductance on PFN (Adjacent neighbour)	μH
M_2	Mutual inductance on PFN (Next nearest neighbour)	μH
n	Number of segments passing normal discharge current	
n_o	Preionisation electron density	cm^{-3}
n_e	Temporal electron density	cm^{-3}
n_p	Number of passes for the resonator	
n_T	Number of segments in ballasted electrode	
N	Neutral particle density	cm^{-3}
N_{tw}	Number of trigger wires	

p	Gas pressure	mb
P_m	Gas pressure where positive mismatch regime is encountered	mb
P_d	Discharge power (generally with flow-shaping installed)	W
P_d'	Discharge power, no flow-shaping	W
$P_{e\rho}$	Experimental, mean output power density	Wcm^{-3}
P_{RT}	Power deposited in ballast resistance	W
P_N	Power available from network (E_N/τ_p)	W
PCU	Pulser control unit	
PFN	Pulse forming network	
r_f	Front mirror reflectivity	%
R_c	Radius of curvature of rear mirror	m
R_i	Radius of curvature of mirror i	m
R_p	Responsivity of photon drag monitor	$mVkW^{-1}$
R_T	Total ballast resistance	Ω
R	Resistance of one segment of ballasted electrode	Ω
SEM	Standard error of the mean ($SEM = \sigma/\sqrt{N_s}$, where N_s is the sample size of the data)	
T1	Charging thyatron	
T2	Discharge thyatron	
T3	Tailbiter thyatron	
TP	Preioniser thyatron	
T_i	Cone calorimeter inlet temperature	$^{\circ}C$
T_o	Cone calorimeter outlet temperature	$^{\circ}C$
v_g	Gas velocity	ms^{-1}
v_s	Speed of sound in gas	ms^{-1}
V_a	Discharge anode voltage (Chapter 3)	V
V_a	Active mode volume (Chapter 5)	cm^3
V_d	Discharge voltage	V
V_{dc}	DC voltage on the main supply	V
V_{ds}	Dead space volume	cm^3
V_m	Measured voltage across discharge and ballast resistance	V
V_N	Network voltage	V
V_{RT}	Voltage drop across ballast resistance	V

V_S'	Steady-state discharge breakdown voltage	V
V_S	Pulsed discharge breakdown voltage	V
$V(t)$	Voltage as a function of time	V
V_T	Total mode volume	cm ³
V_{tw}	Trigger wire voltage	V
V_O	Supply voltage	V
V_p	Voltage Pulse amplitude	V
V_{00}	Mode volume of TEM ₀₀ mode	cm ³
V_{01}	Mode volume of TEM ₀₁ mode	cm ³
w	Useful electrode width	mm
w_o	Beam waist radius	mm
$w(L)$	Beam radius at L	mm
W	Power rating of each ballast resistor	W
W_e	Electron drift velocity	cms ⁻¹
z_c	Critical distance for streamer propagation for uniform discharges	m
Z_d	Discharge impedance	Ω
Z_N	Network impedance	Ω
Z_o	Ideal transmission line impedance	Ω
α	Ionisation coefficient	cm ⁻¹
α_1	Incident angle of beam with wedge	.
γ	Generalised, secondary net ionisation coefficient	cm ⁻¹
γ_r	Ratio of molar heat capacities	
ϵ_b	Transfer efficiency, PFN to discharge and ballast resistance	
ζ	Transfer efficiency from PFN to load	
η	Attachment coefficient	cm ⁻¹
η_b	Ratio of powers in discharge to ballast resistance	
η_i	Laser output efficiency, $i = n_p$ (subscript a indicates aperture is present)	
η_T	Total laser output efficiency assuming 100 % coupling efficiency	

λ_e	Electron mean free path	cm
ξ	Ratio of 10^{10} As^{-1} to the measured dI_{tw}/dt	
ρ	Gas density	kgm^{-3}
τ	Pressure in torr	mmHg
τ_d	Delay time between discharge current and laser output	μs
τ_b	Formative time lag	μs
τ_c	Convective clearing time	μs
τ_l	Laser pulse length	μs
τ_p	Pumping pulse width	μs
τ_p'	Pre-breakdown phase width	μs
τ_{pb}	Post-breakdown phase width	μs
τ_1	Delay time between TP and T2 (thyatron trigger pulses)	μs
τ_2	Delay time between TP and T2 (Pulses from PCU)	μs
ΔP	Pressure differential, dynamic minus static pressure	Pa
ΔT	temperature difference between T_i and T_o	$^{\circ}\text{C}$
ΔV	Discharge overvoltage	V

CHAPTER ONE

INTRODUCTION

1.1 WORKPIECE INTERACTION MECHANISMS

CO₂ lasers play a significant role in processing materials for industrial applications. However, since 1964, when the first CO₂ discharge laser was realised by Patel [1.1], their design and development have been led by philosophies to maximise the laser power and miniaturise the system, little attention has been paid to the interaction process. The present work is based on a philosophy that precedes the laser design. The physical mechanisms that occur during the interaction process were studied by Bakewell et al [1.2] in an attempt to optimise the laser characteristics for the laser-workpiece interaction.

Highly reflective and/or refractory materials, for example: aluminium and nickel, which have reflectivities of 96 % and 94 % respectively at ambient temperatures, are difficult to process with CW CO₂ lasers. Bakewell analysed the response of reflective metals to incident I.R. laser pulses, the important results from this work are briefly discussed.

Figure 1.1 shows the temporal, surface temperature response and the incident and absorbed flux for a pulse of CO₂ laser radiation incident on aluminium. Figure 1.2 [1.2], shows the reduced surface temperature as a function of the absorbed power intensity for Al, Cu, Ti, Ta, Fe and Ni. Bakewell calculated the time taken for the surface temperature to reach 90 % of the steady state level as a function of the absorbed power intensity, see Figure 1.3. It is generally recognised that for incident, absorbed intensities greater than $\approx 10^{11}$ W m⁻², absorption is significantly reduced by the plasma formed above the workpiece, and consequently, it is wasteful to generate intensities beyond this value. For an absorbed incident flux of approximately 5×10^{10} W m⁻² over a 4 μ s period, the surface temperature quickly rises to 4500 K. As the incident flux reduces, the surface temperature cools at a much lower rate, and remains greater than 3000 K for approximately 100 μ s. Moreover, the absorbed power intensities at the workpiece are sufficient to encounter the non-conduction limited interaction processes. The reflectivities of materials are generally, inversely proportional to their surface temperature [1.3]. Consequently, during the relatively slow cooling phase of the workpiece and while the surface temperature is high, any incident radiation is significantly absorbed. If laser pulses are incident on the workpiece with a frequency of 10 kHz, then quasi-continuous processing occurs, with substantial improvement in the coupling of energy between the laser and the workpiece resulting.

For CW processing, decoupling of the plasma formed above the workpiece can seriously degrade the energy delivered into the material. However, in the present case, for the predicted short duration laser pulses to achieve surface temperatures of 4500 K, the plasma decays between pulses and does not represent a loss mechanism for the interaction process. More recently, a theoretical model of the interaction of pulsed infra-red radiation with metals has been developed by Byabagambi [1.4], where the non-equilibrium phonon-electron populations were considered.

To summarise: for laser pulse lengths above 4 μ s duration, a focused spot size of 0.5 mm², 50 kW plateau powers and an operating frequency of 10 kHz an enhanced interaction between the beam and workpiece is to be expected.

1.2 Laser Systems Review

The last two decades have seen rapid developments in the technology of pulsed, CO₂-TEA lasers. In general, the laser output from discharge lasers is inhibited by the fundamental limitations of the maximum discharge energy before arcing occurs. CO₂ laser discharges are only stable for periods less than the arc formation time which decreases as the gas pressure increases. Consequently, the laser output pulse lengths from many TEA lasers are usually the order of fractions of a microsecond. For example, Vizir [1.5] reports a laser pulse length of 200 ns for a small TEA CO₂ laser, the maximum pulse repetition frequency (PRF) that was observed was 1 kHz.

A prototype laser was developed by Kharha [1.6] to both investigate the design requirements for an industrial laser capable of delivering the pulse characteristics as defined by Bakewell and the affect of the gas mixture on the laser output. The power supply and pumping circuit for the prototype gas discharge were developed by Spall [1.7]. Kharha [1.6] calculated the electron energy distribution function by solving the Boltzmann transport equation, and found the fractional energy coupled into the vibrational states of N₂ and CO₂, and consequently, solved the laser rate equations to predict the laser output characteristics. Chatwin [1.8] made a detailed study of the theoretical laser output characteristics by developing a model incorporating the transient development of the intensity of the beam per unit volume. The effects of the gas mixture composition are well understood. Spall [1.7] analysed the development of an unstable, positive branch, optical resonator. A 300 W and 5 kW industrial design for a laser suitable to achieve the enhanced material interaction processes was proposed by Chatwin [1.8].

Enhanced cutting of aluminium using a pulsed CO₂ laser has been demonstrated by Hoesslin et al [1.9]. The pulses were generated by Q-switching the laser with a mechanical chopper. An oscillator-amplifier system was used with pulse energies of up to 70 mJ available over a pulse half-width of 200 ns. The average power was 1.4 kW. Peak powers and maximum repetition rates were 8 kW and 20 kHz respectively. When the laser was operated in the pulsed mode, only half the laser power was required to cut 6 mm thick aluminium as compared to the CW mode. This is a dramatic improvement in material processing and confirms the results of Bakewell et al. However, the pulse characteristics could be improved in order to optimise the interaction process. Moreover, the increased complexity of the Q-switched, oscillator-amplifier system, precludes extensive use in laser job shops.

Anisimov et al [1.10] used a high-repetition rate pulsed excimer and CO₂ laser for combined wavelength material processing in air and under water. Enhanced quality of the material processing was achieved with the pulsed CO₂ laser. The pulse width could be changed from 0.5 μ s to 10 μ s, however, the maximum frequency was only 1.3 kHz, and the maximum pulse energy was 0.6 J. It is unclear if these were attainable at the same time.

RF, CO₂ laser discharges have an inherent advantage in the stability they offer before arcing occurs [1.11]. However, the ability to generate high power pulses, suitable for the interaction processes as defined by Bakewell, are limited [1.12]. This is because pulsed, RF excited gas discharges are generally derived from a modulation (i.e. turning on and off) of the power supply rather than switching and storing energy over the inter-pulse period, and consequently, the modulated pulse power is dependent on the power rating of the voltage supply. Whereas for pulsed lasers, energy is stored and subsequently deposited into the gas discharge over a short time, which yields high pulse powers. It is interesting to note however, that a 45 kW, CW, CO₂ laser is commercially available [1.13]. Modulation of this laser would provide the pulse characteristics as defined by Bakewell et al.

Chatwin et al. [1.14] described the construction of an industrial prototype laser capable of delivering the laser pulse characteristics that were defined by Bakewell et al [1.2] as being necessary to achieve the improved material processing capabilities, with a mean power of only 1 – 5 kW. McDonald [1.14] developed the power supply for the laser. The unstable resonator, as proposed by Spall, was rejected on the grounds of the poor focusability of the beam due to its annular profile, edge diffraction effects, and moreover, the expected laser gain is lower than that required for efficient use of unstable resonators [1.4]. A stable resonator was selected because of its high stability to mechanical and optical perturbations. A

brief summary of the laser system can be found in Chapter 2.

1.3 SCOPE OF THE PRESENT WORK

The performance of the laser developed by Chatwin et al [1.13] was investigated. The scope of the present work can be defined as obtaining laser output pulses which fall within the specification of the pulses as defined by Bakewell [1.2], in order to achieve the non-conduction limited and quasi-cw material interaction processing. This can be split into two distinct regions. Firstly, ensuring that stable, uniform glow discharges can be obtained, and secondly, efficient extraction of the laser energy from the discharge volume.

The initial experiments investigating the performance of the system indicated that it fell short of the necessary specification in both of these areas. The preliminary results indicated that the maximum discharge power loading was 3 kW and the laser output power was 14 mJ. This is discussed in detail in Chapters 4 and 5. The maximum frequency achieved was about 1 kHz, which is comparable to Vizir [1.5].

The level of preionisation for the laser was found to be inadequate, consequently, a H.V. preionising system was fabricated to deliver higher peak currents into the trigger wires than that which was obtained from capacitively coupling energy from the main discharge anode pulse. The stray inductance of the trigger wire circuit is estimated to be about 2 μ H. Chapter 3 gives a full explanation of the transient development of the discharge voltage and current. Changes were made to the pumping circuit for the discharge medium in order to improve the preionisation, the discharge stability and the laser output.

The performance of two ballasted cathodes were investigated, where the total ballast resistances were 0.8 Ω and 8.0 Ω . It was found that they gave significant improvement over the plane electrode configuration, see Chapter 4.

Two roots blowers, operating in parallel, were used to pass the gas at high velocity between the electrodes. The velocity profile was examined in detail and the results are discussed in Chapter 4.

To extract the laser power a stable resonator was used. The number of passes of the resonator through the discharge volume were increased to 3 and 5. A code, using the technique of ray matrices, was used to calculate the propagation of the

TEM_{00} and TEM_{01} modes, and a simple technique is developed to estimate the diffraction losses, see Chapter 5.

The beam propagation for the TEM_{00} mode is calculated for an 11 pass symmetric and half-symmetric resonator. Given the spatial constraints of the discharge volume, and, consequently, the small diameter of the optics because of the high number of passes, it was found that the diffraction losses were significant. Hence, the fundamental mode propagation was investigated for the 11 pass symmetric and half-symmetric resonators with an internal, intra-cavity, focusing element (i.e. a concave mirror) introduced into the resonator.

Recent developments and improved performance of unstable resonators make their use an attractive solution to the problems inherent with stable resonators. Some recent developments in this field are briefly described as possible alternatives to using stable resonators.

REFERENCES CHAPTER 1

- [1.1] Patel C., "Continuous-wave laser action on vibrational-rotational transitions of CO₂". Phys. Rev. 6 (3), pp 106-110, 1964.
- [1.2] Bakewell B., Scott B. Journal of Heat and Mass Transfer. To be published.
- [1.3] "Laser processing and analysis of materials". Duley W. Plenum Press, 1983.
- [1.4] Byabagambi C. "Surface heating in metals irradiated by fast I.R. laser pulses". Ph.D. Thesis. Department of Mechanical Engineering, University of Glasgow, 1987.
- [1.5] Vizir V., Osipov V. et al. "Small CO₂ laser with a high pulse repetition frequency". Sov J. Quantum Electron. Vol. 18 (6), pp 793-795, 1988.
- [1.6] Kharha J. "Optimisation of the output characteristics of a pulsed CO₂ laser for processing materials", Ph.D. Thesis. Department of Mechanical Engineering, University of Birmingham, U.K. 1979.
- [1.7] Spall R. "Pulsed Power Supply for an Unstable Resonator" Ph.D. Thesis. Department of Mechanical Engineering, University of Birmingham, U.K. 1979.
- [1.8] Chatwin C. "Thermodynamics of a pulsed CO₂ laser for machining metals". Ph.D. Thesis. Department of Mechanical Engineering, University of Birmingham, U.K. 1979.
- [1.9] Hoesslin M., Lange I., "Cutting of aluminium with a cw and repetitively pulsed CO₂ laser system". SPIE. Vol. 1031, Seventh International Symposium on Gas Flow and Chemical Lasers, 1988.
- [1.10] Anisimov V., Arutyunyan R. et al. "Materials processing by high-repetition-rate pulsed excimer and CO₂ lasers". Applied Optics. Vol. 23 (1), pp 18-25, 1984.
- [1.11] Vitruk P., Baker H., Hall D. "The characteristics and stability of high power transverse radio frequency discharges for waveguide CO₂ slab laser excitation". J. Phys D: Appl. Phys. 25, pp 1767-1776, 1992.

[1.12] Main R. "RF-excited industrial CO₂ lasers: the users viewpoint". SPIE Vol. 1031. Seventh International Symposium on Gas Flow and Chemical Lasers, 1988.

[1.13] United Technologies Industrial Lasers, 300 Pleasant Valley Road, PO Box 981, South Windsor, CT 06074-0981.

[1.14] Chatwin C., McDonald D., Scott B. "Design of a high PRF CO₂ laser for processing high damage threshold materials". Selected papers on laser design. SPIE Milestone Series, Vol. MS 29, Editor Weichel H. pp 425-433. 1991.

[1.15] McDonald D.W. "10 kHz pulse repetition frequency laser for processing high damage threshold materials" Ph.D. Thesis. Department of Mechanical Engineering, University of Glasgow, U.K. 1989.

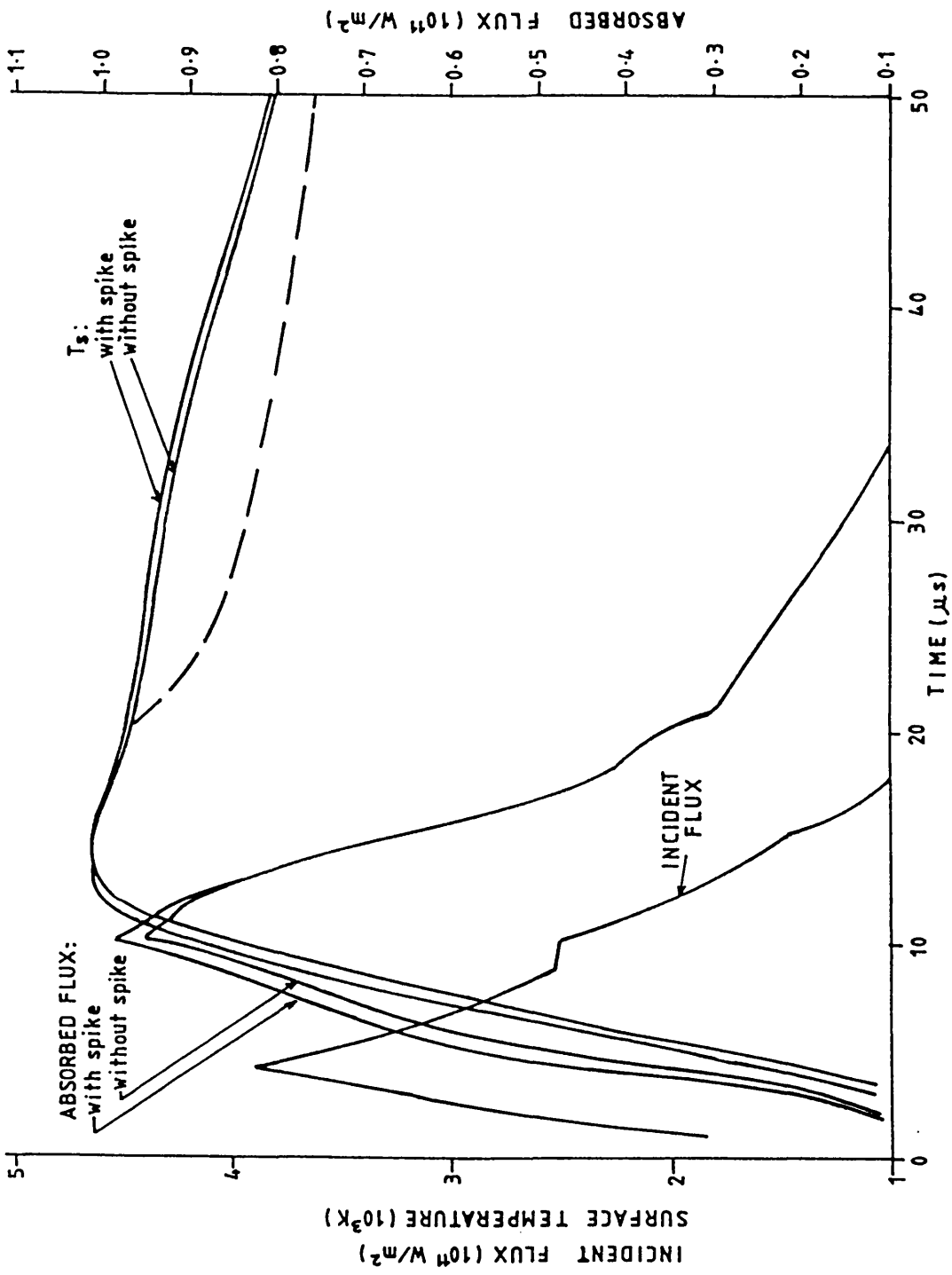


FIGURE 1.1 RESPONSE OF ALUMINIUM TO PULSED CO₂ LASER HEATING

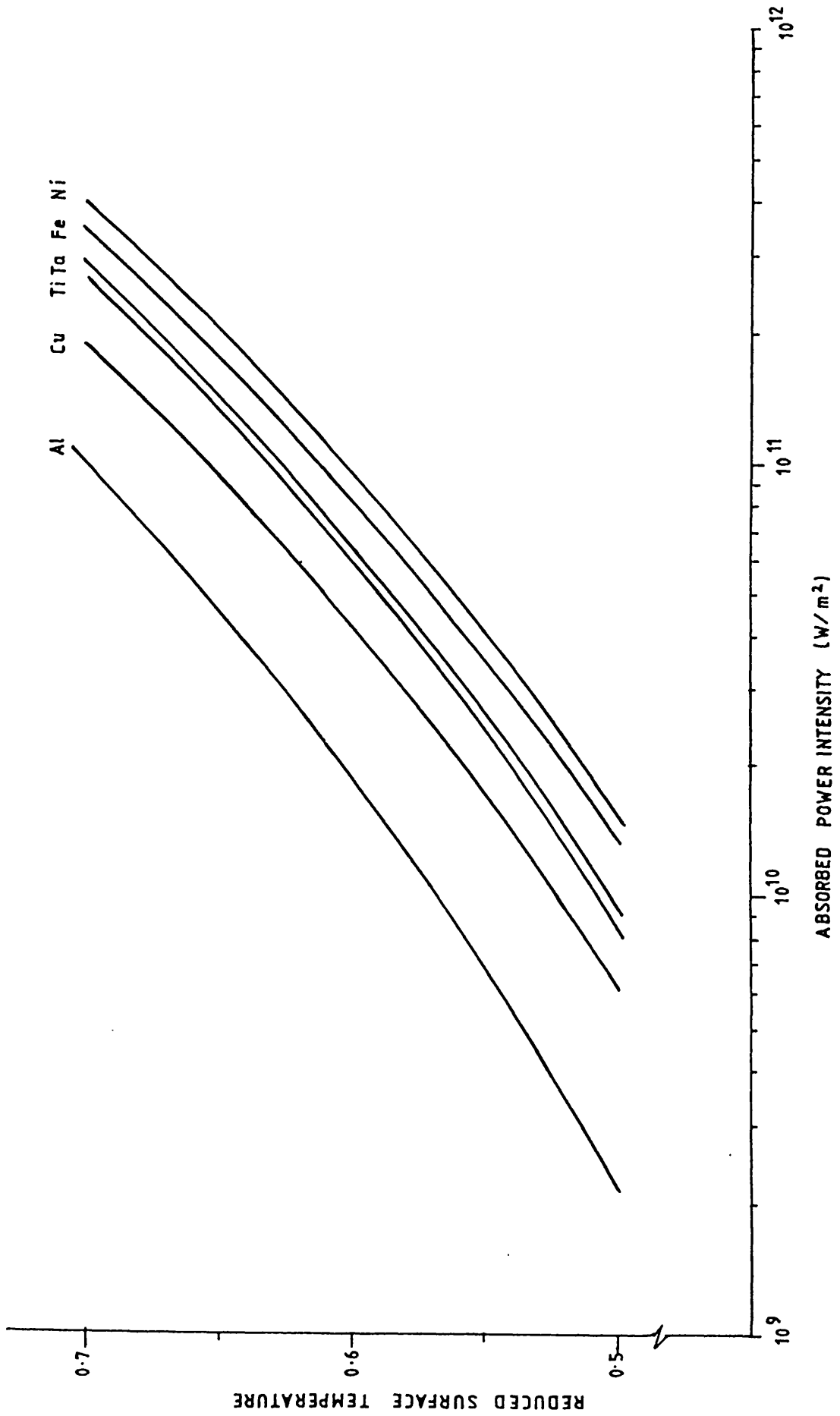


FIGURE 1.2 STEADY STATE SURFACE TEMPERATURE RESPONSE

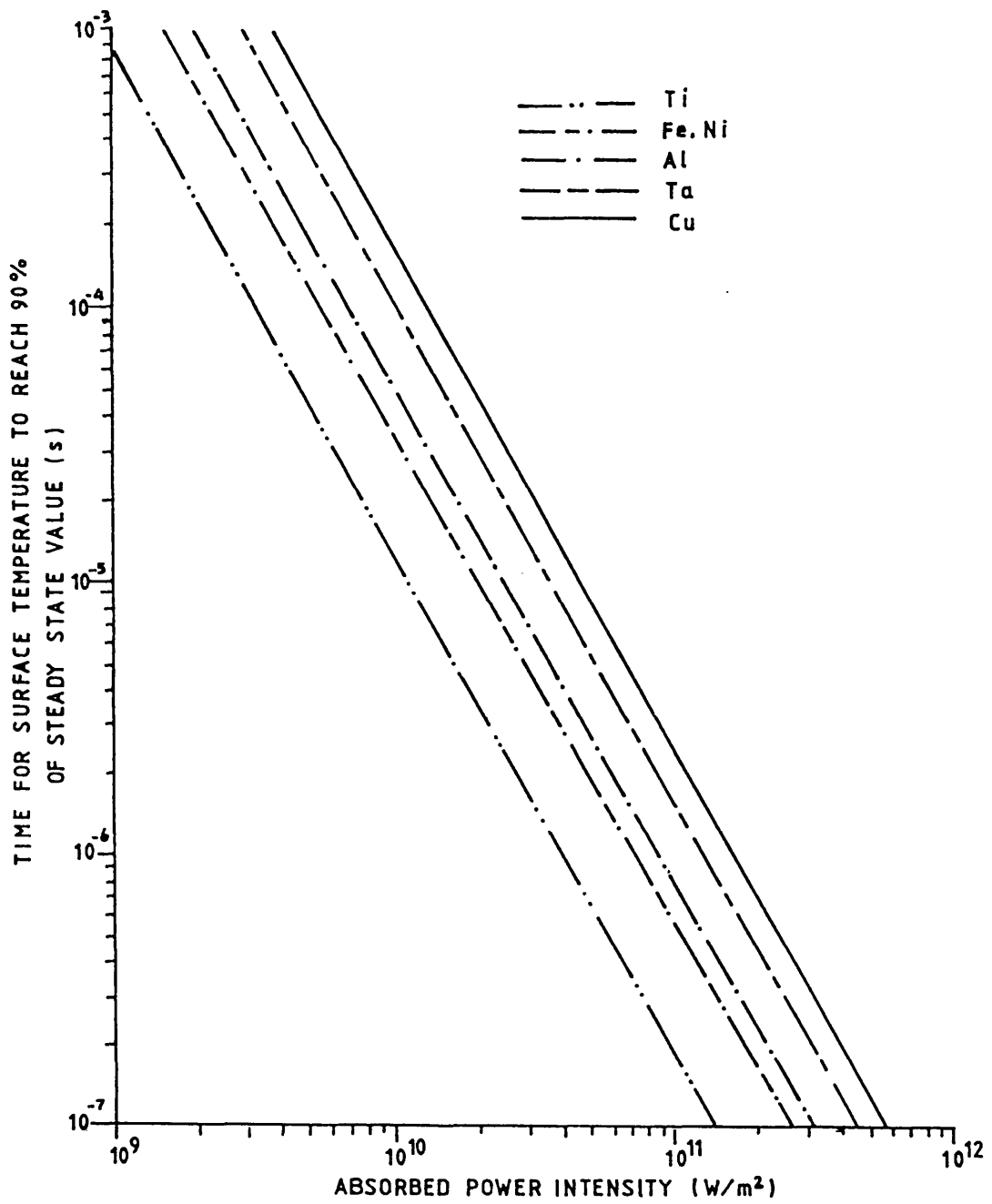


FIGURE 1.3 TIME TO REACH STEADY STATE RELATED TO POWER INTENSITY

CHAPTER TWO

LASER SYSTEM

INTRODUCTION

The prototype laser developed by Kharha [2.1] operated successfully in single shot mode and for short bursts before arcing occurred. The laser output pulse shape was consistent with the theoretically predicted requirements for enhanced material processing capabilities [2.2]. However, because of arcing no extensive material processing trials were conducted. When arcing occurs, the voltage drop across the electrodes collapses, resulting in a short circuit condition, the E/p value reduces, changing the electron energy distribution function (EEDF). This results in the pumping efficiency of the upper laser level greatly reducing, and consequently, no laser output is obtained. It is essential to avoid this regime. Glow discharges suitable for laser pumping can deteriorate into arcs via several mechanisms; for example: insufficient preionisation, a non-uniform electric field between the anode and cathode or thermal instabilities.

Transverse excited (TE), gas discharge lasers often use blower systems to pass the gas at high velocity between the electrodes, this enables higher depositions of energy into the discharge prior to the onset of arcing. Kharha was limited to a static discharge with a small gas purge, the development of thermal instabilities through gas heating and the build up of dissociation products would have been a major reason for the arcing. Also, little attention was given to the effects of preionisation; abstracting information from [2.1], it is likely that the level of preionisation was low and another factor contributing to the discharge instabilities. Following the development of the prototype laser by Kharha, a full scale, 5 kW, industrial laser system was developed by Chatwin et al [2.3] and McDonald et al [2.4]. The design of the complete laser system is briefly described.

The basic components of the laser system are shown in Figure 2.1 and seen to be: the DC charging supply; electrical circuit devices to create the pumping pulse (commonly called the pulser), the laser cavity, gas recirculator, fore-optics and workpiece handling equipment. Each component of the laser system, as defined, will be discussed. Particular attention is given to the pulser as the circuit components dictate important characteristics associated with the discharge development and quasi-steady operating levels.

Figure 2.2 shows a 3 dimensional representation of the cavity structure, gas recirculator, positioning of the flow shaping and the heat exchangers. The laser

cavity houses the anode, cathode and trigger wire assembly, the resonator and part of the flow shaping. The complete structure is fabricated from stainless steel sheet and designed by Chatwin [2.3] who performed detailed analysis of the ducting, laser cavity and compressor suitability for a 300 W and 5 kW system [2.5]. The compressor that was selected for the industrial prototype was a pair of roots blowers operating in parallel, this was a compromise between cost and performance.

The initialisation process for the laser discharge system can be seen in Appendix A1.

2.1 DC CHARGING SUPPLY

A schematic of the DC charging supply is shown in Figure 2.3. The major components are the step up transformer, mercury arc rectifiers (MAR's) and their control circuits, the smoothing capacitance and voltage monitoring device.

2.1.1 Transformer

The 3 phase, delta–star configured transformer is rated at 133.5 kVA with a 13.35 kV rated output line voltage, which can be varied by physically adjusting the tapsettings via rotary dials on the transformer. The tapsettings are coarse with only 5% increments allowed with a minimum of 50 %, this corresponds to half the full voltage rating of the transformer.

2.1.2 Rectification

Mercury arc rectifiers (MAR's) are gaseous diode devices which provide rectification of the output from the step up transformer. MAR's have a high current capacity and can readily take the full supply current in the event of a fault, their maximum power rating is 600 kW. Figure 2.4 shows a schematic of an AR64 excitron tube, which is the type that was used for the rectifier. The devices are old and are gradually becoming less reliable. It was found that after a period of operation, mercury vapour condensates on the glass envelope and there is a visual deterioration in the quality of the discharge in the tube. Performance could be enhanced by using a heat gun and blowing hot air onto the glass walls; consequently, the mercury runs into the mercury pool and replenishes the level.

McDonald [2.6] developed extensive control circuitry to both enable system initiation and trip-out in the event of a fault, for example: component failure or discharge arcing. The external circuitry ensures conduction during the correct period, this is achieved by optimising the phase between the grid AC signal and the excitron anode supply. The phase shifter and remote control unit are used for the optimisation process, see Figure 2.3. The pulser control unit, see Section 2.2.5, also houses a remote switch for the excitron grid drives. If the grid drive is off, the DC supply and the pulser are electrically isolated; consequently, modifications to the laser system can be safely undertaken. However, in practice and for complete safety, the DC voltage was generally turned off at the main switch. The current passing through the MAR's is monitored with current probes, these are connected to the MAR overload module. If the current is greater than some predefined amount the moulded case circuit breakers (MCCB) are de-energised, the system trips and the high voltage supply is disabled. The transformer and MAR's are in a safety enclosure which is situated outside of the laboratory from where the laser is housed.

2.1.3 Smoothing and Voltage Monitoring

The rectified output from the MAR is smoothed with a $0.25 \mu\text{F}$ capacitance, denoted by C_{dc} , see Figure 2.3. The DC voltage is simply monitored via a potential divider network and its value is displayed on a LED digital panel meter in the laboratory. The charging supply connects to the pulser, which in turn connects to the electrodes of the discharge, and when the laser cavity is filled with the gas mixture, then this is said to constitute the load.

2.2 PULSER

The pulser is the name given to the collection of electrical components that are used to generate the pumping pulse for the laser gas discharge, i.e. the load. Figure 2.5 shows a simplified schematic of the basic elements for a line type pulser [2.7]. It is seen that connected to the pulser is the rectified DC voltage and the load. The firing of the switch labelled S1, controls the time at which energy is fed to the energy storage and pulse shaping device – called the pulse forming network and abbreviated to PFN. Switch S2 controls the time at which the energy stored on the PFN is deposited into the load. The method of operation is as follows: with no energy stored on the PFN, switch S2 and S3 are open while S1 remains closed. This allows energy to be stored on the PFN and isolates the

charging supply from the load. Once the PFN is fully charged and storing a quantity of energy, S1 is opened and then some time later S2 is closed. Thus, the energy stored on the PFN is deposited into the load, which is still isolated from the charging supply. If both switches are closed simultaneously a fire-through condition is said to occur and the load experiences the full DC supply voltage. The fire-through condition is to be avoided. If it does occur, all the energy on the smoothing capacitance, C_{dc} , is dumped into the load, and manifests itself as an arc between the electrodes. If C_{dc} is too large the deposited energy is large and severe damage will occur on the electrodes through spark erosion and sputtering processes. If C_{dc} is too small then the voltage is not adequately smoothed. It was observed that once arcing occurs at a particular point, the probability of arcs occurring at the same position increases, eventually the electrodes have to be removed from the cavity, cleaned and reinstalled. This is a time consuming process and inhibits progress. The switch labelled S3 is used to dissipate any positive residual voltage on the PFN between pulses, and the inverse diode stack dissipates any negative residual voltage on the PFN, see Section 2.2.1. A more complete representation of the electrical circuit of the pulser can be seen in Figure 2.6. The high voltage switches are thyratrons, type CX1528 [2.8]. The switches labelled: S1, S2 and S3 in Figure 2.5 are replaced by: T1, T2 and T3. Where T1 is called the charging switch, T2 the discharge switch and T3 the tailbiter switch.

The PFN is briefly discussed as it is important in determining the characteristics of the pumping pulse, and in particular, the breakdown mechanism of the discharge – which is discussed in Chapter 3. The operation of the inverse diode stack and tailbiter are considered, and the load conditions under which they are necessary.

2.2.1 Pulse Forming Network (PFN)

As the name implies the PFN design effects the shape and in particular the duration of the pumping pulse appearing across the load. In practice, a gas discharge will have a dynamic impedance and is complex to model – see Chapter 3 – to simplify analysis a load of constant resistance will be assumed and defined as R_L . The physical phenomena behind the operation of the PFN can be understood in terms of an EM wave propagating along the PFN [2.9].

Ideal rectangular pulses can be generated by lossless transmission lines. The pulse duration is dependent on the length of the line, the stray inductance and stray capacitance. Usually the inductance and capacitance are expressed per unit length.

PFN's consisting of lumped circuit components were developed from network theory to simulate transmission lines in order to obtain approximately rectangular pulses – typically with tens of micro seconds duration – without using long lengths of cable. It can be shown that a type E network, see Figure 2.7, is approximately equivalent to a transmission line, where E stands for equivalent component values. This is the type of PFN that was used by Spall and McDonald. It can be seen that the PFN is composed of a number of LC meshes. The design is important because the PFN dominates the pumping pulse shape and in particular, the last mesh determines the discharge breakdown characteristics. The advantages of the E network over other PFN types are: ease of design and fabrication. Increasing the number of meshes, with the appropriate values of capacitance and inductance, improves the approximation to the ideal lossless transmission line, i.e. the pulse will become squarer; 14 meshes were found to be adequate. The characteristics for the PFN to deliver the required pulse shape into the discharge, as defined by Spall [2.10], are detailed below in Table 2.1.

Table 2.1 PFN Design Characteristics

Network impedance	Z_N	=	100 Ω
Pumping pulse duration	τ_p	=	5 - 10 μs
Pulse rise time	t_r	=	1 μs
PFN charge voltage	V_N	=	10-20 kV
Peak pulse power	P_{max}	=	1 MW
Maximum Pulse Repetition Frequency	PRF_{max}	=	10 kHz
Mean output power	P_{mean}	=	100 kW
Number of meshes	N	=	14

The inductor is wound on a long former, and the total inductance of the PFN is given by $L_N = \tau_p Z_N / 2$, where Z_N and τ_p are the network impedance and pulse width respectively. In designing the PFN, the mutual inductances existing between each mesh and the next nearest neighbour must be taken into account. The total capacitance of the network is given by $C_N = \tau_p / 2Z_N$. Defining the value of $\tau_p = 10 \mu s$, and with a fixed network impedance of 100 Ω , yields values for the network inductance and capacitance of 512 μH and 50 nF respectively. The individual design values for delivering the pulse characteristics as defined in Table 2.1, can be seen in Figure 2.7.

By simply tapping off from the network at the appropriate mesh the required pulse length can be obtained, i.e. the value of τ_p is dependent on the number of meshes used. It is found that the quality of the pulse shape does not vary much with a reduced number of meshes.

Figure 2.8 shows an ideal transmission line with characteristic impedance Z_0 ,

representing the PFN, charged to a voltage V_N and connected to a load resistance R_L , switches S_1 and S_2 are open. As S_2 is closed the voltage appearing across R_L is some fraction of V_N , the magnitude of this voltage is dependent on the ratio Z_0/R_L . The EM wave associated with the current flow is partly reflected and transmitted through R_L . The reflected wave travels towards the charging end of the PFN. It can be shown that the voltage drop V_1 across R_L is given by

$$V_1 = \frac{V_N R_L}{R_L + Z_0} \quad 2.1$$

The charging switch is open circuit which implies an infinite impedance; hence, when the reflected wave eventually arrives at the charging end it is totally reflected and experiences no attenuation or phase change. From the moment S_2 is closed it takes a time δ for the wave to reach the charging switch, where δ is called the one way transmission time. It should be mentioned that during this period V_1 is ideally constant. The wave reflected from the charging end is now travelling towards the load and will take a time δ before undergoing reflection and transmission for the second time at the load. On arrival at the load, the total time from when the switch S_2 was initially closed is $2\delta = \tau_p$ where τ_p is the pulse width. The voltage across the load is now given by [2.7].

$$V_2 = V_N R_L \frac{R_L - Z_0}{(R_L + Z_0)^2} \quad 2.2$$

A fraction of the incident voltage will be reflected and the same process continues. It is seen that the load voltage, and hence the current, experience sudden step changes every $p\tau_p$ seconds, where p is some integer. It is the first τ_p seconds, i.e. $p = 1$, which is important for the pulse generation. However, it is necessary to consider subsequent pulses, i.e. $p > 1$, in order to establish the effects of Z_N and R_L on the load voltage. Moreover, it becomes apparent that there is a requirement for extra circuit components, namely: the inverse diode stack and tailbiter thyatron. For the case of the PFN, the ratio Z_N/R_L determines the initial and subsequent voltage drop across R_L ; three cases are considered.

1) $Z_N = R_L$: Under this condition all of the energy stored on the network is deposited into the load in a time τ_p , no residual energy remains on the network, matched conditions are said to exist. If this equality is substituted into 2.1 it is seen that $V_1 = V_N / 2$, and moreover, it can be shown that the reflected wave $V_r = V_N - V_1 = -V_N/2$, hence after time τ_p , $V_2 = 0$. It is important to realise

that matched conditions can be obtained if the transmission line, or the PFN, are charged to twice the voltage drop across the load.

2) $Z_N < R_L$: A positive mismatch is said to occur for this condition. Under these circumstances a positive residual voltage exists on the line after time τ_p , successive reflections result in step reductions of the residual energy until it is all dissipated. Under these conditions the third switch, called the tailbiter, is closed to ensure that the residual energy is dissipated. The tailbiter can be used to control the length of the pulse by closing it at the desired time and dumping the remaining energy on the PFN to ground. This is inefficient but does provide a high degree of tunability of the pulse length, which has obvious applications to enhance the material workpiece process interaction.

3) $Z_N > R_L$: This condition is termed a negative mismatch, a negative residual exists on the line after time τ_p . Subsequent pulses are of alternating sign and decreasing magnitude. This could lead to excessively high voltages on the PFN if the residual voltage is not dissipated before the next charging cycle of the PFN. To dissipate the residual energy an inverse diode stack is used to dump the energy when the voltage pulse is negative. A series resistor, R_{ds} , limits the peak current through the diodes and the value is generally chosen to dissipate the residual voltage in a time short compared to the pulse width, i.e. the time constant $R_{ds}C_N \approx 5 \mu s$.

Figure 2.9 shows the voltage across R_L for three particular conditions; namely, matched conditions, $R_L = Z_N$; a positive mismatch, $R_L = 2Z_N$; and a negative mismatch, $R_L = Z_N/2$. The step changes every τ_p (i.e. 2δ) seconds are clearly seen.

If there is a load mismatch then the energy transfer efficiency from the PFN to the load in the first pulse is not 100 %; however, the transfer efficiency only drops by 3 % if the load varies from 70 % to 142 % of the PFN impedance [2.7] (the transfer efficiency is examined further in Appendix A7).

2.2.2 Resonant Circuits and the PFN Charging Cycle

Figure 2.6 shows that a charging inductor, denoted by L_C , is positioned before the PFN. This serves to approximately double the DC voltage on the PFN from that on the smoothing capacitor: it is a resonant circuit. Resonant circuits play a vital role in many laser systems, where high voltages are necessary to ensure suitable

discharges for laser pumping. An equivalent circuit of the pulser with the charging thyatron T1 represented by a simple switch can be seen in Figure 2.10. The smoothing capacitance $C_{dc} = 0.25 \mu\text{F}$ and is charged to the DC voltage, V_{dc} . The charging thyatron T1 is open. The charging inductor $L_c = 0.5 \text{ mH}$, the PFN inductance is smaller than L_c and is neglected. If the initial voltage on the PFN is $V_N(0)$, then it is easy to show that the transient response of the voltage across C_N , denoted by $V_N(t)$, is given by

$$V_N(t) = V_{dc} + \left[V_N(0) - V_{dc} \right] \cos \left[\frac{t}{\sqrt{L_c C_{eff}}} \right] \quad 2.3$$

Where C_{eff} is the effective capacitance of C_{dc} in series with C_N and given by

$$C_{eff} = \frac{C_{dc} C_N}{C_{dc} + C_N} \quad 2.4$$

The current flowing through the circuit is

$$I(t) = I_o \sin \left[\frac{t}{\sqrt{L_c C_{eff}}} \right] \quad 2.5$$

Where I_o is the peak current which is given by

$$I_o = \left[V_{dc} - V_N(0) \right] \left[\frac{C_{eff}}{L_c} \right]^{1/2} \quad 2.6$$

The time t_c to charge the network to the maximum voltage is given when the following condition is satisfied:

$$\cos \left[\frac{t}{\sqrt{L_c C_{eff}}} \right] = -1 \quad 2.7$$

Hence, rearranging with $t = t_c$

$$\Rightarrow t_c = \pi \sqrt{L_c C_{eff}} \quad 2.8$$

For the circuit described in Figure 2.10, when $t > t_c$ the current swings negative and $V_N(t)$ reduces; however in practice, the property of the thyatrons is such that they are unable to conduct on reversal of the current, i.e. they act like a switch in series with a diode and pass current in only one direction. Thus, V_N stays high

and the current is zero. Figure 2.11 shows $V_N(t)$ and $I(t)$ over the charging cycle. At time $t_c = \pi/L_c C_{eff}$ and if $V_N(0) = 0$, the voltage on the PFN is $2V_{dc}$ and the current is zero. If a negative residue exists on the line, i.e. $V_N(0) < 0$, then $V_N(t_c) > 2V_{dc}$; conversely, if $V_N(0) > 0$, a positive residual voltage exists on the line and $V_N(t_c) < 2V_{dc}$. Figure 2.11 shows the charging voltage and current for these three conditions.

It can be shown that the final network voltage V_N is capacitively distributed between C_{dc} and the equivalent network capacitance, C_N . Assuming that the initial network voltage $V_N(0) = 0$, then the final network voltage is

$$V_N = \frac{2 V_{dc} C_{dc}}{C_{dc} + C_N} \quad 2.9$$

From equation 2.8 it can be seen that the time to charge the PFN to nearly double the V_{dc} voltage is proportional to the square root of the product of the charging inductor and the effective capacitance. Some experimental waveforms of the PFN charging cycle that were observed are discussed in Appendix A7.

For an error of less than 10 %, it can be assumed that $C_{eff} \approx C_{dc}$. For example, with $C_{dc} = 0.25 \mu F$ and $C_N = 50 \text{ nF} \rightarrow C_{eff} = 41.7 \text{ nF}$; which results in a difference of 8.7% in the calculation of the peak current.

2.2.3 Thyratrons

Thyratrons are high voltage switches, and the model CX1528 [2.8] were the type selected by Spall [2.10] and consequently used by McDonald [2.6], and throughout the present work. Their specification can be seen in Appendix A2; the choice of thyatron was a compromise between cost, performance and availability. The hold off voltage is 35 kV which is sufficient rating for each switch. However, the mean current rating is only 5 A, depending on the load impedance and the pulse operating frequency T1 and T2 are possibly underrated.

For T1, the resonant charging time is $50 \mu s$ and if $V_{dc} = 10 \text{ kV}$, the mean current at 10 kHz is approximately 15 A, thus T1 is underrated by a factor of 3 at this frequency. The maximum system frequency to stay within the limits of the mean current for T1 is only 1 kHz. A specific example will illustrate the problem for T2. With a PFN voltage of 15 kV and assuming load conditions such that 5 kV is dropped across the load, the load pulse plateau current is calculated to be

100 A. With a duty cycle $D = 0.1$ – corresponding to a frequency of 10 kHz and pulse width $10 \mu\text{s}$ – the mean current is 32 A. For these operating conditions and the constraint of 5 A mean current, the maximum PRF is only 250 Hz. For the full voltage rating of 20 kV, the pulse plateau current is 150 A and the maximum allowed PRF is 111 Hz. Hence, it is apparent that for the maximum network voltage and a PRF of 10 kHz, T2 is underrated by a factor of 13 for the mean current.

Several times during the research period, thyatron failure was evident through their inability to hold off any reasonable voltage. The thyatrons history, and the calculations in the previous paragraph, indicate periods of overrating [2.1,2.10] which possibly accounts for these problems. A process known as spot knocking [2.11] can improve a thyatrons hold off capability, and was used successfully on several occasions, the technique is described in Appendix A3. One spare thyatron was available, however, it soon became evident that one thyatron was beyond repair. It was necessary to use the tailbiter thyatron and associated trigger circuitry (see Section 2.2.4) for a preionising circuit, detailed in Chapter 3, leaving the system without the tailbiter. Consequently, no experiments were conducted under positive mismatch conditions. For high discharge currents and PRF tests only short bursts were used – typically less than 1 minute – in order to prevent excessive anode heating.

A major factor contributing to thyatron failure is excessive cathode heating, consequently, sufficient cooling is crucial to prevent this. The thyatron must dissipate the power developed in it due to the load current and the cathode heater. From Appendix A3 it is seen that the cathode heater contributes 227 W to the total power load. McDonald [2.6] used forced convective cooling on one side of the thyatrons. This was improved by mounting the thyatrons into ABS tubing with a diameter of 18 cm and placing fans underneath, forced convective cooling was directed at the cathode. Ideally the thyatrons should be mounted in transformer oil.

2.2.4 Thyatron Trigger Units

The trigger units provide the pulses of the required shape, size and duration in order to trigger the thyatrons into conduction. The prototype trigger units developed by Spall [2.10] experienced spurious triggering of the thyatrons because of poor isolation of the trigger units from large noise transients that were generated from the fast switching action of the thyatrons and the high voltages

employed. McDonald [2.6] redesigned the trigger units and successfully managed to irradicate these spurious triggering problems. It was found that the trigger units were robust and practically trouble free.

2.2.5 Pulser Control Unit (PCU)

The correct sequence for triggering the thyratrons is crucial to ensure safe and reliable operation of the pulser, this task is achieved by the PCU, see Plate 1. Three fibre optic cables link the PCU to the thyatron trigger units associated with T1, T2 and T3. The fibre optic cable provides immunity from noise – Spall used 24 V signals down conventional copper cable. Figure 2.12 shows a schematic of the network voltage and the relative firing time between the thyratrons triggering for 10 kHz operation, 10 μ s pulse lengths and a negative mismatch ($Z_N > R_L$). A PFN charging cycle of 50 μ s allows up to 20 μ s for the recovery periods of T1 and T2. If the tailbiter, T3, is used the time differential between T2 and T3 firing must be equal to the pulse length.

The grid drive for the MAR can be controlled remotely from this unit.

2.3 LASER CAVITY

The laser cavity houses the electrodes and the trigger wires, the resonator and flow shaping. The position of the laser cavity can be seen in Figure 2.2. The pulser is housed in a safety enclosure, approximately 5 m from the laser cavity.

2.3.1 Anode and Cathode

Trunking runs under the floor from the cage enclosing the pulser, to below the centre of the laser cavity. A 5 m length of URm74 cable runs through the trunking and connects the cathode of the discharge thyatron to a high voltage connector which is mounted to an insulated box positioned under the laser cavity which, in turn, houses the coupling capacitors. Figure 2.13 shows a schematic of the high voltage connector. An anode bus bar, fabricated from copper, attaches the high voltage connector to 4, high voltage vacuum lead throughs – a modified type EFT10 [2.12] – which in turn connects to the discharge anode. A schematic of the electrical connections can be seen in Figure 2.14. The EFT10's with

extended lead throughs were connected in parallel via the anode busbar and directly attached to the anode by copper connecting rods.

Figure 2.15 shows a schematic of the side view of the electrodes. The anode and cathode are fabricated from brass, with a flat top and a 1/4" edge, radius of curvature on the corners. Water cooling channels pass through the electrodes and are used to prevent them from becoming hot. The anode and cathode are identical in order to keep the electric field uniform and prevent arcing. The total length of the electrodes was 1165 mm and they were 74 mm wide, the flat region was 1000 mm by 60 mm wide. Figure 2.16 shows how the electrodes were mounted into the laser cavity. The anode was held in position horizontally by 6 moulded epoxy castings, which also provided the electrical isolation between the anode and the cavity walls. The height of the anode can be adjusted by a series of anode support bolts positioned along its length. The bolt heads rest on the epoxy castings and locking nuts were used to secure the bolts. The cathode is mounted approximately 40 mm above the anode. Three supports are used for the cathode, two micrometer adjusters positioned near the rear of the cavity and one pivot support, which can be seen in Figure 2.17, placed towards the front of the cavity. The three cathode supports pass through the top of the laser cavity where the micrometer adjusters can be used to accurately align the electrodes.

Kharha [2.1] found that a tolerance on the parallelism of the electrodes of under 0.5% was necessary to prevent the discharge developing into arcs. The alignment procedure adopted herein is briefly explained. The pivot support and the cathode micrometer adjusters are initially positioned so that the electrodes are approximately parallel. The anode-cathode gap is then determined using inside calipers within the cavity, and then vernier calipers to accurately measure the gap distance from the inside calipers outwith the laser cavity. Unfortunately, the vernier calipers could not fit inside the cavity. Readings were taken near the four corners of the electrodes on the flat face, any discrepancy and the micrometer adjusters would be turned accordingly. With patience, errors of less than 0.5 % could be obtained, corresponding to a distance of ± 0.2 mm for a gap size of 40 mm.

The removal of the anode and cathode from the laser cavity takes approximately 6 man hours. The anode and cathode can be removed independently of each other.

2.3.2 Trigger Wires

In order to obtain a uniform glow discharge, the double discharge technique [2.13] was employed to preionise the electrode volume. Energy is capacitively coupled from the main anode voltage pulse and deposited into the auxiliary discharge. This provides the preionisation of the main gap and subsequent discharge breakdown – this is discussed fully in Chapter 3. The auxiliary discharge is created by a series of trigger wires, placed parallel and close to the cathode. Kharha [2.1] positioned the trigger wires longitudinally and in the present system they are mounted transversely, this is because of the mechanical difficulties of securely mounting longitudinal trigger wires within the gas flow.

The trigger wires consist of 4.0 mm diameter brass rods which pass longitudinally either side of the cathode. Attached to these rods at an 8mm pitch are 2.0 mm brass rods, which are clad with pyrex glass tubing which has inside and outside diameters of 2.0 mm and 3.5 mm respectively. The glass clad, brass rods run transversely across the electrodes, a total of 156 were used. The trigger wires are supported by 5 PTFE pillars and clamps which attach to the 4.0 mm diameter brass rod and down both sides of the cathode support plate, see Figures 2.18 and 2.19. The height of the trigger wires relative to the cathode can be adjusted using brass shims. The optimum trigger wire gap used by Kharha [2.1] was 2.0 mm. Consequently, the shims thicknesses were selected to provide a range of possible values incorporating the option of 2.0 mm.

2.3.3 Cavity Flow Shaping

Sufficient space existed between the epoxy castings and the side walls of the laser cavity to pass through flow-shaping mounted on aluminium sheet while the electrodes were in position. The ability to install the flow-shaping independently of the electrodes has obvious advantages in that the affect of different flow-shaping geometries on the discharge stability can be assessed relatively easily.

The flow shaping was made from 2 mm thick acetal sheet, with a rigid 5mm thick structural framework as support. It was designed to provide insight into the effects of the flow-shaping and discharge performance prior to undertaking manufacture of expensive epoxy castings of the finally selected flow-shaping configuration. Figure 2.16 shows an end view of the laser cavity with the flow-shaping in position.

2.3.4 Resonator

A major difficulty with transverse discharge lasers is efficient coupling of the laser energy out from the discharge volume. Spall [2.10] assessed the theoretical performance of a positive, confocal unstable resonator. Although efficient extraction of the laser power can be obtained, the mode shape is not conducive for high quality material processing. However, recent developments of novel unstable resonators have improved their output beam profiles, this is discussed in Chapter 5. The initial resonator configuration that was tested was a stable, half-symmetric resonator with 3 passes through the discharge volume, i.e. the so called Z resonator, a schematic of this resonator can be seen in Figure 2.20. The radius of curvature of the rear mirror was 20 m, 2 plane folding mirrors provided the Z configuration, and a water cooled aperture could be used to limit the laser oscillation to the fundamental Gaussian mode, i.e. TEM_{00} . The output window is a flat AR/R coated ZnSe optic; various reflectivities were available, namely: 75%, 85% and 90%. All of the reflecting mirrors were water cooled, gold coated, copper-substrate optics. The rear mirror was housed in a commercially available gimbal mirror mount [2.14], and was adjustable from outside of the laser cavity via two vacuum lead through, micrometer adjustment assemblies. The alignment of the rear mirror could be optimised with the laser running. The rear end plate is fabricated from perspex with holes positioned accordingly to accommodate the vacuum lead throughs. The flat folding mirrors are mounted in aluminium mirror housings. The folding and rear mirror mounts are rigidly supported by aluminium blocks – called the mirror mount tables – which were positioned at the front and rear of the laser cavity and securely bolted down in order to minimise the effect of vibration from the roots blowers. The combined height of the mirror mount table and the mirror mounts is such that the centre of the optics, i.e. the optical axis, corresponds to the central position between the anode surface and the bottom of the trigger wires. Any difference between the two can be corrected by shimming underneath the mirror mounts.

The output window mounting is connected via flexible bellows to the stainless steel front flange, which fits over the laser cavity. The mounting is supported by 3" square hollow section welded to the front flange, see Figure 2.21. The output window is cooled by water and forced convection of filtered, compressed air on the ambient pressure side of the optic. Specifically designed channels guide the air over the window to minimise the temperature gradients introduced by the beam [2.3]. Two micrometers allow the front window to be accurately positioned.

2.3.5 Resonator Alignment

A HeNe laser is used to assist in the alignment of the resonator, it is mounted at the same position as where the workpiece focusing lens assembly joins to the fore-optics box, see Section 2.5.1. Figure 2.22a shows a schematic of the Z resonator and the alignment procedure. An aperture is used on the fore-optics box to limit the spatial extent of the beam and provide a screen to observe the return beam reflected from the front window or the rear mirror. A perspex cover is placed over half of the front of the laser cavity with a hole bored in the position where the CO₂ laser beam should come from. An aluminium disk with a small aperture drilled through its centre is positioned into the bored hole. The beam from the HeNe laser is lined up with this aperture, and the first fold mirror is approximately positioned at the rear of the cavity. The first fold mirror is then adjusted so that the incident laser beam strikes its centre and the reflected spot strikes the centre of the second fold mirror, which is positioned at the front of the laser cavity. The position of the second fold mirror was then adjusted so that the reflected spot was incident on the centre of the rear mirror. The position of the fold mirrors were optimised so that the laser beam passed evenly between the discharge region. It was found that the fixed, fold mirrors were particularly difficult to align because of the need to use shim. The effect of this is that when the mounts were bolted down, the beam shifted quite substantially. To align the fold mirrors an iterative approach proved most successful, where the mirrors were repeatedly and alternately tweaked.

Once the fold mirrors are positioned the end plates, the rear micrometer vacuum lead throughs and the front window are assembled. The rear mirror and front window were simple to align, see Figure 2.22b. The front window is displaced off axis so that the reflected spot is not incident on the aperture, i.e. the screen. The return beam from the rear mirror is made to return along the incoming path to the aperture on the fore-optics box so that the larger return beam – due to the laser beams divergence – is central on the aperture. The return beam from the front window is moved so that it overlaps the aperture. The resonator is aligned and the chamber is ready to evacuate.

2.4 GAS RECIRCULATOR

Figure 2.2 shows a schematic of the gas recirculator. It is seen that it consists of 2 roots blowers, ducting and flow shaping. The initial designs were by Chatwin [2.5]. A more detailed drawing of the gas recirculator construction can be seen in

Figure 2.23.

2.4.1 Roots Blowers and Ducting

The technical specification of the roots blowers (type Starvac 7500) can be seen in Appendix A4. A maximum volumetric flow rate of approximately 15 000 m³/hr is possible from the two roots blowers. A pulley system couples an 18 kW motor to the shaft of the roots blower. In this way, the gearing ratio can be adjusted by changing the pulley diameters. This provides a range of possible volumetric flow rates through the system.

A condition for satisfactory development of stable, uniform glow discharges is that a uniform velocity profile exists between the electrodes. For this reason, flow shaping is positioned on the inlet and outlet side of the laser cavity and adjacent to the electrodes, see Section 2.3.3. The inlet diffuser is shown in Figure 2.24, the outlet diffuser has a similar design. Diffuser flow splitters are used, and a nozzle to give uniform flow. Chatwin [2.5] showed that the pressure drop around the circuit was low and as a consequence, the effect on the gas flow is minimal.

The inlet to the laser cavity is partially blocked by 4 struts which act as a structural support to the laser cavity and prevent deflection of the laser cavity when the system is under vacuum conditions. The outlet side has 5 supporting struts. The inlet and outlet orifices can be seen in Figure 2.25. The affect of the inlet struts on the gas velocity flow profile is discussed in Chapter 4.

As the area of the inlet orifice to the cavity is approximately 400 cm², the minimum and maximum gas velocities that could be obtained with the pullies that were available were approximately 33 ms⁻¹ and 103 ms⁻¹ respectively.

2.4.2 Heat Exchangers

The maximum, mean power that is deposited into the gas is approximately 100 kW, the blowers generate an additional maximum heat load of 36 kW. If the laser produces 5 kW mean power, the 4 heat exchangers positioned around the gas recirculator must dissipate a maximum of 131 kW excess power. McDonald [2.6] evaluated the heat exchanger design specification, calculated the coil performance and the number of coils required. It was found that the cooling system provides excellent performance across a range of discharge power levels and gas mixtures

typical of CO₂ lasers. Figure 2.2 shows the positions of the 4 heat exchangers around the system and Figure 2.26 shows a schematic of the water cooling system. The mains water supply was inadequate to supply the required flow rate for cooling the system, consequently, a cooling water tank, with a volume of 6.75 m³, and a Wier centrifugal pump – type SNC2 – were used. The tank and pump are situated remote from the laser laboratory.

2.4.3 Gas Control System

Figure 2.27 shows a schematic of the gas system. There are three vacuum isolating valves which are controlled by solenoids and labelled S1, S2 and S3 in the figure, they control the gas flow and the evacuation process. When S1 and S2 are closed and S3 is open, the laser cavity is exposed to atmospheric pressure. With the valves in this state the cavity is either allowed up to atmosphere, or if the vacuum pump (type Leybold S60) is on the chamber will be evacuated, which takes approximately 20 minutes from ambient pressure conditions. The chamber is then tested for vacuum leaks in order to assess the likely atmospheric contamination during an experiment. A leak rate of greater than 1 mbar/hr was considered unacceptable. After a satisfactory vacuum is achieved, the laser gas mixture can be added to the system. CO₂, N₂ and He gas bottles are connected to solenoid control valves, labelled V₁, V₂ and V₃ respectively in Figure 2.27; initially all three valves are closed. The gas bottles and regulators are opened to a pressure of about 1 Bar, then V₁ is opened and the required partial pressure of CO₂ is administered to the laser cavity. A pressure monitor – type Edwards EMV 251 – is connected to the cavity to indicate when the system has reached the required partial pressure, V₁ is then closed and V₂ opened; N₂ is then added to the cavity, V₂ is closed and V₃ opened, allowing the addition of He. The laser cavity is now ready for excitation from the pulser. A system is available to allow a gas refresh. Gas is mixed in the appropriate proportions in the mixing chamber, and valves S₁ and S₂ are opened allowing the gas mixture into the laser cavity. This is particularly useful for long term running of the laser where the dissociation of the gas species has a deleterious effect on the laser performance, this is evident from long term running of sealed off laser systems [2.15].

2.4.4 Gas Recirculator Control Unit

The gas recirculator control unit houses all the electronics and switches to control the vacuum pump, water pumps for the heat exchangers and the fore-optics

system, and the valves for administering the gas to the system. Plate 1 shows the gas recirculator control unit.

2.4.5 Gas Recirculator Instrumentation

Figure 2.28 shows a schematic of the gas recirculator and how a series of sensors are positioned around the recirculator in order to facilitate assessment of the gas recirculator performance. Temperature probes are positioned both on the gas flow and the water cooling circuit. It is seen that the gas temperature is measured on the inlet and outlet side of the laser cavity and the roots blowers, and at various points around the recirculator. The water flow rate and outlet temperatures from the four heat exchangers are monitored.

The sensors are connected to an instrumentation display box, which houses the instrumentation circuitry and panel meters. Only one water flow rate, and one gas and water cooling temperature can be viewed simultaneously. A rotary switch is used to toggle between the different readings from the sensors in order to view the value of the measurand on the panel meter. Appendix A6 details the integration of an IBM PS/2 data acquisition system with the gas recirculator instrumentation and the laser gas control system, the acquisition unit can be seen in Plate 1.

2.5 FORE-OPTICS AND WORKPIECE HANDLING

The fore-optics and workpiece handling equipment is situated in a safety, polycarbonate enclosure. An aluminium tube covers the laser output window and is attached to the safety enclosure by a flange assembly. The tube prevents accidental exposure to the beam.

2.5.1 Fore-Optics

The fore-optics assembly is placed on a sturdy table with ample space for development of detector systems and beam analysis equipment; for example: photon drag monitor (PDM), cadmium-mercury-telluride (CMT) detector, beam profilers or spectrometers. Figure 2.29 shows the fore-optics assembly. The photon drag monitor is held in position by a mount that has micrometer adjustments in the transverse directions, this allows precise alignment of the monitor with the

incident laser beam. The flexibility of the detector systems provides the opportunity to remove the PDM and use a CMT detector positioned on the fore-optics table.

The beam dump mirror is used to deflect the laser beam into a water cooled cone calorimeter, which provides an absolute measurement of the laser power. It is seen from Figure 2.29 that the beam dump mirror is located above the cone calorimeter and it is placed at an angle of 45° to plane of the laser beam. The beam dump mirror can be up or down. If it is down, the beam is reflected into the cone calorimeter and if it is up, the beam travels towards the workpiece.

The cone calorimeter consists of a black, anodised aluminium cone mounted in a thick perspex cylinder which minimises the heat losses. Water flows at a specific rate over the outside of the cone and passes through specially designed flutes which maximise the heat transfer from the cone to the water. The water flow rate, and the inlet and outlet water temperatures are monitored; thus, an estimate of the laser output power can be obtained. The beam dump mirror also provides a method of safely dumping the optical energy whilst optimising the system components within the safety enclosure.

With the beam dump mirror up, the beam passes through the fore-optics box and it reflects off a mirror which is placed at an angle of 45° to the horizontal. The beam is reflected down towards the focusing lens assembly where it is focused onto the workpiece, which is securely mounted on the workpiece translation stage. The mirror has a micrometer adjustment facility to ensure that the beam passes through the nozzle of the focusing lens assembly.

Between the two 45° mirrors, space is provided for positioning a beam sampling wedge mounted on a rotary table mount. The wedge reflects a small fraction of the beam, typically about 1 %, and diverts this energy towards the CMT detector. The three detection systems briefly described, namely: the cone calorimeter, photon drag monitor and the CMT detector are detailed more explicitly in Chapter 5.

The focusing lens assembly is shown in Figure 2.30. The lens is mounted so that the periphery of the lens is in contact with a water cooled, copper heat sink. An air jet provides a positive pressure to avoid ingress of dust, dirt or vapour from the material being processed. Assist gases can be administered coaxial to aid the processing. Variable nozzle sizes are available to optimise the coupling between the assist gases and the workpiece. The focusing lens assembly is attached to a lead screw and servo motor. Rotation of the servo motor moves the lens vertically, and enables precise focusing of the beam onto the workpiece.

When the resonator is aligned, it is important to ensure that the optical axis of the fore-optics assembly coincides with the optical axis associated with the resonator. The latter is determined primarily through the resonator design and how the beam couples with the discharge volume. To ensure coincidence between the two optical axes, the height of the fore-optics table top was adjustable. A spirit level was used to ensure that the table top was horizontal.

2.5.2 Workpiece Handling

The workpiece handling stage is positioned underneath the focusing lens. However, it only has 1 degree of freedom, but this is sufficient for initial tests in assessing the laser performance over a wide range of operating regimes. For example, the effects of frequency or pulse length on the cutting or drilling performance. The velocity can be varied from 38 mm/min to 633 mm/min, and is controlled from the fore-optics control unit described below in Section 2.5.4.

2.5.3 Water and Air Optical Cooling Circuit

As the mean laser output power is high, the optics must be cooled to prevent thermal distortion and degradation of the laser output beam. Consequently, every optic within the system is water cooled, and in addition, forced convective cooling is used on the front window. The air then passes down the aluminium tube which couples the output window to the polycarbonate enclosure, this prevents an excessive temperature rise and perturbations in the refractive index of the air within the tube. A schematic of the complete cooling system, with the Z resonator installed in the laser cavity, is shown in Figure 2.31. A small water cooling tank ($\approx 1 \text{ m}^3$) was used with a Lafert, type RG100 pump. The separate cooling supply from the gas recirculator heat exchanger cooling system provided greater flexibility. For example, the water flow rate around the optical cooling circuit can be adjusted without influencing the performance of the heat exchangers cooling circuit.

2.5.4 Fore-optics Control Unit (FOC)

The electronic circuitry and controls for the fore-optics control box were situated outside of the enclosure in a position where it was possible to view the laser-workpiece interaction. The beam dump mirror, focusing lens and the

workpiece translation table are controlled from this unit, which can be seen in Plate 1. However, it was found that it was necessary to optimise the position of the focusing lens while actually in the enclosure. Hence, a remote unit which mirrored some of the actions of the FOC was positioned in the enclosure. The remote unit allowed positioning of the beam dump mirror, the focusing lens, moving the workpiece and changing its direction of motion.

2.5.5 Flow Meters

Flow meters are used to ensure that the cooling water is flowing satisfactorily. The positioning of the flow meters, denoted by F_i , are shown in Figure 2.31, where $i = 1$ to 4. If the water cooling supply fails due to, for example, pump failure or the system leaking, the flow monitors register this drop in the flow rate and disable the laser by tripping the grid drive. This prevents excessive heating of the optical components and permanent damage occurring because of the "thermal runaway" effect. A series of LED's positioned on the FCU give a visual indication that the flow is satisfactory. Figure 2.32 shows the flow sensor circuitry.

2.5.6 Cone Calorimeter and Mean Power Indicator

The position of the cone calorimeter in the water cooling circuit can be seen in Figure 2.31. The inlet and outlet temperatures of the water flowing over the cone are monitored by two 4-wire, platinum resistance, temperature probes - type RS Pt-100. The two voltage signals from the probes, which are proportional to the temperature, are fed into the FOC where the signals are subtracted, amplified and passed to a galvanometer meter. The deflection on the meter is proportional to the laser output power, Figure 2.33 shows the electronic circuit.

CHAPTER TWO REFERENCES

- [2.1] Kharha J. "Optimisation of the output characteristics of a pulsed CO₂ laser for processing materials". Ph.D. Thesis. Department of Mechanical Engineering, University of Birmingham, U.K. 1979.
- [2.2] Bakewell B., Scott B. Journal of Heat and Mass Transfer. To be Published
- [2.3] Chatwin C., McDonald D., Scott B. "Design of a high PRF CO₂ laser for processing high damage threshold materials". Selected papers on laser design. SPIE Milestone Series, Volume MS 29, Editor Weichel H. pp 425-433, 1991.
- [2.4] McDonald D., Chatwin C., Scott B. "100 kW, 10 kHz, line type pulser for gas laser pumping". SPIE, Pulsed Power for Lasers II, pp 106 - 112, Volume 1046-14, 1989.
- [2.5] Chatwin C. "Thermodynamics of pulsed CO₂ laser for machining metals". Ph.D. Thesis. Department of Mechanical Engineering, University of Birmingham, U.K. 1982.
- [2.6] McDonald D.W. "10 kHz pulse repetition frequency laser for processing high damage threshold materials". Ph.D. Thesis. Department of Mechanical Engineering, University of Glasgow, U.K. 1989.
- [2.7] "Pulse generators". Glasoe G., Lebacqz J. Radiation Laboratory Series, McGraw Hill, 1948.
- [2.8] "Hydrogen thyratron product data". EEV, Chelmsford, Essex, U.K.
- [2.9] "Transmission lines with pulse excitation". Metzger G., Vabre J. Electrical Science series. Academic Press, 1969.
- [2.10] Spall R. "Pulsed power supply for an unstable resonator". Ph.D. Thesis. Department of Mechanical Engineering, University of Birmingham, 1979.
- [2.11] Barry Newton. Personal communication. EEV, Chelmsford, Essex, UK.
- [2.12] Vacuum Generators, Hastings, Surrey, U.K.

[2.13] Foster H. "High power CO₂ lasers - a review". Optics and Laser Technology, pp 121-127, June 1972.

[2.14] Gimbal mount, Model GM50. Photon Control Ltd, Cambridge CP4 2PF, U.K.

[2.15] Willis C. "Catalytic control of the gas chemistry of sealed TEA CO₂ laser systems". Journal App. Phys. 50 (4), pp 2539-2543, 1979.

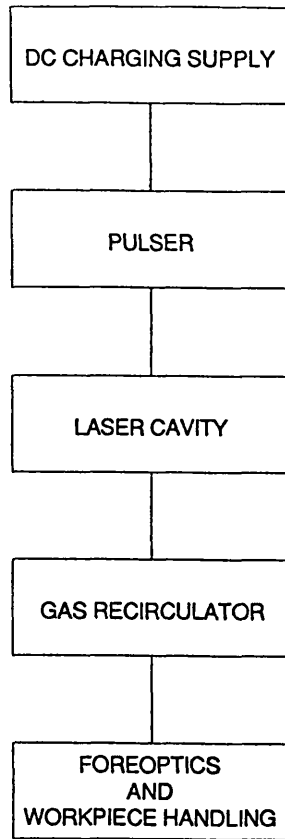


FIGURE 2.1 BASIC COMPONENTS OF THE LASER SYSTEM

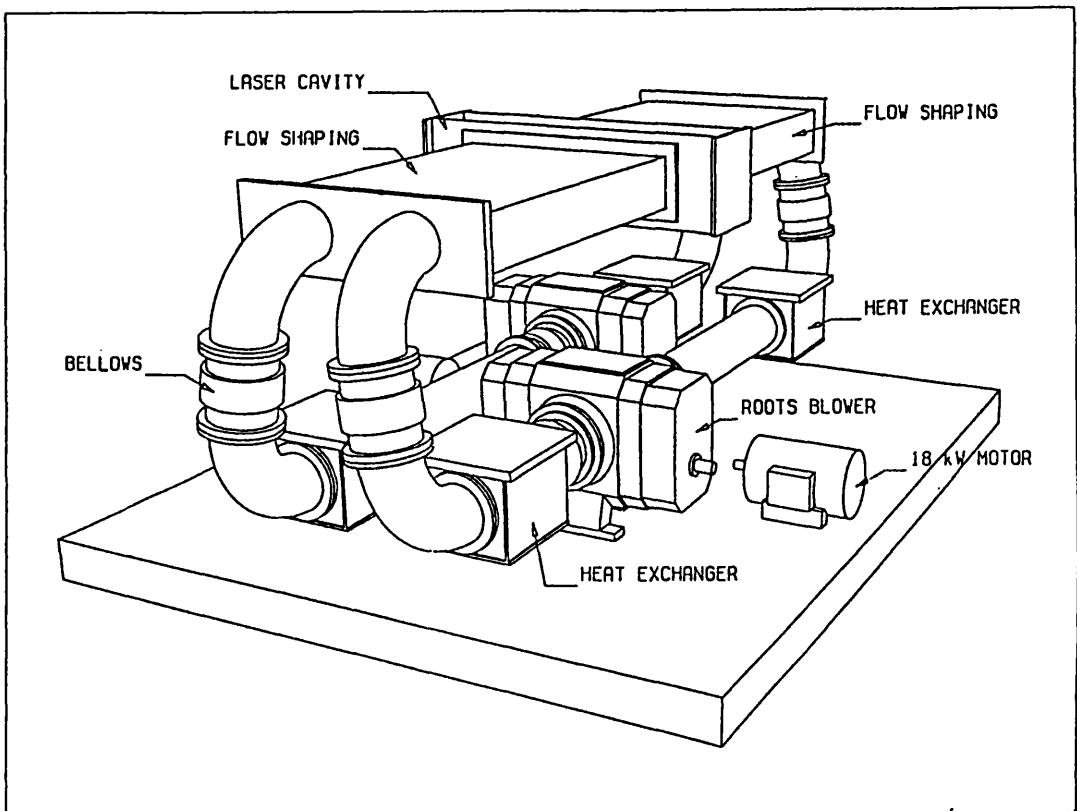


FIGURE 2.2 3-D MODEL OF THE GAS RECIRCULATOR

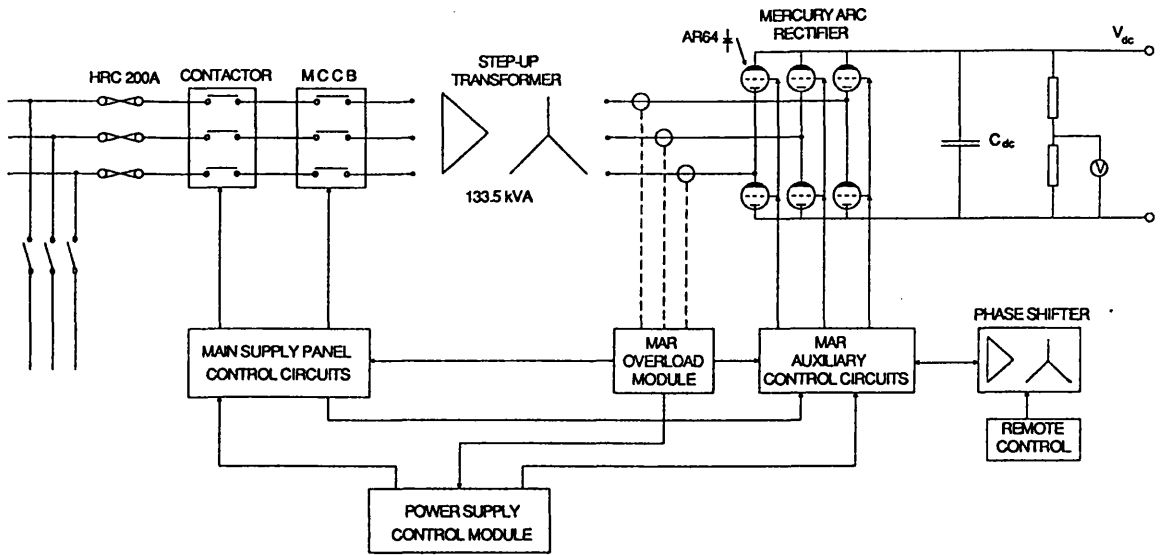


FIGURE 2.3 SCHEMATIC OF THE DC CHARGING SUPPLY

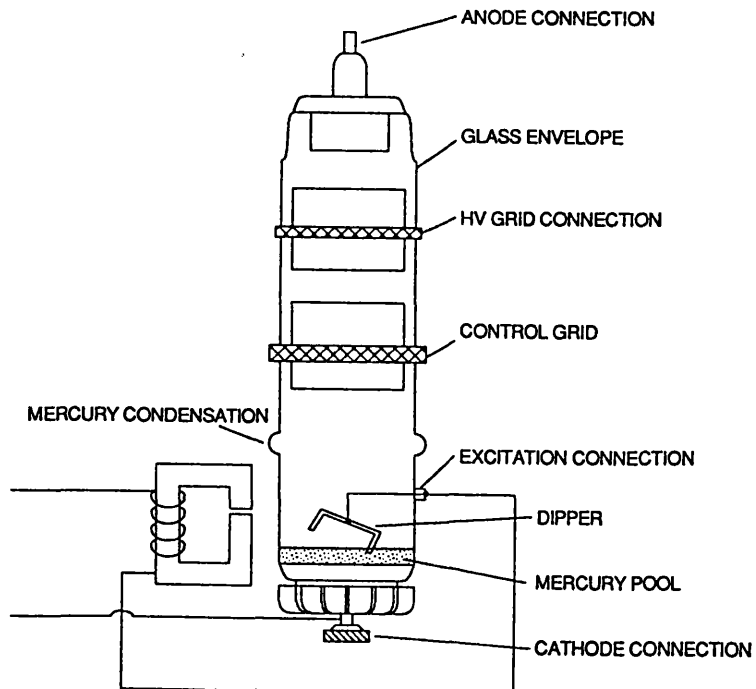


FIGURE 2.4 AR64 EXCITRON TUBE

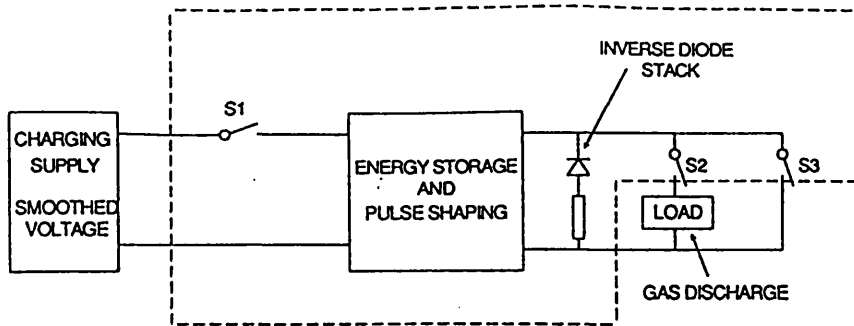


FIGURE 2.5 BASIC COMPONENTS OF THE LINE TYPE PULSER

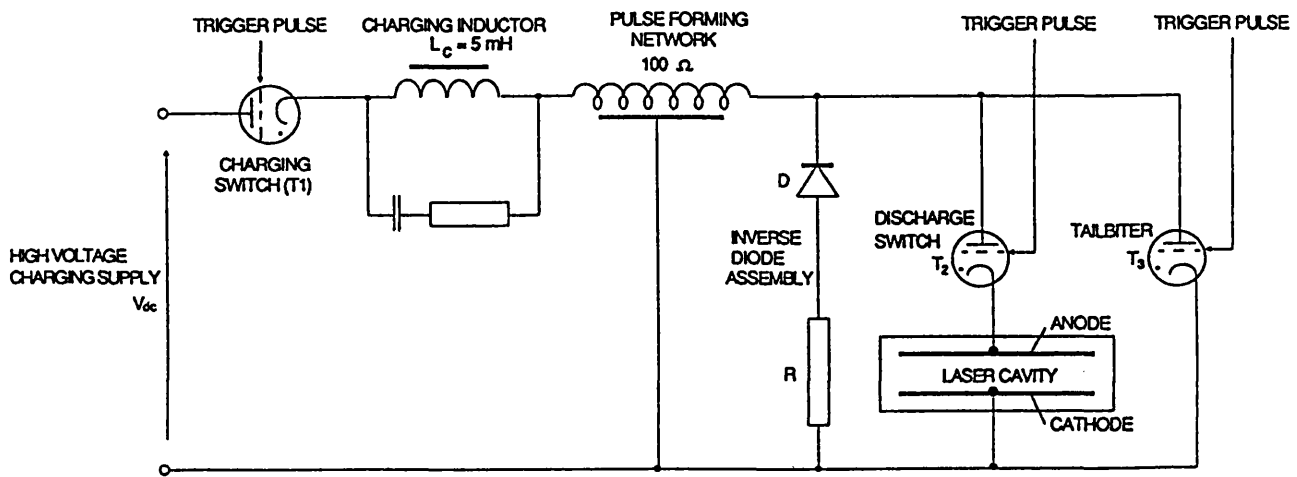


FIGURE 2.6 LINE TYPE PULSER CIRCUIT DETAILS

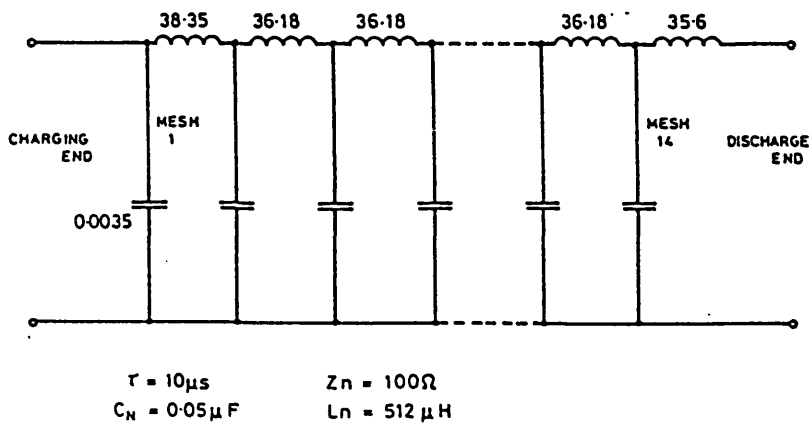


FIGURE 2.7 SPALLS 14 SECTION 100 Ω PULSE FORMING NETWORK

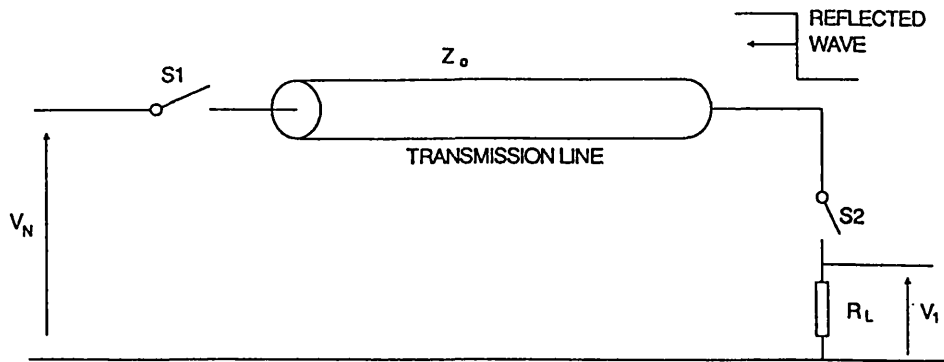


FIGURE 2.8 LOSSLESS TRANSMISSION LINE

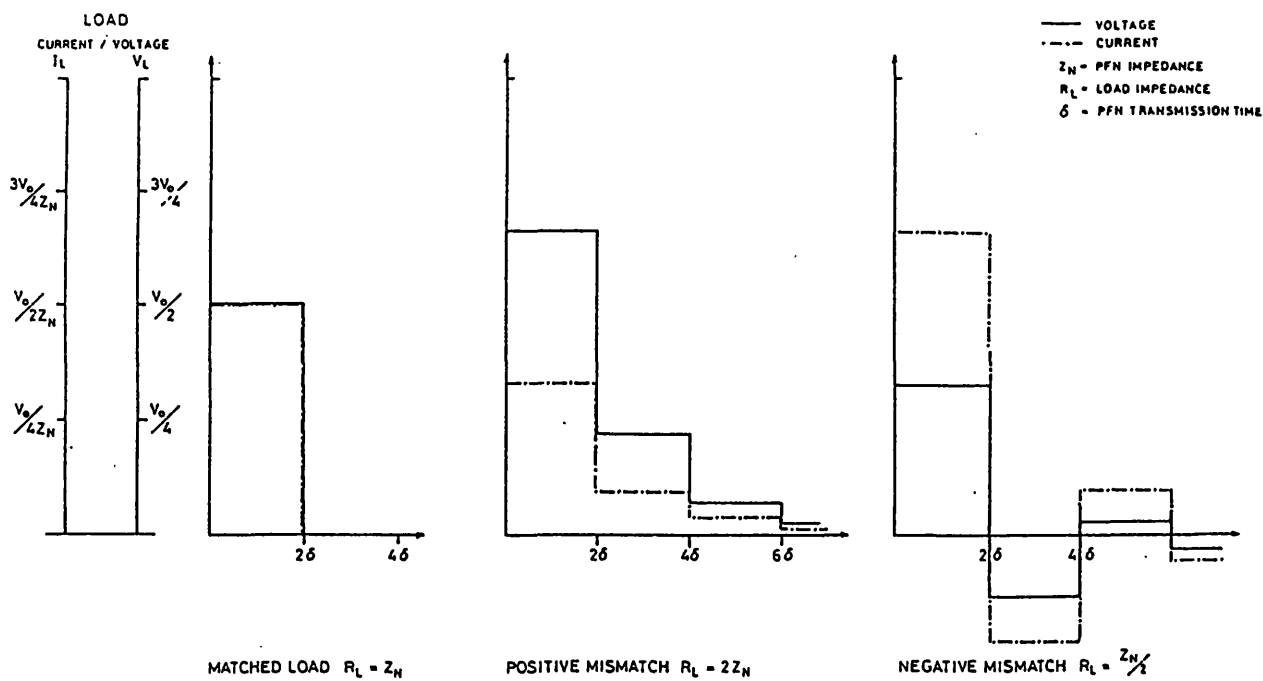


FIGURE 2.9 VOLTAGE AND CURRENT CHARACTERISTICS OF A LOSSLESS TRANSMISSION LINE WITH CONSTANT LOAD RESISTANCE

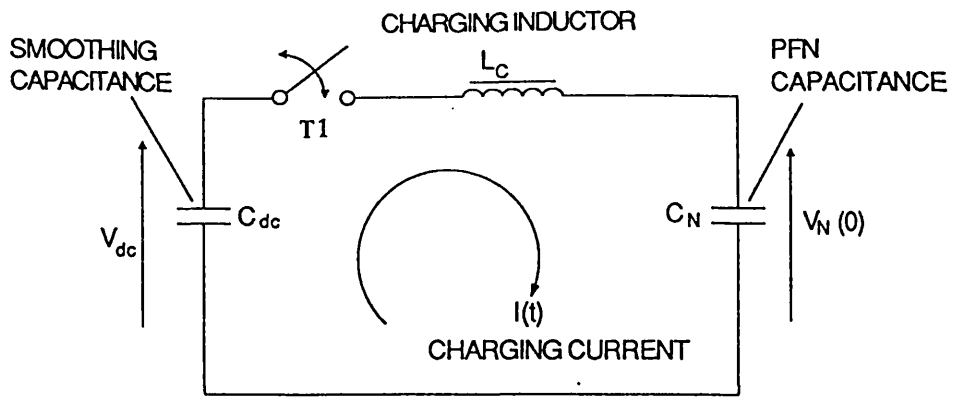


FIGURE 2.10 SIMPLIFIED EQUIVALENT CHARGING CIRCUIT OF THE PULSER

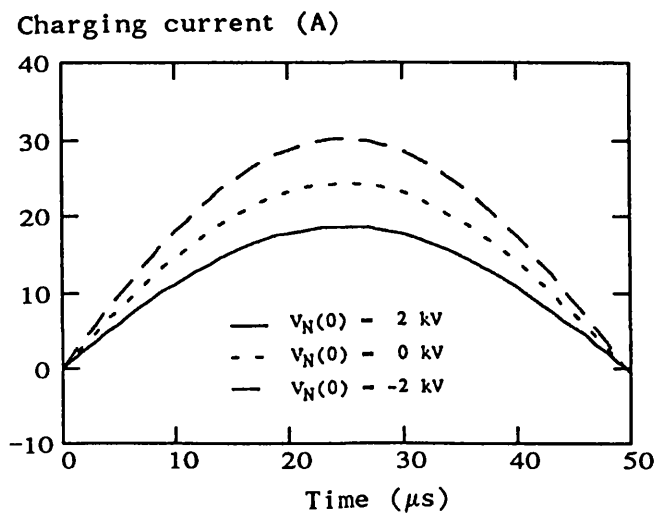
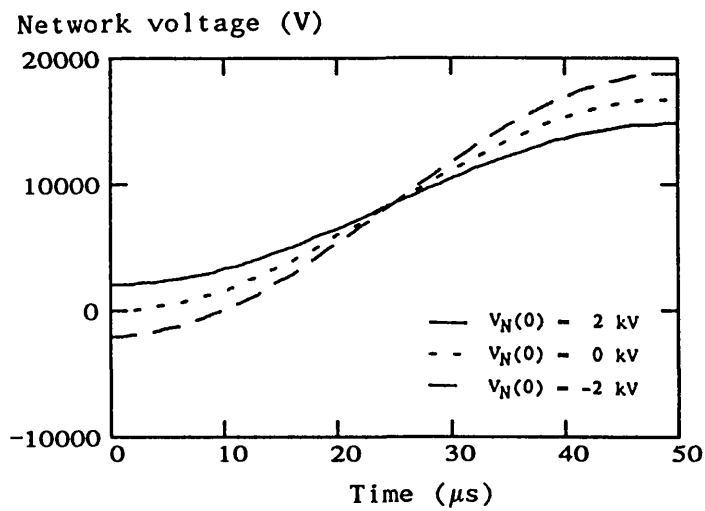


FIGURE 2.11 CHARGING CURRENT AND VOLTAGE WAVEFORMS

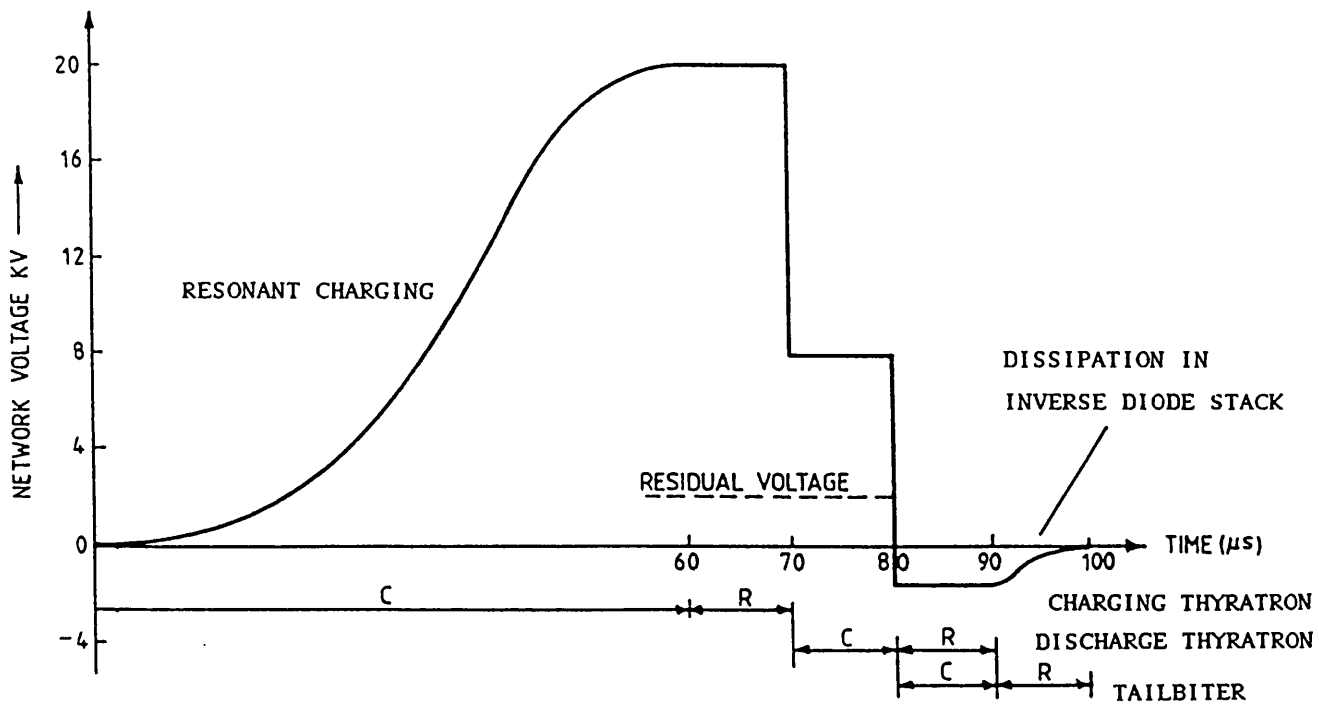


FIGURE 2.12 NETWORK VOLTAGE AND RELATIVE FIRING TIMES OF THE THYRATRONS

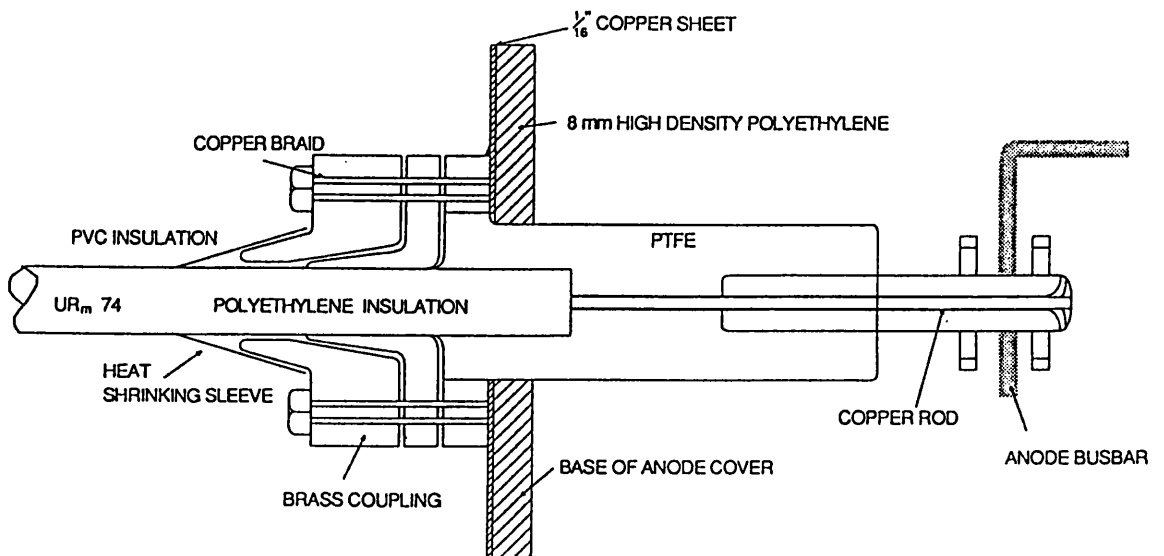


FIGURE 2.13 HIGH VOLTAGE CONNECTOR

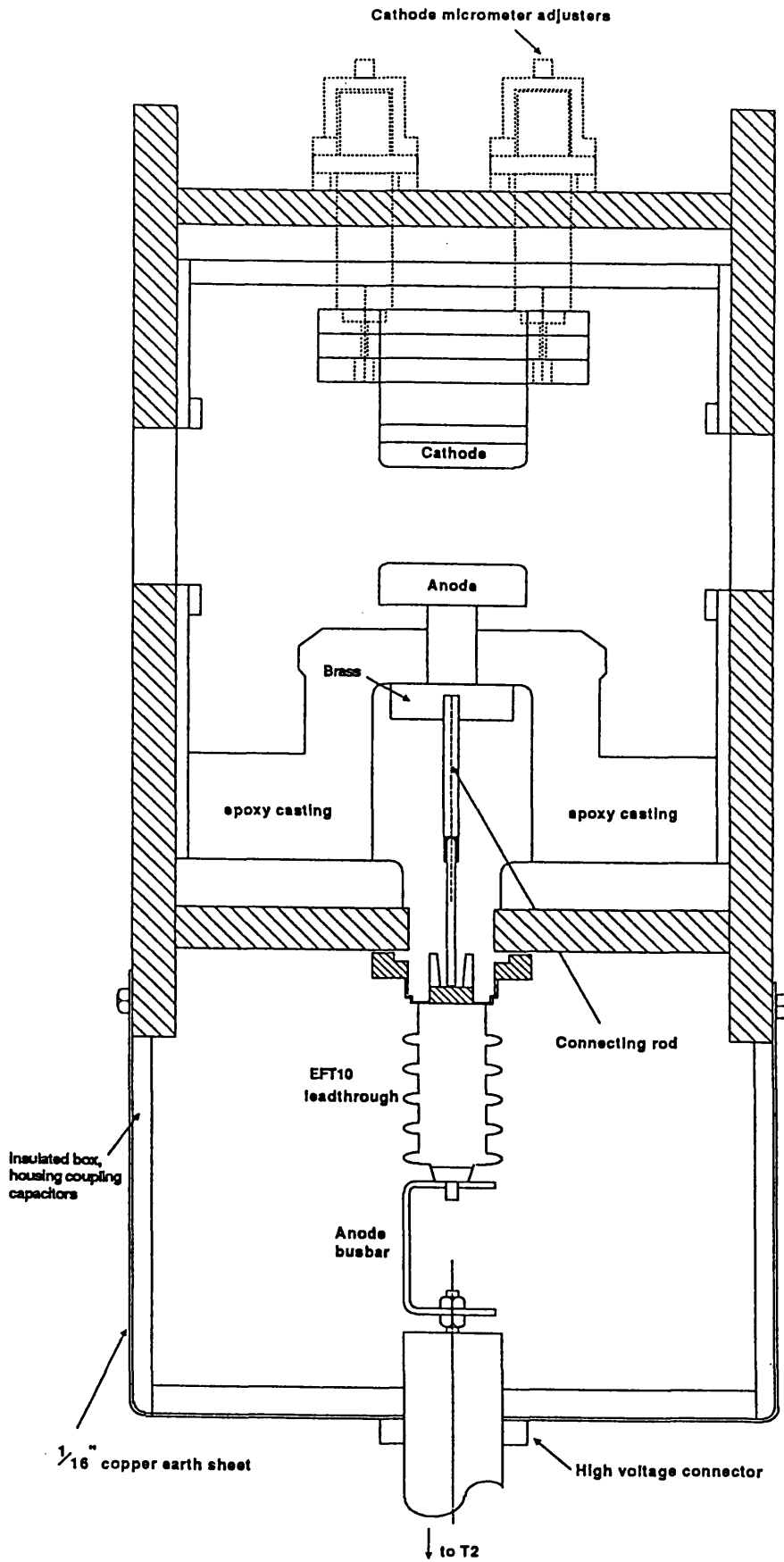


FIGURE 2.14 SCHEMATIC OF THE ELECTRICAL CONNECTIONS AND LASER CAVITY

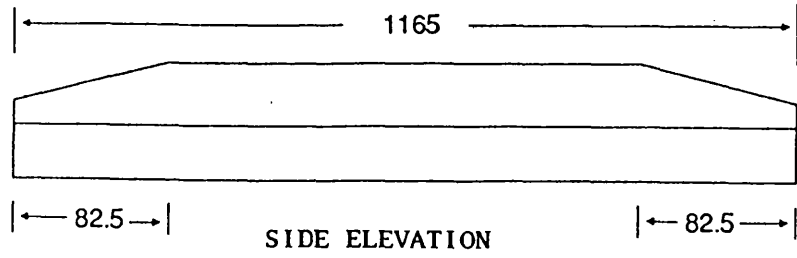


FIGURE 2.15 ELECTRODE DESIGN

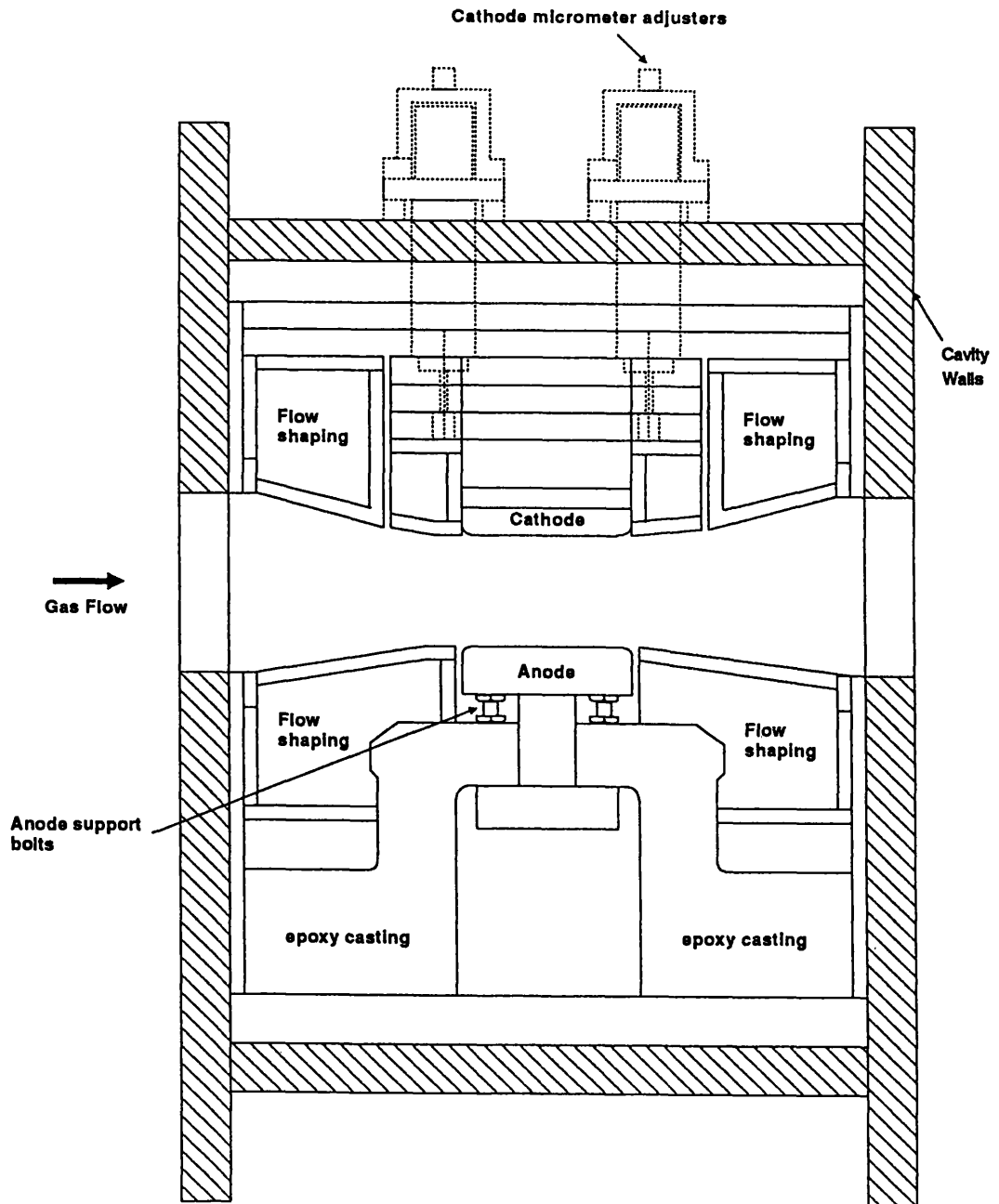


FIGURE 2.16 LASER CAVITY ASSEMBLY WITH FLOW-SHAPING

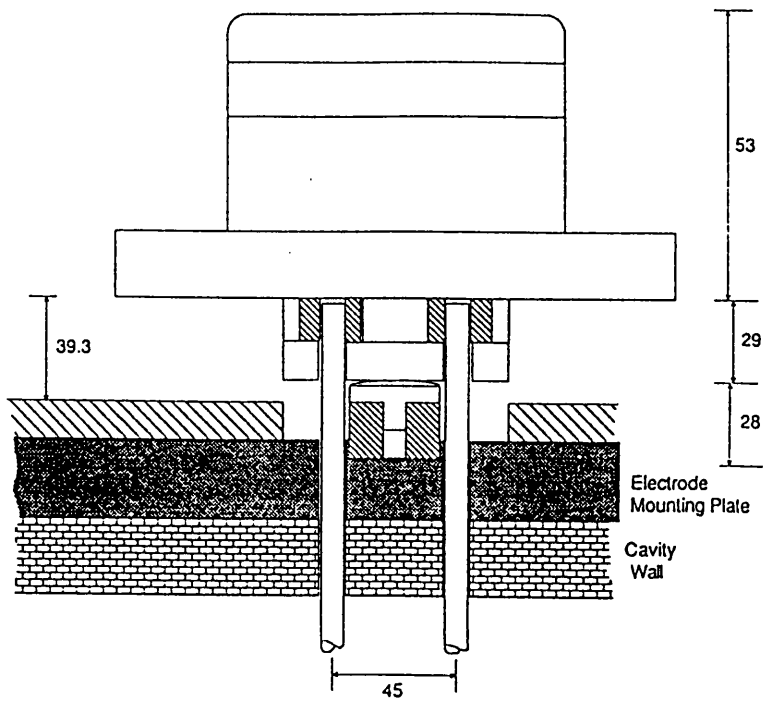


FIGURE 2.17 CATHODE PIVOT SUPPORT

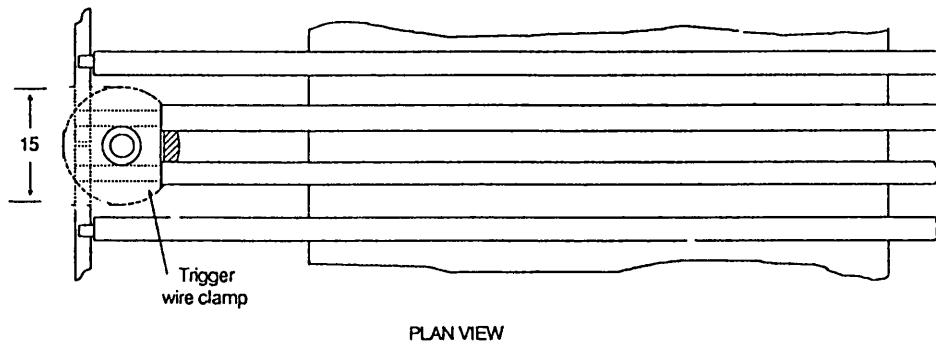


FIGURE 2.18 TRIGGER WIRE ASSEMBLY

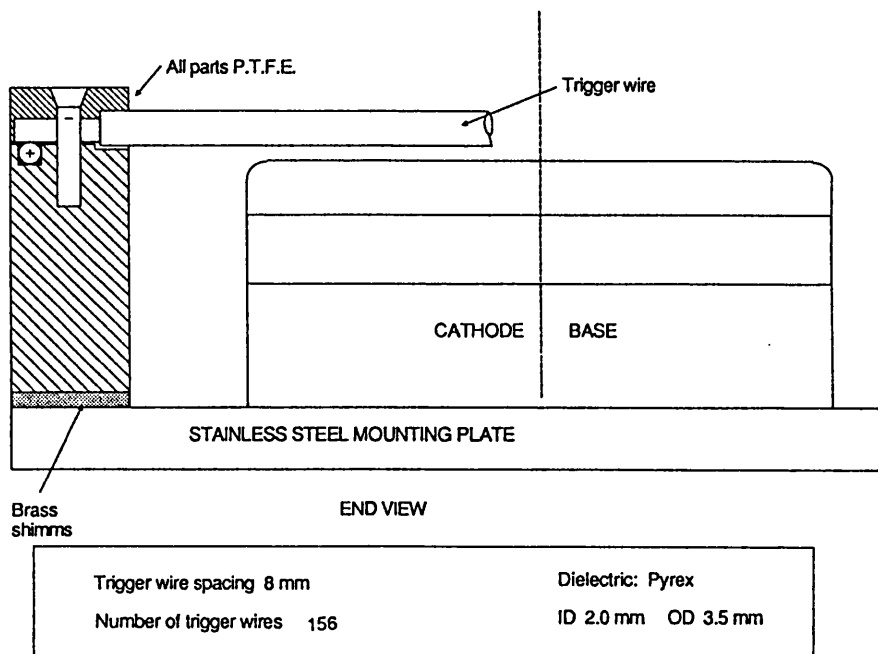


FIGURE 2.19 TRIGGER WIRE ASSEMBLY SHOWING TRIGGER WIRE GAP

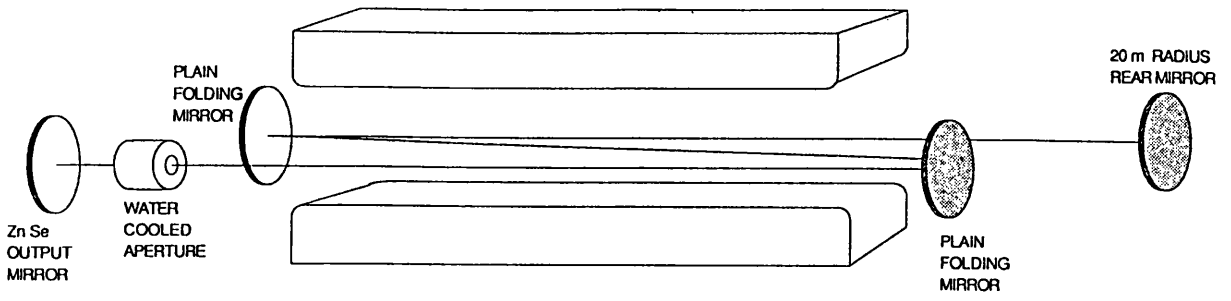


FIGURE 2.20 SCHEMATIC OF THE STABLE Z RESONATOR

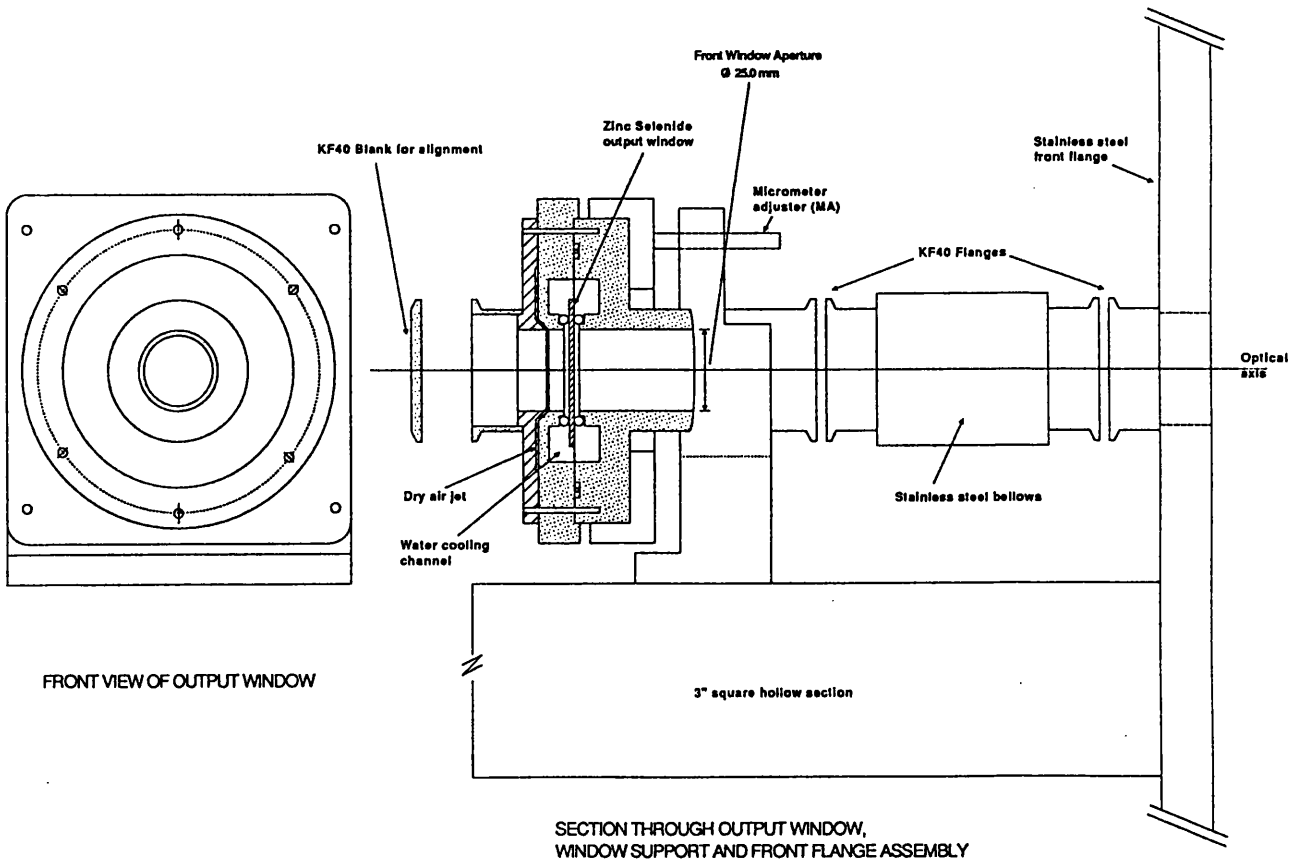


FIGURE 2.21 OUTPUT WINDOW MOUNT

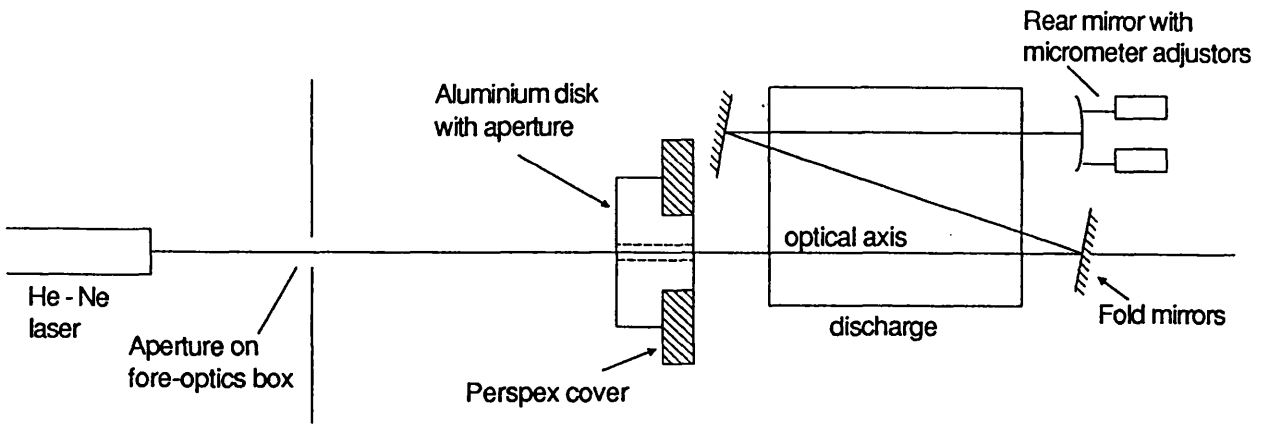


FIGURE 2.22a SCHEMATIC OF THE ALIGNMENT PROCEDURE

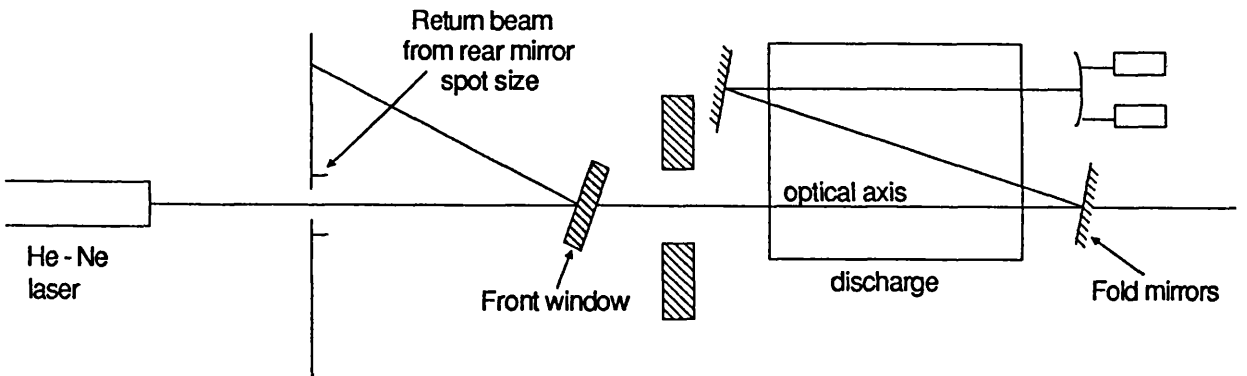
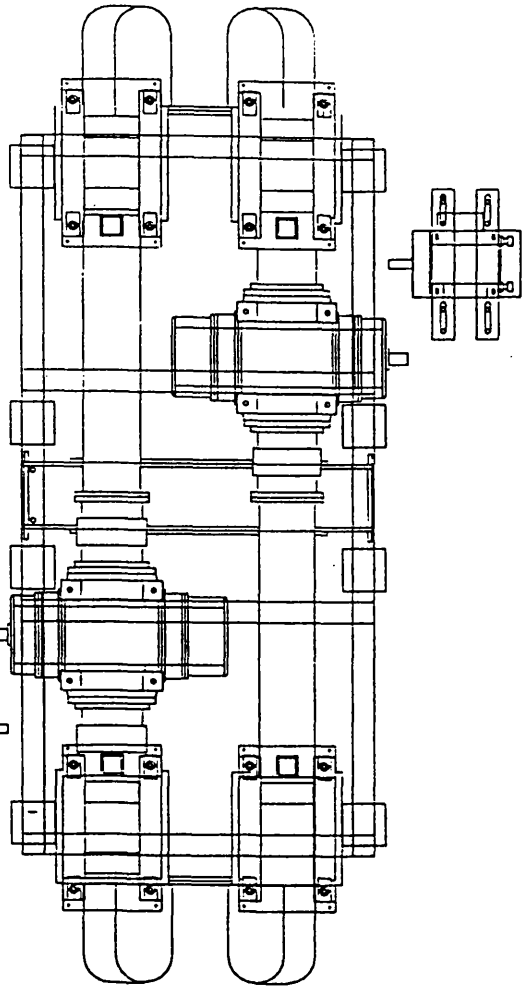


FIGURE 2.22b ALIGNMENT OF THE FRONT AND REAR MIRRORS

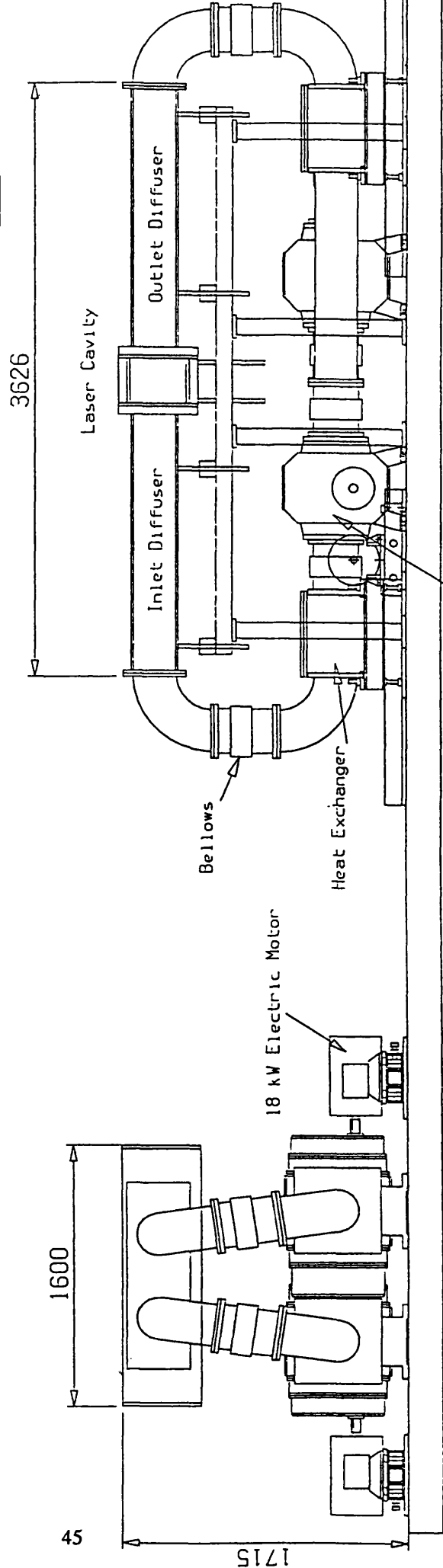
Roots Blowers
STARVAC 7500

BOTTOM VIEW



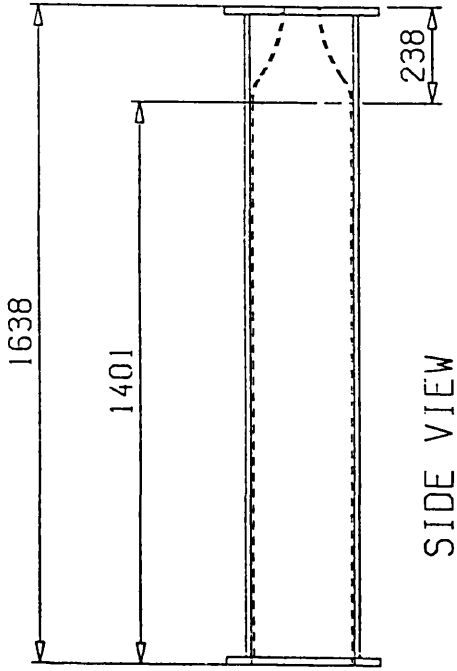
1715
45
1600

END VIEW

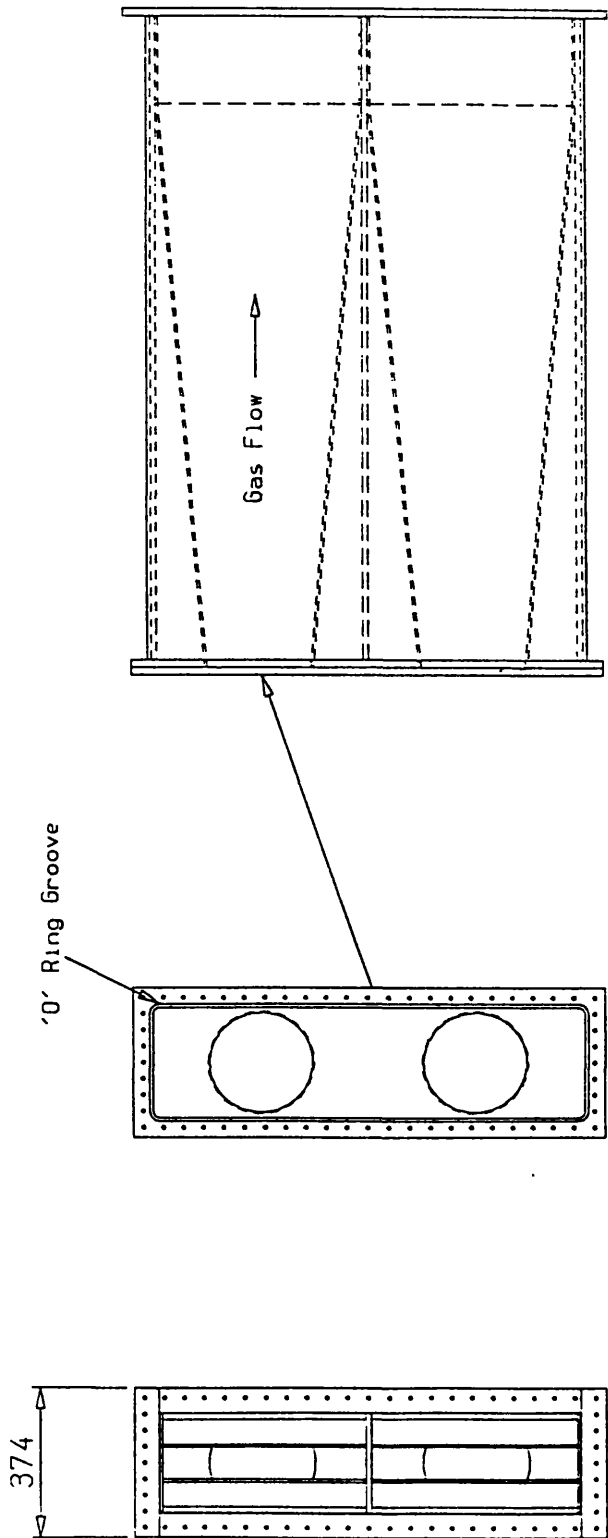


FRONT VIEW

FIGURE 2.23 GAS RECIRCULATOR CONSTRUCTION



Diffuser: all parts 1/4" aluminium plate
 Duct: all parts 1/2" stainless

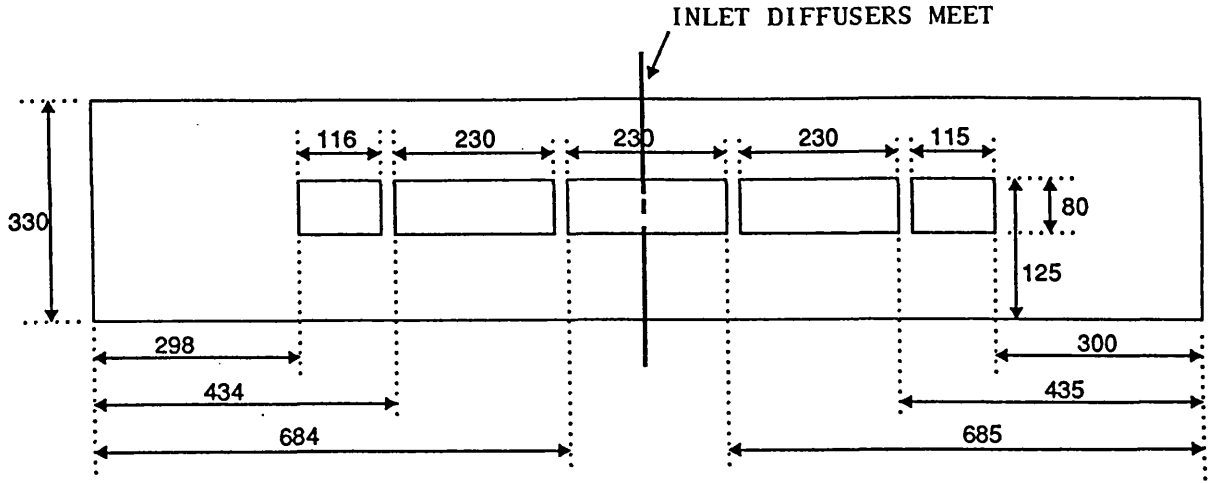


END VIEW

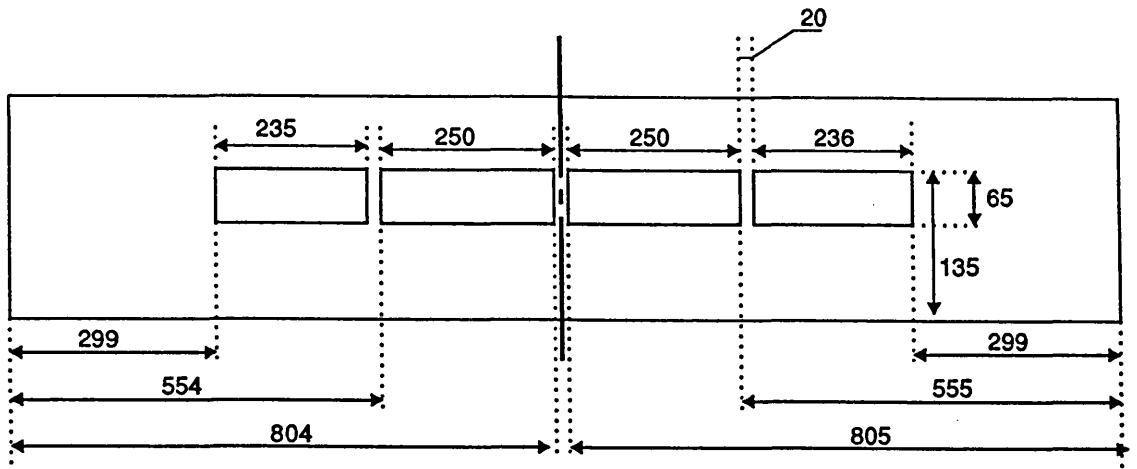
FLANGE

PLAN VIEW

FIGURE 2.24 INLET DIFFUSER



INLET ORIFICE



OUTLET ORIFICE

FIGURE 2.25 INLET AND OUTLET ORIFICES

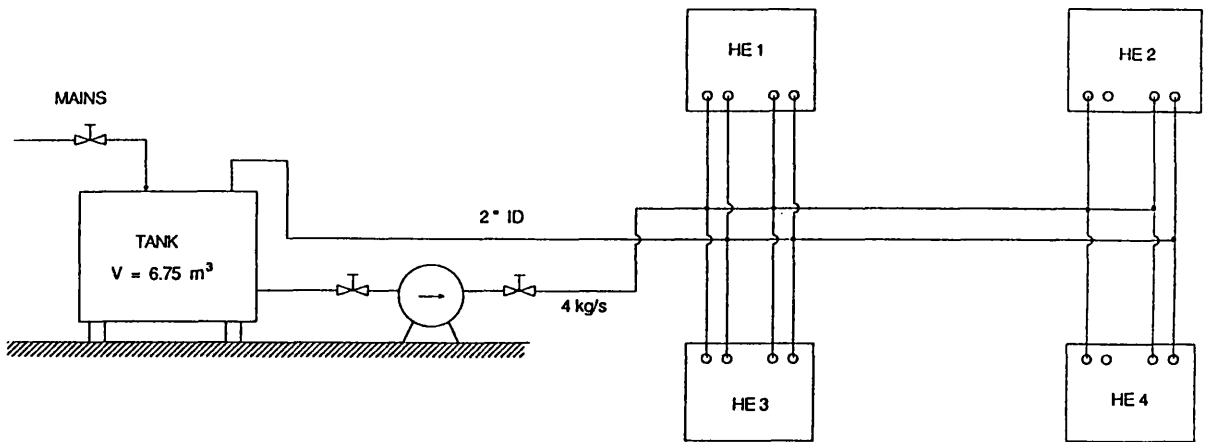


FIGURE 2.26 COOLING WATER CIRCUIT

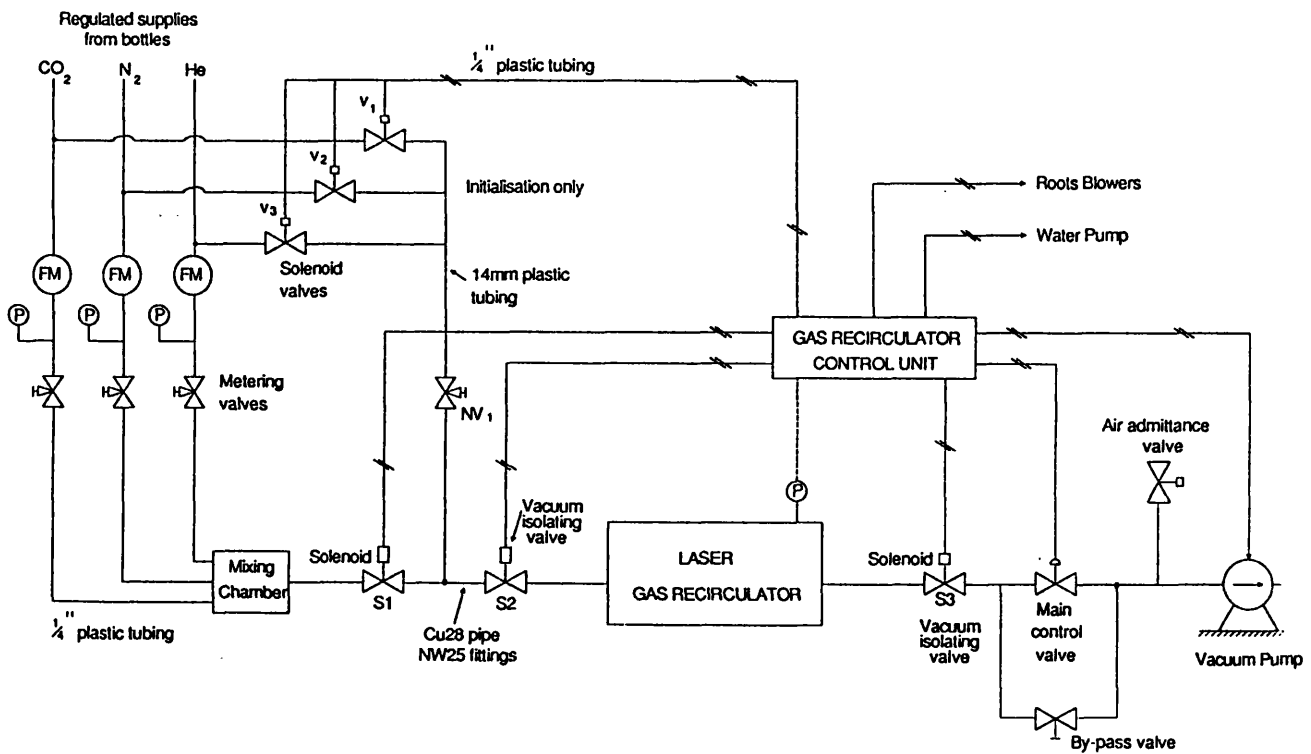


FIGURE 2.27 LASER GAS CONTROL SYSTEM

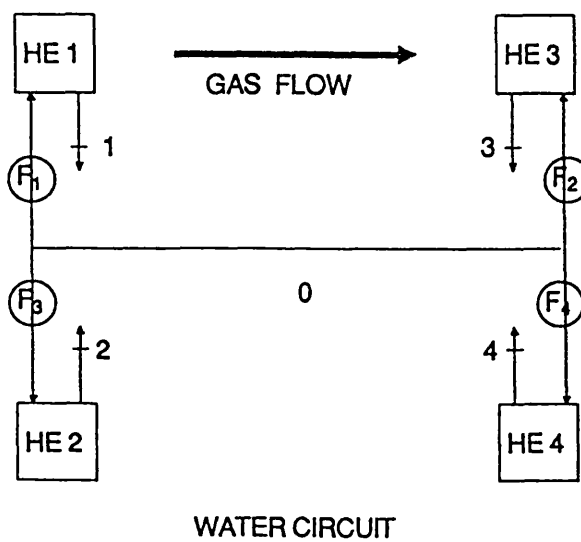
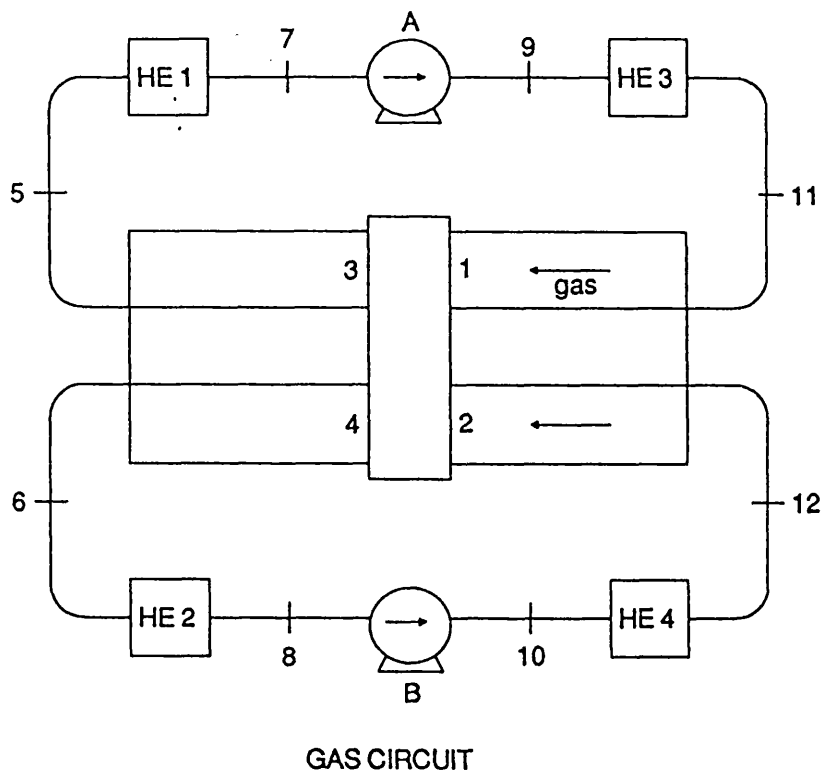


FIGURE 2.28 INSTRUMENTATION POINTS AROUND THE GAS RECIRCULATOR

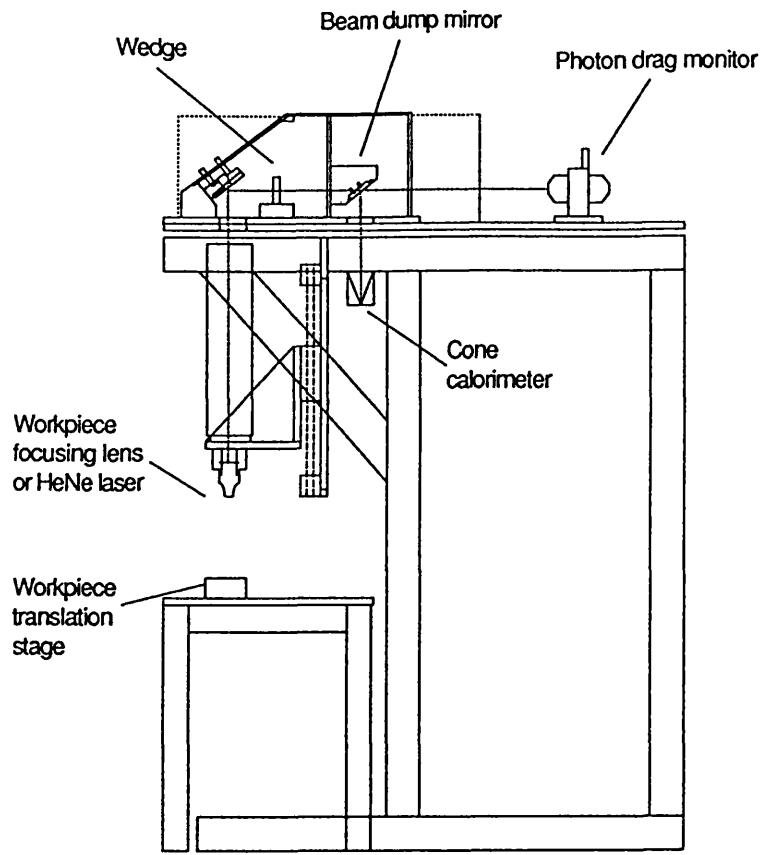


FIGURE 2.29 FORE-OPTIC ASSEMBLY

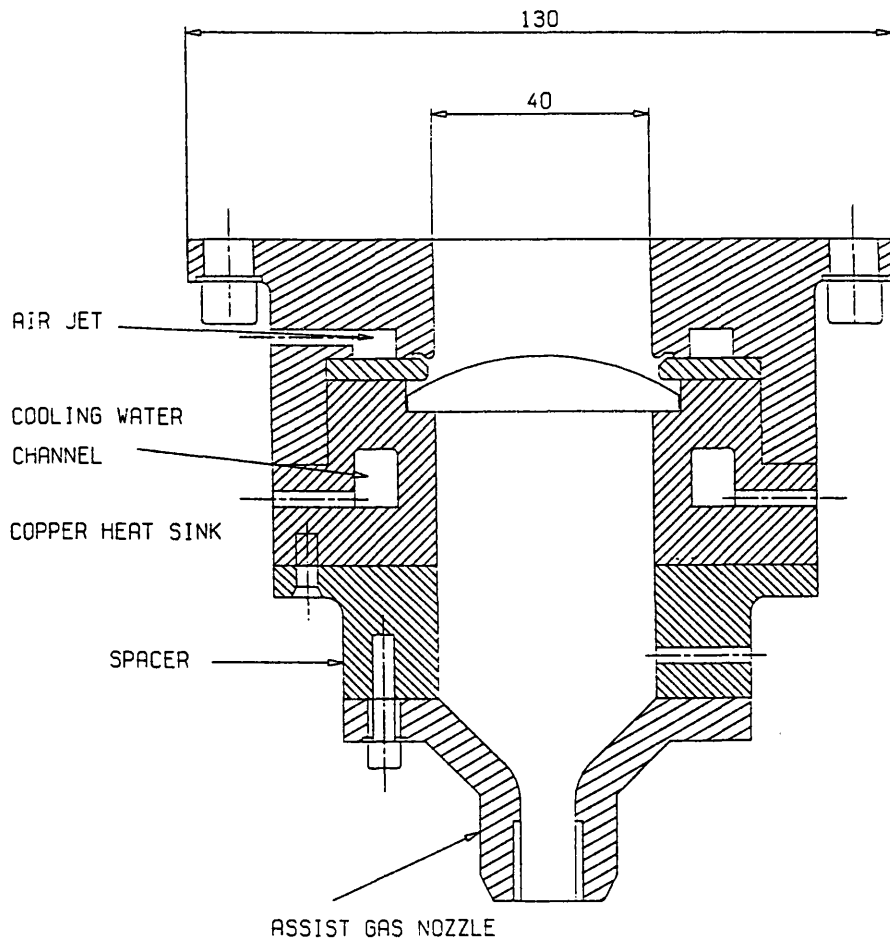
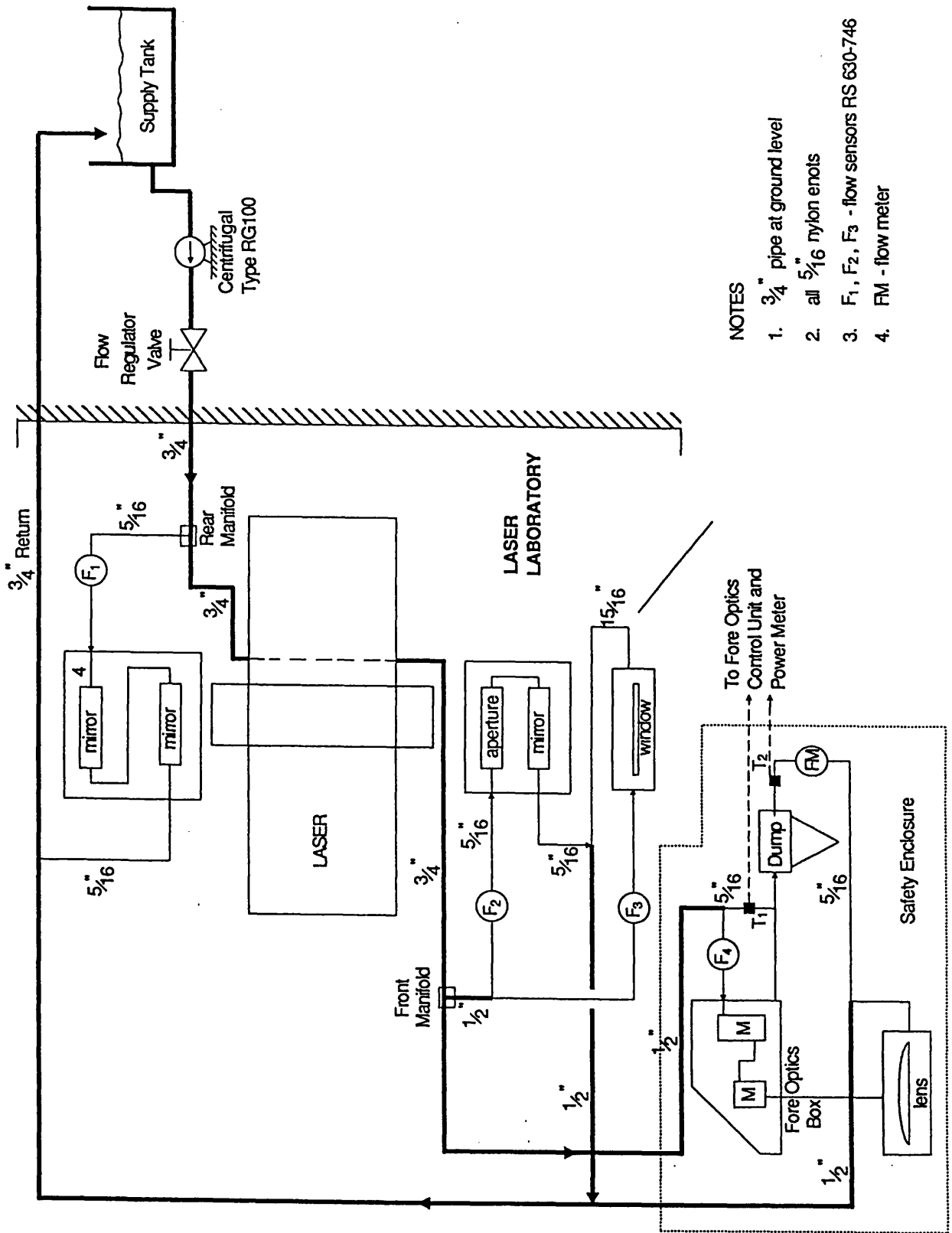


FIGURE 2.30 FOCUSING LENS ASSEMBLY



NOTES

1. 3/4" pipe at ground level
2. all 5/16" nylon encls
3. F₁, F₂, F₃ - flow sensors RS 630-746
4. FM - flow meter

FIGURE 2.31 OPTICAL WATER COOLING CIRCUIT

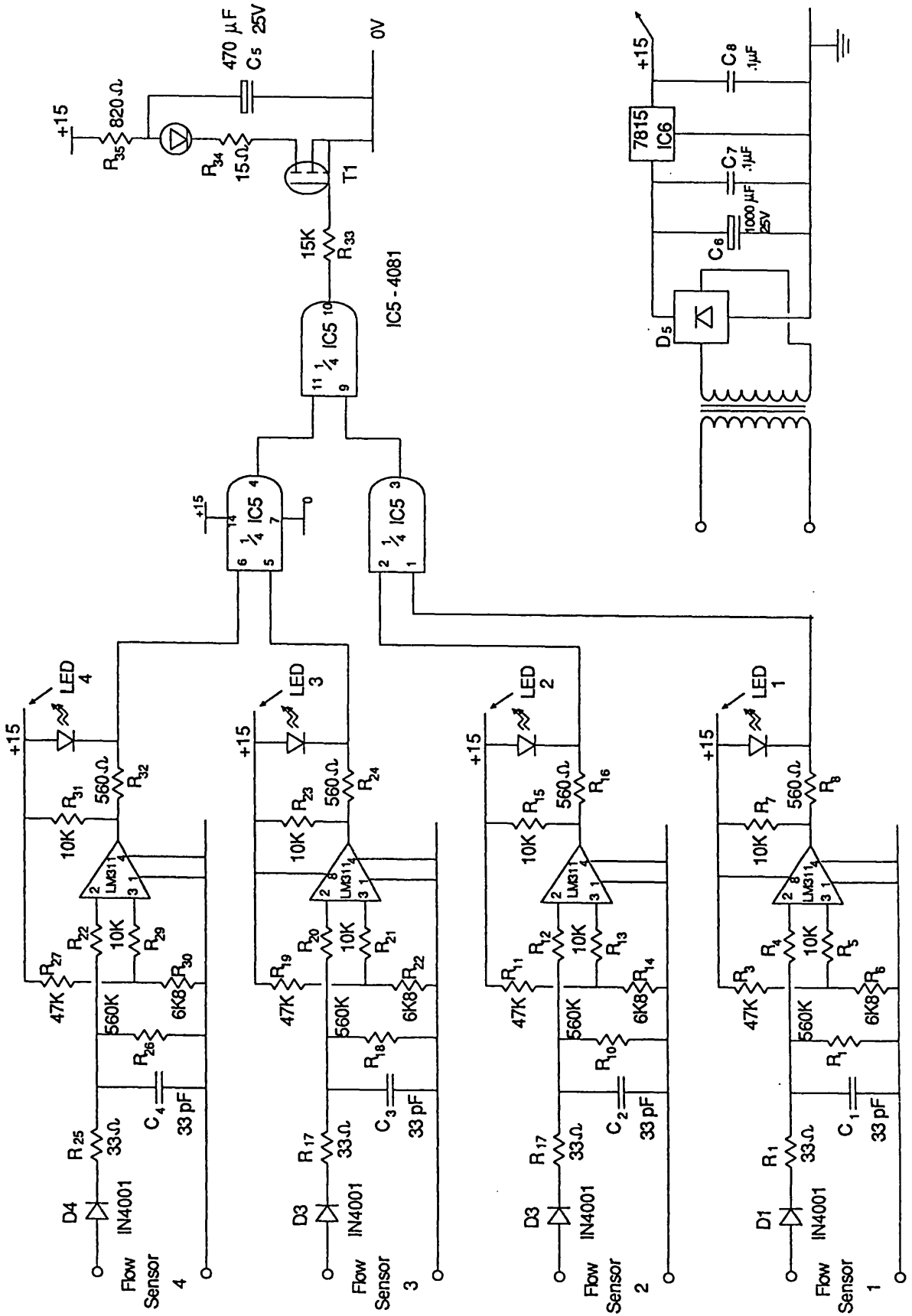


FIGURE 2.32 FLOW SENSOR CIRCUITRY

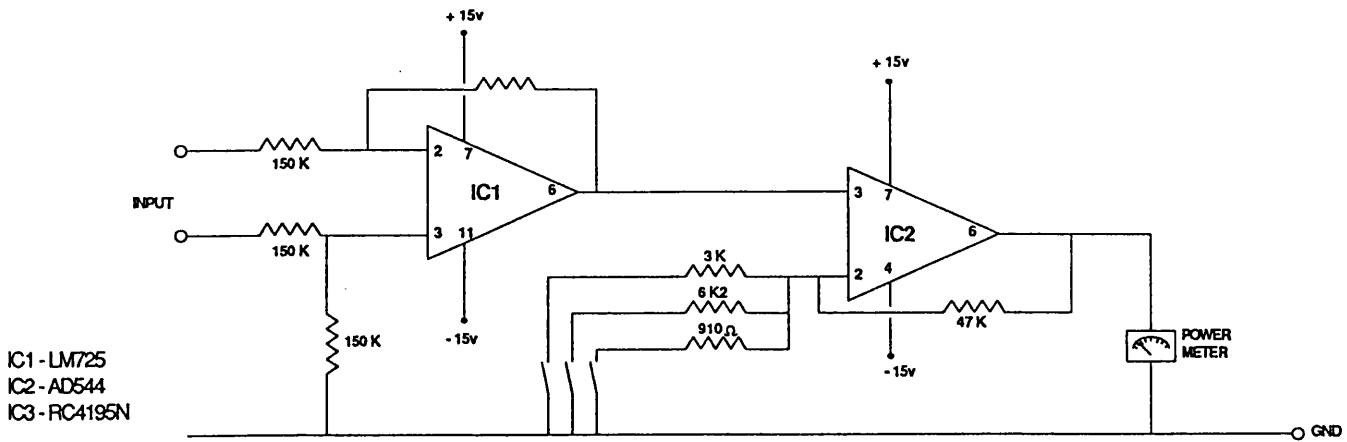


FIGURE 2.33 TEMPERATURE SUBTRACTING AND AMPLIFICATION CIRCUIT

CHAPTER THREE

DISCHARGE PARAMETERS, INITIATION AND PREIONISATION

INTRODUCTION

The performance of the discharge and laser system, as described in Chapter 2, was assessed and compared to the characteristics necessary to achieve the non-conduction limited and quasi-cw interaction processes. It was found that low discharge energy loadings – between 2 and 5 J – developed into satisfactory glow discharges, see Plate 2. Experiments were performed to fully investigate the behaviour of the glow discharge and examine the regime in which arc-free discharges were achievable. It soon became evident that arcing occurred for discharge energies above 7 J and with pulse repetition frequencies (PRF) of approximately 150 Hz. However, it was possible to conduct a series of experiments examining some fundamental discharge properties. For example, the discharge E/N values with different gas mixtures, pressures and discharge currents, see Section 3.1. These experiments were undertaken at a PRF \approx 100 Hz and with low energy loadings, i.e. < 5 J.

Having established good agreement between the measured E/p values and published results, the single shot stability limits of the discharge were investigated; the results compared moderately well with those obtained by Kharha [3.1], see Section 3.2.1. Whilst conducting these experiments, several modifications to the electrode geometry were found necessary to enhance the discharge operating performance, these are discussed in Section 3.2.2.

The effect of running the discharge at PRF > 100 Hz was investigated and is discussed fully in Chapter 4. Briefly, it was found that the maximum mean power that could be deposited into the discharge, prior to the onset of arcing, was approximately 3.5 kW; this is much lower than that required to obtain a mean laser output power of 5 kW. More worrying was the laser output, this is discussed in Chapter 5. Basically it was low, efficiencies of less than 0.5 % were obtained, whereas at least 6 % was expected, both theoretically and experimentally [3.1,3.2].

It has been reported that the laser output power [3.3] and discharge stability [3.4] of CO₂ TEA lasers is heavily dependent on the level of preionisation within the discharge. However, in the present case, measurement of the discharge formative time lags and the rate of change of the trigger wire current, i.e. dI_{tw}/dt , indicated

a low level of discharge preionisation; this is in itself a sufficient reason for the poor laser output power and discharge stability. Subsequently, efforts were directed towards increasing the level of preionisation. The affect of the level of preionisation on discharge stability and the laser output power was examined by changing the inductance placed on the anode of the discharge thyatron and using a separate preioniser supply.

A theoretical examination of the Townsend and streamer breakdown mechanisms established values for the initial preionisation electron densities necessary to ensure evolution of stable, glow discharges for the laser. Formative time lags for the streamer breakdown process are calculated.

A SPICE code is developed to simulate the transient development of pulsed, gas discharges, where the affects of circuit components are analysed.

Appendix B1 details the calculation of the transfer efficiency from the PFN to the load for different load conditions, and the system gas pressure at which the positive mismatch regime is encountered. This is particularly important because no tailbiter thyatron was available, consequently, the discharge must not be operated under positive mismatch conditions.

3.1 E/N MEASUREMENTS

The affect of the discharge current, gas mixture and pressure on the plateau characteristics of the discharge voltage are examined and compared to experimental and theoretical results [3.1,3.2]. Hasan [3.2], showed that small quantities of CO gas, as a substitute for He or N₂, has a beneficial effect on CO₂ gas discharge lasers. Consequently, these effects are examined.

The role of CO in CO₂ gas mixtures is, in some respects, similar to N₂. Electron impact collisions with CO molecules cause excitation of the molecule to its first vibrational level, $\nu = 1$. A resonance exists between this metastable level and the upper laser level of the CO₂ molecule; thus, energy is transferred readily to the upper laser level. If N₂ is present, energy can be transferred to excite its first quantum state through collisions with electrons and excited CO. The first vibrational state of N₂ is in resonance with the upper laser level of CO₂ and the $\nu = 1$ level of CO. Unlike N₂, CO is beneficial in deactivation of the lower laser level, through collisions with CO₂ molecules in this state.

All the measurements of E/N were taken at a frequency of approximately 100 Hz. The plateau values of the voltage and current traces were measured for a range of gas mixtures, pressures and different tapsettings on the transformer, see Section 2.1. The gas mixture composition is expressed in the ratio CO₂:N₂:He, where a variable partial pressure is denoted by X. For measurements including CO, the partial pressure of N₂ or He includes the partial pressure of CO.

3.1.1 Measurement of E/N with Different Partial Pressures of He And N₂

The gas mixtures selected for the experimental investigation were 1:1:X, 1:2:X and 1:3:X, where X is the partial pressure of He. Figure 3.1 shows a graph of E/N versus gas pressure, in torr, for the gas mixtures 1:1:X where X = 2, 4, 6 and 8. It is seen that for a particular gas mixture and pressures greater than about 80 torr, the value of E/N is constant with increasing pressure. The value of E/N is lower for mixtures with higher helium content. For values of the gas pressure which are approximately less than 80 torr, there is a slight increase in the E/N value as the pressure is reduced; this is due to the cathode fall becoming a significant fraction of the voltage drop across the positive column.

Figure 3.2 shows, for the same gas mixtures as Figure 3.1, that the E/N values are independent of the current passing through the discharge. For currents greater than 100 A there is a slight increase in E/N with current, which again, can be attributed to the cathode fall and recombination processes which become dominant for high discharge currents [3.5]. Over a finite region of the graphs E/N is seen to be a property of the gas mixture.

Table 3.1 shows the experimental and theoretical values of E/N for the gas mixtures 1:1:X, 1:2:X and 1:3:X. The theoretical results are obtained from Hasan [3.2], it is seen there is excellent agreement between these values.

Figures 3.3 and 3.4 show the variation of the quasi-steady values of E/N as a function of the CO₂ and He content respectively. It is apparent that increasing the CO₂ content results in an increase in the quasi-steady E/N value. This can be explained in terms of the electron energy distribution function (EEDF). Increasing the CO₂ content, decreases the mean electron energy of the gas mixture. This is due to the electrons colliding with the increased fraction of CO₂ molecules and losing energy through vibrational excitations. Increasing the He content, decreases the quasi-steady E/N value and increases the mean electron energy of the gas. Because of the monatomic nature of He, no electrons lose energy through

vibrational excitation with the He atoms – as this process cannot occur. Consequently, electrons are accelerated to a greater degree by the applied electric field, which increases the mean electron energy of the gas and decreases the quasi-steady E/N value of the discharge.

3.1.2 Measurement of E/N With Additions of CO

The variation of E/N with CO as a substitute for He and N₂ was examined, the results are shown in Table 3.2, the partial pressures are expressed in the ratio CO₂:N₂:He:CO. Figure 3.5 shows the theoretical values of E/N as a function of the ratio of the partial pressures CO/CO₂ with gas mixtures of 1:1:6 and 1:2:6 [3.2]. For the 1:1:6 gas mixture, the last partial pressure (6) is the sum of the He and CO content; and for the 1:2:6 gas mixture, the second partial pressure (2) is the sum of the N₂ and CO content. It is seen that the values agree. The addition of CO to the gas discharge reduces the average electron energy. Moreover, increasing the CO concentration increases the population of the upper laser level of the CO₂ molecule through a resonance transfer of energy from CO ($v = 1$) to CO₂ (001).

3.2 DISCHARGE EXPERIMENTAL RESULTS

After success in obtaining the quasi-steady E/N values across a range of gas mixtures and pressures, the maximum single shot energy depositions into the discharge prior to arcing were found, and compared to the experimental results measured by Kharha [3.1] from the prototype laser system.

Two distinct types of arc can be defined: a) those attributed to instabilities within the discharge, and b) those that occur due to poor design of the electrode and/or electrode support structure. It was found that arcs had a higher probability of occurring at certain places within the discharge – the arcing fell into category b). The arcing was due to the design of the electrode configuration, and not to any breakdown mechanisms occurring within the discharge. These problems and their solutions are detailed in Section 3.2.2.

The voltage and current waveform characteristics of the main discharge and trigger wire gap are discussed in Sections 3.2.3 and 3.2.4.

Experimental results of varying: the trigger wires gap, coupling capacitance, peaking capacitance and low ionisation potential seedant (LIPS) concentration are discussed in Section 3.2.6.

3.2.1 Single Shot Stability Limits

The single shot stability limits measured by Kharha [3.1] were, essentially, in a static gas mixture. A gas purge was possible, but in the 10 μ s pulse period the effect of this can be assumed negligible. In an attempt to validate these single shot stability limits the roots blowers were left off and there was no gas purge; i.e., the PFN energy was deposited into a static gas mixture. Three gas mixtures were selected for comparison to the single shot stability limits measured by Kharha, namely: 20:20:80, 20:20:40 and 30:30:0; these are the partial pressures expressed in torr. They were then converted to the nearest reading in mbar because this was the pressure range setting of the EMV251 pressure monitor. As the maximum energy depositions into the discharge prior to arcing were required, it was decided to use a 0–240 V variac, 20 kV RMS high voltage supply and charge the PFN resistively. This allowed greater control over the maximum voltage, and hence discharge energy deposition, as compared to that available from the main transformer which only has tapsettings at 5 % increments. Figure 3.6 shows a schematic of the gas discharge circuit. The coupling capacitor, C_c , was 10 μ F. Three possible positions are shown for the current transformer namely: A, B and C. If the probe is placed at A, both the main discharge current and the preionising current are monitored; at B, the preionising current is measured and at C, only the main discharge current is detected. The observed waveforms at each position are discussed in detail in Sections 3.2.3 and 3.2.4. For the single shot stability measurements, the current probe was placed at position A. Tables 3.3 and 3.4 show the results obtained by Kharha [3.1] and those measured in the present case respectively.

Table 3.3 Kharha's Single Shot Stability Limits

Gas Mixture torr	E/p $Vcm^{-1}torr^{-1}$	V_d kV	V_N kV	I_d A	E_{dm} J
20:20:80	11.0	5.41	17.1	117	6.32
20:40:40	18.0	7.34	19.0	116	8.56
30:30:0	29.2	7.13	20.0	129	9.00

Table 3.4 Single Shot Discharge Stability Limits

Gas Mixture mbar	E/p $Vcm^{-1}torr^{-1}$	V_d kV	V_N kV	I_d A	E_{dm} J
26:26:104	11.3	4.8	19.7	151	7.56
27:54:54	16.1	6.6	19.0	127	7.34
40:40:0	26.8	6.4	19.0	133	7.18

It is apparent that the first reading for the maximum discharge energy, denoted by E_{dm} , compares favourably with Kharha's and is approximately 20 % greater; however, the next two are lower by 15 % and 20 % respectively. Probably, the major factor accounting for these discrepancies is the degree of sophistication of the detection equipment used, which in the present case is much more sophisticated than that used by Kharha. The energy is calculated automatically by the oscilloscope (see Appendix A6); whereas Kharha took photographs of the voltage and current traces which were captured on a lower bandwidth oscilloscope, the negatives for the photographs of the traces were then projected onto graph paper and the energy calculated manually by "counting the squares".

It is interesting to note that for the values of E_{dm} measured in the present case, the maximum frequency that the discharge could operate at was ≤ 200 Hz, whereas repetition rates of 5 kHz were obtained for short bursts on the prototype [3.6].

In order to establish the optimum value of the coupling capacitor and trigger wire gap a series of experiments were undertaken, these are discussed in Section 3.2.5.

3.2.2 System Modifications

After preliminary experiments examining the arc-free operating regime of the discharge, it was found that arcing was most likely to occur from the same positions on the electrodes. Hence, some initial modifications to the discharge system were necessary to irradicate the source of these arcs.

For moderate discharge energy loadings of 5 - 7 J, arcs were observed on the downstream side of the gas flow at the knee of the electrodes, i.e. where the flat surface and the taper meet. The electric field is non-uniform over this transition region of the electrode profile. Also, the trigger wires were close to this region, enabling the discharge to grow, and because of the non-uniform electric field, it

soon developed into arcs. By adjusting the position of the cathode relative to the anode, the arc could be moved to the knee of the electrode on the upstream side, the electrodes were then misaligned by approximately 1 mm. The electrodes were actually longer than the gas inlet window to the laser cavity; hence, a poor gas velocity profile would exist in this region. This poor gas flow coupled with the trigger wire position favours arc development within the discharge. The electrodes were modified by reducing their total length to be the same as the gas inlet window, 1000 mm, and increasing their radii of curvature to 3/8", see Figure 3.7. The number of trigger wires were reduced so a significant distance (5 mm) existed between the knee of the electrodes and the ends of the trigger wires, see Figure 3.8. Subsequent testing of the modified electrodes and trigger wires showed that this source of arcing had been irradiated.

The consequence of these modifications is to decrease the volume of the discharge from 2.400 to 2.016 litres, a reduction of 16 %. Thus, there is an enhanced probability of arcing due to the higher specific input energy densities. However, large energy depositions into CO₂ laser gas mixtures have been reported by Kline [3.7] and no immediate problem was envisaged from reducing the discharge volume. The system used by Kline had dimensions of 10 x 10 x 100 cm³, and was preionised by an array of 480 sparks, each spark dissipated about 40 mJ, yielding a total of 19.2 J for the preionisation source. The total discharge energy deposition was, approximately 1000 J, which gives a specific energy density of 0.1 J/cc, this compares to a value of only 4.96×10^{-3} J/cc in the present case.

Subsequent testing of the modified electrode and trigger wires showed that successful glow discharges were obtained with no preferential place for arcing. However, occasionally, arcs occurred from the anode to the base plate which supports the epoxy anode mounts, see Chapter 2, Section 2.3. Also, faint corona were visible from the ends of the trigger wire assembly, they were particularly prominent at a PRF \approx 1 kHz. At this frequency the anode leadthrough's, type EFT10, broke down, see Figure 3.9a. Trackmarks left by the arc indicated that the arc had followed a path from the central conductor, along the ceramic insulating pillar to the base of the flange.

These minor arcing problems were irradiated in the following manner. The arcing from the anode to the base plate was prevented from forming by insulating the back face of the anode with a PTFE cover, this constitutes the anode backing plate. The corona, although not a severe problem, was overcome by placing PTFE covers over the ends of the trigger wires. The EFT10 anode leadthroughs were

further modified by insulating the central conductor with 3 layers of heat shrink sleeving, see Figure 3.9b. PTFE sleeves were then fabricated to fit inside the ceramic insulation of the leadthrough, reducing the possibility of tracking. The top of the PTFE sleeve was made flush to the PTFE anode backing plate, see Figure 3.10.

3.2.3 Voltage and Current Waveforms of the Main Gap

The characteristics of the voltage and current pumping pulse shapes are dependent on the electrical components of the pumping circuit and the composition of the gas mixture. However, certain similarities exist in the shape over a wide range of conditions. As a particular example, the voltage and current traces are described for a 1:1:4 gas mixture at a pressure of 156 mb.

The network was charged to a voltage of 13.0 kV, the trigger wire coupling capacitance was 20 μF and the blowers were running at their penultimate speed, 2453 rpm, this gives a nominal volume flow rate of 12 600 m^3/hr . The current probe was initially positioned at A, see Figure 3.6, i.e. the preionisation and the main discharge current were monitored. The voltage and current traces are shown in Figure 3.11. It seemed that the discharge current grew almost immediately with application of the voltage to the electrodes, this would indicate that the discharge was breaking down via the streamer mechanism, see Section 3.3. The current probe was moved to position C – it was then realised that a delay existed between the rise of the voltage and the current – see Figure 3.12. The initial "back of the envelope" calculation suggested that this time delay corresponded to the electron transit time between the anode and cathode. This tended to suggest that the discharge was breaking down via the Townsend mechanism. The drift velocity for electrons in gases is approximately proportional to the applied electric field, E . As the voltage increases across the gap, electrons created at the trigger wires, see Section 3.2.4, are accelerated towards the anode. Assuming that the average value of the voltage is half the peak value, then the average of the electric field over the transition period is $\approx 9.5 \text{ kV} / 2 / d \text{ V cm}^{-1} = 1.2 \text{ kV cm}^{-1}$ (with $d = 4.0 \text{ cm}$).

For a pressure of 156 mb ($N = 3.77 \times 10^{-18}$ at 300 K) the average $E/N \approx 3.2 \times 10^{-16}$. For this value of E/N an electron drift velocity of $7.114 \times 10^6 \text{ cm s}^{-1}$ is reported by Hasan [3.2]. Thus, for an electron to traverse the gap of 4.0 cm theoretically takes 562 ns, whereas 528 ns was measured, a difference of only 6 %. This is surprisingly close considering the crudeness of the estimation. An

important assumption in this calculation is that the trigger wires are behaving as a source of electrons at the cathode. Each electron is the precursor for an avalanche that develops according to Townsend's theory [3.8]. The number of electrons are multiplied, on their journey to the anode, through ionisation processes within the gas mixture. This is a simple model, neglecting both space charge effects; which can enhance avalanche progress, particularly for high electric fields [3.9]; and electron loss through attachment. This breakdown process contrasts with initial ideas that were developed from examination of Figure 3.11, where it was thought that the trigger wires were providing volumetric preionisation, which enabled the discharge to breakdown practically immediately with the applied voltage. This is discussed in more detail in Section 3.3.

The breakdown time, often called the formative time lag [3.10], is defined as the period between the application of a voltage pulse to the discharge gap and the subsequent growth of significant current, with the assumption that the statistical time lag is small. This latter quantity is important historically, and defined as the time before an initial free electron exists between the electrodes. Early discharge analysis experiments generally relied upon cosmic rays as the preionisation source for initiating breakdown of the gap. With the highly random nature of cosmic rays, the statistical time lag can become a considerable fraction of the total time before breakdown. With laser preionisation sources, however, this time lag is negligible, as a sufficient initial electron density is usually present, assuming that the preionisation source is synchronised correctly with application of the main discharge voltage pulse. Various workers [3.11,3.12] quote smaller formative time delays for atmospheric pressure lasers than reported here. Crawford stated that the value of the applied voltage, for TEA discharges, must be at least double the quasi-steady discharge voltage in order to obtain formative time lags of less than 400 ns.

The long formative time lag measured in the present case was, in part, due to the preionisation characteristics of the trigger wires, see Section 3.2.4, as little or no VUV light was being generated, which itself was indicated by the measured rate of change of current through the trigger wires, see Section 3.3.3. The inductance of the laser pumping circuit is important in determining the level of preionisation and hence the discharge development phase, see Sections 3.4 and 3.6.

The level of laser output and the probability of discharge arcing for TEA CO₂ lasers is dependent on the level of preionisation [3.3,3.4]. Thus, the low laser output power, discussed in Chapter 5, and the low energy loadings prior to arcing supported the argument of poor preionisation.

3.2.4 Trigger Wire Characteristics and Modelling

The trigger wire voltage and current characteristics for the 1:1:4 mixture at a total pressure of 156 mb, a network voltage of 12.85 kV and PRF = 100 Hz, are shown in Figure 3.13. The trigger wires are coupled to the anode via a 10 nF coupling capacitor.

These results were taken in conjunction with McDonald who subsequently developed a model predicting the trigger wire behaviour [3.13]. The model enables optimisation of the controlling parameters for the trigger wires, and was based purely on their capacitive characteristics, with no account taken of the perturbing nature of the discharge. However, the model provides a good basis to predict the behaviour and optimum design for the trigger wires and an independent preioniser, see Section 3.6.

As the trigger wires are capacitively coupled to the main anode pulse, the voltage across the trigger wires, V_{tw} , will follow the anode voltage, V_a . This is consistent with Kharha [3.1] who also, incorrectly, stated that preionisation was occurring during the whole pulse. This view was reached because of the inability to measure the preionisation current, which was due to excessive noise levels during the thyatrons switching period. Interestingly, these large noise transients experienced by Kharha suggest a rapid rate of rise of current. High di/dt 's (typically 10^{10} As^{-1} , see Section 3.3.3) are a pre-requisite for efficient preionisation, such values were not measured under the present experimental arrangement, and were a major reason for assuming insufficient preionisation of the discharge.

It is seen from Figure 3.13 that the trigger wire current only flows when the trigger wire voltage is changing and that it is the same sign as dV_a/dt . This indicates that the trigger wire current is a displacement current – given by $I = C dV/dt$ – hence, a capacitive nature can be attributed to the trigger wires. After the pulse, a negative residual, typically -1 kV , exists across the trigger wires.

A capacitance meter, an Avo LCR meter type B183, was used to measure the stray capacitance between the trigger wires and cathode, denoted by C_{tw} , a value of 0.36 nF was recorded. This value is dependent on the design of the trigger wires. A large value is usually required in order to maximise the initial current drawn through the trigger wire gap, and consequently maximise the level of preionisation. From Figure 3.13, the voltage rise time is approximately 600 ns. The estimated value of the rate of rise of the voltage is $dV_{tw}/dt \approx 9.23 \text{ kV}/\mu\text{s}$, and during this period the current rises to a value of 70 A. Substitution of these values into the equation for the displacement current yields a value for the

effective capacitance, C_e , of 7.6 nF. This is much larger than the initial measured stray capacitance, and was attributed to the breakdown of the trigger wire gap. A fraction of the total electrons attach to the outer surface of the pyrex tubing whilst the remainder avalanche towards the anode. C_e is that capacitance existing between the trigger wires to the outside of the dielectric surface, and can be calculated per unit length from the equation for capacitance of cylindrical dielectric material of relative permittivity ϵ_r , in this case pyrex, which is given

$$C_\ell = \frac{2 \pi \epsilon_0 \epsilon_r}{\ln (D/d)} \quad \text{F m}^{-1} \quad 3.1$$

Where C_ℓ is the effective capacitance of the trigger wires per unit length, D and d are the outer and inner diameters of the glass tubing respectively.

Table 3.5 summarises the characteristics of the trigger wires which enable calculation of the value of C_e .

Table 3.5 Trigger Wire Geometry

Trigger Wire Conductors	Brass rod
Dielectric: Pyrex glass tubing	$\epsilon_r = 5$
Inside diameter	$d = 2.0 \text{ mm}$
Outside diameter	$D = 3.5 \text{ mm}$
Transverse Length of one Trigger wire, l_t	130 mm
Distance between Trigger Wires	8 mm
Number of Trigger Wires	$N_{tw} = 104$
Trigger Wire - Cathode gap	$d_{tw} = 0.53 \text{ mm}$

Substitution of these values into 3.1 gives a value of 0.5 nF/m. C_e can then be found by multiplying C_ℓ by the number of trigger wires and the length of one trigger wire, C_e is thus given by

$$C_e = C_\ell \cdot N_{tw} \cdot l_t \quad \text{F} \quad 3.2$$

C_e is found to be 6.76 nF which is moderately close, within 11.1 %, to the experimental value of 7.6 nF.

The transition region between the measured capacitances of 0.36 nF and 7.6 nF, corresponds to the breakdown of the trigger wire gap. This can be seen as a small glitch on the trigger wire voltage, see Figure 3.14, and is also visible on the main

anode voltage waveform, see Figure 3.11. The breakdown occurred at a voltage of between 1 – 1.5 kV for $d_{tw} \approx 0.5$ mm.

For gas discharges, the physical phenomena occurring in the discharge are dependent on the E/N value. In order to optimise the processes responsible for the creation of the preionising electrons (see Section 3.2.5 and 3.3.3) it is important to optimise the value of E/N for the trigger wire discharge. To calculate the optimum E/N value the Boltzmann transport equation must be solved and, as photonic processes are important, they too must be included. However, an estimate of the processes occurring can be obtained by calculating the value of E/N from measurement of the trigger wire voltage, trigger wire gap and the gas pressure. It is difficult to precisely calculate the value of the electric field when the trigger wire gap breaks-down; this is because of the non-uniform trigger wire geometry, which by definition, is responsible for the corona characteristics. To accurately calculate the electric field numerical techniques would be required which take account of the trigger wire geometry and the development of the space charge effects within the discharge, which inevitably perturb the electric field. The minimum estimate for the electric field between the trigger wires when the gap breaks-down is simply given by the ratio of the breakdown voltage divided by the trigger wire gap, which in this case yields a value of 7.5 kV cm^{-1} . For a neutral particle density of $3.766 \times 10^{18} \text{ cm}^{-3}$, i.e. a pressure of 156 mb at a temperature of 300 K, then the E/p value for the moment the trigger wire gap breaks-down is approximately $2 \times 10^{-15} \text{ Vcm}^2$. This is discussed further in Section 3.2.5.

Prior to breakdown of the trigger wire gap, the trigger wire current is typically 8 – 10 A, and $dV_{tw}/dt \approx 1.9 \times 10^{10} \text{ Vs}^{-1}$. Calculating the capacitance of the trigger wires in the pre-breakdown stage, i.e. the initial stray capacitance, yields a value of between 0.42 and 0.53 nF, which compares moderately well with the measured value of 0.36 nF. It is evident that following the collapse of the trigger wire voltage, in this pre-breakdown stage, the current increases to its' peak value which is determined by the trigger wire geometry and the rate of change of the applied voltage; the latter is inevitably dependent upon the circuit inductance.

Once the trigger wire gap has broken down, the ratio of the anode and trigger wire voltage is constant and given by

$$\frac{V_a}{V_{tw}} = \frac{C_c + C_e}{C_c} \quad 3.3$$

Where C_e is the effective trigger wire capacitance. It is seen from equation 3.3 that the affect of the coupling capacitance, C_c , on the trigger voltage is that it simply couples some fraction of V_a across the trigger wires. The larger the ratio C_c/C_e then the nearer V_{tw} approaches V_a . This obviously fixes the upper limit of V_{tw} and consequently the peak trigger wire current. Hence, changing the value of C_c above a certain value will not significantly alter the trigger wire characteristics; this is consistent with the results of Kharha [3.1]. Figure 3.15 shows the trigger wire and anode voltages, the attenuation of the trigger wire voltage is clearly seen – the trigger wire waveform has been repositioned to highlight the differences between the voltage waveforms. The ratio V_a/V_{tw} was measured at 1.40, as the value of the coupling capacitance is known (20 μF in this case) equation 3.3 can be rearranged to give a value for C_e , this yields a value of 6.2 nF. This seems to compare favourably with the measured value of 7.6 nF, originating from the displacement current calculation.

3.2.5 Preionisation: A Threshold Process

Preionisation is discussed in detail in Section 3.3.3, however, it is convenient at this stage to introduce a parameter that expresses the efficiency of the preionisation source at creating VUV flux. Several authors indicate two conflicting possibilities to maximise VUV production, they are: high di/dt 's [3.14], typically 10^{10} As^{-1} or large corona currents [3.15]. The first technique implies a very fast rate of switching, whereas, the second method requires large values of current, perhaps the order of kilo-Amps. It is apparent that the creation of the VUV flux is a threshold process, requiring the decay of excited electronic states of N_2 . Some of the preionising electrons are then created by the subsequent absorption of the VUV flux by impurities within the gas mixture, this occurs at wavelengths of 120 nm and 175 nm [3.16].

Ideally, it would be useful to quantify the efficiency of the preionisation source through a measurement of the VUV flux, however, as such equipment was unavailable, it was decided to define the requirement of a rate of change of the trigger wire current to be 10^{10} As^{-1} as the threshold for VUV creation. It is interesting to note that for the present case, the rate of change of current passing through the trigger wires was measured at only 675 $\text{A}/\mu\text{s}$.

The parameter used in an effort to quantify the VUV flux level is defined as the ratio of 10^{10} As^{-1} to the measured value of di/dt ; and given by

$$\xi_x = \frac{10^{10}}{di/dt} \quad 3.4$$

The subscript x is used to distinguish between the rate of rise of current for the trigger wires and the main gap, where at this stage it is unclear if a high rate of change of current for the main gap is necessary. For the former case x is not included, if $x = mg$ then it is the rate of change of current of the main gap which is being specified. From this definition values of $\xi < 1.0$ are required, whereas for the example given in Figure 3.14, $\xi = 14.8$. It is thus recognised that the value of di/dt must be increased by at least this factor to obtain significant levels of VUV flux. This gives an indication of how poor the trigger wire system is at creating uniform preionisation.

It should be mentioned that the electrons in the high energy tail of the electron energy distribution function (EEDF) will be responsible for excitation of the electronic states in N_2 , and the subsequent creation of the VUV flux. Also, some of these electrons will be energetic enough to directly ionise N_2 , CO_2 and gas impurities, however, it is unlikely that He will be ionised with an ionisation potential of 24.481 eV as compared to 15.576 eV and 13.769 eV for N_2 and CO_2 respectively. The minimum estimate of the peak value of the E/N for a 1:1:4 gas mixture at a pressure of 156 mb was calculated in Section 3.2.4 as approximately $2 \times 10^{-15} \text{ V cm}^2$. For this value of E/N considerable energy is coupled into electronic excitation of N_2 and, to a lesser extent, some directly into ionisation of N_2 and CO_2 . Thus it is probable that for values of $\xi > 1$ some VUV flux will be created by the decay of excited states of N_2 which were excited by electrons in the high energy tail of the EEDF.

3.2.6 Affect of Trigger Wire Gap, Coupling Capacitance, Peaking Capacitor and Low Ionisation Potential Seedants on the Discharge Performance

Kharha [3.1] found significant difference in the discharge stability by changing the trigger wire gap, d_{tw} , and the coupling capacitor, C_c . Experiments varying the values of these parameters and also using a peaking capacitor [3.16] and low ionisation potential seedant (LIPS) [3.17], which were not used by Kharha, were undertaken in an effort to understand the discharge behaviour and to examine their affect on the discharge quality. The objective was to substantially improve the arc-free operating regime of the discharge.

Experimentally, the simplest parameter to vary is the coupling capacitor. Values were selected ranging from 20 nF to 5 nF. The trigger wire gap was adjusted from 0.35 mm to 2.2 mm. The experiments were conducted by observing the discharge while gradually increasing the pulse repetition frequency (PRF). At a specific frequency, denoted by f_1 , faint filamentary arcs were observed. If the frequency was increased further, the arcs became brighter, more severe and regular; this level of arcing was defined as the maximum system frequency, denoted by f_m . The latter condition has a detrimental effect on the electrodes, through spark erosion, and potentially on pulser components. By observing f_1 , the regime of f_m was avoided. It was considered satisfactory and simpler to define the system performance from the value of f_1 than, for example, by measuring the laser output energy. This avoided the added complication of installing the resonator and measuring the laser output energy. Moreover, without the resonator in position the discharge is easily viewed.

During the series of experiments no significant improvement was found of the magnitude required to ensure operation of the laser within the necessary specification.

The effect of varying the coupling capacitor was examined with a gas mixture of 1:1:4 at a pressure of 156 mb. Figures 3.16 and 3.17 show traces of the trigger wire voltages and currents which were obtained for values of the coupling capacitance equal to 20 nF and 5 nF respectively. It is seen that the rate of change of the trigger wire current for each waveform is significantly different. Values of $\xi_{20} \approx 313$ and $\xi_5 \approx 15.2$ were measured, where the subscript in this case refers to the value of the coupling capacitance (C_c) in μF . For the definition of ξ see Section 3.2.5. The peak current is approximately the same in each case, 33 ± 1 A. A further difference lies in the width of the current pulse, approximately 800 ns and 583 ns for the coupling capacitance values of 20 nF and 5 nF respectively. However, there was no significant difference in the discharge performance for the different values of the coupling capacitor; the required power levels could not be deposited into the discharge. This is consistent with the view that when $\xi > 1$, the level of preionisation is inadequate for enhanced discharge performance. The effect of higher values of C_c is to increase the fraction of the anode voltage developed across the trigger wires; however, the rise time increases as well, and the resulting rate of change of trigger voltage (dV_{tw}/dt) remains approximately constant. Consequently, no immediate benefit was observed from changing the value of the coupling capacitance.

Peaking capacitors are used in laser discharge pumping circuits to improve the

discharge stability [3.17], they are placed in parallel with the electrodes. For TEA lasers they normally have a small value, typically 10's-100's of pico-Farads. However, when such small values were tested no significant difference was found in the trigger wire voltage and current traces. It was not until the peaking capacitor was the order of "nano-Farads" that any significant effects were noticed. Figure 3.18 shows the voltage and current traces of the main gap, with a peaking capacitance $C_p = 10$ nF, compared to the case with no peaking capacitor placed across the discharge, defined at this stage as $C_p = 0$. Clearly, C_p has a dramatic influence on the formative time lag, τ_b ; dV_d/dt and dI_d/dt . It is important to note that the values are tending to move in the opposite direction from that desired, i.e. large values of C_p have, apparently, adverse affects on the waveform characteristics - increasing the value of ξ_{mg} . Table 3.6 gives values of the following waveform parameters abstracted from Figure 3.18: the breakdown time τ_b , dV_d/dt , dI_d/dt , the peak current I_p , and ξ_{mg}

Table 3.6 Affect of peaking capacitor on discharge characteristics

C_p nF	τ_b ns	dV_d/dt CV s ⁻¹	dI_d/dt A μ s ⁻¹	I_p A	ξ_{mg}
"0"	507	1.55	718.3	113	13.9
10	1141	0.68	279.2	133	35.8

Quite clearly, the rate of change of the discharge current is much greater for the condition $C_p = "0"$, however, as expected the peak current is reduced, in this case by about 20 A. Also, the formative time lag is much shorter for the condition with the lower value of peaking capacitor, see Section 3.4.5.

Small additions of low ionisation potential seedants (LIPS) to CO₂ laser gas mixtures, have been reported to substantially increase the laser output performance [3.18]. Thus, experiments were performed to see if any improvement in the laser output could be obtained by using LIPS.

Low concentrations were added to the discharge by the following technique. A small cylindrical reservoir of volume V_2 , was connected to the laser cavity of volume V_1 , see Figure 3.19. When the laser cavity is pumped down, valves VS_1 and VS_2 are open and the regulator on the gas supply bottle is closed, thus the complete laser cavity and LIPS gas assembly is evacuated. The valves are left open until the system is filled with the laser gas mixture to pressure p . Valve VS_1 is closed and then the reservoir is filled to a pressure $p + \Delta p$, where Δp is the partial pressure of the LIPS gas. VS_2 is closed and VS_1 is opened, allowing the pressures between the laser cavity and reservoir to equalise. The laser cavity now

has a small partial pressure of LIPS which is dependent on the ratio of the volumes V_1 and V_2 , which are 2.4 m^3 and $(1000 \pm 50) \text{ cm}^3$ respectively. As an example, to add 10 ppm of the LIPS gas to the laser gas mixture, the following ratio must be satisfied:

$$\frac{\Delta p}{p} = \frac{10 \times 2.4}{1 \times 10^6 \times 1000 \times 10^{-6}} = 0.024$$

With a system pressure $p = 156 \text{ mb}$, for every Δp increment of 3.74 mb , an extra 10 ppm of LIPS is added to the gas mixture. It is possible to fill the reservoir with the LIPS gas to a much higher pressure than p , and use the VS_1 valve to regulate the flow until the required partial pressure has been filled to the laser chamber. This was quicker but slightly harder to control, for this reason the first technique was usually adopted.

The effect of the LIPS, in this case propylene (C_3H_6) was used, was to produce a discharge with small, spherical regions of intense light which existed for short periods of time. A satisfactory explanation could not be given, however, localised regions of intense ionisation must have occurred. No improvement in the laser output was observed.

An important future experiment would be to replace the LIPS with impurities, for example O_2 or air, to examine the affect of these contaminants on the discharge quality.

3.2.7 Gap Voltage Prior to the Discharge Thyatron, T2, Triggering

It was noticed during the experimental programme, discussed above, that the voltage between the discharge anode and cathode was not at ground potential when the discharge thyatron, denoted by T2, was triggered. This can be seen from Figure 3.15 on the discharge anode voltage trace. Figure 3.20 shows the PFN charging cycle and the voltage across the gap. When the charging thyatron (denoted by T1) fires, the PFN charging cycle starts and the voltage across the gap begins to rise in a similar fashion. This was explained in terms of the stray capacitance across T2 (denoted by C_{st2}) which coupled the voltage across T2 and charged the stray capacitance across the discharge gap, C_d . It was found that the stray capacitance on the laser head side was dominated by the cable stray capacitance C_{ca} , and the trigger wire stray capacitance C_{tw} (typically 0.36 nF) thus $C_d \approx C_{tw} + C_{ca}$, where the stray capacitance of the electrodes is only $\approx 10 \text{ pF}$ and clearly negligible. The connecting cable had characteristics of 100 pF/m

and 100 nH/m. With a cable length of 5 m the total cable capacitance is approximately 0.5 nF, thus, $C_d \approx 0.86$ nF, which is close to the measured value of 1.01 nF. The total cable inductance, L_{ca} , is 0.5 μ H, and negligible compared to the inductance placed on the anode of the discharge thyatron, denoted by L_a , which is placed there to minimise the rate of rise of current through the CX1528 thyatron ($L_a = 36$ μ H). An estimate for the value of stray capacitance across T2 was $C_{st2} \approx 60$ pF. Figure 3.21 shows the equivalent circuit of the laser and the last stage of the PFN. The stray inductances of the anode and cathode connections, and the trigger wires are denoted by L_{sa} , L_{sc} and L_{tw} respectively. It is seen that C_{ca} is behaving like a large peaking capacitor which will substantially alter the discharge performance.

It was noted in Section 3.2.6 that no significant difference was found for the discharge characteristics when small peaking capacitors were used. It can now be appreciated that this is due to the cable capacitance dominating the capacitances when small values were tested. With $C_p = 10$ nF, it was found that the formative time lag increased as compared to that condition which was defined as $C_p = 0$, i.e. when no peaking capacitor was intentionally placed across the discharge. This ' $C_p = 0$ ' condition must be modified to $C_p = 1.01$ nF to take account of the the cable capacitance.

It is interesting to note that Kharha positioned T2 close to the anode and hence the value of the stray capacitance measured across the discharge gap would have been smaller. Many laser systems position the final switch close to the anode to minimise the stray inductance in the circuit in order to maximise the rate of change of the discharge current; however, in the present case, the inductance is practically equivalent to the prototype as it is dominated by L_a . Because of the marked difference in waveforms obtained with $C_p = 10$ nF and when no peaking capacitor was intentionally placed across the discharge, it was decided to move T2 to underneath the laser cavity where the trigger wire coupling capacitors were initially placed. The results are discussed in Section 3.6.

3.2.8 Patterns Formed on the Anode and Cathode

During routine removal of the anode and cathode it was noticed that patterns existed on both electrodes, they ran transversely and seemed to correspond to shadows from the trigger wires. Hypotheses were developed to explain this physical phenomenon, Figure 3.22 shows a possible way in which these patterns were formed. The discharge is developing in a non-uniform manner across the trigger

wire - anode gap and the trigger wire - cathode gap. This results in non-uniform contact of the discharge with the electrodes, manifesting itself as the observed patterns due to the non-uniform sputtering processes. When the electrodes were subsequently installed, careful inspection of the discharge between the trigger wire gap and cathode supported this view. The discharge was non-existent between adjacent trigger wires but corona were visible surrounding their edge - a characteristic speckle pattern danced randomly over a small area of the cathode with a distinctive absence of glow between the trigger wires, this is evident from Plate 2, which shows the glow discharge - the cathode is the top electrode. This was more evident as the distance increased away from the trigger wires, and down the radius of curvature of the side of the cathode. It was impossible to observe this occurring on the anode through visual inspection of the discharge. If this is a correct interpretation of the discharge, the discharge volume is not that given by the dimensions of the electrodes but a smaller value dependent on the discharge spatial formation, which is in itself, dependent on the trigger wire geometry. Gain only occurs where there is discharge, this reduces the possible gain of the laser by an estimated factor of 2 and could account for the poor laser output characteristics. Figure 3.22 illustrates how the discharge splits into regions of gain and loss, depending on where the discharge is located. Further investigation would be needed to substantiate this view. For example, the spatial measurement of the electron density and the laser gain would provide invaluable information on the discharge processes at work.

Sometime after this hypothesis it was found that Tallman [3.19], in a general review of preionisation techniques, described a laser system with a mesh cathode and solid anode - the preionisation source was placed behind the cathode. It was observed that a pattern of the mesh electrode occurred on the anode, with a corresponding reduction in the discharge volume. Taylor [3.20] has reported laser action only occurring within the preionised volume. This tends to substantiate the view, mentioned above, of limited laser gain occurring within the discharge due to the poor spatial-uniformity characteristics of the discharge. Kharha [3.1] used longitudinal trigger wires and would have had gain throughout the complete length of the discharge. However, if poor preionisation was present in the prototype system, then this would be evident from a poor transverse mode structure because of the losses in this direction. Unfortunately, no mention is given on the transverse mode structure.

It is important to mention that as these patterns are observed they are indicative of a non-uniform electric field, which is in itself, a sufficient reason for arcing to develop in gas discharges [3.21].

3.3 DISCHARGE INITIATION THEORY

So far, experimental results have been presented without recourse to theoretical examination. This section describes the basic theory of transient discharges. Particular attention is given to the preionisation processes and the breakdown mechanisms which are relevant to the conditions encountered in the laser. The theory and experimental work in the literature is biased towards transverse excited atmospheric (TEA) lasers and is not strictly applicable to the present case, where the pressure is typically $\approx 40 - 300$ mb. Thus, some of the models developed for atmospheric pressure laser conditions require modification in order to study the discharge operation at lower pressures. Calculations are presented for the voltages satisfying the Townsend criterion for breakdown of the discharge gap. The streamer breakdown mechanism is analysed, values are calculated for the critical distance a streamer must propagate to ensure evolution of stable, glow discharges and the corresponding preionisation electron densities.

3.3.1 Discharge Breakdown Mechanisms

Consider two parallel, plane electrodes separated a distance d , with a gas mixture at pressure p between them. The cathode is irradiated with UV light which generates a constant photoelectric current, I_0 . If a voltage pulse of amplitude V_p , is applied to the anode then when $V_p = V_s$, where V_s is called the pulse breakdown voltage, electron avalanches start to develop between the electrodes. When these avalanches reach the cathode, breakdown of the discharge gap has occurred. There are many definitions for the precise moment at which breakdown is said to happen, for example, it occurs at the moment when substantial current starts to flow between the anode and cathode or when the secondary processes are able to sustain the current flow. The former definition is easier to determine experimentally and is the subject of discussion in Section 3.3.4.

When the discharge gap breaks-down, the secondary processes sustain the current flow, even if the initial source of ionisation is removed, i.e. $I_0 = 0$; the discharge is now called self-sustained. If a glow to arc transition (GAT) develops, the voltage between the electrodes collapses and the current flow increases exponentially, its growth is only limited by the external circuit resistance.

An important parameter for establishing the discharge development mechanism is the overvoltage, denoted ΔV , and defined as

$$\Delta V = V_p - V_s$$

3.6

The self-sustained discharge only develops when $\Delta V > 0$. Four different breakdown mechanisms can be defined, each with a separate model, the operative one depends on the magnitude of the overvoltage applied to the electrode, in each case the discharge is still self-sustained. In order of increasing ΔV , the models are [3.9]: the Townsend, streamer, avalanche chain and the continuous acceleration model. The last two are for high overvoltages, typically 200 – 300 % of V_s , they lie outside the region of interest and are not discussed. The first two breakdown mechanisms are approximately split as follows, Townsend breakdown for $\Delta V < 20$ % of V_s , and streamer breakdown for $\Delta V > 20$ % of V_s . The former is characterised by the absence of space charge effects perturbing progression of the avalanching wave, whereas space charge effects are crucial for development of the streamer breakdown mechanism. Unification of the models into a single model, applicable for all four breakdown regimes has been given [3.22]. For simplicity, however, the single models developed for predicting the Townsend and streamer breakdown mechanisms will be used.

With increasing ΔV the formative time lag is reduced, i.e. it takes less time for the current to grow after application of the voltage to the electrodes [3.9]. This can be explained as follows: increasing ΔV , increases the applied electric field, E , consequently the primary ionisation coefficient, α , increases. The ionisation processes increase and electron multiplication occurs more efficiently. At a particular overvoltage the streamer breakdown mechanism becomes operative, which reduces the formative time lag still further.

For uniform electric fields and constant E/p values, the pre-breakdown current, I , develops according to Townsend by [3.8]

$$I = \frac{I_0 \alpha \exp([\alpha - \eta]d) - \eta}{[\alpha - \eta - \alpha \gamma \exp([\alpha - \eta]d - 1)]} \quad 3.7$$

Where the symbols represent the following coefficients

α : ionisation coefficient

η : attachment coefficient

γ : generalised, secondary net ionisation coefficient

The value of the applied voltage at which the current becomes self-sustainable can be found from the Townsend sparking criterion [3.8], and is obtained by setting the denominator in equation 3.7 to 0, thus

$$1 - \frac{\alpha\gamma}{\alpha - \eta} \left[\exp([\alpha - \eta]d - 1) \right] = 0 \quad 3.8$$

For steady state conditions, equation 3.8 is satisfied when the applied voltage, denoted by V_s' , is slightly less than V_s , i.e. the pulse breakdown voltage is normally greater than the steady state breakdown voltage. However, it is informative to solve equation 3.8, and in doing so, it is important to have accurate data for both α and η which are functions of E/N , i.e. $\alpha = \alpha(E/N)$ and $\eta = \eta(E/N)$. The value of γ is generally not known and estimates are used, typically $\gamma = 0.1$; it is usually assumed γ is independent of E/N [3.8]. Hasan [3.2] solved the Boltzmann transport equation for various gas mixtures pertinent for CO_2 gas lasers, found the electron energy distribution function (EEDF), and calculated the values of $\alpha(E/N)$ and $\eta(E/N)$ by summing over the inelastic processes responsible for electron production and electron losses respectively. However, the results were not consistent with other published values, for example Lowke [3.5]. Consequently, values were abstracted graphically from Lowke, whose results have agreed with subsequent workers, both theoretically and experimentally [3.23,3.24]. The estimated error from reading the data was approximately $\pm 7\%$.

It is conventional to fit ionisation and attachment data in the form $A \exp(-BN/E)$, where A and B are constants, but such fits are usually inaccurate over a wide range of E/N . Hence, it was attempted to use high order polynomials, up to degree 8, but similar inaccuracies were observed over the E/N range of interest. Typically, errors for $E/N > 3 \times 10^{-16} \text{ Vcm}^2$ were $< 10\%$, but for lower E/N values the errors were as great as 500% . Because of these errors, the data was fitted using splines. However, no extrapolation can occur with reliability outside the range of values over which the data is taken [3.25].

By solving equation 3.8 with the data for a 1:1:8 gas mixture, the voltage V_s' was found and compared to the measured values of the quasi-steady discharge voltages, denoted by V_d . Appendix B2 details the code. Figure 3.23 shows the breakdown voltage, denoted by V_s' , as a function of gas pressure for a discharge gap of 4 cm. Assuming that $V_s \approx kV_s'$ where k is some constant approximately equal to but greater than unity, then the breakdown voltage as indicated from Figure 3.23 is, as one would expect from Paschens law, proportional to the gas pressure. The value of V_d was calculated by multiplying the value of E/p by the gas pressure and the electrode spacing. V_s' was multiplied by 1.2 to give the approximate regime in which the streamer breakdown was observed. It is seen that V_s' is greater than V_d . For a 1:1:8 gas mixture at 160 mb with the DC voltage at 8.2 kV (60% tapsetting) and $L_a = 36 \mu\text{H}$ the maximum applied voltage between the electrodes

was measured as 7.087 ± 0.031 kV, and $V_d = 3.986 \pm 0.025$ kV, where the errors are the standard error of the mean for a sample size of 10. The measured peak value is about 1.78 times larger than the measured value of V_d . If $k \approx 1$, it is probable that the discharge would breakdown via the streamer mechanism. However, if $k \approx 2$ or greater, the streamer breakdown mechanism will not occur.

For the above discussion it was assumed that $\gamma = 0.1$ and that it was independent of E/N . Figure 3.24 shows a graph of V_s' and $1.2 \times V_s'$ as a function of γ for a pressure of 160 mb and 1:1:8 gas mixture. It is evident that the value of V_s' is fairly insensitive to the value of γ , a 50 % change in γ results in only ≈ 500 V change in V_s' . It is also interesting to note that increasing γ slightly decreases the value of V_s' . This is because with a higher secondary ionisation coefficient the voltage does not need to be so great to provide the necessary feedback to sustain the discharge.

3.3.2 Streamer Breakdown

For overvoltages in excess of 20 % of V_s , the streamer breakdown mechanism occurs, this is characterised by short formative time lags and a filamentary discharge. TEA laser discharges generally operate under streamer breakdown conditions, with $Pd \approx 1500$ torr-cm and applied voltages in excess of 20 kV. The overvoltage causes photoionisation in the gap ahead of the avalanche. Raether [3.26] states that the photoionisation occurs when the avalanche reaches a critical dimension, the size of which depends on the space charge effects introduced by the avalanching wave. This photoionisation causes enhancement of the electric field, with a resultant increase in the local value of α . Electron multiplication occurs more efficiently, and the space-charge cloud increases rapidly in size, eventually growing to the same size as the initial parent cloud, and closer to the anode. This streamer process repeats until the family of avalanches reach the anode. A secondary wave then starts propagating towards the cathode. Kline [3.27] solves spatio-temporal continuity equations in order to examine the discharge initiation phase in overvolted parallel plane gaps.

Palmer [3.28] developed criterion for the initial electron density necessary to ensure development of stable, atmospheric-pressure glow discharges via the streamer breakdown mechanism. The space-charge field for a single avalanche was calculated and equated to the applied electric field, E . This resulted in an expression for the critical distance, z_c , over which the avalanche must propagate for initiation of uniform, streamer breakdown; z_c is given by Palmer as

$$\alpha z_c = \ln \left[\frac{4 \pi \epsilon_0 E \lambda_e}{e} \right] + \ln z_c \quad 3.9$$

Where λ_e is the electron mean free path, and given by [3.8]

$$\lambda_e = \frac{1}{\pi \sum_r \left[n_r d_{er}^2 \left[1 + \frac{m_e}{M_r} \right]^{0.5} \right]} \quad 3.10$$

The summation is taken over the molecular species present in the laser gas mix, subscripted r ; n_r is the partial molecular number density of species r , such that

$$\sum_r n_r = N \quad 3.11$$

d_{er} is the average diameter of: the molecular species r , denoted d_r , and the electrons. M_r and m_e are the species r molecular and electron mass respectively. Clearly some simplifying assumptions can be made. The molecular mass is much greater than the electrons, i.e. $M_r \gg m_e$; hence, $m_e/M_r \ll 1$, and can be neglected. The molecular diameters for CO_2 , N_2 and He are, in units of 1×10^{-8} cm, 3.32, 3.28 and 2.35 respectively [3.29]. The electron radius is, classically, 5.6×10^{-13} cm [3.30] and negligible. For the 1:1:8 mixture the weighted average molecular diameter squared, d_a^2 , is 6.596×10^{-16} cm². With all of these assumptions equation 3.10 reduces to

$$\lambda_e = \frac{4}{\pi N d_a^2} \quad 3.12$$

Substituting $d_a^2 = 6.596 \times 10^{-16}$ cm, and using $N=p/kT$, then for $T=300$ K, the value of λ_e is given by

$$\lambda_e = \frac{7.995}{p} \quad \text{cm} \quad 3.13$$

Where λ_e is expressed in cm and p in mb. It is seen that reducing the gas pressure, increases the mean distance travelled by the electrons between collisions. Thus, for a given applied voltage, the affect of reducing the pressure is to increase the mean electron energy of the gas mixture. The number of electrons in the high energy tail of the EEDF will increase, and electron production through collisional ionisation and photo-ionisation will occur more readily. Consequently, it

is to be expected that the streamer breakdown mechanism will occur, in the present case, for lower values of applied field than is common for TEA lasers. However, the reduction in pressure implies a reduction in the number of species available for producing the VUV radiation, i.e. from the excited states of N_2 . To compensate for this, gas mixtures rich in N_2 would serve to increase the VUV production and consequently increase the level of preionisation, provided that enough gas impurities were present within the gas; also the high N_2 content would increase the reservoir of energy for the upper laser level of CO_2 . This argument is consistent with the experimental results of Kharha [3.1], where it was found that mixtures with a higher content of N_2 than CO_2 were more stable.

The term in square brackets, in equation 3.9, is a slowly varying function, and for air has a value of 20 in MKS units [3.28]. If $z_c = d$ then Raethers criterion is obtained for the streamer breakdown mechanism, and is given by:

$$\alpha d = 20 + \ln d \quad 3.14$$

To analyse development of the discharge operating under the streamer breakdown conditions for the present laser system, it is necessary to calculate the term in square brackets in 3.9, and solve for z_c .

A necessary constraint to ensure discharge uniformity is an initial electron number density, n_0 , such that spatial overlap of the parent avalanches occur. For every initial electron an avalanche develops which has its own space-charge field; thus, if n_0 is sufficiently high, the space-charge associated with every avalanche becomes uniform over the electrode area. This smoothing of the electric field results in uniform glow discharges which do not possess the normal streamer filamentary characteristics. Palmer [3.28] concluded that the requirement for n_0 is given by

$$n_0^{-1/3} < (\lambda_e z_c)^{1/2} \quad 3.15$$

Where z_c is found by solving equation 3.9. Palmer states that for TEA CO_2 lasers, the value of the initial preionisation electron density must satisfy the inequality: $n_0 > 10^4 \text{ cm}^{-3}$, and that this is consistent with experimental observations.

Substituting in values of E and λ_e typical of the present laser system, then given a value of d the applied voltage to the electrodes is known and the corresponding value of z_c can be calculated by solving 3.9. Substituting these values into 3.15 the minimum required electron density can be determined. A MathCad code was developed to fit the data, solve 3.9 for z_c and calculate n_0 , see Appendix B3.

Figure 3.25 and 3.26 show the variation of n_0 and z_c respectively, as a function of E/N , for a 1:1:8 gas mixture. Clearly, with increasing E/N the required initial electron density must increase to ensure uniform glow discharges. With low values of E/N , z_c is large and the value of n_0 is small.

As a particular example, consider the 1:1:8 gas mixture at a pressure of 160 mb, typical values of the applied electric field are $\approx 8 \text{ kV} / 4 \text{ cm} = 2 \text{ kV cm}^{-1}$, assuming that the discharge is breaking-down via the streamer mechanism, then this results in $z_c \approx 3 \text{ cm}$. A uniform glow discharge is occurring; but only in the lower quarter of the discharge, i.e. for a distance greater than 3 cm from the cathode. This is difficult to prove experimentally, but the consequences are dramatic. Most of the discharge is developing in an unstable manner, and as indicated by Palmer [3.28] it is of vital importance to ensure that the discharge is initiated uniformly. Any discharge inhomogeneities rapidly develop into arcs – leading to non-uniform discharges. After the discharge development phase, the discharge shape is dependent upon the spatial form of the secondary ionisation coefficient. For a transverse trigger wire arrangement – the uniformity of γ is severely degraded. Thus the affect of the non-uniform electric field and the positioning of the trigger wires is to enhance the probability of the discharge developing into arcs. It would be interesting to analyse the spatial variation of the laser gain in an attempt to further understand the physical processes at work and assess the dependence of the laser gain on the discharge initiation phase.

It is seen that as E increases the value of z_c decreases. Provided that the initial electron densities are met, then for high overvoltages a greater proportion of the discharge volume is uniform. For example, if $E = 6 \text{ kV cm}^{-1}$, then $z_c \approx 0.20 \text{ cm}$. If $d = 4 \text{ cm}$ this corresponds to an applied voltage of 24 kV, and $n_0 \approx 10^5 \text{ cm}^{-3}$, which is typical of TEA laser systems.

3.3.3 Requirements for Efficient Preionisation

It is important that the preionisation perpendicular to the applied electric field is homogeneous in order to ensure discharge uniformity [3.21]. Evidence from operation of the laser indicates poor preionisation. The preionisation requirements are discussed, clarifying the objectives for proper development of the laser preionising system.

The processes involved in VUV preionisation of CO_2 gas discharge lasers are well known [3.31]. Photoionisation processes occur by the interaction of VUV light with

impurities in the laser gas mixture about two gas transmission windows, at the wavelengths of 120 nm and 175 nm; the corresponding photon energies are 10.33 and 7.08 eV respectively. Low ionisation potential impurities were found to be responsible for generation of the photoelectrons through a single step ionisation process. For efficient preionisation two conditions must be met: VUV radiation at the correct wavelength must be generated and low ionisation impurities must be present in the gas mixture. The discharge uniformity is determined by the geometrical interaction of the VUV flux with the discharge volume, and absorption of the flux by the LIP gases. Several authors indicate 2 possible processes responsible for maximising VUV production; namely, high di/dt 's [3.14], typically 10^{10} A s^{-1} or high currents [3.15]. As can be seen from Section 3.2.4 neither of these conditions are met; this results in poor preionisation uniformity, and consequently, low laser output power and the development of discharge instabilities.

VUV light is one method of preionisation, other techniques exist, for example, electron beam preionisation, which is an excellent method of initiating and stabilising discharges [3.32]. An electron beam is injected between the electrodes, the electron range must be greater than the electrode spacing to ensure a uniform spatial electron density distribution. Continuous and precise control of the electron density is available by adjusting the electron beam current, this provides additional stability through optimisation of the electron density at any moment in time. The injected electrons provide the secondary mechanism to sustain the discharge. The operating E/p value of the discharge can be optimised to maximise the pumping rate of the upper laser level. Fortunately, the required electric field between the electrodes for optimum pumping is much lower than that required for self-sustained discharges. Thus, the Townsend breakdown mechanism is not operative and the discharge cannot develop into arcs via this mechanism.

X-rays are also used as preionising sources and this method dominates preionisation of excimer lasers [3.33]. Several authors have used X-ray preionisation for CO_2 lasers [3.34]; however, the most widely used source of preionisation is VUV radiation. This is due to the relative ease with which the light can be generated as compared to the complex engineering designs for electron beam, X-ray, or even gamma-ray preionisation [3.35]. Because of the simplicity of VUV preionising techniques; it was decided to maintain corona preionisation, which by definition, relies on non-uniform electric fields for the generation of the VUV light and subsequent creation of the initial preionising electrons. However, improvement of the preionising system was crucial to enhance the discharge and laser performance.

In order to develop a satisfactory preionisation source it is useful to quantify the

preionisation requirements, they are as follows:

1) Generate VUV flux for efficient volumetric preionisation, i.e. $di/dt's \geq 10^{10} \text{ As}^{-1}$ and/or large corona currents. The lateral uniformity of the applied electric field perpendicular to the trigger wires is important to ensure the glow is uniform [3.21].

2) Ensure there are impurities within the gas mixture, industrial grade He is sufficient; however, improved performance may be obtained by deliberately adding small quantities of LIPS.

If the above requirements are met, then the initial electron densities will be sufficient - i.e., $n_0 \geq 10^4 \text{ cm}^{-3}$ - to ensure development of stable, uniform glow discharges and an increased laser output power.

McDonald [3.13] considered the propagation of the ionising wave due to the initial trigger wire current. For a 1:1:4 gas mixture at 156 mb, it was concluded that the effective trigger wire current was $\approx 2 \text{ A}$. This yields, for a discharge area of $84 \times 6 \text{ cm}^2$ and an electron drift velocity of $0.97 \times 10^7 \text{ cm s}^{-1}$, an average, initial preionising electron density of $\approx 2.6 \times 10^9 \text{ cm}^{-3}$. This value is sufficient for efficient preionisation. But, a further requirement is that the electron density is spatially uniform, such information is unavailable from this simple calculation. However, the patterns observed on the electrodes (see Section 3.2.8) tend to indicate the development of a non-uniform discharge, which in itself, maybe due to a non-uniform preionising electron density. A measurement of the spatial distribution of the preionising electron density would provide important information for developing a preionising system.

For VUV generation at the trigger wires, assuming that the criterion $dI_{tw}/dt > 10^{10} \text{ As}^{-1}$ must be met; then, from the circuit in Figure 3.21

$$\frac{dI_{tw}}{dt} = \frac{V_{tw}}{L_{tw} + L_{sc}} \quad 3.16$$

Where V_{tw} is the trigger wire voltage, L_{tw} the effective inductance of the trigger wires and L_{sc} the stray inductance of the cathode and cathode support. From Figure 3.21, it is apparent that the total inductance L_T is given by the anode inductance, L_a , in series with the stray inductance of the URm74 connecting cable, L_{ca} , and the stray inductance of the laser structure, L_{st} ; thus

$$L_T = L_a + L_{ca} + L_{st} \quad 3.17$$

Where $L_{st} \approx L_{sa} + L_{sc}$

From Section 3.2.4, the voltage at which the trigger wire gap broke-down, and the rate of change of current were measured as 1.5 kV and $6.75 \times 10^8 \text{ A s}^{-1}$ respectively. This leads to a value for the inductance of the trigger wire circuit and the cathode stray inductance of: $L_{tw} + L_{sc} \approx 2.2 \text{ } \mu\text{H}$.

From equation 3.16, it is apparent that there are two methods to increase the rate of change of current through the trigger wire gap, dI_{tw}/dt . The simplest technique is to reduce L_{tw} and/or L_{sc} . The second method is to increase the voltage; however, the maximum voltage is fixed by the requirements of the discharge energy, a maximum of 20 kV is possible with the 50 nF capacitance of the PFN – i.e. a total energy of 10 J. This is insufficient to obtain the necessary di/dt 's; hence – the inductance must be reduced. The voltage across the trigger wires can be increased by reducing the inductance L_a .

Improved laser performance has been reported by Tallman [3.19] in systems where a separate preionising system was used. This allows greater control over the timing of the pulse with respect to the main anode pulse; although for CO_2 lasers, this timing is not critical, as it is for example with excimer lasers. Moreover, for CO_2 lasers, the amplitude of the voltage and current pulses are easily controlled, thus the level of preionisation can be finely tuned. McDonald [3.13] fabricated an independent preioniser, and successfully showed that the discharge could be initiated. However, the preioniser was designed to deliver trigger wire voltage and current pulses of the same magnitude as that obtained by capacitively coupling energy from the main anode pulse. These pulses typically had a voltage amplitude of 3 kV and a peak trigger wire current of 70 A. Hence, the same level of preionisation was obtained from both systems – consequently, no improvement in the discharge stability was observed. No experiments were undertaken to examine the possible affect on the laser output power.

It was decided to investigate the performance of the laser with a high voltage preioniser. As the main transformer was limited in its range of tapsettings, it was decided to supply the power for the preioniser from an independent high voltage supply. Section 3.6 details the design and performance of the H.V. preioniser

The PFN design, discussed in Chapter 2, had a specification of a $1 \text{ } \mu\text{s}$ rise time on the voltage and current pulse. It can now be appreciated that this will not help the discharge development and stability. The component values of the last mesh –

and the associated stray values close to the laser head - are of the utmost importance in determining the rise time of the pumping pulse and, consequently, the probability of the discharge arcing. Partly as a consequence of this, the discharge thyatron was repositioned underneath the laser cavity to minimise the stray inductances.

3.3.4 Formative Time Lag Calculations

Calculation of the formative time lags, denoted by τ_b , in gas discharges usually requires numerical solution of spatio-temporal continuity equations; expressing all electron, positive and negative ion loss and creation processes [3.27]. Fortunately, with some simplifying assumptions, moderately accurate estimates can be obtained. In practice, it is difficult to experimentally determine the moment of breakdown of the gap. As a consequence, Crawford [3.12] arbitrarily defined the formative time lag as the period for the discharge current to grow to 10 A. This relatively high value of discharge current - as compared to the pre-breakdown current which is typically fractions of micro-amps - is easy to measure, hence, this definition facilitates measurement of the formative time lag.

Klines and Denes [3.21] derive a simple equation to estimate the time for the discharge current density to grow to the value j_b , where

$$j_b = \frac{i_b}{A} \quad 3.19$$

i_b is the current flowing between the electrodes of area A.

If losses to the electrodes are neglected then the formative time lag is given by

$$\frac{1}{\tau_b} = \frac{\frac{W_e}{N} (\alpha - \eta)}{\ln \left[\frac{j_b}{e W_e n_0} \right]} \quad 3.20$$

Where W_e is the electron drift velocity.

W_e , α and η are functions of the applied field and the gas pressure. For given values of the applied voltage, discharge gap and gas pressure, values of W_e , α and η at this specific value of E/N are substituted into equation 3.20 and then τ_b can be found. This expression is only valid for formative time lags, less than or equal

to half the electron transit time between the electrodes.

The electron drift velocity is approximately proportional to the applied electric field, the constant of proportionality being mobility, denoted μ , thus $W_e = \mu E$. From the data abstracted from Lowke [3.5], and given in Appendix B2, values of τ_b were calculated as a function of E/N for various initial preionisation electron densities, denoted n_0 . Figure 3.27 shows the results with $n_0 = 10^4, 10^6$ and 10^8 cm^{-3} . Clearly, with increasing preionisation electron densities the formative time lag decreases for a given applied E/N . With increasing E/N , i.e. increasing applied voltage or a reduction in pressure, the formative time lag reduces.

3.4 PULSED DISCHARGE SIMULATION USING PSPICE

It was noted in Section 3.2.7, by Crindland [3.12], Kline [3.21] and Scott [3.36] that circuit components have a large influence over the breakdown characteristics of gas discharges. Most models which predict the discharge development phase take little account of their affects; clearly in the present case, circuit components are dominating discharge development. Most discharge modelling is complex and requires extensive effort to obtain results that are, in reality, only as reliable as the input data. The ability to calculate approximate solutions, providing quick and quantitative assessment of the affects of circuit components, is a valuable tool in optimising the laser system. PSPICE, a commercially available software package, is specifically designed to facilitate modelling of electrical circuits, and ideal for studying the transient development of the discharge for different component values. However, it was necessary to develop a method of modelling discharges on PSPICE, as no such facility previously existed. The result is an easily accessible code which provides insight into the affects of circuit components on gas discharge initiation and development.

Following a discussion on the PSPICE code, attention is given to the predicted results for a laser gas mixture of 1:1:8, in which the affects of: the gas pressure, network voltage, peaking capacitance, inductance on the anode of T2, and the initial preionisation electron density, are examined

3.4.1 Model of the CO₂ Laser Gas Discharges

The temporal electron continuity equation is solved, this gives the number of electrons, at any time, that exist between the electrodes. The current flow is

simply calculated from knowledge of: the electron density, electrode area, drift velocity of the electrons and the electronic charge. The primary assumptions of the model are that the discharge volume is perfectly preionised with an electron density n_0 ; and that no electrode losses occur, i.e. the current flow causes no electron losses, this implies that the anode and cathode currents are equal. If short formative delay times occur then the discharge can be modelled as a homogenous positive column [3.21]. If recombination is assumed negligible, then the temporal electron continuity equation is

$$\frac{dn_e}{dt} = \alpha W_e n_e - \eta W_e n_e \quad 3.21$$

Integration of this equation leads to

$$n_e(t) - n_e = n_0 \exp \left[\int_0^t (\alpha - \eta) W_e dt \right] \quad 3.22$$

Where n_0 is the electron density at time 0. The current, as a function of time, is related to the electron density through the relation

$$I(t) = n_e e A W_e \quad 3.23$$

A is the electrode area, and e the electronic charge. Substituting for n_e from 3.22 into 3.23, then equation 3.23 becomes

$$I(t) = n_0 e A W_e \exp \left[\int_0^t (\alpha - \eta) W_e dt \right] \quad 3.24$$

The PSPICE circuit model of the discharge can be seen in Figure 3.28. The behavioural modelling option on PSPICE is used, where the Keyword [3.37] is specified as TABLE. The values for α , η and W_e are then entered at specific values of E/N , i.e. as a table. As the voltage pulse V_p is applied between the anode and cathode, the E/N value is calculated for the given gas pressure and electrode spacing and the corresponding values of W_e , α and η are determined. PSPICE performs linear interpolation between the values entered in the table. When the values have been found the current source, GI, assumes the value $(\alpha - \eta)W_e$. It is seen from equation 3.24 that this function has to be integrated; this is achieved by placing a 1 F capacitor across the terminals of the current source. The resistor R_3 is necessary because PSPICE does not allow nodes to float from earth potential. Thus, the voltage at node 3 is given by

$$V_3 = \int_0^t (\alpha - \eta) W_e dt \quad 3.25$$

The current source, GD, is then used to calculate the discharge current; $\exp[V(3)]$ is multiplied by the appropriate values to obtain the expression:

$$\text{GD } \langle \text{anode} \rangle \langle \text{cathode} \rangle \text{ VALUE} = \{ n_0 * W_e * A * e * \exp(V(3)) \}$$

In Figure 3.28, the resistors labelled R_4 , R_5 and R_6 are used to prevent nodes 4, 5, and 6 respectively, from floating.

Various values associated with the laser system are entered as parameters, for example: the discharge gap, d ; gas pressure, p ; initial preionisation electron density, n_0 ; peaking capacitance, C_p ; and the network voltage, V_N . Entering the parameters in this manner enables PSPICE to perform parametric analysis. The chosen values of one parameter are entered, then the PSPICE code solves the circuit for each value defined for that parameter. The corresponding graphs give an immediate indication of the affect of varying that parameter.

3.4.2 Evaluation of the Simulation Validity

In an attempt to validate the code, comparisons were initially made to the results reported by Kline [3.21] where the initial preionisation electron densities were sufficient to satisfy the assumptions used in developing the model; and also, short formative time lags were observed. The circuit used by Kline is shown schematically in Figure 3.29; the corresponding voltage, discharge and capacitance current, as predicted by the model, can be seen in Figure 3.30. Unfortunately, the comparison is not exact as a 1:7:0 gas mixture was used by Kline and, as the data for this mixture was unavailable, the data for a 1:1:8 composition was used. However, the system pressure was increased so that the same quasi-steady voltage was developed across the electrodes. It is seen that the model predicts a formative delay time of 35 ns, which is typical of that observed by Kline.

Clearly, the most reliable method to validate the code is to compare the experimental and theoretical waveforms obtained under identical conditions. In order to achieve this under the present conditions, a more realistic representation of the pulser components must be incorporated into the model. The PFN is modelled as lumped component values (see Chapter 2, Section 2.2) which are charged to the network voltage, V_N . The initial condition command is used on all the PFN capacitors, i.e. $IC = \{V_N\}$, where V_N is defined as a parameter. The

thyratrons are modelled as switches in series with diodes; the affect of the stray capacitance, C_{st} , across the thyatron can easily be included. Figure 3.31 shows the equivalent circuit that was developed to model the thyratrons. Switches in PSPICE have an "on" and "off" resistance, represented by R_{on} and R_{off} respectively. The value chosen for R_{on} was low, typically 1Ω , which is representative of the expected tube losses for the experimentally measured current levels, i.e. a voltage drop of a few hundred volts can exist across the thyatron while it is conducting. The complete PFN circuit coupled to the discharge circuit model can be seen in Figure 3.32.

Figure 3.33 shows the V-I characteristics predicted from the model for a 1:1:8 gas mixture at a pressure of 160 mb, with $V_N = 8.4$ kV and an electrode spacing of 4.0 cm. Clearly, the pulse characteristics are similar during the latter stages of the pulse to those obtained experimentally, see Section 3.2.3. But as expected, the formative delay time is not accurately modelled because of the inherent assumptions of the model, i.e. the discharge volume is perfectly preionised with an initial electron density of n_0 , in this particular case a value of 10^8 cm^{-3} was selected.

3.4.3 Affect of Gas Pressure on Discharge Performance for a 1:1:8 Gas Mixture

Figures 3.34 and 3.35 show the voltage and current traces for the 1:1:8 gas mixtures at pressures of 120 mb, 140 mb and 160 mb, the time base is from 0 to $12 \mu\text{s}$, the discharge thyatron is triggered after 100 ns from time 0. The values of the parameters are shown as inserts within the graphs. Clearly, the pulse shapes are similar to the experimentally obtained waveforms described in Section 3.2.3, see for example Figure 3.12. As expected, increasing the pressure results in an increase in the discharge voltage and a corresponding reduction in the discharge current.

Figures 3.36 and 3.37 show the same graphs as the previous two, but on an expanded time base, between 100–300 ns. They show that the formative time lag is practically independent of gas pressure over this small pressure range. The lower pressures have a slightly lower value, but all are approximately 125 ns for the given conditions.

It can be concluded that the affect of the system gas pressure is most predominant over the quasi-steady pulse shape characteristics (i.e. the plateau values); and for the pressure range considered in the present case, the affect on the formative time

lag can be neglected. Figures 3.38 and 3.39 show the rate of change of the discharge voltage and current with respect to time for a gas pressure of 120 mb.

3.4.4 Affect of Network Voltage

The network voltage, V_N , assumed values of: 10 kV, 15 kV and 20 kV. Figures 3.40 and 3.41 depict the discharge voltages and currents respectively for a pressure of 160 mb at these values of V_N . It is immediately apparent that the formative time lag decreases for the higher network voltages. This can be appreciated because: with higher values of V_N , the applied electric field is greater, consequently the ionisation coefficient increases, resulting in a larger electron gain and faster breakdown of the gap. Figure 3.42 and 3.43 show the rate of change of the discharge voltage and current respectively, for different network voltages. It is seen that as V_N increases dV/dt and dI/dt increase.

3.4.5 Affect of Peaking Capacitance

The affect of placing a peaking capacitor parallel to the electrodes can be seen in Figures 3.44 and 3.45, they show the voltages and currents respectively for peaking capacitor values of: 11 pF, 50 pF, 200 pF and 1010 pF. Clearly, increasing the size of the peaking capacitor, decreases the rate of rise of the discharge voltage and increases the formative time lag. Energy is stored in the peaking capacitor prior to breakdown of the gap; when the discharge current starts to flow, the stored energy quickly transfers to the discharge, manifesting itself as a larger current than if the peaking capacitor was not present. Figures 3.46 and 3.47 show the rate of rise of voltage and current, with respect to time, as a function of the value of the peaking capacitor. It can be seen that the advantage of using a large peaking capacitor is that it increases the rate of change of current through the discharge. However, there is no extra benefit in increasing C_p beyond a certain value as di/dt does not increase; i.e. compare the graphs for $C_p = 200$ pF and $C_p = 1010$ pF. According to Bushnell [3.17], for example, increasing C_p results in an increased level of preionisation and laser output. It must be remembered that for this analysis the peaking capacitor is directly connected to the anode of the laser with no stray inductance included in the circuit, which of course would limit the rate of change of discharge current considerably.

It is important to remember that the model assumes the gap is perfectly preionised with a uniform electron density, which in this case is 10^8 cm⁻³.

3.4.6 Affect of Discharge Thyatron Anode Inductance

Figures 3.48 and 3.49 show the theoretical discharge voltages and currents that are obtained with different inductances placed on the anode of the discharge thyatron (T2), this inductance is represented by L_1 for the PSPICE model (i.e. the last inductance on the PFN). The values selected for comparison were: 1 μH , 9 μH and 32.6 μH . The mutual inductances M_1 and M_2 were kept constant at 0.15 and 0.05 respectively. It is seen that, from Figures 3.50 and 3.51, reducing the value of L_a : reduces the formative time lag, increases the rate of change of the discharge voltage and the rate of change of the discharge current.

3.4.7 Affect of Initial Preionisation Electron Density

Figures 3.52 and 3.53 show the voltage and current traces respectively, for initial preionisation electron densities of 10^7 cm^{-3} , 10^8 cm^{-3} and 10^9 cm^{-3} . It is seen that increasing the value of n_0 reduces the formative time lag and the initial peak current. Figures 3.54 and 3.55 show the rate of change of the discharge voltage and current respectively, for different values of n_0 . It is seen that decreasing the initial electron density results in a higher rate of change of the discharge voltage and current.

3.5 INDEPENDENT PREIONISER

The effect of changing the coupling capacitance was discussed in Section 3.2.6. It was found that changing C_c had negligible influence on the peak current flowing through the trigger wires and on the discharge performance. It is apparent that the trigger wire voltage will rise to a value determined by the L-C characteristics of the laser circuit and the time taken for the electrons to traverse the trigger wire gap. In order to develop high values of dI_{tw}/dt , it is important that the trigger wires are hit with a fast voltage pulse, which quickly rises before the trigger wire voltage has a chance to collapse. When the trigger wire voltage does collapse, the trigger wires are capable of passing substantial current without any change on the preionisation of the laser volume.

Because of the inability to finely control the voltage developed across the trigger wires whilst using the capacitive coupling technique of preionisation, it was decided to fabricate a separate preioniser supply, from which high values of dI_{tw}/dt could be generated, and hopefully, a higher level of preionisation would be obtained. A

further advantage is that the triggering of the preionisation pulse, relative to the main switch (T2) firing, can be optimised. McDonald [3.13] fabricated a separate preioniser, but the design was such that it delivered voltage and current pulses of the same magnitude as that which was readily available from the capacitive coupling source of preionisation. Hence, no improvement in the laser output power or discharge stability was observed. However, it was demonstrated that a glow discharge could be obtained. The major disadvantage of using a separate preioniser is the corresponding increase in the system complexity. Capacitively coupling energy from the main anode voltage is simple and hence preferable if satisfactory performance can be obtained. There are methods to increase the performance of this technique, for example, increasing the relative permittivity of the dielectric medium (ϵ_r) [3.38].

3.5.1 Preioniser Design

The preioniser circuit can be seen in Figure 3.56. The high voltage transformer was rated at 30 kVA, with a maximum available voltage of 10 kV. Figure 3.57 shows the rectified, but unsmoothed output voltage from the transformer. The smoothing capacitance, C_{sp} , was 0.5 μF . Capacitor C_{1p} was resonantly charged via the inductor L_{cp} , within a time of 80 μs , this allows operation of the preioniser at the full specification frequency of 10 kHz. The inverse diode stack dissipates any negative residual on C_{1p} . The tailbiter thyatron (type CX1528) was used, and the trigger circuitry developed by McDonald [3.13]. The charging diode D_p prevents any current reversal through L_{cp} . The 1:1 pulse transformer (PT_p) provides electrical isolation between the trigger wires, the thyatron and C_{1p} . The advantages of using the pulse transformer are that the cathode of the thyatron (TP) can be grounded, and the trigger wire polarity easily reversed by changing the connections from the pulse transformer. Marchetti [3.38] reports obtaining significant differences in the preionising electron density by reversing the polarity of the preionising source.

To commission the preioniser with the trigger wires as the load, the smoothing capacitor was resistively charged from a 20 kV RMS supply, which was rated at only 200 VA; thus, only single shot experiments could be performed. However, it was hoped that this would provide insight into the value of the stray inductance of the laser structure, and the general behaviour of the trigger wires and the preioniser. With a gas mixture of 1:1:0 at a gas pressure of 40 mb, the voltage and current pulse widths were measured at, typically, 30 ns. It was estimated – from knowledge of the capacitance of the trigger wires and the measured pulse

width - that the inductance of the preioniser, the trigger wires and the laser structure was approximately, only $0.450 \mu\text{H}$. However, the pulse shape was found to be extremely irregular and erratic on the first pulse and this value is likely to be erroneous. These results are not presented explicitly, however, the affect on the trigger wire characteristics of running the preioniser under single shot and burst mode conditions is discussed in Section 3.5.3.

According to the model discussed in Section 3.2.4 the trigger wire behaviour can be split into two regimes: the pre-breakdown and the post-breakdown phase. The capacitance of the trigger wires attributed to each phase is, approximately, 0.36 nF and 7.6 nF , and denoted by C_{tw} and C_e respectively. The effective capacitance of the last stage of the preioniser, prior to breakdown of the trigger wire gap, and denoted by C'_{ep} , is given by the series combination of $C_{1\text{p}}$ and C_{tw} . In this case $C_{\text{tw}} = 0.36 \text{ nF}$ and $C_{1\text{p}} = 5 \text{ nF}$, hence $C_{\text{ep}} = 0.3358 \text{ nF}$. The time of this current pulse is denoted by τ'_{p} . When the trigger wires breakdown, the trigger wire capacitance assumes a different value, denoted by C_e , thus the effective capacitance after the breakdown of the trigger wire gap is given by the series combination of C_e and $C_{1\text{p}}$, and denoted by C_{ep} and has a value of 3.0159 nF . The width of this current pulse is denoted by τ_{pb} . Thus it is apparent that the ratio of the current pulse widths during the pre-breakdown and post-breakdown phase is given by

$$\frac{\tau'_{\text{p}}}{\tau_{\text{pb}}} = \left[\frac{C'_{\text{ep}}}{C_{\text{ep}}} \right]^{1/2} \approx 0.11 \quad 3.26$$

Similarly, the peak current flowing through the trigger wires, which is dependent on the ratio of the square root of the effective capacitances, is approximately 11 % larger once breakdown has occurred. This is assuming that the voltage is constant across the trigger wires.

From Section 3.2.4 it was noted that the trigger wire breakdown voltage was typically 1.5 kV and the trigger wire current 70 A . The effective capacitance was found to be 7.6 nF , thus a measure of the stray inductance of the trigger wires, cathode and laser structure is found to be, approximately, $3.5 \mu\text{H}$. This will obviously limit the maximum current that can be drawn through the trigger wires under the present experimental conditions. It is normal practice in many laser systems to use copper grounding sheets to earth the cathode. However, in the present case the cathode is supported by 3 pillars, see Chapter 2, Section 2.3.1, the result of this is the relatively large stray inductance. For the coupling capacitive technique of preionisation the inductance is, in general, dominated by

L_a , so the stray inductance is negligible. It is apparent that the stray inductance will severely affect the operation of the independent preioniser – however, it was decided to test the preioniser under these normal, high circuit inductance conditions to compare the performance of the two systems of preionisation.

3.5.2 Delay Time Calibration

An important parameter that will affect the performance of the laser output and discharge stability whilst using the independent preioniser is the time between the preioniser and the discharge thyatron firing, denoted by τ_1 . The preioniser and the discharge thyatron are abbreviated to TP and T2 respectively. The most convenient way to determine the value of τ_1 is to monitor the trigger output pulses from the pulser control units, see Section 2.2.5, these pulses are low voltage signals that drive the emitter for generation of the optical pulses which are then sent down the fibre-optic cable to the thyatron trigger unit. This technique avoids monitoring the high voltage thyatron trigger pulses and is thus safer. However, due to the slight differences in the characteristic impedance of the trigger units, it was found necessary to calibrate the time between the thyatron trigger pulses occurring against the time between the fibre-optic output pulses. Figure 3.58 shows a schematic of the square output pulses which drive the emitter and the corresponding thyatron trigger pulses which are generated by the trigger units. The calibration involves plotting τ_1 against τ_2 , where τ_2 is the measured delay between the output trigger pulses from the pulser control unit. Figure 3.59 shows the measured thyatron trigger pulses from TP and T2 for a time delay of 840 ns. Figure 3.60 shows the trigger pulses from TP and T2 on an expanded time base for a delay time of 287 ns.

A 10 turn potentiometer was positioned on the back of the pulser control unit to control the relative firing time between TP and T2 triggering; a maximum delay of 3 μ s was possible. Figure 3.61 shows the calibration curve of τ_1 vs τ_2 , it is seen that a simple linear relationship exists between them, given by the equation in the figure. The coefficient of correlation is extremely high with a value of 0.999985.

It was attempted to test the accuracy and repeatability of this calibration by trying to obtain a time delay of $\tau_1 = 300$ ns; from the equation in Figure 3.61 this required a value of $\tau_2 = 1124$ ns. Because of the bandwidth of the oscilloscope, this precise value of τ_2 cannot be obtained in practice. A value of (282.8 ± 0.7) ns was obtained for τ_2 , where the standard error of the mean is quoted for a sample size of 17. The error from the expected value of 300 ns is 5.7 %. Thus,

the calibration equation given in Figure 3.61 can be simplified to $\tau_1 \approx \tau_2 - 810$ ns where the error from this approximation is less than 2 % of τ_1 , the delay should then be known to at least 20 ns. It was felt that this accuracy was sufficient for optimisation of the preionisation trigger pulse. In practice, the potentiometer controlling the value of τ_1 would be tweaked to optimise the laser output while the laser is in operation.

Following calibration of the relative firing time between the preioniser and discharge thyatron, the preioniser was used in the single shot and burst mode, and on the laser output power was measured. The results are reported in Sections 3.5.3 and 3.5.4.

3.5.3 Testing into Trigger Wires : Single Shot and Burst Mode

Table 3.7 gives the system characteristics that were used to test the performance of the preioniser with the trigger wires as the load. The H.V. supply was connected to commission the preioniser in the single shot and the burst mode. While operating the laser in the single shot mode, it was noticed that the voltage across the trigger wires rose rapidly to a value much greater than that measured from continuous, pulsed operation with the capacitive coupling technique of preionisation.

Table 3.7 System characteristics for preioniser testing

Gas mixtures	1:1:0 or 1:1:1
Partial gas pressures	20:20:20 mb
Transformer tap-setting	60 %
Preioniser DC voltage	7 - 10 kV
Transverse trigger wires	105
Plane electrodes	
Anode inductance on T2 (L_a)	36 μ H

Figure 3.62 shows the trigger wire voltage and current characteristics that were obtained, with the parameters as described in Table 3.7, for the single shot mode (or equivalently the first pulse of a pulse train) with the preioniser voltage at 7 kV. However, subsequent pulses, when the laser is operating in the continuous pulsed mode, show distinctly different characteristics - the traces become smoother and temporally broader. The time of the current pulse width was measured as

approximately 450 ns, which is significantly different from the 40 ns measured from the first pulse. Figure 3.63 shows the voltage and current traces for the second pulse, the preioniser voltage was at 7 kV and the system conditions are those listed in Table 3.7. For the first pulse, there is no resonant charging effect of the capacitor C_{1p} ; hence, for $V_{dcp} = 10$ kV, the energy stored on C_{p1} for the first and subsequent pulses is 0.25 J and 1 J respectively. Consequently, the current flow for the first pulse will be substantially lower – by a factor of 2 – than it is for subsequent pulses.

Initially it was considered that the different breakdown characteristics were due to the different charging characteristics between the first and subsequent pulses. However, this effect of the first pulse showing different breakdown characteristics was subsequently observed when capacitive coupling was employed on the discharge system. Clearly, the trigger wires, once breakdown has been initiated, are much easier to breakdown on subsequent pulses.

This fact tends to suggest that metastable states which are created in the first pulse exist, if the operating frequency is high enough or their lifetime is long enough, in a large enough quantity to perturb the behaviour of the discharge sufficiently to alter the breakdown characteristics of the next pulse. The electronic metastable states of N_2 , for example, may become ionised by a multi-photon absorption process which is occurring over several pulses, or perhaps, the excited metastable states of N_2 are emitting UV radiation. Thus as these states are created in the first pulse, they will be present to some degree – depending upon their lifetime and the laser frequency – when the next pulse arrives. Thus the multi-photon ionisation, or the UV flux, provides an additional source of preionisation aiding the breakdown mechanism of the trigger wires for the later pulses. It would be interesting to verify this experimentally, however, unfortunately, such measurement equipment was unavailable. There are some experimental measurements that could be taken which would support this view. For example, if the discharge stability was purely dependent on the level of preionisation, then increasing the frequency would increase the initial level of preionisation. The discharge could run at higher frequencies more efficiently because of the higher level of preionisation within the discharge. This of course assumes the exponential decay of the metastable states and/or the UV flux. However, it is probable that another form of discharge instability will arise with the increase in PRF, for example, thermal instabilities.

Figures 3.64 and 3.65 show, arbitrarily, the fifteenth trigger wire voltage and current pulse respectively. A clear transition region can be seen, representing the

breakdown of the trigger wire gap, this is particularly visible on the current trace, where a sharp peak is observed, prior to the main displacement current. The current pulse widths are about in the ratio of 1:10, but the peaks are approximately 1:2, clearly the drop in voltage across the trigger wires, once the trigger wire gap has broken down, is reducing the expected size of the displacement current. It is seen that $dI_{tw}/dt \approx 2.7 \times 10^9 \text{ As}^{-1} \Rightarrow \xi = 3.7$, it seems that the rate of change of current is still too low. However, the peak current has increased considerably and it was decided to examine the laser output whilst using the independent preioniser.

3.5.4 Laser Output Results

A gas mixture of 1:1:0 was used at a pressure of 40 mbar and with the transformer tap settings at 60 %. A single pass resonator was installed with a rear mirror radius of curvature of 10 m and output mirror reflectivity of 75 %. The delay, τ_1 , was adjusted and 10 laser output pulses were measured at each value of τ_1 . The mean of the pulsed laser output energy and the standard error of the mean were calculated. It was noticed that for long and short time delays, such that $\tau_1 > 535 \text{ ns}$ or $\tau_1 < 120 \text{ ns}$ the discharge became very striate and filamentary, the laser output power dropped and the pulse shape became distorted, high order ripples appeared on the plateau, and the output delay increased. For delays 20 to 30 ns beyond these limits the discharge arced. The DC voltage on the preioniser was at 8.35 kV.

The independent preioniser was disconnected and a 10 nF coupling capacitor was connected between the trigger wires and the discharge anode, the laser output was then measured, the same gas fill was used as for the previous experiment. Figure 3.66 shows the variation of the pulsed laser output energy, E_0 , as a function of τ_1 , with the H.V. preioniser and the coupling capacitor connected: the latter is drawn as a straight line for comparison of the two preionisation techniques. It is seen that the optimum value of τ_1 is about 200 ns and the output is comparable in both cases at this value with an overlap in the error bars.

It has been shown that the H.V. independent preioniser is capable of initiating the discharge and providing comparable laser output. However, it appears that no improvement has been obtained even though $\approx 300 \text{ A}$ is passing through the trigger wires. A possible reason for this is that the value of L_a used in these experiments (i.e. 36 μH) limits satisfactory development of the discharge. Also, the stray inductance of the laser structure severely limits the growth of the trigger wire

current and production of VUV radiation.

3.6 REPOSITIONING OF T2 AND THE LAST PFN MESH

Sections 3.2.7, 3.4.4 and 3.4.5 detail some experimental and theoretical aspects of the effects of circuit components on the discharge and laser performance. It is clear that stray inductances and, in some cases, capacitances are potentially undesirable and can lead to degradation of the discharge quality and laser output. In an attempt to improve the discharge stability, the discharge thyatron and the last mesh of the PFN were moved closer to the laser cavity – they were positioned underneath the cavity. An aluminium enclosure was fabricated to house the components leaving space for future developments; for example, using magnetic switches to limit the initial rate of rise of current through the discharge thyatron. A perspex window was fitted over the side of the enclosure, this was a safety precaution and provided a means to observe the circuit components. A port hole was made on one side of the enclosure so as to pass the current and voltage probe cables safely to the oscilloscope. The high voltage connector, see Section 2.3.1, was mounted to the bottom of the aluminium box, the other end of the URm74 cable was connected to the penultimate mesh of the PFN. Figure 3.67 shows a schematic of the modified electrical circuit. The inductance of the connecting cable is negligible; the capacitance between the cathode of the discharge thyatron and ground was measured as ≈ 200 pF, this is in contrast to the value 1.01 nF which was measured previously, see Section 3.2.7.

The experimental programme continued, initially, by investigating the capacitive coupling technique of preionisation with the laser operating in the single shot mode. The effect of applying overvoltage to the discharge was to be analysed by measuring the laser output energy and assessing the quality of the gas discharge for different values of L_a . However, it was found that in the single shot mode, the large transients experienced at the moment T2 was triggered saturated the oscilloscope, and no information could be abstracted about the degree of overvoltage applied to the discharge.

The experiment was subsequently devised so as to determine the affect of the measurand on the laser output pulse energy. A major disadvantage with this method is that the resonator inhibits the view of the discharge; however, if arcs do occur it is usually evident from observation of the captured traces on the oscilloscope. For example, Figure 3.68 shows the laser output and current trace when the discharge arcs. It is seen that the laser output suddenly reduces as the

current rises to the full fault current. The increase in the laser output power after the current pulse can be attributed to lasing action occurring because of the reservoir of energy stored in the metastable states of N_2 . In an attempt to maximise the laser output power it was decided to use the single shot mode of the laser and charge the smoothing capacitance from the 20 kV RMS supply and use the 0-240 V variac. Thus the voltage doubling effect of the PFN would still be utilised with maximum control over the PFN voltage and the energy deposited into the discharge. In order to achieve the maximum PFN voltage of 20 kV, the DC voltage on the smoothing capacitor of the pulser circuit must be equal to 12 kV.

Because the single shot mode was used, it was considered not worth while at this stage to measure the laser output with the independent preioniser connected. This is because the voltage doubling - i.e. the resonant effect - is not obtained from the preioniser until the second pulse.

The resonator and detector configuration can be seen in Table 3.8

Table 3.8 Resonator and detector geometry

Single pass			
Output window reflectivity	90 %		
Rear mirror:	Cu-substrate Au-coated		
	Radius of curvature	10m	
Distance between mirrors	1.61 m		
Fundamental mode shape diameter:	front window	7.04	mm
	rear mirror	7.69	
Diameter of TEM_{01} mode:	front window	12.20	
	rear mirror	13.32	
Photon-drag detector (PDD) Ge crystal			
Diameter of active area	25 mm		
Responsivity	6 mV/kW		
Distance of PDD from output window	\approx 2.35 m		
Diameter of fundamental mode on PDD	8.36 mm		
Measured diameter	15 - 16 mm		
Calculated diameter of TEM_{01} mode	14.48 mm		

The values quoted in Table 3.8 are discussed thoroughly in Chapter 5.

To ensure optimum alignment of the resonator, the pulser was connected to the main transformer and then, while the discharge was running at 100 Hz, the front and rear mirror were tweaked to yield the maximum laser output power.

3.6.1 Results With Capacitive Coupling Preionisation: Single Shot Mode

The system variables are shown in Table 3.9. the coupling capacitance was kept constant at 10 μF . The main parameters that were varied were the DC network voltage, gas pressure and L_a .

Table 3.9 System parameters

DC voltage V_{dc}	8 - 12 kV
Coupling capacitance C_c	10 nF
T2 anode inductance L_a	\approx 9 - 36 μH
Trigger wire gap	2 mm
Number of trigger wires	105
Electrode length	1000 mm (see Figure 3.7)
Gas mixtures:	1:2:0
Gas pressure \approx	40 - 130 mb
Low Ionisation Potential impurity (LIPS)	C_3H_3

V_{dc} was varied between 8 kV and 12 kV for a fixed gas pressure, in this case 1:2:0 at 78 mb was selected. Then the affect of increasing the gas pressure for a fixed value of $V_{dc} = 12$ kV was investigated. These experiments were repeated with inductance values of 9 μH and 36 μH on the anode of the discharge thyratron.

Figure 3.69 shows the laser output power for a 1:2:0 mixture at 78 mb, with the anode inductance $L_a = 36$ μH and V_{dc} set at: 8 kV, 10 kV and 12 kV. Clearly, as would be expected, increasing V_{dc} results in an increase in the network voltage and the energy deposited into the discharge (denoted by E_d); thus, the laser output power increases. The laser output is discussed in more detail in Chapter 5.

It was found that for $L_a = 36$ μH the pumping pulse shape of the voltage and current trace did not significantly alter; however, for $L_a = 9$ μH , increasing V_{dc} resulted in an increased time before the voltage and current reached their plateau values. Figure 3.70 shows the voltage and current traces that were obtained with the conditions: $V_{dc} = 12$ kV and $L_a = 36$ μH at 78 mb; and Figure 3.71 shows the voltage and current traces for $V_{dc} = 12$ kV and the pressure at: 78, 96 and

114 mb. It is seen that the affect of reducing L_a on the input pumping pulse shape is to slightly decrease the value of E_d for a given value of V_{dc} , typically by about 0.3 to 0.5 J. The divergence between the values of E_d for the different values of L_a is more noticeable for either lower operating pressures or higher values of applied voltage. This affect can be explained in terms of the impedance matching between the discharge and the PFN. It has been shown that the electrical components on the last mesh are important in determining the pumping pulse shape of the laser medium.

Figure 3.72 shows the laser output pulse energy E_o as a function of the input pulse energy E_d for values of L_a equal to 9 μ H and 36 μ H. It can be seen that E_o is greater for the lower value of L_a and that E_o increases with E_d . Figure 3.73 shows the efficiency of the laser (defined as $\eta = E_o/E_d$) for the anode inductances of: 9 μ H and 36 μ H. It is seen that the efficiencies are greater for the lower value of L_a . This represents a significant improvement in the laser output compared to the initial results, which are discussed in Chapter 5, where efficiencies of ≈ 0.3 % were reported. Clearly, there is a slight benefit in decreasing the anode inductance in that the laser efficiency increases. The maximum output energies were slightly over 0.07 J with efficiencies of 1.2 %, the pumping pulse energy was approximately 7 J. With $V_{dc} = 12$ kV, the energy stored on the network is 10 J, however, the value of E_d is less than 10 J because of the mismatch in impedances between the discharge and the PFN.

It is noticed, from Figures 3.68 and 3.69, that it takes a finite time before any laser output occurs after application of the voltage to the discharge. The time it takes for the current to rise to 10% of its peak value to the time it takes the laser output power to rise to 10 % of its peak, is called the delay time, and denoted by τ_d . Figure 3.74 shows the delay time as a function of E_d for the anode inductances of 9 μ H and 36 μ H. Interestingly, the affect of reducing the anode inductances is to slightly reduce the delay time.

Figure 3.75 shows the peak output power as a function of E_d for the anode inductances of 9 μ H and 36 μ H. It is seen that increasing E_d increases the peak power and, for values of $E_d > 5$ J, the peak power is significantly greater for the lower value of L_a .

The plateau power of the output pulse is plotted against E_d in Figure 3.76 for the cases $L_a = 9$ μ H and $L_a = 36$ μ H. It can be seen that the plateau power increases with increasing E_d , and that the plateau power is slightly greater for the lower value of L_a . However, the differences do not appear to be as significant as

they were for the peak powers.

It seems that the affect of reducing the anode inductance, at least in the single shot mode, is to significantly increase the peak laser output power and to slightly increase the plateau power. It appears that the lower values of inductance are affecting the initial part of the laser pulse more so than the latter part of the pulse.

In order to increase the value of E_d with a fixed value of V_{dc} the pressure must be increased, this increases the discharge impedance and at a specific pressure, denoted by P_m , the energy transfer efficiency is 100 %. Appendix B1 derives an expression for calculating P_m . Substituting in the appropriate values for the E/p value of the gas mixture and $V_N = 20$ kV then it is found that $P_m = 140$ mb. So it is seen that the gas pressure can be increased by a factor of approximately 1.8 from 78 mb before the positive mismatch regime is encountered.

The next experiment was to investigate the affect of increasing the gas pressure on the laser output and discharge stability whilst keeping the supply voltage fixed at 12 kV and using the anode inductances of 9 μ H and 36 μ H. However the results are not presented explicitly, this is due to the "lack of confidence" in the values because the laser was operating under poor vacuum conditions, with a leak rate in excess of 2 mb/hr. To complete one experiment can take up to 1 hour. However, in general, the laser output energy for pressures up to 120 mb with $L_a = 9$ μ H was slightly in excess of 0.1 J, for higher pressures the discharge arced. It is possible that the arcing was due to the high atmospheric contamination of the gas mixture.

The next phase of the experimental programme was to investigate the affect of PRF on the discharge operating under the conditions in which the output energy was 0.1 J. Unfortunately, problems were experienced with the trigger wires breaking which fore-shortened these experiments.

3.7 REDESIGNING THE ELECTRODE CONFIGURATION

Uniform Field Electrodes (UFE) are often used to provide a highly regular electric field transversely across the electrode, several designs have been tried. Firstly, Rogowski [3.39] who developed UFE from empirical relationships, used three segments which joined together to make one electrode. The disadvantage of this profile is that the discharge width is small in comparison to the electrodes, also

the three segments make manufacturing complex. Chang [3.40] approached the problem analytically, using conformal transformations, and developed expressions enabling fabrication of UFE with a discharge width closer to the electrode width than was available from the Rowgowski profile. More compact electrode profiles were developed by Ernst [3.41], where the discharge width is comparable to the electrodes. The advantage of this is that the preionising source can be placed closer to the discharge volume, ensuring maximum penetration of the VUV flux and development of a stable, uniform glow discharge.

To date, only plane electrodes have been used. It was decided to examine the affect of using UFE. A program was written in C to produce a CNC code to mill the electrodes on a CNC milling machine [3.42].

Two pairs of electrodes were fabricated, the first had a reduced electrode width of 35 mm and the second was 75 mm wide. Although the electrodes were fabricated they were untested, consequently, no results can be presented of their performance.

CHAPTER THREE REFERENCES

- [3.1] Kharha J. "Optimisation of the output characteristics of a pulsed CO₂ laser for processing materials". Ph.D. Thesis. Department of Mechanical Engineering, University of Birmingham, U.K. 1979.
- [3.2] Hasan M. "Thermodynamics of transiently pumped CO₂ gas laser plasmas". Ph.D. Thesis. Department of Mechanical Engineering University of Glasgow, U.K. 1989.
- [3.3] Suzuki S., Ishibashi Y. et al. "Dependence of laser output on initial photoelectron density in TEA CO₂ lasers". *App. Phys. Letts* Vol. 36(1), pp 26-28, 1980.
- [3.4] Marchetti R., Penco E. "A new type of corona-discharge photopreionization source for gas lasers". *J.Appl.Phys* Vol. 56(11), pp 3163-3168, 1984.
- [3.5] Lowke J., Phelps A., Irwin B. "Predicted electron transport coefficients and operating characteristics of CO₂-N₂-He laser mixtures". *J.A.P* Vol. 44(10), pp 4664-4671, 1973.
- [3.6] Scott B. Personal communication. Mechanical Engineering Department, University of Glasgow.
- [3.7] Kline L., Denes L., Pechersky M. "Arc suppression in CO₂ laser discharges". *App. Phys. Letts*. Vol. 29(9), pp 574-576, 1976.
- [3.8] Howatson A. "An introduction to gas discharges". Pergamon Press. 1965.
- [3.9] Kunhardt E. "Electrical breakdown of gases: the pre-breakdown stage". *IEEE Transaction on Plasma Science*, Vol. PS-8, No. 3, pp 130-138.
- [3.10] Dutton J., Haydon S. et al. "Formative time lags in the electrical breakdown of gases". *British J.A.P.* Vol. 4, pp 170-175. 1953.
- [3.11] Crawford E., Phelps A. "Formative time lags in CO₂ laser discharges". *App Phys Lett* Vol. 25(1), pp 59-61, 1974.

- [3.12] Crindland J., Howells S. "The dependence of transversely excited atmospheric CO₂ laser performance on circuit configuration". J. Appl. Phys. Vol. 53(6), pp 4016-4019, 1982.
- [3.13] McDonald D. "10 kHz pulse repetition frequency laser for processing high damage threshold materials". Ph.D. Thesis. Department of Mechanical Engineering, University of Glasgow, U.K. 1989.
- [3.14] Levatter J., Lin S. "Necessary conditions for the homogeneous formation of pulsed avalanche discharge at high pressures". J. Appl. Phys. Vol. 51(1), pp 210-218, 1980.
- [3.15] Mcken D., Seguin H., Tulip J. "Photoionisation parameters in the CO₂ laser gas". IEEE Journal QE QE12 (8), pp 470-482, 1976
- [3.16] Seguin H., Mcken D., Tulip J. "Photoabsorbtion cross-sections in a seeded CO₂ laser mixture". Applied Optics, Vol. 16(1), pp 77-82, 1977.
- [3.17] Bushnell A., Gundersen M., Burkes T. "Effect of a small capacitor in parallel with a pulsed CO₂ TEA laser". IEEE Journal of Q.E. July 1976, p 447. Also see [3.12].
- [3.18] Morikawa E. "Effects of low ionisation gas additive with uv photo-preionisation on CO₂ TEA laser operation". JAP Vol. 48(3), pp 1229-1239, 1977.
- [3.19] Tallman C. "Preionization techniques for discharge lasers". SPIE Vol. 1046 Pulse Power for Lasers II, 1989, pp 2-14.
- [3.20] Taylor R. "Preionisation and discharge stability study of long optical pulse duration UV-preionised XeCl lasers". App Phys B4 1 - 1 - 24, 1986.
- [3.21] Kline L., Denes L. "Investigation of glow discharges with volume preionisation". JAP Vol. 46(4), pp 1567-1574, 1975.
- [3.22] Kunhardt E, Byszewski W. "Development of overvoltage in high pressure gases". Phys Rev A Vol. 21, pp 2069-2077, 1980.
- [3.23] Sierra R. et al. "Effective swarm parameters and transport coefficients in CO₂ laser mixtures". J.Phys D: Applied Physics Vol. 14, pp 1791-1801, 1981.

- [3.24] Hasegawa H. "Measurement of the ionisation coefficient in binary and ternary mixtures of CO₂, N₂ and He". J.Phys D: Applied Physics, Vol. 18, pp 1361–1370, 1985.
- [3.25] "MathCad 3.0 Users Guide". 1991
- [3.26] Raether R. "Electron avalanches in gases". London, 1964.
- [3.27] Kline L. "Calculations of discharge initiation in overvolted parallel plane gaps". JAP Vol. 45(5), pp 2046–2054, 1974.
- [3.28] Pamler A. "A physical model on the initiation of atmospheric–pressure glow discharges". App Phys Letts Vol. 25(3), pp 138–140, 1974.
- [3.29] "Handbook of chemistry and physics". 55th Edition. CRC press. 1974–1975.
- [3.30] "An introduction to physics for scientists and engineers". Beuche. McGraw Hill.
- [3.31] See [3.12,3.15,3.16,3.18,3.19,3.21,3.36,3.38]
Kopeika N., "The role of excited atoms in UV photopreionization TEA lasers". IEEE Journal Quantum Electronics QE-13(12), pp 968–972, 1977.
- [3.32] Apollonov V. et al. "High power CO₂ laser pumped by a self–sustained volume discharge initiated by an electron beam". Sov. Tech. Phys. Letts. Vol. 12(4), pp 163–164, 1986.
- [3.33] Scott S. "Experimental investigation on an x–ray preionizer test bed". JAP Vol. 64(2), pp 537–543, 1988.
- [3.34] Jayaram K. Alcock A. "X–ray preionisation of self sustained, transverse excitation CO₂ laser discharges". J. Appl. Phys. Vol. 58 (5), pp 1719–1726, 1985.
- [3.35] Couceiro I., Zannon R. "Experimental analysis of the γ –ray ionization effects of a DC discharge CO₂ laser". Optics and laser Technology, Vol. 22 (5), pp 348–350, 1990.
- [3.36] Scott, Smith. "Ultra–violet photopreionization in CO₂ TEA lasers". JAP Vol. 64(2), pp 528–536, 1988.

- [3.37] "PSPICE circuit analysis users guide". Microsim corporation. 1991.
- [3.38] Marchetti R., Penco E. "Optimisation of corona discharge photopreionisation for CO₂ lasers". J.Appl.Phys Vol. 54(10), pp 5672–5675,
- [3.39] Rogowski Arch. Elecktrotech. 12(1) 1923.
See, for example, W. J. Witteman. "The CO₂ laser". Springer Series in Optical Sciences, Vol. 53. Springer Verlag. 1987.
- [3.40] Chang T. "Improved uniform electrode profiles for TEA laser and high voltage applications". Rev Scientific Instruments, Vol. 44(4), pp 405–407, 1973.
- [3.41] Ernst G. "Uniform-field electrodes with minimum width". Optic Communications, Vol. 49(4), pp 275–277, 1984.
- [3.42] Stevely, D. "Production of a Uniform field electrode". Undergraduate report, Department of Mechanical Engineering, Glasgow University, U.K. 1990/1991.

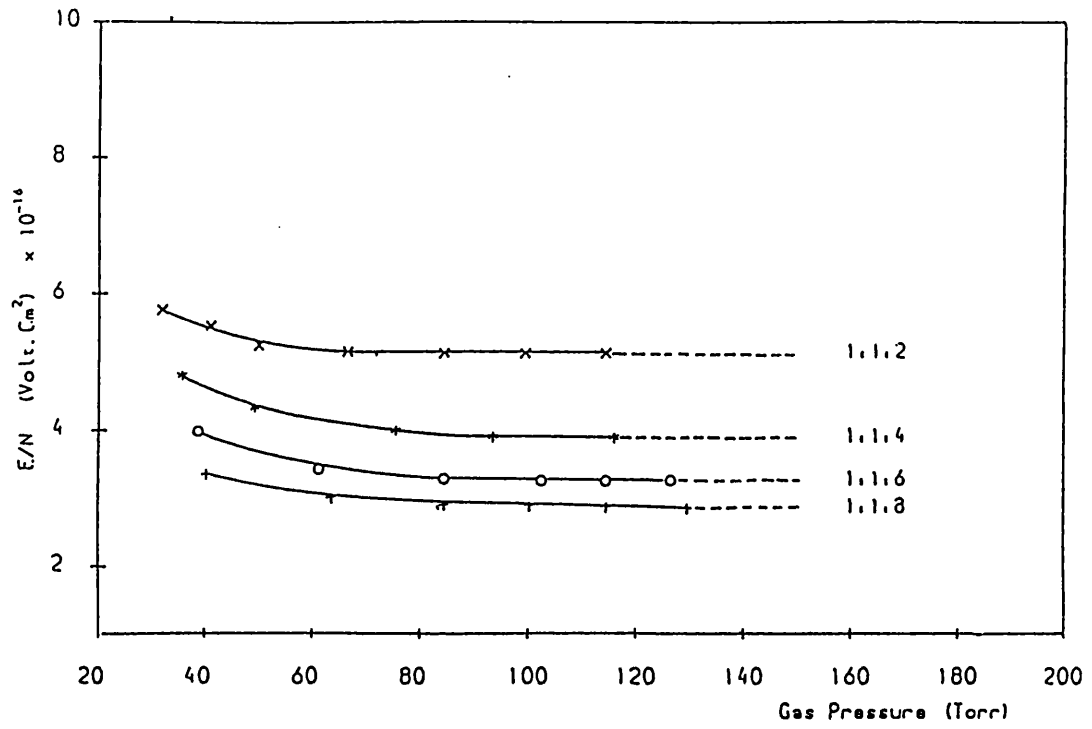


FIGURE 3.1 E/N VS GAS PRESSURE

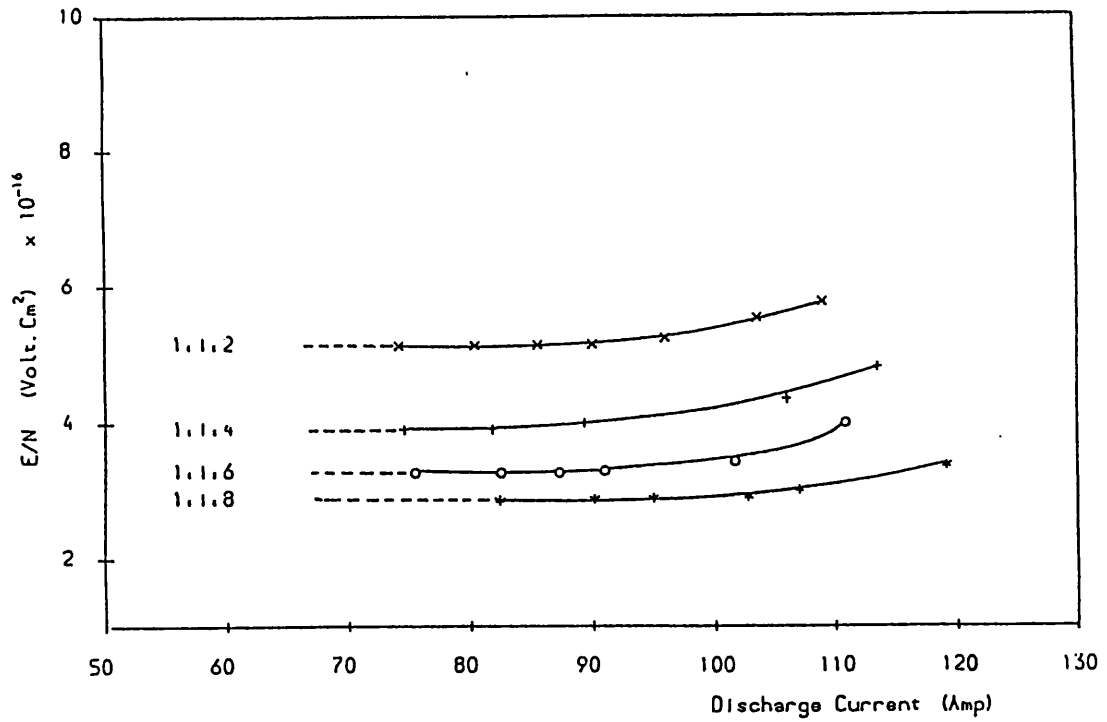


FIGURE 3.2 E/N VS DISCHARGE CURRENT

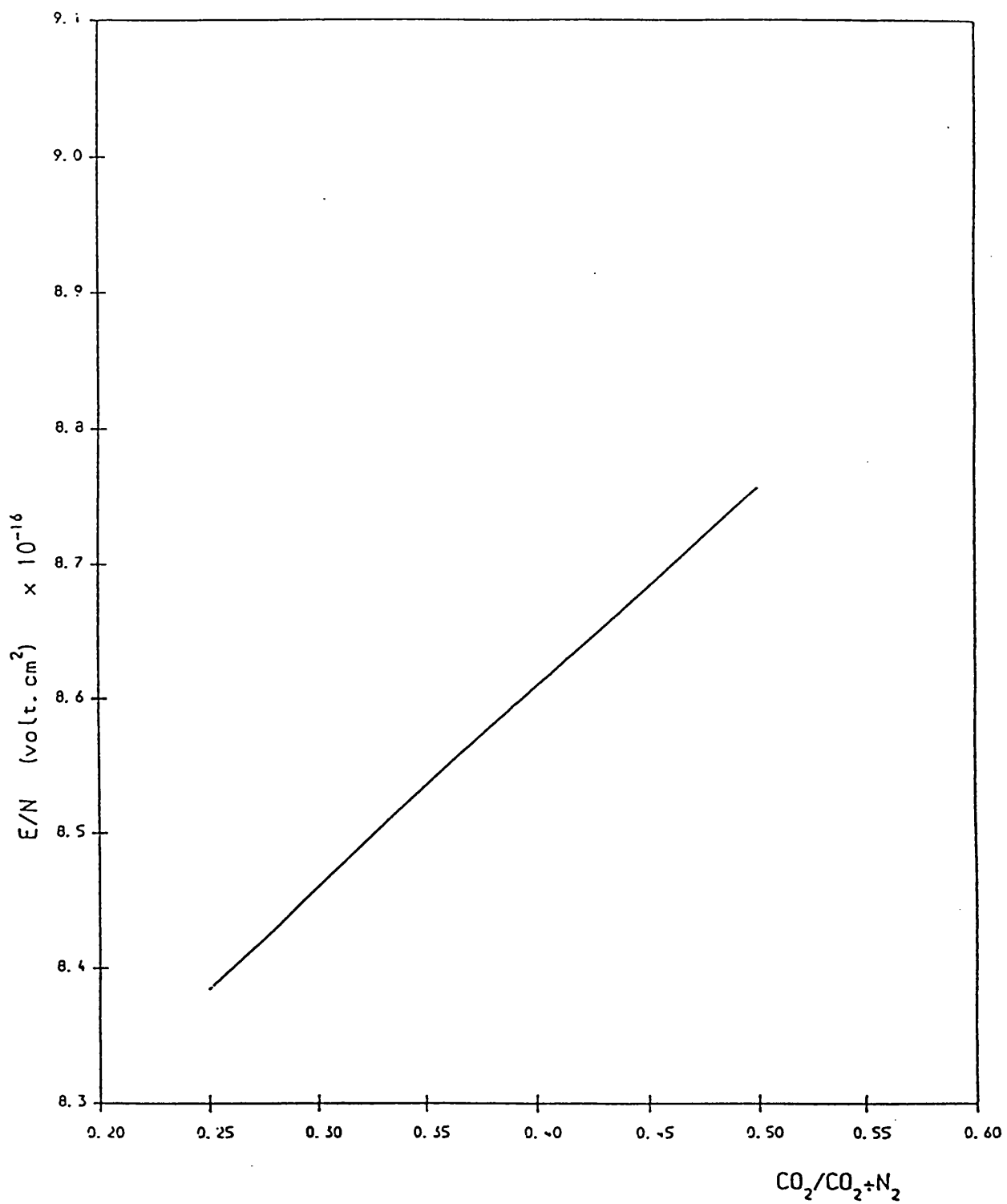


FIGURE 3.3 E/N VS CO_2 CONTENT

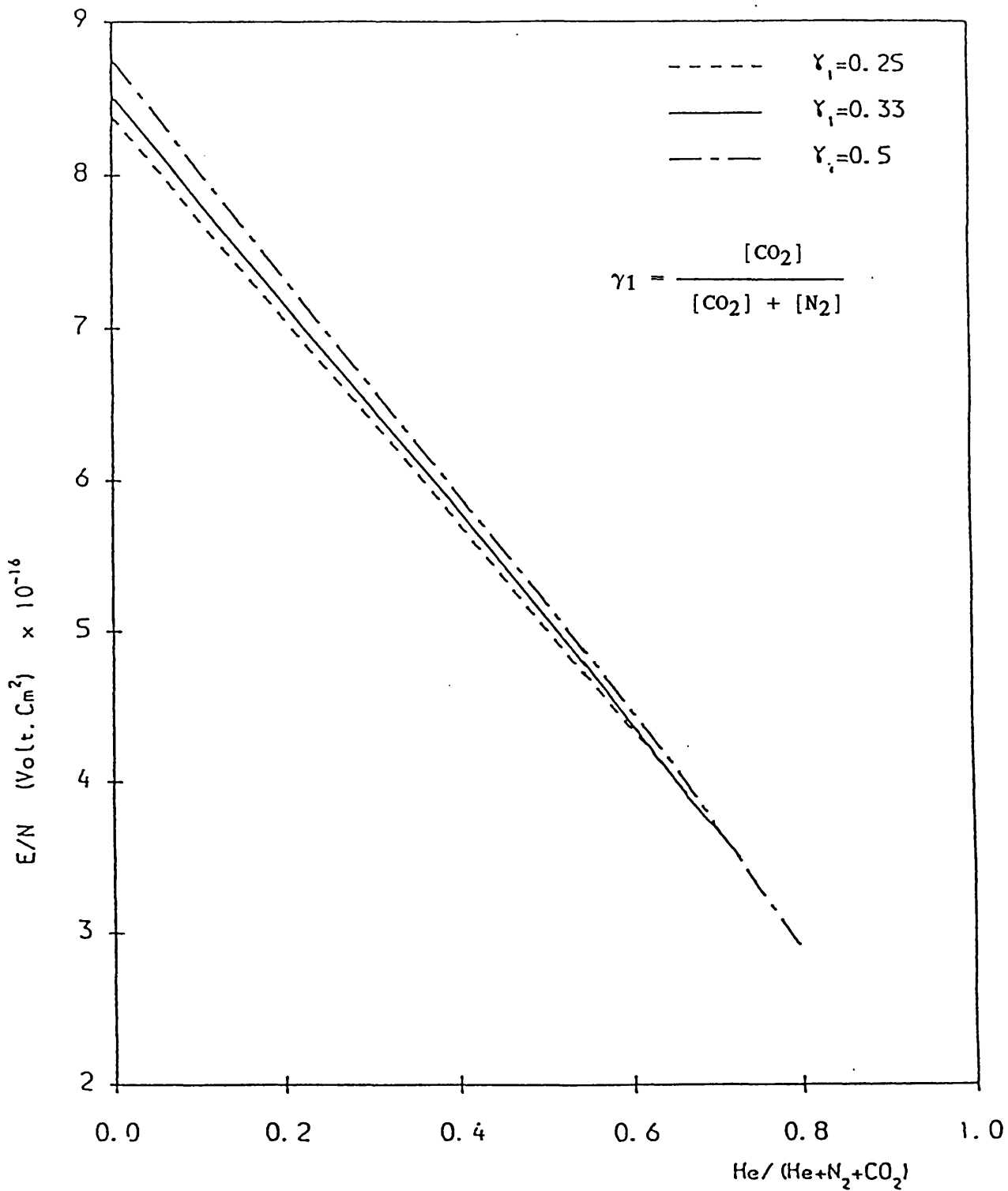


FIGURE 3.4 E/N VS HE CONTENT

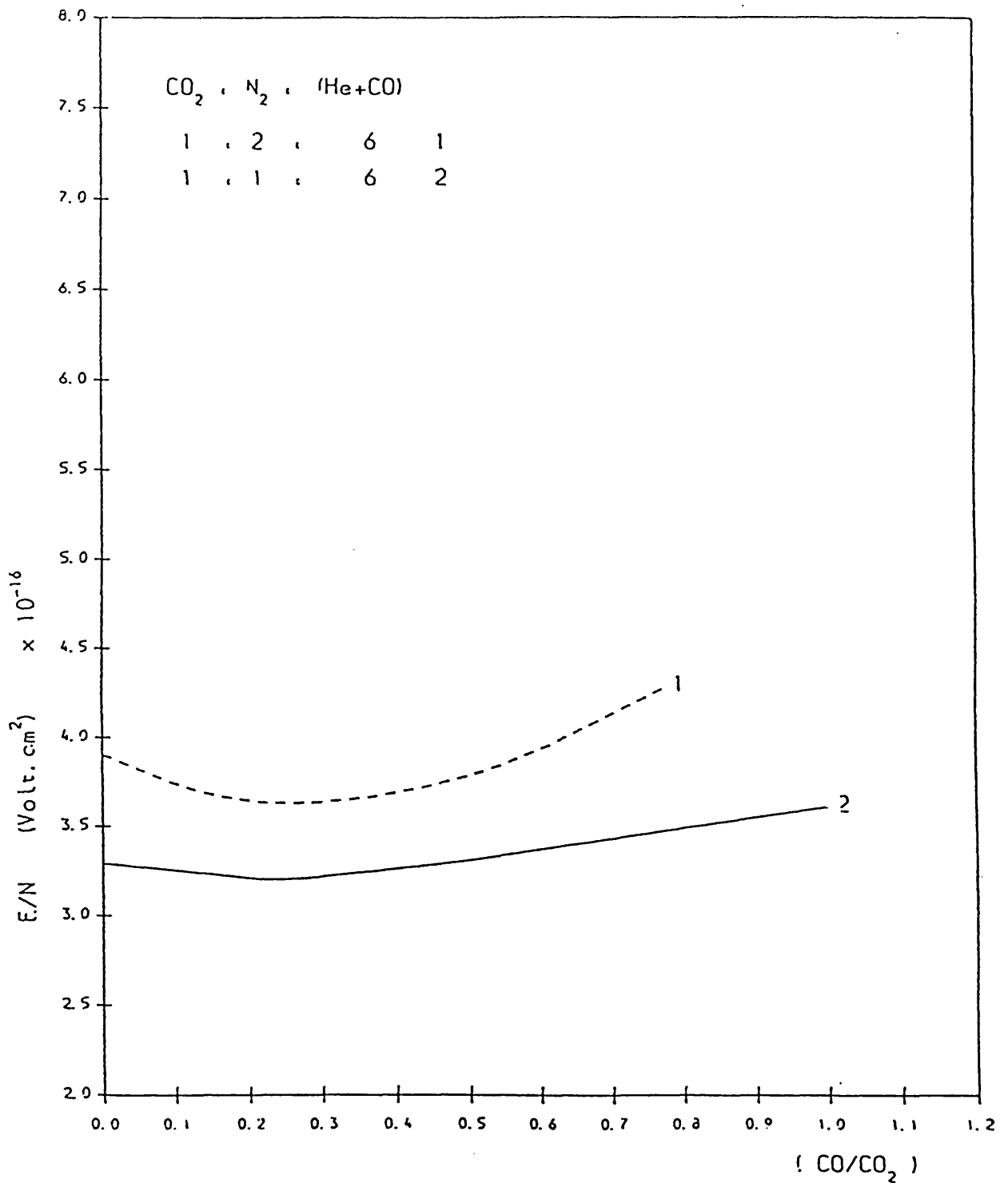


FIGURE 3.5 THEORETICAL E/N VALUES VS CO CONTENT

TABLE 3.1 EXPERIMENTAL AND THEORETICAL VALUES OF E/N

Gas Mixture	Theoretical E/N × 10 ¹⁶ Vcm ²	Experimental E/N × 10 ¹⁶ Vcm ²
1:1:0	8.6269	8.7571
1:1:1	6.3216	6.3933
1:1:2	5.1360	5.2283
1:1:4	3.9048	3.9892
1:1:6	3.2509	3.2912
1:1:8	2.4823	2.8942
1:2:0	8.4119	8.5213
1:2:1	6.7464	6.8121
1:2:2	5.7279	5.8287
1:2:4	4.5304	4.6065
1:2:6	3.8389	3.9023
1:2:8	3.3681	3.5002
1:3:0	8.2972	8.3848
1:3:1	6.9925	7.0581
1:3:2	6.1096	6.2041
1:3:4	4.9815	5.0408
1:3:6	4.2835	4.3583
1:3:8	3.7891	3.9272

TABLE 3.2 EXPERIMENTAL VALUES OF E/N

Gas Mixture	Experimental E/N × 10 ¹⁶ Vcm ²
1:1.0:6:0.0	3.291
1:0.5:6:0.5	3.041
1:0.0:6:1.0	3.135
1:2.0:6:0.0	3.902
1:1.5:6:0.5	3.422
1:1.0:6:1.0	3.496

Gas Mixture	Experimental E/N × 10 ¹⁶ Vcm ²
1:1:8.00:0.00	2.894
1:1:7.78:0.22	2.722
1:1:7.50:0.50	2.903
1:1:7.22:0.78	2.991
1:1:7.00:1.00	3.261
1:1:6.00:0.00	3.291
1:1:5.78:0.22	3.201
1:1:5.50:0.50	3.311
1:1:5.22:0.78	3.479
1:1:5.00:1.00	3.607
1:1:4.00:0.00	3.989
1:1:3.78:0.22	3.896
1:1:3.50:0.50	4.063
1:1:3.22:0.78	4.245
1:1:3.00:1.00	4.545
1:2:6.00:0.00	3.902
1:2:5.78:0.22	3.632
1:2:5.50:0.50	3.782
1:2:5.50:0.50	4.287

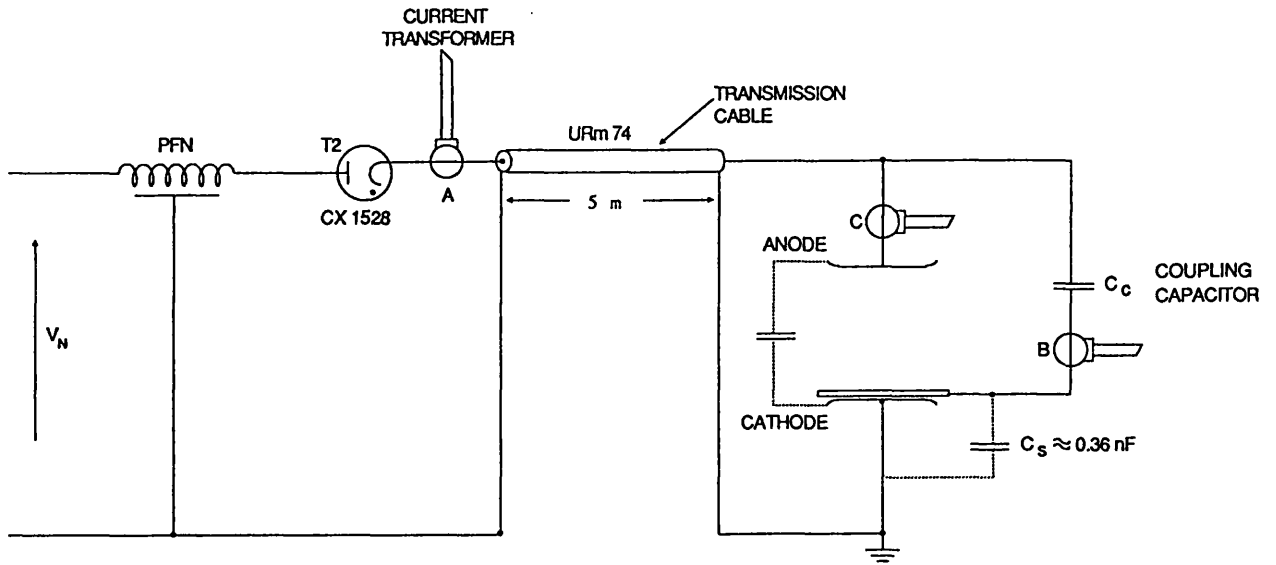


FIGURE 3.6 SCHEMATIC OF GAS DISCHARGE CIRCUIT

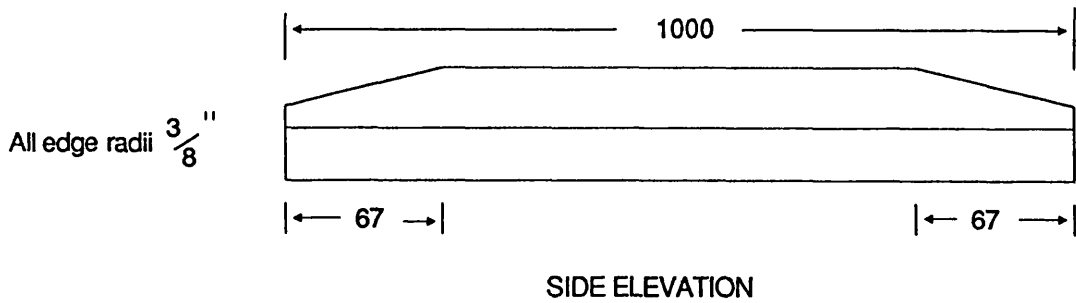


FIGURE 3.7 MODIFIED ELECTRODE PROFILE

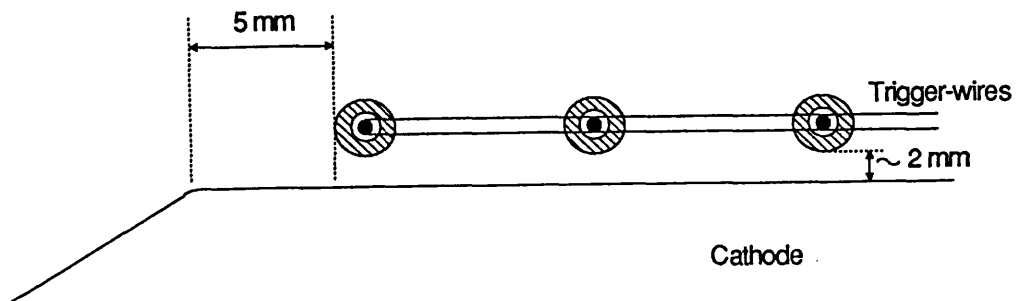


FIGURE 3.8 ELECTRODE EDGE AND TRIGGER WIRES

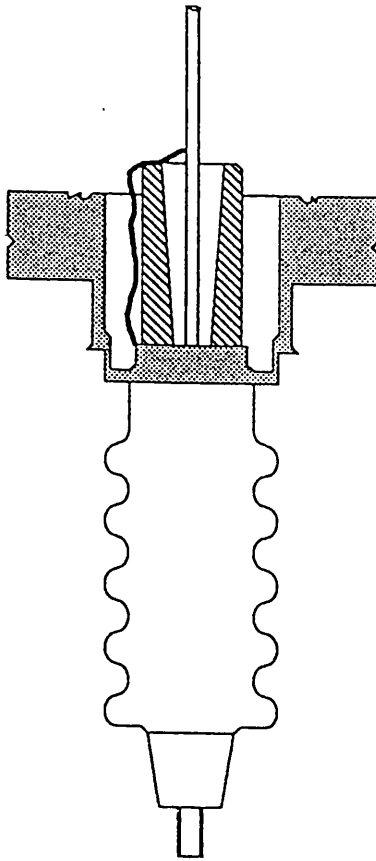


FIGURE 3.9a BREAKDOWN IN ANODE LEADTHROUGHS

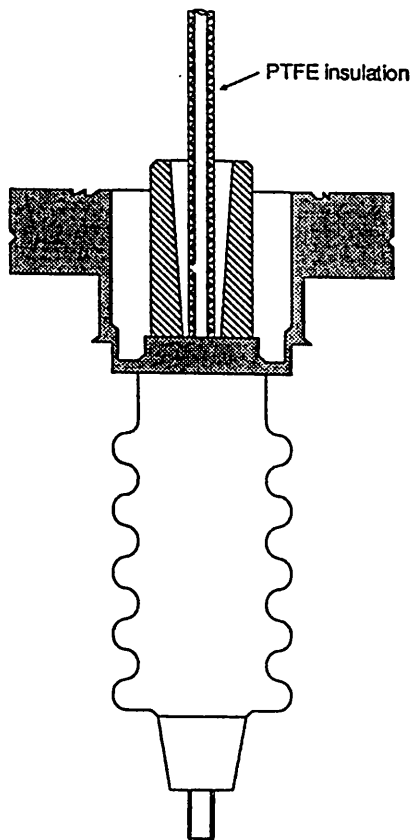


FIGURE 3.9b MODIFIED ANODE LEADTHROUGH

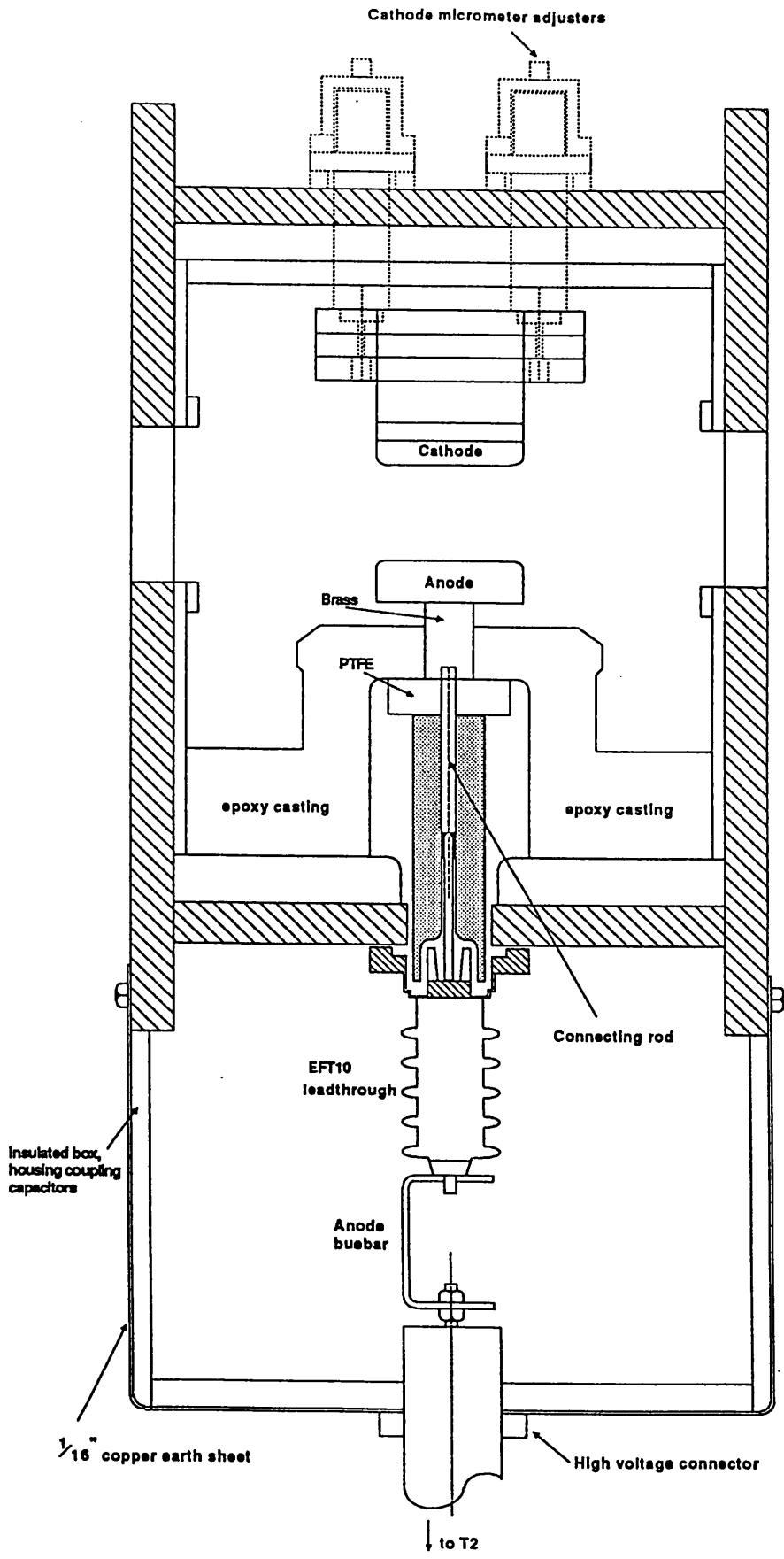


FIGURE 3.10 INSULATED EFT10 AND LASER CAVITY ASSEMBLY

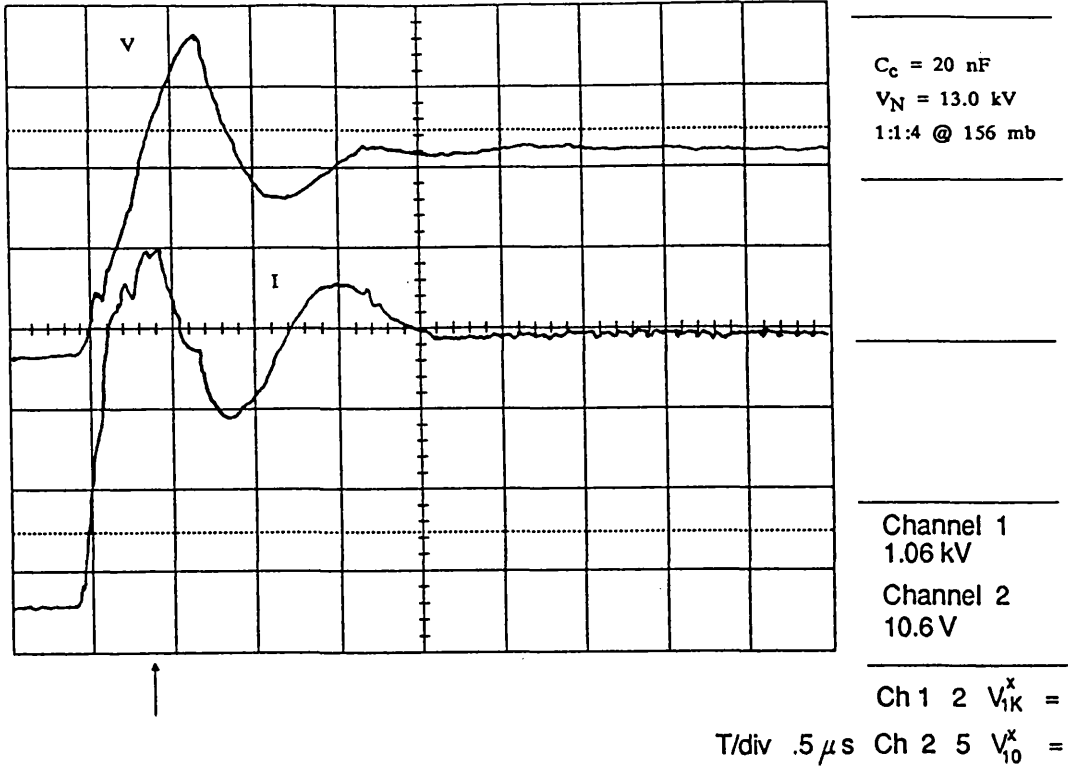


FIGURE 3.11 DISCHARGE VOLTAGE AND CURRENT: MONITORED AT A

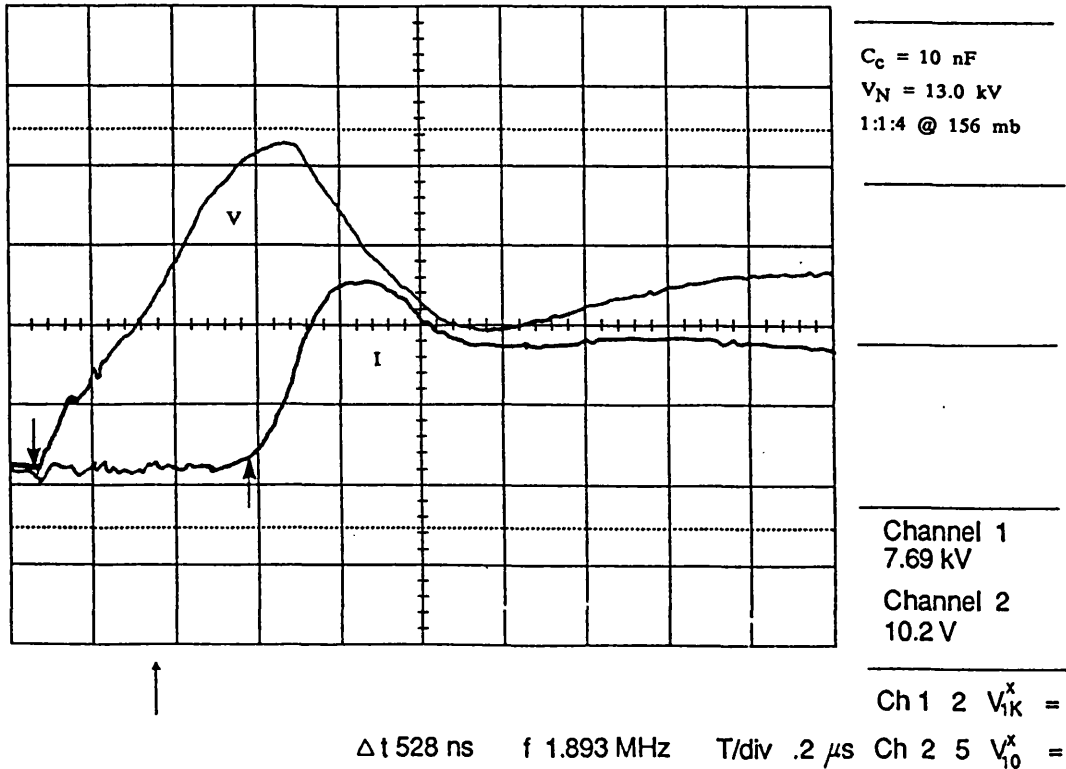


FIGURE 3.12 DISCHARGE VOLTAGE AND CURRENT: MONITORED AT C

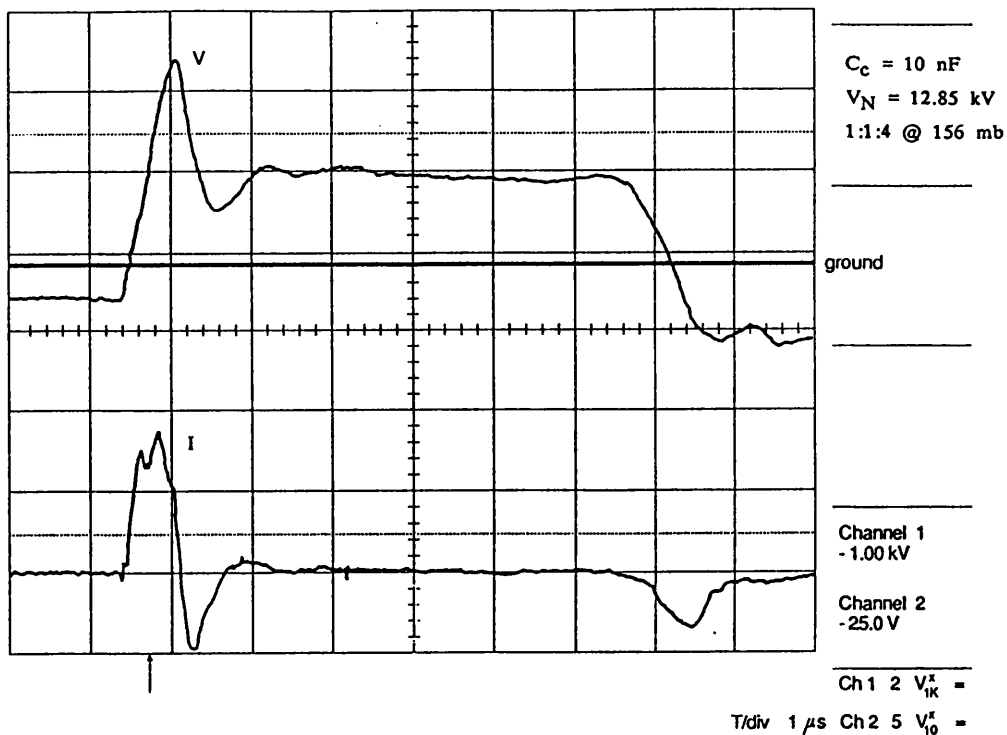


FIGURE 3.13 TRIGGER WIRE VOLTAGE AND CURRENT

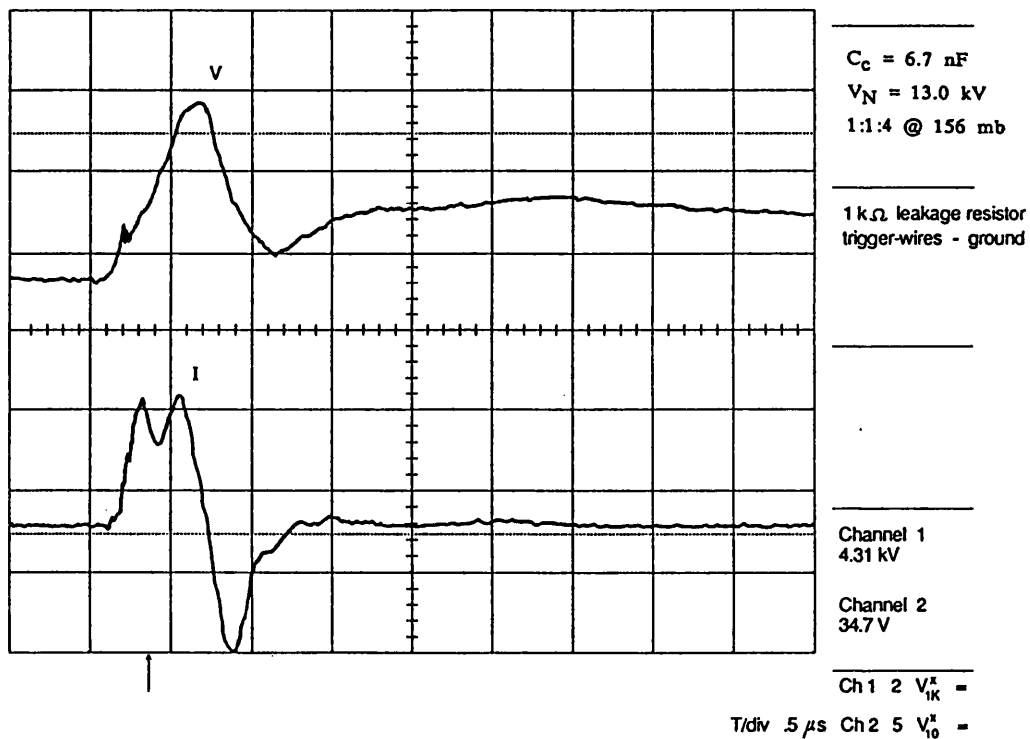


FIGURE 3.14 TRIGGER WIRE VOLTAGE AND CURRENT

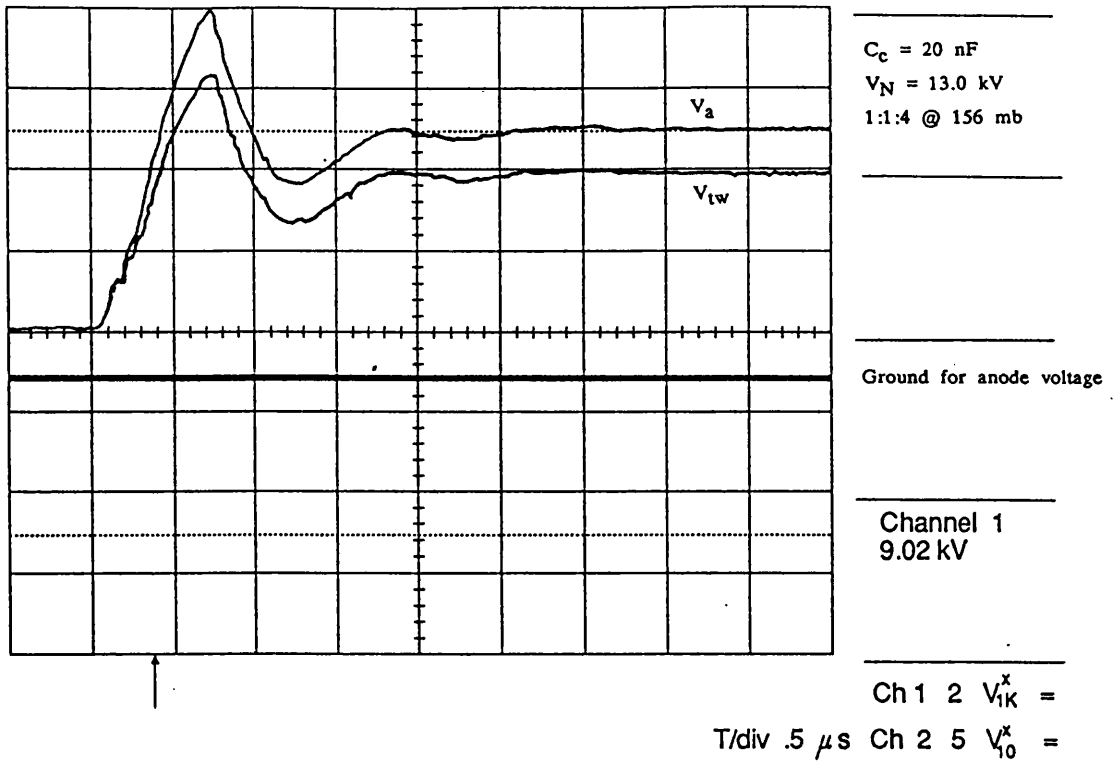


FIGURE 3.15 TRIGGER WIRE AND ANODE VOLTAGES

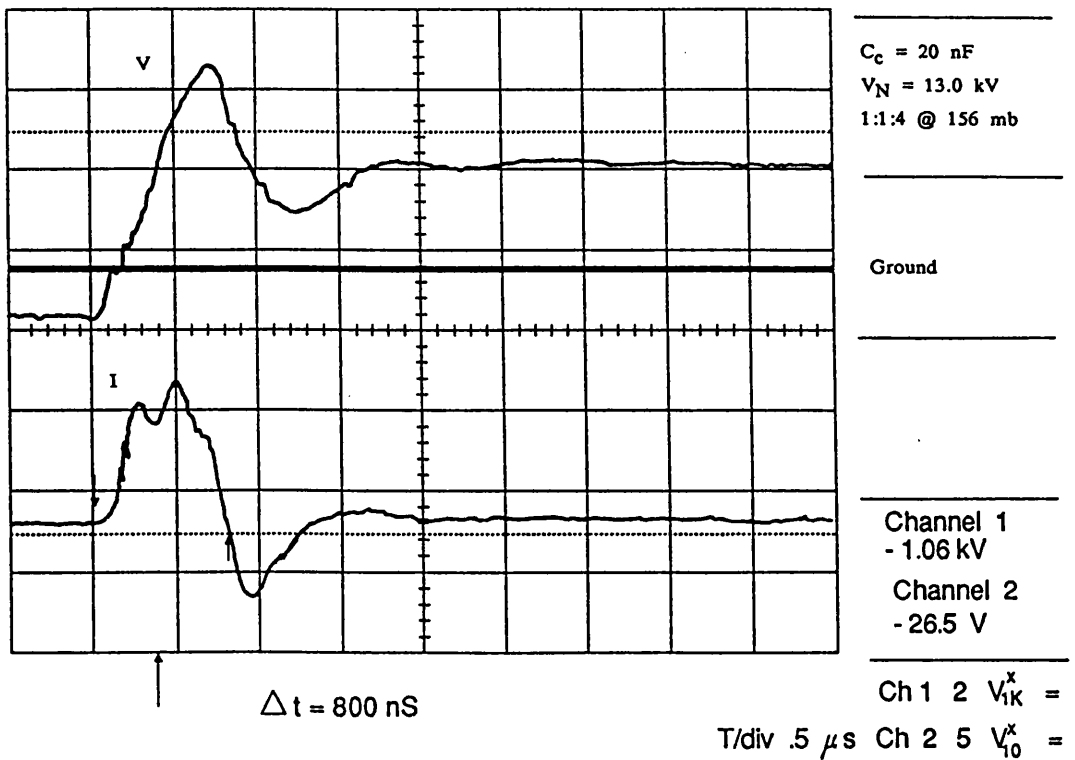


FIGURE 3.16 TRIGGER WIRE VOLTAGE AND CURRENT

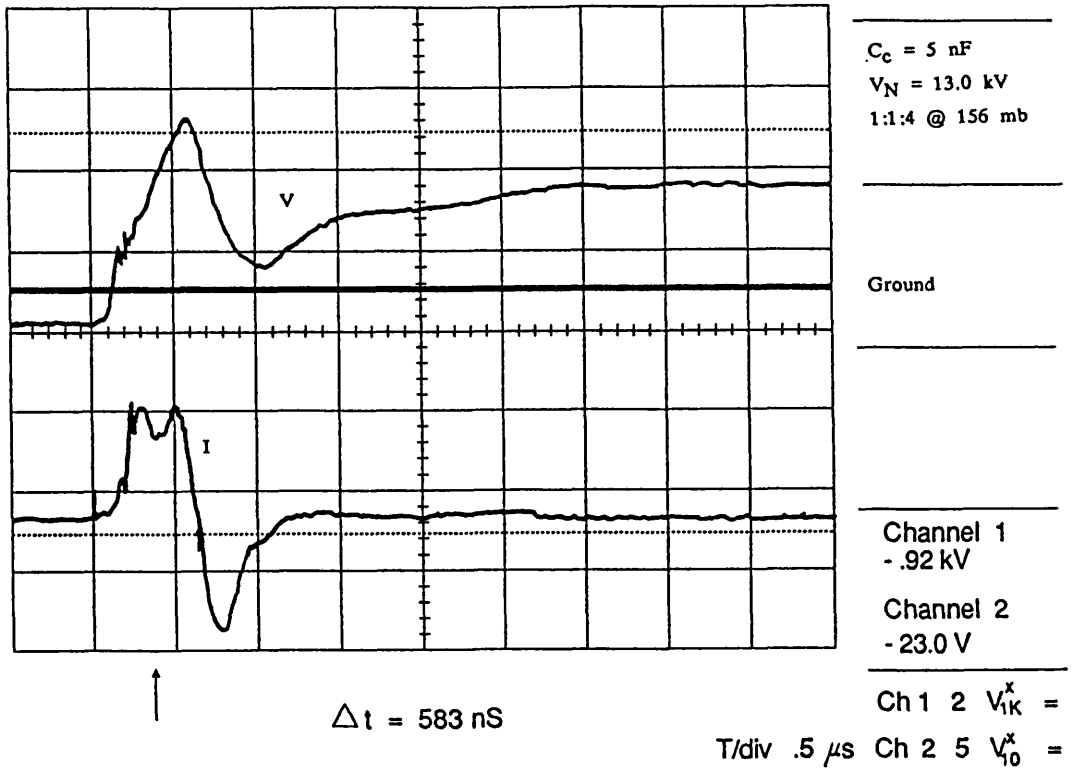


FIGURE 3.17 TRIGGER WIRE VOLTAGE AND CURRENT

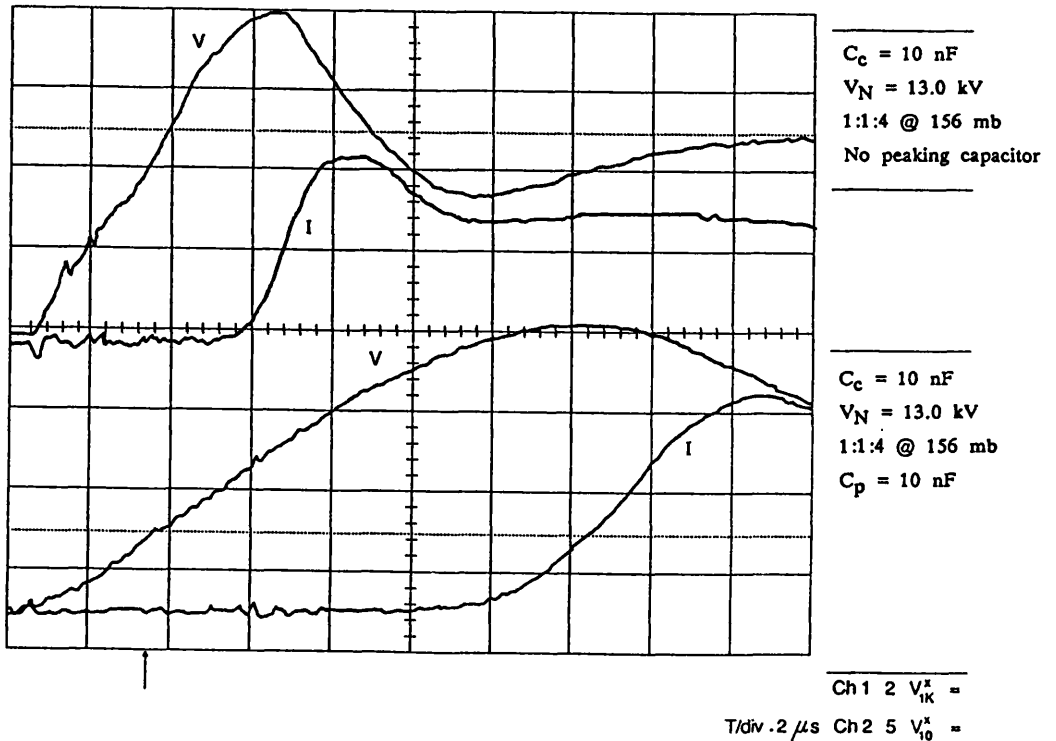


FIGURE 3.18 AFFECT OF PEAKING CAPACITOR

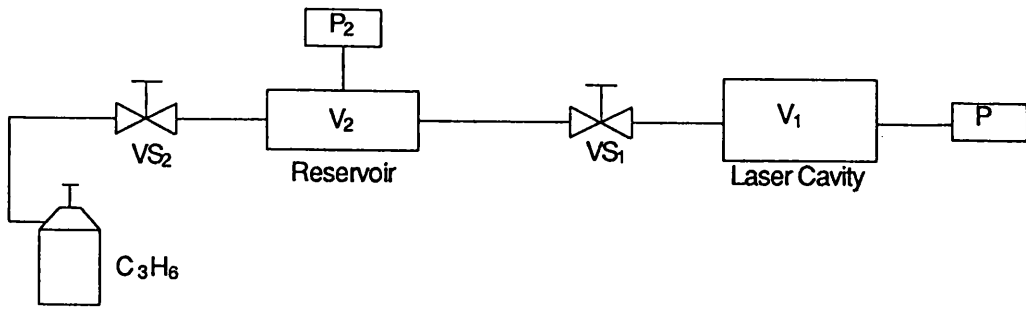


FIGURE 3.19 LIPS GAS SUPPLY SYSTEM

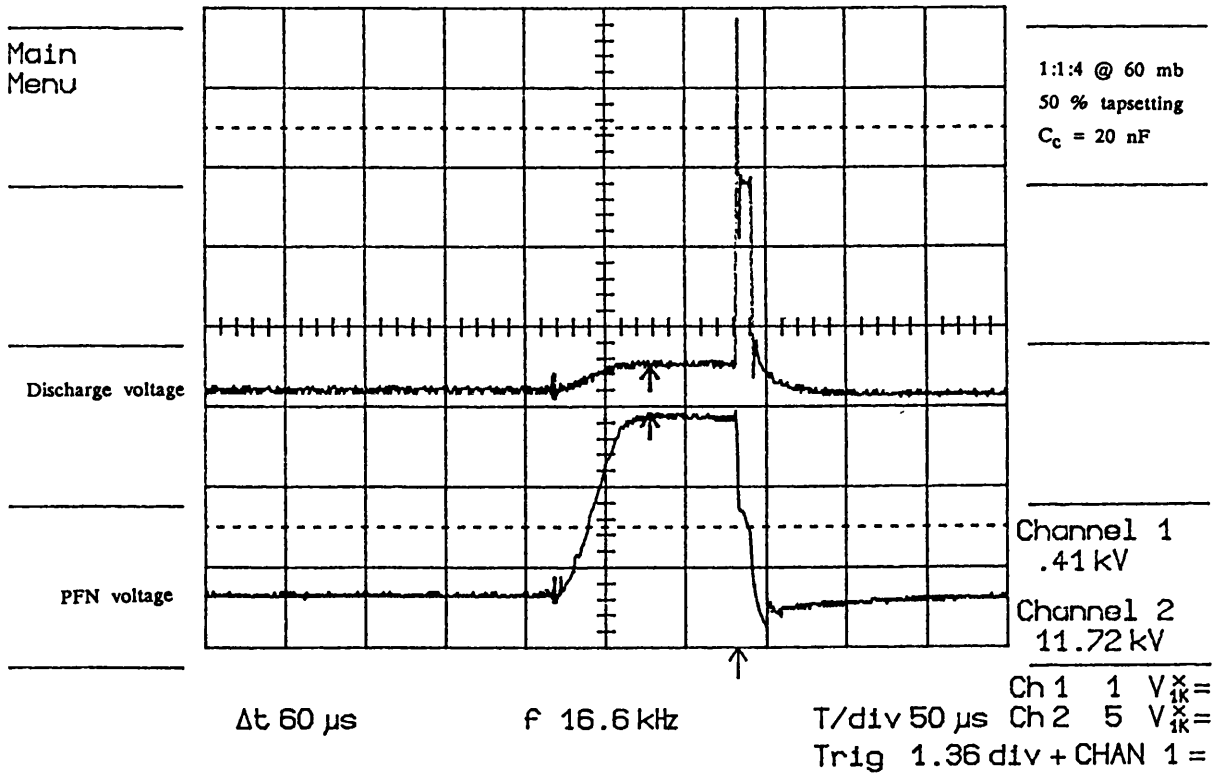


FIGURE 3.20 DISCHARGE AND PFN VOLTAGE TRANSIENTS

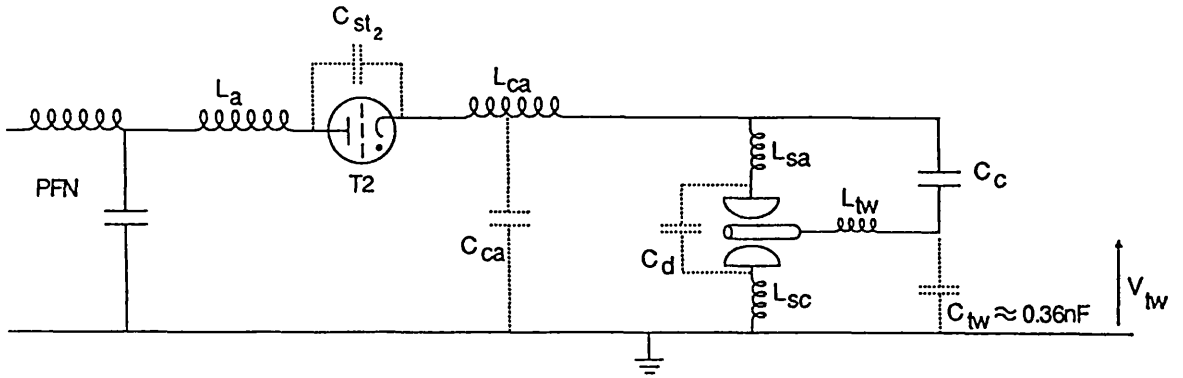


FIGURE 3.21 EQUIVALENT LASER CIRCUIT

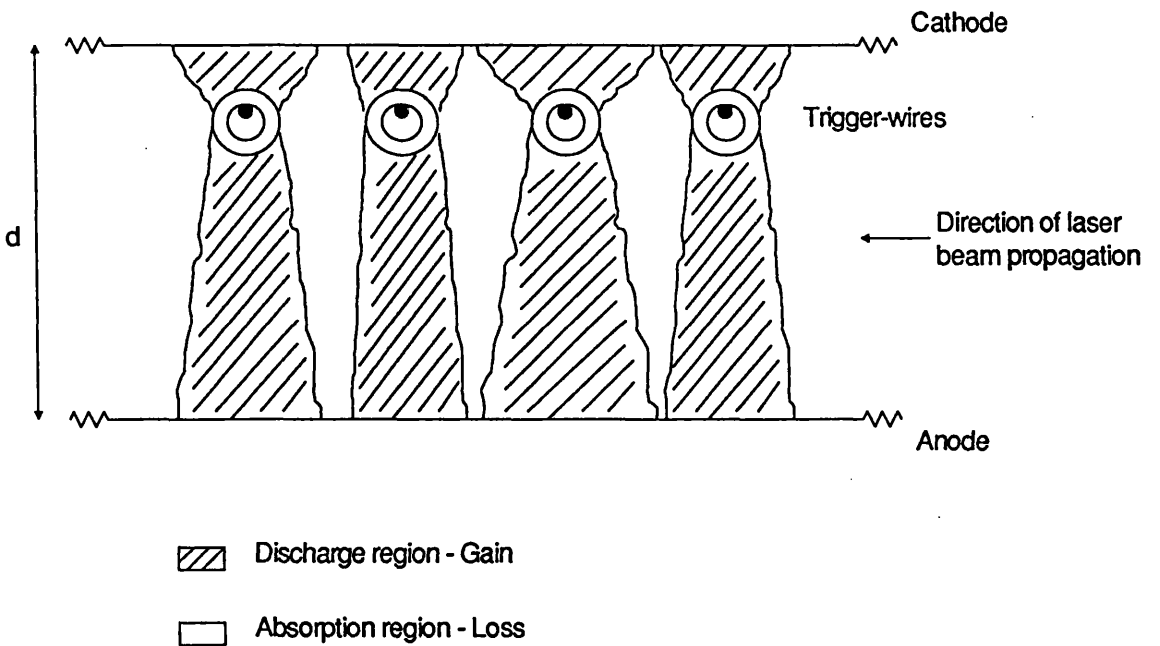


FIGURE 3.22 DISCHARGE SPATIAL DEVELOPMENT

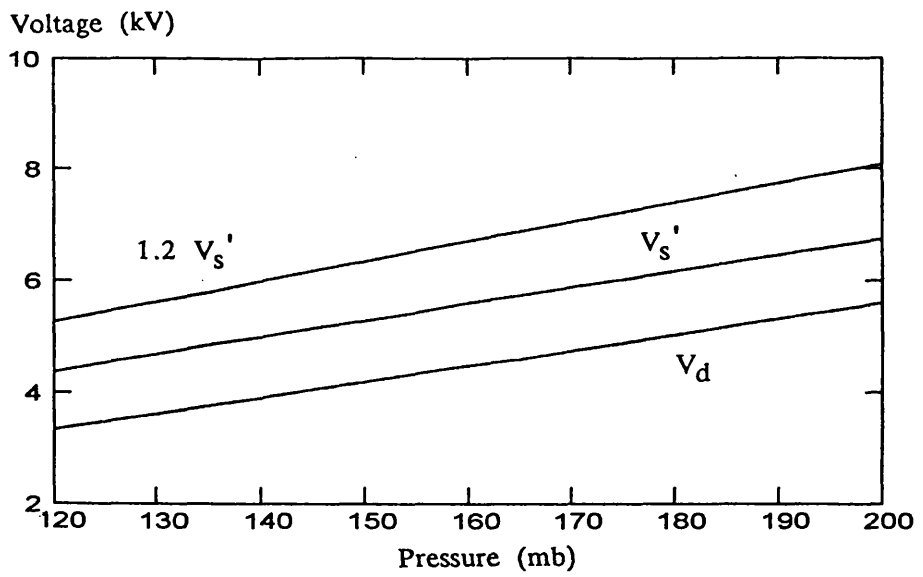


FIGURE 3.23 DISCHARGE BREAKDOWN VOLTAGE VS GAS PRESSURE

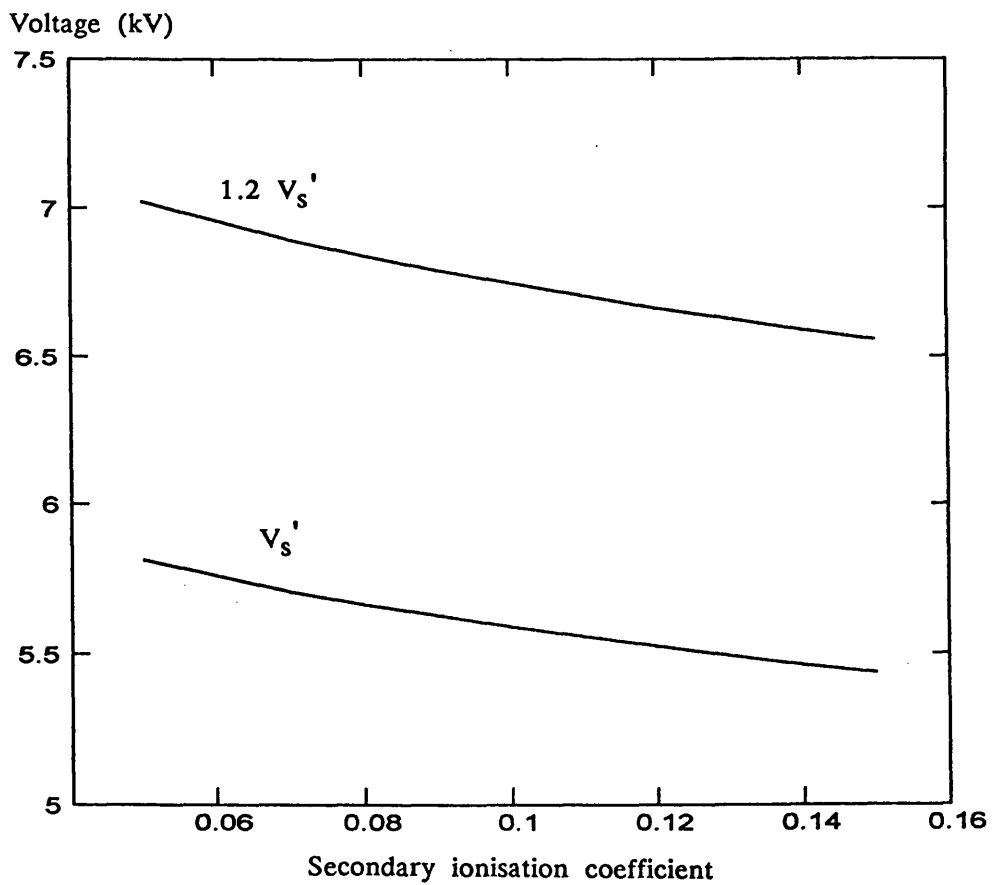


FIGURE 3.24 BREAKDOWN VOLTAGE VS SECONDARY IONISATION COEFFICIENT

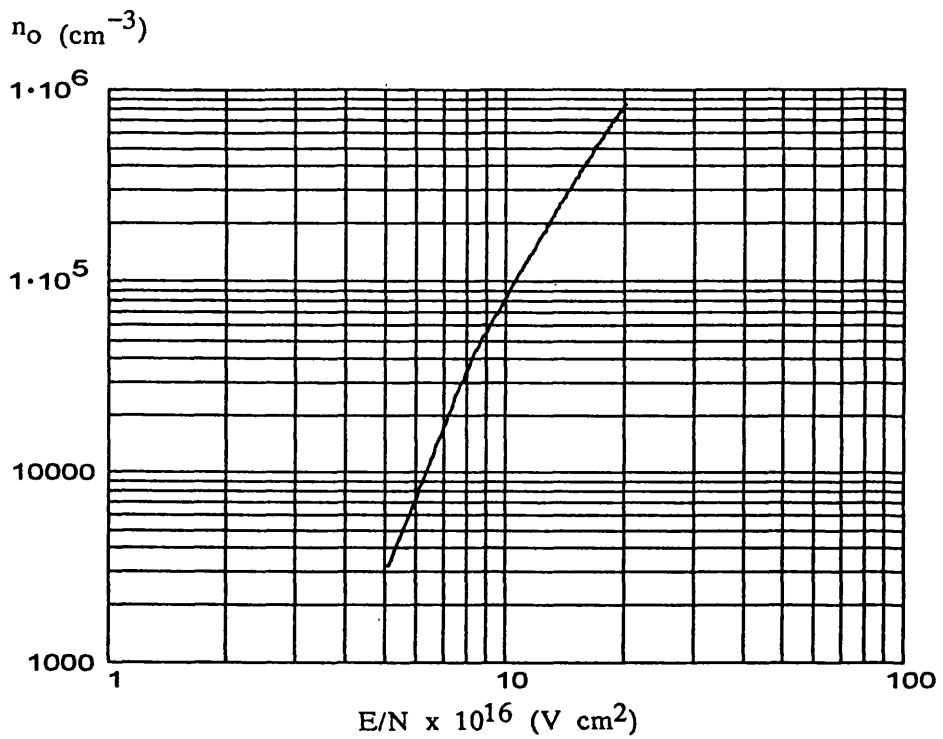


FIGURE 3.25 INITIAL PREIONISATION ELECTRON DENSITY VS E/N

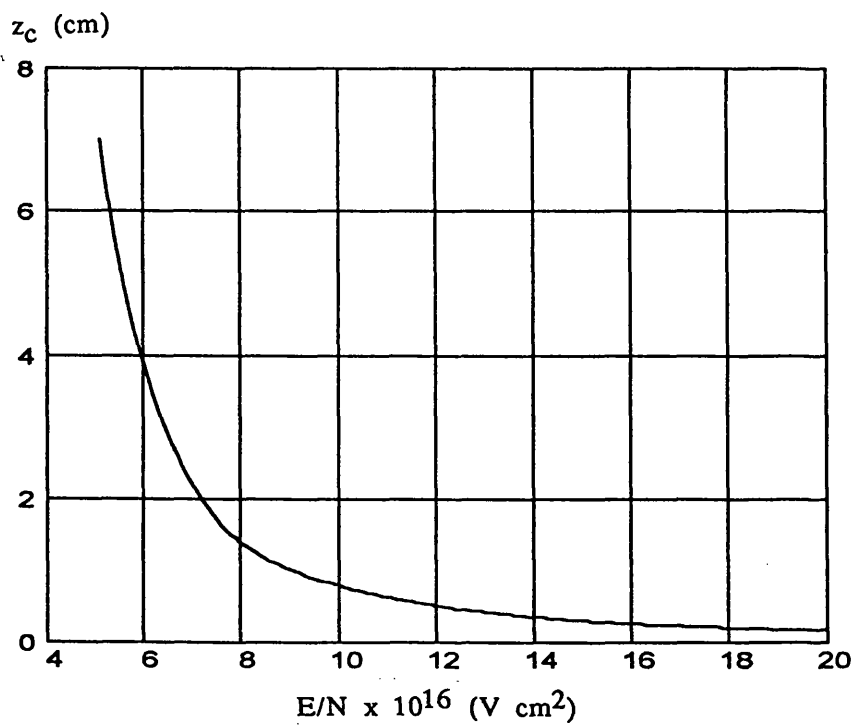


FIGURE 3.26 z_c VS E/N

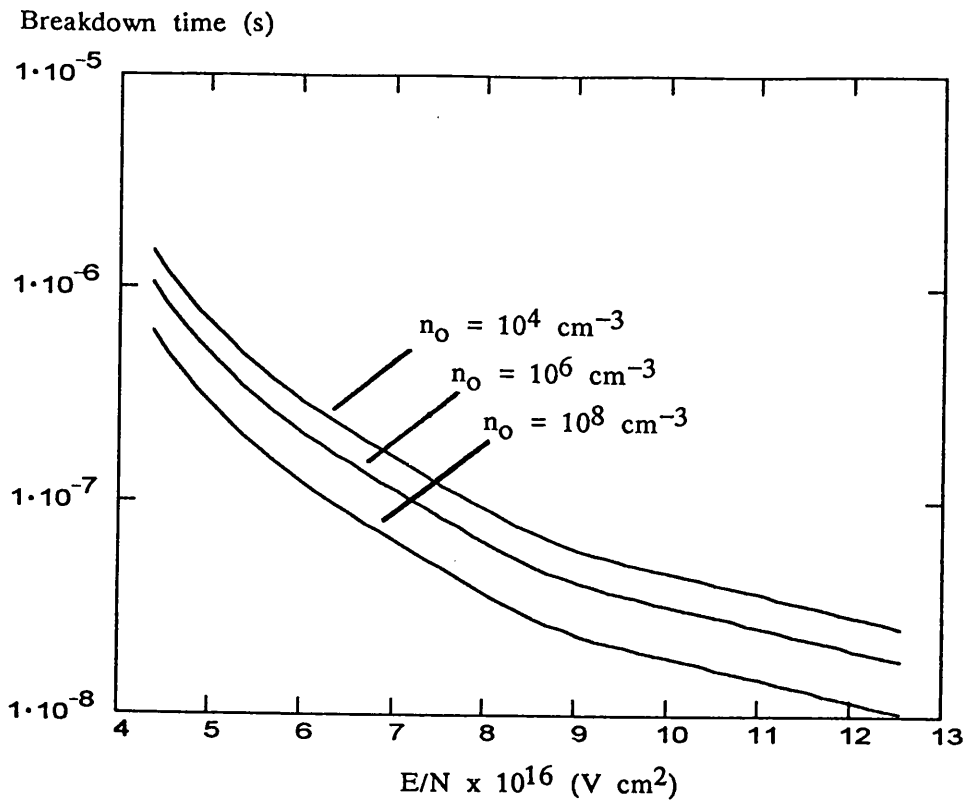


FIGURE 3.27 FORMATIVE TIME LAG VS E/N

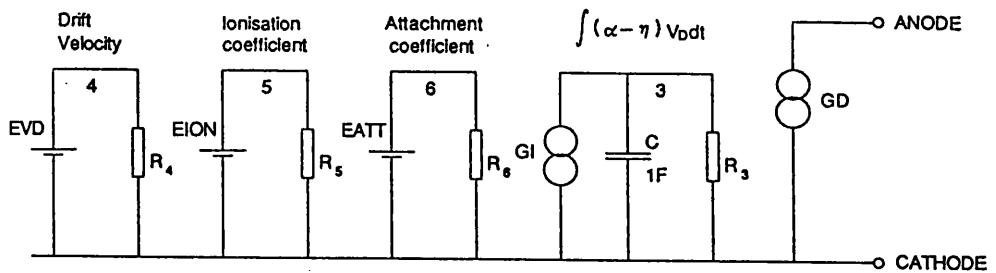


FIGURE 3.28 PSPICE CIRCUIT DISCHARGE MODEL

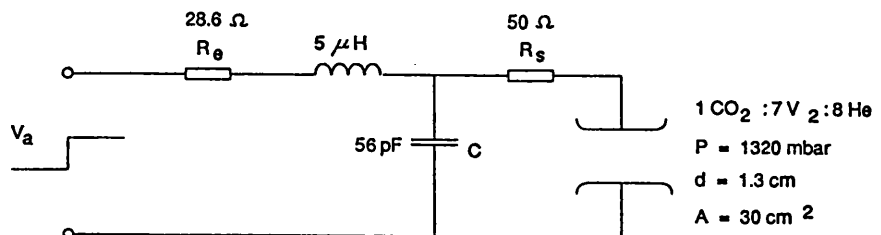


FIGURE 3.29 KLINES DISCHARGE CIRCUIT

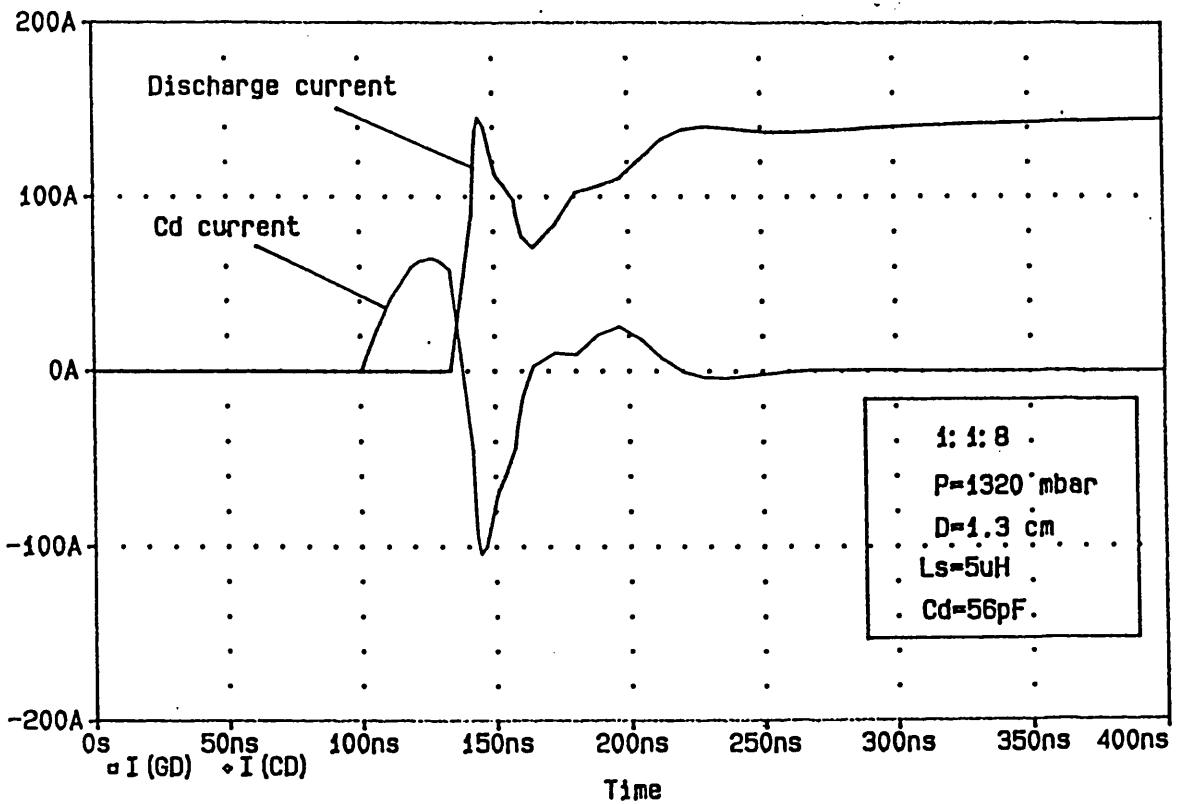
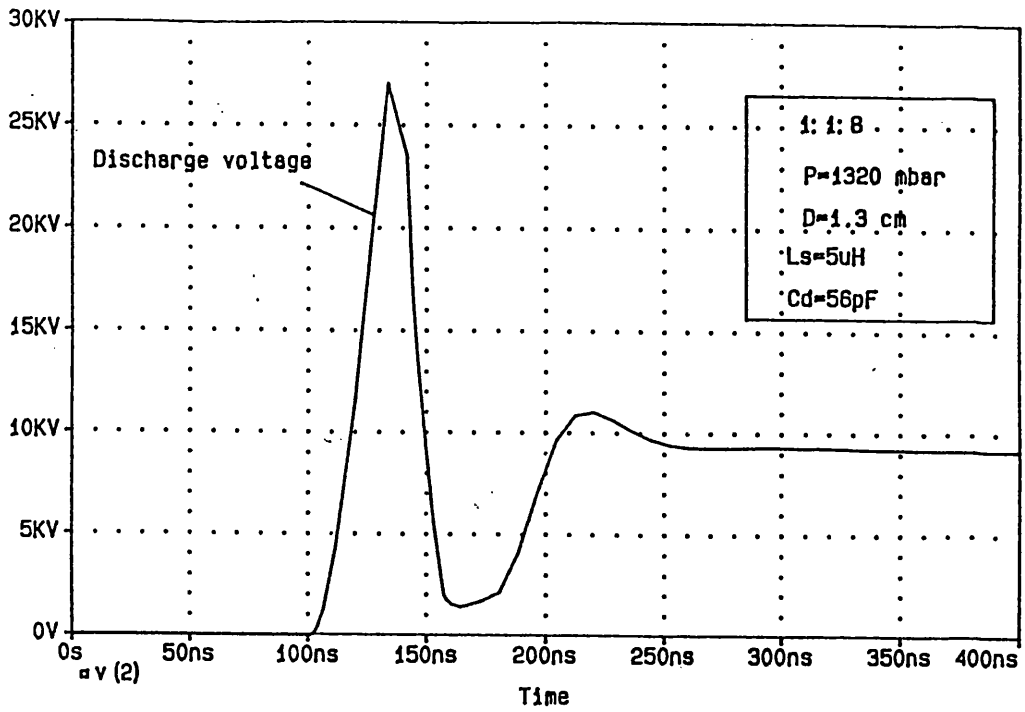


FIGURE 3.30 DISCHARGE VOLTAGE AND CURRENT CHARACTERISTICS

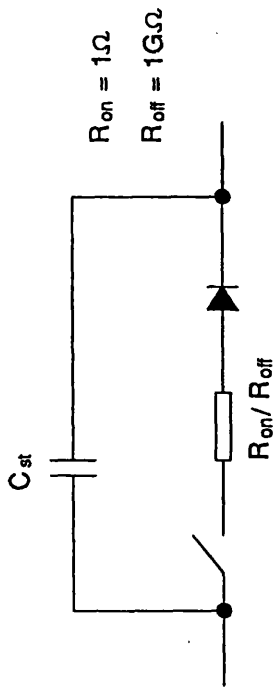


FIGURE 3.31 THYRATRON EQUIVALENT CIRCUIT MODEL

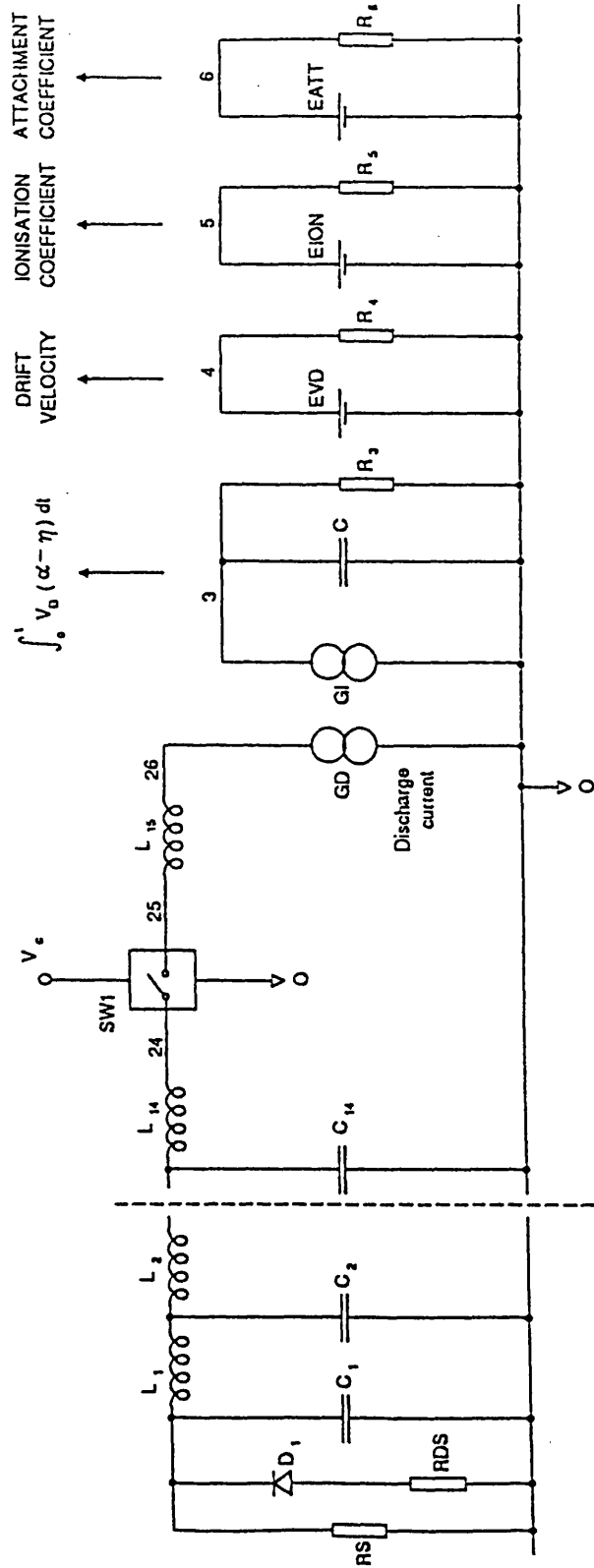


FIGURE 3.32 SPICE MODEL OF PFN DISCHARGE CIRCUIT

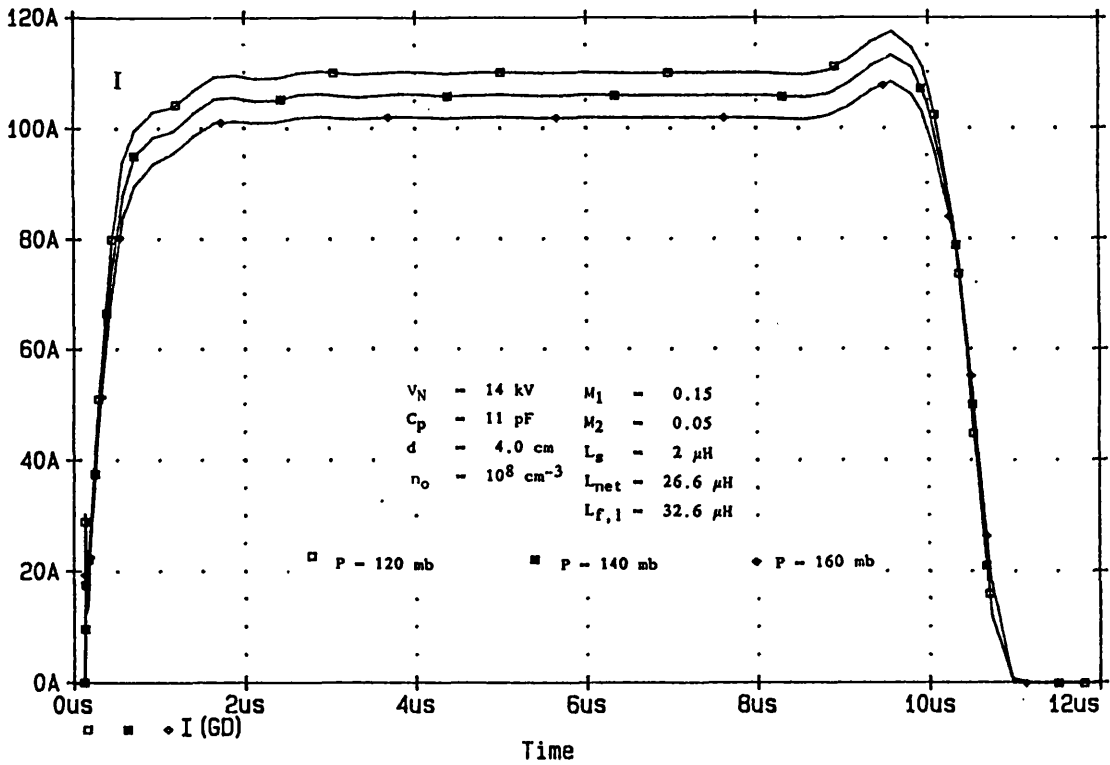
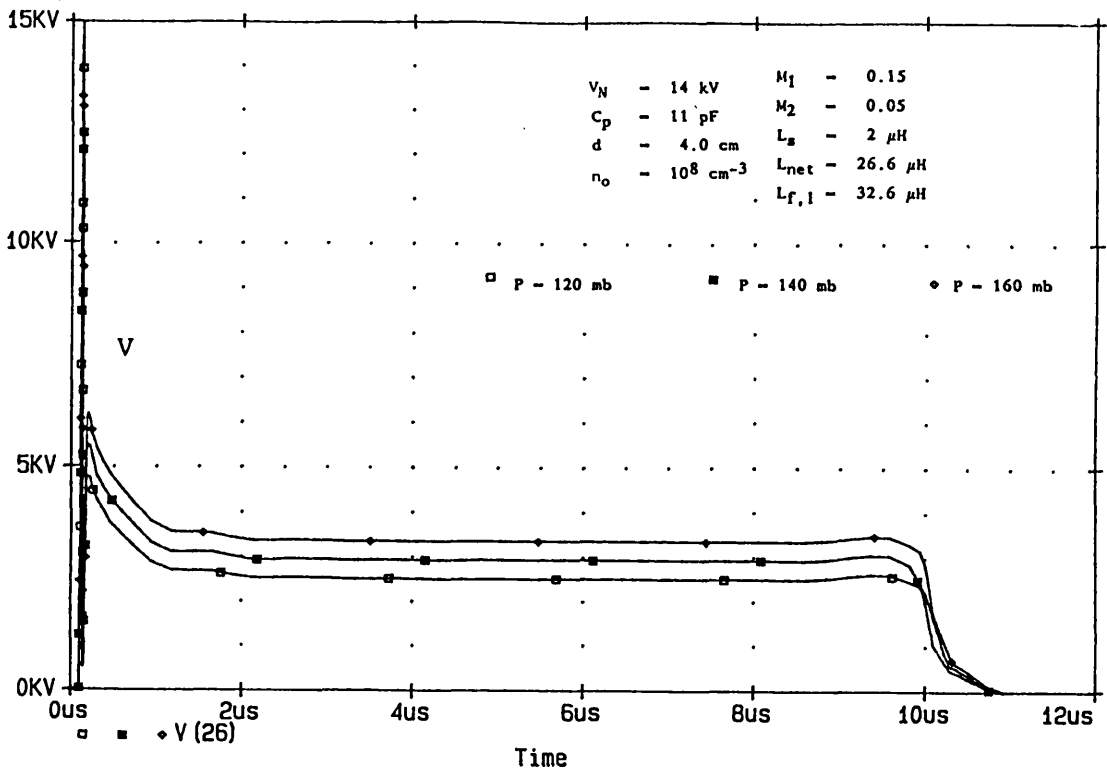


FIGURE 3.33 V-I CHARACTERISTICS FOR 1:1:8 GAS MIXTURE

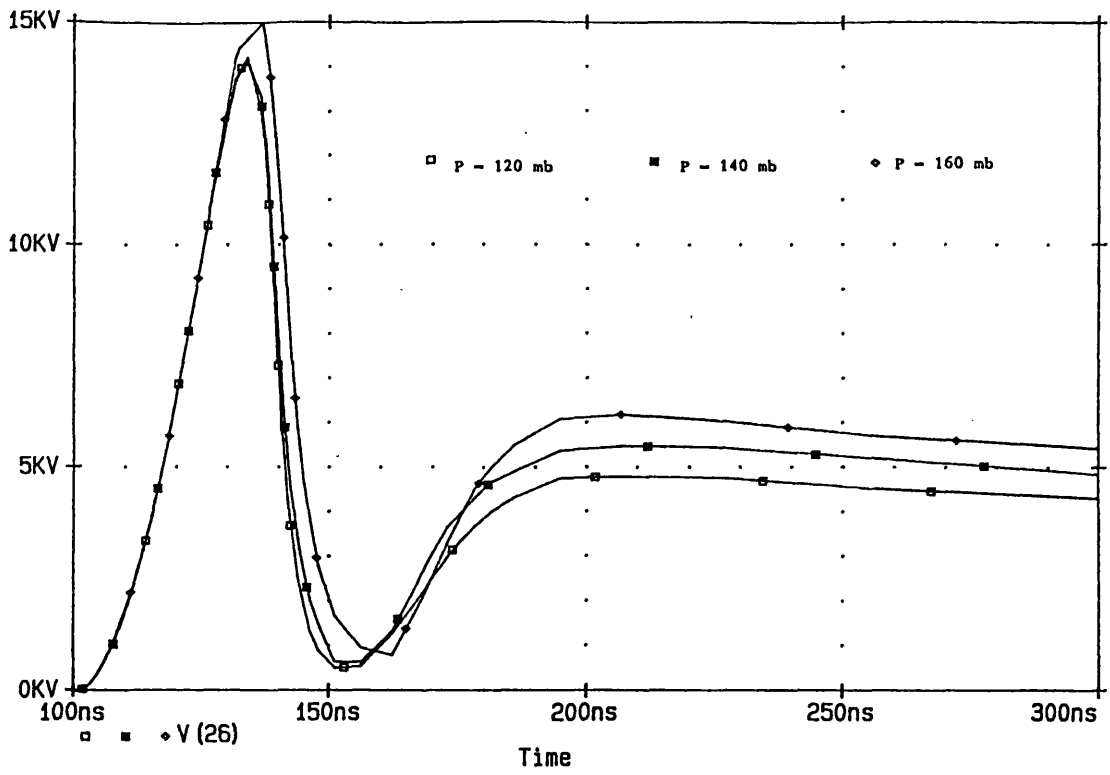


FIGURE 3.34 DISCHARGE VOLTAGE

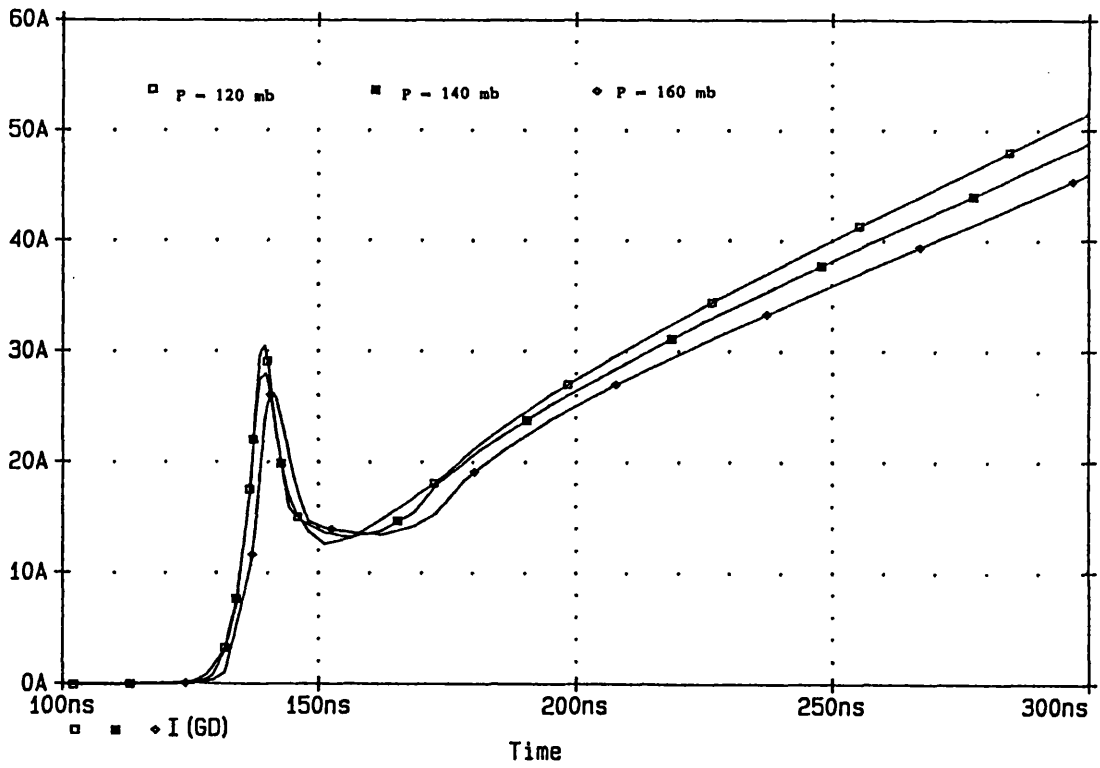


FIGURE 3.35 DISCHARGE CURRENT

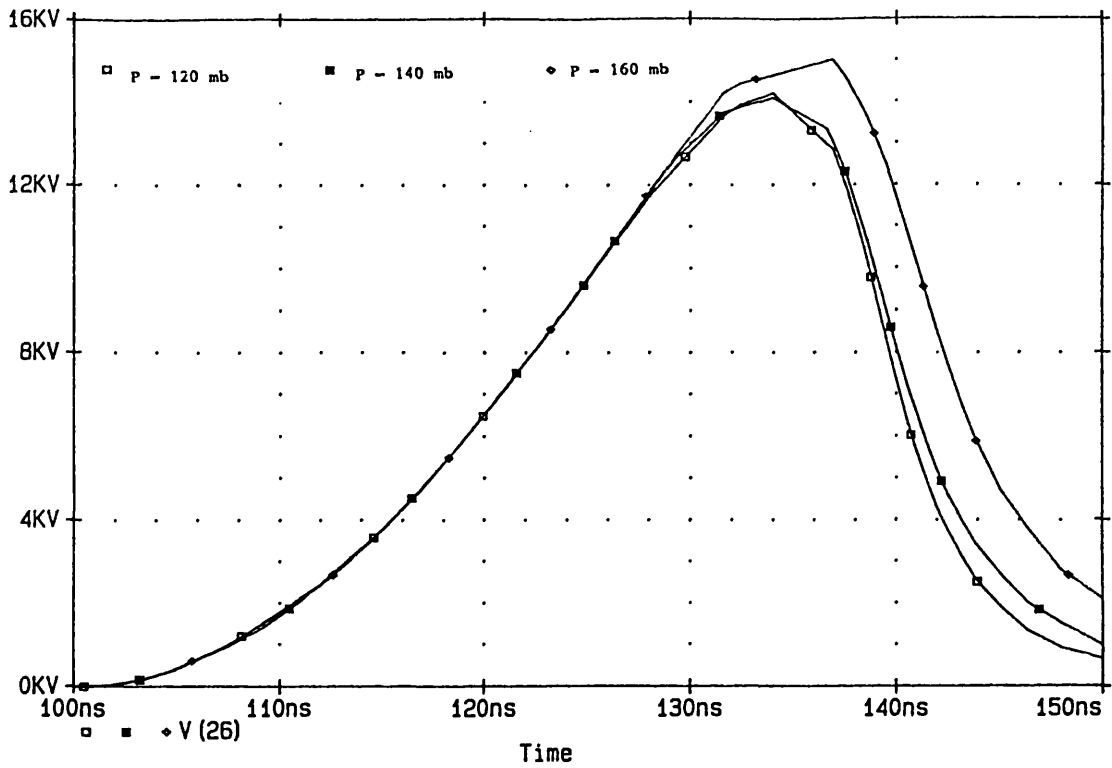


FIGURE 3.36 DISCHARGE VOLTAGE ON EXPANDED TIME BASE

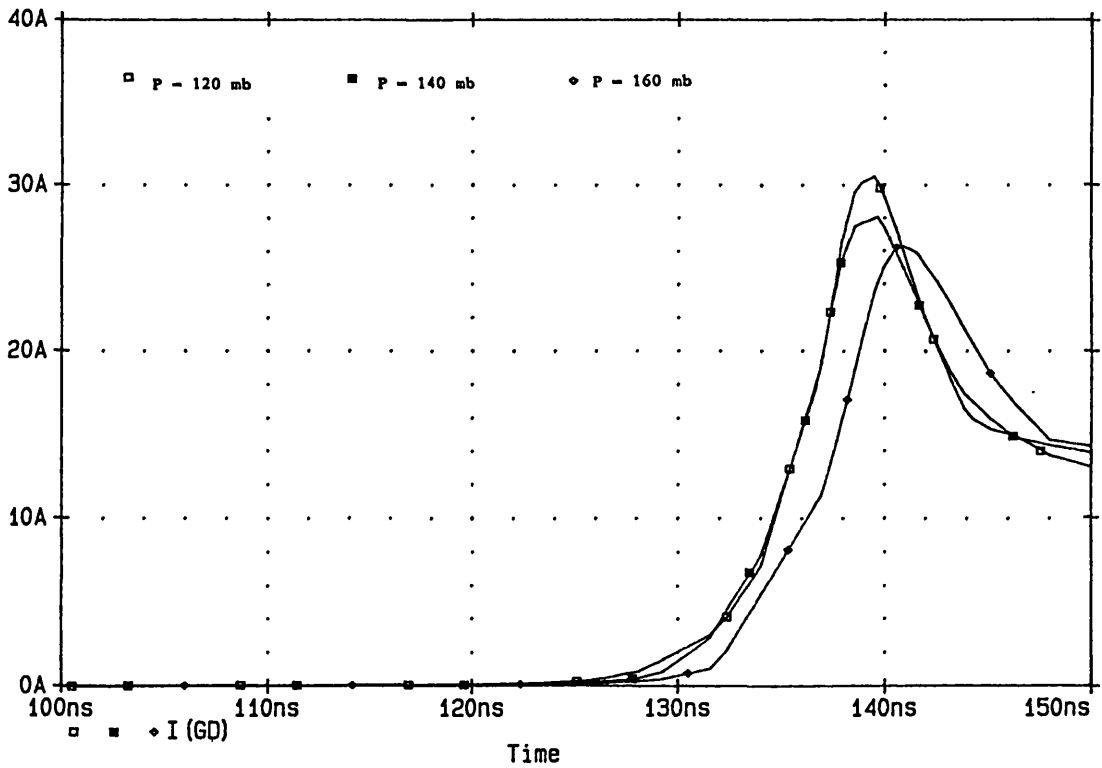


FIGURE 3.37 DISCHARGE CURRENT ON EXPANDED TIME BASE

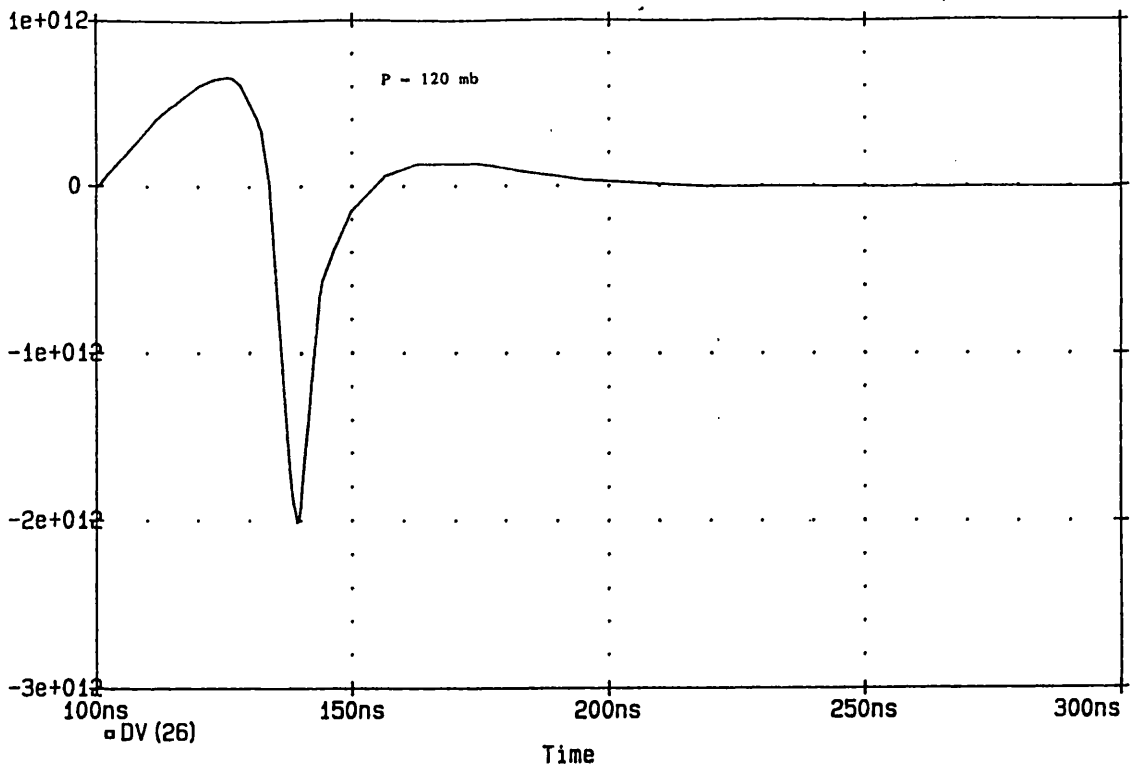


FIGURE 3.38 RATE OF CHANGE OF VOLTAGE

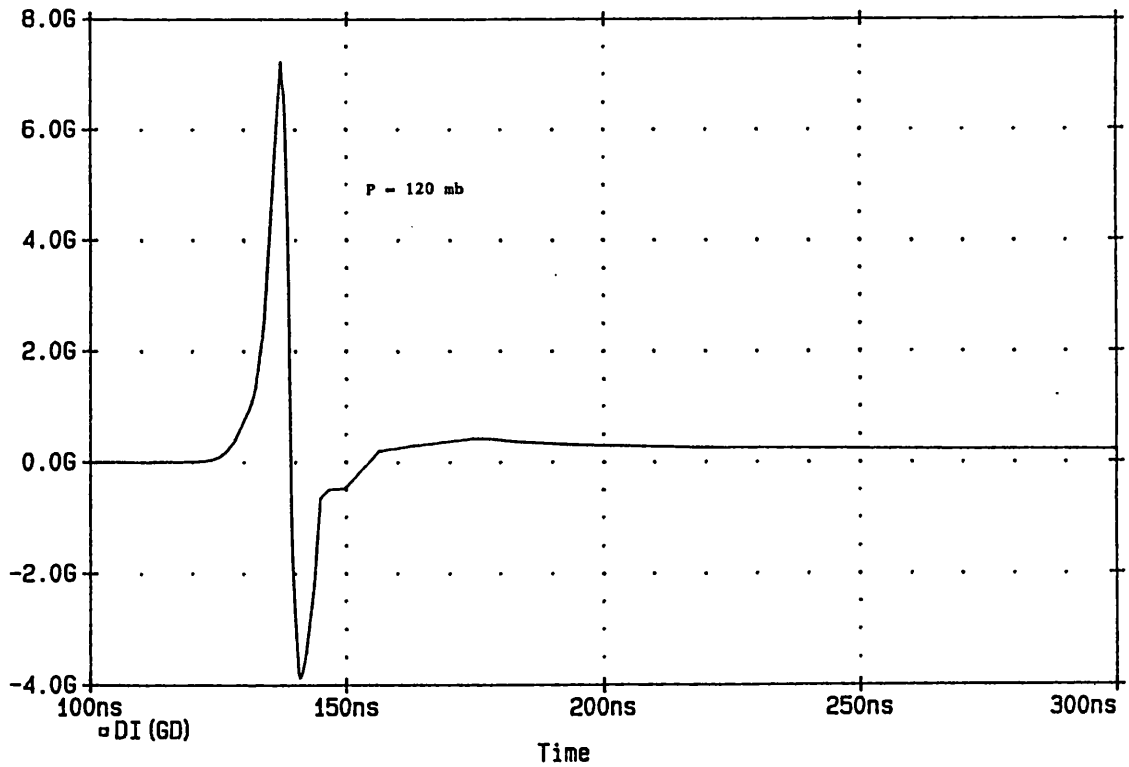


FIGURE 3.39 RATE OF CHANGE OF CURRENT

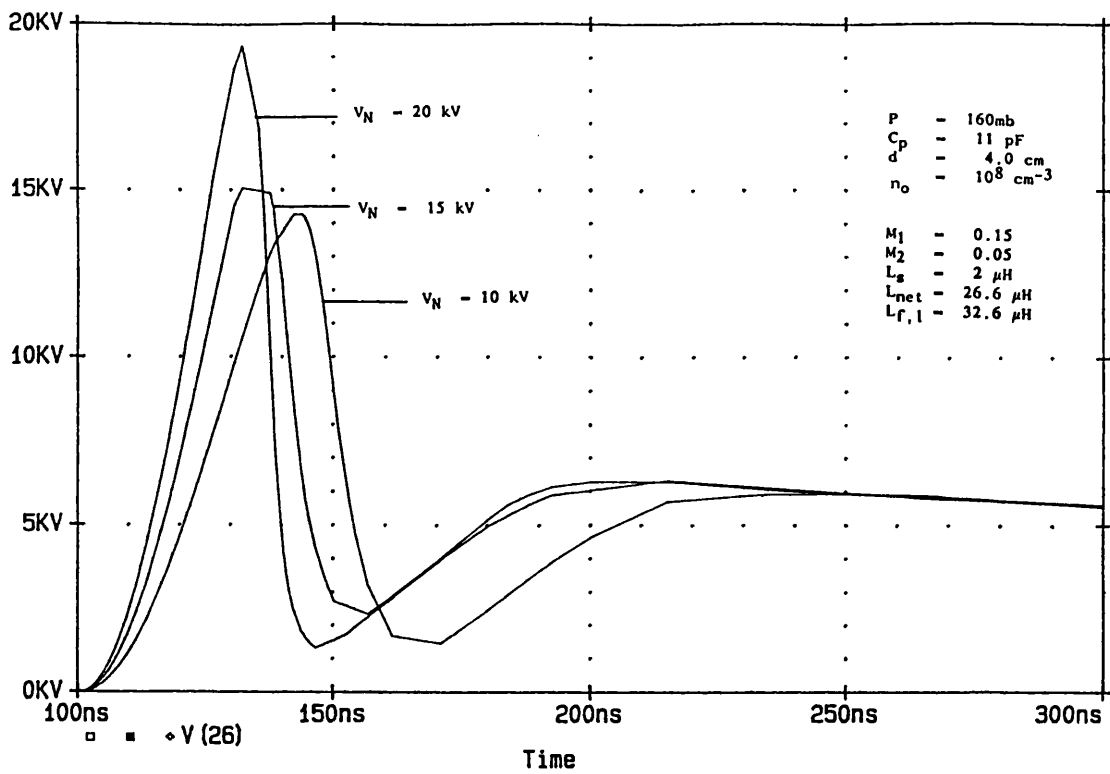


FIGURE 3.40 DISCHARGE VOLTAGE FOR DIFFERENT NETWORK VOLTAGES

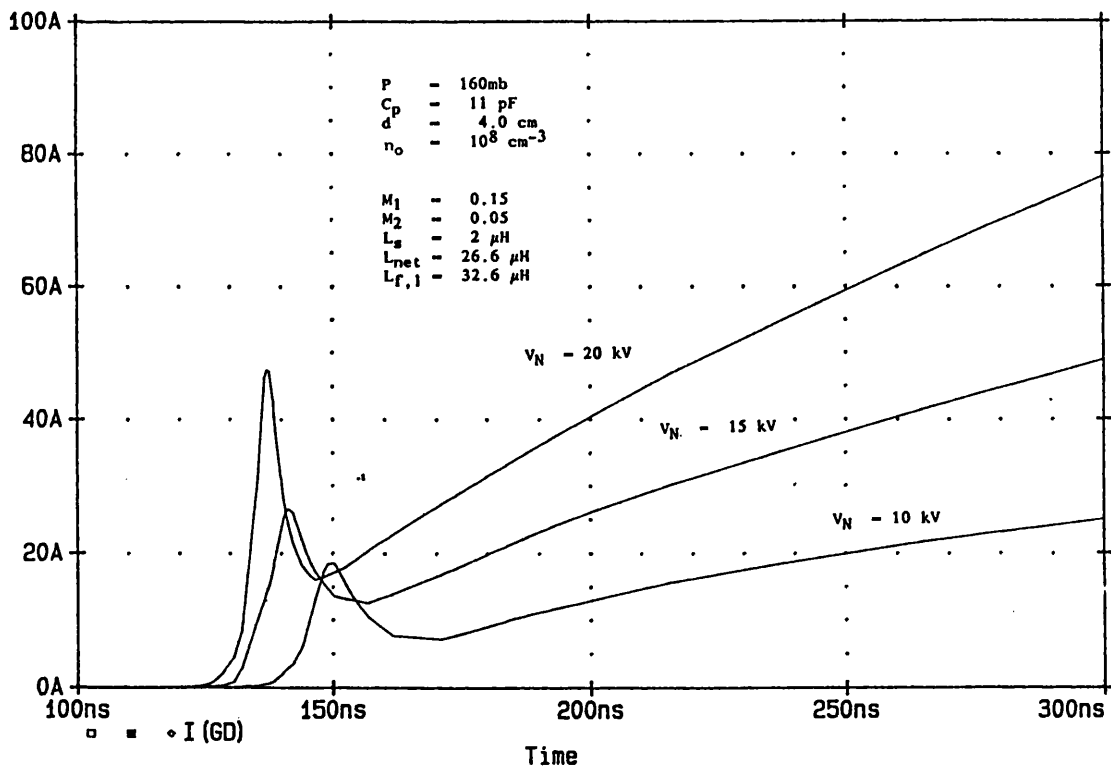


FIGURE 3.41 DISCHARGE CURRENT FOR DIFFERENT NETWORK VOLTAGES

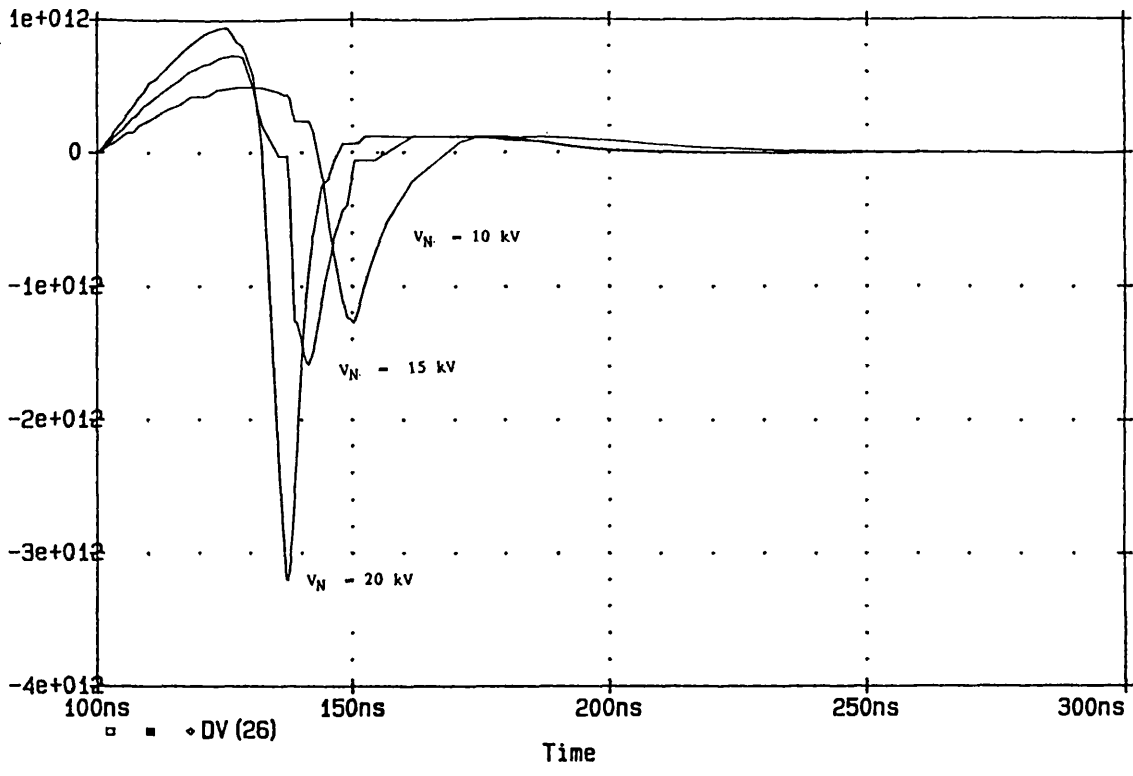


FIGURE 3.42 RATE OF CHANGE OF VOLTAGE FOR DIFFERENT V_N

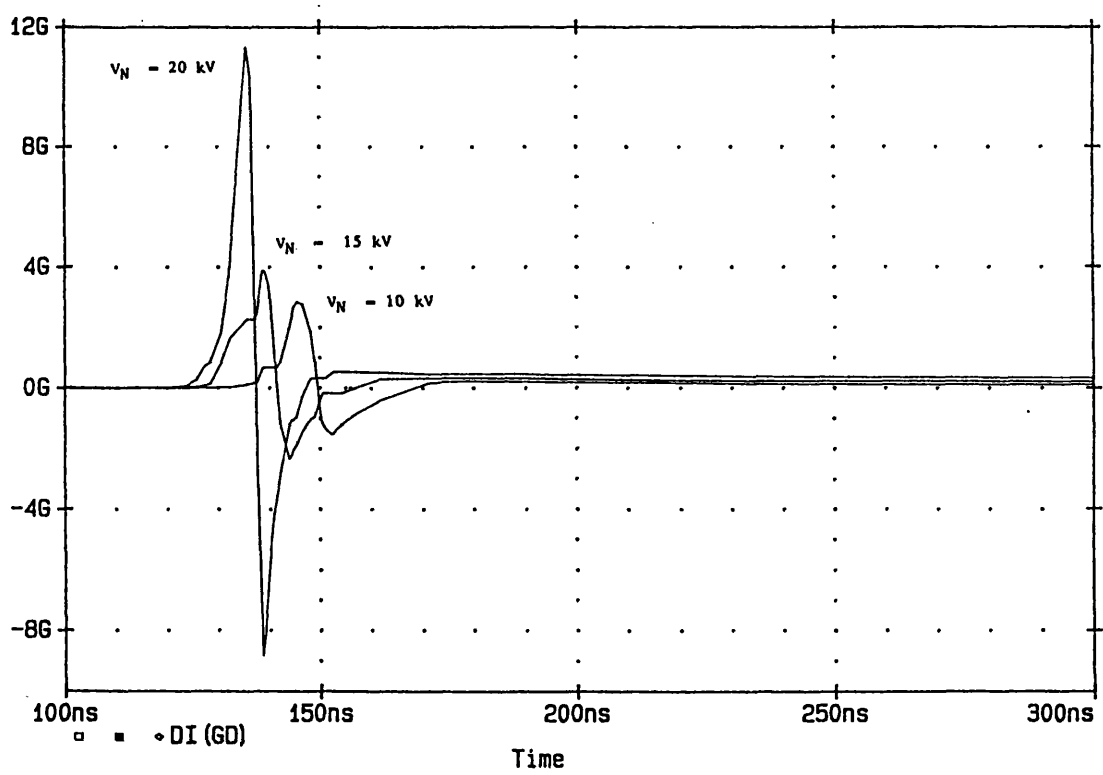


FIGURE 3.43 RATE OF CHANGE OF CURRENT FOR DIFFERENT V_N

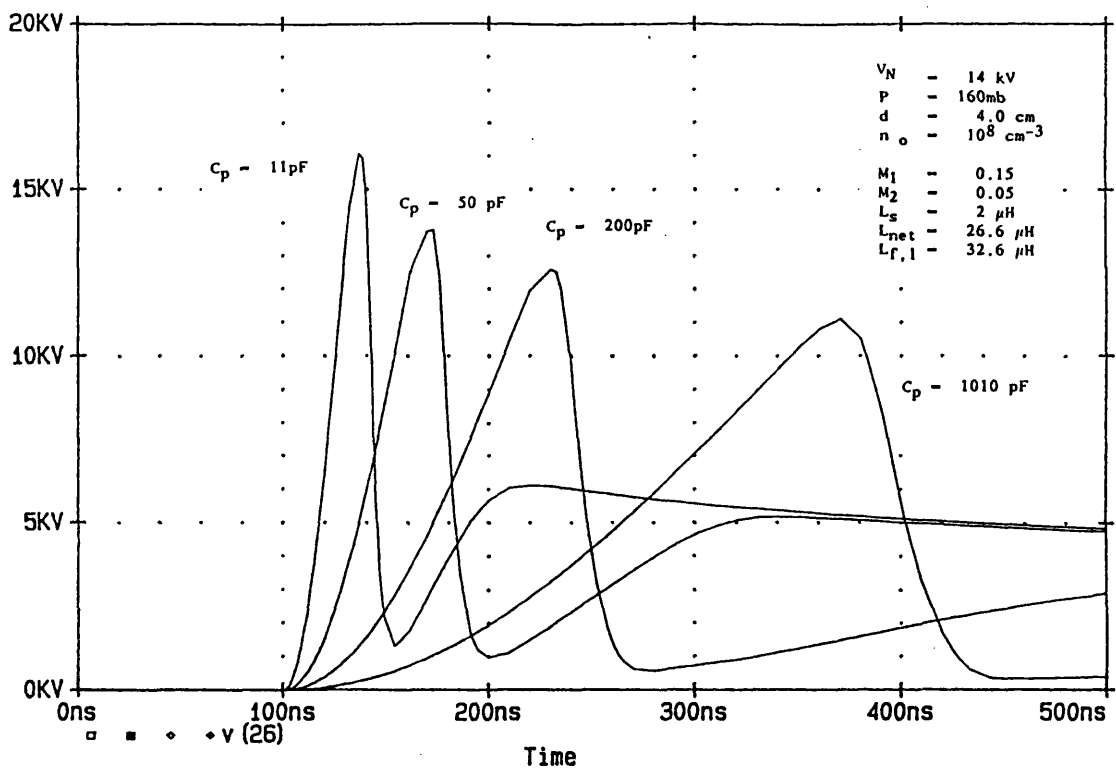


FIGURE 3.44 DISCHARGE VOLTAGE: AFFECT OF PEAKING CAPACITANCE

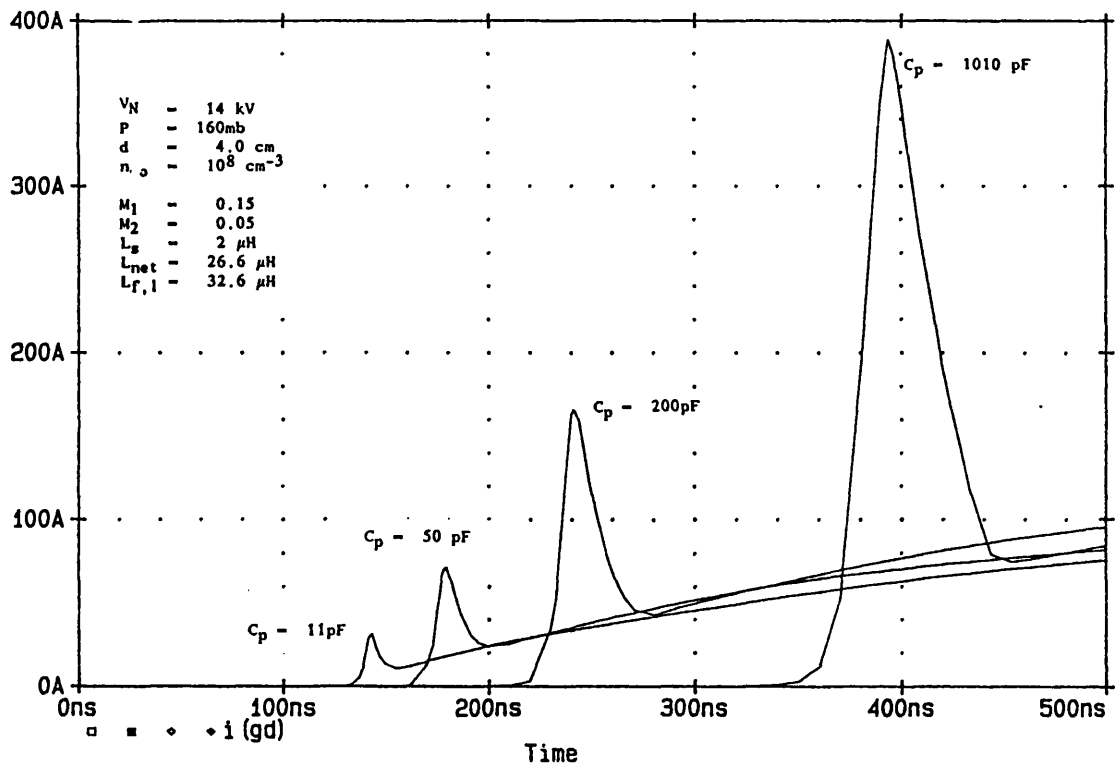


FIGURE 3.45 DISCHARGE CURRENT: AFFECT OF PEAKING CAPACITANCE

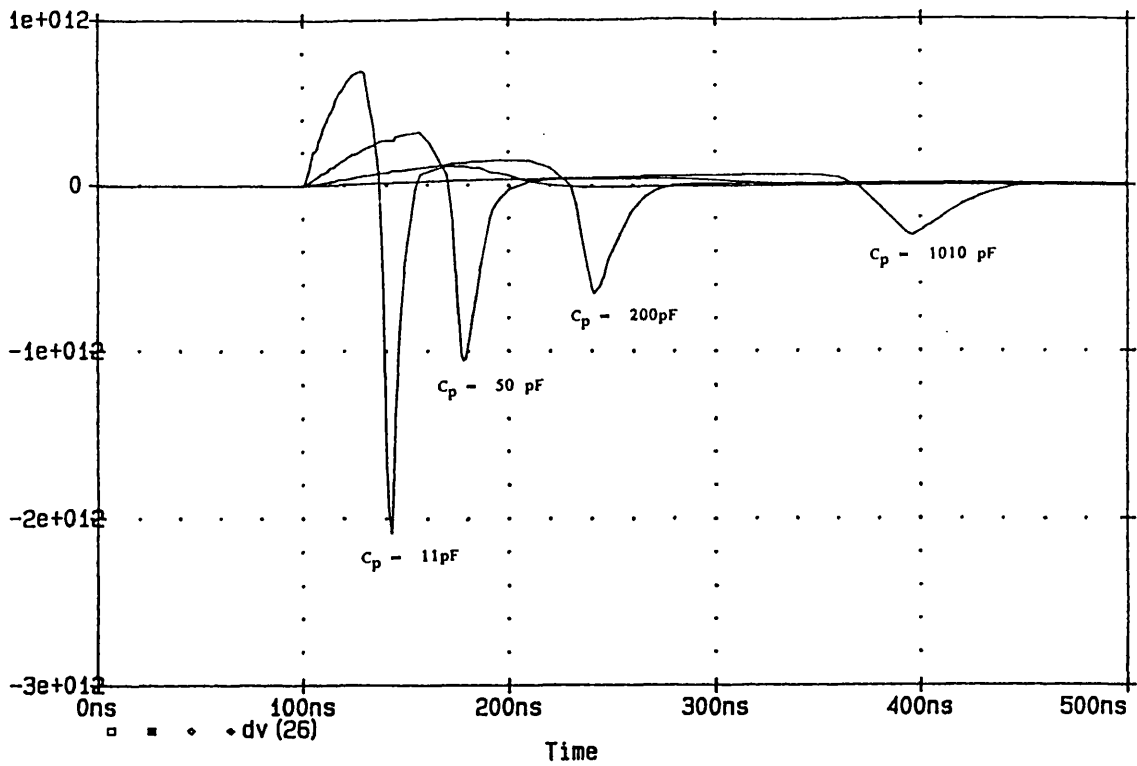


FIGURE 3.46 RATE OF CHANGE OF VOLTAGE: AFFECT OF C_p

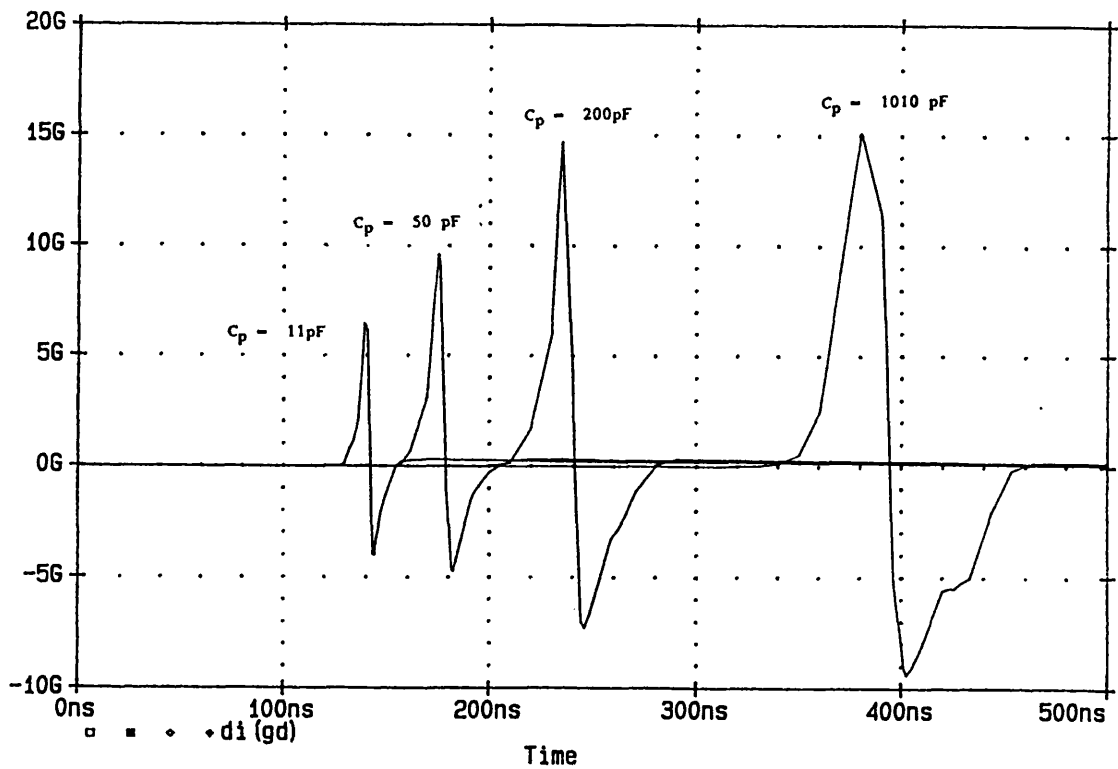


FIGURE 3.47 RATE OF CHANGE OF CURRENT: AFFECT OF C_p

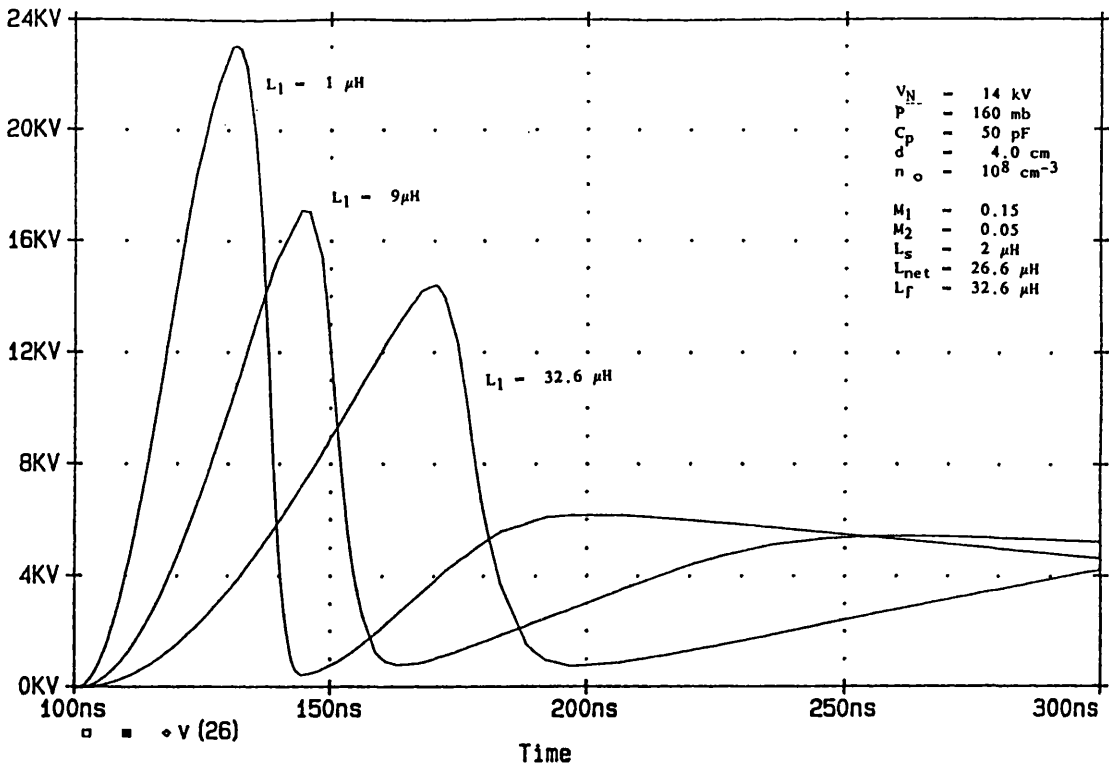


FIGURE 3.48 DISCHARGE VOLTAGE: AFFECT OF INDUCTANCE

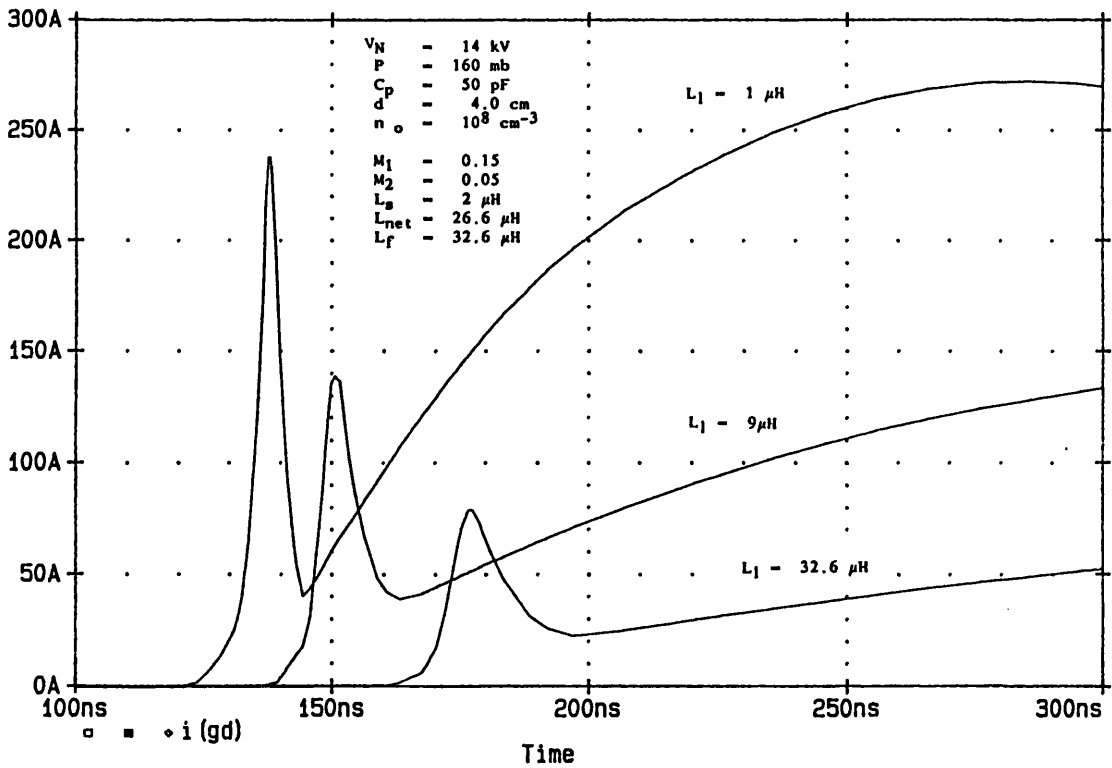


FIGURE 3.49 DISCHARGE CURRENT: AFFECT OF INDUCTANCE

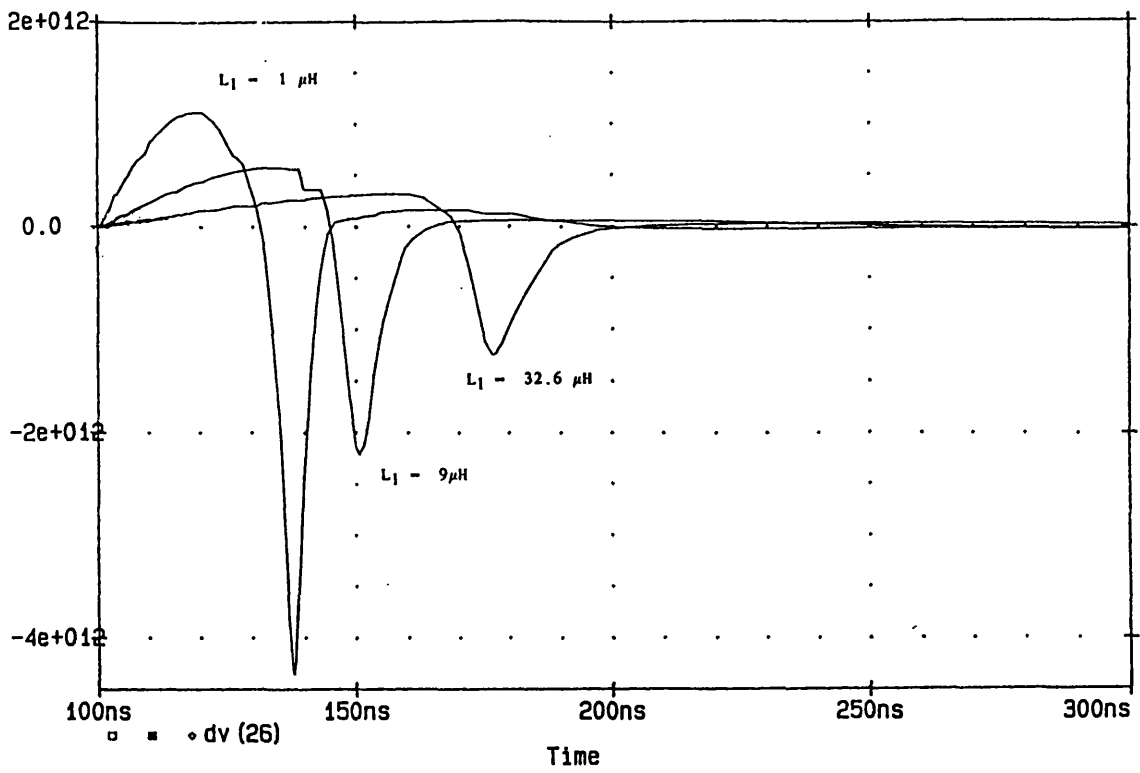


FIGURE 3.50 RATE OF CHANGE OF VOLTAGE: AFFECT OF INDUCTANCE

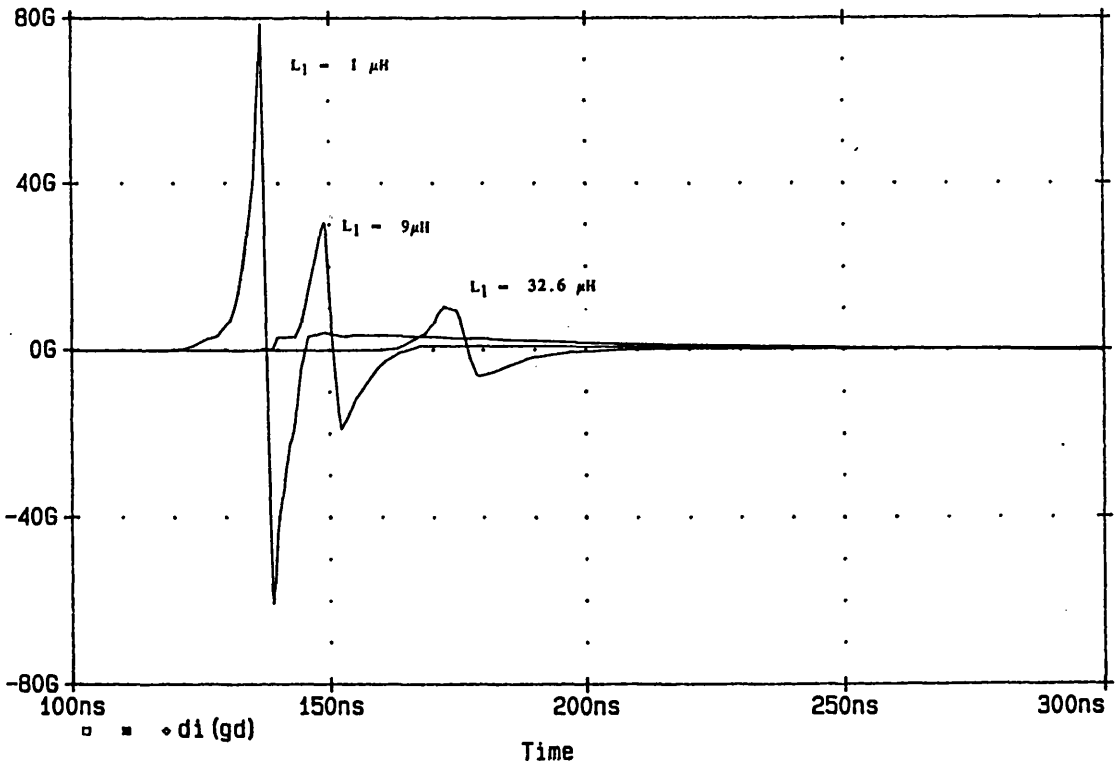


FIGURE 3.51 RATE OF CHANGE OF CURRENT: AFFECT OF INDUCTANCE

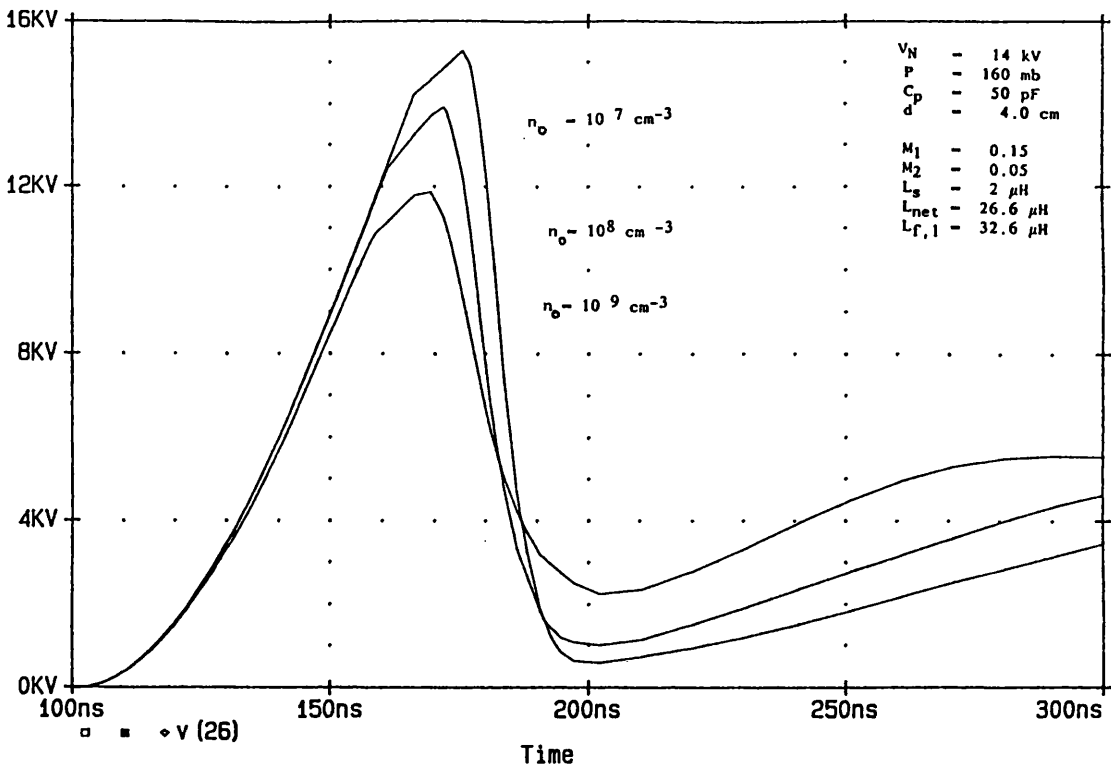


FIGURE 3.52 DISCHARGE VOLTAGE: AFFECT OF n_o

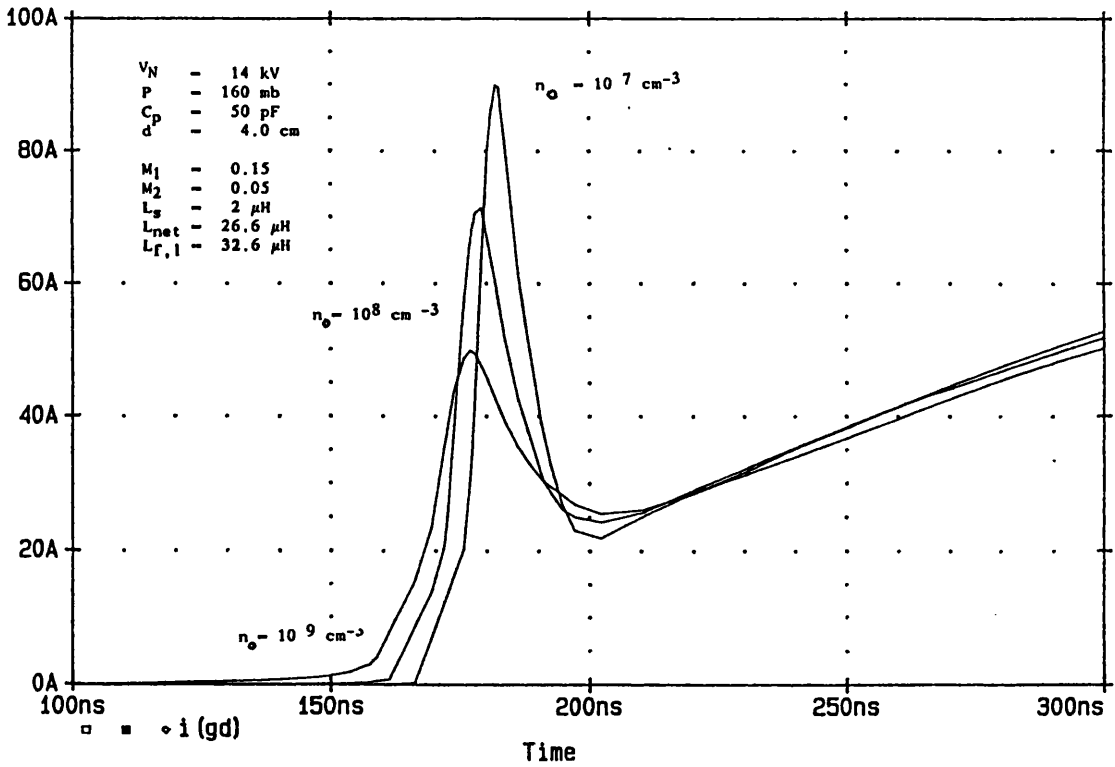


FIGURE 3.53 DISCHARGE CURRENT: AFFECT OF n_o

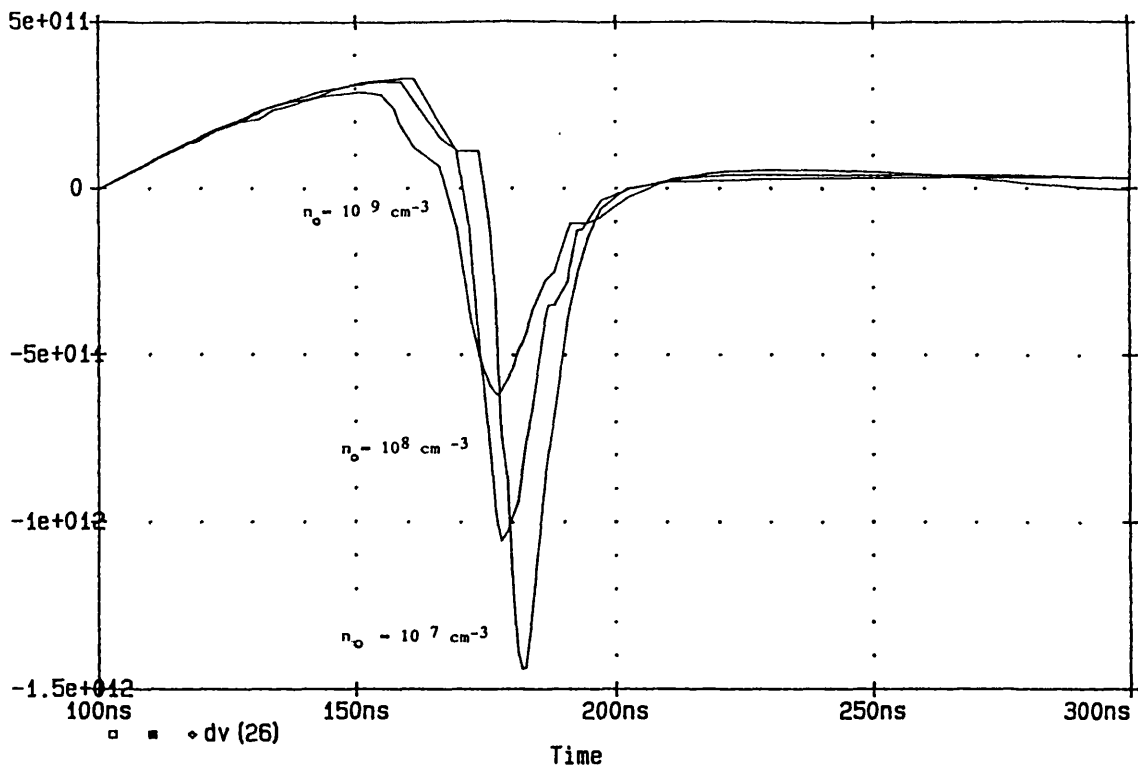


FIGURE 3.54 RATE OF CHANGE OF VOLTAGE: AFFECT OF n_0

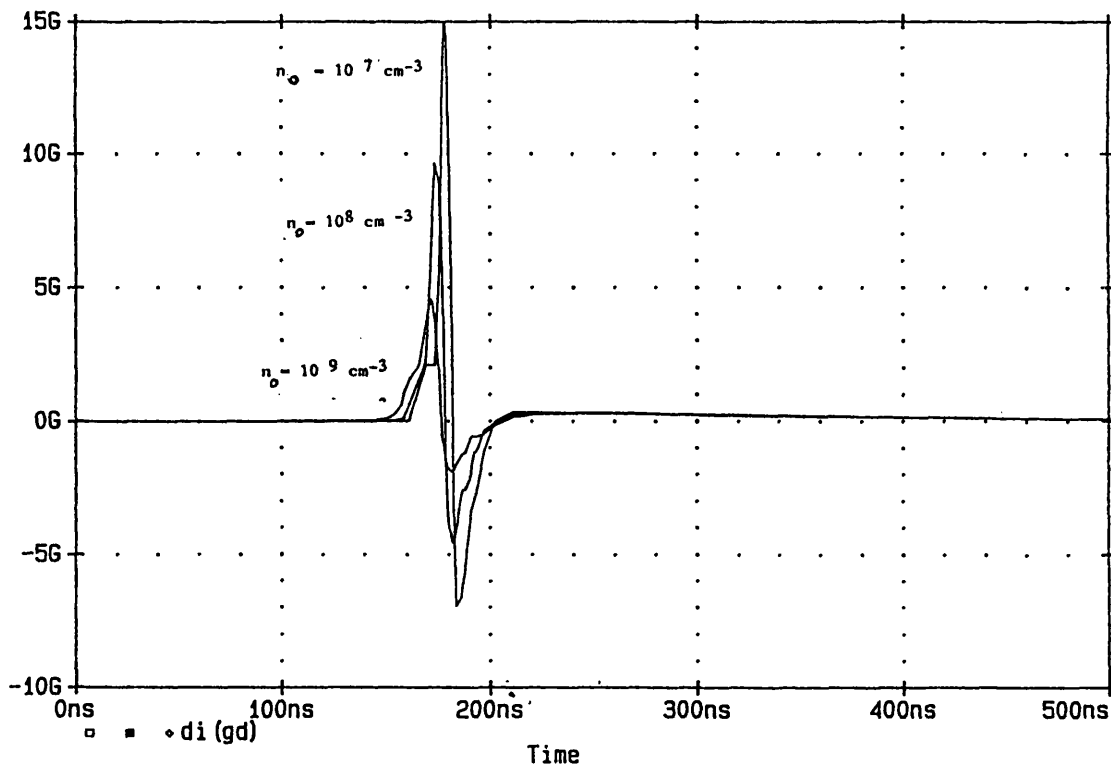


FIGURE 3.55 RATE OF CHANGE OF CURRENT: AFFECT OF n_0

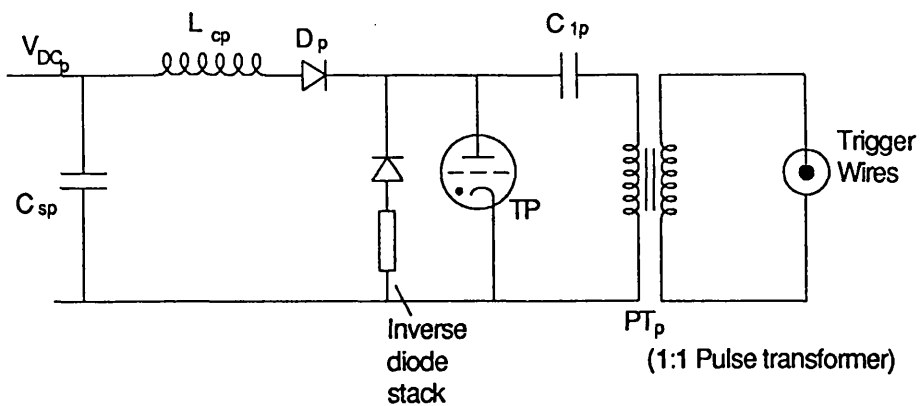


FIGURE 3.56 HIGH VOLTAGE PREIONISER CIRCUIT

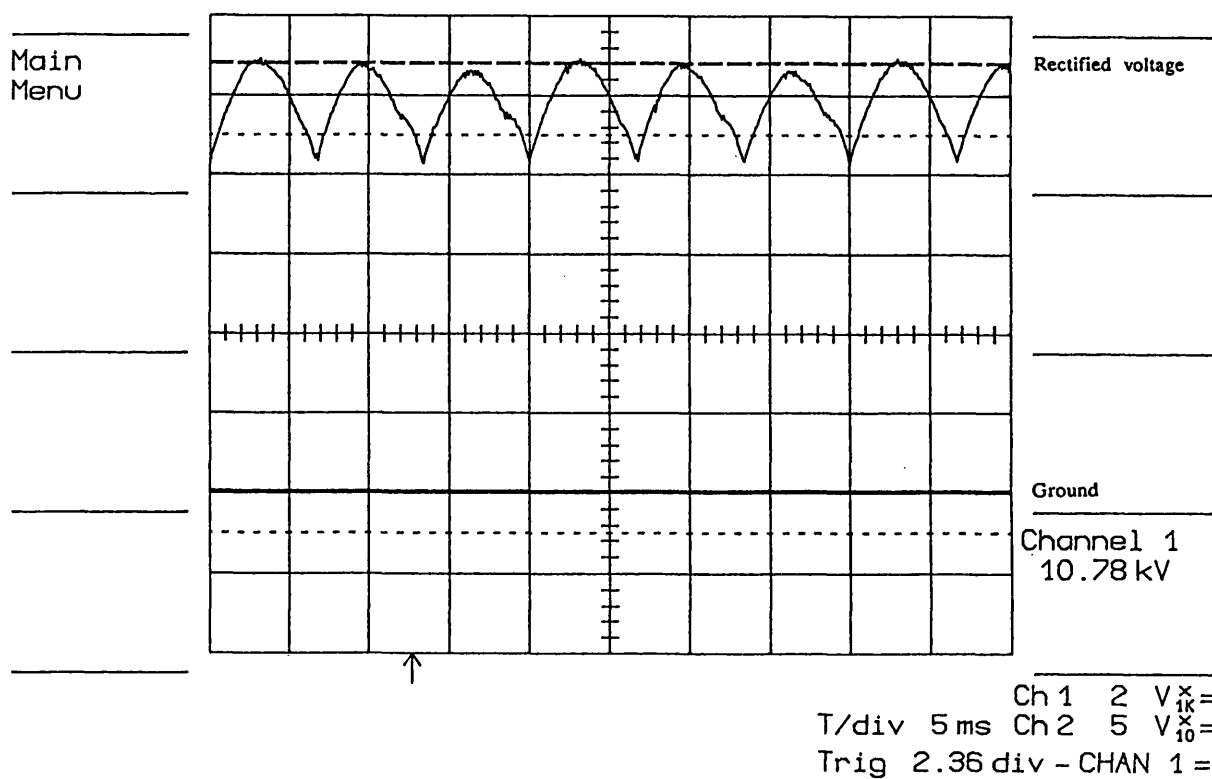


FIGURE 3.57 RECTIFIED PREIONISER VOLTAGE

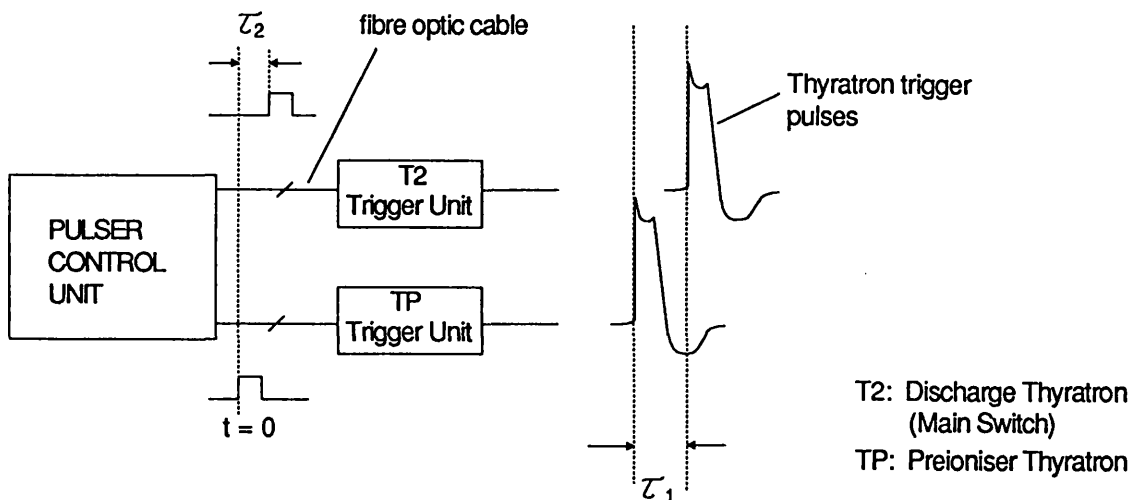


FIGURE 3.58 SCHEMATIC OF TP AND T2 TRIGGER PULSES

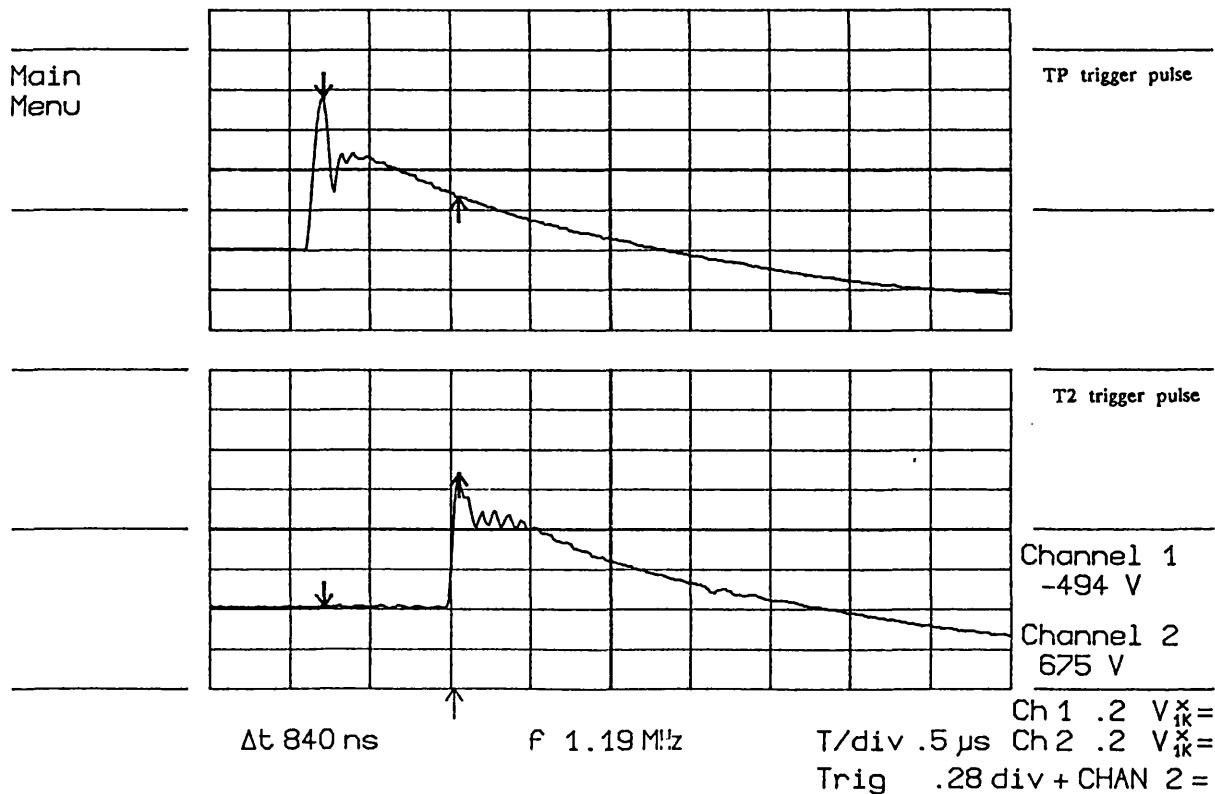


FIGURE 3.59 TP AND T2 TRIGGER PULSES

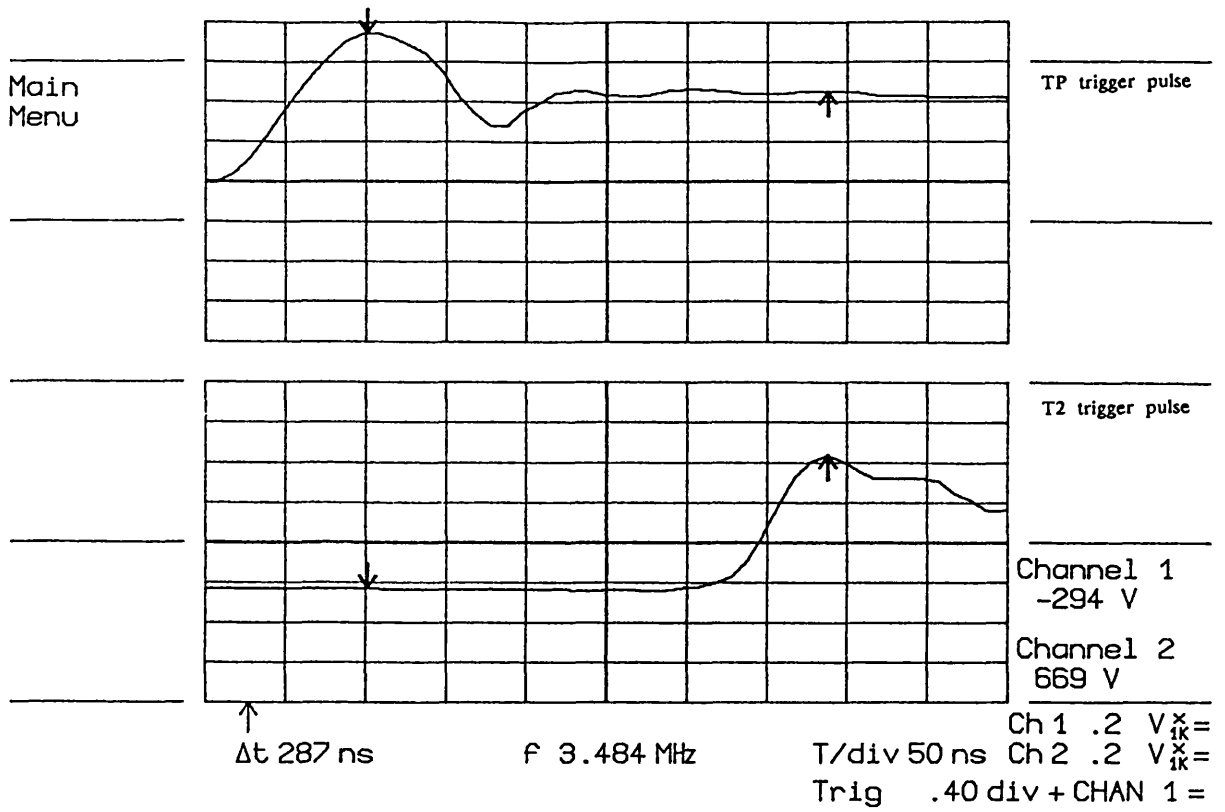


FIGURE 3.60 TP AND T2 TRIGGER PULSES

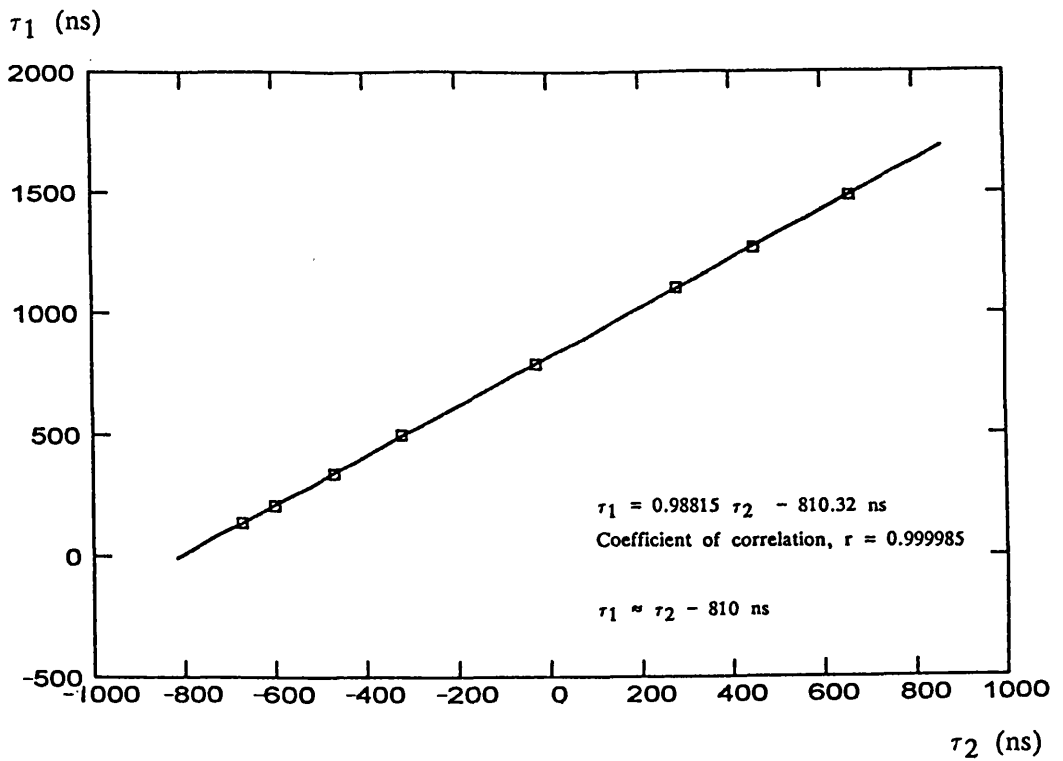


FIGURE 3.61 CALIBRATION CURVE: τ_1 VS τ_2

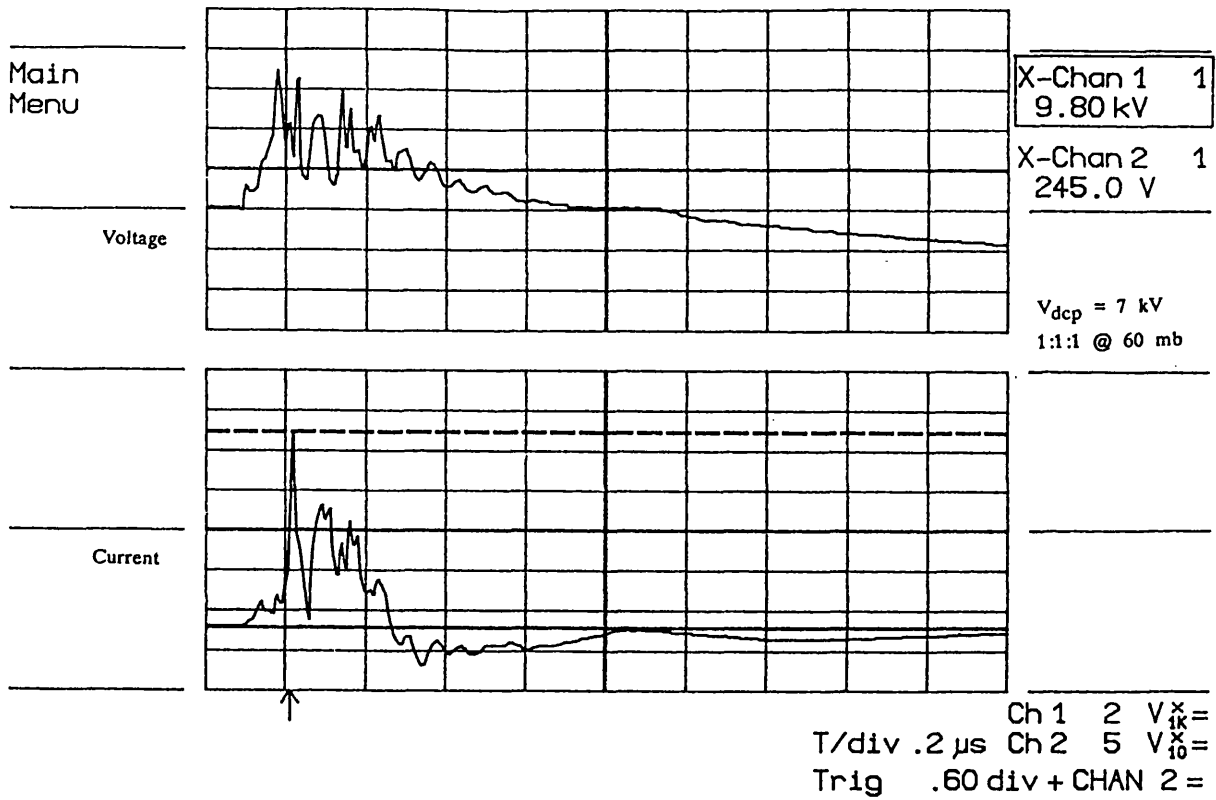


FIGURE 3.62 TRIGGER WIRE VOLTAGE AND CURRENT: 1 ST PULSE

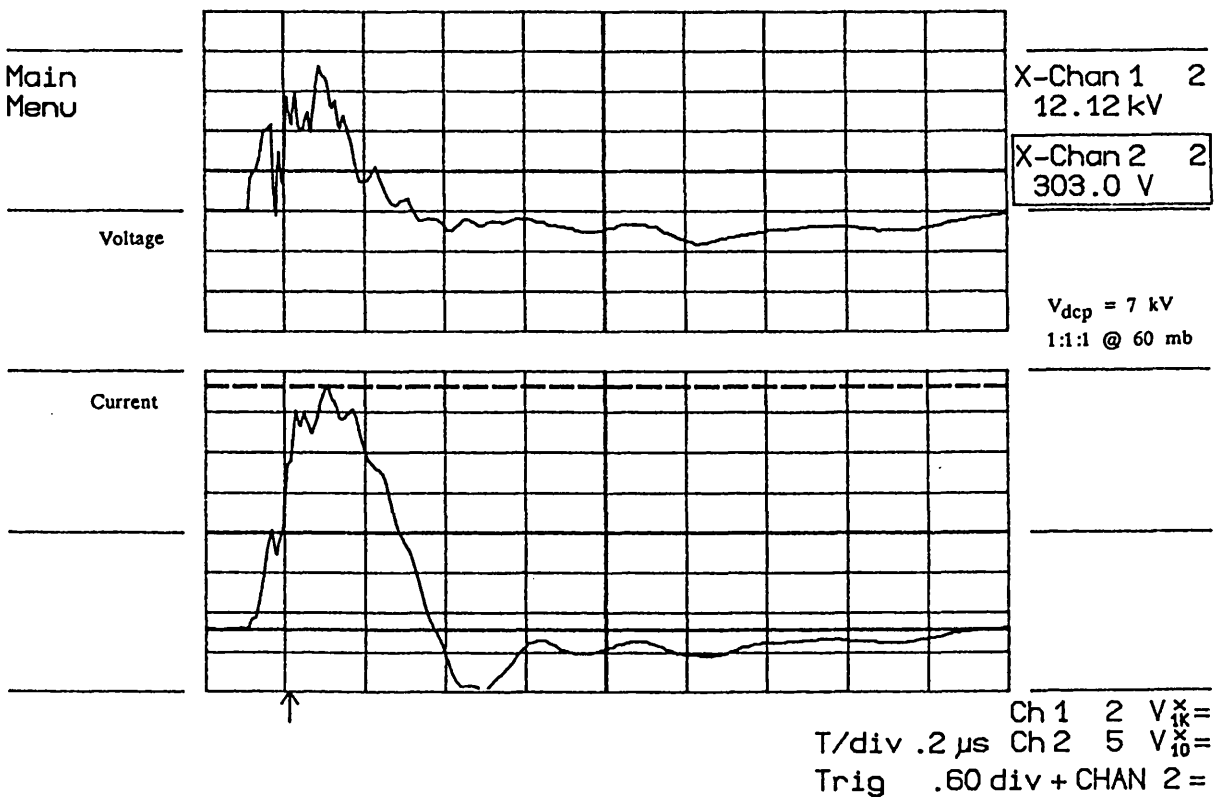


FIGURE 3.63 TRIGGER WIRE VOLTAGE AND CURRENT: 2 ND PULSE

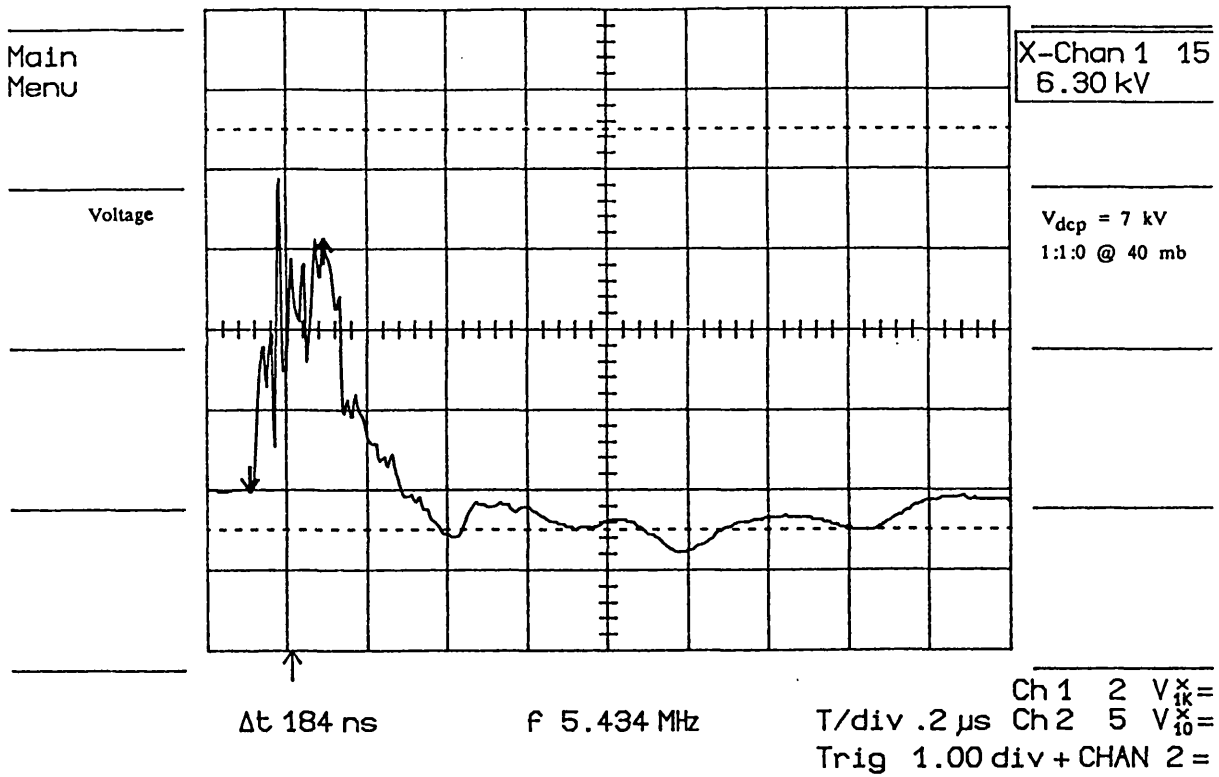


FIGURE 3.64 TRIGGER WIRE VOLTAGE

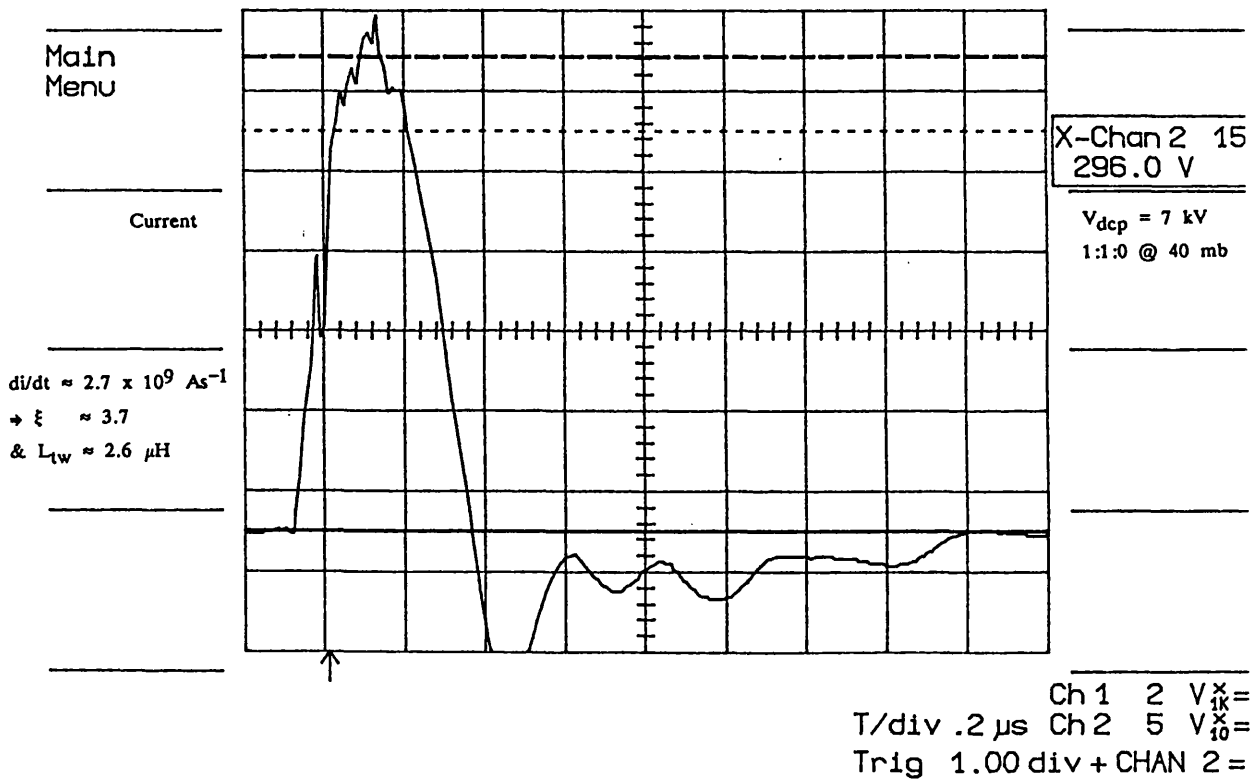


FIGURE 3.65 TRIGGER WIRE CURRENT

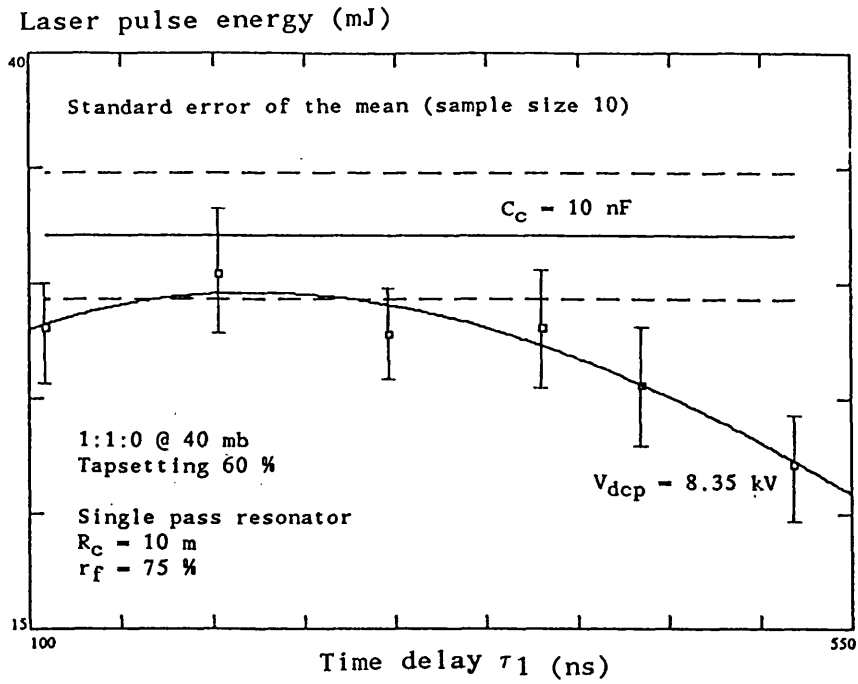


FIGURE 3.66 LASER OUTPUT ENERGY WITH INDEPENDENT PREIONISER

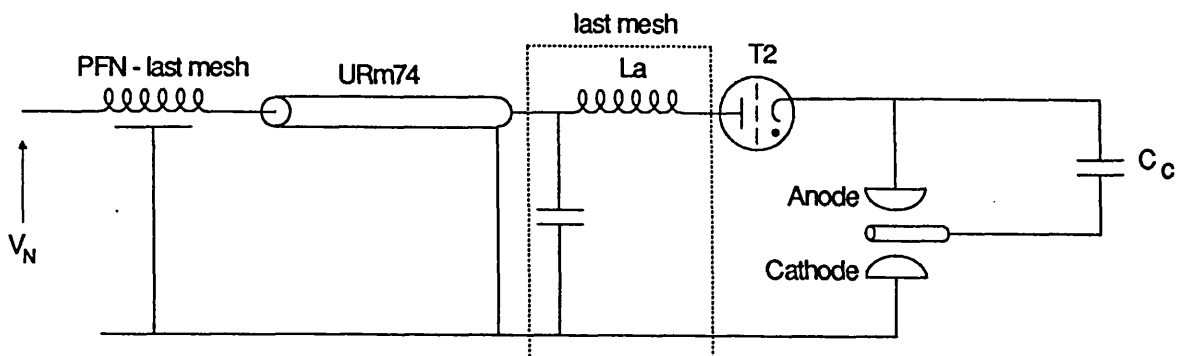


FIGURE 3.67 MODIFIED PUMPING CIRCUIT

Main
Menu

1:2:0 @ 78 mb

$V_{dc} = 12 \text{ kV}$

$L_a = 36 \mu\text{H}$

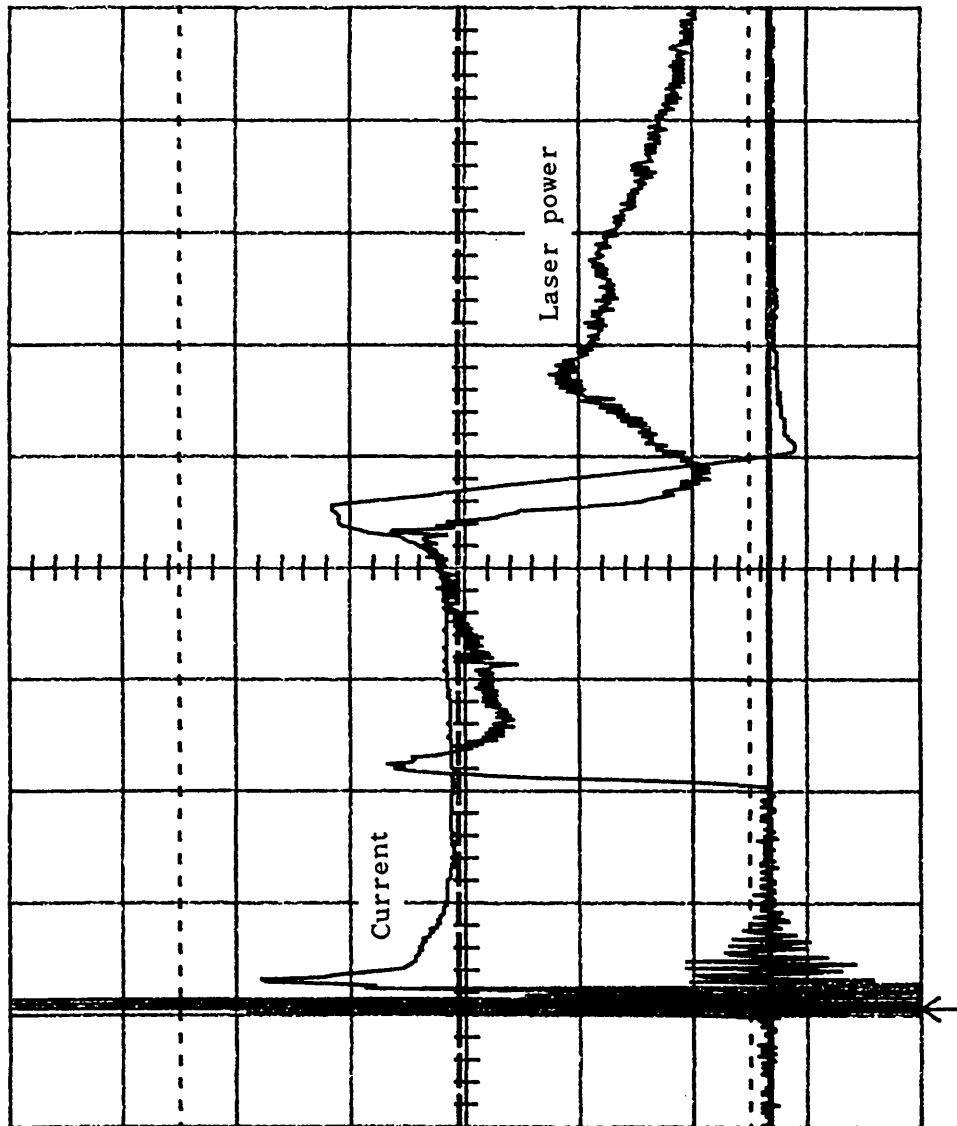
$C_c = 10 \text{ nF}$

Single pass resonator

$R_c = 10 \text{ m}$

$r_f = 90 \%$

$R_p = 6 \text{ mv/kW}$



Channel 1

54.6 mV

Channel 2

136.5 V

Ch 1 20 mV $\frac{50}{\Omega}$

T/div 2 μs Ch 2 5 $V_{10}^{\times} =$

Trig- .96 div + CHAN 2 =

FIGURE 3.68 LASER OUTPUT WITH DISCHARGE ARCING

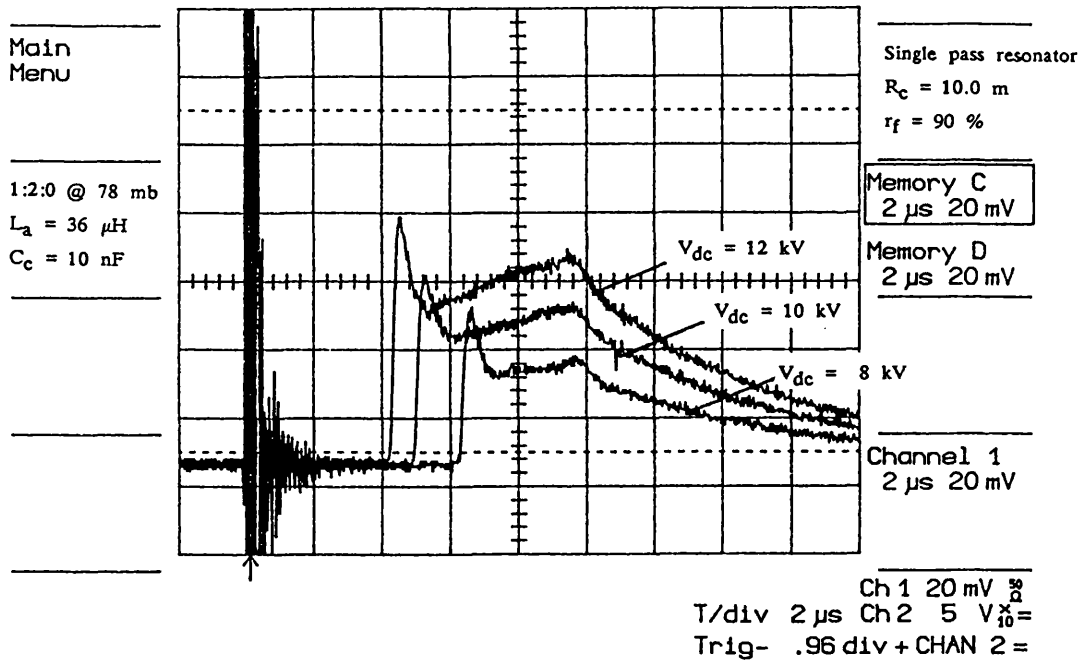


FIGURE 3.69 LASER OUTPUT PULSES

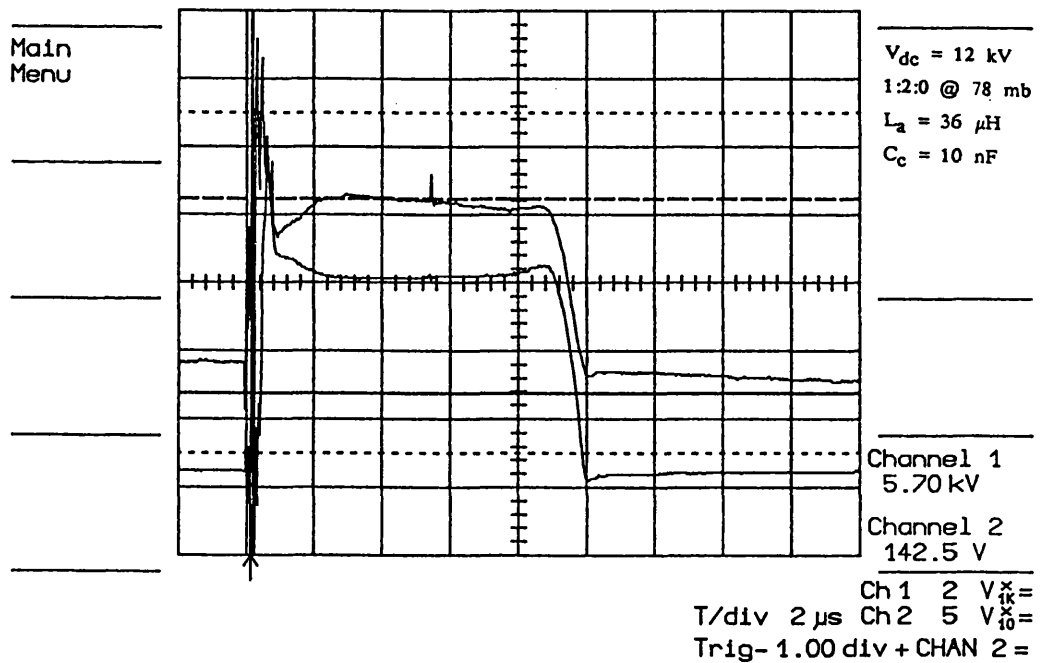


FIGURE 3.70 DISCHARGE VOLTAGE AND CURRENT: $L_a = 36 \mu\text{H}$

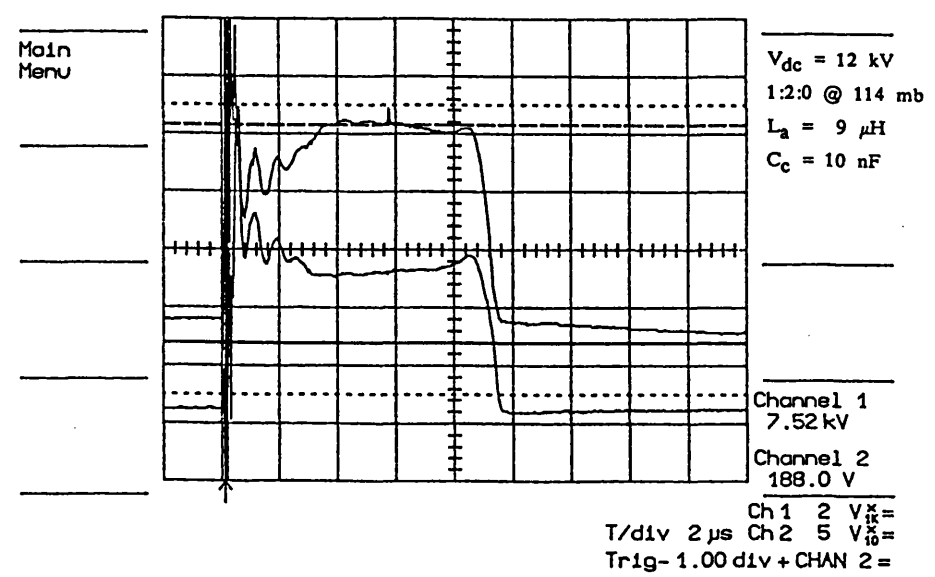
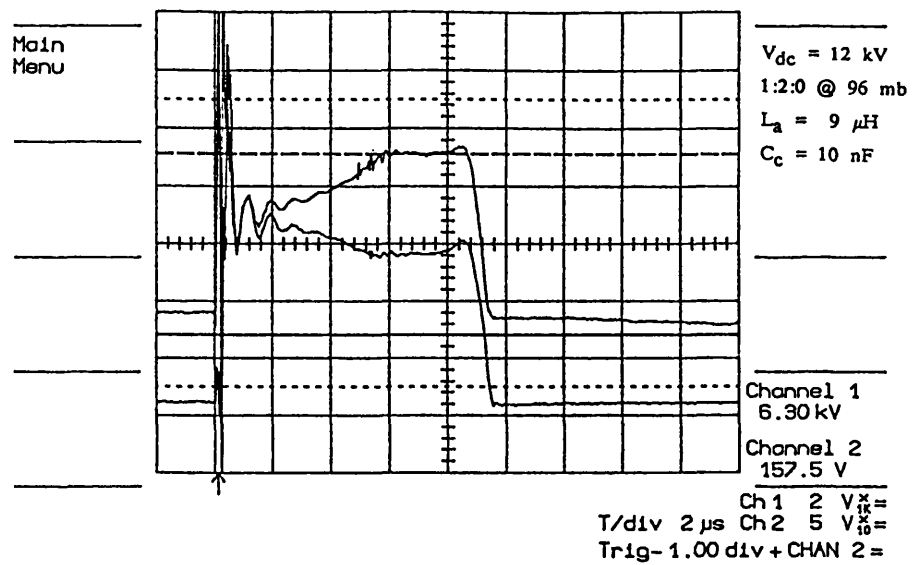
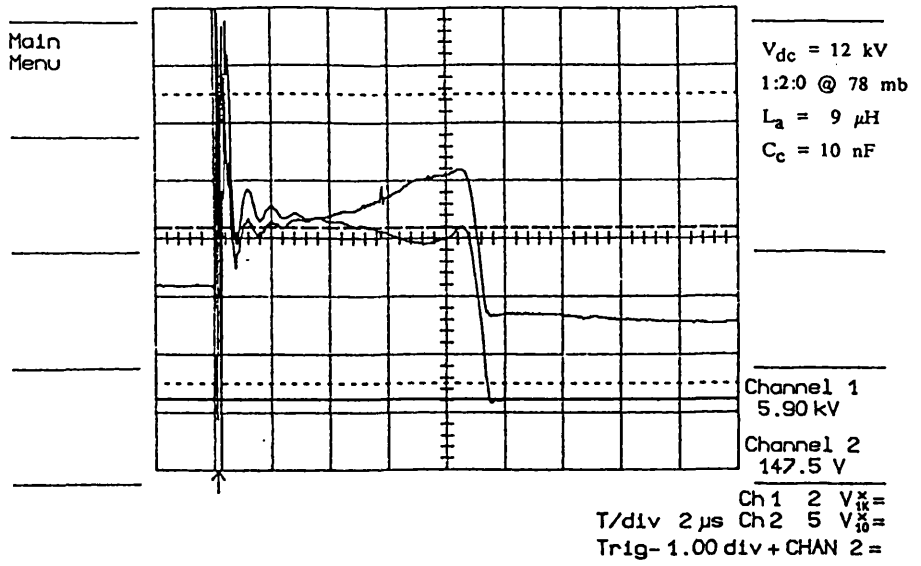


FIGURE 3.71 DISCHARGE VOLTAGE AND CURRENT: $L_a = 9 \mu\text{H}$

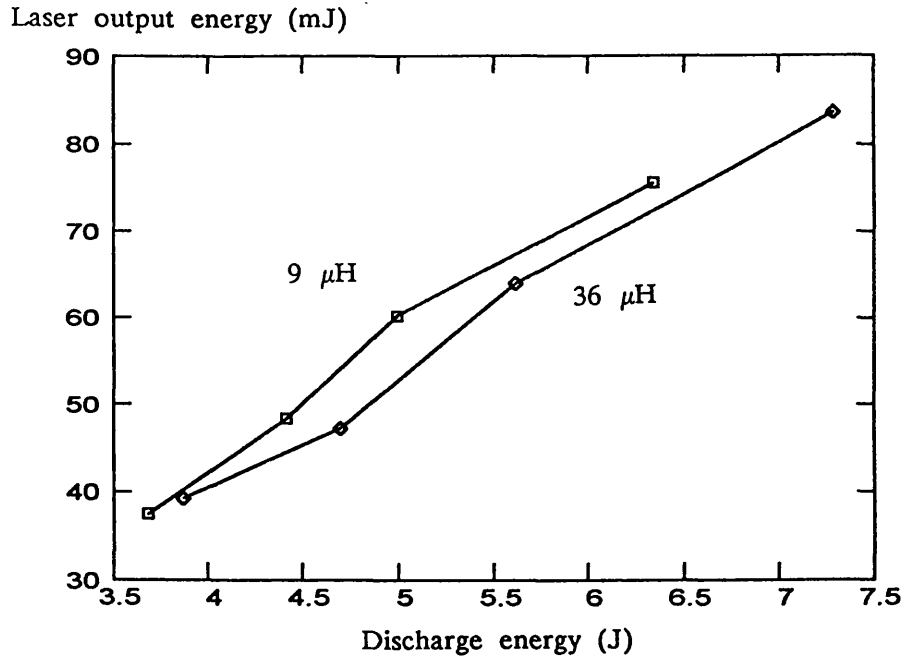


FIGURE 3.72 LASER OUTPUT ENERGY VS DISCHARGE ENERGY

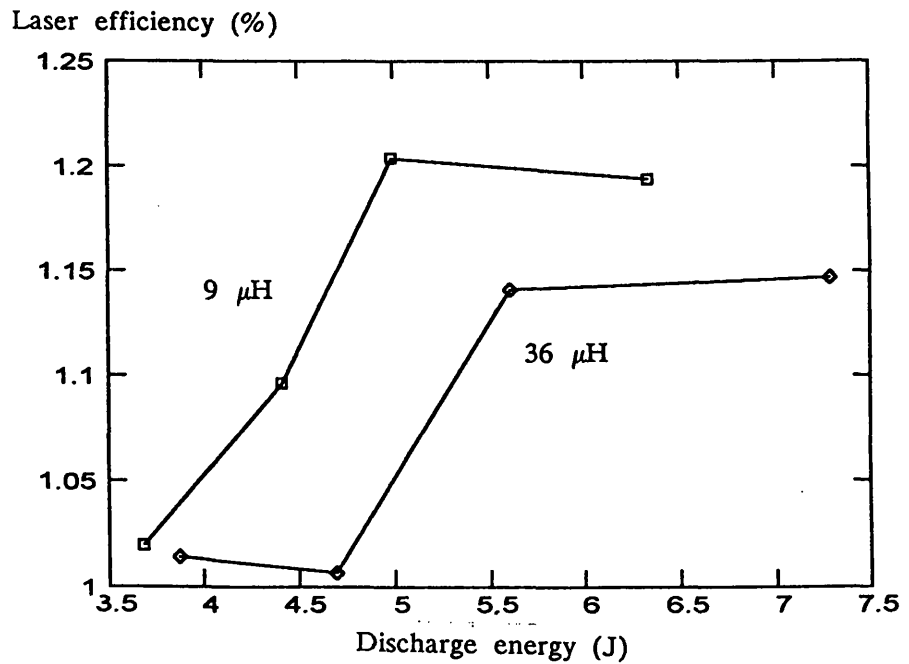


FIGURE 3.73 LASER EFFICIENCY VS DISCHARGE ENERGY

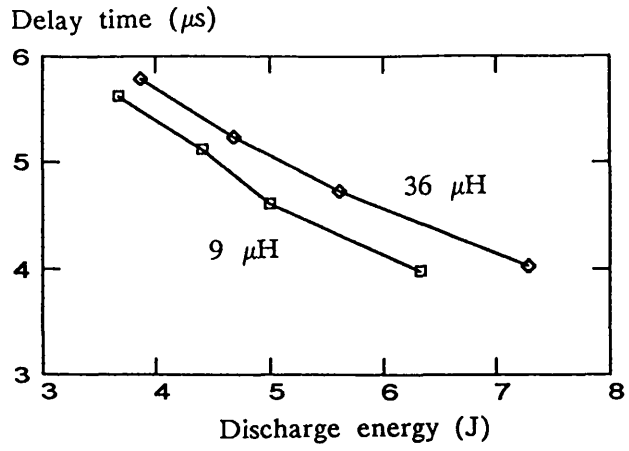


FIGURE 3.74 DELAY VS DISCHARGE ENERGY

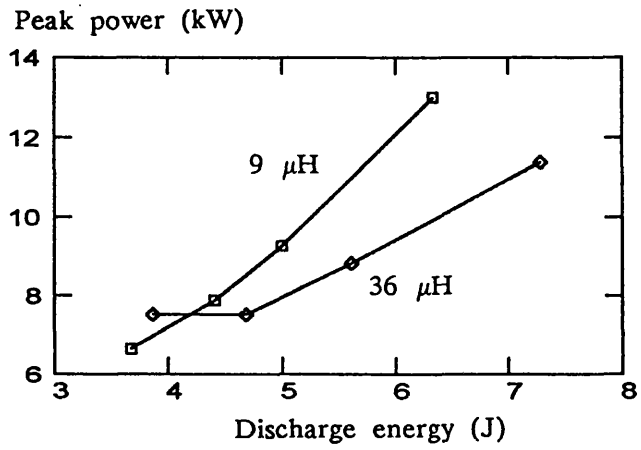


FIGURE 3.75 PEAK POWER VS DISCHARGE ENERGY

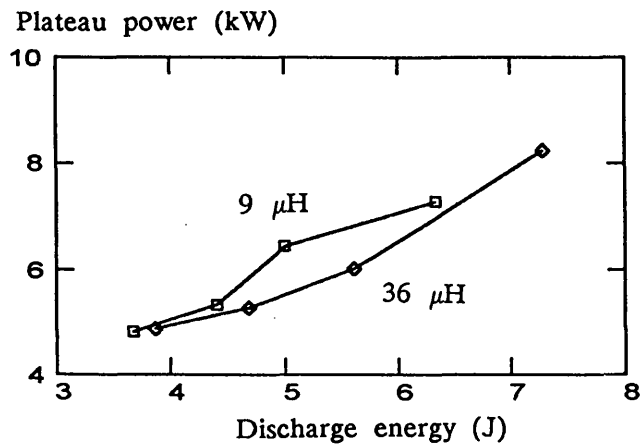


FIGURE 3.76 PLATEAU POWER VS DISCHARGE ENERGY

CHAPTER FOUR

GAS FLOW AND DISCHARGE STABILITY

INTRODUCTION

Depositing energy into the gas mixture increases the temperature of the gas through relaxation processes of excited gas species to translational modes and by direct electron gas heating. This increase in the gas temperature is possibly detrimental to the discharge stability and consequently the laser output. Local inhomogeneities of the temperature distribution in the gas discharge results in an uneven gas density and electrical conductivity. These changes caused by the local temperature variation will increase the local mean electron temperature as the electrons can now accelerate to a greater degree before colliding with any other molecules. Moreover, the local electron density will increase through an increase in the ionisation events that occur because of the increase in the local mean electron energy. Hence, the ohmic heating increases which in turn increases the gas temperature and reduces its density still further. This process continues via this positive feedback mechanism until eventually the growth of the local instability is sufficient to cause the discharge to arc, and a glow to arc (GAT) transition is observed [4.1,4.2]. The discharge voltage collapses, which significantly alters the electron energy distribution function (EEDF) and drastically reduces the pumping efficiency of the upper laser level. The laser output will reduce, even possibly to the extent that no laser output will be observed at all.

For pulsed, transverse, gas discharge lasers the instability growth time is primarily dependent on the gas residence time between the electrodes. Hence, gas recirculators are often employed to convectively clear the heated gas from the discharge region prior to deposition of energy from the next pulse. This substantially increases the maximum amount of energy that may be deposited into the discharge before arcs occur. However, in the present case, in order to clear the heated gas from the discharge region between pulses a gas velocity of at least 667 ms^{-1} is required: this is assuming an electrode width of 60 mm and the convective time as $90 \mu\text{s}$, i.e. the interpulse period for laser operation at 10 kHz. The specification of the roots blowers indicate that a maximum gas velocity of only approximately 100 ms^{-1} is attainable (see Appendix A4 for the specification of the roots blowers). Thus it is apparent that about 6 pulses have to be deposited into what appears to be a static gas mixture.

An approximate indication to the likely maximum operating frequency of the laser can be obtained by taking the ratio of the maximum gas velocity to the electrode

width, and in this case is found to be 1.67 kHz. In practice, however, expansion of the gas occurs due to the heating of the gas primarily by the discharge, this effect was called "puffing" by Dzakowic [4.3]. When the gas expands some of the discharge products puff upstream, these will then take longer to convect past the electrodes. Consequently, the maximum system frequency will be reduced to the reciprocal of the time it takes to convectively clear these discharge products from the electrode region. Dzakowic [4.3] stated that for laminar flow conditions, it takes about 1.7 times longer to clear the gas from the inter-electrode region than the gas convective time, which is determined simply from the ratio of the electrode width to the gas velocity. If this effect is taken into account the maximum system frequency becomes 982 Hz. The experimentally determined maximum system frequency is discussed in more detail in section 4.1.

Biblarz [4.4] and Wasserstom [4.5] have reported observing increased stability of gas discharges if turbulence is introduced into the gas flow. The major reason why the discharge stability is enhanced is attributed to an increase in the effective thermal conductivity of the gas, which tends to homogenise the temperature distribution and reduce the possibility of hot-spots forming. Experiments were performed to examine the affect of turbulence on the maximum system frequency. The turbulence was introduced into the flow by inserting stainless steel mesh into the upstream gas flow.

It has been mentioned that the magnitude of the gas velocity is crucial in determining the operational characteristics of the laser. The critical points of interest are the magnitude and uniformity of the gas velocity profile between the electrodes. In order to assess the inter-electrode gas velocity profile a computer controlled experimental rig, using stepper motors and a Pitot-static tube, was constructed to measure the gas velocity in 2 dimensions for a selection of gas pressures and mixtures. This is described fully in section 4.2.

It is well known that ballasting gas discharges substantially improves their performance. The implications of a ballasted cathode coupled to the PFN are discussed and a model is developed for predicting the requirements for the ballasted electrode. The design and fabrication of two prototype ballasted electrodes with the resistors placed inside the laser cavity is discussed. The effect of partial breakdown of some of the elements is considered, and experimental results are shown.

In order to assess the quality of the discharge for many of the experiments in this chapter it is necessary to see clearly all of the discharge region. For this reason

the resonator was not installed, as doing so severely limits the view of the discharge.

For all of the experiments reported in this chapter the discharge thyratron (T2) was housed in the pulser enclosure, and the anode inductance on T2 was $36 \mu\text{H}$.

4.1 AFFECT OF FLOW-SHAPING AND MESH ON DISCHARGE STABILITY

A series of experiments were undertaken to assess the affect of the flow-shaping on the discharge stability. The discharge frequency was increased until faint filamentary arcs were observed, this was defined as f_1 , and taken as the maximum frequency of the laser, see section 3.2.6. The values of f_1 were determined for a variety of flow-shaping geometries in an attempt to maximise the value of f_1 and the discharge power. Flow-shaping could be placed upstream and downstream - this was described as longitudinal flow-shaping, as it ran parallel to the electrodes - the results are discussed in section 4.1.1. In an attempt to maximise the gas flow, "edge flow-shaping" was introduced perpendicular to the ends of the electrodes, these results are reported in section 4.1.2.

4.1.1 Affect of Longitudinal Flow Shaping On Discharge Stability

For the initial experiments the affect of using the longitudinal flow-shaping on the discharge stability was investigated. The values of f_1 were determined for a 1:1:8 gas mixture as a function of the total gas pressure between 60 mb and 140 mb, both with and without the longitudinal flow-shaping.

Figure 4.1 shows the values of f_1 as a function of the total gas pressure with and without the flowshaping present. It is clearly seen that the values of f_1 are significantly greater when the flow-shaping is installed. The product $f_1 E_d$, where E_d is the measured discharge energy, gives the maximum power that is deposited into the discharge, and is denoted by P_d' and P_d for the cases of no flow-shaping and with flow-shaping respectively. Figure 4.2 shows P_d' and P_d plotted as a function of the total gas pressure. Clearly, greater power can be deposited into the discharge when the longitudinal flow-shaping is present. A best fit polynomial is fitted through both sets of data. As the gas pressure p is increased, the value of E_d rises as the impedences of the discharge and PFN become closer, see Appendix B1.

It is interesting to note that as p increases an optimum value of P_d' is observed, beyond which the value of P_d' rapidly decreases. However, it appears that for $p > 80$ mb the value of P_d decreases almost linearly with increasing gas pressure, and with no apparent sign of an optimum value. This may be due to the way in which the curve is fitted to the data or the effect of the flow-shaping.

In order to highlight the significant differences between P_d and P_d' the ratio P_d/P_d' , derived from the fitted curves in Figure 4.2, is plotted in Figure 4.3. Clearly, greater energy depositions into the discharge are possible for the experimental condition when the flow-shaping is present, this is indicated in Figure 4.3 where the ratio of the discharge powers is greater than unity. It is interesting to note that these differences are greater for either higher or lower values of E_d . Obviously, the minimum value of the curve will occur at the discharge energy at which the maximum value of P_d' was observed and, it is the point at which the values of P_d' and P_d are closest. This minimum point represents an increase of more than 10 % between the maximum discharge powers with the different flow-shaping geometries.

It was mentioned at the beginning of this chapter about the importance of the gas velocity in determining the maximum operating frequency of the discharge. The clearing time of the discharge products from the inter-electrode region prior to deposition of energy from the next pulse was found to be greater than the convective clearing time. In order to quantify the results of experiments examining the effect of gas velocity Dzakowic [4.3] defined the clearing ratio (CR) as

$$\begin{aligned}
 \text{CR} &= \frac{\text{minimum time between arc free pulses}}{\text{time for gas to traverse gap}} \\
 \text{CR} &= \frac{v_g}{f_m w} \approx \frac{v_g}{f_1 w} \qquad 4.1
 \end{aligned}$$

Where v_g is the gas velocity, w the electrode width and f_m is the maximum system frequency. However in practice, it can be assumed that $f_m \approx f_1$ with only a small error resulting.

Table 4.1 shows the continuous discharge stability limits that were measured for a 1:1:8 gas mixture at a constant gas pressure of 100 mb. The experimental conditions are exactly the same as for those in which the data for Figure 4.1 were obtained.

Table 4.1 Continuous discharge stability limits with longitudinal flow-shaping

V_N kV	E_d J	f_1 Hz	P_d W	CR
10.96	2.32	980	2268	1.49
13.15	2.98	808	2399	1.81
15.79	3.77	600	2262	2.43

1:1:8 gas mixture. Blower speed 2453 (penultimate).
 The value of v_g was assumed at 87.5 ms^{-1} and
 the electrode width $w = 60 \text{ mm}$. Discharge volume $\approx 2.0 \text{ l}$

It is seen that the clearing ratio increases with increasing discharge energy E_d , a higher clearing ratio implies a lower attainable PRF prior to the development of discharge instabilities and arcing. If $CR = 1$ then the condition occurs at which the maximum PRF is given by the inverse of the convective clearing time (τ_c) of the gas through the inter-electrode region. τ_c is simply given by

$$\tau_c = \frac{v_g}{w} \tag{4.2}$$

In the present case if $CR = 1$, this results in a maximum system frequency of $60 \times 10^{-3} / 87.5 = 1.48 \text{ kHz}$. From the values quoted in Table 4.1, it is apparent that more than one complete gas change is required per pulse. However, it is assumed that $v_g = 87.5 \text{ ms}^{-1}$.

4.1.2 Affect of Edge Flow-shaping on Discharge Stability

As there is a discrepancy between the lengths of the cavity inlet orifice (1.0 m) and the cavity (1.60 m) it was felt that a reduction in the gas velocity may be occurring due to this mismatch (see Figure 2.25). Hence, it was decided to place "edge flow-shaping" perpendicular to the longitudinal flow-shaping across the width of the laser cavity and close to the ends of the electrodes; this was an attempt to improve the gas flow. Figure 4.4 shows the edge flow-shaping and its position relative to the electrodes, the laser cavity, location of the resonator and the support structures on the inlet and outlet orifices. The edge flow-shaping was fabricated from perspex and had windows bored in position so that the laser beam could pass through unaffected.

The values of f_1 were determined for the longitudinal flow-shaping installed, and the longitudinal and edge flow-shaping. The values of f_1 can be seen in Figure

4.5; Figure 4.6 shows the discharge power as a function of the discharge energy E_d . The gas mixtures tested were 1:1:8 and 1:1:4 at gas pressures of 160 mb and 114 mb respectively. It is seen that a significant improvement is obtained with the edge flow-shaping in position. The average percentage increase in the maximum power depositions into the discharge for the 1:1:8 and 1:1:4 gas mixtures is $11.6 \pm 1.9 \%$, where the error is the standard error of the mean (SEM) for a sample size of 10. The maximum discharge power obtained with a gas mixture of 1:1:0 at a pressure of 60 mb and just with the edge and the longitudinal flow-shaping in position is also shown in the figure. It is clear that the greatest discharge power is obtained with a 1:1:8 gas mixture with the longitudinal and edge flow-shaping installed.

It is thus apparent that the quality of the gas flow uniformity and velocity is of vital importance in determining the maximum power depositions into the gas discharge. The simple measure of inserting the edge flow-shaping into the cavity results in an average increase in the maximum discharge power of $\approx 12 \%$. The gas velocity profiles were examined experimentally and the results are discussed in section 4.2.

4.1.3 Affect of Turbulance on Discharge Stability

It has been reported [4.4,4.5] that a turbulent gas flow can enhance the discharge stability for ambient pressure discharges through homogenisation of the temperature distribution of the gas medium. In order to examine the effect of turbulence on the discharge stability in the present case, stainless steel mesh was inserted into the upstream flow-shaping. However, no significant change was found in the maximum power depositions for a variety of mesh sizes, consequently, no results are discussed. It is possible that no turbulence was introduced into the gas flow in the discharge region, because for example, the mesh may have been positioned too far upstream, and laminar flow established by the time it reached the discharge.

4.2 MEASUREMENT OF THE GAS VELOCITY PROFILES

Section 4.1 demonstrated the importance of using flow-shaping to extend the operational regime of the discharge before the growth of the discharge instabilities were sufficient to cause arcing. It was found that significant improvement was observed by using both the longitudinal and the transverse edge flow-shaping. In an attempt to quantify the continuous discharge stability limits a series of

experiments were undertaken to determine the gas velocity profile between the electrodes. The experimental rig and data acquisition code is first discussed followed by the results. The gas velocity profiles were examined both parallel and perpendicular to the plane of the electrodes surfaces. However, because of severe constraints on the available space within the laser cavity only a restricted number of experiments could be reliably undertaken.

The effect of the upstream longitudinal flow-shaping was investigated, and the result of placing flow-shaping around the support pillars on the gas inlet window. The edge and downstream flow-shaping could not be installed simultaneously with the experimental rig, thus unfortunately, their affect on the gas velocity profiles could not be ascertained.

4.2.1 Experimental Arrangement

The gas velocity was measured by using a Pitot-static tube and a micromanometer transducer, which under full scale deflection gave a 10 V output signal corresponding to a pressure differential $\Delta P = 20 \text{ mm H}_2\text{O}$. The gas velocity is calculated from

$$v_g = \left[\frac{2 C \Delta P}{\rho} \right]^{0.5} \quad 4.3$$

Where ρ is the gas density and C a constant. The output voltage from the transducer is converted into a value for the pressure differential in Pascals, this represents the difference between the dynamic and the static pressure reading. Then given some gas mixture and temperature, the gas density is known and hence, the velocity can be calculated.

The constant C is dependent on the compressibility of the gas and is approximately given by [4.6]

$$C = 1 + \frac{M^2}{4} \quad 4.4$$

Where M is the Mach number, i.e. the ratio of the velocity of the gas to the velocity of sound in the gas mixture which is denoted by v_s ; M is given by

$$M = \frac{v_g}{v_s} = v_g \left[\frac{\rho}{\gamma_r P} \right]^{0.5} \quad 4.5$$

Where p is the static gas pressure and γ_r the ratio of the molar heat capacities. As a specific example, the value of ρ for a 1:1:8 gas mixture at 300 K and 160 mb is $0.06675 \text{ kg m}^{-3}$ and $\gamma_r = 1.224$, thus $v_s \approx 542 \text{ ms}^{-1}$. If the gas velocity v_g is assumed to be 100 ms^{-1} then it is found that $M = 0.18$. Consequently the error correction to the measurement of the gas velocity, due to the compressibility of the gas, is given by substituting the value of M into expression 4.4, it is found that $C = 1.008$. This correction is negligible for the present work where errors of 5 - 10 % are acceptable.

Figure 4.7 shows a schematic of the experimental arrangement that was used to measure the gas velocity profiles. The outlets from the Pitot-static tube were passed through a vacuum flange assembly to the micromanometer. The output voltage from this transducer was measured using the Keithly 175 digital volt meter, which was attached to the data acquisition system via a GPIB cable. To measure the spatial velocity distribution it is necessary to move the position of the Pitot-static tube and collect the data at each point. In order to achieve this process relatively easily, the positioning of the Pitot-static tube must be adjustable from outside of the laser cavity while it is under operational conditions, i.e. with the appropriate gas mixture in the system. The simplest technique is to electronically control a stepper motor to position the Pitot-static tube. The data acquisition and control system, which is discussed in Appendix A6, was extended to provide this facility.

The Pitot-static tube was secured in a clamp which was attached to a fine screw thread with a pitch of 40 turns per inch. The end of this thread was secured to a stepper motor (type RS 4-phase stepper motor size 2) which was interfaced to the computer and software controlled. This stepper motor provided the transverse (i.e. up and down) motion of the Pitot-static tube relative to the electrodes. Through the centre of the base of the mount which supported the stepper motor an 8 mm thread was tapped. Screwed rod was passed through the mount and secured to both ends of an aluminium track that ran the complete length of the gas inlet window. Rotation of the freely supported screwed rod provided the longitudinal motion of the Pitot-static tube along the aluminium sliding track, see Plate 3. Initially, a stepper motor was attached to the screwed rod to provide computer control of the motion along this degree of freedom; however, the inexpensive screwed rod proved extremely difficult to align reliably and accurately enough for the stepper motor to move the mount. Brass rod was attached to the end of the

screwed rod using a split pin and was passed through the perspex rear end plate. The longitudinal motion was obtained by physically rotating a handle attached to the brass rod. A stuffing box was fabricated which screwed into the rear, perspex end plate and the brass rod was passed through it, see Figure 4.8.

The pulses controlling the stepper motor were generated from software developed using ASYST [4.7] and the digital output ports on the MetraByte Dash 16 data acquisition board. The digital output pulses from the acquisition board were fed into the stepper motor driver control card, see Figure 4.9, and the output pulses from this card were used to drive the stepper motor; 1 pulse rotated the motor shaft 7.5 degrees. The drive pulses were passed into the laser cavity via a 20 pin, low voltage, electrical lead-through flange assembly (see Figure 4.7). The software was developed to provide automatic acquisition of a complete 2-D profile of the gas velocity, following the possible paths as indicated in Figure 4.10. The longitudinal profiles could be taken from the rear to the front of the cavity or vice-versa; the transverse profiles could be taken from the anode towards the cathode or vice-versa. This flexibility was designed within the software to facilitate ease of data acquisition and also for this reason, the program was fully menu driven.

Initial measurements of the gas velocity profiles indicated that the transducer was extremely sensitive, and a small variation of readings were observed over a short period of time – even with the usual shielding precautions taken against noise. For this reason, a number of readings were taken at a specific position and the average value and the standard error of the mean were calculated.

The total time to collect the data representing the velocity profile is dependent on the number of positions at which the velocity is measured, the time taken to capture and store the data from one position, and finally, the time taken to reposition the Pitot-static tube. The number of values taken at each position was kept low, a value of 5 was finally selected, enabling some statistical assessment, and a relatively fast acquisition rate of the data. With a sample size of 5, the major overhead in the speed of the data collection is the repositioning of the Pitot-static tube. However, in order to speed the acquisition rate still further, processing of the captured data was undertaken at a latter stage, i.e. only the raw voltage values from the transducer were saved to file. Approximately 1 reading was taken and stored to file every 0.7 seconds; no attempt was made to improve this acquisition rate as compared to the repositioning of the Pitot-static tube this time is insignificant.

A simple calculation illustrates the problem of capturing detailed 2-D profiles. Assuming that a measurement of the gas velocity is required every square centimeter, the total area is $\approx 100 \times 4 = 400 \text{ cm}^2$, then if 5 readings are taken at each point this gives the total number of readings of 2000. The time to collect 5 points, store the data to file and move the Pitot-static tube to the next position was approximately 40 seconds. For 400 positions the total time would be an impractical 4.5 hours, of which only 23 minutes is CPU time dedicated towards acquiring and storing the data. The 2-D data collection option could, more realistically, be used to study a small portion of the gas flow.

It was decided to examine the longitudinal and transverse velocity profiles independently of each other. For the longitudinal profile, the Pitot-static tube was positioned at the desired height relative to the anode and cathode, and the required position from the front of the sliding track. After the data collection was initiated and the 5 data values had been collected for this position, the captured data was automatically saved to file as an array of 5 numbers, whilst the Pitot-static tube was being manually advanced to the next position. Saving the data between each reading provides security of the captured data in the event of a system fault. The spatial separation between each velocity measurement was 5 mm. The estimated time to cover a distance of about 1 m was approximately 45 minutes, and the time for the experiments to determine the transverse velocity profiles was less than a few minutes.

4.2.2 Gas Velocity Measurements as a Function of Time

As the estimated length of time for an experiment investigating the longitudinal profile was 45 minutes, it was decided to examine the velocity at one position, as a function of time, to see how stable the blowers were, and moreover, to see if any corrections to the data were necessary. It is important to establish if any corrections are required in order to quantify the experimental results and to be able to reliably compare the velocity readings across the discharge length; and moreover, to see if there are steady flow conditions. Corrections may be necessary because of variations in the gas temperature or pressure as a result of heating from the power dissipated by the blowers or leakage of the vacuum system.

A gas mixture of 1:1:0 at a total gas pressure of 40 mb was selected for the study of the temporal behaviour of the blowers and vacuum system. The ASYST code was slightly modified to capture 1 reading every 3 seconds, the corresponding cavity temperature was noted every minute and the total leak rate for the system

was approximately 1 mb hr^{-1} .

The variation in the measured gas temperature during this experiment and the corresponding calculated change in the gas density can be seen in Figure 4.11. The error in assuming a constant temperature when calculating the gas velocity results in an error for the gas velocity of $\approx \pm 0.2 \%$, which for a velocity of 100 ms^{-1} is only 10 cm, this is clearly negligible for the present work where an error of 5 – 10 % is acceptable. The velocity as a function of time is shown in Figure 4.12 along with the temperature corrected data. The error is small and the two traces are indistinguishable on this scale. For clarity, the velocity correction due to the temperature variation is shown in Figure 4.13. Thus, the variation in the gas temperature can be neglected in the present work. It is interesting to examine the variation in temperature over the period of this experiment. Initially forced convective cooling occurs resulting in a reduction of the temperature, then gradual heating occurs due to the power dissipated by the blowers.

Figure 4.14 shows the temporal variation in the gas velocity. The uncorrected top trace shows a gradual rise in the velocity with increasing time, this is particularly prominent after approximately 1000 seconds: the velocity is calculated assuming a constant gas temperature and pressure. If the atmospheric contamination due to the system leaking is taken into account, then with the approximate leak rate of 1 mb hr^{-1} , the lower trace is obtained. The contribution to the density of the gas due to the system leaking was calculated assuming that the air was dry [4.8]. It is seen that the corrected curve is much flatter, but still starts increasing after about 2000 s, indicating that the leak rate is probably slightly in excess of that estimated. It is difficult to obtain an accurate measurement for the leak rate over short time scales as the minimum resolution of the EMV 251 pressure monitor is only 1 mb. The velocity error correction due to the leak rate of 1 mb hr^{-1} , which is shown explicitly in Figure 4.15, is only approximately 50 cm s^{-1} after 45 minutes, and clearly negligible in the present case.

It has been shown that over the period of the experiment, the variation of the gas velocity due to changes in the gas temperature or the system leaking is negligible and it is not necessary to correct the data.

4.2.3 Gas Velocity Profiles Without Flow-shaping

Figures 4.16, 4.17 and 4.18 show the longitudinal velocity profiles for the gas mixtures 1:1:0, 1:1:4 and 1:1:8 at total gas pressures of 40, 120 and 200 mb

respectively. The Pitot-static tube was positioned 14.6 mm from the anode surface. Plotted under the graphs of the longitudinal gas velocity profiles in Figures 4.17 and 4.18 is the standard error of the mean (SEM) for the sample of data taken at each point (sample size 5). It is seen that the SEM is generally less than 0.5 ms^{-1} , with the occasional peak above this value. This shows that the measured values are consistent. Figure 4.17 is not complete because the cables connecting the stepper motor and its driver board became entangled in the ceramic castings which support the anode - this problem occurred several times during the experiments and limited the scope of the results that were achieved. However, it is immediately apparent from the figures that the support structures on the inlet window are having an adverse effect on the uniformity of the gas velocity profiles across the length of the electrodes. To highlight this, Figure 4.16 shows the position of the support structures (labelled S). It is also evident that the flow uniformity is perturbed downstream from where the diffuser flow splitters are positioned and at the middle of the electrodes, labelled M in the figure.

It is clear that the gas uniformity is far from ideal, for example, in Figure 4.16 the maximum velocity is about 50 ms^{-1} and the minimum is approximately 35 ms^{-1} . This is a large variation (30 %) and will result in non-uniform cooling - and hence heating of the gas under excitation conditions - and is a sufficient reason for thermal instabilities developing and the discharge breaking down.

The measured values of the gas velocity seemed rather low. The maximum flow rate of the system is $15\,000 \text{ m}^3 \text{ hr}^{-1}$ with a blower speed of 2920 rpm, the area of the inlet window is $\approx 100 \times 4 \text{ cm}^2 = 400 \text{ cm}^2$. Thus the maximum velocity with the blowers running at their full speed is 103 ms^{-1} . However, the blowers were running at their penultimate speed of 2453 rpm, consequently, the expected gas velocity is 87.5 ms^{-1} . The measured values, where no obstruction occurred due to the support structures, were typically 50 ms^{-1} .

Although minima in the velocity profiles are observed, it cannot conclusively be said that arcing was more probable in these regions when the discharge was running. This is difficult to observe while the discharge is in operation, but would have been readily apparent from inspection of the electrodes after a period of time. However, it was noted on several occasions that arcing had occurred on the upstream side of the middle of the electrode. Prior to the knowledge of the gas velocity profiles this was normally attributed to, for example, a trigger wire cracking. But it is possible that the trigger wires cracked because of the arcs which were due to thermal instabilities developing because of the irregular flow.

4.2.4 Gas Velocity Profiles With Upstream Flow-shaping

Figures 4.19 and 4.20 show the gas velocity profiles with the upstream flow-shaping installed in the laser cavity for the gas mixtures 1:1:0 and 1:1:4 at gas pressures of 40 and 120 mb respectively. It is apparent that the affect of the flow-shaping is to increase the gas velocity, and it is nearer the expected value. For example, for the 1:1:0 gas mixture, the maximum velocity has increased from approximately 50 ms^{-1} to 70 ms^{-1} , an increase of 40 %; and the minimum velocity has increased from about 35 ms^{-1} to just under 60 ms^{-1} , an increase of 71 %. The variation in velocities between the maximum and minimum values without flow-shaping are 30 % and, in the present case are only about 17 %. Thus it is apparent that the profiles are more uniform when the flow-shaping is installed.

Thermal instabilities are more likley to develop where the velocity is at a minimum. It is interesting to consider that the clearing ratio is now known to be a function of longitudinal distance along the length of the discharge. Thus, a maximum and minimum clearing ratio will exist corresponding to the positions of the maximum and minimum velocity. However, if consideration is given to the maximum frequencies (i.e. the values of f_1) that were obtained for the experiments with and without the longitudinal flow-shaping, it is apparent that the increase in performance, due to the inceased velocity with the flow-shaping, does not scale in direct proportion with the gas velocity. If the case of the minimum clearing ratio is considered, then an increase of about 70 % may be expected in the value of f_1 when the flow-shaping is installed, whereas in practice an average increase of only 19.2 % was observed. A possible explanation for this fact lies in the behaviour of the SEM of the data taken for the longitudinal profiles. If Figures 4.17 and 4.20 are compared, it is seen that the the general trend of the SEM values is that they are much greater for the case with no flow-shaping. This is particularly the case where the velocity is a minimum, adjacent to the support structures. This local variation in the measurements of the gas velocity may be due to turbulence caused by the support structures themselves, and tends to be minimised by the installation of the flow-shaping. Biblarz [4.4] reported increased discharge stability by generating tubulance, this effect maybe occurring under the present circumstances, and possibly the reason why only a 20 % improvement was observed in the values of f_1 under the different flow-shaping geometries.

It was estimated that the downstream and edge flow-shaping would be to increase the gas velocity to approximately the specification value.

4.2.5 Transverse Velocity Profiles

The transverse velocity profiles were determined at the position labelled T in Figure 4.16, without the longitudinal flow-shaping in position and for the gas mixtures 0:1:0 at pressures of 25 mb and 50 mb. The profiles can be seen in Figures 4.21 and 4.22. Obviously, this gas mixture is unsuitable for the laser mixture and was only selected to test the performance of the experimental rig. It can be seen that the velocity is approximately 50 ms^{-1} and is uniform to less than 2.0 % over a considerable proportion of the electrode gap. However, the boundary layers at the anode and cathode were estimated to be between 7.5 mm and 10.5 mm. A small boundary layer is crucial in ensuring arc free discharges. Essentially, the boundary layer is a stagnant region, consequently the temperature of the gas in this region will rise much faster, a temperature gradient will be introduced into the discharge and the probability of arcing will increase.

It is interesting to note that changing the N_2 pressure seems to have little or no influence on the gas velocity. A 1:1:8 laser gas mixture at 160 mb was selected for analysis of the transverse velocity profile, the results can be seen in Figure 4.23. Unfortunately this graph is not complete because the portion of the gas flow data captured near the anode was unreliable because the plastic tubes connecting the Pitot-static tube to the micromanometer were restricting the movement of the Pitot-static tube.

4.2.6 Gas Velocity Profiles With Flow-shaping around the Support Structures

The measurement of the spatial variation of the gas velocity has indicated that the support structures on the gas inlet orifice are introducing perturbations into the gas velocity profiles. In an attempt to generate a more uniform flow it was decided to fabricate flow-shaping to fit around these structures. This was considered a quicker method of testing the discharge under uniform flow conditions than, for example, stripping the laser cavity and machining out the support structures.

A Mathcad program [4.9] was used to analyse the foil design to estimate their affect on the gas velocity profile. Figure 4.24 shows the approximate shape of the flow-shaping and the theoretical longitudinal velocity profile. It is seen that laminar flow is established within a short distance from the end of the flow-shaping. Four foils were fabricated from acetal sheet and secured around the structural supports. The longitudinal velocity profile was measured and it can be seen in Figure 4.25. The gas mixture was 1:1:0 at a total gas pressure of 40 mb. It is apparent that

there is no significant change in the profile shape or in the magnitude of the velocities. Moreover, this was also found to be the case when experiments were performed to measure the values of f_1 and determine the discharge stability thresholds with this gas mixture and flow-shaping geometry – no significant change was found, hence, the results are not presented.

4.2.7 Gas Velocity as a Function of Pressure

Because of some of the difficulties experienced with the cables and tubing entangling on the ceramic anode supports, only a limited number of experimental results were achieved. To quantify these results, it was decided to investigate the velocity at one particular position, slightly off centre of the electrodes centre, as a function of the total gas pressure for a 1:1:4 gas mixture. The pressure was incremented from 102 to 192 mb in steps of 18 mb. Figure 4.26 shows the velocity as function of the gas pressure – the flow-shaping was not installed. The error bars show a 1 % error in the velocity, so it is seen that the velocity is independent of the gas pressure, and as a consequence, the density. It can be concluded that the affect of the gas mixture and pressure on the velocity profiles is insignificant.

4.2.8 Summary of the Gas Velocity Measurements and the Clearing Ratios

Section 4.2.7 showed that the gas velocity is independent of the gas pressure. However, it is seen from the figures showing the longitudinal velocity profiles that a small differences exist in the magnitude of the recorded velocities. On one occasion it was noticed that a small offset voltage was present on the voltmeter whereas 0 volts was assumed. The error from this assumption is less than 8 %. Another possible source of error is the angle that the Pitot-static tube makes with the direction of the gas flow. If the tube is inclined at an angle, the static pressure will increase due to a component of the dynamic pressure being added. Because of the geometry of the Pitot-static tube it is likely that the dynamic pressure will reduce at a lower rate, consequently, the measured value of ΔP would decrease as would the apparent gas velocity.

Table 4.2 summarises the average maximum and minimum values of the gas velocities that were measured with and without the flow-shaping installed.

Table 4.2 Summary of the gas velocities.

Blower Speed 2453 rpm	v_{gmin} ms ⁻¹	v_{gmax} ms ⁻¹	$\frac{v_{gmax}}{v_{gmin}}$
With flow-shaping ¹	62.1	75.2	1.21
Without flow-shaping ²	43.9	58.9	1.34

It is seen that

$$\frac{v_{gmax}^1}{v_{gmax}^2} = 1.27 \quad \text{and} \quad \frac{v_{gmin}^1}{v_{gmin}^2} = 1.41$$

Figure 4.27 shows the clearing ratios as a function of the discharge energy, calculated from the data shown in Figure 4.5 and assuming the minimum measured value for the gas velocity, which for the condition with the flow-shaping present is $\approx 60 \text{ ms}^{-1}$; the value of 65 ms^{-1} was assumed for the data with the edge flow-shaping installed. It is clear that the clearing ratio can have values less than one. This means that more than one pulse can be deposited into the gas before it is convectively cleared from the inter-electrode region. This is lower than the limit defined by Dzakowic [4.3], the reason is probably due to the energy density of the discharge. Which in this case is typically 3 mJ/cc, whereas for the work done by Dzakowic the energy densities were approximately 100 mJ/cc.

It is important to note that the clearing ratio is substantially lower than that required to operate at 10 kHz. Also, it is apparent from the graph that CR increases with the pulse energy. This is probably due to the increased effect of the discharge products puffing upstream as the discharge energy increases. Consequently, it takes longer to clear them from the inter-electrode region and the maximum discharge frequency reduces. It is seen that the differences in the values of the clearing ratios for the 1:1:4 and 1:1:8 gas mixtures are small.

4.3 BALLAST ELECTRODE

Continuous wave and pulsed CO₂ lasers often employ series ballast resistance to limit the growth of the discharge current to 10's of milli-Amps [4.10]. The reason for using ballast resistance lies in the dynamic impedance of the gas discharge and its propensity to arc for high discharge current densities. A schematic of the static discharge characteristics, showing the discharge voltage as a function of the discharge current, can be seen in Figure 4.28. The discharge current I_d is given

by

$$I_d = \frac{V_o - V_d}{R} \quad 4.6$$

Where V_d is the discharge voltage, V_o the supply voltage and R the series resistance. The V - I curve is obtained by varying the value of R and measuring the values of V_d and I_d . The point labelled S corresponds to the voltage at which the Townsend breakdown criterion is met. If the resistance is reduced, the discharge current increases and the discharge voltage remains constant – this is called the normal glow phase. As R is decreased further, it is seen that both the discharge voltage and current increase; an abnormal glow is then said to exist, which is characterised by a positive V - I discharge characteristic. When point c is reached, it is possible that the discharge breaks-down via an arc and the voltage collapses to a low level – a glow to arc transition (GAT) is observed. A load line of gradient equal to R can be drawn on the graph of the V - I characteristics, for example R_1 and R_2 where it is seen that $R_2 < R_1$. In order for the discharge to remain stable the following condition must be met

$$\frac{dV_d}{dI_d} + R > 0 \quad 4.7$$

Where dV_d/dI_d is the gradient of the V - I characteristic at the point of intersection with the load line. It is seen that the points B , C and D are stable and that c is unstable. It also becomes clear that if a resistance is intentionally placed in series with the discharge, the discharge current is limited and the discharge will remain in the stable regime provided that the above equation is satisfied. Hence, the major reason why gas discharges often employ ballast resistance is to limit the discharge current in order to maintain the discharge stability.

For large volume discharges, any discharge instability that develops into an arc will severely degrade the discharge – the discharge voltage collapses and the current develops to the full fault current. However, if the discharge volume is split into a number of smaller volumes, then it is possible that if the discharge for one segment breaks-down, the discharges for the other segments remain stable and laser output will still be obtained but at a slightly lower level. For this reason, electrodes are often segmented and if each segment is individually ballasted, the stable operational envelope of the laser gas discharge will be extended.

It was decided to fabricate a relatively inexpensive segmented ballasted cathode in order to examine the affect of such an electrode geometry on the discharge

stability and the laser output power. However, a difficulty lies in theoretically selecting the correct value of the ballast resistance because of the inherent complexity in modelling the discharge system. It is clear that if the ballast resistance is too high then the transfer efficiency of the energy from the PFN to the discharge will be low and most of the energy will be deposited into the ballast resistance. If the resistance is too low then there may not be any significant effect on the discharge stability. Thus it is apparent that an optimum value will exist. In practice, it is usual to optimise the ballast resistance experimentally.

The design of the prototype segmented ballasted cathode consisted of 588 individually ballasted elements. Two electrodes were fabricated, their only difference being the total ballast resistance, the values were $\approx 0.8 \Omega$ and $\approx 8.0 \Omega$. These low values were selected in an attempt to minimise the power deposited into the ballast resistance. The resistors were housed inside the laser cavity and formed an integral part of the cathode structure. See section 4.4 for a more detailed discussion of the electrode design and performance.

The initial prototype electrodes led to a significant increase in the maximum discharge power before the development of discharge arcing. This success led to an improvement in the design by placing the ballast resistance external to the laser cavity, however, this is not reported. The improved design facilitates the ease with which the experimental work to optimise the ballast resistance can be achieved.

4.3.1 Ballasted Electrode Design Equations

Figure 4.29 shows a schematic of the equivalent circuit of the laser with the ballasted cathode. It is seen that the ballast resistors are housed in the laser cavity, and thus, they are subjected to vacuum conditions. The total ballast resistance is R_T , Z_N is the network impedance and V_N the voltage on the PFN at the moment the discharge thyatron T_2 is fired, see Chapter 2. V_d and I_d are the discharge voltage and current respectively. Using Kirchoffs law it can be shown that the discharge current I_d is given by

$$I_d = \frac{V_N - V_d}{Z_N + R_T} \quad 4.8$$

As a specific example, Figure 4.30 shows the effect of R_T on the discharge current for a 1:1:4 gas mixture at 160 mb with three values of the network voltage: 12 kV, 16 kV and 20 kV. As one would expect, for a given value of the

network voltage, as R_T increases the discharge current is reduced, so less energy is deposited into the discharge. For a given ballast resistance, provided that $R_T + Z_d < Z_N$, where Z_d is the discharge impedance, then increasing the network voltage will increase the discharge current.

In order to design the ballasted cathode it is important to appreciate the power requirements of the ballast resistors and stay within their specified power rating, denoted by W . Appendix C1 derives an equation to find the necessary power rating W of the ballast resistors given some power loading of the discharge, W is given by

$$W = \frac{I_d^2 R_T \tau_p f}{n_T} \quad 4.9$$

Where $D = \tau_p f$, and is called the mark to space ratio; τ_p is the pumping pulse width, n_T the number of discharge segments and f the discharge frequency. For the full specification frequency of 10 kHz and pulse width of 10 μ s, $D = 0.1$.

Worthwhile points to note are that the number of elements required is inversely proportional to the individual mean power rating of the resistors and, proportional to the total ballast resistance and the frequency. The maximum frequency F_m above which the power rating of the resistors will be exceeded, can be calculated by setting $f = F_m$ in equation 4.9 and rearranging, then as $\tau_p = 10 \mu$ s, F_m is given by

$$F_m = \frac{W n_T}{I_d^2 R_T \tau_p} = \frac{W n_T}{I_d^2 R_T 10 \mu s} \quad 4.10$$

It is seen that the value of F_m increases for a greater value of the power rating of the total ballast resistance (i.e. $W n_T$), and lower discharge currents, ballast resistance or pulse width. These equations provide a method to calculate the power rating of the total ballast resistance given the values of the ballast resistance, maximum operating frequency and the number of elements in the segmented cathode.

4.3.2 Power Transfer Efficiency

Appendix B1 described how the energy, or equivalently the power, transfer efficiency from the PFN (pulse forming network) to the gas discharge varies with the discharge impedance. The affect of the ballast resistance on the power transfer efficiency requires full appreciation in order to fully understand the design implications for the ballasted electrode coupled to the power supply. This is particularly important when the system is operating without a tailbiter as the discharge must operate under negative mismatch conditions; ie, $Z_d + R_T < Z_N$, where Z_d is the discharge impedance, R_T the total ballast resistance and Z_N the network impedance. The maximum transfer efficiency occurs when the impedance of the PFN and the load are matched. Where for a ballasted cathode, it is useful to think of the load as R_T in series with the discharge impedance.

With zero ballast resistance, the power transfer efficiency can be expressed as the ratio of the power available on the network over the pulse period, denoted by P_N , to the power deposited into the discharge, denoted by P_d . If the effect of the ballast resistance is taken into account, the power transfer efficiency is given by

$$\epsilon_b = \frac{P_d + P_{RT}}{P_N} \quad 4.11$$

Where P_{RT} is the power developed in the total ballast resistance. Figure 4.31 shows, as for the same conditions as Figure 4.30, the transfer efficiency ϵ_b (expressed as a percentage) as a function of the total ballast resistance. For a particular gas mixture and network voltage, it is apparent that an optimum transfer efficiency will occur for some specific value of R_T .

The voltage developed across the discharge during matched conditions with a ballast resistance can be calculated from the principal of conservation of energy. It is shown in Appendix C2 that for matched conditions the discharge voltage is given by

$$V_d = \frac{V_N}{2} - V_{RT} \quad 4.12$$

Where V_{RT} is the voltage drop across the total ballast resistance ($V_{RT} = I_d R_T$).

4.3.3 Ratio of Discharge Power to Power Developed in the Ballast Resistance

An obvious requirement for satisfactory performance of the segmented ballasted cathode is to maximise the power deposition into the discharge and minimise the power deposited into the ballast resistance. However, it may be necessary to "invest" in a high value of R_T as this is a small price to pay if the benefits of greater discharge stability are realised. In an attempt to assess the relative losses within the ballast resistance, it was found useful to define the quantity η_b as the ratio of the powers developed in the discharge to the ballast resistance. Thus, η_b is given by

$$\eta_b = \frac{P_d}{P_R} = \frac{V_d}{I_d R_T} \rightarrow \eta_b \propto \frac{1}{I_d} \quad 4.13$$

With increasing discharge current it is seen that η_b decreases; thus, proportionately more energy is deposited into the ballast resistance than the discharge. Increasing I_d for a particular gas mixture means that a larger fraction of the energy will be deposited into the ballast resistance. Figure 4.32 shows η_b plotted against R_T for a 1:1:4 gas mixture at 160 mb with the network voltage at 12 kV, 16 kV and 20 kV. It is seen that for a given network voltage, as the ballast resistance increases the fractional energy deposited into the ballast resistance increases. Increasing the network voltage, whilst keeping R_T constant, results in a greater fraction of the energy being deposited into R_T .

4.3.4 Ballasted Electrode Discharge Energy Measurements

Figure 4.29 shows a schematic of the ballasted cathode coupled to the PFN. It is clearly seen that the ballast resistors are placed inside the laser cavity. Consequently, the high voltage probe which measured the discharge voltage for the plane electrode geometries, will in this case, measure the voltage drop across the ballast resistance and the discharge, and is denoted by V_m . This presents a problem in directly determining the discharge energy. However, if the discharge current is monitored and, as the ballast resistance is known, the energy deposited into the ballast resistance can be found and the discharge energy calculated. The energy E_m which is deposited into the ballast resistance and the discharge is given by

$$E_m = \int_0^{\tau_p} V_M I_d dt \quad 4.14$$

The value of E_M is calculated using the built in functions from the oscilloscope and the data acquisition code. The value of E_m is also given by

$$E_m = E_d + E_{RT} \quad 4.15$$

Where E_{RT} is the energy deposited into the total ballast resistance. Substituting for E_{RT} , 4.15 becomes

$$E_m \approx E_d + I_d^2 R_T \tau_p \quad 4.16$$

Thus
$$E_d \approx E_m - I_d^2 R_T \tau_p \quad 4.17$$

Using expression 4.17 the discharge energy can be determined by obtaining a measure for the value of E_m from the oscilloscope functions, and subtracting the value of E_{RT} obtained from knowledge of the discharge current, total ballast resistance and pulse width.

4.3.5 Fault Current Analysis

With a segmented cathode design the elements are electrically isolated from each other. It is possible, if the discharge develops into arcs, for some of the elements to conduct the correct discharge current whilst the remainder conduct the fault current. For cathode designs that have a high number of segments it is difficult to determine if the discharge is arcing. It is impractical to measure the current flowing through each segment and visual assessment of the discharge may not be a reliable method to indicate if the discharge is arcing. The reason why the last method of arc detection is limited can be explained as follows. The fault current passing through one element will be moderately low, and consequently, the number of radiation transitions occurring will be low, resulting in a low luminosity arc; as compared, for example, to a single pair of electrodes where any discharge arcing generally results in one bright arc which passes the full fault current.

In order to quantify the extent of the discharge arcing it is necessary to develop an equation that can be used to predict the discharge current given that a number of segments n are passing the correct discharge current and a number m are passing the fault current. Where the normal and fault currents which can pass through one segment are denoted by i and i_f respectively. The total measured discharge current I_{dm} is given by

$$I_{dm} = ni + mi_f \quad 4.18$$

Where if $m = 0$ then $I_{dm} = I_d$.

If no elements are passing the fault current it can be shown that the total discharge current I_d , in terms of the number of elements n_T , is given by

$$I_d = \frac{n_T (V_N - V_d)}{n_T Z_N + R} \quad 4.19$$

Where $n_T = n + m \quad 4.20$

It is shown in Appendix C3 that the number of segments n conducting the correct discharge current is given by

$$n = \frac{n_T V_N - I_{dm} (n_T Z_N + R)}{V_d} \quad 4.21$$

If the discharge current is measured, the number of elements conducting the normal discharge current can be found, then using expression 4.20 the number conducting the fault current can be determined. Section 4.4.5 describes some of the graphs that were obtained under partial breakdown of the discharge, and the relationship between the value of m and the discharge power.

4.4 PROTOTYPE BALLASTED ELECTRODE DESIGN

In order to examine the affect of using a segmented ballasted cathode on the discharge stability it was decided to fabricate and test an inexpensive electrode. This would at least provide an indication of the likely performance of a ballasted system and whether to pursue a design capable of industrial performance.

A major cost of developing a segmented electrode with a high number of elements and the resistors housed externally to the laser cavity is the electrical lead throughs. To minimise this element of the cost, it was decided to house the resistors within the laser cavity. However, problems then arise over spatial constraints, for example, the resistors are packed in close proximity to each other. It was thought that this may cause a reduction in their power rating. This is mainly due to over heating as thermal conduction of heat away from the resistors with high packing densities would be severely degraded. The value of the thermal

conductivity of the gas mixture will be critical in determining the effectiveness of the heat dissipation from the ballast resistors.

Figure 4.33 shows the design of the prototype ballasted segmented cathode. It can be seen that the resistors are placed behind the cathode. The design was dictated by the available space and using suitably sized resistors. The cathode consisted of brass, countersunk rivots embedded into a 10 mm thick sheet of acetal. This material was chosen because it is cheap, easy to machine and has a low moisture absorbtion. However, it has a relatively low melting point of 165° C [4.12], thus it was necessary to carefully test the electrode assembly to prevent the material from melting. The acetal provided the necessary electrical insulation between adjacent segments; it was also used as the walls of the cathode and provided the housing for the ballast resistors. The connection leads from the resistors were tinned and individually soft soldered to the rivots via a small hole drilled in the back of them; the other end of the resistor was connected to an earthed brass plate.

As a certain amount of guess work was involved in designing the cathode, in particular the geometrical spacing between the segments, it was decided to use countersunk rivots, this would provide some control over the spacing between the elements. For example, if the segments were too close to each other, then the distance could be increased by milling down the plate thickness. Plate 4.4 shows the finished ballasted electrode. A schematic of the geometrical layout of the cathode segments can be seen in Figure 4.33 and was designed in an effort to maximise the uniformity of the laser gain across the electrode width to ensure propogation of the TEM_{00} fundamental Gaussian mode from the laser. And moreover, to prevent any apparent structure of the segmented discharge showing in the laser beam profile.

4.4.1 Ballast Resistance Selection

As the effect of using a segmented cathode on the discharge stability was unclear, it was decided to initially opt for a low ballast resistance. The factors leading to this decision were the power rating specifications of the resistors available with small enough dimensions to fit into the cathode housing. A high number of elements will reduce the current passed through each segment; 588 were chosen in order to reduce the requirements for the power rating of the resistors. As the size of resistors is usually in direct proportion to their power rating, this high number of segments means that a smaller sized resistor can be used.

2 W, 470 Ω carbon film resistors were used for the first prototype and 7 W, 4.7 k Ω vitreous enamel for the second. With 588 segments the total power rating of the first ballast resistance was only 1.2 kW, while the second was rated at 4.1 kW. However, this rating is for free air at typically 70 °C, whereas in practice the resistors would be exposed to the normal CO₂ laser gas mixtures and pressures as low as 40 mb. No information was found regarding the performance of the resistors under such adverse conditions. It was anticipated that a reduction in the limiting element voltage (LEV) would occur and possibly outgassing of the encapsulation material surrounding the resistors, this would lead to a decrease in their power rating and premature overheating. The principal heat transfer mechanism for the excess heat generated through ohmic heating of the resistors is thermal conduction through the gas mixture. An estimate of the likely effect of using the resistors for the laser gas mixtures can be obtained by considering the ratio of the thermal conductivity of air to that of the laser gas mixture. Figure 4.34 shows the thermal conductivity K_g for various CO₂ laser gas mixtures as a function of the gas temperature [4.13]. It is seen that increasing the He content increases the thermal conductivity of the gas. The resistors have a derating curve with increasing temperature. If operation is assumed at room temperature then it is seen that K_g varies from approximately 2 to 9 x 10⁻² W m⁻¹ K⁻¹ for the different gas mixtures. For air, the thermal conductivity K_a is about 0.241 W m⁻¹ K⁻¹ [4.14]. Thus K_g/K_a ranges from 0.08 with zero He content, to 0.40 with a 1:1:8 gas mixture. It can be assumed that the thermal conductivity is independent of the gas pressure. From this calculation it is apparent that the resistors are more likely to exceed their power specification for gas mixtures which are low in He.

However, the problem is not as severe as is described above. This is because it is possible to overrate both types of resistors by a factor of about 2 for short durations, i.e. up to several seconds [4.15].

It can be concluded that for continuous discharge running, the power rating of the resistors inside the laser cavity would be reduced by at least a factor of about 2.5 for a 1:1:8 gas mixture. This derating is mainly due to the lower thermal conductivity of the laser gas mixture and the proximity of the resistors to each other because of their high packing density. However, because the resistors can be overrated for short durations, it can be assumed that the power rating is approximately equal to the atmospheric specification for He rich gas mixtures.

The maximum frequency rating F_m of the prototype ballasted cathode with $R_T = 0.8 \Omega$ can be calculated using equation 4.10. Knowing that $R = 470 \Omega$ and $n_T = 588$, it is found that $F_m = 8.7$ kHz. The approximate discharge power can be

calculated assuming that, typically, the discharge voltage $V_d \approx 5$ kV and the discharge current $I_d \approx 130$ A, the discharge energy is ≈ 6.5 J, thus at F_m the mean discharge power is ≈ 57 kW.

4.4.2 Discharge Initiation

All of the experiments that were conducted with the prototype ballasted cathodes were performed using the double discharge technique with the trigger wire geometry that is reported in Chapter 3, Section 3.2.2. This was not the most efficient form of preionisation geometry for the ballasted electrode, as significant overlap of the trigger wires and the discharge elements occurred. However, it would at least, provide an indication of the possible benefits of using a ballasted electrode system. The coupling capacitance was 10 nF and the trigger wire gap was 2.0 mm.

4.4.3 Experimental Procedure for the Prototype Ballasted Electrode

In order to examine the affect of the ballasted cathode on the discharge stability it was decided to determine the value of f_1 – defined in section 3.2.6 – as a function of E_d for various gas mixtures and pressures. A total of 5 readings of the values of E_m , V_m and I_d were measured so that the discharge energy could be found, see section 4.3.4. This enabled an average value to be calculated and an assessment of the standard error of the mean (SEM) for the experimental results. The five readings were taken when the discharge was operating at ≈ 100 Hz, i.e. for a low power rating. This facilitated ease of the data acquisition whilst ensuring that the discharge was arc free, moreover, the temperature rise of the acetal was minimal and the resistors were not overrated.

It was typically found that for the measured values of E_m and I_d the SEM was approximately 1 %. As the readings were taken at 100 Hz it was important to establish if E_m and I_d varied as a function of frequency, as of course, it is important to determine the discharge energy at f_1 . Experiments were undertaken to examine the dependency of E_m and I_d with frequency. Figure 4.35 shows the discharge energy and the SEM as a function of frequency. The gas mixture and pressure were 1:1:0 and 60 mb respectively, the transformer tapsetting was at 50 %. Statistically, no significant difference was found (95% level, sample size 5 per reading). However, it should be noted that the SEM increased for the higher frequencies, but still lied within the expected statistical range. It was concluded

that the discharge measurements could be taken at 100 Hz and inferred from this, the values at higher PRF.

In order to minimise the risk of melting the acetal and decrease the time that the resistors may be overrated, it was decided to perform the experiments in the burst mode. However, to do this it must be established that no significant difference exists between the short burst mode, typically 1 – 10 seconds, and longer burst modes, above 10 seconds.

A major reason for arcing in CO₂ lasers is the presence of long lived dissociation products [4.16]. In the present case, once the products are created they will enter the discharge again after a finite time which is dependent on the gas velocity and the distance around the closed system that the gas travels. Hence, it is informative to use a burst length much greater than this gas transit time.

The flow path length L_g is approximately 8.9 m and without the flow-shaping installed in the laser cavity the maximum gas velocity $v_g \approx 50 \text{ ms}^{-1}$ (see section 4.2). Thus the time for one cycle of the gas is 0.178 s, in one second 5.6 cycles have occurred. If the flow-shaping is installed then the maximum gas velocity $v_g \approx 70 \text{ ms}^{-1}$, then in one second 7.9 cycles of the gas have occurred. Experiments were undertaken to assess the probability of the discharge arcing for different burst lengths. It was found that the longer burst modes – up to 3 minutes – gave the same results as the 1 second burst mode. Thus, it was concluded that no errors would occur by assuming that the discharge stability could be ascertained over a one or two second pulse train. The advantages of performing the experiments over this short length of time are that it prevents excessive heating of the acetal material and prolonged overrating of the ballast resistors.

4.4.4 Calibration of the Frequency Control Potentiometer

For preliminary testing of the ballasted cathode only short pulse trains were used, typically $< 0.5 \text{ s}$. However, this is below the response time of the frequency meter (type RS LED frequency meter 5 Hz – 600 MHz). Hence, it was necessary to calibrate the potentiometer, which controls the discharge operating frequency, against the reading of the frequency from the frequency meter. Figure 4.36 shows the calibration curve used in the experiments for the 1 kHz and 10 kHz switch settings. However, with a pulse train of 1 second, which was used in the experiments to evaluate f_1 , the frequency meter was used quite successfully.

4.4.5 0.8 Ω Ballasted Electrode Performance

During the experimental investigation into the performance of the 0.8 Ω ballasted electrode it was noticed that the Lecroy oscilloscope was giving erroneous readings on the second input channel, unfortunately, and partly as a consequence of this, only a limited number of experimental results were taken on the discharge performance of the 0.8 Ω ballasted system. However, it was immediately apparent that the electrodes performance was a substantial improvement over the previously tested electrode geometries. Following this success, the immediate objective was to install the resonator and investigate the laser output power, these results are discussed in Chapter 5. While the oscilloscope was under repair, the 8.0 Ω ballasted electrode was installed and a more detailed investigation was initiated into the discharge stability - these results are reported in section 4.4.6.

Although the experiments to determine the values of f_1 across a range of experimental conditions were fairly limited, some of the results of the discharge stability experiments are discussed because of the dramatic improvements that were observed.

It was found that with a 1:1:4 gas mixture at a pressure of 60 mb and the tapsetting at 50 %, the maximum discharge frequency, i.e. f_1 , was approximately 3 kHz. This represents an increase of about a factor of 3 for the value of f_1 compared to that obtained with the plane electrode geometry. The energy deposited into the discharge and the ballast resistance was 2.160 J, the discharge current was measured at 92 A. Thus, the energy deposited into the ballast resistance is only 0.068 J, and it is found that $E_d = 2.092$ J. At 3 kHz the maximum mean discharge power is 6.28 kW and the power deposited into the ballast resistance is 204 W. It is seen that $\eta_b = 30.8$, so ≈ 31 times as much power is being deposited into the discharge as compared to the ballast resistance. For this small sacrifice in the discharge energy, considerable gains have been made in the maximum discharge power before arcing occurs. Of course, these benefits may not be entirely due to the ballast resistance, but could for example, be due to the fact that the electrode is segmented. In order to determine the primary reason for the improvement in the discharge stability it would be necessary to fabricate another electrode with $R_T = 0$ and compare the values of f_1 . However, it was hoped to perhaps determine more information on the effect of the ballast resistance from testing the second prototype with $R_T \approx 8 \Omega$.

It was noticed that at high frequencies, the discharge was spatially displaced from the electrode region, i.e. it was swept downstream by the blowers - this effect was

more prominent for higher frequencies. The consequences of this observation are important for designing a resonator configuration that can "follow" the discharge with frequency. The resonator must either be able to tolerate a misalignment with the discharge by positioning one of the folds of the resonator downstream, or perhaps, actually move with the displaced discharge as the frequency is increased. There is currently much research activity into the field of adaptive control of optical systems, some of which is particularly relevant to the design of an "intelligent resonator" which could optimise its position relative to the position of the discharge [4.17].

Figure 4.37 shows the discharge voltage and current with the transformer tapsettings at 50 %, a 1:1:4 gas mixture at a gas pressure of 72 mb and with $f_1 = 3$ kHz. It is seen that for approximately the first 3 μs of the pulse, the discharge voltage and current are normal. However, after 3 μs the voltage collapses to a lower level, but not 0; and the current increases to a higher value, but not the full fault current. It can be appreciated that partial breakdown of the discharge has occurred. If equation 4.21 is used it is found that the number of segments n conducting the normal discharge current is approximately 311 and the number of segments m conducting the fault current is 277; the ratio $m/n_T = 0.47$. It is seen that only 53 % of the segments are conducting the correct discharge current. Figure 4.38 shows the partial breakdown of the discharge for a 1:1:4 gas mixture at 96 mb operating at 3 kHz. It is found that $n = 66$ and $m = 522$, thus the ratio $m/n_T = 0.88$, nearly all of the segments are conducting the fault current.

These two and some other results were used in an attempt to find the relationship between m and the discharge power. Figure 4.39 shows n and m plotted against the discharge power and Figure 4.40 shows the ratio m/n_T as a function of the discharge power. It is clearly seen that as P_d increases the value of m increases, whilst the value of n decreases. It is important to realise that these results are collected from experiments at different gas pressures and consequently, it is not necessarily justifiable to plot them on the same graph. They do, however, seem to indicate a plausible way in which the number of elements conducting the fault current will vary with the discharge power. It is evident that for low values of P_d , the value of m will be 0 and the curve for the ratio of m/n_T against P_d will cross the $m = 0$ line at the point at which the discharge is operating at its highest and most perfectly stable power rating, i.e. $\approx E_d f_1$. Moreover, any further increase in P_d will result in the collapse of the discharge for one segment; the ratio will then collapse to $1 - 1/n_T$. As P_d increases, it would be expected that the value of m would eventually reach the line equal to n_T . However, it appears that m does not quite reach the expected asymptotic line. This may be due to the

fact that the data was taken at slightly different gas pressures - 60 to 96 mb - or a combination of errors from measuring the discharge current, the network voltage, the network impedance and assuming the value of the total ballast resistance from the individual specification values. It must be appreciated that the total ballast resistance is only 0.8Ω , and no stray resistance has been taken into account. It is likely that the total resistance is considerably more than 0.8Ω .

Figure 4.41 shows the PFN voltage for a train of pulses. The discharge was operating at $f_1 \approx 3.125$ kHz with a 1:1:8 gas mixture at 160 mb and 50 % tapsetting, the longitudinal flow-shaping was used. The discharge energy was 2.17 J, which for this value of f_1 results in a discharge power of 6.8 kW. The discharge stability for frequencies greater than f_1 - i.e. where arcing was first observed - was examined. It was found that with increasing frequency, arcing was more likely to develop in the centre of the electrodes along both the longitudinal and transverse directions, at a position where the longitudinal velocity profile was found to be a minimum. For long burst modes - greater than 10 seconds - the discharge arcing was severe. However, it was found that for shorter burst modes - less than 50 ms - arcing only occasionally occurred; again, when arcs were observed they were in the same position. For these short pulse trains the system frequency could be increased to 5.2 kHz; Figure 4.42 shows the PFN voltage for a short burst of pulses at this frequency. This apparently anomalous behaviour of increasing the discharge power for very short pulse trains could not be explained satisfactorily. Perhaps the arcing from the central part of the electrode was acting as a preionising source and enhancing the stability of the discharge, prior to the growth of any thermal instabilities. Or perhaps, more simplistically, the length of the burst mode before any arcing is observed, gives an indication of the characteristic growth time of the instabilities, where burst lengths longer than some critical value results in the discharge arcing because the instability has sufficient time to grow.

Over a period of time, it was found that arcing gradually became more probable for lower operating powers. Because of this and the technical problems experienced with the oscilloscope, the experiments had to prematurely cease.

It is clear that the electrode has delivered a substantial improvement in the maximum power depositions into the discharge before arcing is observed. However, it is difficult at this stage to quantify what effect the value of the ballast resistance and the electrode geometry are having on the discharge stability. It is probable that an optimum design would exist, in order to find this design a series of experiments would have to be performed.

4.4.6 8.0 Ω Ballasted Electrode Performance

Following the success of the 0.8 Ω ballasted cathode, it was decided to test the 8 Ω electrode, with the objective of obtaining more information about the maximum discharge power ratings. The values of f_1 and the corresponding discharge power were found as a function of the discharge energy for the gas mixtures: 1:1:8, 1:1:4 and 1:1:0 at pressures of: 160 mb, 114 mb and 60 mb respectively, the longitudinal flow-shaping was installed. These three gas mixtures and pressures were carefully selected as it was found that the pulse energy was approximately the same in each case (to less than 10 %). The effect of 10 μs and 7 μs pulse lengths was investigated. Figures 4.43 and 4.44 show the values of f_1 and P_d respectively, as a function of the discharge energy for the selected gas mixtures, pressures and with $\tau_p = 10 \mu\text{s}$; a best fit polynomial of degree 2 was fitted through the data in Figure 4.44. It is seen that the maximum frequency f_1 decreases as the discharge energy is increased, and that the maximum frequencies are observed for gas mixtures rich in He and low in the partial pressure content of N_2 and CO_2 . The values of P_d are seen to reach an optimum value and then decline as E_d is increased further. The maximum values are approximately 11 kW, 8 kW and 5.75 kW for the gas mixtures 1:1:8, 1:1:4 and 1:1:0 respectively. It is apparent that He is having a beneficial effect on the discharge stability either through increased preionisation or, more likely, because of the higher thermal conductivity of this gas mixture and the inherent stability this yields for He rich discharges. For all of these operating conditions no partial collapse of the discharge was observed.

It was mentioned in section 4.4.5 that $P_d \approx 6.8 \text{ kW}$ for the 0.8 Ω electrode with a 1:1:8 gas mixture at 160 mb and 50 % tapsetting, whereas in the present case and under these conditions, $P_d = 7.4 \text{ kW}$. It is apparent that the value of P_d is slightly greater for the 8 Ω electrode. However, in order to quantify the effect of the ballast resistance on the discharge stability it would be necessary to perform a further series of detailed experiments. For the latter case, considerably more energy is deposited into the ballast resistance, for apparently only a small gain in the value of P_d . However, it is clear that the value of P_d can be increased up to 11 kW – this was not found to be the case for the experiments that were performed on the 0.8 Ω electrode.

Figures 4.45 and 4.46 show, as for the same gas mixtures and pressures as for Figures 4.44 and 4.45, the values of f_1 and P_d as a function of E_d respectively, but in this case for 7 μs pulse lengths. In addition, the values of f_1 obtained for a 1:1:4 gas mixture at 156 mb are shown in Figure 4.45. Interestingly, the effect

of increasing the gas pressure for the 1:1:4 mixture, is that it just seems to continue the same decreasing trend in the value of f_1 with increasing E_d as is observed for the 1:1:4 mixture at 114 mb.

If Figures 4.43 and 4.45 are compared, it is seen that the frequencies are slightly higher for the lower pulse lengths. If Figures 4.44 and 4.46 are compared, it is apparent that the total discharge powers are approximately 10.5 kW, 10 kW and 7.5 kW for the gas mixtures 1:1:8, 1:1:4 and 1:1:0. Interestingly, this represents a significant increase in the value of P_d for the 1:1:4 and 1:1:0 gas mixture, however, for the 1:1:8 mixture it seems that no apparent improvement in the total discharge power rating has been observed. To clarify this, the best fit curves were plotted onto the same graph, see Figure 4.47. This clearly shows that there are larger differences in the values of the discharge power for different pulse lengths when the mixture has a reducing He content. For low discharge energies and the 1:1:0 gas mixtures, it is apparent that the discharge power is greater for the longer pulse length. However, care must be taken in not extrapolating too much information from these graphs because of the assumed best fit to the data is a polynomial of degree 2 - in reality this may not be the case. The differences between the 1:1:8 gas mixtures for the two pumping pulse lengths seems to be small. These experiments were repeated and the same conclusions were drawn. With the 7 μ s pulse lengths no more power could be deposited into the 1:1:8 gas mixture than that which was attainable from the 10 μ s pulse lengths. It is possible that the breakdown process occurring at 11 kW is a different mechanism than that which is occurring at the lower discharge powers, and is a mechanism that is independent of the pulse length.

Figure 4.48 shows the values of f_1 as a function of the gas pressure for a 1:1:4 and 1:1:0 gas mixture with the ballasted electrode and flow-shaping installed. Also on the same graph, the values of f_1 for a 1:1:4 gas mixture with the planar electrode geometry, no flow-shaping and $C_c = 20$ nF are shown for a direct comparison of the performance of the two systems. In all cases the transformer tapsettings were at 50 %. It is seen that the values of f_1 are considerably greater for the ballasted electrode than they are for the planar geometry.

Figure 4.49 shows the discharge power as a function of the gas pressure for the same experimental conditions as for Figure 4.48. Clearly, the values of P_d are greater for the ballasted electrode. For small increases in the gas pressure the incremental rise in the value of E_d is small, consequently, the drop in frequency and the discharge power are relatively slowly varying functions of the gas pressure.

Over a period of time it was found that for the ballasted electrode arcing gradually became more probable for lower operating powers. Latter inspection of the cathode showed that distinctive burn marks had developed around the central elements of the cathode – this can be seen in Plate 5. There were corresponding signs that arcing had occurred on the trigger wires – see Plate 6. It is interesting that the arcing had developed at a place where the velocity was found to be a minimum, which highlights the importance of maximising the gas flow.

REFERENCES CHAPTER FOUR

- [4.1] Nighan W., Wiegand W. "Causes of arcing in CW CO₂ convection laser discharges". *App. Phys. Letts.* Vol. 25(11), pp 633–636, 1974.
- [4.2] Wasserstrom E., Crispin Y. "Stability of glow discharges". *J. App. Phys.* Vol. 53(8), pp 5565–5577, 1982.
- [4.3] Dzakowic G., Wutzke S. "High pulse rate glow-discharge stabilization by gas flow". *J. App. Phys* Vol. 44(11), pp 5061–5063, 1974.
- [4.4] Biblarz O., Nelson R. "Turbulence on an ambient pressure discharge". *J. App. Phys.* Vol. 45(2), pp 633–637, 1974.
- [4.5] Wasserstrom E., Crispin Y. et al "The interaction between electrical discharges and gas flow". *J. App. Phys.* Vol. 49(1), pp 81–86, 1978.
- [4.6] Smith D., Houghton J. "Fluid mechanics". Cleaver Hume Press Ltd, London. 2nd Edition 1961.
- [4.7] "ASYST 2.0 Users Manual: Modules 1, 2, 3 and 5". Macmillan software Company.
- [4.8] "Handbook of chemistry and physics" 55th Edition. CRC press 1974–1975.
- [4.9] "Mathcad 3.0 Users Guide". 1991.
- [4.10] Martin K., Du K. "High power laser development within the Eureka project". *SPIE* Vol. 1031. Seventh symposium on gas flow and chemical lasers, pp 24–30, 1988.
- [4.11] "Electrical breakdown and discharges in gases: macroscopic processes and discharges". Editors Kunhardt, Luessen. Nato series ASI series. Series B Physics, Vol. 89b.
- [4.12] "Technical and design data: Precision engineering with plastics". Published by Polypenco, Herts. U.K. 1988.
- [4.13] McDonald D. "10 kHz pulse repetition frequency laser for materials processing high damage threshold materials". Ph.D Thesis. Department of

Mechanical Engineering, University of Glasgow, 1989.

[4.14] "Tables of physical and chemical constants". Kaye and Laby. 14th Edition. Longman 1973.

[4.15] RS Components, PO Box 99, Corby, Northants, NN17 9RS, U.K

[4.16] Wiegand W., Nighan W. "Plasma chemistry of CO₂-N₂-He discharges". App. Phys. Letts. Vol. 22(11), pp 583-586, 1973.

[4.18] "Principal of adaptive optics". Tyson R. Academic press, 1991.

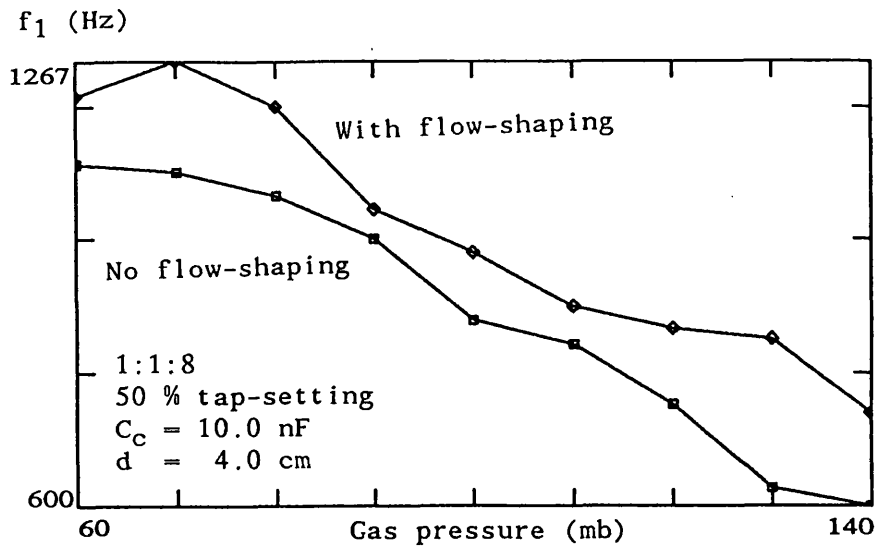


FIGURE 4.1 f_1 AS A FUNCTION OF GAS PRESSURE

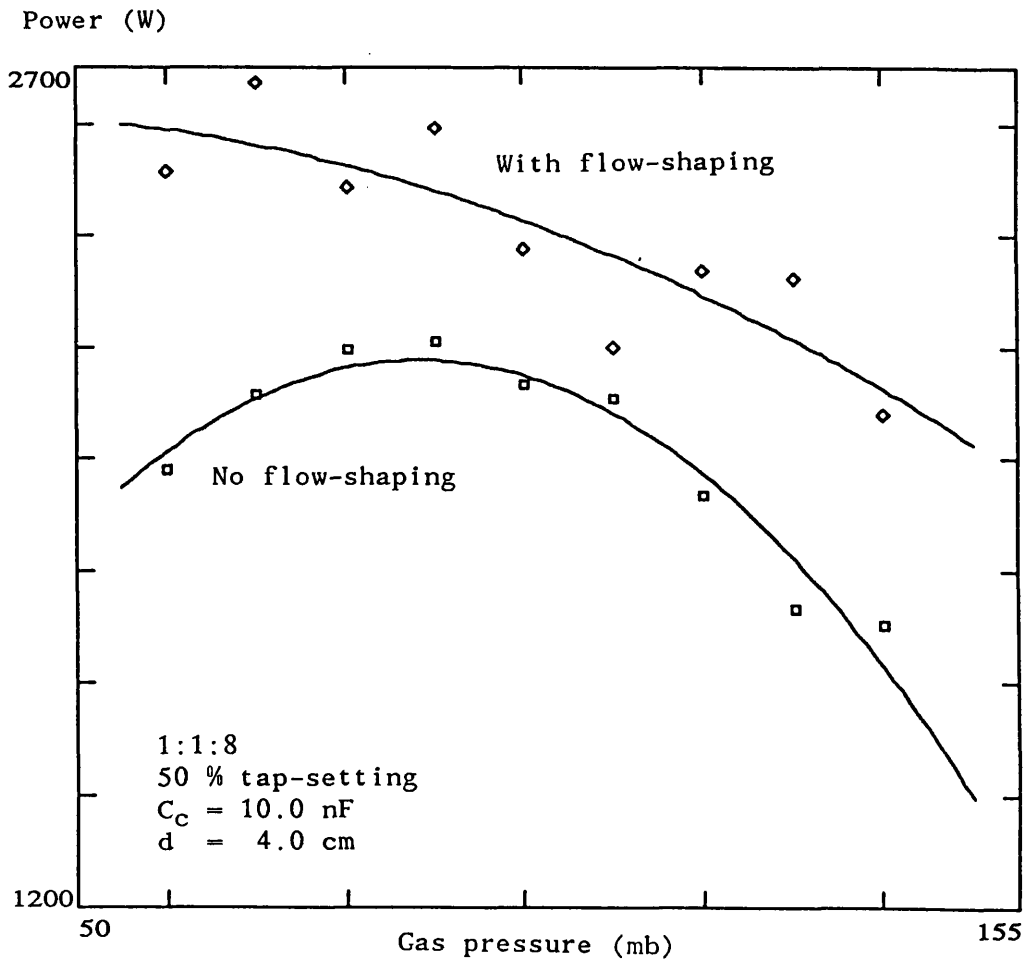


FIGURE 4.2 MAXIMUM DISCHARGE POWER AS A FUNCTION OF GAS PRESSURE

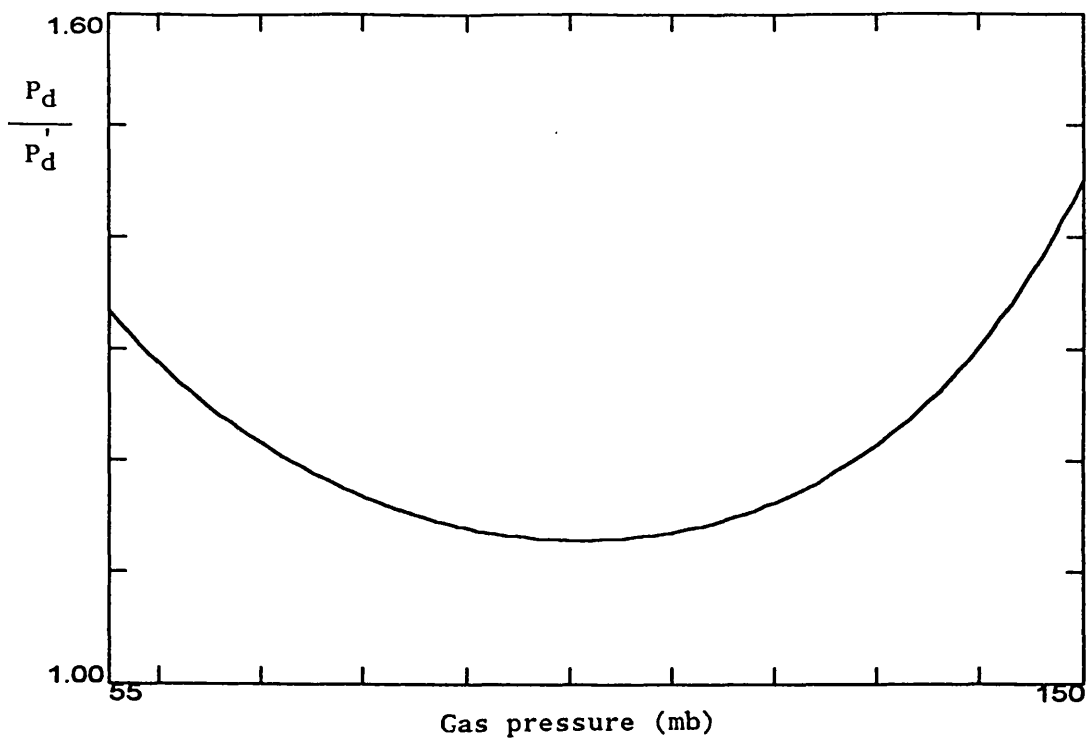


FIGURE 4.3 RATIO OF THE DISCHARGE POWER WITH AND WITHOUT FLOW-SHAPING

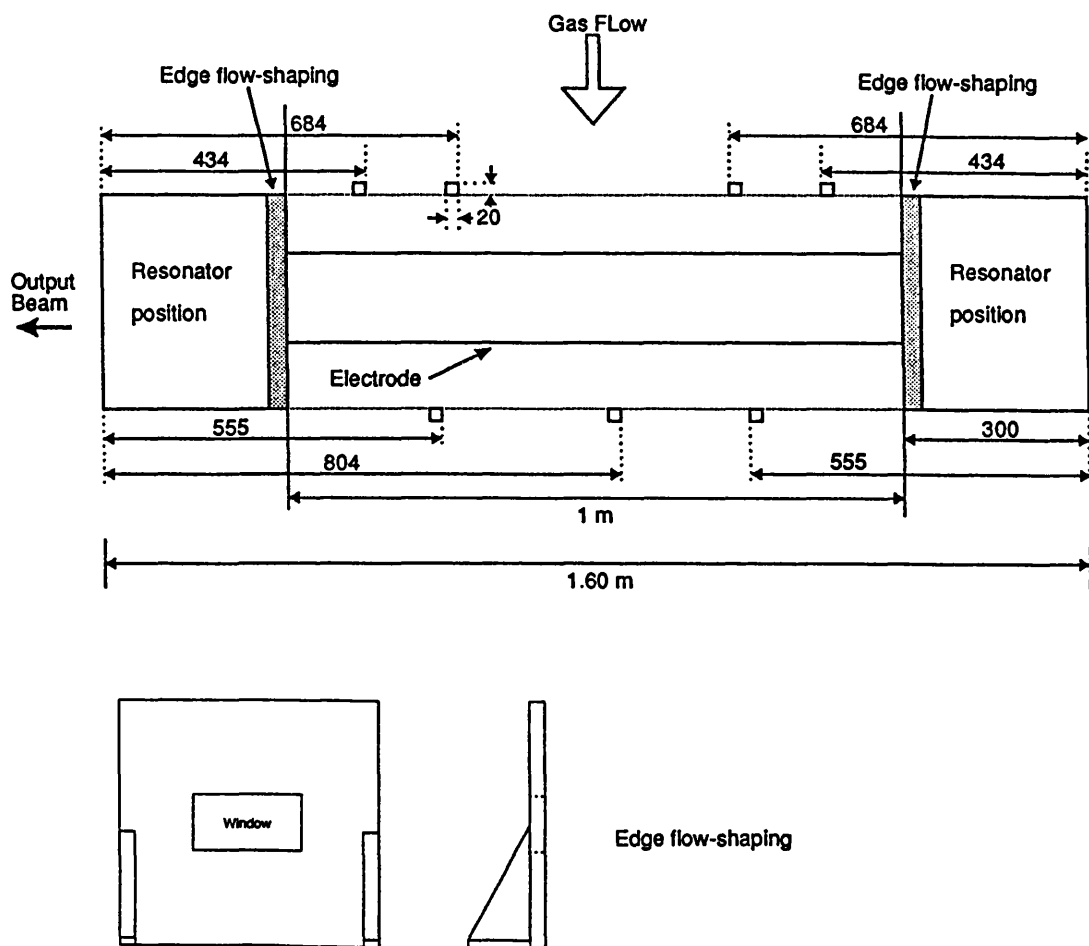


FIGURE 4.4 POSITIONING OF THE EDGE FLOW-SHAPING

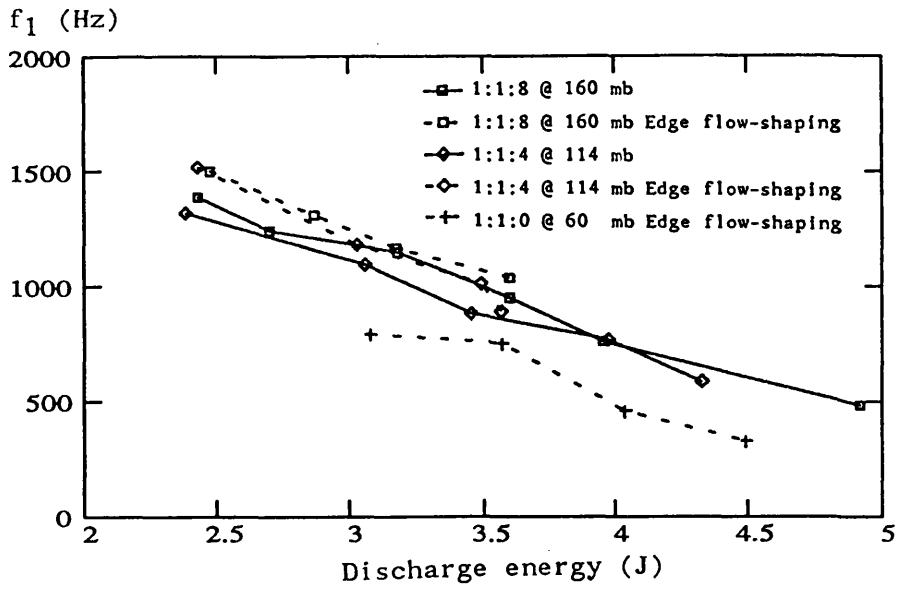


FIGURE 4.5 f_1 VS DISCHARGE ENERGY WITH EDGE AND LONGITUDINAL FLOW-SHAPING

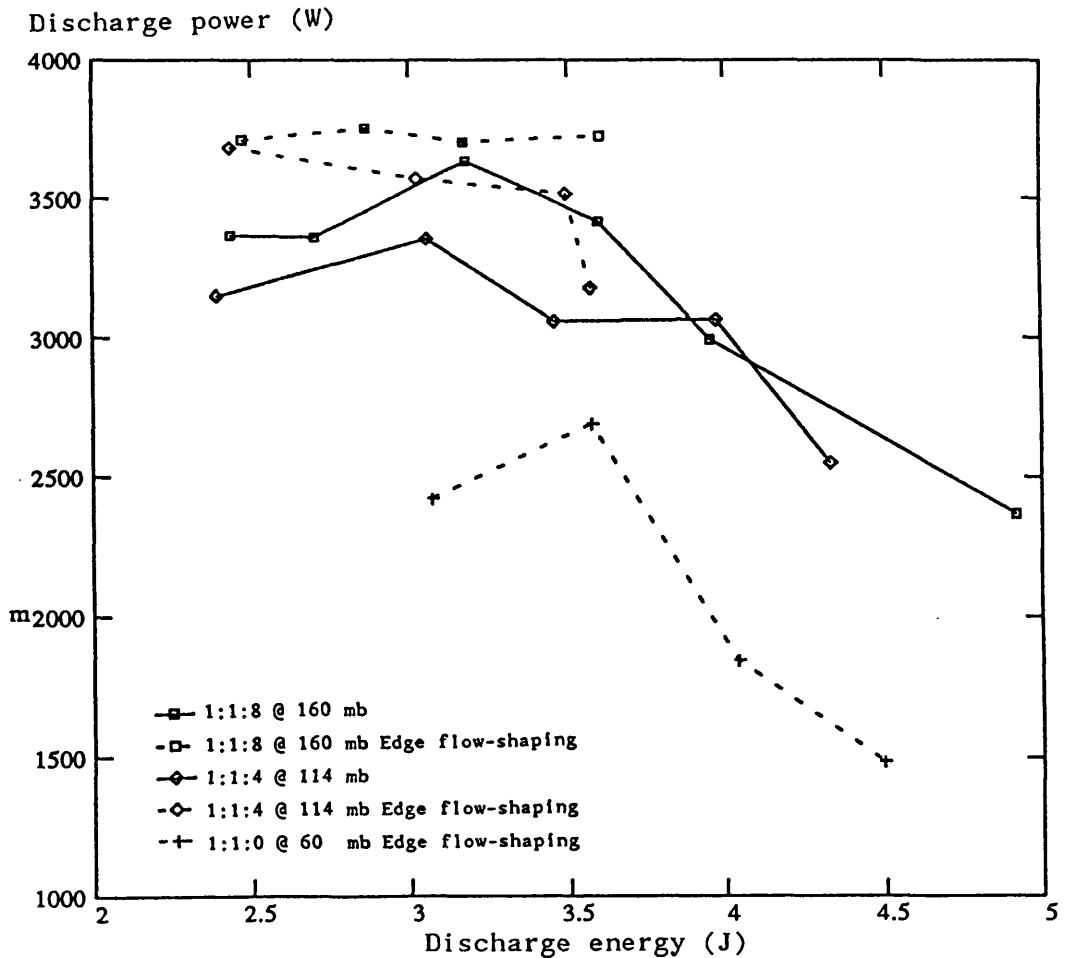


FIGURE 4.6 AFFECT OF EDGE FLOW-SHAPING ON THE MAXIMUM DISCHARGE POWER

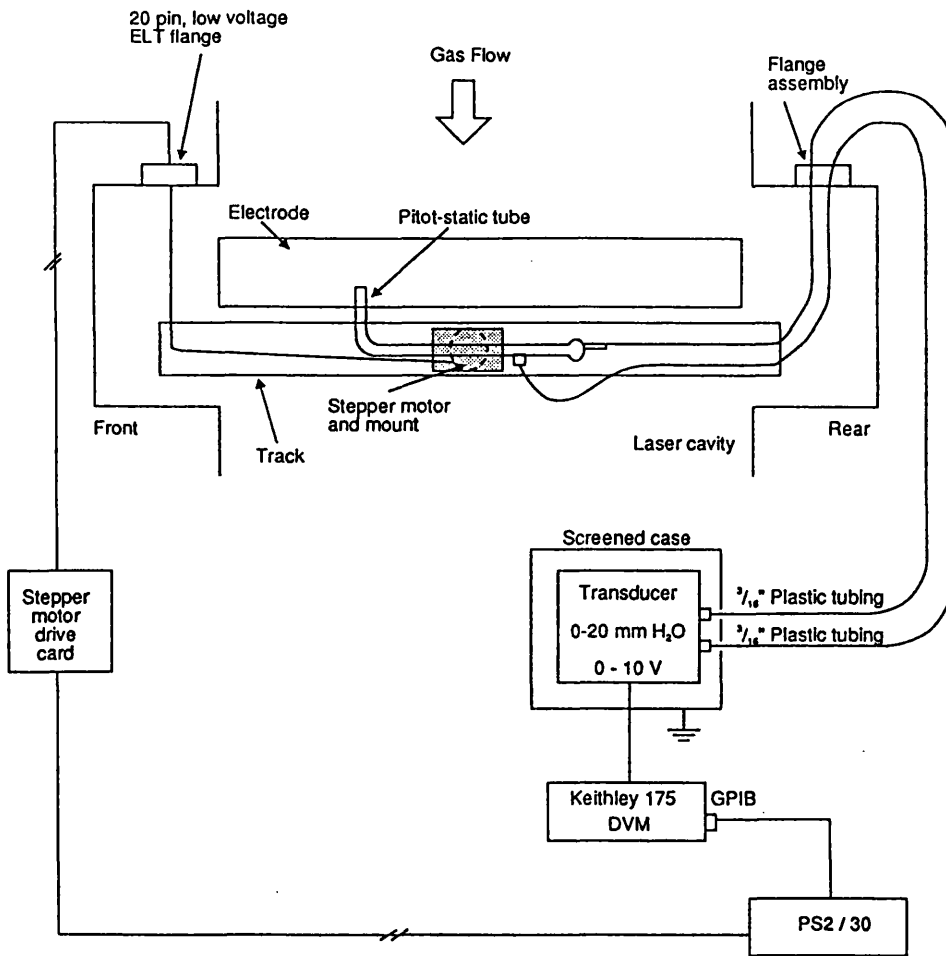


FIGURE 4.7 GAS VELOCITY EXPERIMENTAL ARRANGEMENT

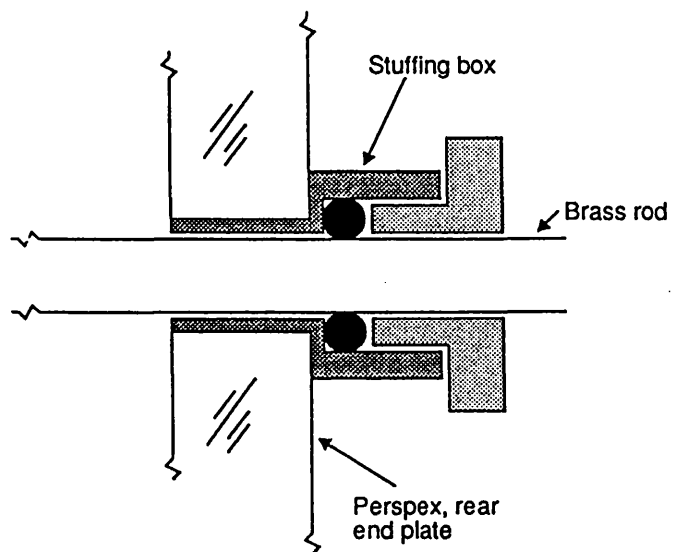


FIGURE 4.8 STUFFING BOX

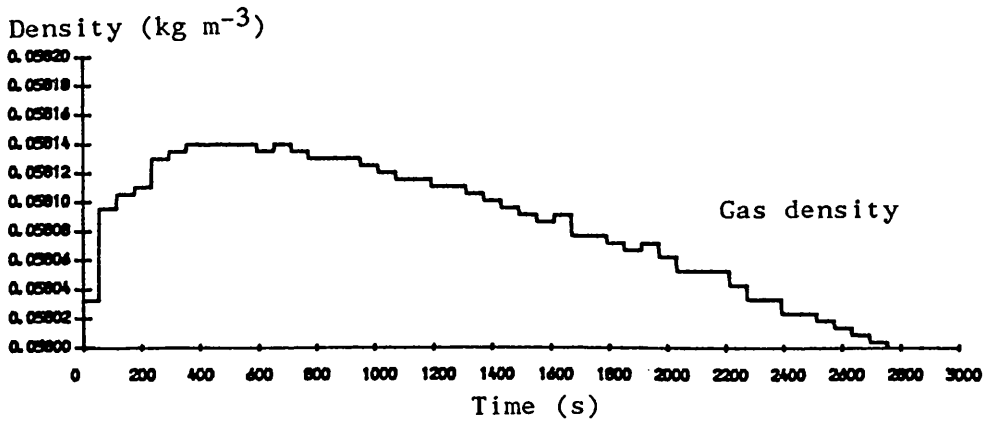
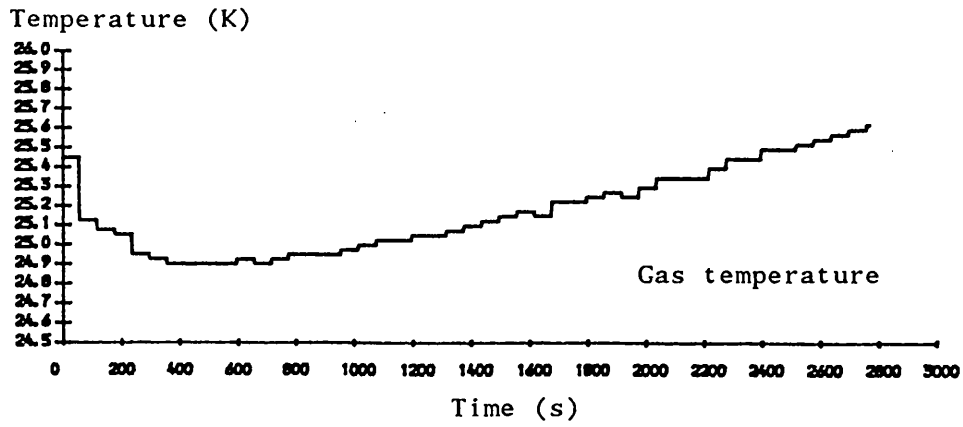


FIGURE 4.11 GAS TEMPERATURE AND DENSITY AS A FUNCTION OF TIME

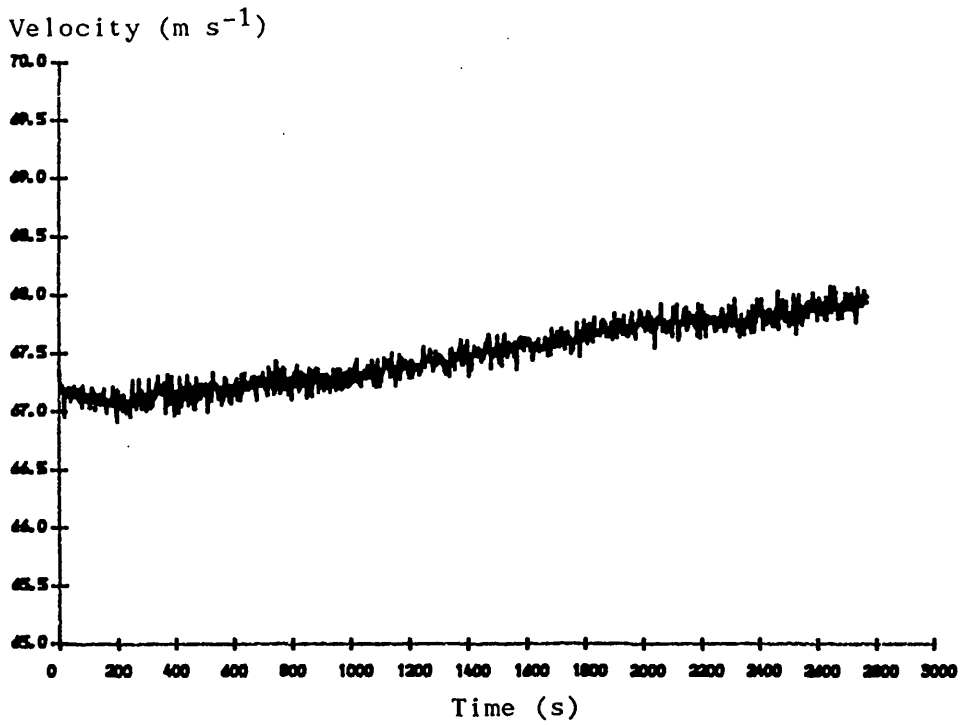


FIGURE 4.12 VELOCITY AND TEMPERATURE CORRECTED VELOCITY VS TIME

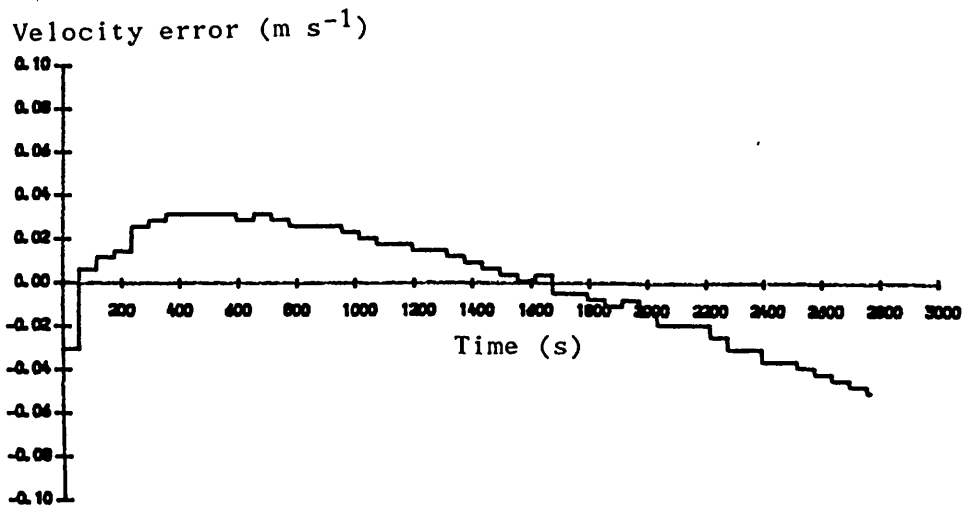


FIGURE 4.13 VELOCITY ERROR DUE TO TEMPERATURE CHANGE

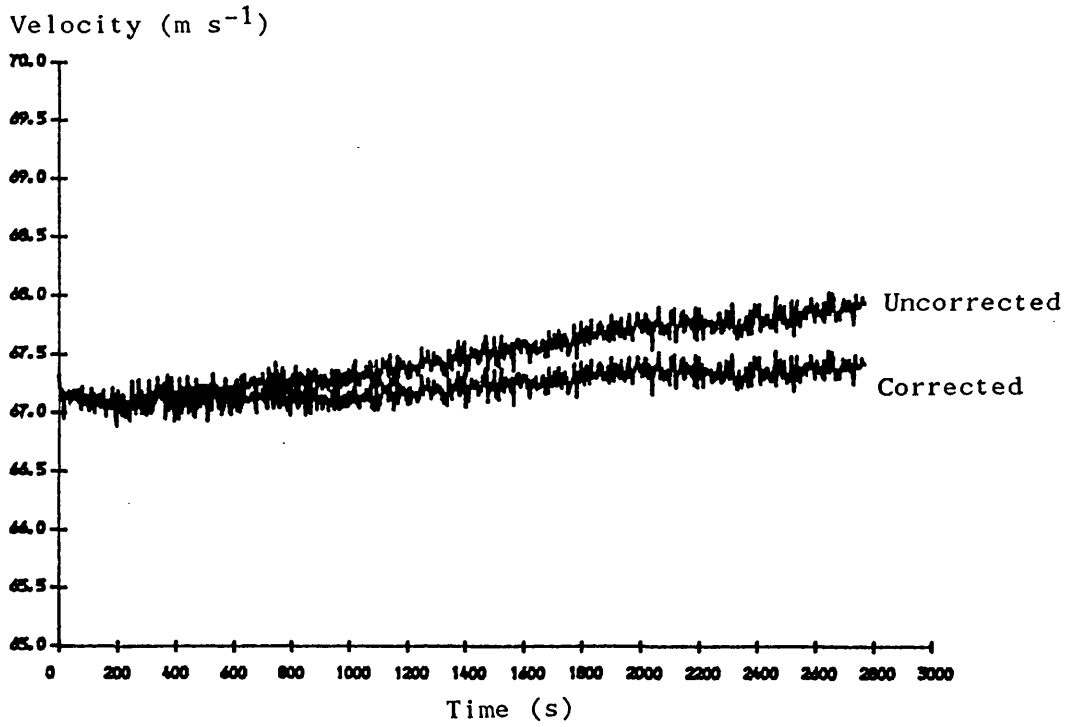


FIGURE 4.14 VELOCITY AND LEAK RATE CORRECTED VELOCITY AS A FUNCTION OF TIME

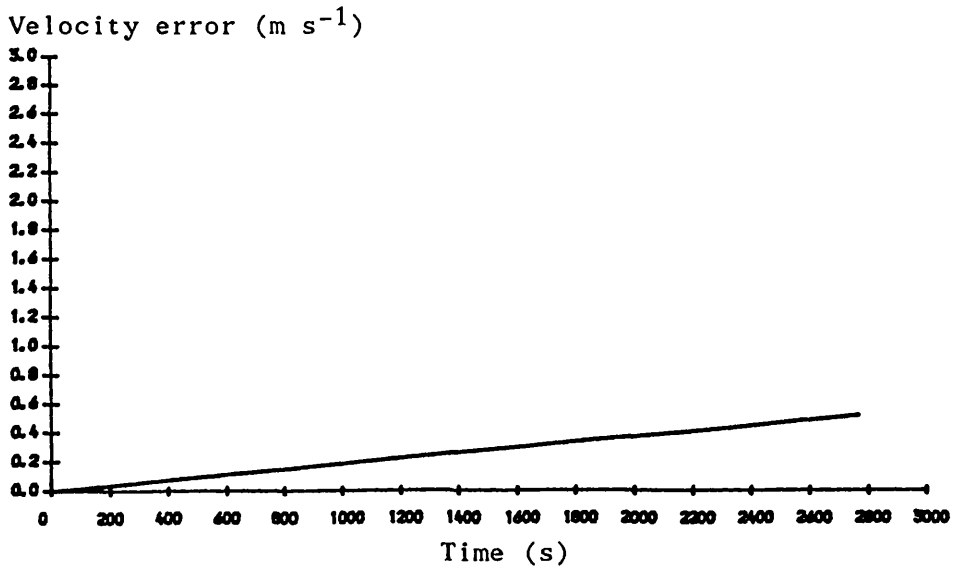


FIGURE 4.15 VELOCITY ERROR DUE TO SYSTEM LEAKING

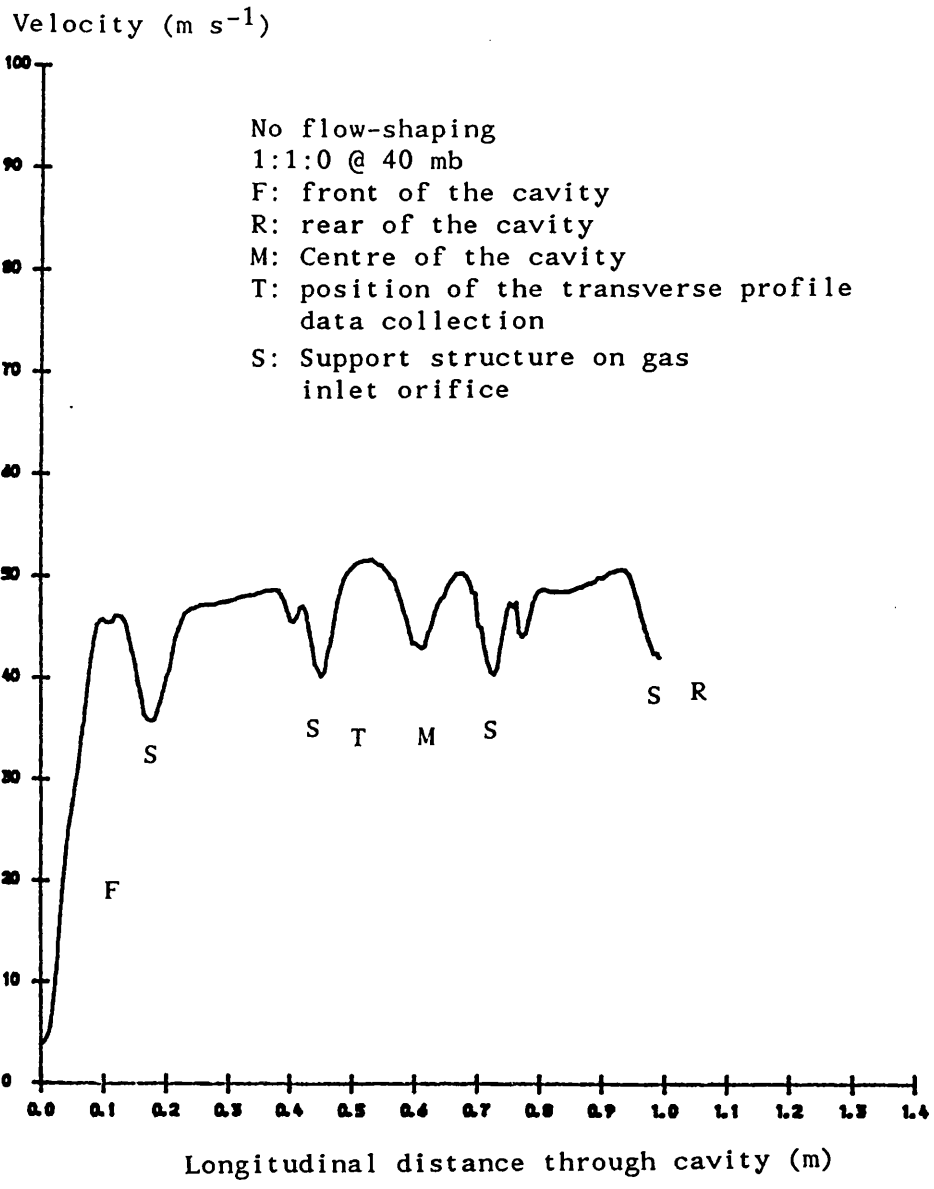


FIGURE 4.16 LONGITUDINAL VELOCITY AND POSITION OF SUPPORT STRUCTURES

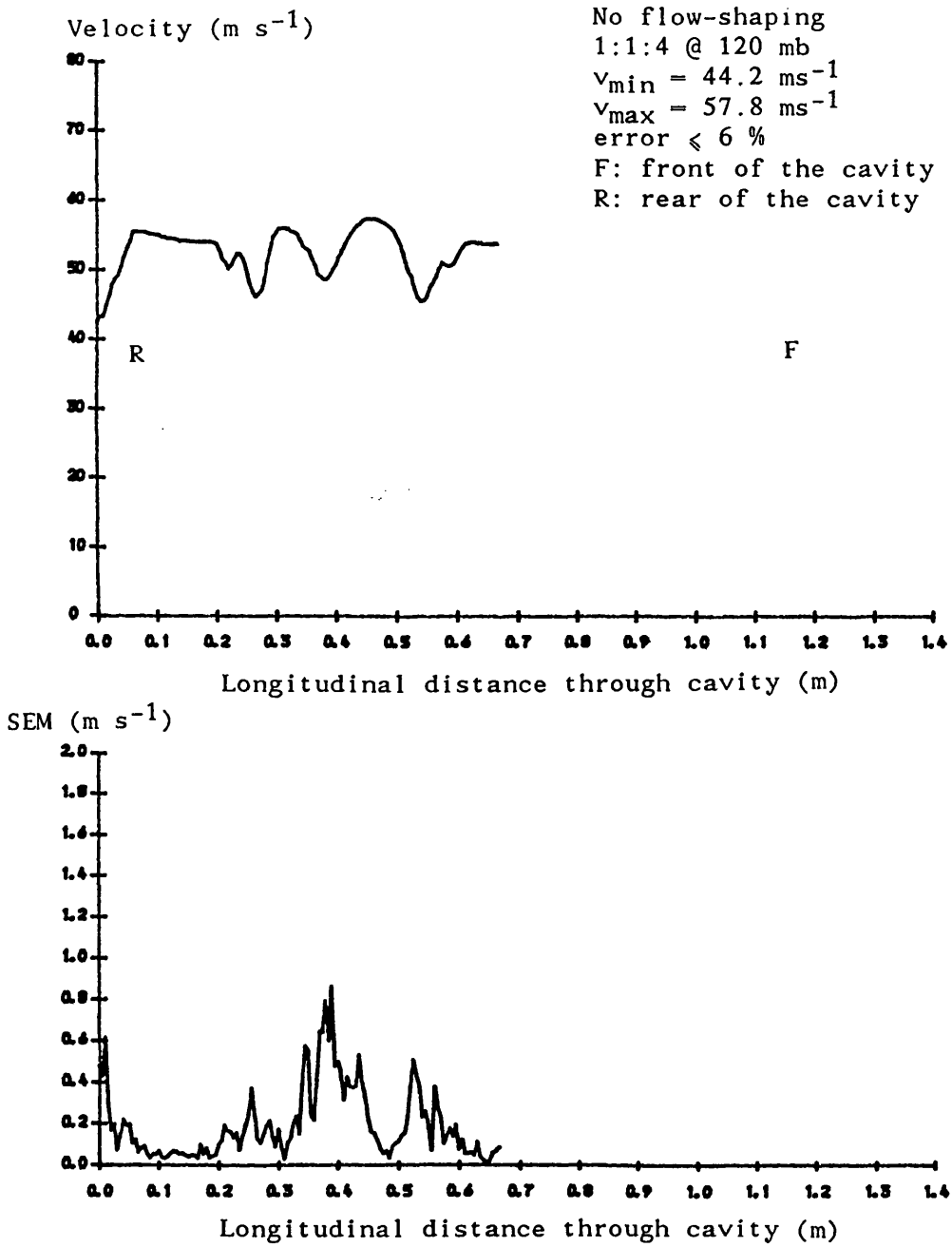


FIGURE 4.17 LONGITUDINAL VELOCITY PROFILE AND THE SEM

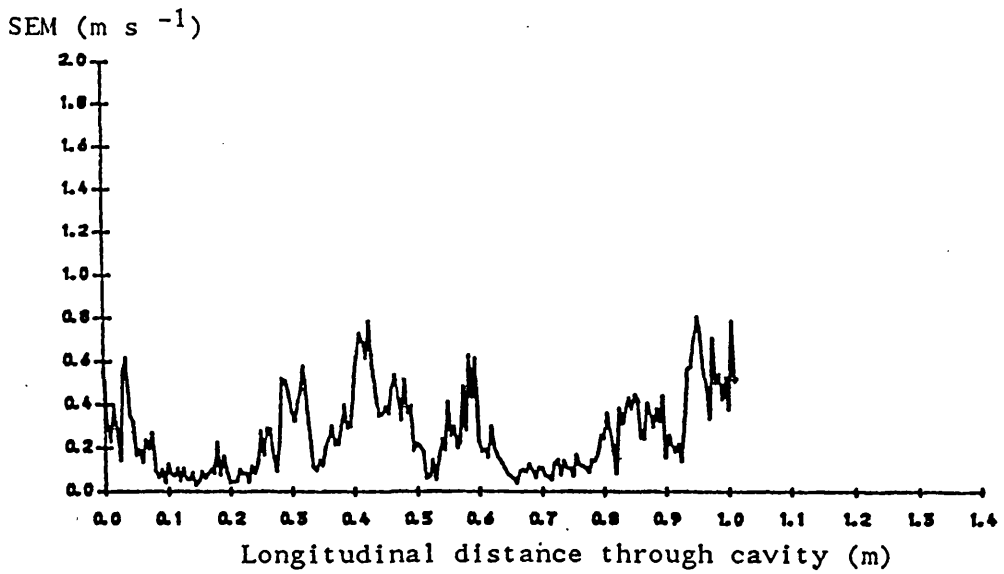
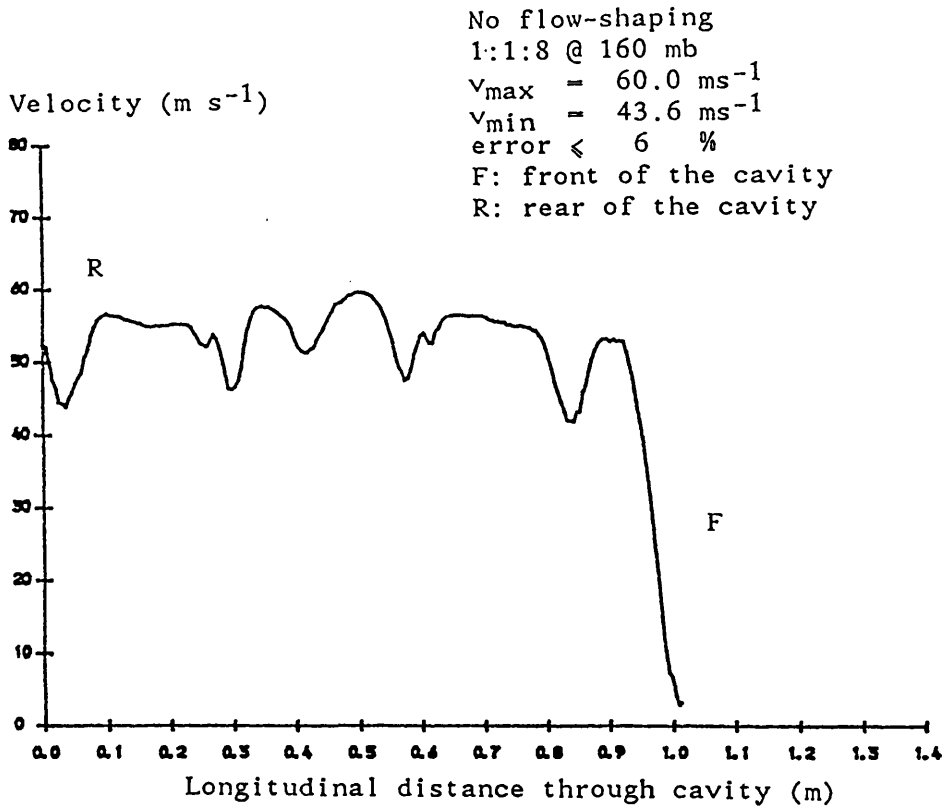


FIGURE 4.18 LONGITUDINAL VELOCITY PROFILE AND THE SEM

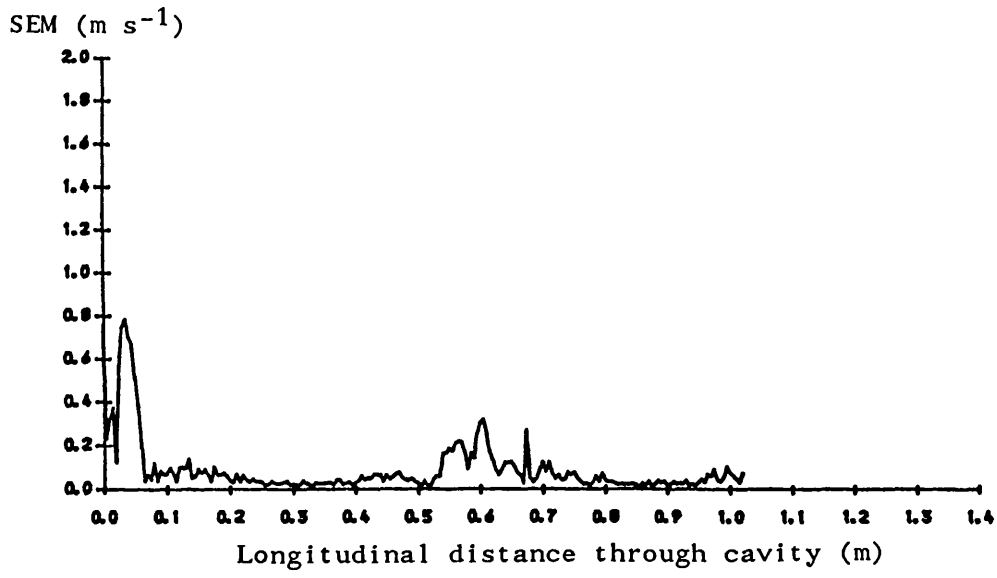
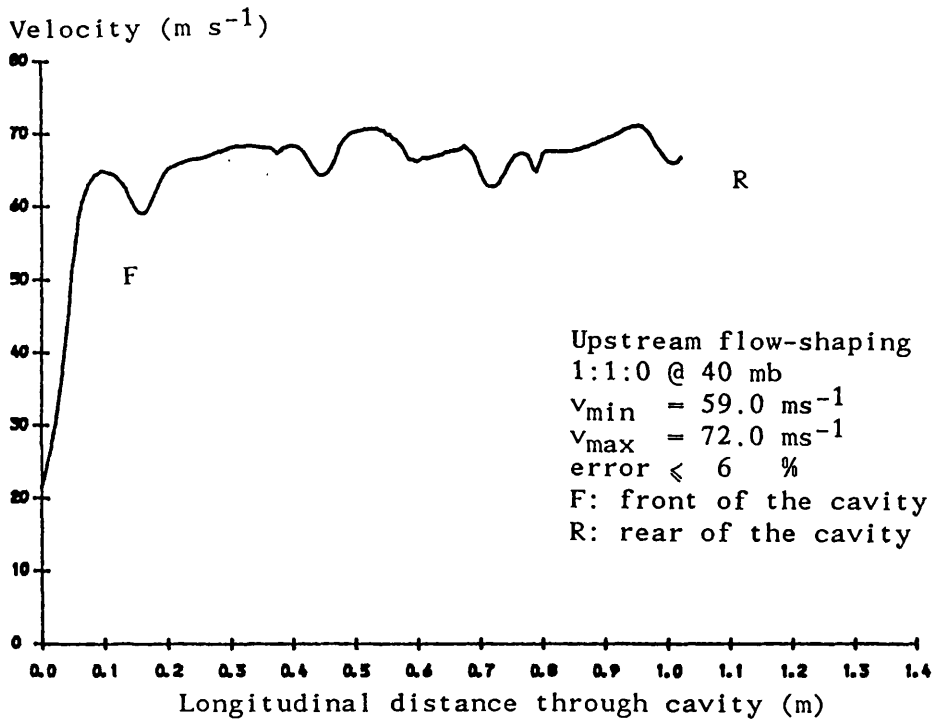


FIGURE 4.19 LONGITUDINAL VELOCITY PROFILE AND THE SEM

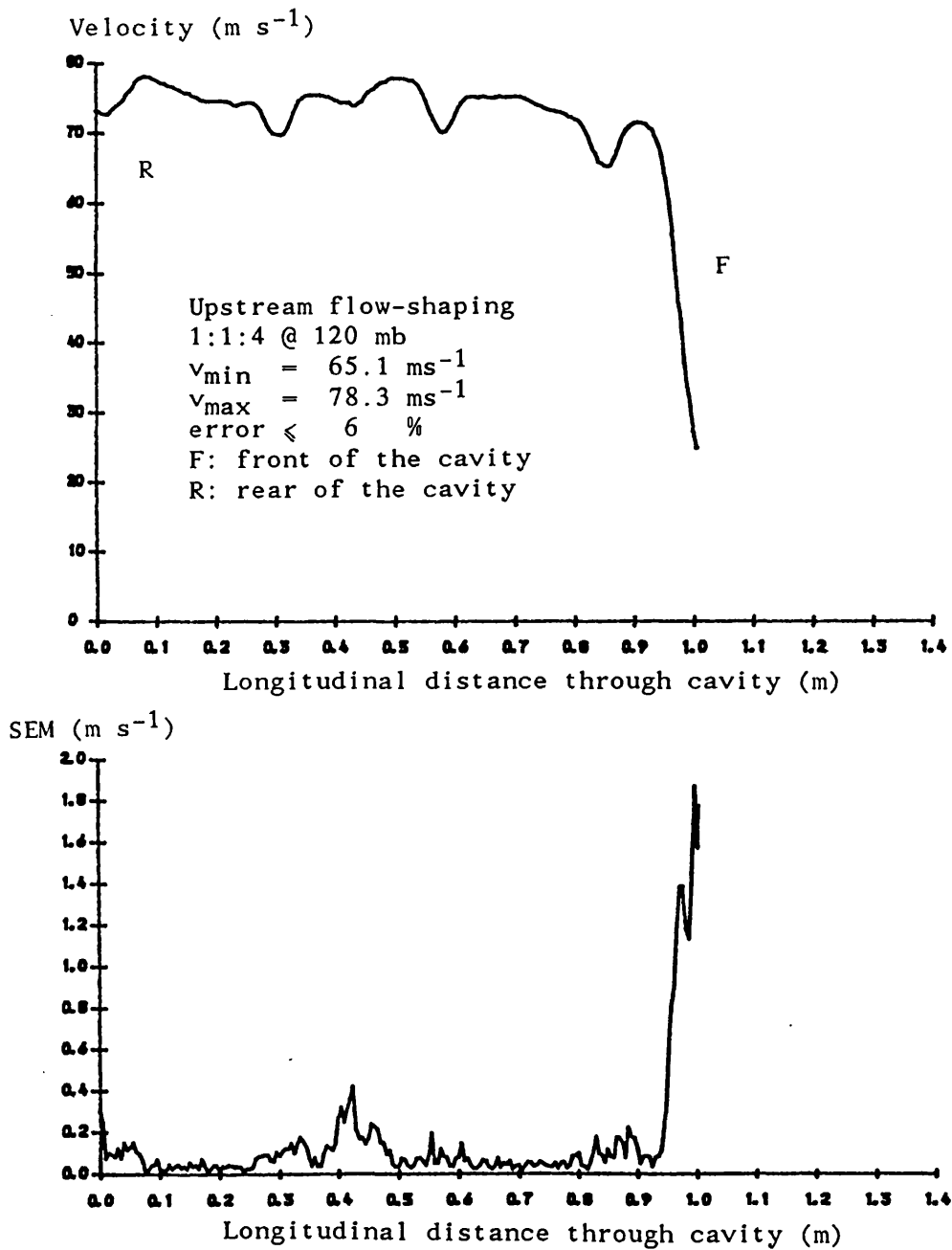


FIGURE 4.20 LONGITUDINAL VELOCITY PROFILE AND THE SEM

Distance from cathode (mm)

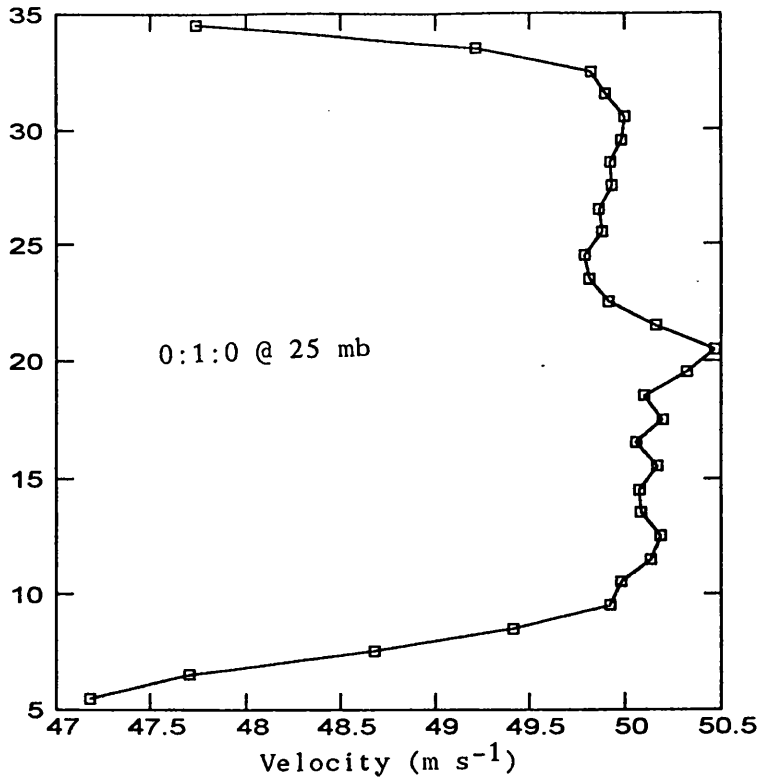


FIGURE 4.21 TRANSVERSE VELOCITY PROFILE AT POINT M

Distance from cathode (mm)

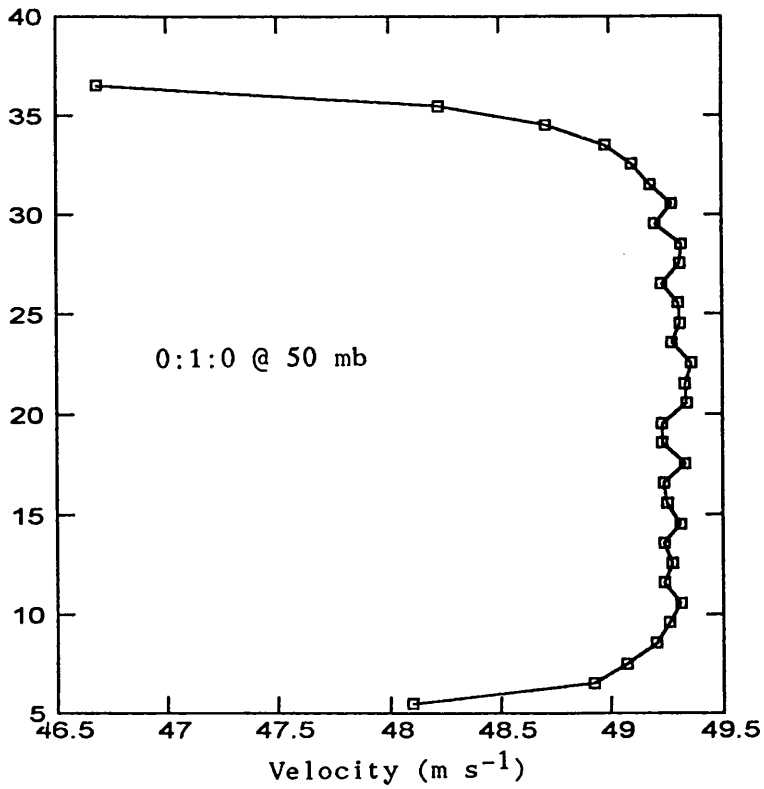


FIGURE 4.22 TRANSVERSE VELOCITY PROFILE AT POINT M

Distance from cathode (mm)

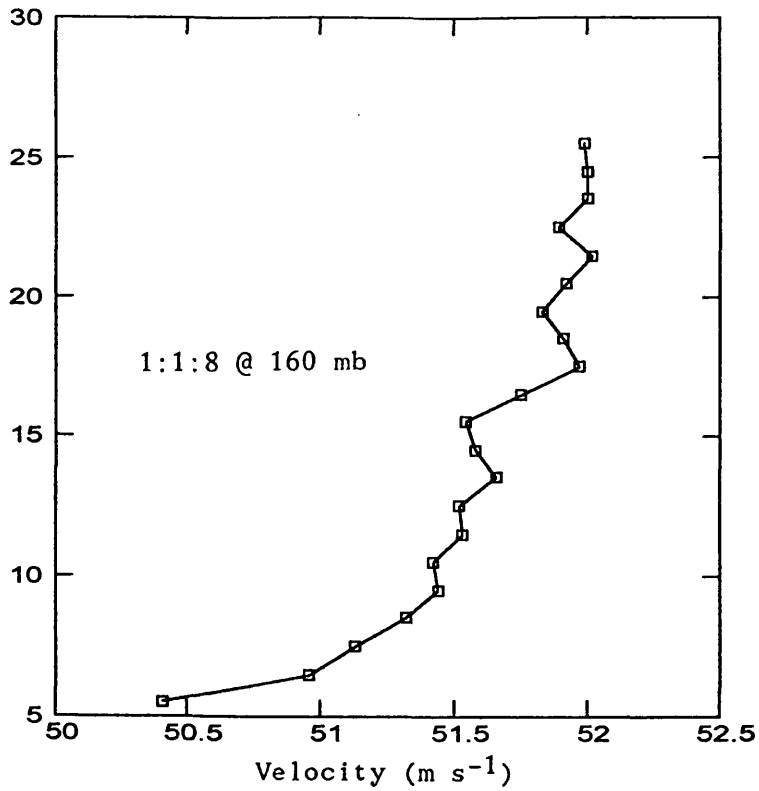


FIGURE 4.23 TRANSVERSE VELOCITY PROFILE AT POINT M

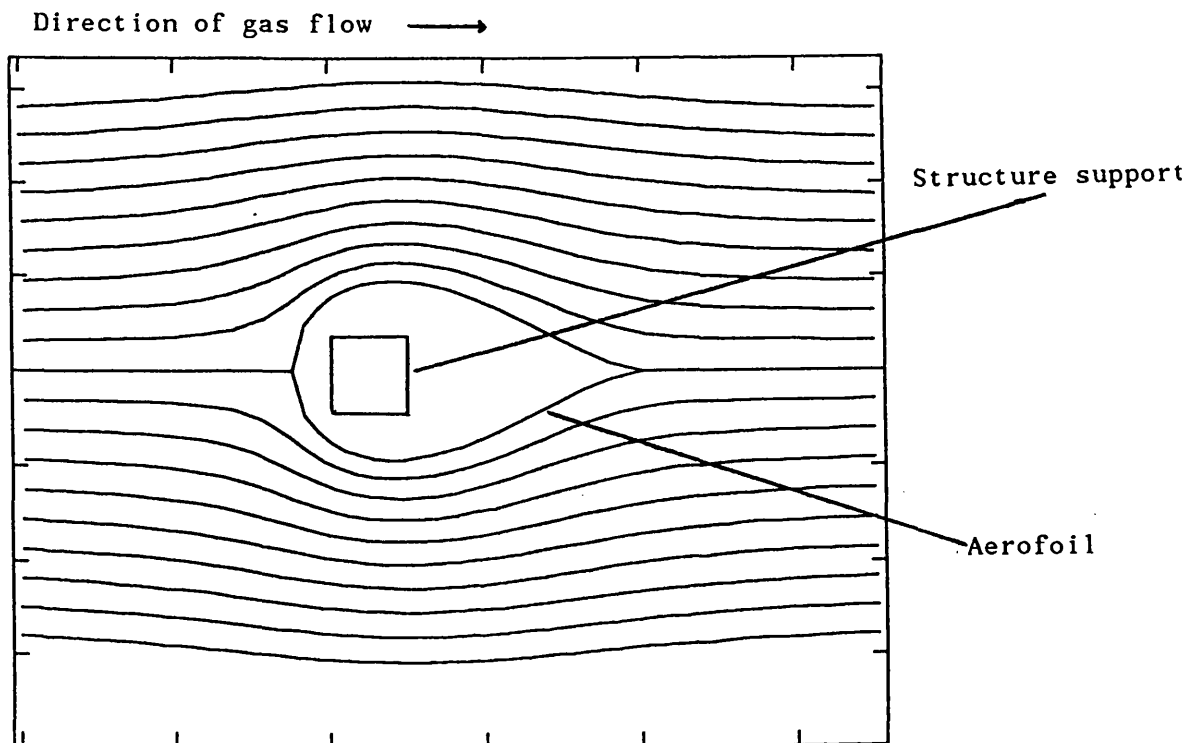


FIGURE 4.24 AEROFOIL AROUND SUPPORT STRUCTURE AND THEORETICAL FLOW PROFILE

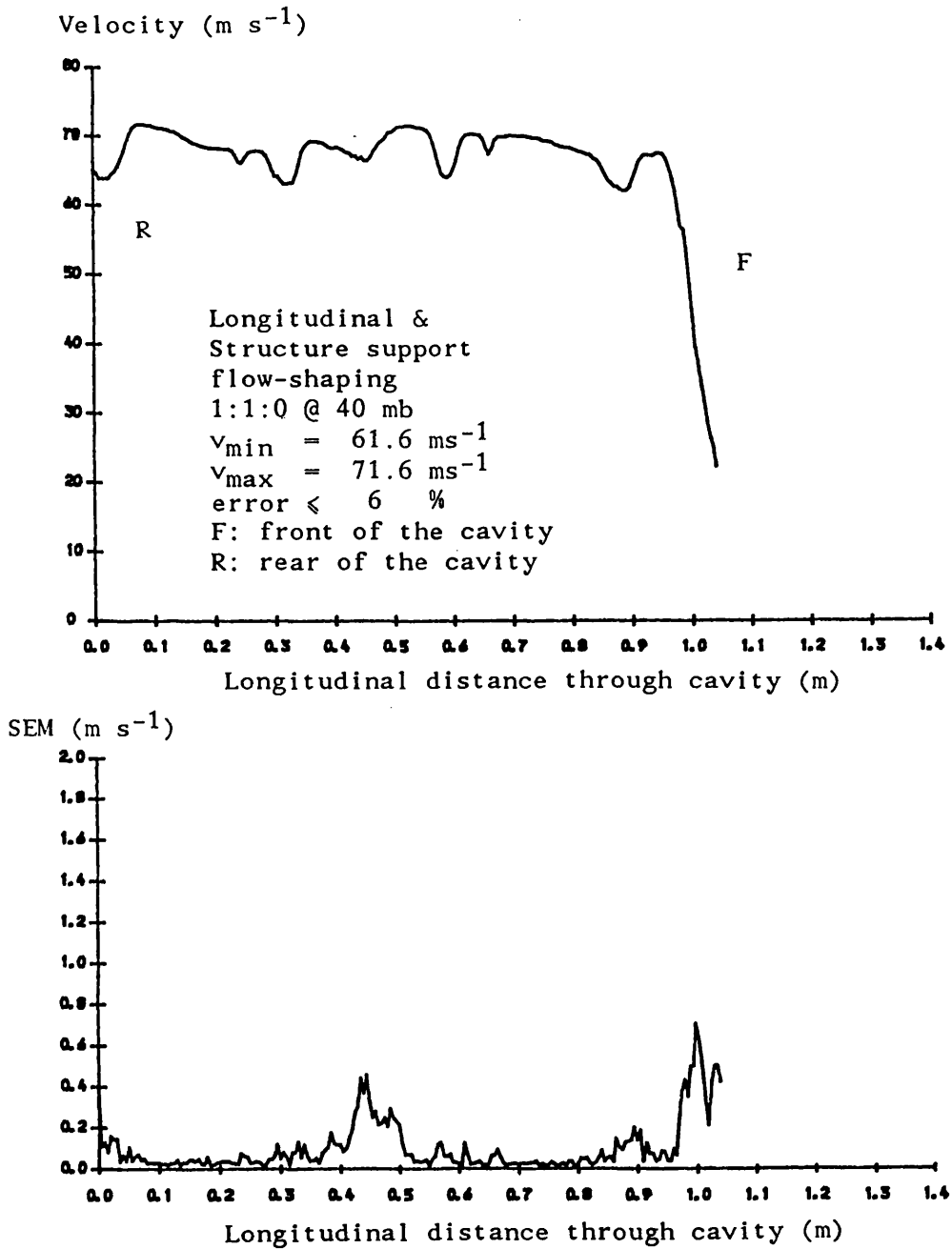


FIGURE 4.25 LONGITUDINAL VELOCITY PROFILE WITH AERO-FOILS POSITIONED

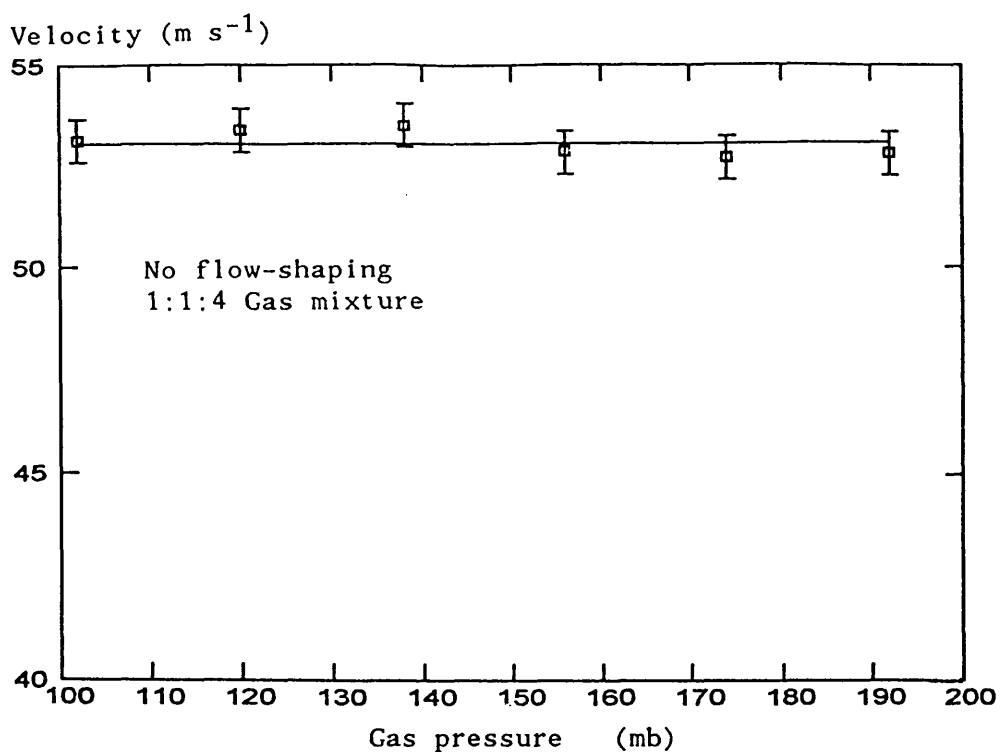


FIGURE 4.26 GAS VELOCITY AS A FUNCTION OF THE GAS PRESSURE

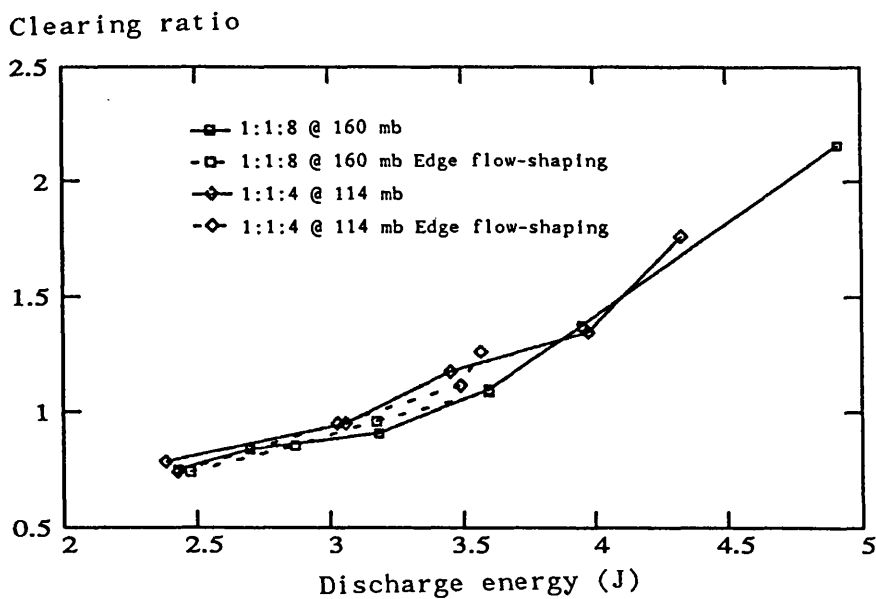


FIGURE 4.27 CLEARING RATIO AS A FUNCTION OF DISCHARGE ENERGY

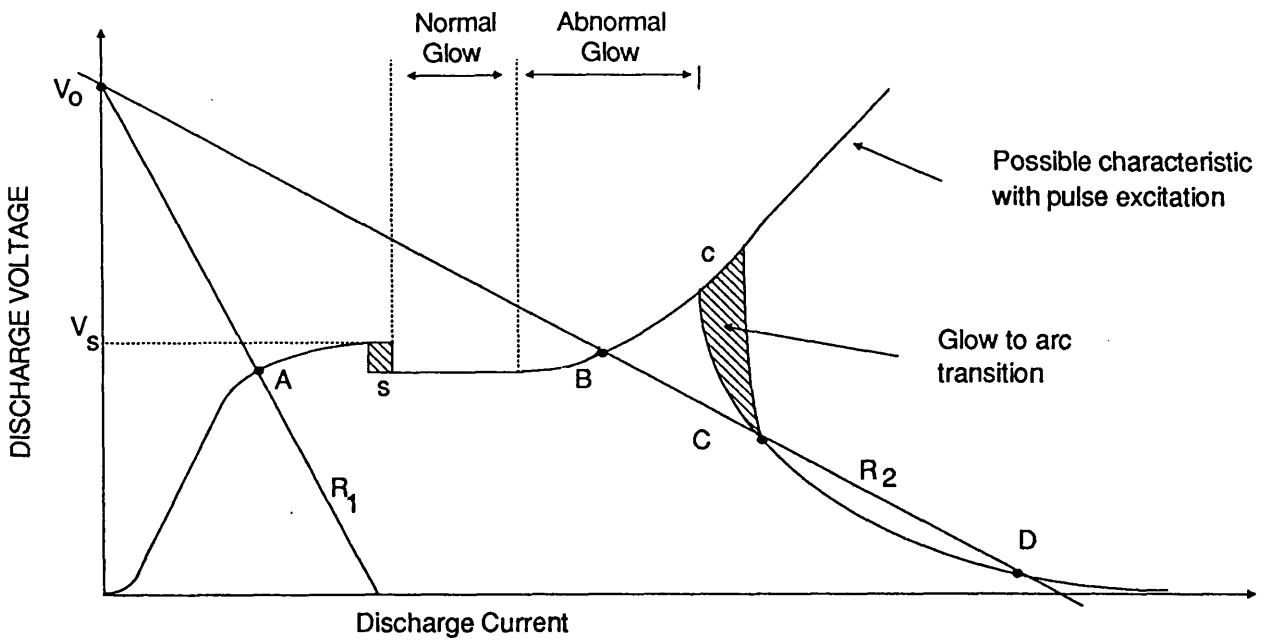


FIGURE 4.28 STATIC GAS DISCHARGE CHARACTERISTICS

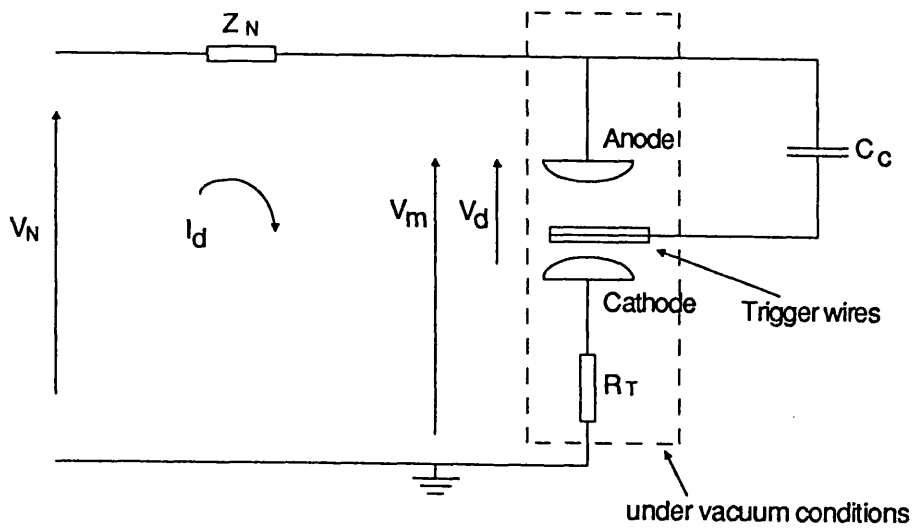


FIGURE 4.29 EQUIVALENT CIRCUIT OF THE BALLASTED CATHODE AND PULSER

Discharge current (A)

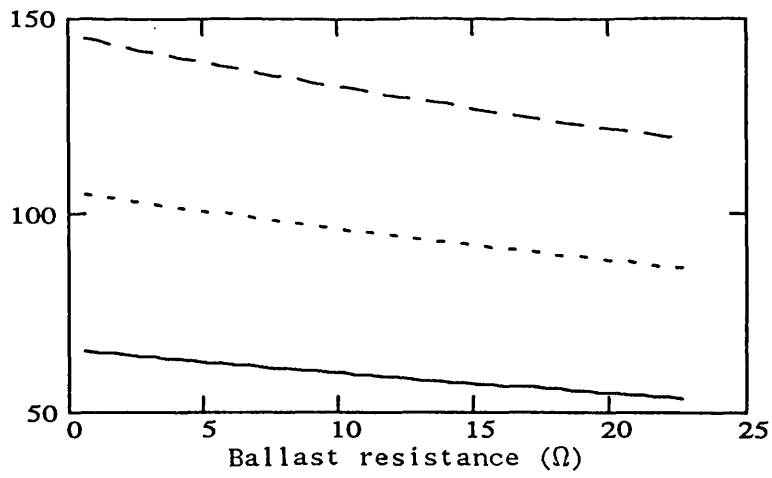


FIGURE 4.30 DISCHARGE CURRENT VS BALLAST RESISTANCE

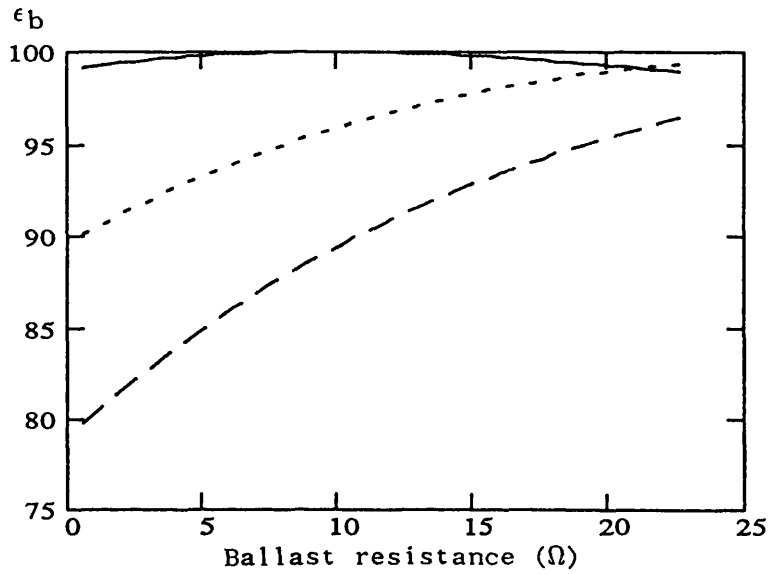


FIGURE 4.31 TRANSFER EFFICIENCY VS BALLAST RESISTANCE

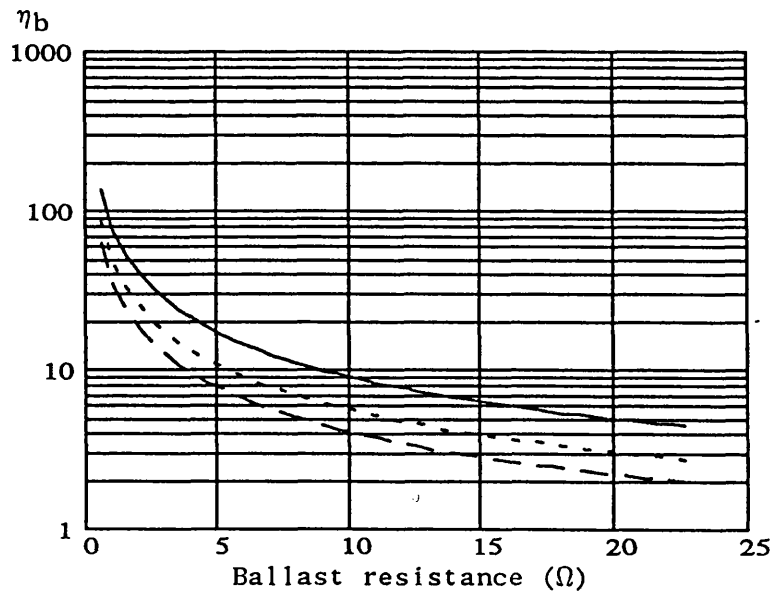


FIGURE 4.32 η_b VS BALLAST RESISTANCE

Figures 4.30 - 4.32

1:1:4 @ 160 mb
 — $V_N = 12$ kV
 - - $V_N = 16$ kV
 - · - $V_N = 20$ kV

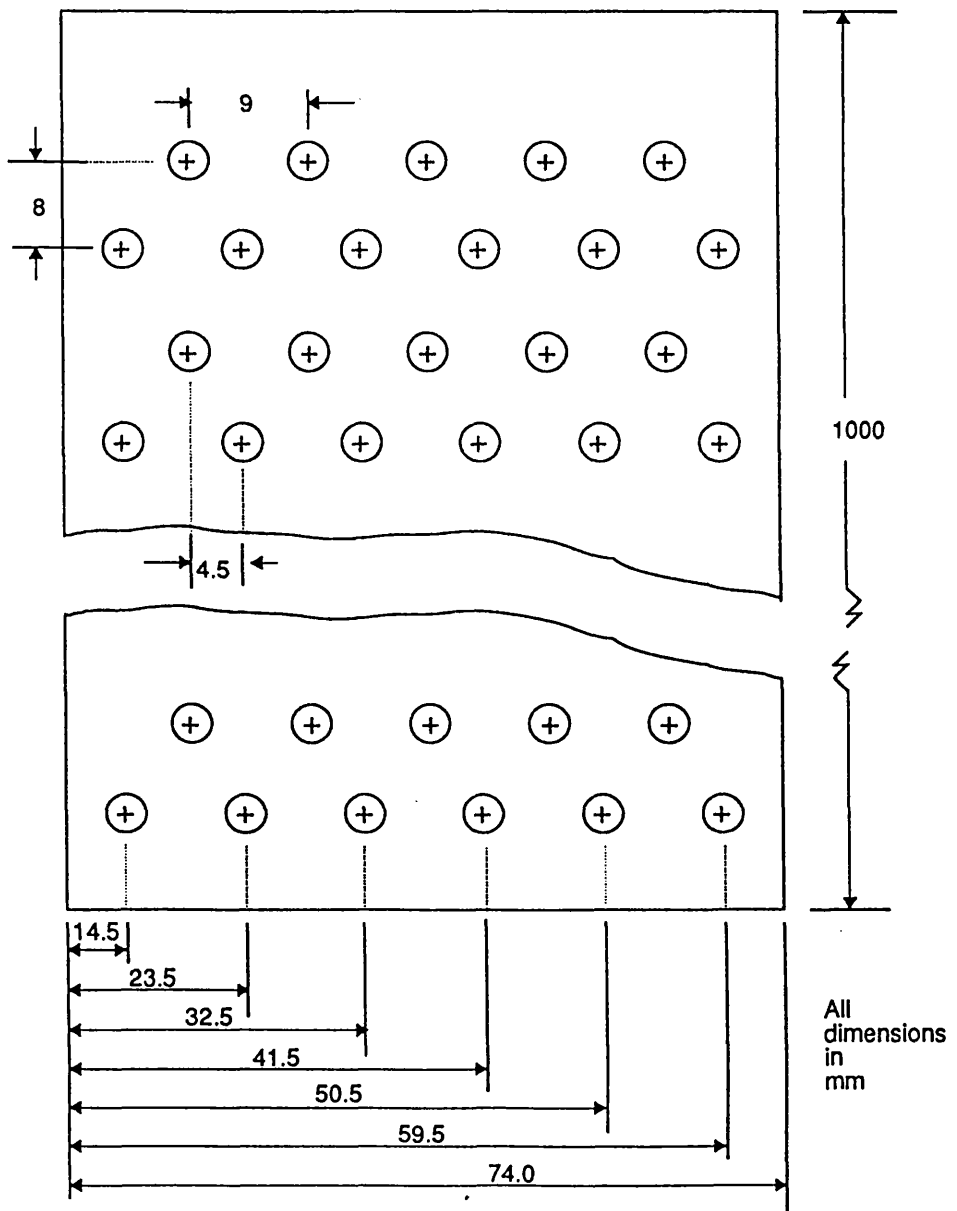
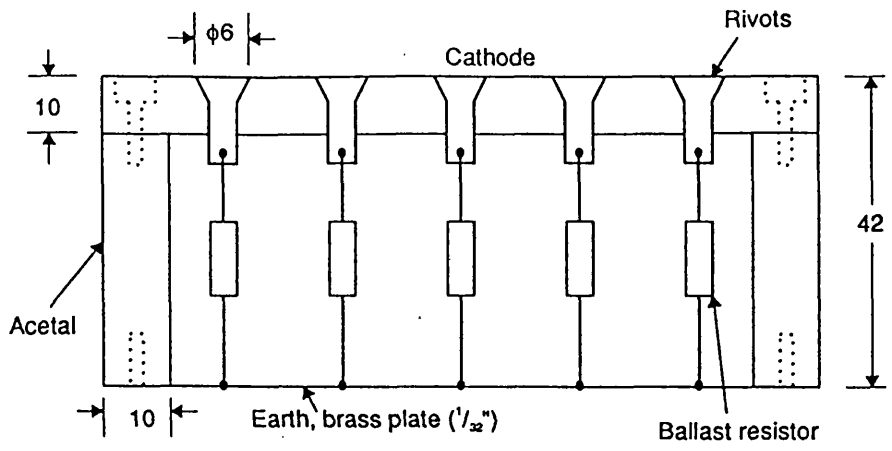


FIGURE 4.33 PROTOTYPE BALLASTED CATHODE DESIGN

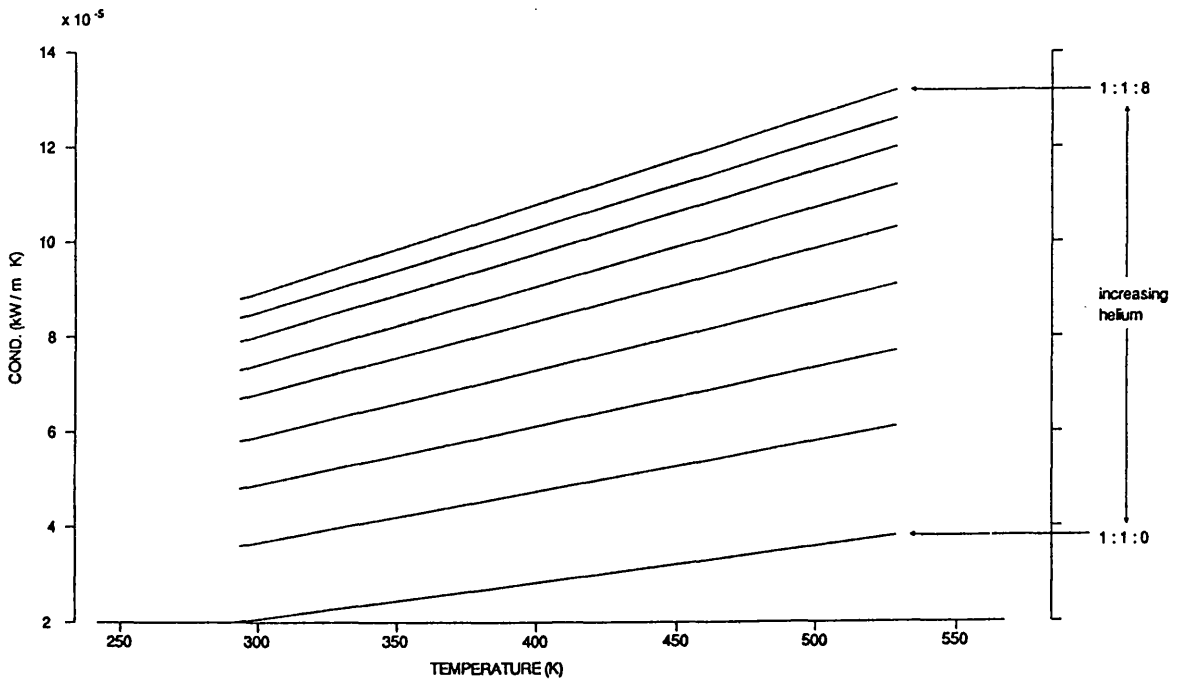


FIGURE 4.34 GAS MIXTURE THERMAL CONDUCTIVITY AS A FUNCTION OF TEMPERATURE

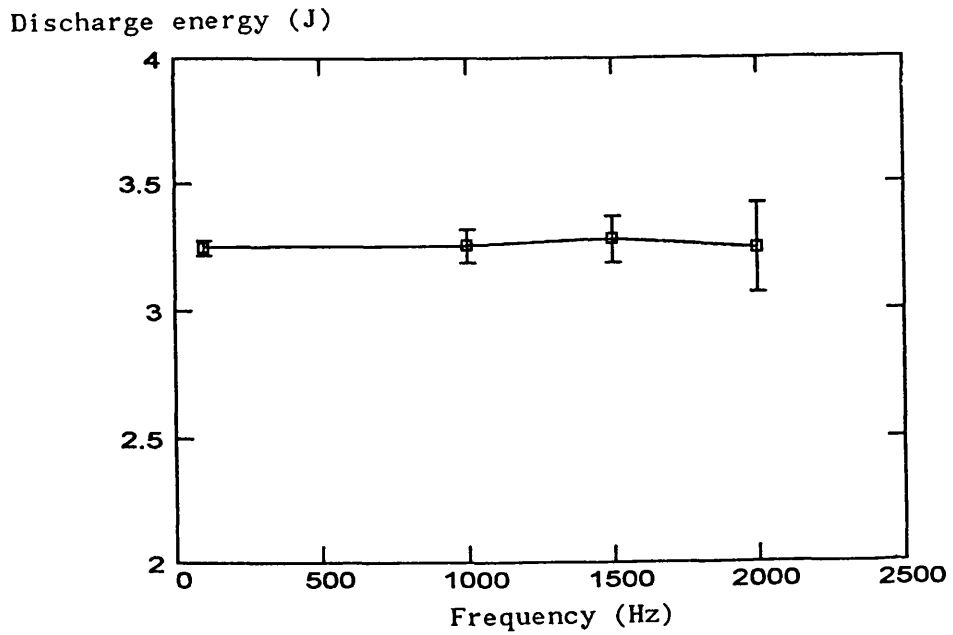


FIGURE 4.35 DISCHARGE ENERGY AS A FUNCTION OF FREQUENCY

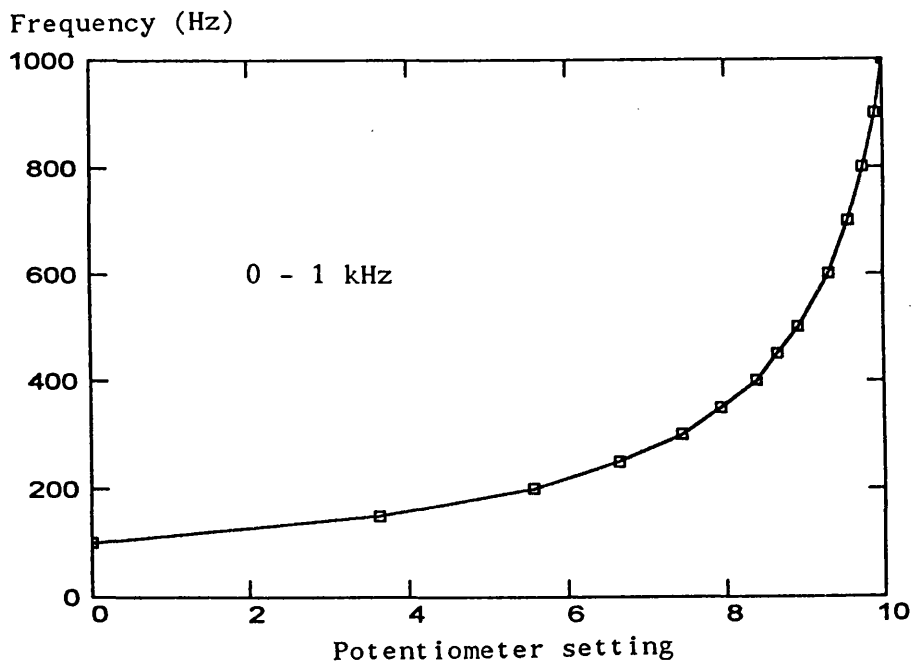
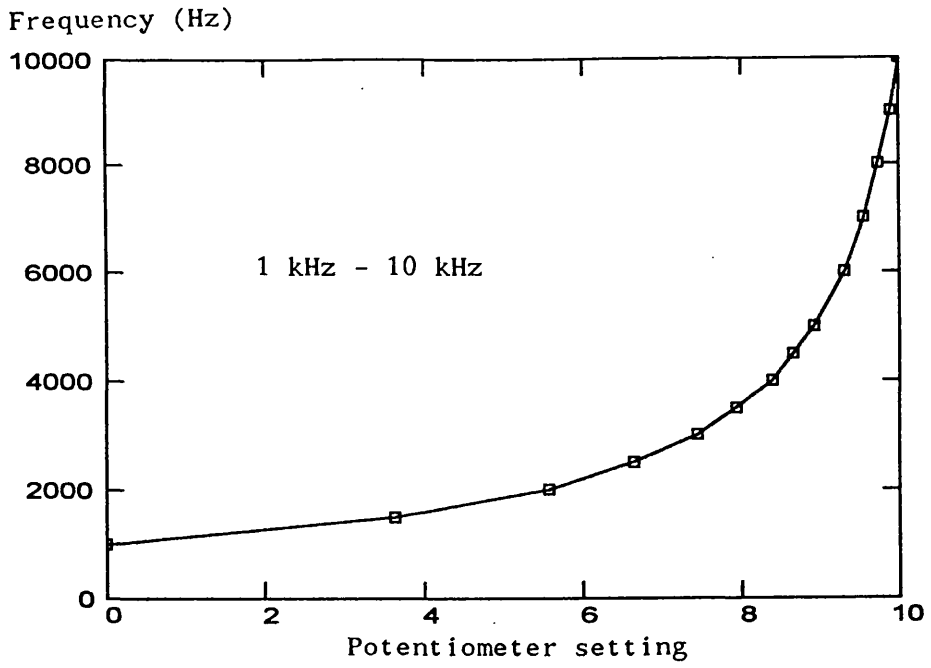


FIGURE 4.36 CALIBRATION OF FREQUENCY CONTROL POTENTIOMETER

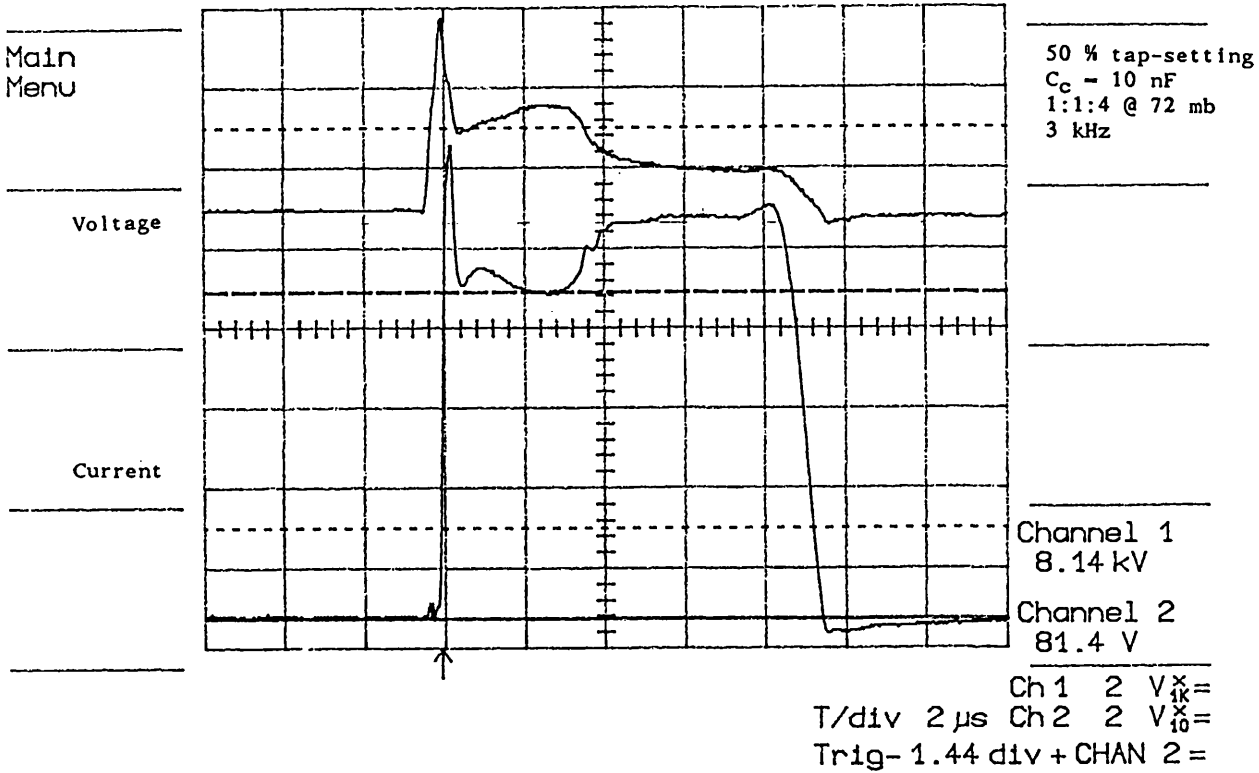


FIGURE 4.37 DISCHARGE CURRENT AND VOLTAGE WITH PARTIAL DISCHARGE BREAKDOWN

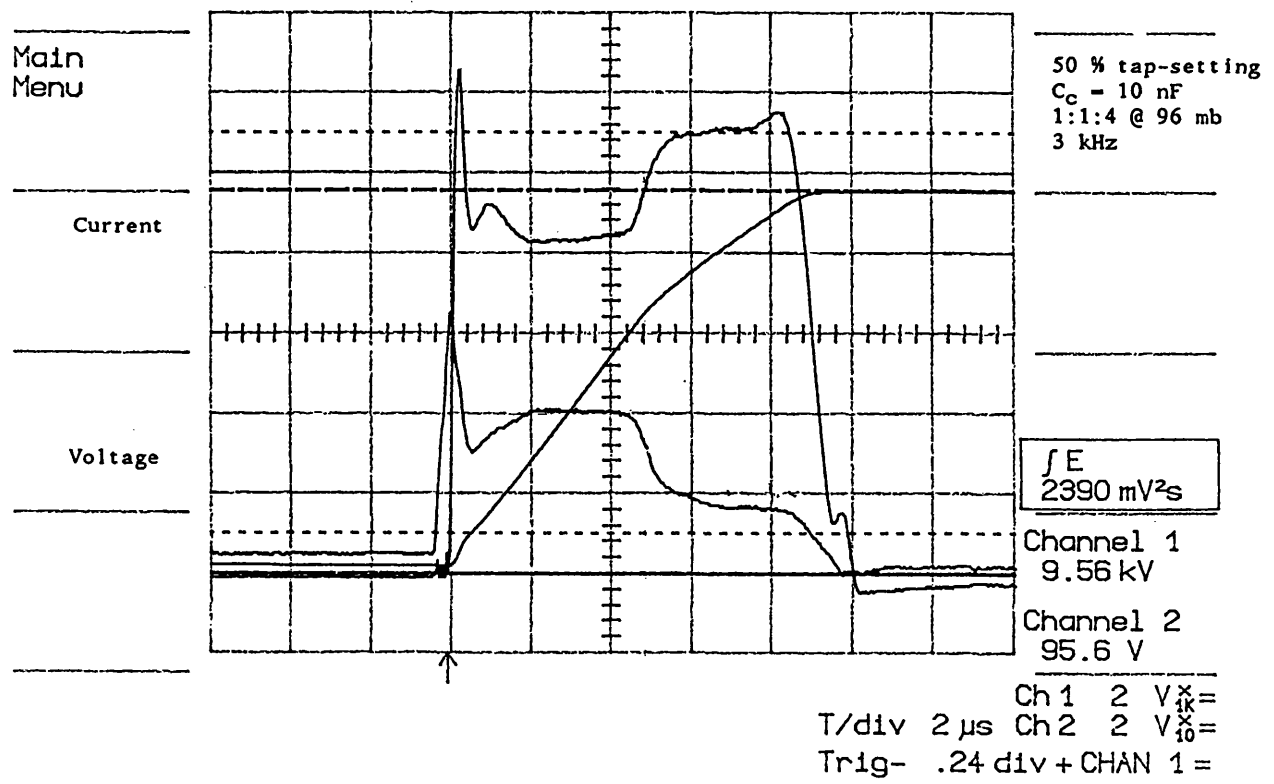


FIGURE 4.38 DISCHARGE CURRENT, VOLTAGE AND ENERGY WITH PARTIAL DISCHARGE BREAKDOWN

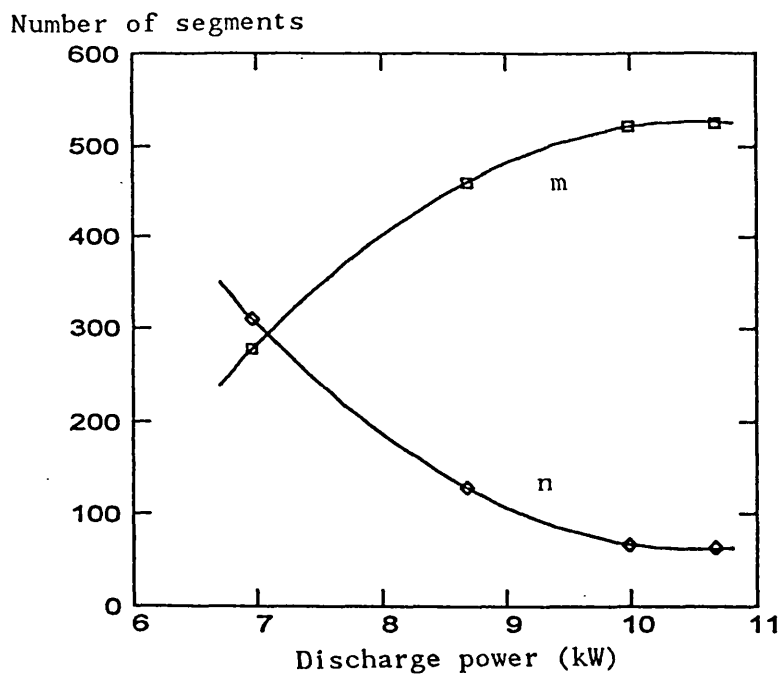


FIGURE 4.39 m AND n VS DISCHARGE POWER

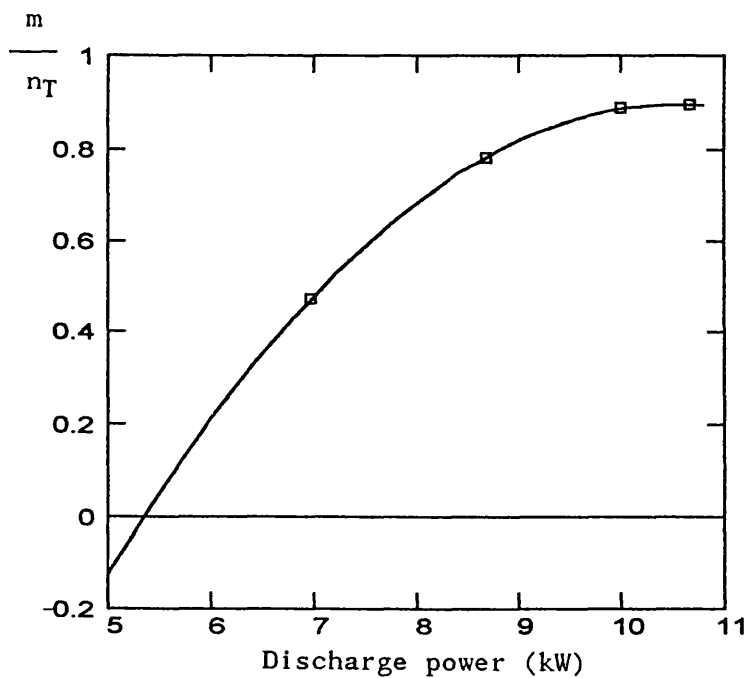
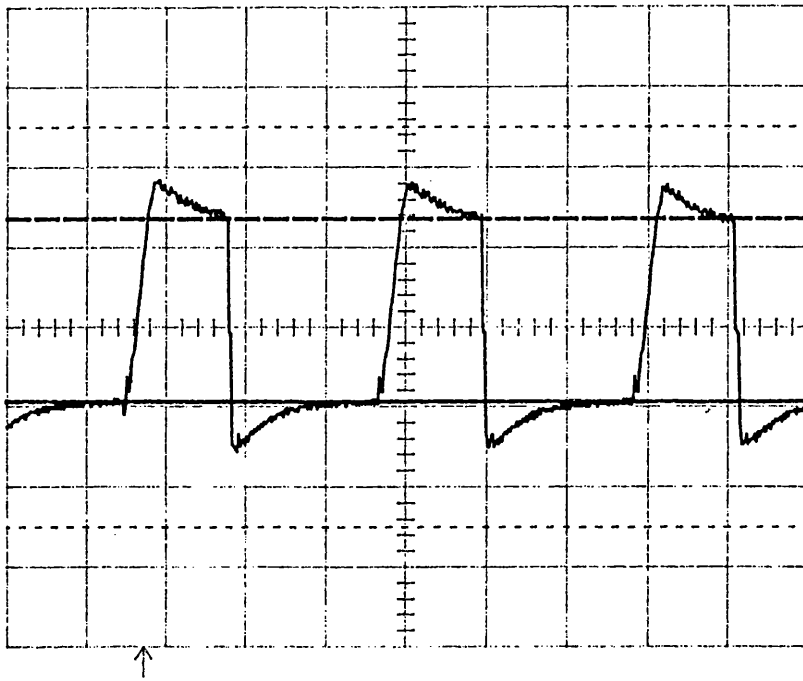


FIGURE 4.40 FRACTIONAL DISCHARGE BREAKDOWN VS DISCHARGE POWER

n number conducting normal discharge current
 m number conducting fault current
 $n_T = n + m$

Main
Menu



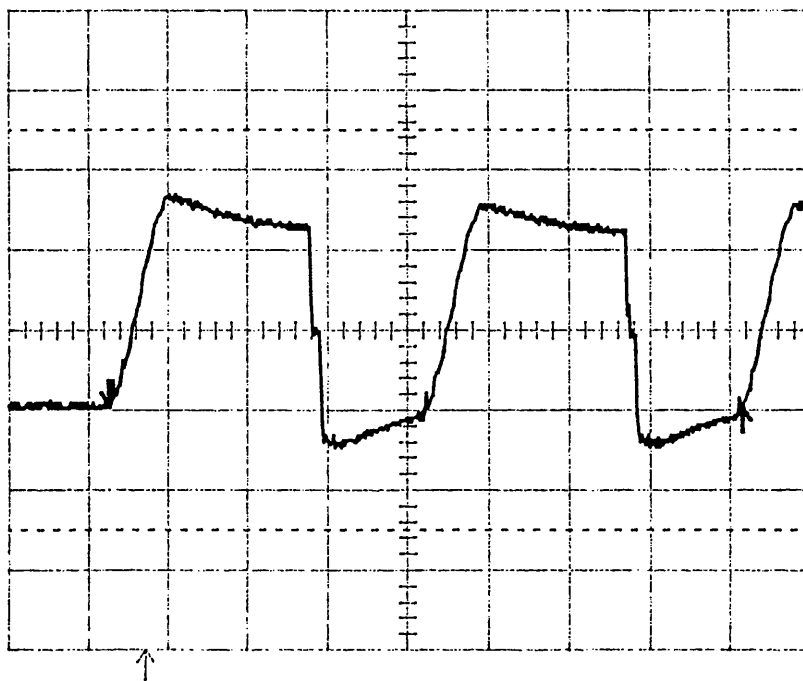
$R_T = 0.8 \Omega$
50 % tap-setting
 $C_c = 10 \text{ nF}$
1:1:8 @ 160 mb
3.125 kHz
Flow-shaping installed

Channel 1
11.45 kV

Ch 1 5 V_{1k}
T/div .1 ms Ch 2 5 V₁₀
Trig .60 div - CHAN 1 =

FIGURE 4.41 PFN VOLTAGE AT 3.125 kHz

Main
Menu



$R_T = 0.8 \Omega$
50 % tap-setting
 $C_c = 10 \text{ nF}$
1:1:8 @ 160 mb
5.2 kHz
Flow-shaping installed

Channel 1
-.16 kV

$\Delta t 395 \mu\text{s}$

f 2.531 kilz

Ch 1 5 V_{1k}
T/div 50 μs Ch 2 5 V₁₀
Trig .60 div - CHAN 1 =

FIGURE 4.42 PFN VOLTAGE AT 5.2 kHz

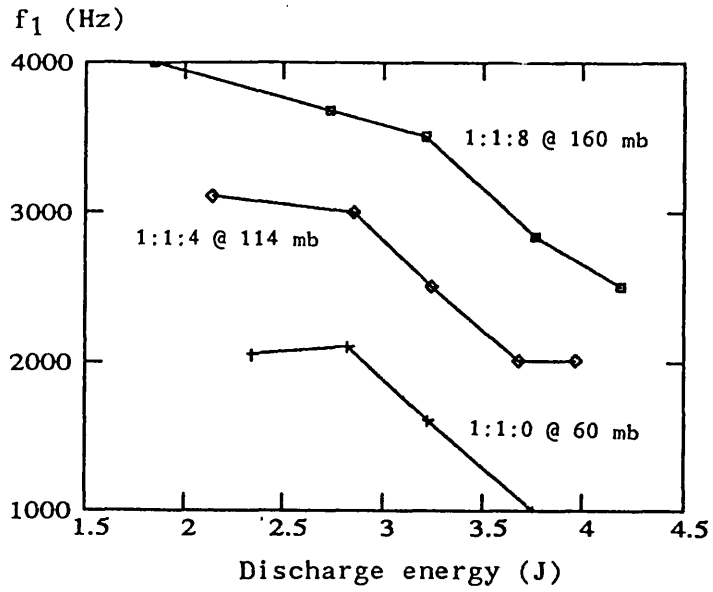


FIGURE 4.43 f_1 VS DISCHARGE ENERGY - $\tau = 10 \mu s$

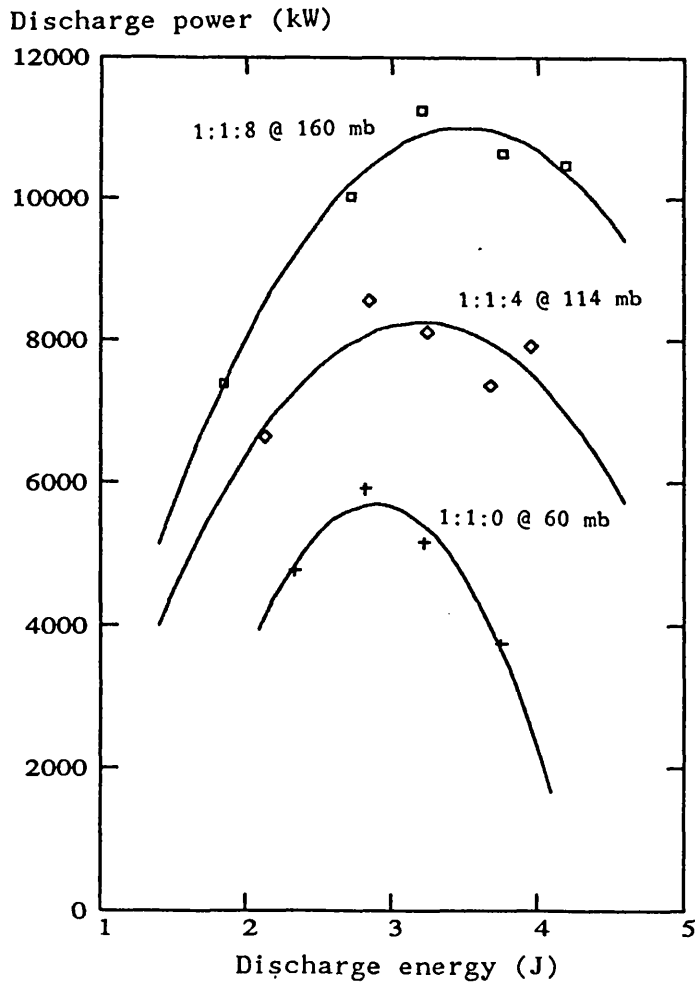


FIGURE 4.44 DISCHARGE POWER VS DISCHARGE ENERGY - $\tau = 10 \mu s$

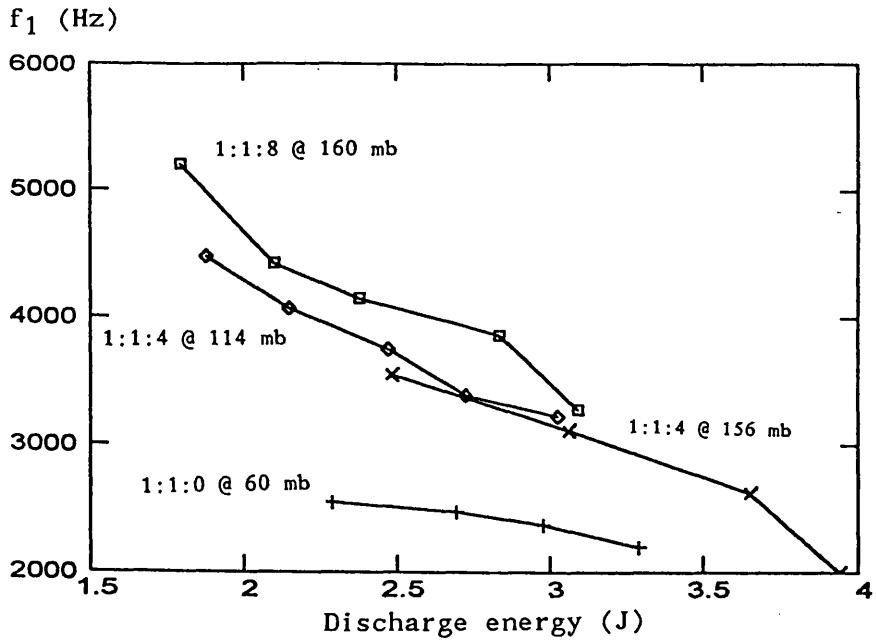


FIGURE 4.45 f_1 VS DISCHARGE ENERGY - $\tau = 7 \mu s$

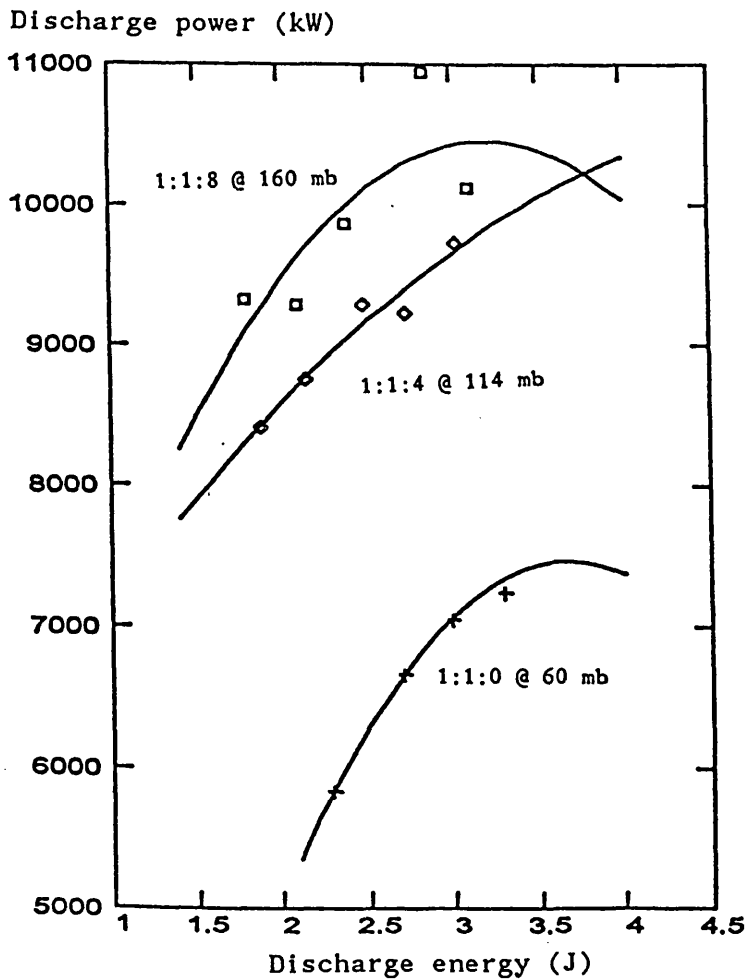


FIGURE 4.46 DISCHARGE POWER VS DISCHARGE ENERGY - $\tau = 7 \mu s$

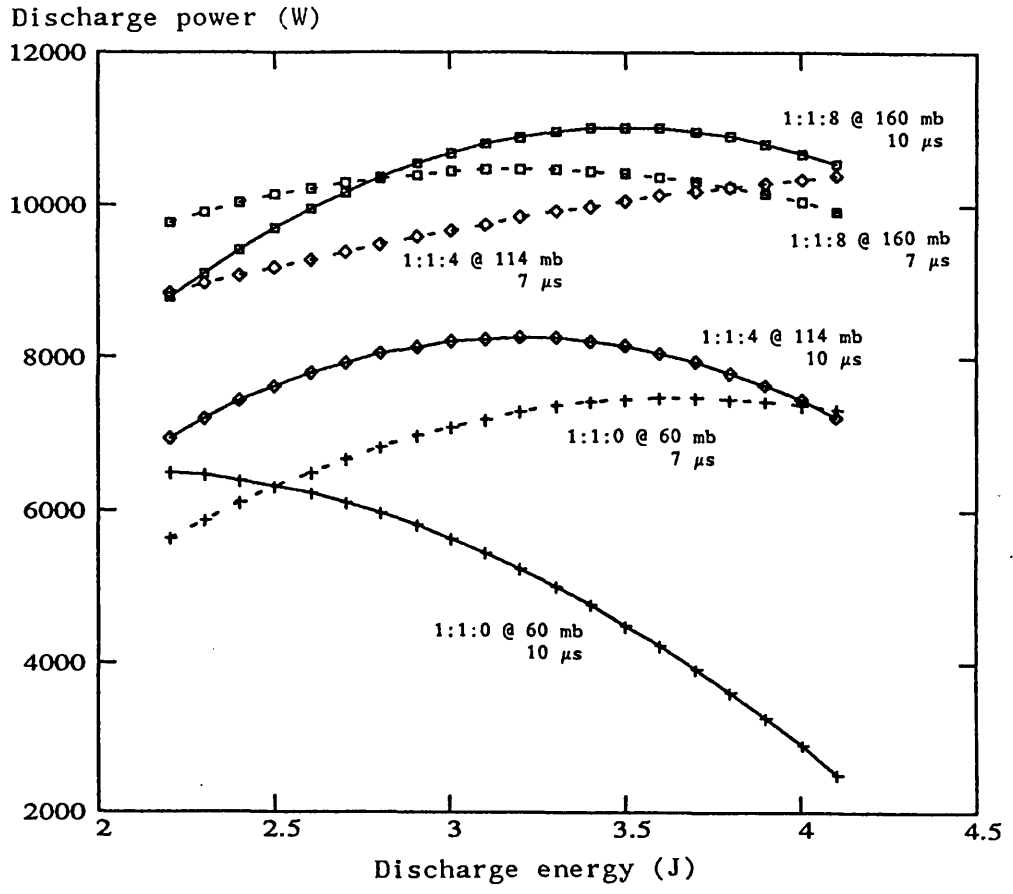


FIGURE 4.47 BEST FIT CURVES FOR 8 Ω BALLASTED ELECTRODE
DISCHARGE POWER VS DISCHARGE ENERGY

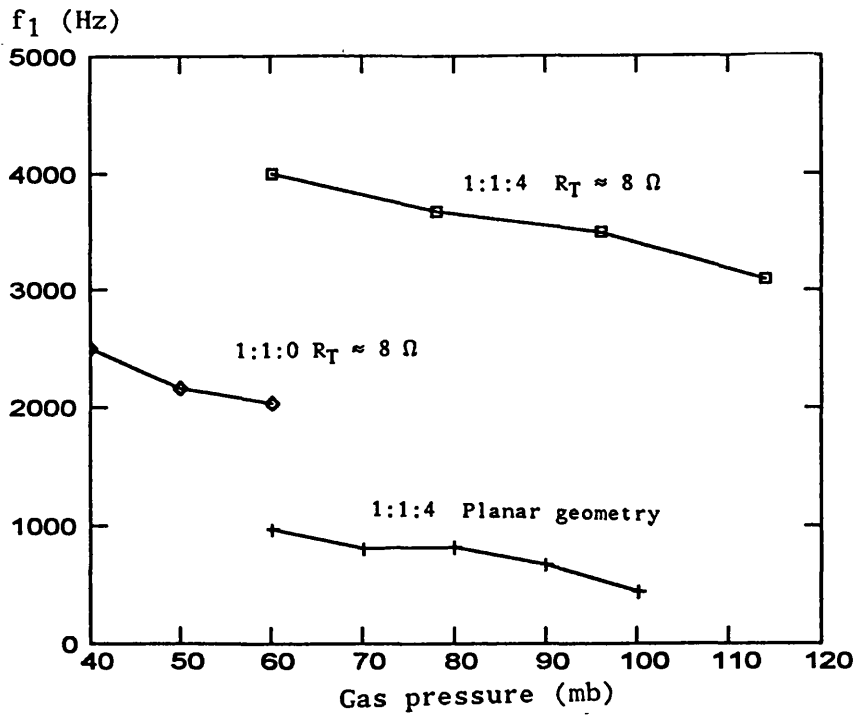


FIGURE 4.48 f_1 VS TOTAL GAS PRESSURE

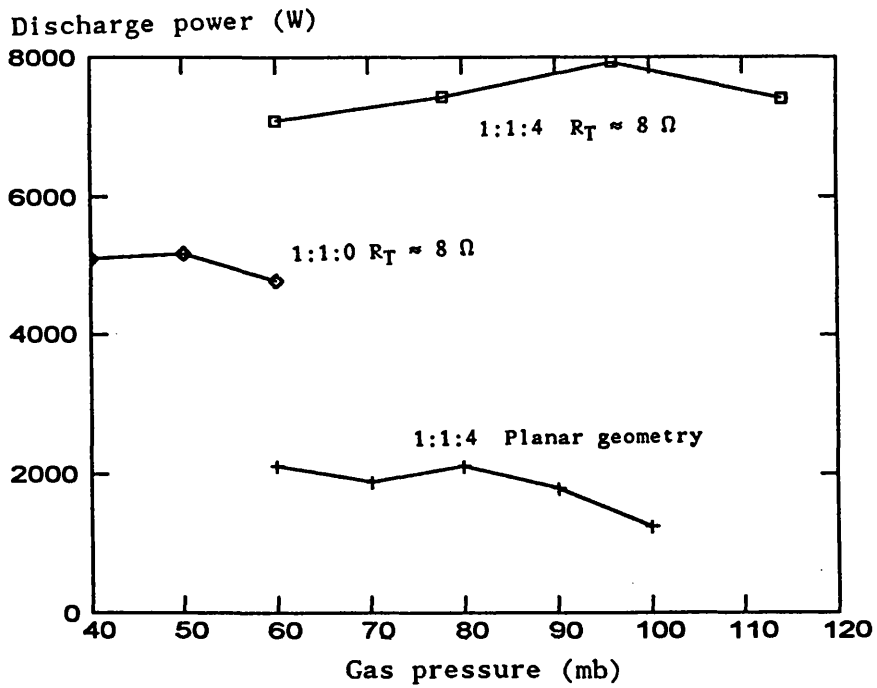


FIGURE 4.49 DISCHARGE POWER VS TOTAL GAS PRESSURE

CHAPTER FIVE

LASER OUTPUT CHARACTERISTICS

INTRODUCTION

Bakewell [5.1] found the theoretical characteristics of a laser pulse in order to achieve the non-conduction limited material interaction processes. It was calculated that with laser pulse lengths of about 10 μ s duration and an operating frequency of 10 kHz, the temperature of the workpiece remained approximately constant during the inter-pulse period. Moreover, the plasma formed above the workpiece during the interaction process would decay between pulses. Consequently, energy from the laser beam is delivered into the workpiece and not the plasma. Thus, the coupling between the laser and the workpiece material increases. In contrast, the mechanism of CW laser processing relies upon the formation of the plasma to help in the conduction of energy to the workpiece.

In order to measure the laser output power three monitoring devices were available namely: a cone calorimeter, a photon drag monitor (PDM) and a cadmium-mercury-telluride (CMT) detector. The simplest detection system to utilise and the most frequently used was the photon drag monitor. Section 5.1 discusses these systems in more detail.

After performing a series of experiments characterising the performance of the discharge – see Chapter 4 – the single pass resonator was installed and the first laser output power measured; the results are reported in Section 5.2. It was found that the laser output pulse energy was comparable with that which was reported by Kharha [5.2] only if the laser output was scaled, with the assumption that all of the possible laser energy could be extracted from the discharge. However in practice, the power was below the levels necessary to achieve the non-conduction limited material interaction processes. As a result of these experiments considerable effort was directed towards increasing the laser output power by, for example, increasing the number of passes of the resonator through the discharge volume whilst still maintaining a stable resonator configuration.

In order to optimise the stable resonator design a program was written to assess the propagation of the TEM_{00} and the TEM_{01} mode of the resonator and calculate the approximate diffraction losses – see Section 5.4.

Lastly, unstable resonators and recent developments are briefly described.

5.1 DETECTION AND MONITORING SYSTEMS

It is useful at this stage to define a fundamental property of the laser – the electrical to optical conversion efficiency. If the laser output pulse energy is denoted by E_o and the energy deposited into the discharge for a single pulse by E_d , then the electrical to optical conversion efficiency is given by

$$\eta = \frac{E_o}{E_d} \quad 5.1$$

Chatwin [5.3] developed a theoretical code to simulate the laser output pulse and found it useful to define certain pulse characteristics; these are shown in Appendix D1. However, because of the experimental uncertainty in determining the laser characteristics, it was deemed at this stage not worthwhile to record them for the laser pulse when the laser output was assessed. For example, the laser output efficiencies were defined by Chatwin for a 10 μ s and 20 μ s period, whereas in practice, to measure E_o over these time scales requires a long time base on the oscilloscope; this results in a reduction in the resolution of the shape of the pulse. Moreover, the contribution to E_o over the longer time base is smaller than the statistical error associated with a series of readings – this is particularly true for mixtures with a low N_2 concentration. The laser efficiency, unless otherwise stated, was calculated by using equation 5.1, where E_o and E_d were measured using the data acquisition and analysis system which is described in Appendix A6. The time over which the efficiency is found by the oscilloscope is dependent on the position of the trigger, the time base of the oscilloscope and the delay time of the laser output pulse. In practice, a value of between 8 μ s and 15 μ s was obtained. This range is mainly due to the difference in the laser output pulse lengths for different discharge energies and resonator configurations.

Three devices were available for detecting the laser output energy, these were: the cone calorimeter, a photon drag monitor and a cadmium–mercury–telluride (CMT) detector. Each detector has its own particular advantages and disadvantages. The methods used to monitor the laser output energy are briefly described.

5.1.1 Cone Calorimeter

The cone calorimeter provides a measure of the mean laser output power. It was reported in Chapter 2 that the cone calorimeter was positioned under a mirror placed at an angle of 45° to the plane of the laser beam. The mirror could be either up or down. If the mirror is down, the laser beam is directed into the cone calorimeter and if it is up, the laser beam passes towards the focusing optics and

the workpiece translation stage. The principal disadvantage of the cone calorimeter is that whilst it is being used the laser cannot be used for material processing applications.

The method of operation is simple: water flows over the cone at a rate \dot{m} , then if the inlet and outlet water temperatures (T_i and T_o respectively) are monitored and the mean specific heat capacity of the water \bar{c} is known, the mean power can be calculated from

$$P_o = \dot{m} \bar{c} \Delta T \quad 5.2$$

Where ΔT is the temperature difference: $T_o - T_i$. Although this technique was used satisfactorily on several occasions it was found that the period before thermal equilibrium was established was quite long - the order of five to ten minutes - and the error of this simple approximation was about 5 - 15 %. It should be noted that this response time can be reduced by decreasing the water flow rate or increasing the laser output power. No efforts were made to improve the accuracy of the calculation by, for example, incorporating the effects of: heat losses, the non-ideal reflection coefficient of the cone at 10.6 μm and/or the effects of misalignment. The major reason for this was because the other detecting systems had the ability to temporally resolve the laser output pulse; consequently, the pulse energy could be determined and if the frequency is known, the mean power can be found accurately and quickly.

5.1.2 Photon Drag Monitor (PDM)

The photon drag monitor has a response time of ≈ 2 ns and is capable of resolving the temporal characteristics of the laser output pulse. Generally PDM's do not require calibration and are easy to use - the detector is simply placed into the beam path. The monitor that was used absorbed approximately 25 % of the incident power from the beam, consequently, the energy left for the material interaction processing trials is slightly diminished. However, this detection method was the one most frequently used to determine the laser output pulse energy and, from knowledge of the laser frequency, the mean laser output power can be found.

The detecting element of the photon drag monitor is p type germanium [5.4]. The monitor has a responsivity $R_p = 6$ mV/kW. The noise level was approximately 1 mV; this corresponds to a minimum detectable pulse power of 600 W. The full

specification of the monitor can be seen in Appendix D2.

The photon drag monitor was secured in a mount and could be moved in the transverse direction via two micrometers. It was found that it was necessary to electrically isolate the monitor from the fore-optics table, otherwise erroneous readings were observed in the laser output energy. This was due to noise picked up by the monitor during the discharge thyatron switching period. The useful diameter of the monitor was 25 mm; if the beam diameter is greater than this the beam would be clipped, resulting in a lower measurement for the value of E_O . In order to reduce beam clipping for large beam diameters, an aluminium bracket could be mounted prior to the monitor, on which could be positioned a series of lenses to focus or, if necessary, expand the diameter of the beam. The latter technique of using a beam expanding telescope to widen the size of the laser beam, is used so that the beam can be focused to a smaller spot size at the workpiece.

When the laser output energy was first measured the values seemed very low when they were compared to the theoretical predictions and experimental results from the prototype laser [5.2,5.3]. So, in order to test the validity of the measurement of E_O while using the PDM, it was decided to compare the value of E_O with the results from the cone calorimeter detection method. This would indicate satisfactory performance of the PDM and that the correct responsivity was being used.

As a specific example, the mean laser output power was measured using the PDM and the cone calorimeter with a water flow rate of 50 cm³/min. A 1:1:4 laser gas mixture at a total pressure of 156 mb was used, the transformer tap settings were at 60% and the frequency of the laser was 887 Hz. A three pass resonator was installed with the front mirror reflectivity $r_f = 75\%$. The outlet temperature was noted every 30 seconds, Figure 5.1 shows the graph of T_O against time. After 6 minutes from turning the laser on, it was found that the outlet water temperature remained constant; after 8 minutes the laser was turned off and T_O was monitored for a further 15 minutes. The transition regions of where the laser is turned on, thermal equilibrium is established and the laser turned off are clearly seen in the figure. However, the temperature rise of the water is very small, only 4.2 ± 0.1 °C. The specific heat capacity of water over this temperature range is $4.18 \text{ J g}^{-1} \text{ K}^{-1}$ and has a deviation of less than 0.2 % [5.5]. From equation 5.2, the mean power is calculated to be only 14.6 W; at 887 Hz the average laser output pulse energy is 16.46 mJ. The discharge energy E_d was measured as $3.885 \pm 0.70 \text{ J}$, where the error is the standard error of the mean (SEM) for a sample size of 10. It is seen that the electrical to optical conversion efficiency $\eta = 0.42\%$. It is

apparent that this electrical to optical conversion efficiency is very low for CO₂ lasers. For example, Hidekazu et al [5.6] report, for a TEA laser, efficiencies of 7.5 %.

The laser output pulse energy E_0 was measured with the PDM and found to be 17.5 mJ. With the laser operating at a frequency of 887 Hz the mean power is calculated to be 15.50 W. Considering that no corrections were applied to the simple cone calorimeter detection system, it is apparent that the values for the mean pulse energy and mean laser output power from these two techniques compare favourably; the difference between the two methods is only 5.8 %. This placed confidence in the readings that were taken with the PDM. If the effect of the corrections were taken into account the corrected power would increase and be closer to the value obtained from the PDM.

5.1.3 Cadmium - Mercury - Telluride (CMT) Detector

The third option available to measure the laser output power is the CMT detector, which requires only a small fraction of the laser beam to obtain a reading, and for this reason is ideal for using whilst performing interaction studies between the beam and the workpiece. However, to implement this detection system is considerably more complex than the photon drag. The damage threshold for CMT detectors is 1 W cm^{-2} , so it is necessary that the beam is attenuated sufficiently to avoid irreparable damage occurring to the detector. Sections 5.1.4 and 5.1.5 detail methods of attenuating the laser beam to levels suitable for the CMT detector. Appendix D2 details the characteristics of the CMT detector.

5.1.4 Beam Sampling Wedge

For CO₂ lasers it is common practice to use an AR/AR coated ZnSe wedge to divert a small fraction of the incident beam towards the detector. An advantage of using a wedge is that the reflections off of the front and rear face are spatially separated, however, the transmitted beam is slightly deviated.

Figure 5.2 shows the reflection coefficient both parallel and perpendicular to the plane of incidence (denoted by R_s and R_p respectively), as a function of the angle of incidence α_1 for an AR/AR coated ZnSe wedge. These values were obtained from the Original Equipment Manufacturer [5.7]. It is seen that the minimum reflection coefficient is about 0.1 % of the incident power and occurs at $\alpha_1 \approx$

25°; however, it should be noted that to obtain this minimum value for the reflection coefficient requires a high degree of accuracy in the alignment of the wedge and the incident beam. During the analysis of the detection system, it was realised that a novel detection system could be employed by using an uncoated wedge that had the rear face positioned such that the angle of incidence was equal to the Brewster angle. Because the wedge has a small angle, the incident ray on the front face is slightly deviated from the Brewster angle and this results in partial reflection from the front face. The technique is used for linearly polarised light and is fully described in Appendix D3.

A simple example will illustrate that using an AR/AR coated ZnSe wedge does not solve all of the problems for attenuating the beam sufficiently for the CMT detector. If the total beam power is 5 kW and the beam is 10 mm in diameter, then it is apparent that the minimum intensity of the reflected beam is approximately 1.6 W cm^{-2} . This is too high for directing into the CMT detector, and the beam must be further attenuated. Furthermore, if additional beam attenuation techniques are used then this allows greater tolerance in selecting the angle of incidence α_1 . This is important because the deviation of the light through a wedge is dependent upon the value of α_1 . Because of the importance of ensuring that the beam is satisfactorily attenuated some of the methods that are used in practice are briefly discussed in Section 5.1.5.

For a wedge angle of 1°, the deviation of the beam is less than 2.5° for an incident angle of up to 45°, and the displacement of the beam through the wedge is less than 0.5 mm. In the present case, the distance from the wedge to the focusing optic is approximately 0.75 m; consequently, the expected deviation of the beam is less than 4 mm. However, this misalignment is tolerable since the 45° mirror can be used to redirect the beam through the focusing lens. In practice, the interaction studies that were performed were undertaken without the wedge in position as the PDM was generally used.

5.1.5 Beam Attenuators

Some examples of the techniques available to attenuate the beam are shown below, however, only convex reflective surfaces are discussed in detail as this was the method that was used in the CMT detection system:

- 1) Partially reflective surfaces
- 2) Convex reflective surfaces: ball bearing, convex mirrors
- 3) Diffraction techniques: circular pin holes, rectangular slits
- 5) Holographic beam samplers [5.8]

Brief mention is given to partially reflective surfaces and the relatively new technique of holographic beam samplers. Partially reflective surfaces are cumbersome if large attenuation of the beam is required because the only control over the level of attenuation is the number of surfaces – this makes alignment more difficult and the system more expensive. The major advantages of holographic beam samplers are that no deviation of the beam occurs as the sampler is positioned normally to the incident beam, and the beam attenuation is large enough such that other optical components are not needed.

Convex reflective surfaces – for example ball bearings – are ideal attenuators as they are relatively inexpensive. Provided that their diameter is small in comparison to the radius of curvature of the phase front of the laser beam, they will diverge the beam to a greater extent than the natural divergence of the laser. This increased divergence will mean that the intensity will rapidly decrease as the distance is increased away from the ball bearing. This provides a simple method of obtaining any required attenuation by placing the detector a specified distance from the convex reflective surface. However, if the ball bearing is inserted into the path of the main beam, it is obvious that the laser will not be able to be used for material processing applications. For this reason, a partially reflective surface – for example a wedge – can be used to divert a small fraction of the laser beam towards the ball bearing, where the radiation is then scattered over a wide area. This decreases the intensity to a value suitable for safe operation of the CMT detector and enables compact detection systems. This technique was adopted in practice; Figure 5.3 shows a schematic of the CMT detection system. With the laser running, the CMT detector was placed a considerable distance from the centre of the ball bearing and gradually moved towards the ball bearing until a suitable laser output was observed on the oscilloscope. The major disadvantage of the CMT detector is that it requires calibration against a known source. However, it was found possible to calibrate the CMT detector from knowledge of the laser output obtained from the PDM. A further disadvantage is that CMT detectors require cooling to liquid N₂ temperatures in order to increase the signal to noise ratio.

5.2 LASER OUTPUT CHARACTERISTICS: PLANE ELECTRODE GEOMETRY

For the preliminary experiments examining the laser output power the 3 pass resonator was first installed into the laser cavity. The design and alignment procedure for this resonator are discussed in Chapter 2. It should be noted that the alignment of the front output window and the rear mirror are optimised via

micrometers, and the position of the fold mirrors are fixed. No laser output was detected. It was felt that this could be due to unsatisfactory alignment of the fold mirrors. Consequently, the three pass resonator was replaced with a single pass; for this resonator the alignment of both optics, i.e. the front window and rear mirror, can be optimised, externally from the laser cavity with micrometers. Hence, the alignment was much simpler than it was for the 3 pass resonator. Laser output was successfully obtained – the results are reported in Section 5.2.1. It was found that the laser output was substantially lower than that expected from consideration to the theoretical [5.2,5.3] and experimental work [5.2]. In order to increase the laser output power the number of passes were increased to 3, and a series of experiments were performed to investigate the affect of the water cooled aperture on the laser output power, see Section 5.2.3. The number of passes were further increased to 5 – this required a different resonator design – the resonator design and the laser output results are discussed in Sections 5.2.4 and 5.2.5. The laser output power for the 0.8 Ω ballasted electrode was assessed, see Section 5.3.

It should be noted at this stage that the laser output reported in this chapter was obtained whilst the discharge thyatron was located in the pulser cage with the inductance on the discharge thyatron $L_a = 36 \mu\text{H}$. A schematic of the electrical circuit can be seen in Chapter 3, Figure 3.6. The coupling capacitance was 10 nF and the discharge gap was 40 mm. In general, the laser output was assessed as a function of the discharge energy with the laser operating at ≈ 100 Hz.

5.2.1 Single Pass Resonator

In order to examine the laser output for the single pass resonator a 1:1:4 gas mixture at a pressure of 156 mb was selected. The front window reflectivity $r_f = 75 \%$, and the rear mirror radius of curvature $R_c = 20$ m. The laser output power was measured with the photon drag monitor which was inserted directly into the beam path; the beam dump mirror was down. The laser output energy E_o was determined as a function of the tapsettings which were varied from 60 % to 75 % – the corresponding change in the discharge energy E_d was from 4.09 J to 6.02 J. The laser output pulse energy with the transformer tapsettings at 60 % can be seen in Figure 5.4; E_o was found to be only 14.3 mJ. Table 5.1 summarises the experimental results. It is clearly seen that the electrical to optical conversion efficiency, denoted by η_{1a} (the subscript 1 refers to the number of passes for the resonator and "a" indicates that the water cooled aperture is in position) is much less than 1 % in all cases. Values of about 6 % were reported by Kharha [5.2]. E_s is the specific discharge energy density, i.e. the discharge energy E_d divided by

the discharge volume and the gas pressure expressed in torr (denoted by τ in the tables).

Table 5.1 Laser output characteristics for a 1:1:4 gas mixture at 156 mb. Single Pass Resonator - with aperture

Tap settings %	E_s $\mu\text{Jcc}^{-1}\tau^{-1}$	E_D J	E_o mJ	η_{1a} %
60	17.34	4.09	14.3	0.35
65	19.96	4.71	16.1	0.34
70	23.31	5.50	18.6	0.33
75	25.51	6.02	32.0	0.53
Reflectivity of the front window $r_f = 75.0\%$ Back mirror radius of curvature $R_c = 20.0\text{ m}$ (Output window radius of curvature is infinite) Total discharge volume $V = 2016\text{ cm}^3$ Cavity length $L = 1.62\text{ m}$ Beam waist radius (TEM ₀₀) $w_o = 4.3\text{ mm}$ Beam radius on rear mirror " " $w(L) = 4.5\text{ mm}$ Pumping pulse length $\tau_p = 10\ \mu\text{s}$ System frequency $f = 100\text{ Hz}$ Water cooling Aperture in position Diameter $D = 20\text{ mm}$				

It is well known that the power available from lasers and their efficiency increases in proportion to the specific energy density of the pumping medium [5.2], this was the main reason for the development of the TEA laser [5.9]. The laser output power from CO₂ discharge lasers is only limited by the maximum energy loading of the discharge, which is in itself, limited by the development of the glow to arc transition. In the present case, the values of E_s are much lower than, for example, TEA lasers, where energy depositions in excess of 200 J/litre/atm have been reported [5.6]; thus, for TEA lasers $E_s \approx 263\ \mu\text{Jcc}^{-1}\tau^{-1}$. However, Kharha [5.2] reports observing efficiencies of approximately 6 % with similarly low specific energy densities as were used in the present case and with a single pass resonator.

The total mode volume, V_T , can be defined as that volume which the beam occupies between the optics of the resonator. This can be split into two regions: the active mode volume V_a and the dead space region V_{ds} , where V_a is that part of the mode volume which coincides with the discharge volume, and V_{ds} is the remainder. V_T is given by

$$V_T = V_a + V_{ds}$$

5.3

Figure 5.5 shows a schematic of the positions of V_a and V_{ds} for a single pass resonator – it is seen that the active mode volume only occupies a small fraction of the discharge volume. Obviously, V_T increases with the number of passes, moreover, the total gain of the laser increases as it is proportional to the cavity length L .

It is unclear if the efficiencies calculated by Kharha were from a direct measure of the ratio of the output to input energies or if they were calculated with the assumption that the modal coupling efficiency was 100 %. This would require scaling the output energy from an assumed mode volume to that expected if all of the available power could be extracted from the resonator; the efficiency calculated in this manner is denoted by η_T . In the present case, as $R_c = 20$ m it is apparent that the beam waist is large and the divergence of the laser beam is small. Hence, it is satisfactory to calculate V_a assuming that the active mode volume is a cylinder with a radius equal to the average of the beam radius on the front window and rear mirror. If the laser is operating in the TEM_{00} mode then the active mode volume is $V_{00} \approx 51$ cm³, consequently, the output energy density for the 75 % tapsetting is about 0.624 mJ cm³. The total output energy if the modal coupling efficiency was 100 % would be 1.26 J, giving $\eta_T \approx 21$ %. This value is in excess of the values that were estimated by Kharha [5.2] and Chatwin [5.3].

Several assumptions are implicit with this simple calculation of η_T . It is apparent that the values of the output energy per unit volume are sensitive to the estimated value of V_a . It was assumed that the resonator was operating in the TEM_{00} mode. Although no beam profiles were examined in detail, a perspex burn print of the beam diameter suggested that the laser was operating in a higher order mode – the beam diameter was about 15 mm. The TEM_{01} mode has a diameter given by $w(z)/\beta$ [5.10], where $z = 0$ at the beam waist, i.e. the output window, and $z = L$ at the rear mirror. In this case, the expected size of the beam at the perspex is given by $w(2.35)/\beta = 8.09 \times 10^{-3}$ m; the diameter is about 16 mm which is close to the measured value. Consequently, the laser will be operating in the TEM_{00} and TEM_{01} mode. To the first order, it is found that the active mode volume with the laser running in both modes is $V_{01} \approx 169$ cm³, and for this case the expected laser output energy for 100 % modal coupling efficiency is 0.169 J, giving an efficiency of $\eta_T = 6.3$ %. The magnitude of the scaled output pulses are of the same order as the values that were reported by Kharha. In order to approach the values of E_0 to ensure that the non-conduction limited processes

occur at the workpiece, it is apparent that the laser output power must be increased. The simplest technique to achieve this is to increase the number of passes of the resonator through the discharge region.

The codes that were developed [5.2,5.3,5.12,5.13] to simulate the laser output pulse give the output power per unit volume in units of W cm^{-3} . In order to quantify the theoretical results and obtain a measure for the theoretical laser output, it is necessary to multiply the laser output power distribution by V_a , where $V_a \approx V_{00}$ or $V_a \approx V_{01}$, depending upon the operating mode of the laser. For the examples given, the experimental mean output power density, denoted by $P_{e\rho}$, is given by

$$P_{e\rho} = \frac{E_o}{V_a \tau_\rho} \quad 5.4$$

Where τ_ρ is the time over which the laser output is detected. It was found that $\tau_\rho \approx 5 \mu\text{s}$ for the experimental conditions reported in Table 5.1 and with the tapsettings at 75 %. If it is assumed that the TEM_{00} mode is propagating it is seen that $P_{e\rho} \approx 126 \text{ W cm}^{-3}$, and for the larger mode volume of 169 cm^3 where both modes are oscillating: $P_{e\rho} \approx 38 \text{ W cm}^{-3}$. This is a large variation and introduces substantial uncertainty into the predicted laser output power because the value of V_a is difficult to determine.

In an effort to increase the modal coupling efficiencies and the laser output energy, the number of passes for the resonator was increased to 3, i.e. the so called "Z resonator" was installed. The effect of using longer resonator lengths has the added advantage of improving the output pulse shape by suppressing the gain switched spike, so it is more suitable for laser material processing applications [5.3].

5.2.2 Three Pass Resonator: With the Aperture

In order to compare the values of E_o with the values that were obtained whilst using the single pass resonator, the same gas mixture and pressure were used. The optical components for the front and rear mirror were identical – but the resonator length was now 4.10 m – see Chapter 2 for a description of the 3 pass resonator. Table 5.2 shows the experimental results. The last column shows the ratio of the laser output efficiencies for the three and single pass resonator geometries. This is given because it gives an indication of the approximate

performance of the two systems. However, it must be noted that when the ratios of the efficiencies are given there is usually a small discrepancy in the value of E_d (≈ 0.2 J) for the two resonator geometries, but the error introduced into the ratio is typically less than 5 %.

Table 5.2 Laser output characteristics for a 1:1:4 gas mixture at 156 mb. Z resonator - with aperture

Tap settings %	E_S $\mu\text{Jcc}^{-1}\tau^{-1}$	E_D J	E_O mJ	η_{3a} %	η_{3a}/η_{1a} %
60	17.67	4.17	21.0	0.51	1.46
65	20.26	4.78	32.6	0.68	2.00
70	22.89	5.40	41.0	0.76	2.30
75	25.69	6.06	43.1	0.71	1.34
$r_f = 75\% : R_c = 20 \text{ m} : L = 4.1 \text{ m} : \tau_p = 10 \mu\text{s}$					

It is clear that the overall efficiency has increased, i.e. $\eta_{3a} > \eta_{1a}$. But, on a mode for mode basis for the different resonators, the increase is not directly proportional to the increase in the total modal coupling efficiency; which has increased by about a factor of 3, whereas the maximum observed increase was only a factor of 2.3 – moreover, the average percentage increase was only 75 %. If the mode volume is calculated assuming that only the TEM_{00} mode is propagating then $\eta_T = 5.9\%$. However, if it assumed that both the TEM_{00} and the TEM_{01} modes are propagating then $\eta_T = 2.0 \%$.

At this stage, the mode shape was assessed by examining the effect of irradiating a 10 mm thick sheet of perspex with the laser beam. However, the determination of the beam diameter from the perspex burn print is difficult in practice. This is mainly due to lateral diffusion of heat away from the beam, which tends to make a larger beam print than is the actual beam diameter. It was found that the burn print was slightly elliptical; the major and minor axis were approximately 14 mm and 12 mm respectively. The theoretical beam diameters of the TEM_{00} and TEM_{01} modes are ≈ 11 mm and ≈ 19 mm respectively. It is probable that the TEM_{01} mode is not propagating within the resonator. This accounts for the reason why η_T was low if the active mode volume was taken as V_{01} – i.e. V_{01} overestimates the active mode volume for the 3 pass resonator.

The beam eccentricity could not be corrected by tweaking the front window or the rear mirror. So, it was concluded that the resonator alignment must have been slightly off axis due to the misalignment of the fold mirrors. Later experiments with a single pass resonator, indicated that it was possible to obtain an elliptical

output beam profile by deliberately offsetting the rear mirror from the position of ideal alignment.

Figure 5.6 shows the values of η_T as a function of the specific energy density of the pumping medium for the 1 and 3 pass resonators, and with a 1:1:4 gas mixture at 156 mb. The values of η_T were calculated assuming the active mode volume was equal to V_{00} and/or V_{01} . On the same graph can be seen the theoretical and experimental laser output efficiencies for a 1:1:4 gas mixture at the slightly higher (2.5 %) gas pressure of 160 mb; this data was abstracted from the results of Kharha [5.2]. It should be noted that in the present case, the front mirror reflectivity $r_f = 75\%$, and for the abstracted data, $r_f = 90\%$. It can be seen that, in general, there is approximate agreement between the two experimental data sets. Scaling the laser output efficiency for the single pass resonator gives efficiencies close to the theoretical if the active mode volume is calculated assuming propagation of the TEM_{00} and TEM_{01} modes. Measurement of the laser output beam diameter tended to support the view that both modes existed. For the three pass resonator, the experimental values agree moderately well if the active mode volume is calculated assuming that only the TEM_{00} mode is propagating. Again, the perspex burn prints supported this view. Figure 5.6 also shows the scaled laser output efficiency for the 3 pass resonator, assuming that the active mode volume is obtained from both modes oscillating. It can be seen that this calculation of the efficiency is much less than the other values.

It has been shown that if the correct mode volume is assumed, the laser efficiencies in the present case are consistent with the values that were reported by Kharha. However, it is evident that the actual value of the laser output energy is low; this is primarily as a result of the poor coupling between the resonator and the discharge volume.

The laser output was measured for the same resonator configuration as described above but for a 1:1:0 gas mixture at a total pressure of 60 mb. Table 5.3 shows the experimental results. The resonator was left unchanged.

Table 5.3 Laser output characteristics for a 1:1:0 gas mixture at 60 mb. Z resonator - with aperture

Tap settings %	E_S $\mu\text{Jcc}^{-1}\tau^{-1}$	E_D J	E_O mJ	η_3 %
60	44.19	4.01	25.8	0.64
65	51.57	4.68	34.3	0.73
70	57.08	5.18	37.8	0.73
75	63.70	5.78	40.4	0.70
$r_f = 75\% : R_C = 20 \text{ m} : L = 4.1 \text{ m} : \tau_p = 10 \mu\text{s}$				

Figure 5.7 shows the laser output pulse with the tapsettings at 75 %. It is seen that the pulse has a long plateau and the plateau power is $\approx 6 \text{ kW}$. This is considerably below the necessary values to obtain the non-conduction limited material interaction processes.

If the values from Tables 5.2 and 5.3 are compared, it is seen that there is a small increase in E_O for the 1:1:0 gas mixture. This was attributed to the fact that slightly higher partial pressures of CO_2 and N_2 exist within this mixture.

5.2.3 Three Pass Resonator: Without the Aperture

In order to examine the affect of the water cooled aperture on the laser output, the aperture was removed from the resonator and exactly the same exeperimental conditions were used as those that are reported for Table 5.3. The alignment of the fold and rear mirrors was not changed. It should be noted that the effective diameter of the front window is only 25 mm. This is due to the aperturing effect of the window support - see Figure 2.21 in Chapter 2 - consequently, there still is aperturing of the output laser beam even when the water cooled aperture is not in position. The water cooled aperture has a diameter of 20 mm.

Table 5.4 Laser output characteristics for a 1:1:0 gas mixture at 60 mb. Z resonator - no aperture.

Tap settings %	E_S $\mu\text{Jcc}^{-1}\tau^{-1}$	E_D J	E_O mJ	η_3	η_3/η_{3a}
60	43.97	3.99	28.8	0.72	1.12
65	51.02	4.63	34.4	0.75	1.02
70	57.86	5.25	42.0	0.80	1.097
75	64.69	5.87	50.8	0.87	1.24
$r_f = 75\% : R_C = 20 \text{ m} : L = 4.1 \text{ m} : \tau_p = 10 \mu\text{s}$					

It is seen that the average percentage increase in the value of E_0 when the aperture is removed is approximately 12 %. The standard error of the mean for the values of E_d and E_0 were typically less than 0.5 % and 1.4 % respectively (sample size 10). It is seen that this increase is significant.

5.2.4 Five Pass Resonator: 10 μ s Pulse Length

In an attempt to increase the value of E_0 still further, the number of passes of the resonator through the discharge volume was increased to 5. This necessitated a redesign of the optical mounts for the resonator. As the discharge width is 60 mm severe constraints are placed on the maximum diameter of the optics as the number of passes is increased. Moreover, the effect of using mirrors with a smaller diameter is to increase the diffraction losses; therefore, severe constraints are placed on the minimum size of the optics – see Section 5.4. An optimum mirror diameter will exist for any given resonator configuration.

It is apparent that for a resonator configuration with a number of passes n_p , the number of optics required is $n_p + 1$. Consequently, for five passes 6 optics are required: 3 are positioned at each end of the laser cavity. In the present case, where the discharge width is 60 mm, the maximum diameter of the mirrors that can fit within this space is 20 mm. However, if the optics are staggered then larger diameter mirrors can be used. Figure 5.8 shows a schematic of the fold mirror mounts and Plates 7 and 8 show how the mirrors located at the rear and front of the cavity were mounted. The front window and rear mirror mountings that were used for the 3 pass resonator were employed.

The fold mirror mounts were designed in order to reduce some of the problems in lining up the resonator that were experienced with the 3 pass resonator. The mirrors were mounted into 25 mm diameter blind holes that were partly bored through the side of the 20 mm diameter aluminum rod, they were held in position by a grub screw, see Figure 5.8. Water cooling channels ran behind the optic to facilitate cooling of the optics. A 6 mm clearance hole was bored through the centre along the entire length of the rod. The mirror mounts were mounted onto a sheet of aluminium that had two slots milled through it; this was the resonator table top. The advantage of this was that the resonator could be removed from the cavity without affecting its alignment. A 6 mm bolt was passed through the centre of the aluminium rod and through the slot on the resonator table top. The 6 mm bolt protruded through the table top; T-nuts were used to secure the mirror mounts to the table top. The height of the mirror was determined by its

position along the length of the aluminium rod; the rod could be rotated so that the resonator was easily aligned. Various thicknesses of washers were fabricated and were used as shims to optimise the height of the fold mirrors. Once in position the bolt was tightened and the resonator was ready for testing.

Table 5.5 shows the experimental results of the 5 pass resonator and a 1:1:0 gas mixture at a gas pressure of 60 mb.

Table 5.5 Laser output characteristics for a 1:1:0 gas mixture at 60 mb. 5 pass resonator - no aperture

Tap settings %	E_S $\mu\text{Jcc}^{-1}\tau^{-1}$	E_D J	E_O mJ	η_5 %	η_5/η_3
50	29.35	2.66	30.8	1.160	-
55	39.23	3.56	42.0	1.180	-
60	46.51	4.22	53.8	1.276	1.77
65	51.68	4.69	65.9	1.405	1.87
70	59.18	5.37	76.5	1.424	1.78
75	65.34	5.93	85.9	1.450	1.67
$r_f = 75\% : R_c = 20 \text{ m} : L = 6.58 \text{ m} : \tau_p = 10 \mu\text{s}$					

It is clear that the values of E_O have increased compared to the values that were obtained for the three pass resonator. The average increase in the laser efficiency is 77.3 % - and the corresponding increase in the mode volume is approximately 66 %. The mode shape tended to indicate that the resonator was poorly aligned, however, it was likely that only the fundamental mode was propagating. An estimate for V_{00} is 310 cm^3 . Consequently on the basis of this active mode volume, $\eta_T \approx 9.44 \%$ and $E_O \approx 0.187 \text{ J}$ for the 75 % tapsetting. It is seen that η_T is greater for the 5 pass resonator than it is for the 3 - by about 62 %. This is probably due to the increased laser gain because of the longer resonator.

In order to increase the maximum frequency of the output laser beam, the pulse length was reduced to $7 \mu\text{s}$.

5.2.5 Five Pass Resonator: $7 \mu\text{s}$ Pulse Length

It was shown in Chapter 4, Section 4.4.6, that the effect of decreasing the pumping pulse length for the ballasted system was that the maximum system frequency f_1 could be increased before the discharge developed into arcs. Although not reported explicitly, this was found to be the case for the present laser head

geometry. The affect of reducing the pulse length to 7 μs on the laser output is reported for the 5 pass resonator and with a gas mixture of 1:1:0 at 60 mb.

Table 5.6 Laser output characteristics for a 1:1:0 gas mixture at 60 mb. 5 pass resonator - no aperture

Tap settings %	E_S $\mu\text{Jcc}^{-1}\tau^{-1}$	E_D J	E_O mJ	η_5 %	η_5/η_3
50	22.59	2.05	15.2	0.739	-
55	28.65	2.60	23.2	0.889	-
60	34.38	3.12	35.3	1.129	1.57
65	34.82	3.16	55.0	1.524	2.00
70	45.07	4.09	50.4	1.231	1.54
$r_f = 75\% : R_c = 20 \text{ m} : L = 6.58 \text{ m} : \tau_p = 7 \mu\text{s}$					

It is seen that both the discharge and the laser output energy are reduced for the shorter pulse lengths. The average increase in the laser efficiency when compared to the 3 pass resonator with a 10 μs pumping pulse (data from Table 5.4) is about 70%.

5.2.6 Summary of the Laser Output Efficiencies

Figure 5.9 shows the laser output energy as a function of the discharge energy obtained from the different resonator configurations that have been discussed in the previous sections. It is clearly seen that the affect of increasing the number of passes is to increase the laser output power for a given discharge energy, gas mixture and pressure. Figure 5.10 shows the laser output efficiencies for the same data as shown in Figure 5.9, it is apparent that the efficiency increases with the number of passes. The efficiency of the laser is, obviously, highly dependent on the resonator design. For this reason attention was given to optimising the resonator and the investigation into the effects of the gas mixture was, at this stage, considered of secondary importance and not examined in any detail.

In order to reach the required specification for the laser output pulses, the modal coupling efficiency must be increased. Section 5.4 discusses in detail some of the possible options to achieve this.

The development of the laser output power is dependent on the satisfactory performance of the glow discharge. It was shown in Chapter 3 that the discharge is not ideal for the development of stable, uniform glow discharges and high laser

gain. This is primarily as a result of the non-uniform electron density due to the poor performance of the trigger wires. It was reported in Chapter 3 that the laser output energy and the electrical to optical conversion efficiency is dependent on the value of L_a – the anode inductance on the discharge thyatron. Values of $E_0 \approx 0.1$ J, with $\eta \approx 1$ % were obtained with a single pass resonator and 1:2:0 gas mixture at slightly higher gas pressures (≈ 100 mb) than were used for the experiments discussed in this section. If the active mode volume V_{01} is calculated, then it is found that if all of the energy could be coupled out from the discharge region then $E_0 = 1.2$ J and $\eta_T = 11.9$ %. It should be noted that the discharge thyatron and the last mesh of the PFN were positioned under the laser cavity for this experiment.

5.2.7 Affect of the Number of Passes on the Delay Time

The delay time τ_d is that period of time between the start of the discharge current and the laser output pulse. Figure 5.11 shows the delay time as a function of the discharge energy for the different resonator geometries. It is seen that as the number of passes n_p increases, the delay time reduces. This is because with a higher number of passes, the gain of the laser is higher and it takes less time before the resonator losses are overcome. Consequently, the laser output is obtained much earlier after the growth of the discharge current. The values obtained for τ_d with the single pass resonator are similar to the values that were reported by Kharha [5.2].

5.2.8 Affect of the Number of Passes on the Plateau Power

As the number of passes increases, it is seen from Figure 5.12 that, for a given discharge energy, the plateau power increases. More energy is being coupled out from the discharge as n_p and the modal coupling efficiency increases.

5.3 LASER OUTPUT CHARACTERISTICS: BALLASTED ELECTRODE DESIGN

From the experimental investigation into the laser output characteristics with the plane electrode geometry, it was apparent that the maximum energy which could be extracted from the laser was dependent on the number of passes of the resonator. Consequently, in order to obtain the maximum laser output power, the 5 pass resonator was installed whilst the 0.8Ω ballasted electrode was in the laser

cavity. The characteristics of the pumping circuit remained unaltered - i.e. the discharge thyatron was in the pulser safety cage and $L_a = 36 \mu\text{H}$.

The diameter of 1 segment was approximately 6 mm, as there were 588 segments and the discharge gap was ≈ 4 cm, the total discharge volume is approximately 665 cm^3 . The specific energy density for the ballasted electrode system is greater than that for the plane electrode geometry.

It was shown in Chapter 4 that approximately 11 kW of mean power could be deposited into the discharge for the $\approx 8.0 \Omega$ electrode. The results of the laser output are reported for the $\approx 0.8 \Omega$ electrode at 100 Hz.

5.3.1 Five Pass Resonator: 10 μs Pulse Length

A gas mixture of 1:1:0 at a total gas pressure of 60 mb was selected for analysis of the laser output with the 0.8 Ω electrode, the results could then be compared to those obtained from the plane electrode geometry. Table 5.7 shows the experimental results. Figure 5.13 shows the discharge current, laser output pulse and its integral, i.e. the pulse energy E_o , for the 80 % tapsetting.

Table 5.7 Laser output characteristics for a 1:1:0 gas mixture at 60 mb. Five Pass Resonator - no aperture

Tap settings %	$E_{S_1} \mu\text{Jcc}^{-1}\tau^{-1}$	E_d J	E_o mJ	η_5 %
50	85.99	2.574	38.1	1.48
55	101.29	3.032	62.8	2.07
60	118.87	3.558	79.7	2.24
65	137.32	4.110	92.9	2.26
70	154.10	4.613	105.2	2.28
75	168.80	5.053	116.0	2.30
80	191.76	5.740	132.5	2.31

Reflectivity of the front window $r_f = 75.0 \%$
 Back mirror radius of curvature $R_c = 20.0$ m
 (Output window radius of curvature is infinite)
 Total discharge volume $V = 665 \text{ cm}^3$
 Cavity length $L = 6.58$ m
 Beam waist radius $(\text{TEM}_{00}) w_0 = 5.63$ mm
 Beam radius on rear mirror " " $w(L) = 6.87$ mm
 Pulse length $\tau_p = 10 \mu\text{s}$
 System frequency $f = 100$ Hz

Figure 5.14 shows E_0 as a function of E_d for the ballasted and the plane electrode geometry (i.e. the data from Table 5.5); and Figure 5.15 shows, for the same conditions as Figure 5.14, the laser efficiencies. It is seen that the efficiency is considerably greater for the ballasted electrode. However, it cannot conclusively be said whether this increase is due to better alignment of the fold mirrors or the greater input specific discharge energy densities.

The benefits of using the ballasted electrode geometry are clear. The electrical to optical conversion efficiency and the maximum discharge energy, before arcing occurs, are greater than they are for the plane electrode geometry.

It is seen that the average, maximum value of E_0 was 0.1325 J. This represents nearly an order of magnitude improvement over the initial laser output energy that was reported in Table 5.1. Moreover, this magnitude of the laser output power is sufficient to encounter the non-conduction limited processes at the workpiece. Figures 5.16 and 5.17 show the plateau power and delay time respectively, as a function of the discharge energy for the ballasted and plane electrodes. It is seen that for the ballasted geometry, the minimum value of τ_d is about 4.2 μs and the maximum value of the plateau power is 17.2 kW.

It is calculated that $\eta_T \approx 9\%$ for the condition with 80% tapsetting. This is assuming that only the TEM_{00} mode is propagating within the resonator.

It is interesting to note that a segmented longitudinal discharge CO_2 laser with a variable ballast resistance is reported by Kukreja et al [5.11]. The laser could operate in burst and pulsed mode with maximum frequencies of up to 50 Hz. The electrical to optical conversion efficiency was 13%. This maximum efficiency was observed with zero resistive and inductive ballast.

A CW, transverse flow laser is reported by Sliwinski et al [5.12]. Efficiencies of 11.4% were observed, with an output laser power of about 8 kW. The system was segmented with 1022 cathodes, the discharge volume was about 6.5 l and the gas velocity was 110 ms^{-1} . The typical pressures were 115 mb. An unstable resonator was used for efficient extraction of the laser power.

Appendix E1 shows some holes that were successfully drilled in aluminium with the laser, while the ballasted electrode and the 5 pass resonator were installed in the laser cavity.

5.4 MODELLING STABLE RESONATORS

It was shown in Section 5.2 that the laser output power is dependent on the number of passes n_p of the resonator through the discharge volume; moreover, the total efficiency of the laser increased with n_p . The computer codes that were developed by Kharha [5.2], Chatwin [5.3], Byabygambi [5.13] and Hasan [5.14] simulate the laser output pulse, and give an output power per unit volume. Consequently, in order to calculate the theoretical laser output power, it is necessary to multiply the laser output power distribution by the mode volume of the resonator that coincides with the discharge volume – this was defined as the active mode volume and denoted by V_a in Section 5.2.1 (Equation 5.3). The experiments in the previous sections have indicated that the relationship between the active mode volume and the laser output power for 1, 3 and 5 passes is approximately consistent if the correct mode volume is assumed.

The laser output per unit volume from a simple calculation of the mode volume is somewhat tenuous. Several factors are not taken into account. For example, Cheo [5.15] mentions that for CW CO_2 lasers, molecules that are in the upper laser level can diffuse into the active mode volume and contribute to the laser output. However, as the pumping pulse length is only $10 \mu\text{s}$ it is assumed that this effect is insignificant because of the low discharge energy densities. The transverse profile of the laser is not included. The theoretical laser output power needs to be recalculated for the longer length resonators, as obviously, the total gain of the laser per pass will increase with n_p . However, quite surprisingly, it does seem that for the first order approximation, the theoretical results can be validated by comparing them to the experimental laser output per unit volume, where the volume is the assumed active mode volume given some resonator configuration.

The resonators that have been used to date are far from ideal, offering electrical to optical conversion efficiencies of only 2.3 %. Whereas approximately 6.5 % is obtainable if 100 % of the laser energy could be extracted from the discharge for $n_p = 1$, and 11 % if $n_p = 5$. Spall [5.16] analysed the theoretical performance of unstable resonators. The major advantage of these resonators is that high modal coupling efficiencies can be obtained, but generally at the expense of a poor mode structure. Whereas, in general, stable resonators have poor output coupling efficiencies and a high quality mode shape. In order to maintain a high beam quality, it was decided to investigate the possibility of using various stable resonator configurations to maximise the laser output power.

Once the value of n_p becomes large, the beam waist and the beam diameter on

the rear mirror and folding optics become large and the diffraction losses for the resonator can become significant. This problem is exacerbated by the fact that as n_p increases, the number of optics must increase and they must fit into the same amount of space, which is dependent on the discharge width. These spatial constraints for the optics dictate the maximum size of the mirrors that can be used for a given resonator configuration. In order to minimise the diffraction losses, it is possible to include optics within the resonator to focus the beam periodically – these are defined as internal focusing optics, and serve to limit the spatial extent of the laser beam and, consequently, the diffraction losses [5.17,5.18].

In order to assess the relative merits of different resonator configurations, equations were derived to predict the diffraction losses for any given stable resonator. To optimise the resonator design, a code was developed in ASYST to predict the radius of the TEM_{00} and TEM_{01} mode throughout the length of the resonator. The code used the technique of ray transfer matrices [5.19]. It was developed so that the mode volume and the dead space region were calculated for the TEM_{00} and TEM_{01} laser modes; and, the resonator stability was found. It was possible to include any number of plane mirrors and a total of three curved mirrors consisting of concave and/or convex mirrors for the resonator. The effect of internal focusing or expanding optics could be examined. However, the effects of the gain medium were not considered. A technique of using ray matrices to model optical systems with loss or gain has been proposed by Kauderer [5.20].

The possibility of extending the number of passes of the resonator to 11, and the effect of using one internal focusing optic with both half-symmetric and symmetric resonators is examined.

The use of convex mirrors as part of a stable resonator configuration has been proposed by Cheng [5.21] as a method to increase the active mode volume of the laser and, consequently, the output power. However, a scraper mirror was used and an annular output beam was obtained. In order to maintain a TEM_{00} mode for the laser output beam, it was decided to investigate the theoretical performance of a concave-convex resonator with a partially transmissive output window. An analysis of the affect of the radius of curvature of the negative lens on the radius of the TEM_{00} mode is analysed and, the consequences of moving the convex lens to different positions within the resonator.

Finally, consideration is given to some recent developments in unstable resonator design which makes their use a much more attractive solution to the problem of

increasing the modal coupling efficiency.

5.4.1 TEM₀₀ and TEM₀₁ Propagation, Diffraction losses and Mode Volume Calculations for Different Resonator Designs

Kogilnik and Li [5.19] describe the basic methods that are used to model the propagation of the TEM₀₀ mode for stable resonators. For simple resonators – i.e. symmetric or half symmetric – it is sufficient to use two basic equations that express the variation of the beam radius and curvature of the phase front as a function of distance from the beam waist – which is defined as the position at which the beam diameter is a minimum. The axis of propagation of the beam is conventionally given the coordinate z ; $z = 0$ is defined as the beam waist position. The beam radius and the radius of curvature of the phase front at z are denoted by $w(z)$ and $R(z)$ respectively, and are defined in Appendix D4.

Appendix D5 describes the theory behind the development of the code. Briefly, the ABCD matrix is found for the equivalent lens waveguide of the resonator configuration, where a plane mirror is represented by the identity matrix. A variable ℓ is introduced into the ABCD matrix that takes on a running value from $\ell = 0$ to $\ell = L$. It is important that the order of the matrices are correct when the ABCD matrix is calculated for the optical system. Once the elements of the ABCD matrix have been found at a distance ℓ from the front window, then the beam radius at ℓ is given by

$$w(\ell)^2 = \frac{\lambda B}{\pi n \left[1 - \left[\frac{A + D}{2} \right]^2 \right]^{1/2}} \quad 5.5$$

Where A, B, C and D are the elements of the ABCD matrix and n the refractive index of the medium – assumed unity in the present case. The radius of curvature of the phase front at ℓ is given by

$$R(\ell) = - \frac{2 B}{A - D} \quad 5.6$$

The values are calculated as a function of ℓ . The code was developed to be user friendly with the intention of incorporating the code into the data acquisition and analysis system (see Appendix A6).

The mode volume is found by dividing the distance L into equal incremental distances of δ . The j^{th} volume element is simply given by

$$\Delta V_j = \pi \delta w^2(j\delta) \quad 5.7$$

Where $j\delta$ is the distance to the j^{th} volume element. The total sum over the distance L will equal the total mode volume V_T which is given by

$$V_T = \sum_{j=1}^{L/\delta} \pi \delta w^2(j\delta) \quad 5.8$$

Part of the input data for the code is a physical description of the distance of the optics from the discharge region and the length of the discharge. In this way, the value of ℓ is indicative of whether the volume element at ℓ has to be added to the active mode or the dead space volume. Eventually when $\ell = L$ the values of V_a , V_{ds} and V_T are known.

The first order expression for the diffraction loss for the TEM_{00} mode incident on mirror i of radius a_i is given by

$$\rho_{00i} = \exp \left[- \frac{2 a_i^2}{w_i^2} \right] \quad 5.9$$

Where w_i is the size of the TEM_{00} on mirror i . Mirror $i = 1$, denoted by M_1 , is defined as the output window, and $i = n_p + 1$ is the rear mirror. For the TEM_{01} mode the diffraction loss for mirror i of radius a_i is given by [5.22]

$$\rho_{01i} = \left[1 + 2 \left[\frac{a_i^2}{w_i^2} \right] \right] \exp \left[- \frac{2 a_i^2}{w_i^2} \right] \quad 5.10$$

As the width of the beam is known as a function of z , it is apparent that the radius of the beam will be known on each optic within the resonator. If it assumed that the right and left travelling waves (denoted by r and l respectively) within the laser resonator are incident upon the front window and rear mirror respectively, and these waves are propagated through the system, then the general term for the diffraction loss of either mode for the right going wave is given by (see Appendix D6 for the derivation)

$$DL_r = \rho_1 + \sum_{n=1}^{np} \rho_{n+1} \prod_{i=1}^n (1-\rho_i) + \prod_{i=1}^{np} (1-\rho_i) \sum_{n=np}^1 \rho_n \prod_{i=n}^{np} (1-\rho_{i+1}) \quad 5.11$$

and the diffraction loss for the left going wave is given by

$$DL_l = \rho_{np+1} + \sum_{n=np}^1 \rho_n \prod_{i=1}^{np} (1-\rho_{i+1}) + \prod_{i=1}^{np} (1-\rho_{i+1}) \sum_{n=1}^{np} \rho_{n+1} \prod_{i=n}^1 (1-\rho_i) \quad 5.12$$

Where the subscripts denoting the resonator mode have been dropped for clarity. The average of these two waves gives the approximate diffraction loss DL for the resonator configuration.

$$DL = \frac{DL_r + DL_l}{2} \quad 5.13$$

It must be remembered that this is only an approximation, but will serve to give moderately accurate results for resonator configurations that have a high Fresnel number - $N_F \gg 2$ (see Appendix D7) - which is defined by

$$N_F = \frac{a_1 a_{np+1}}{\lambda L} \quad 5.14$$

Where a_1 is the effective radius of the front window (or aperture if it is smaller), and a_{np+1} is the radius of the rear mirror. L is the distance between these optics and λ the transition wavelength of the CO₂ laser.

5.4.2 The Single, Three and Five pass Resonator Configurations

Figures 5.18 and 5.19 show, for the 1 and 3 pass resonators respectively, the loci of the $1/e^2$ point of the beams intensity for the TEM₀₀ mode for different values of the radii of curvature of the rear mirror, denoted by R_C . It is seen that increasing R_C increases the radius of the beam, and consequently, the mode volume. However, it must be appreciated that as the beam radius increases then so do the diffraction losses. Eventually, with increasing R_C , the losses for a particular mode are sufficiently high such that that mode is unable to propagate within the resonator. As the higher order modes have a greater spatial extent than the lower order modes, it is obvious that the diffraction losses are higher for the higher order modes. So, increasing R_C will reduce the likelihood of the higher order

modes from developing. This is one method of mode discrimination in resonators [5.23] and preferable over aperturing techniques which tend to introduce diffraction patterns onto the transverse intensity profile of the laser beam [5.24].

Figure 5.20 shows the diffraction losses for the TEM_{00} mode as a function of the fold and rear mirror diameters with 1, 3 and 5 pass resonators, and $R_c = 20$ m. The diameter of the front window a_1 was assumed equal to the diameter of the aperture or the diameter of the front window mount, i.e. $a_1 = 10$ mm or $a_1 = 12.5$ mm respectively. Figure 5.21 shows, for the same conditions as Figure 5.20, the diffraction losses for the TEM_{01} mode. It is clear that for both modes, the diffraction losses increase with the number of passes and reducing mirror diameter, and the losses are greater for the higher order mode. As the diameter of the optics increase it is apparent that the diffraction losses reach a limiting value determined by the value of a_1 . Obviously, the losses are greater for a given resonator geometry with the aperture ($a_1 = 10$ mm) in position than they are for the front window mount. For values of the optics diameter less than ≈ 20 mm, it is clear that the differences between the two possible values of a_1 have little effect on the diffraction losses.

In practice, the diameter of the optics for the 1 and 3 pass resonator were 50 mm, and under these circumstances, it is seen that the diffraction losses in all cases are less than 1 % and clearly negligible. It would be expected that with these low losses the laser would operate in the TEM_{00} and TEM_{01} modes. But, from Sections 5.2.2 and 5.2.3, it seems that the higher order mode is not propagating. This could have been due to misalignment of the resonator, and consequently, larger than expected losses for the TEM_{01} mode. Or, possibly, the convex-lensing effect of the discharge which would increase the beam radius and the losses for the higher order mode.

For the 5 pass resonator the maximum diameter of the mirrors that were used was 25 mm, and it is seen that the losses for the TEM_{00} and TEM_{01} mode are approximately 1 % and 7 % respectively. It is unlikely that the higher order mode will oscillate for this resonator configuration, and indeed this was found to be the case, see Section 5.2.4. It should be noted that a measurement of the laser gain would enable a more precise statement of if the higher order modes would propagate for a particular resonator configuration. The affect of the aperture on the diffraction losses is approximately 0.5 %.

Figure 5.22 shows the diffraction losses of the TEM_{00} and TEM_{01} modes for the 3 pass resonator as a function of the radius of curvature of the rear mirror, and

both with and without the aperture in position. It is seen that for $R_c \geq 10$ m, the diffraction losses increase with R_c and are greater for the TEM_{01} mode. The effect of the aperture is more noticeable for higher values of R_c .

The active mode volume of the TEM_{00} and TEM_{01} mode for the 1 and 3 pass resonator, with the aperture in position is shown in Figure 5.23 as a function of R_c . Clearly, increasing R_c increases the mode volume and, at first sight, it may seem beneficial to increase the value of R_c . However, the diffraction losses increase and this serves to limit the oscillation of higher order modes and possibly reduce the laser output power. Although a series of experiments were undertaken to assess the laser output power as a function of R_c , the results are not presented because of the poor vacuum conditions under which the experiments were taken and the corresponding "lack of confidence" in the results. The calculation of the active mode volume does not, at present, take any account of the beam overlapping itself in the discharge region. Hence, for large beam diameters, the mode volume will be overestimated.

For the three pass resonator, the aperture or front window mount has a considerably smaller diameter than any other optical component, and as a consequence, will limit the development of modes with a higher order than the TEM_{01} . Although multi-mode laser output beams are not ideal for high quality material processing applications, the quantity of laser power extracted from the discharge can be maximised. Figure 5.24 shows a graph of the diffraction losses for the 3 pass resonator as a function of the aperture diameter with $R_c = 20$ m. The diameters of the folding and rear mirrors are 48 mm and 30 mm. The diffraction loss is dominated by the diameter of the aperture when it is smaller than the diameter of the other optics. The losses for the TEM_{00} mode are smaller than they are for the TEM_{01} . Clearly, the TEM_{02} mode will be more likely to develop if the aperture diameter is increased above 25 mm, which was the size that was used for the experiments discussed in the previous sections. Consequently, the extraction efficiency of the laser would increase.

5.4.3 Eleven Pass Resonator Configuration

As the number of passes increases it has been shown in Section 5.2 that the laser output power increases. It is fruitful to consider the likely performance of resonators with a higher number of passes than 5. The design of an 11 pass resonator is discussed. Figure 5.25 shows a schematic of an 11 pass resonator, and Figure 5.26 the locus of the $1/e^2$ point of the laser beams intensity, for the

TEM₀₀ mode throughout the resonator. If low values of R_C are used it is seen that the beam waist size is small, but the divergence of the beam is large; consequently, the beam is large on the optics towards the rear of the resonator. However, if R_C is large, then the beam waist size is larger, but this time, the beam is smaller on the optics towards the rear of the resonator. The divergence of the laser beam is greater for smaller values of R_C . The spatial constraints for positioning the optics are even more severe than they were for the 5 pass resonator, and an absolute maximum diameter for the fold optics is 20 mm. Quite clearly, there will be large diffraction losses if suitable precautions are not taken.

In order to limit the extent of the diffraction losses for multi-pass resonators Hall [5.10] used a concave mirror for every optic. The beam is periodically focused throughout the resonator. In the present case, the effect of using only one internal focusing optic – a concave mirror with a radius of curvature R_2 – is analysed, this optic is also used as a fold mirror.

With 11 passes it is apparent that the focusing optic can be positioned at several possible locations throughout the resonator. The effect of moving the focusing optic through these positions is analysed.

Figure 5.27 shows the propagation of the TEM₀₀ mode through the 11 pass resonator for different focal lengths of the internal focusing optic (i.e. a concave mirror with radius of curvature R_2) placed a distance $d = 1.62$ m from the front window. The front window and rear mirror radii of curvature are $R_f = \infty$ and $R_C = 20$ m respectively, and all mirror diameters are 20 mm. It is seen that for low values of R_2 , the beam radius on the front window is magnified and on the rear mirror it is reduced. It was found that for all cases the diffraction losses were significant. For this resonator the Fresnel number $N_F = 0.841$; consequently, the approximations used in calculating the diffraction losses are no longer valid. However, as a rule of thumb, the mirror diameter should be greater than about $1.7 \times 2 w_i$, where w_i is the beam radius on mirror i . In this case, the diffraction loss past each mirror is about 0.3 %. As the mirror radius is 10 mm, the beam radius should be less than 5.88 mm on each optic to ensure that this condition is met. It is clearly seen that this is not the case. The minimum diffraction losses that was calculated from the code was ≈ 15 %, and this was for the condition $R_C \approx 40$ m.

Figure 5.28 shows the TEM₀₀ mode propagated throughout the 11 pass resonator with $R_2 = 50$ m, and the internal focusing optic located at different distances d from the front window. It is seen that as d is increased, the size of the beam on

the front window and rear mirror reduce and magnify respectively. For all cases, the beam size is considerably greater than the minimum value required to limit the diffraction losses to acceptable levels.

In order to try and limit the diffraction losses the effect of using a symmetrical resonator was examined with $R_2 = \infty$ and $R_f = R_c$. Figure 5.29 shows the beam radius for the fundamental Gaussian mode for different values of R_f and R_c . Obviously, the divergence of the laser beam is less for greater values of R_f and R_c . It is seen that the beam radius is greater than the minimum value required to limit the diffraction losses given the spatial constraints of the maximum size of the optics.

Figure 5.30 shows the beam radius of the symmetrical resonator with $R_f = R_c = 40$ m, and for different values of R_2 at a distance of 1.62 m from the front output window. It is seen that as R_2 decreases, the beam radius on the output window and rear mirror increase and decrease respectively, and the diffraction losses are still significant.

Figure 5.31 shows the effect of increasing the distance d of the internal focusing optic from the front window. As d is increased, the beam size on the output window and rear mirror decrease and increase respectively. The diffraction losses are still too large to make the 11 pass symmetric resonator, with one internal focusing optic, a possible option.

5.4.4 The Concave-Convex Stable Resonator Configuration

Figure 5.32 shows the path of the TEM_{00} mode propagated through resonator configurations for different values of R_2 , and with: a plane output window, $R_c = 10$ m and the convex mirror placed a distance $d = 1.62$ m from the output window. It is seen that as R_2 becomes more negative, the beam radius tends towards the radius that is obtained for $R_2 = \infty$, and the mode volume of the TEM_{00} mode decreases – this serves to limit the oscillation of higher order modes within the discharge. It is seen that the beam diameter is much less than the diameter of the optics (50 mm) and the diffraction losses for the TEM_{00} are small.

Figure 5.33 shows, as for the same conditions as Figure 5.32, the effect of moving R_2 to a distance $d = 2.86$ m from the output window. It can again be recognised that as R_2 is made more negative, the beam radius tends towards the value that

was obtained for $R_2 = \infty$, and the TEM_{00} mode volume decreases.

If Figures 5.32 and 5.33 are compared, it is seen that the width of the fundamental mode is larger for the condition where R_2 is placed 2.86 m from the front window. The mode volume will be larger under these circumstances and the expected extraction efficiency will increase. The diffraction losses for both resonators are minimal.

5.5 RESONATOR DEVELOPMENTS

It is clear that the resonators that have been used so far are far from ideal. It is apparent that more than one internal focusing optic is required to limit the diffraction losses for the 11 pass resonator. However, for resonators with such a long length, the tolerance to misalignment becomes less, and it is harder to ensure that the resonator remains aligned.

If a stable resonator configuration is to be used, then it is more practical to use independent resonators that occupy the lower and upper volumes of the discharge space. The total length of the resonators is less than the 11 pass resonator, and consequently, the resonator is more tolerant to misalignment. Recent developments in hollow waveguide beam delivery systems for CO_2 lasers mean that the two laser beams can easily be guided over short distances, to any particular location and recombined if necessary [5.25]. However, it must be questioned if this is the most suitable approach to follow for the optimum resonator design, the extraction efficiency is still low.

The effect of the 3 pass resonator with beam expanding optics may prove to be a useful way to optimise the extraction efficiency of the laser whilst still maintaining a high quality mode shape. However, it should be remembered that to a certain extent, the discharge region acts as a convex lens, causing the fundamental Gaussian mode to expand [5.26]. This is particularly true when the discharge power loading is high.

Some recent developments in unstable resonators provide high extraction efficiencies with mode shapes that are suitable for high quality material processing. Some of these are briefly described.

The unstable self-filtering resonator (USFR) [5.27] provides a method of obtaining

high laser extraction efficiency from the gain medium with a "top hat" irradiance profile of the output laser beam [5.23].

A major physical phenomena which prevented successful use of the unstable resonator for high quality, material processing has been generally called mode medium instabilities (MMI). The MMI develop in high power CO₂ lasers because of spatio-temporal variations in the refractive index of the gain medium. This has been attributed to uneven heating rates of the discharge medium, introduced via the intensity variation of the beam. For unstable resonators, the effects of diffraction at the output mirror have been a sufficient reason for MMI to develop with the subsequent, and sometimes severe, degradation of the beam quality and output power. However, the problem can be overcome by using Gaussian-reflectivity mirrors, they reduce edge diffraction at hard apertures, and moreover, transform the output mode of an unstable resonator into a smooth Gaussian mode whilst still maintaining a large mode volume – MMI are reduced. An analysis of the MMI for a CO₂ unstable resonator has been performed by Webster et al [5.28]. They conclude that the Gaussian reflectivity mirrors improve the beam quality by reducing the effects of MMI, and consequently, the diffraction ripples on the edge of the beam profile.

The use of a kaleidoscope has been proposed as a method to shape the laser output beam to optimise the interaction process, for example surface heat treatment or welding [5.29].

The general trend in the open literature has been to use unstable resonators in order to maximise the power extracted from the laser medium. The realisation of the variable reflectivity mirror and the SFUR have helped in nearly achieving the far field diffraction limited spot sizes for the laser beam.

A constraint for the successful implementation of unstable resonators is a high laser gain. Although the laser gain has, unfortunately, not been measured in the present case, the theoretical results [5.3] show that it is low, typically 0.001 cm⁻¹. For a discharge length of 1 m, this corresponds to a gain of about 10 % per pass. Whereas, for unstable resonators gains of approximately 50 % are advantageous.

From the experimental results discussed in Section 5.3, it is clear that if efficiencies of about 10 % can be realised, then with a mean discharge power of 11 kW, a laser beam in excess of 1 kW can be obtained with an operating frequency of up to 5 kHz. The pulse energy would be about 0.220 J. If 90 % of

the power occurs within the plateau region, and the pulse length $\tau_Q = 5 \mu s$ then the plateau power is approximately 40 kW; and within the specification for the non-conduction limited interactions and quasi-cw material processing.

Appendix E1 briefly describes some of the results from the laser/workpiece interaction experiments.

CHAPTER FIVE REFERENCES

- [5.1] Bakewell B., Scott B., Journal of Heat and Mass Transfer. To be published.
- [5.2] Kharha J. "Optimisation of the output characteristics of a pulsed CO₂ laser for processing materials", PhD Thesis, Department of Mechanical Engineering., University of Birmingham, U.K. 1979.
- [5.3] Chatwin C. "Thermodynamics of a pulsed CO₂ laser for machining metals". PhD. Thesis University of Birmingham, U.K. 1979.
- [5.4] Gibson A., Kimmitt M., Walker A. "Photon drag in germanium". App. Phys. Letts. Vol. 17 (2) pp 75-77 1970.
- [5.5] "Handbook of chemistry and physics" 55th Edition. CRC press 1974-1975.
- [5.6] Hatanaka H., Kawahara N. et al. "High-repetition-rate, multijoule transversely excited atmospheric laser". SPIE Vol. 1397, Eighth International Symposium on Gas flow and Chemical Lasers (1990). pp 379-382.
- [5.7] V+S Scientific (London) Ltd. Potters Bar, Herts EN6 1BW, England.
- [5.8] II-VI Incorporated. C/O LOT Oriel, Leatherhead, Surrey, England.
- [5.9] Foster H. "High power CO₂ lasers - a review". Optics and Laser Technology, pp 121 - 127, June 1972.
- [5.10] "The physics and technology of laser resonators". Edited by Hall D., Jackson P. Adam Hilger, IOP Publishing Ltd. 1989.
- [5.11] Kukreja L., Sehgal S. et al. "Pulsed operation of a segmented longitudinal discharge CO₂ laser without ballast impedance". Rev. Sci. Instrum. Vol. 56 (11) pp 2021-2024 1985.
- [5.12] Sliwinski G., Rabczuk G. et al. "Investigation of a high-power transverse-flow CO₂ laser". SPIE Vol. 1031. pp 216 - 220, 1988. Seventh International Symposium on Gas Flow and Chemical Lasers.

- [5.13] Byabagambi C. "Surface heating in metals irradiated by fast I.R. laser pulses". Ph.D. Thesis, Department of Mechanical Engineering, University of Glasgow, 1987.
- [5.14] Hasan M.A. "Thermodynamics of transiently pumped CO₂ gas laser plasmas", PhD Thesis, Department of Mechanical Engineering, University of Glasgow 1989.
- [5.15] Christenson C., Freed C., Haus H. IEEE J. Quant. Electron. 5, 276, 1969.
- [5.16] Spall R. "Pulsed power supply for an unstable resonator". PhD. Thesis, Department of Mechanical Engineering, University of Birmingham, 1979.
- [5.17] Kogelnik H., Li T. "Laser beams and resonators". Applied Optics Vol. 5 (10) pp 1550-1567.
- [5.18] Collins S. "Analysis of optical resonators involving focusing elements". App. Optics Vol. 3 (11), pp 1263-1275, 1964.
- [5.19] Kogelnik H. "Imaging of optical modes - resonators with internal lenses". Bell Technical System Journal, pp 455-494, 1965.
- [5.20] Kauderer K. "Gaussian-Schell model sources in one-dimensional first order systems with loss or gain". Applied Optics Vol. 32 (6), pp 999-1017, 1993.
- [5.21] Cheng Z., Seguin H. et al. "Annular-coupled concave-convex stable resonator for large-volume high-quality energy extraction". Applied Optics, Vol. 27 (5) pp 836-842, 1988.
- [5.22] "Laser electronics". Verdeyen J. Prentice-Hall International Editions. Second edition, 1989.
- [5.23] Li T. "Diffraction losses and selection of modes in maser resonators with circular mirrors". Bell System Technical Journal, pp 917-932 May 1965.
- [5.24] "Lasers". A. Siegman. University Science, Mill Valley, California. 1986.
- [5.25] Matsuura Y., Miyagi M. "Bending losses and beam profiles of zinc-selenide coated silver waveguides for carbon dioxide laser light". Applied Optics, Vol. 31 (30), pp 6441-6445, 1992.

[5.26] "The CO₂ laser". W. Witteman. Springer Series in Optical Sciences, Vol. 53, 1987.

[5.27] Gobbi P., Reali G. "A novel unstable resonator configuration with a self filtering aperture". Optics Communication, Vol. 52 (3) pp 195-198, 1984.

[5.28] Webster K., Sung C. "Mode medium instability and its correction with a Gaussian-reflectivity mirror". Applied Optics, Vol. 31 (3), pp 319-328, 1992.

[5.29] Miyamoto I., Maruo H. "Shaping of CO₂ laser beam by Kaleidoscope". SPIE Vol. 1031. Seventh International Symposium on Gas Flow and Chemical Lasers, 1988.

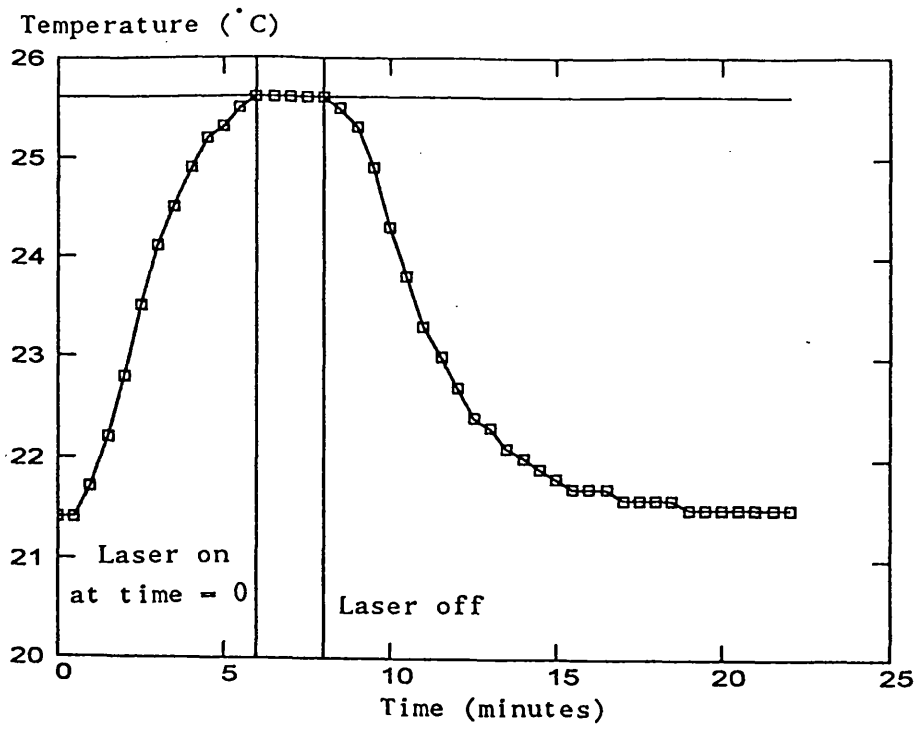


FIGURE 5.1 CONE CALORIMETER TEMPORAL TEMPERATURE RESPONSE

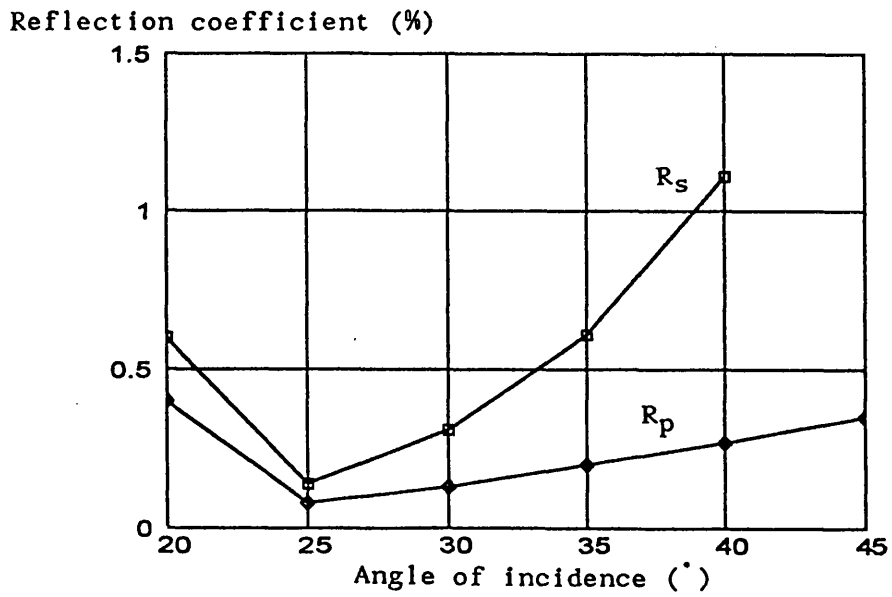


FIGURE 5.2 AR/AR ZNSE REFLECTION COEFFICIENTS

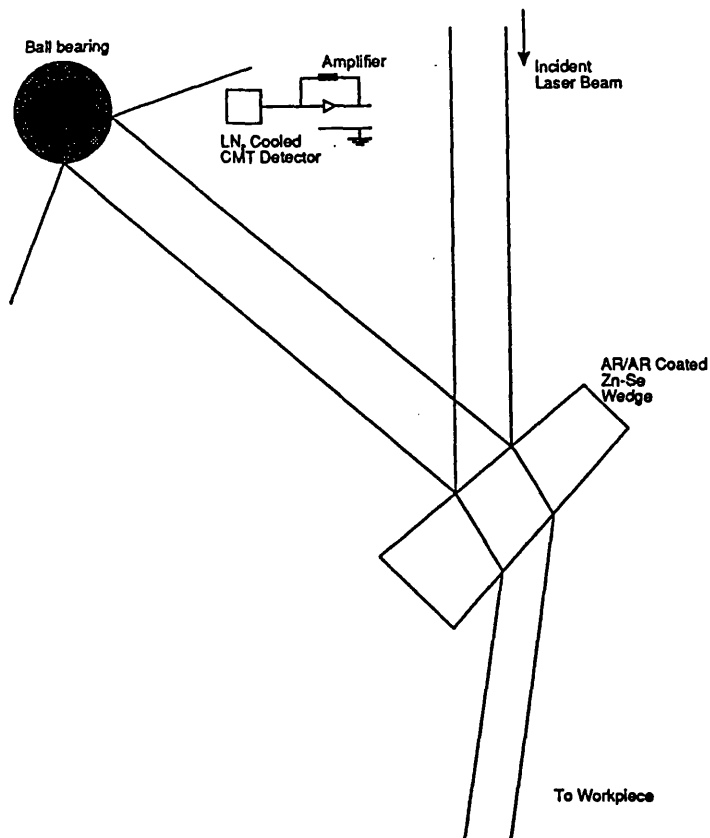


FIGURE 5.3 CADMIUM-MERCURY-TELLURIDE DETECTION SYSTEM

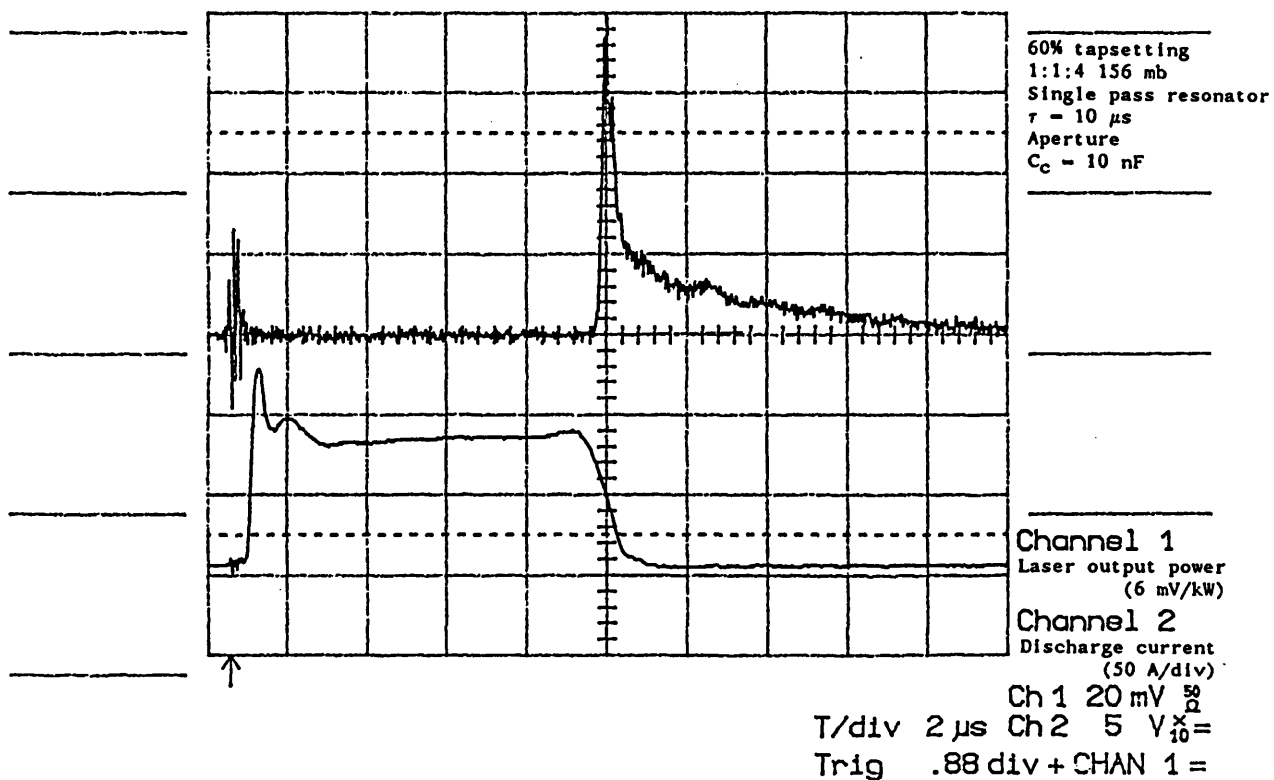


FIGURE 5.4 LASER OUTPUT PULSE AND DISCHARGE CURRENT

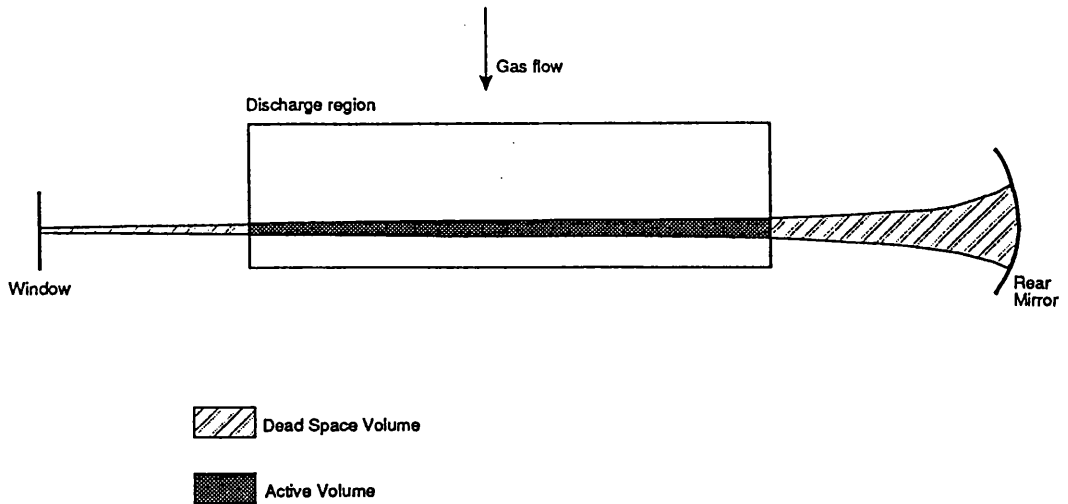


FIGURE 5.5 ACTIVE AND DEAD SPACE REGIONS FOR SINGLE PASS RESONATOR

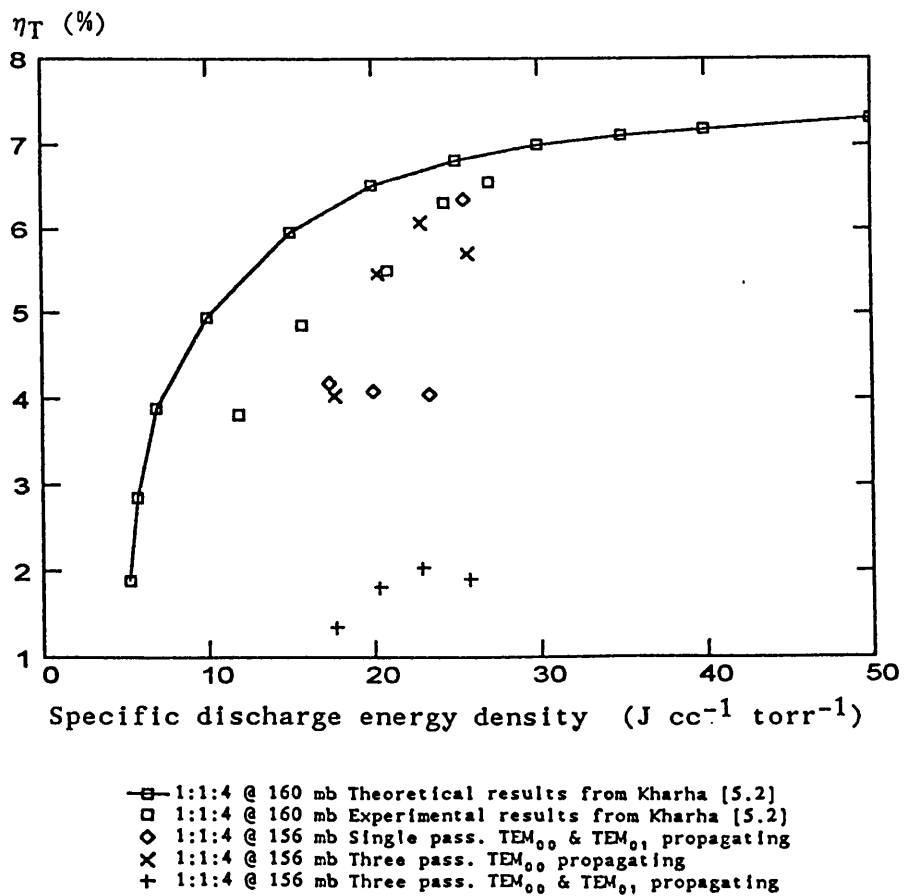


FIGURE 5.6 η_T VS SPECIFIC DISCHARGE ENERGY DENSITY

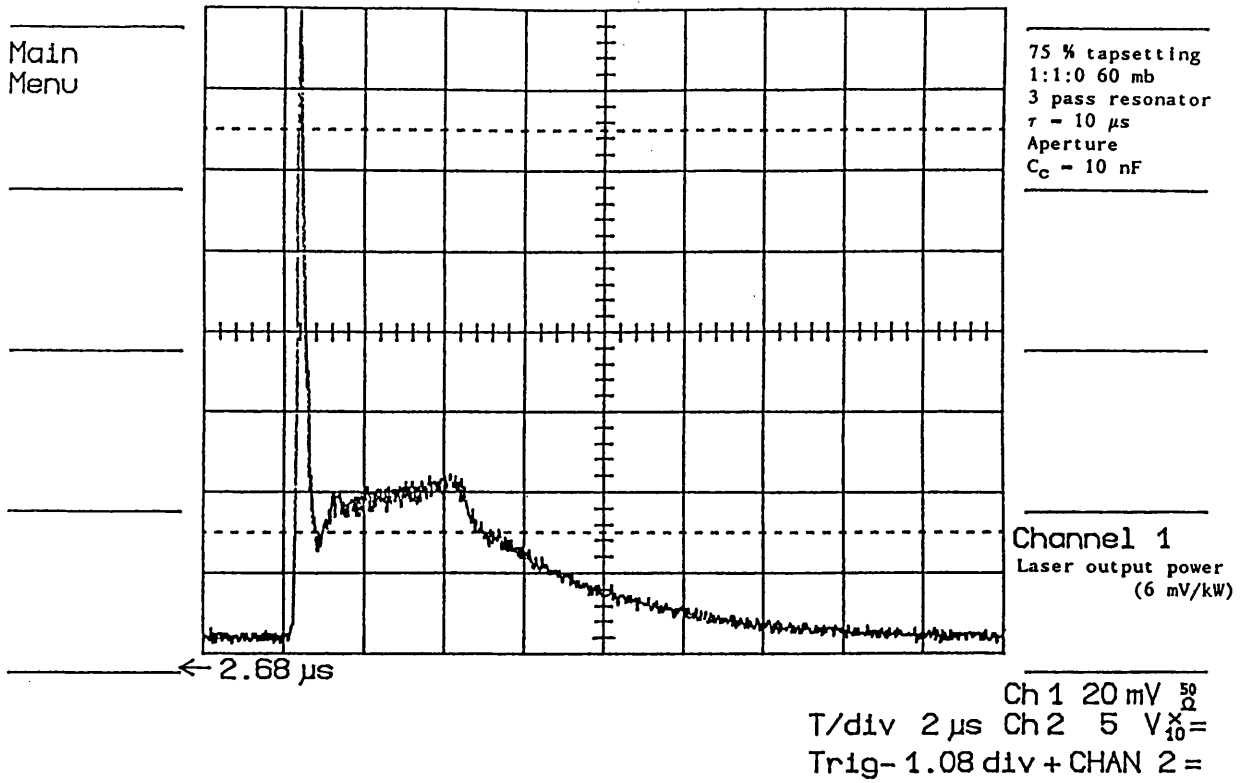


FIGURE 5.7 LASER OUTPUT PULSE

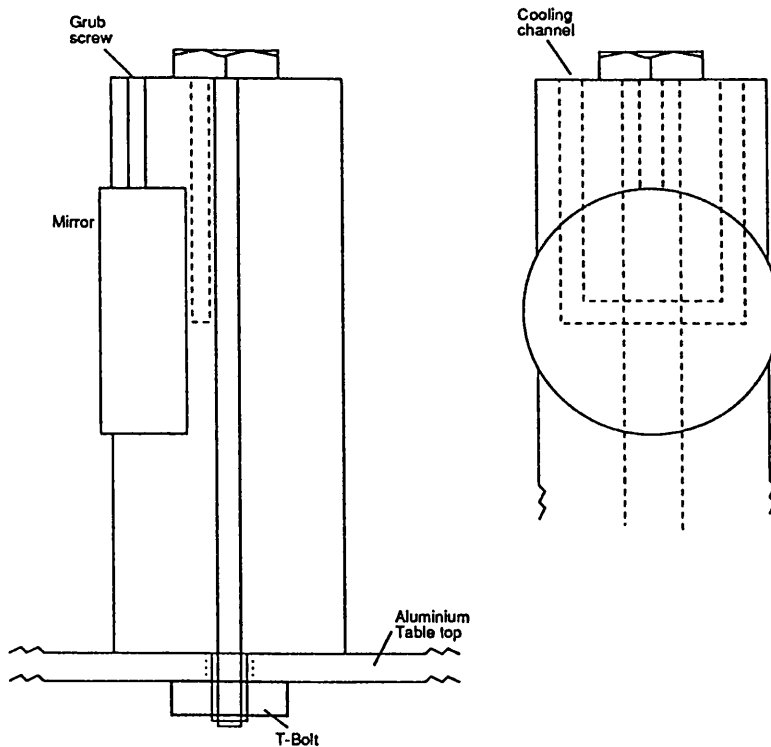


FIGURE 5.8 5 PASS RESONATOR DESIGN

Laser output energy (mJ)

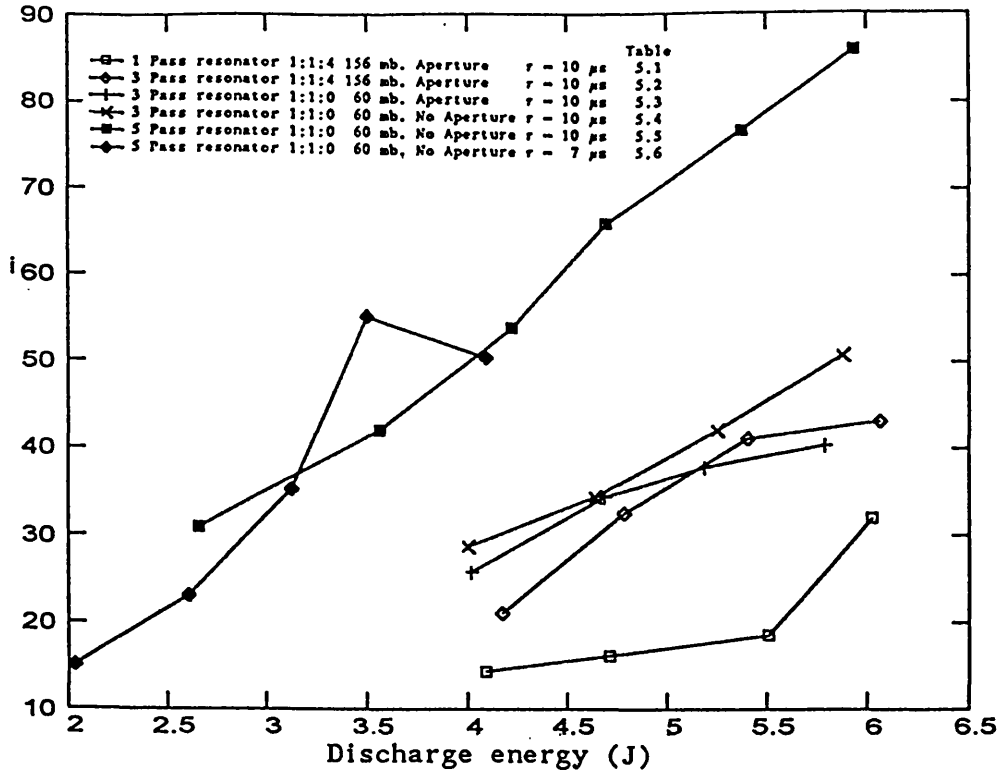


FIGURE 5.9 LASER OUTPUT ENERGY AS A FUNCTION OF DISCHARGE ENERGY

Laser efficiency (%)

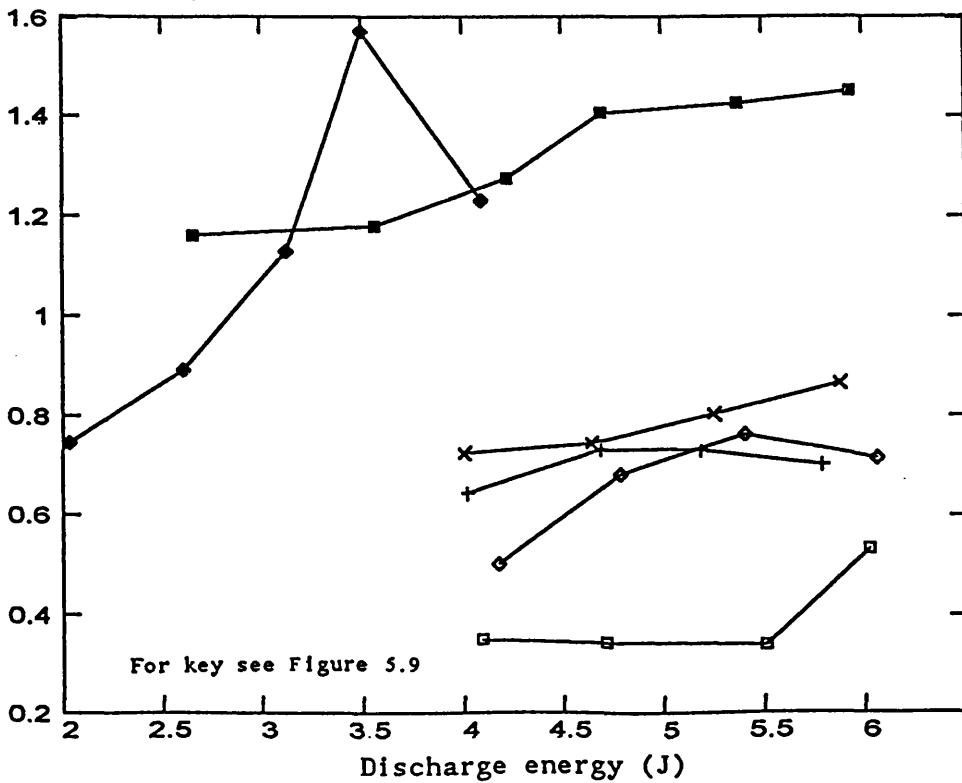


FIGURE 5.10 LASER EFFICIENCY AS A FUNCTION OF DISCHARGE ENERGY

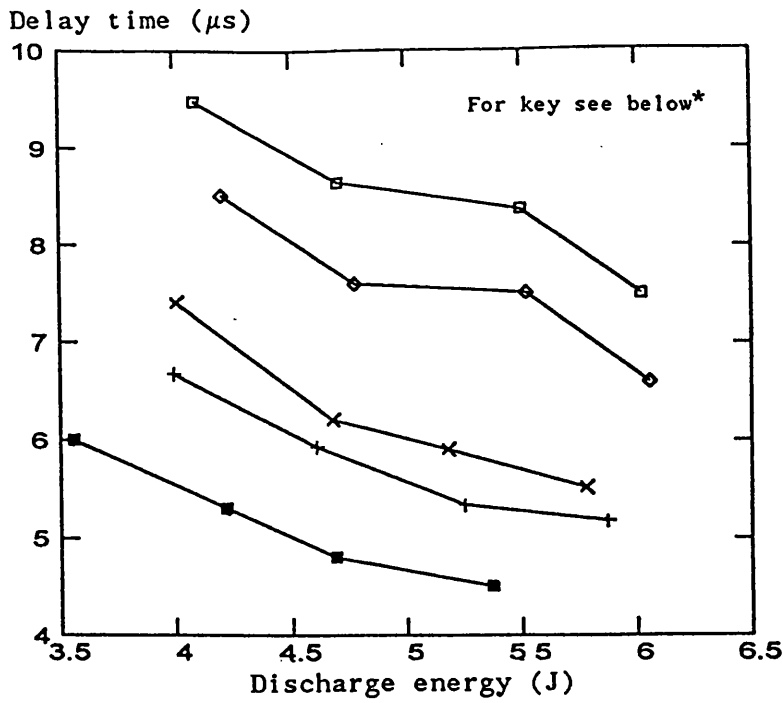


FIGURE 5.11 DELAY TIME VS DISCHARGE ENERGY

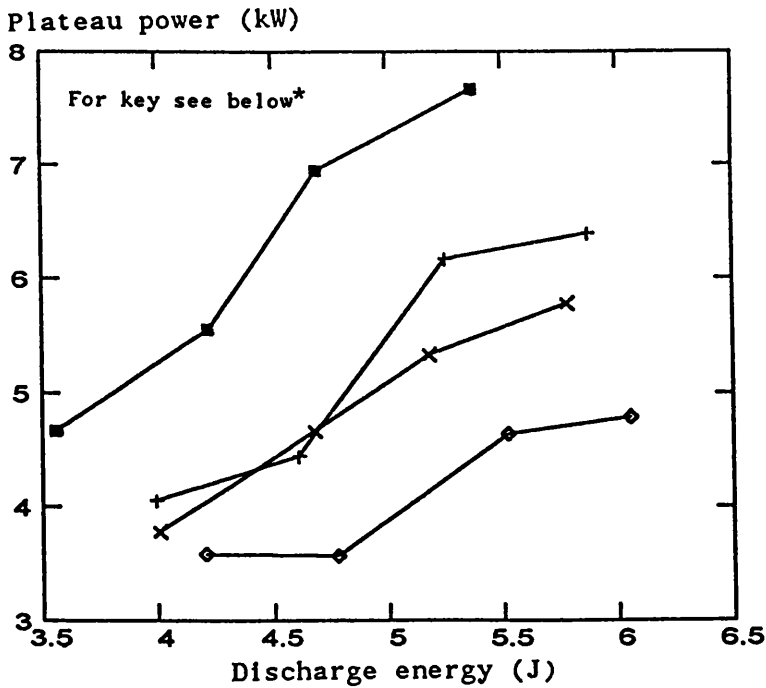


FIGURE 5.12 PLATEAU POWER VS DISCHARGE ENERGY

*Key for above figures

Series	Resonator	Aperture	Table
□	1 Pass resonator 1:1:4	156 mb. Aperture	5.1
◇	3 Pass resonator 1:1:4	156 mb. Aperture	5.2
+	3 Pass resonator 1:1:0	60 mb. Aperture	5.3
×	3 Pass resonator 1:1:0	60 mb. No Aperture	5.4
■	5 Pass resonator 1:1:0	60 mb. No Aperture	5.5

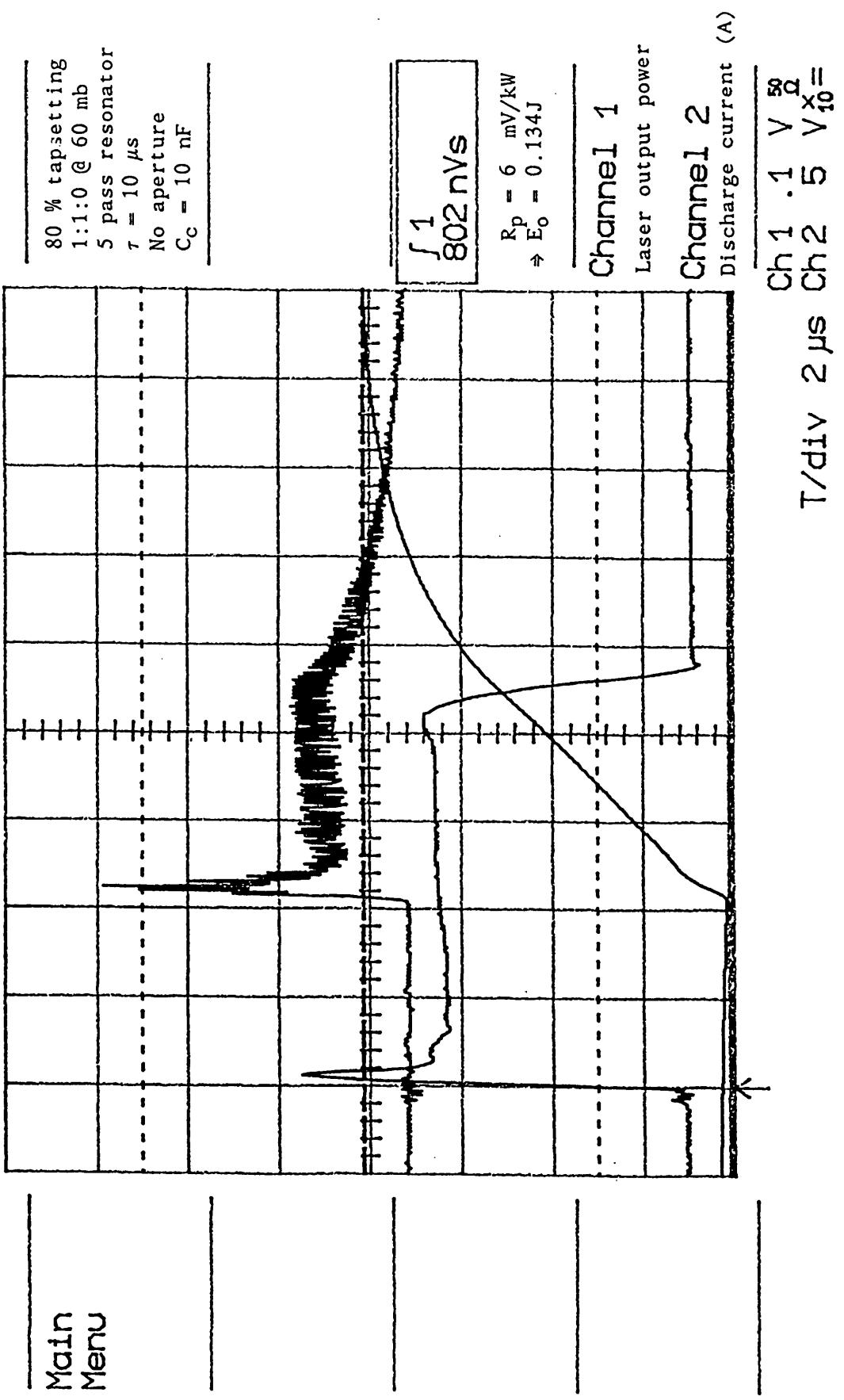


FIGURE 5.13 LASER OUTPUT PULSE AND DISCHARGE CURRENT

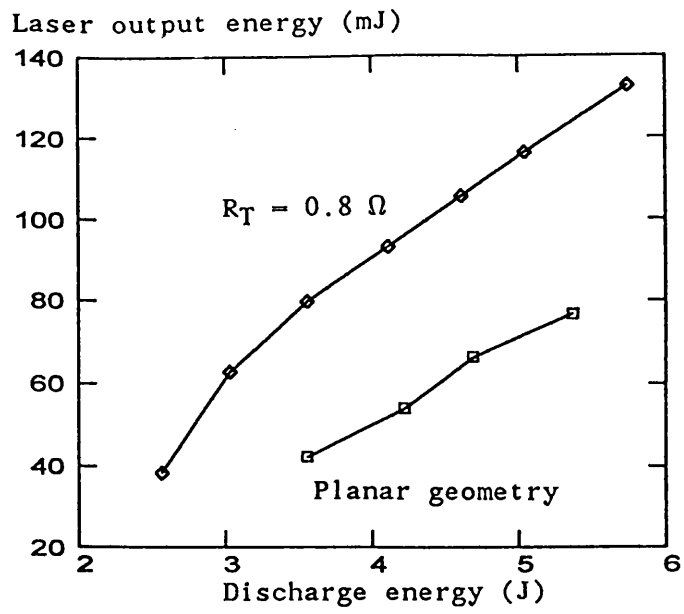


FIGURE 5.14 LASER OUTPUT ENERGY VS DISCHARGE ENERGY

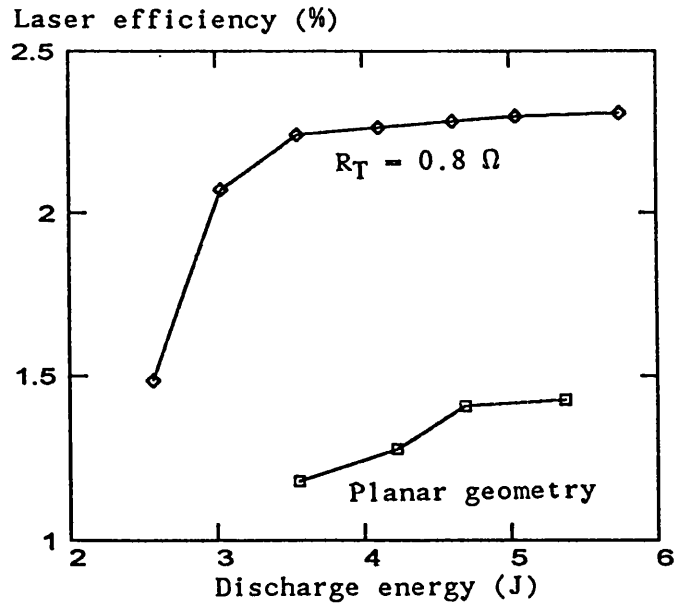


FIGURE 5.15 LASER EFFICIENCY VS DISCHARGE ENERGY

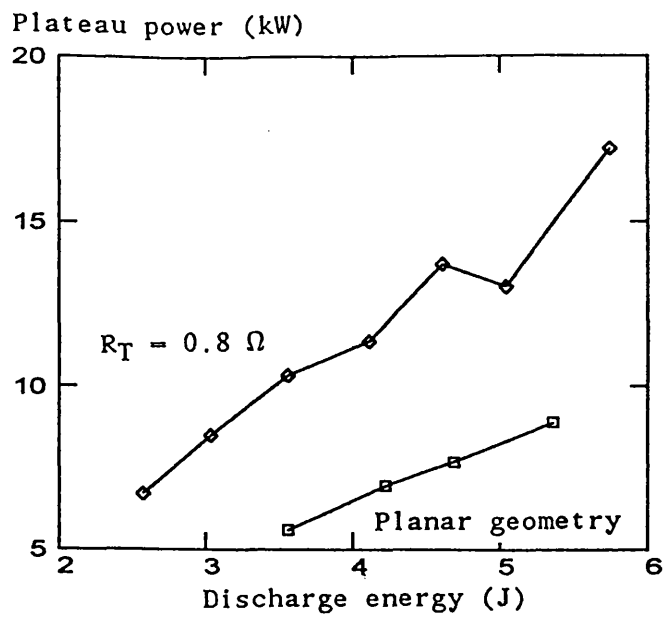


FIGURE 5.16 PLATEAU POWER VS DISCHARGE ENERGY

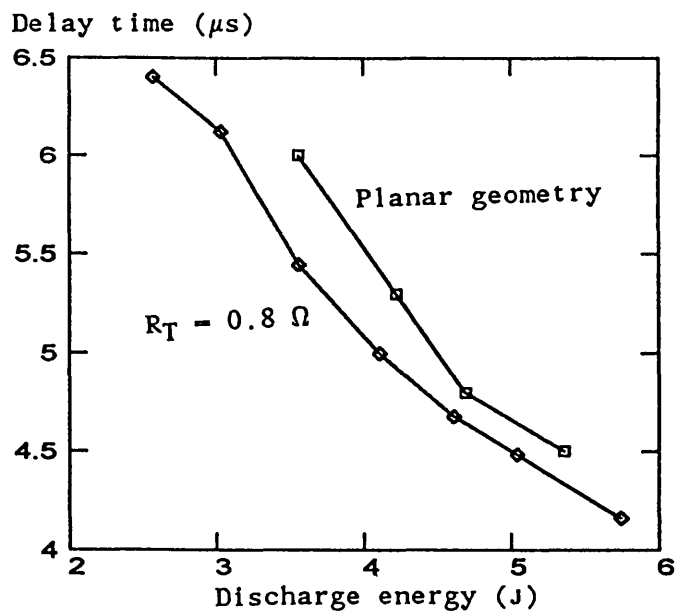


FIGURE 5.17 DELAY TIME VS DISCHARGE ENERGY

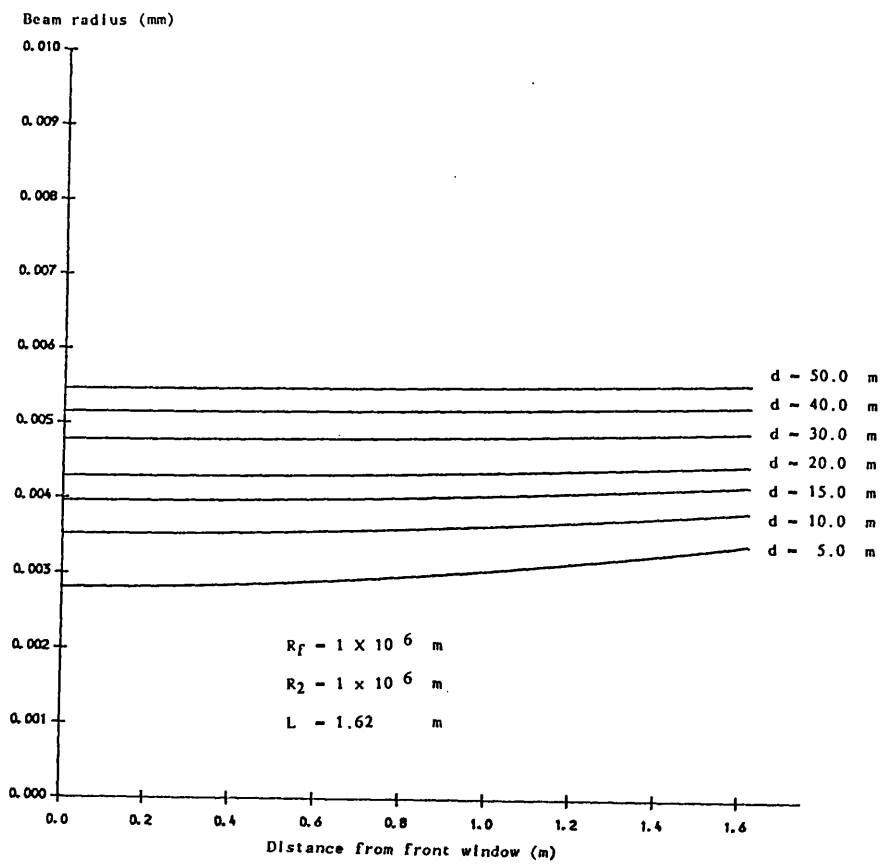


FIGURE 5.18 BEAM RADIUS OF THE TEM_{00} MODE FOR THE SINGLE PASS RESONATOR

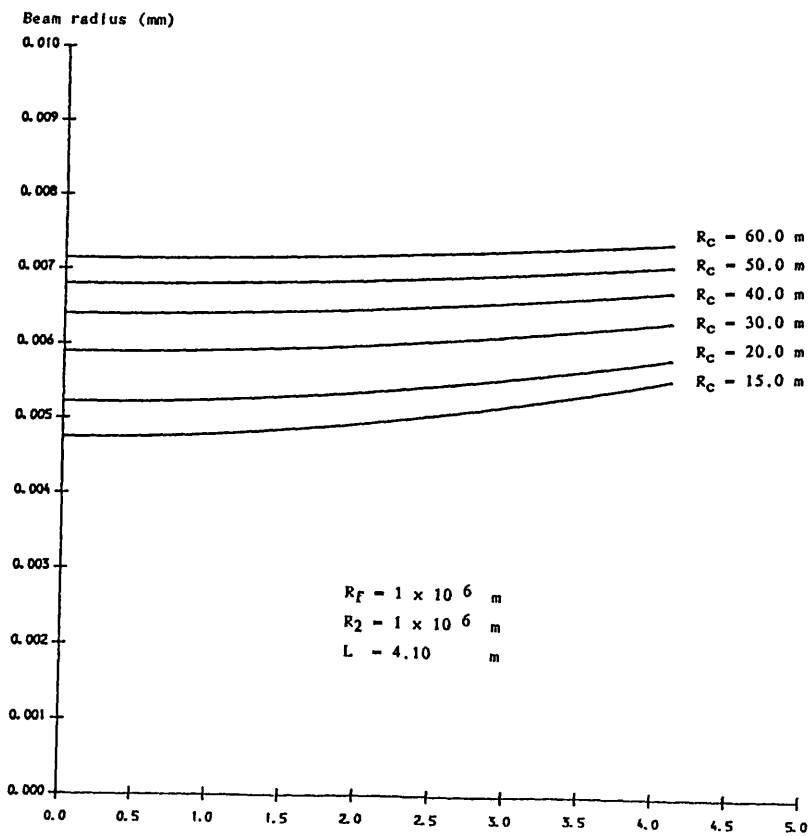


FIGURE 5.19 BEAM RADIUS OF THE TEM_{00} MODE FOR THE 3 PASS RESONATOR

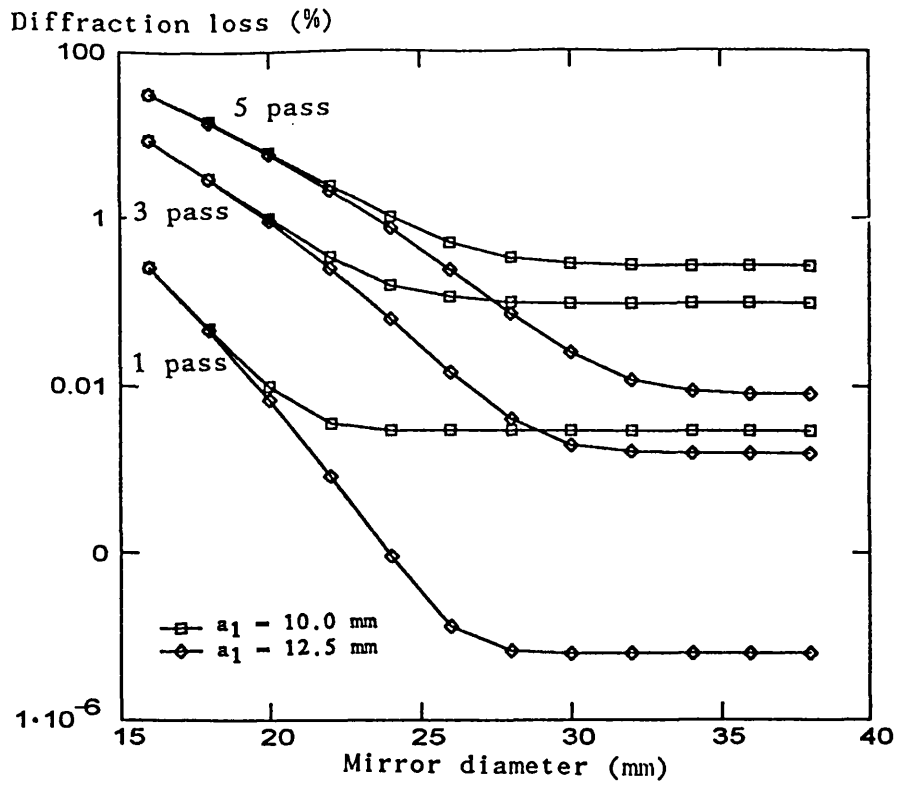


FIGURE 5.20 DIFFRACTION LOSSES OF THE TEM_{00} MODE FOR 1, 3 AND 5 PASSES

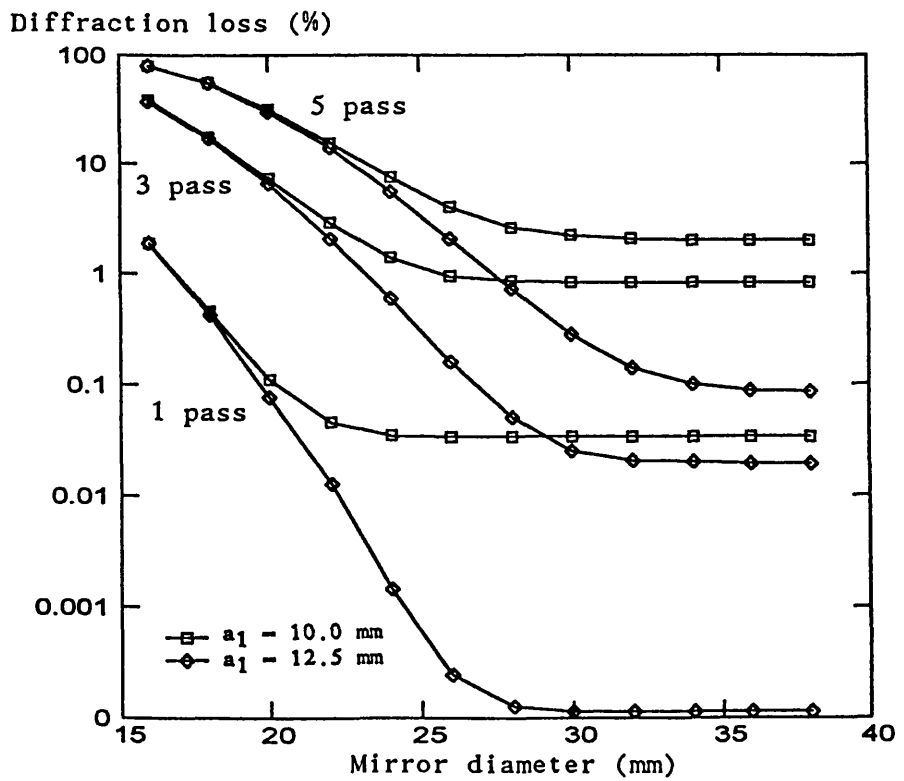


FIGURE 5.21 DIFFRACTION LOSSES OF THE TEM_{01} MODE FOR 1, 3 AND 5 PASSES

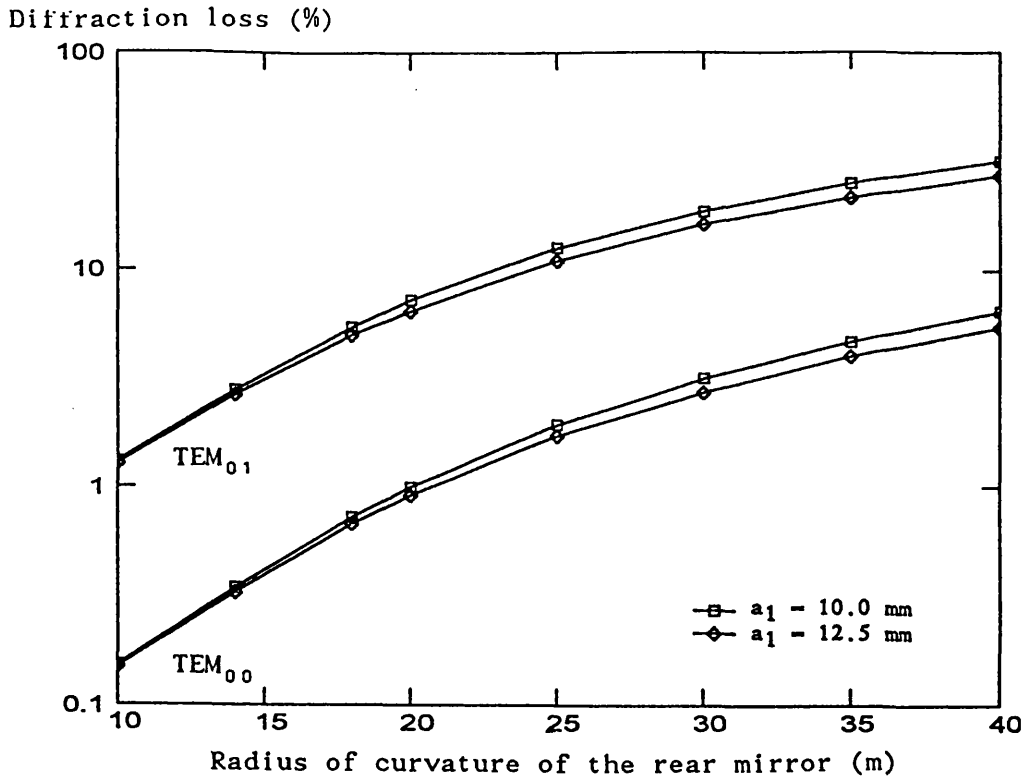


FIGURE 5.22 DIFFRACTION LOSSES AS A FUNCTION OF R_c

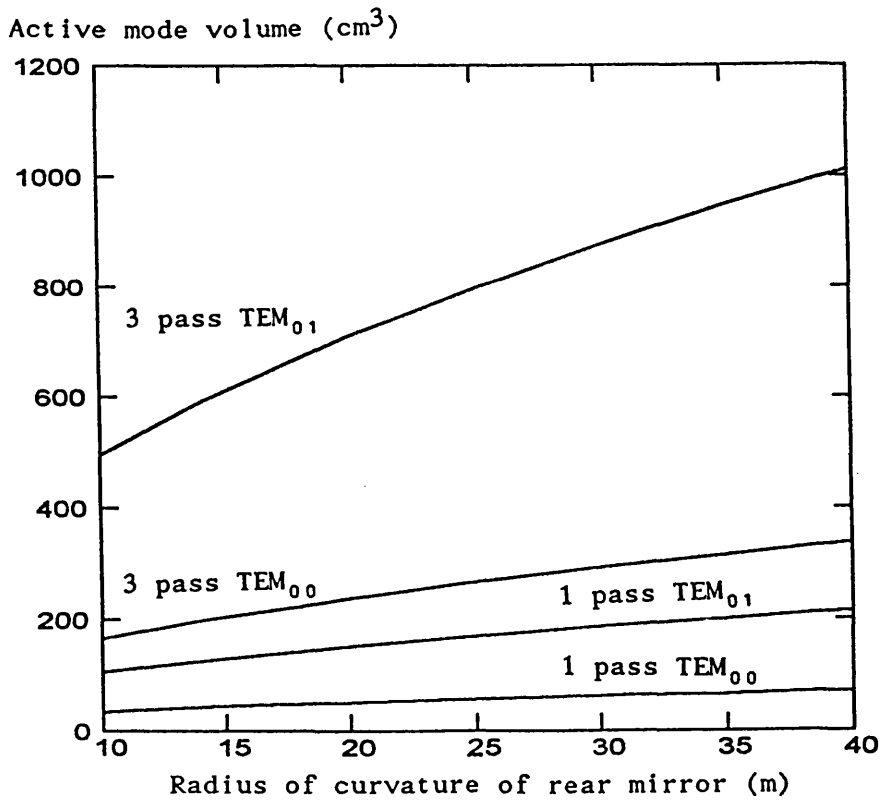


FIGURE 5.23 MODE VOLUME OF THE 3 PASS RESONATOR

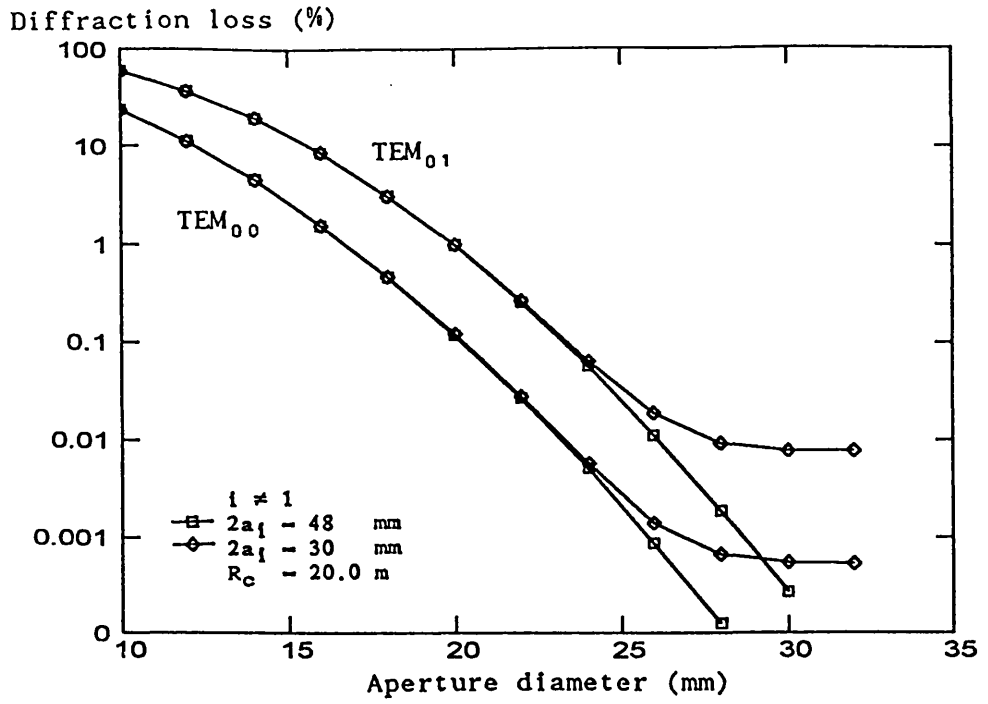


FIGURE 5.24 3 PASS RESONATOR DIFFRACTION LOSSES VS APERTURE DIAMETER

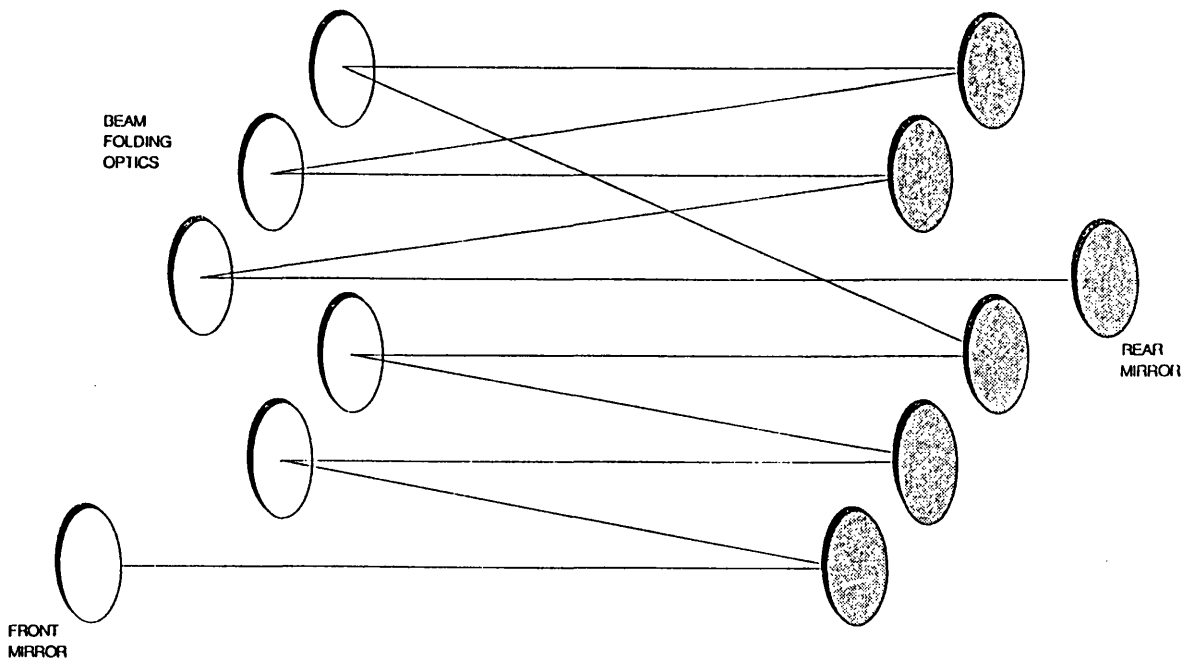


FIGURE 5.25 SCHEMATIC OF THE 11 PASS RESONATOR

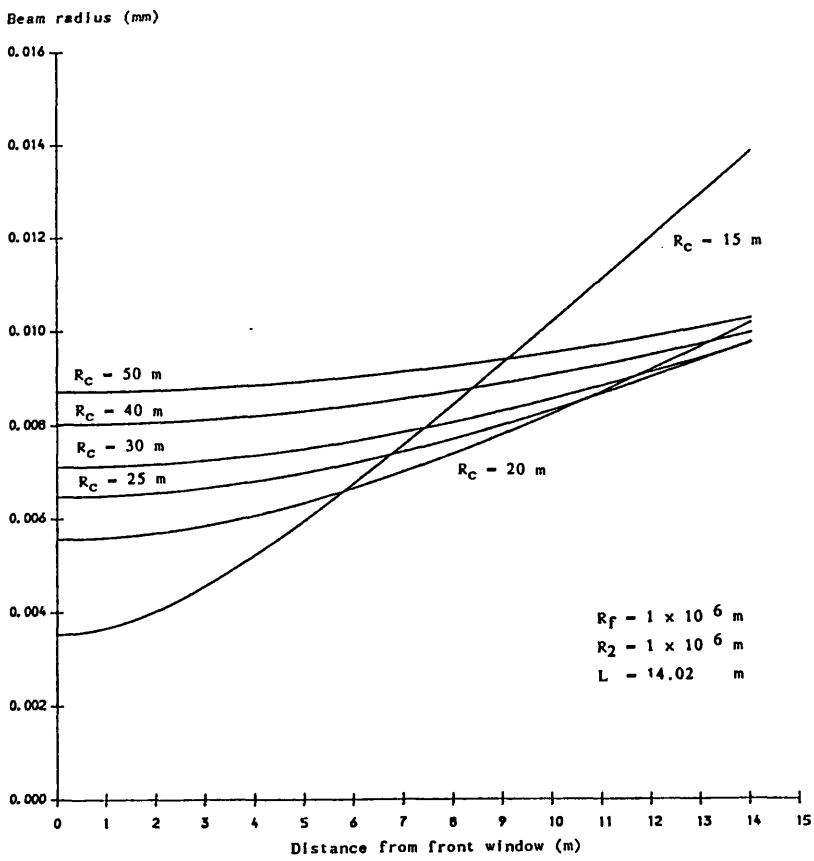


FIGURE 5.26 BEAM RADIUS OF THE TEM_{00} MODE FOR THE 11 PASS RESONATOR

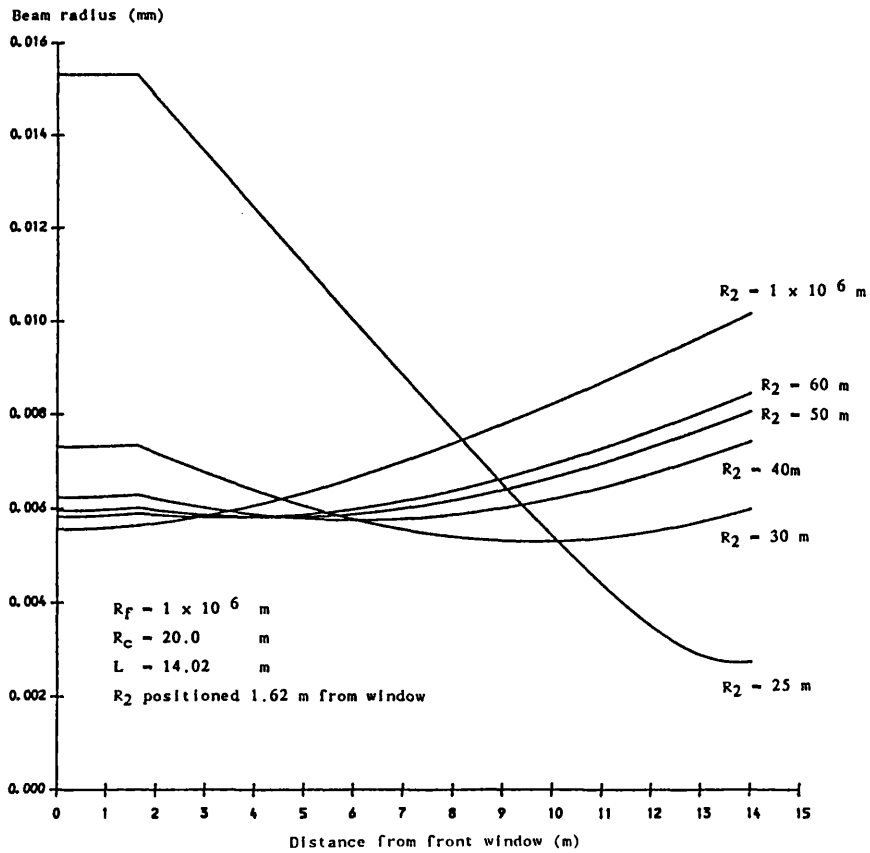


FIGURE 5.27 AFFECT OF THE INTERNAL FOCUSING OPTIC

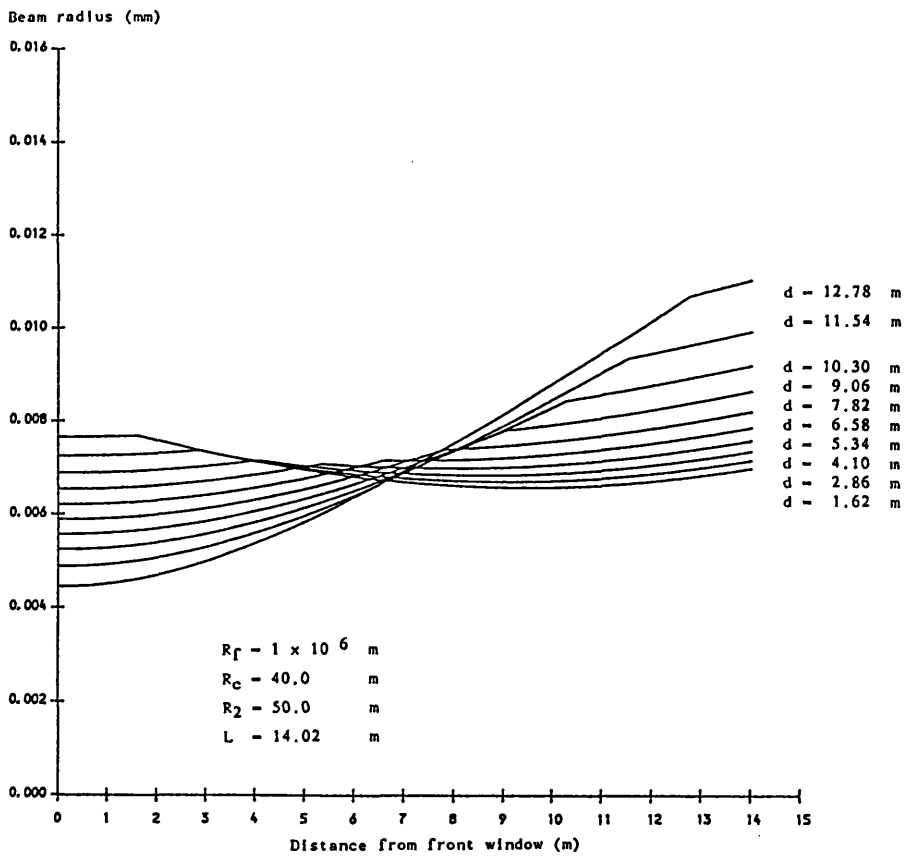


FIGURE 5.28 AFFECT OF INTERNAL FOCUSING OPTIC AT DIFFERENT POSITIONS

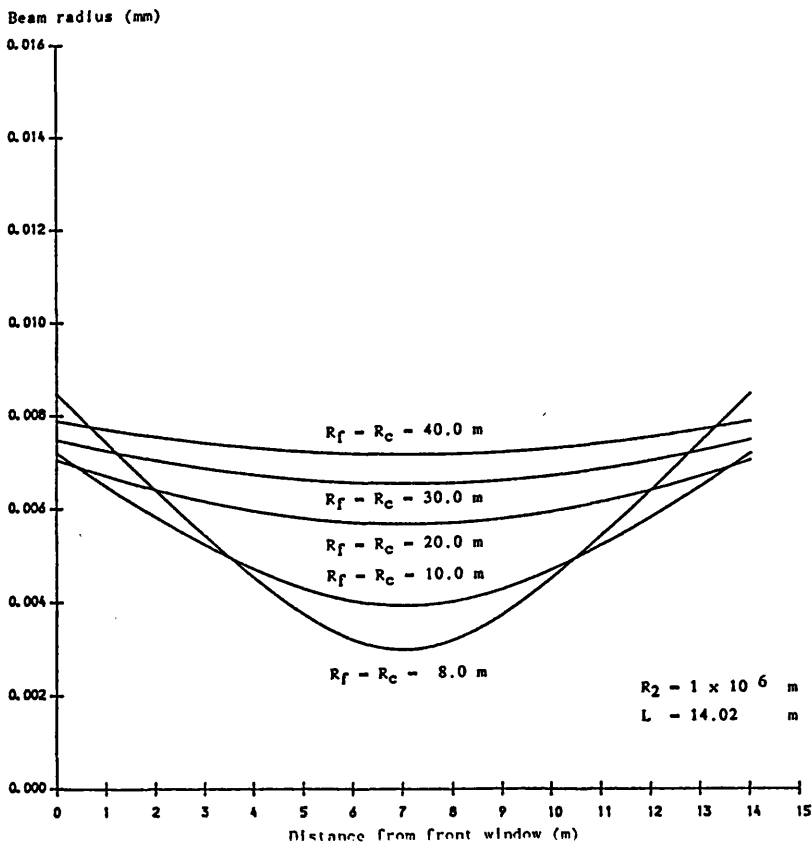


FIGURE 5.29 BEAM RADIUS OF THE TEM_{00} MODE FOR 11 PASS, SYMMETRIC RESONATOR

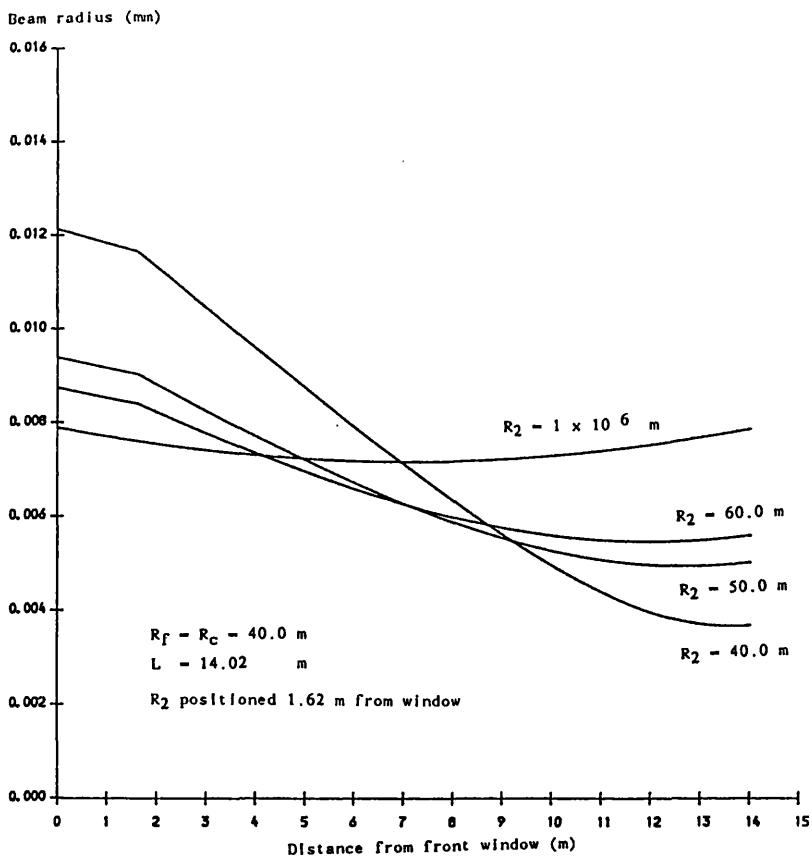


FIGURE 5.30 AFFECT OF THE INTERNAL FOCUSING OPTIC

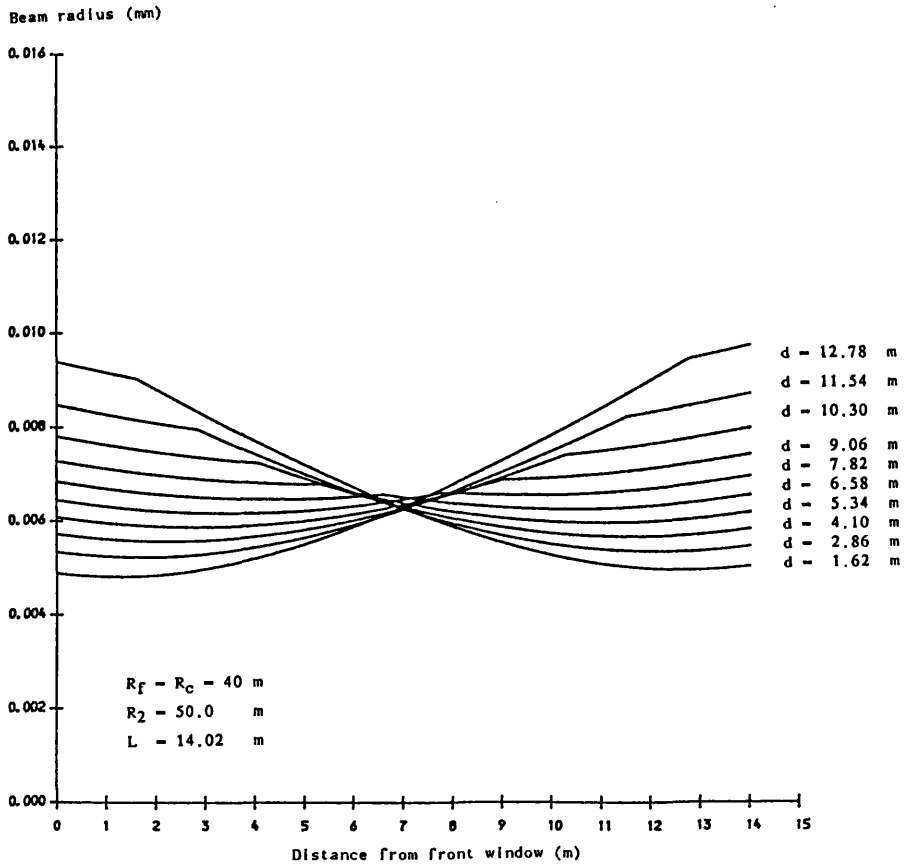


FIGURE 5.31 AFFECT OF THE INTERNAL FOCUSING OPTIC AT DIFFERENT POSITIONS

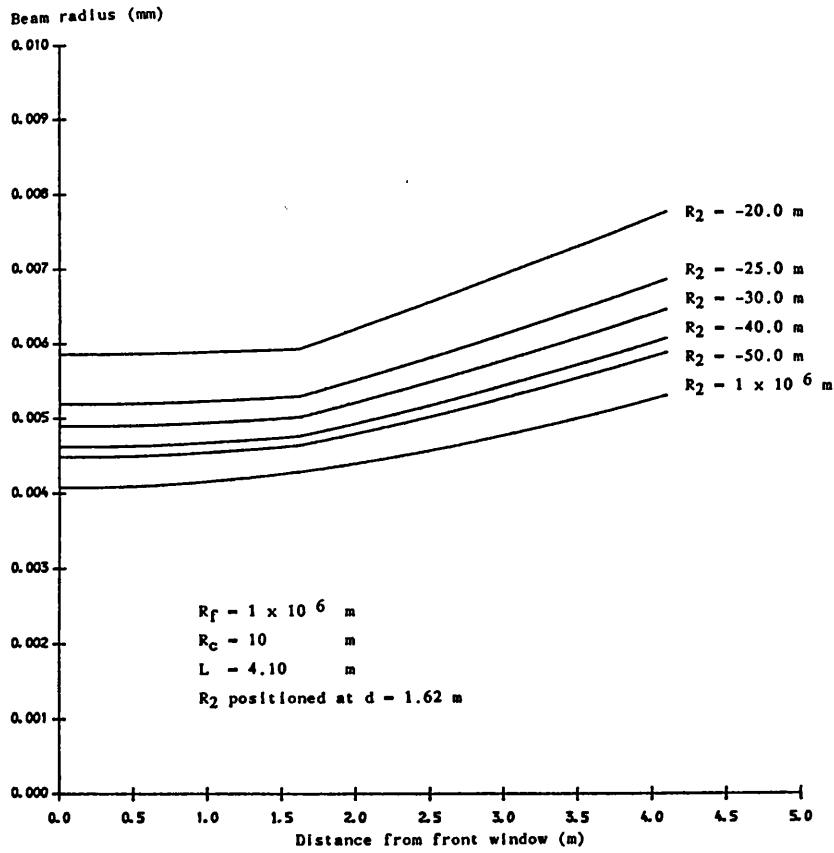


FIGURE 5.32 BEAM RADIUS OF TEM_{00} MODE FOR 3 PASS, CONCAVE-CONVEX RESONATOR

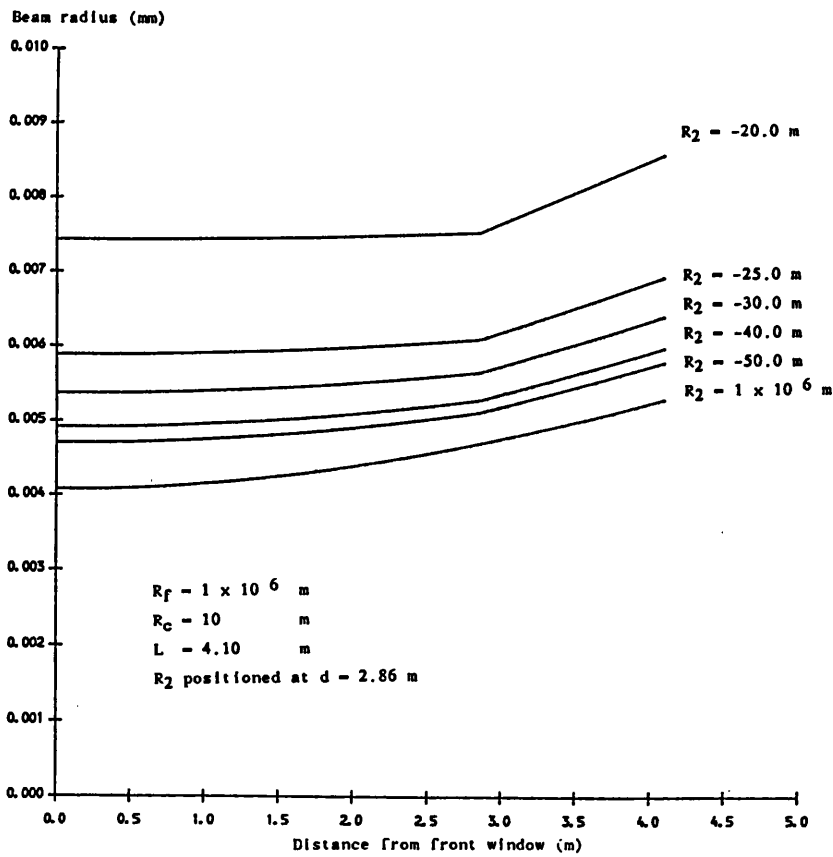


FIGURE 5.33 BEAM RADIUS OF TEM_{00} MODE FOR 3 PASS, CONCAVE-CONVEX RESONATOR

CHAPTER SIX

CONCLUSIONS AND FUTURE WORK

6.1 CONCLUSIONS

The steady state E/N values were measured for a selection of gas mixtures, and the effects of CO were examined. The results compared favourably with theoretical predictions.

Sufficient laser output power has been obtained to successfully demonstrate the non-conduction limited interaction processes occurring at the workpiece (see Appendix E1).

Overall, the laser output pulse energy has been increased by an order of magnitude and the laser frequency by about a factor of 4. The maximum laser pulse energy was 0.13 J for the ballasted electrode system and the 5 pass resonator. However, over 0.1 J has been obtained from the planar electrode geometry with only a single pass resonator. This was achieved by positioning the discharge thyatron (T2) close to the discharge anode, reducing the inductance L_a on the anode of T2 from 36 μH to about 9 μH , and reducing the mismatch in impedances between the PFN and discharge by increasing the gas pressure. It was shown that reducing L_a increased the pulse laser output energy, the plateau and the peak power, and reduced the delay time between the start of the current and laser output pulse. Interestingly, reducing L_a seemed to have a greater affect on the peak power than the plateau power.

It is clear from the literature and the present work, that fast switching circuits are needed in order to develop stable, uniform glow discharges. Moreover, the fast circuits maximise the preionisation electron density, which consequently maximises the laser output.

To determine the efficiency of the trigger wires at creating VUV flux, the parameter ξ was introduced, and defined as the ratio of 10^{10} As^{-1} to the measured rate of change of current. It was found that the effect of reducing the coupling capacitor (C_c) was to reduce the value of ξ . For example, for $C_c = 20 \text{ nF}$ it was found that $\xi \approx 313$; and for $C_c = 5 \text{ nF}$, $\xi \approx 15$. However, there was no significant difference in the discharge stability for these values of coupling capacitor because in practice, it is required that $\xi < 1$. The value of E/N between the trigger wires and the cathode when this gap breaks-down, was calculated to be approximately $2 \times 10^{-15} \text{ V cm}^2$, and consequently, it is expected that some

preionisation will occur.

It was observed that the anode voltage, at the moment the discharge thyatron was triggered, was not at ground potential. This was attributed to the stray capacitance across T2 which coupled a small fraction of the PFN charging voltage to the anode. It is possible that this has a beneficial effect on the discharge stability, as this voltage will naturally tend to pull the preionising electrons away from the trigger wires into the main discharge volume.

Patterns were observed on the electrodes which corresponded to the positions of the trigger wires. It was proposed that this was due to non-uniform sputtering processes occurring in the discharge, as a result of the non-uniform preionising electron density. Moreover, this has the effect of reducing the discharge volume, and consequently the laser gain. The initial electron density was estimated to be about 10^9 cm^{-3} , however, the patterns on the electrodes tend to suggest that the longitudinal electron density was non-uniform, and a major cause of the discharge instabilities that were observed.

The calculation of the Townsend and streamer breakdown voltages, for a 1:1:8 gas mixture, suggested that if the overvoltage applied to the electrodes is increased, the uniformity of the preionising electron density should be enhanced. The critical distance for a streamer to propagate to ensure uniform glow discharges (z_c), was found to about 3 cm for the applied voltages. However, by increasing the overvoltage, z_c rapidly reduces to a fraction of this value, and the lateral uniformity of the discharge increases; mainly because of the efficient generation of the VUV light and the increased rate at which ionisation processes occur. It was found that gas mixtures rich in N_2 improve the discharge stability, through the increased level of the VUV flux, provided that the concentration of low ionisation potential seedants is sufficient.

The formative time lags were calculated for different preionising electron densities and as a function of the E/N value for the 1:1:8 gas mixture. It was shown that increasing E/N reduces the formative time lag.

The measured formative time lag was found to be dominated by the inductance L_a and the URm74 cable capacitance, where the cable connects the anode of the discharge thyatron to the discharge anode. The cable capacitance was behaving like a large peaking capacitor, and tending to slow down the discharge initiation phase. Partly as a consequence of this, and to minimise the stray inductances, the discharge thyatron was repositioned under the laser cavity.

A PSPICE code was developed to model the effect of circuit components on the transient development of gas discharges, by solving the electron continuity equations. It was found that large values of the peaking capacitance made no significant difference to the initial rate of change of the discharge current. Reducing the circuit inductance increased the rate of change of the discharge voltage and current, and reduced the formative time lag.

A high voltage, independent preioniser was fabricated to improve the preionisation of the system. It was found that the laser pulse energy was maximised for a delay of about 200 ns between the preioniser and discharge thyatron firing. The laser output was comparable to that obtained whilst the trigger wires were capacitively coupled to the discharge anode. The effective inductance of the trigger wires and cathode support structure ($L_{tw} + L_{sc}$) were calculated to be about 2 μH . The peak value and rate of change of the trigger wire current were in excess of 300 A and about $2.7 \times 10^9 \text{ A s}^{-1}$ ($\xi \approx 3.7$) respectively. It is clear that to increase dI_{tw}/dt , this stray inductance must be reduced.

It was observed that the first pulse of a pulse train behaves in a different fashion to subsequent pulses. Generally, the first pulse has higher frequency components and is more erratic. It was proposed that ionised discharge products and/or radiation transitions from metastable states of excited gas species were perturbing the behaviour of subsequent pulses and their discharge breakdown characteristics.

The maximum discharge power, prior to the development of arcs, was increased by positioning longitudinal flow-shaping, upstream and downstream, parallel to the electrodes. The discharge power rating was further enhanced by placing edge flow-shaping, transversely, across the ends of the electrodes (see Chapter 4).

To quantify the performance of the flow-shaping the gas velocity profiles were measured in two dimensions. It was found that the longitudinal gas velocity profile was perturbed by the presence of the support structures on the gas inlet orifice and where the inlet diffuser flow splitters join the duct nozzle. The gas velocity varied by about 21 % and 34 % for the cases with and without flow-shaping respectively. This causes non-uniform cooling and introduces density perturbations into the discharge medium, and an increased probability of discharge instabilities growing and developing into arcs.

An attempt was made to make the longitudinal velocity profile more uniform by placing aerofoils around the support structures, these experiments proved inconclusive; however it was found that there was no appreciable improvement in

the gas velocity profile with the aerofoils installed.

The clearing ratio for the gas discharge system is dictated by the minimum gas velocity. For low discharge energy densities of 1.25 mJ cm^{-3} the clearing ratio was about 0.7 and increased to above 2 for discharge energy densities of 2.5 mJ cm^{-3} . Using the upstream flow-shaping the minimum gas velocity increased by about 40 %. However, the fractional increase in the maximum discharge power with and without flow-shaping was only about 15 %. It was noticed that the standard error of the mean for the gas velocity measurements was much greater without the flow-shaping installed, particularly in the vicinity of the support structures. It was concluded that although the gas velocity increased by 40 % when the flow-shaping was inserted, the gas flow was more turbulent without it due to the poor flow dynamics. Consequently, the discharge operated at a higher than expected power loading before arcs formed. Inserting stainless steel mesh into the upstream flow, with the flow-shaping installed, failed to improve the discharge stability. It was assumed that no useful increase in the turbulence was generated in the discharge region because the mesh was positioned too far upstream.

Measurement of the transverse gas velocity profiles indicated that the boundary layers adjacent to the electrodes surfaces were large, typically between 7.5 and 10 mm. This was particularly so near the cathode, and was attributed to the trigger wires restricting the flow.

Two prototype, segmented, ballasted electrodes were fabricated and tested, they yielded substantial improvement over the previously tested electrodes. The maximum discharge frequency was above 5 kHz, and the maximum discharge power was approximately 11 kW.

Using the ballasted electrode and increasing the He content of the gas mixture, increased the maximum discharge power rating. The effect of reducing the pulse length, for a given gas mixture, was to increase the maximum discharge power prior to arcs forming. However, this was not found to be the case for a 1:1:8 gas mixture with a power loading of 11 kW. The $7 \mu\text{s}$ and the $10 \mu\text{s}$ pumping pulse yielded the same discharge power ratings. It was proposed that a different breakdown mechanism was operative at this power loading, that was independent of the pumping pulse length.

The partial breakdown of the ballasted discharge has been investigated, and the number of elements conducting the fault current calculated as a function of the discharge power loading. It was found that the number increased with the discharge

power above a threshold value, below which no breakdown of any segments was observed.

A ballasted system has recently been fabricated where the resistors are housed externally from the laser cavity, however, the system has not yet been tested.

It was apparent that the thyratrons have a low, mean current rating (5 A), which may be exceeded at high PRF. The maximum frequency before the charging switch is overrated is 1 kHz, and for the discharge thyatron its about 250 Hz. Consequently, for the present pulser system, it is recommended that only short bursts are used at high frequency in order to limit possible damage to the thyratrons.

The laser output increased with the number of passes of the resonator through the discharge volume, the maximum number of passes that were tested was 5. Removing the water cooled aperture increased the laser power by an average of about 12 %. The minimum delay time between the growth of the discharge current and obtaining laser output was 4.2 μ s. The corresponding pulse energy was 132 mJ and the plateau pulse power was 17.2 kW. The perspex burn prints indicated that only the TEM₀₀ mode was propagating. Consequently, if the pulse laser output energy is scaled, efficiencies of 9 % and pulse energies of over 0.5 J could be expected.

To assess the development of stable resonators, for the purpose of increasing the modal coupling efficiency, a code was developed which utilised the ray transfer matrix techniques to predict Gaussian beam propagation, for any stable resonator configuration.

An analysis of the performance of 11 pass, symmetric and half symmetric resonators, each with one internal focusing optic, indicated that the diffraction losses were significant and more than one intra cavity focusing optic is required for resonators with a high number of passes.

An extensive data acquisition system was developed to capture data associated with the discharge and the laser output pulse. The pulses were fully analysed and the salient characteristics found.

The non-conduction limited processes were demonstrated by cutting and drilling aluminium, see Appendix E1.

6.2 FUTURE WORK

To maximise the laser output power and operating frequency it is clear that the gaseous discharge and the optical coupling must be optimised. This has already been achieved to some degree, but greater improvement is still needed. From the present work, the areas that need future study and design refinement have been identified.

It is recommended that primary consideration should be given to optimising the flow dynamics. The instrumentation, data acquisition and analysis system have been developed so that the flow profiles can be determined, and any improvements observed. Calculations should be performed to see if it is possible to remove the support structures, without undue deflection of the cavity. However, this will not completely solve the problem. Because, although the system was designed with a nozzle to produce a uniform flow, the perturbations produced by the diffuser flow splitters do not appear to have been eliminated by the flow expansion. Consequently, flow-shaping will need installing in this part of the flow. If a uniform flow cannot be achieved over the length of the gas inlet orifice, it may prove simpler to install 2 or 3 independent pairs of electrodes over the regions where the flow is uniform.

To minimise the boundary layers at the electrodes flow-shaping should be designed to redirect a portion of the flow over the trigger wires and anode or perhaps, a low power blower could be strategically positioned.

It would be interesting to model the breakdown mechanisms of the discharge with non-uniform flow conditions and large boundary layers, in order to understand the physical mechanisms occurring.

The effect of introducing turbulence into the discharge region should be studied, by, for example, inserting mesh into the upstream gas flow. However, it is recommended that a series of experiments are performed to optimise the mesh size and position relative to the electrodes.

The spatio-temporal laser gain, the VUV flux, preionising electron density, and the concentrations of low ionisation potential seedant (LIPS) gases and N_2 should be measured for different pumping circuit configurations. This will provide important information on the physical processes occurring in the discharge, a means to quantify the results and optimise the preionisation.

Two generic routes are clearly available for the development of the electrode geometry, namely: optimisation of the segmented ballast electrode or using a single pair of uniform field electrodes.

Experiments should be performed on the ballasted system where the resistors are housed and cooled externally from the laser cavity. This facilitates optimisation of the ballast resistance prior to development of an expensive, ceramic ballasted system. Moreover, the prototype ballasted system has been successfully demonstrated for discharge powers up to 11 kW, which gives confidence in the development of this electrode geometry. However, the inductance on the anode of the discharge thyatron was high, i.e. $L_a = 36 \mu\text{H}$. It is recommended that the ballasted system is tested with the low inductance, H.V. preioniser supply in order to maximise the preionisation electron density. It may prove useful to develop a preionising system that is electrically independent of the ballast system, i.e. so that the preionising current is not damped by the ballast resistance.

A pair of single electrodes could be used where the circuit inductance has been minimised and the preionisation optimised. The supply for the preionisation source has been developed, future work should concentrate on using this in conjunction with a low inductance, main discharge circuit. This necessitates development of a different arrangement for the preionisation. As a specific example, the uniform field electrodes which have been fabricated, should be tested with the trigger wires running longitudinally, the length of the discharge, near the edge of the electrodes, see Figure 6.1. The optimum value of the coupling capacitors C_{c1} and C_{c2} can be found to provide the maximum level of preionisation for this system. Moreover, if $C_{c1} \neq C_{c2}$, then effectively two preionisation pulses occur. The independent preioniser could be used to drive either or both of these auxiliary discharges. This design avoids the shadowing effect of the trigger wires, and the reduction in the discharge volume and laser gain that was discussed in Chapter 3.

The laser should be operated at gas pressures near the optimum transfer efficiency from the PFN to the load. This naturally means that the laser output will increase because of the higher gas pressure. However, to operate successfully at these elevated gas pressures it is critical that the rise time of the discharge is fast, i.e. the circuit inductance is low.

From the calculation of the inductance of the trigger wires and cathode support, it is clear that a redesign of the cathode support structure and the electrical connection to the trigger wires is necessary to maximise the preionising current. Large copper sheets should be used to ground the cathode.

To limit the rate of rise of current through the discharge thyatron, a saturable magnetic switch can be positioned in series with the discharge anode. When the discharge thyatron switches, the stray cable capacitance is rapidly charged, while the magnetic switch begins to saturate. When the switch has fully saturated, the discharge voltage rapidly rises at a rate determined by the inductance of the circuit and the stray capacitance. By this time, the thyatron has triggered into full conduction and is passing substantial current.

Magnetic pulse compression stages can be implemented on the H.V. preioniser to extend the life of the preioniser thyatron. Moreover, the preioniser voltage can be increased, through the resonant effect, to values above those available from the present design.

The resonator should be designed so that the fold mirrors are simpler to align, for example micrometer mounts can be incorporated. This is relatively simple for 3 passes but the design becomes complex, due to the spatial constraints, for a high number of passes. It was found that for high frequencies the discharge was spatially displaced from the electrode region. To optimise the resonator alignment, it is possible for one leg of the resonator to be positioned on the downstream side, see Figure 6.2.

The diameter of the aperture on the front window mount should be increased to allow operation of the laser in a higher order mode. This will increase the coupling of energy from the discharge region, but at the expense of a poor output mode structure, which is undesirable for material processing. Efficient extraction of the energy means that effectively, more energy can be deposited into the discharge region prior to the development of arcs.

Measurement of the laser gain will indicate if it feasible to use an unstable resonator, where large gains per transit are desirable. If the gain is large, the use of mirrors with non-uniform reflectivities will increase the quality of the output mode shape. Unstable, self-filtering resonators can be used where the quality of the beam and extraction efficiency are extremely high.

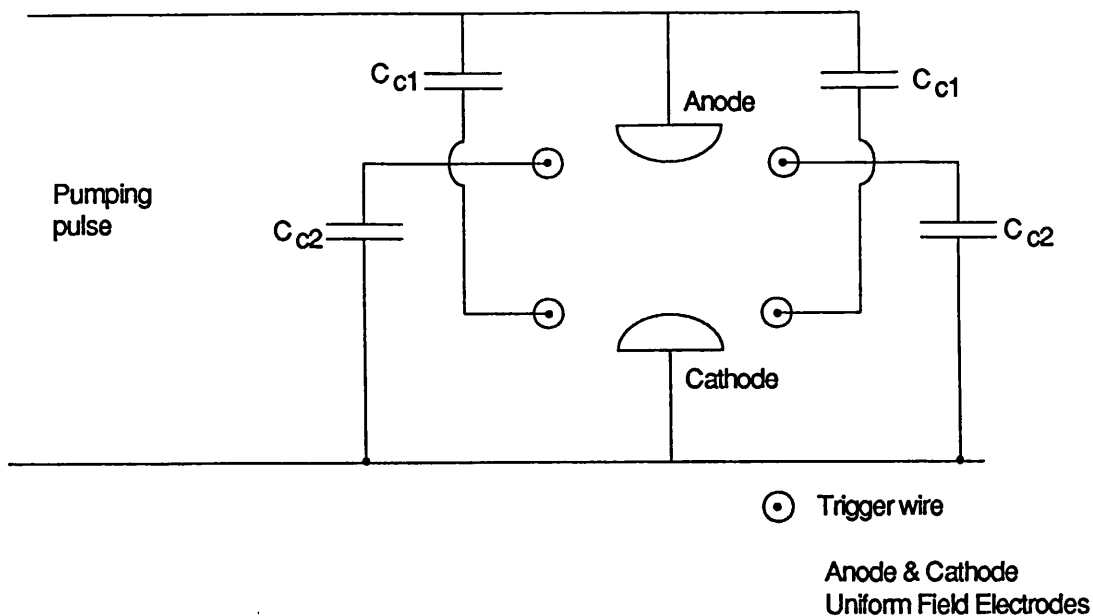


FIGURE 6.1 UNIFORM FIELD ELECTRODE PREIONISATION GEOMETRY

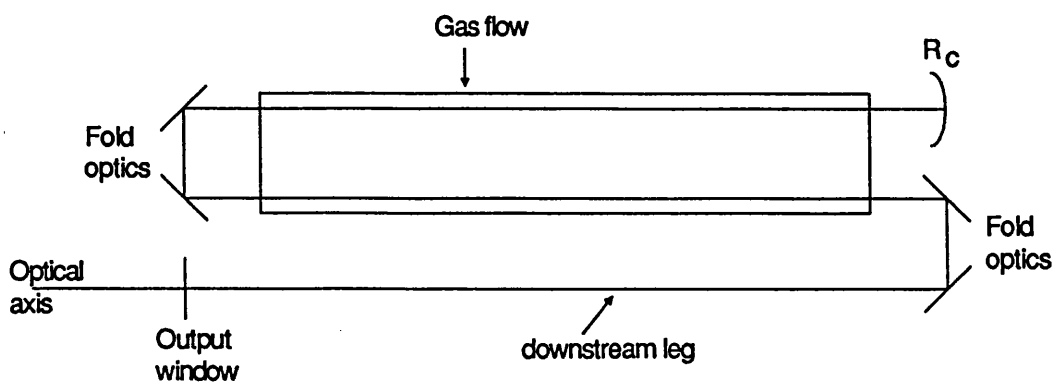
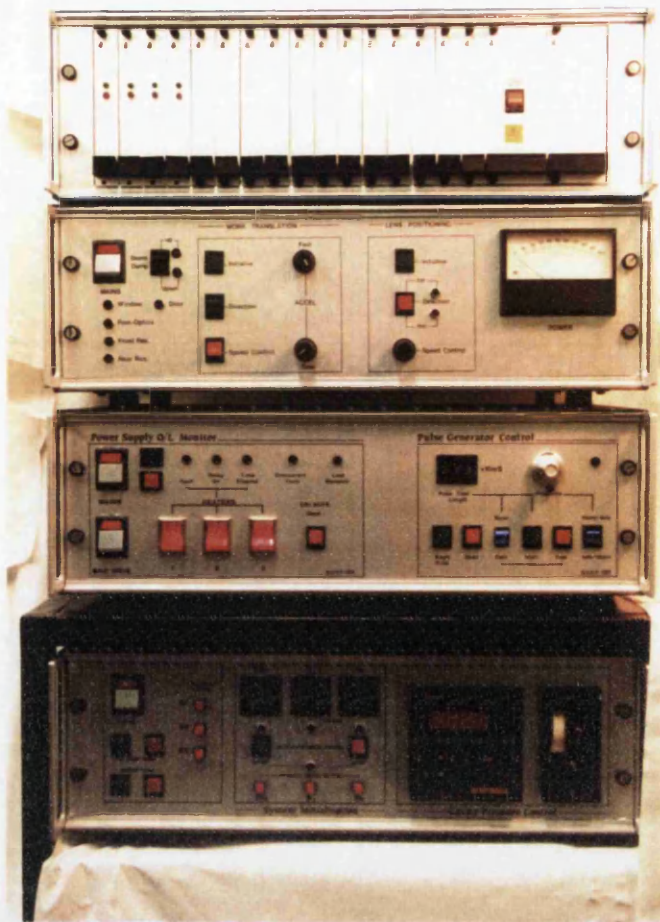


FIGURE 6.2 OPTIMUM 3 PASS RESONATOR DESIGN



AQUISITION

FORE-OPTICS

PULSER

GAS RECIRCULATOR

PLATE 1 LASER SYSTEM CONTROL UNITS

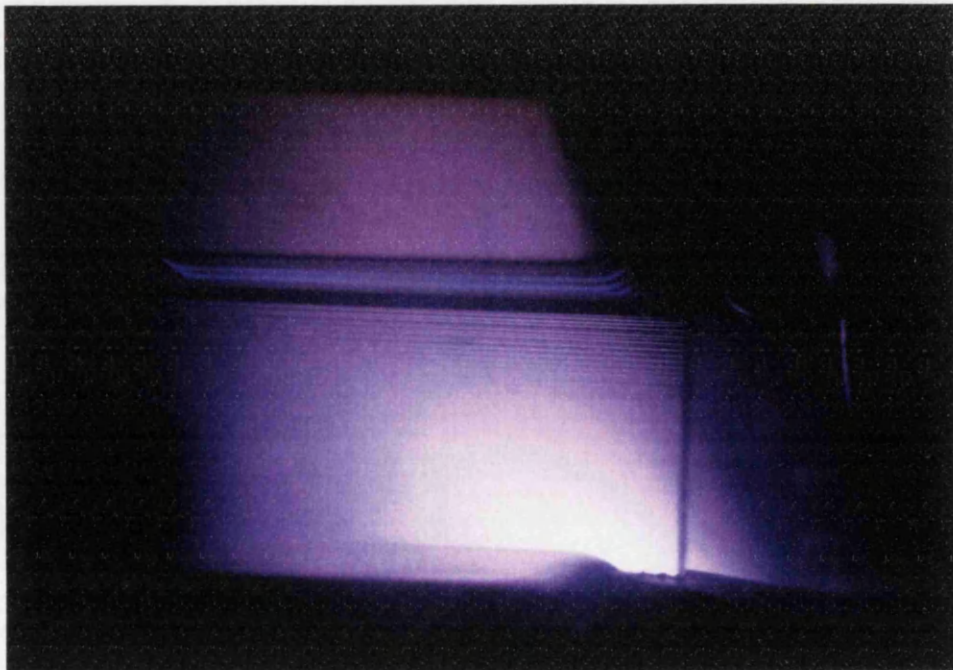


PLATE 2 GAS DISCHARGE

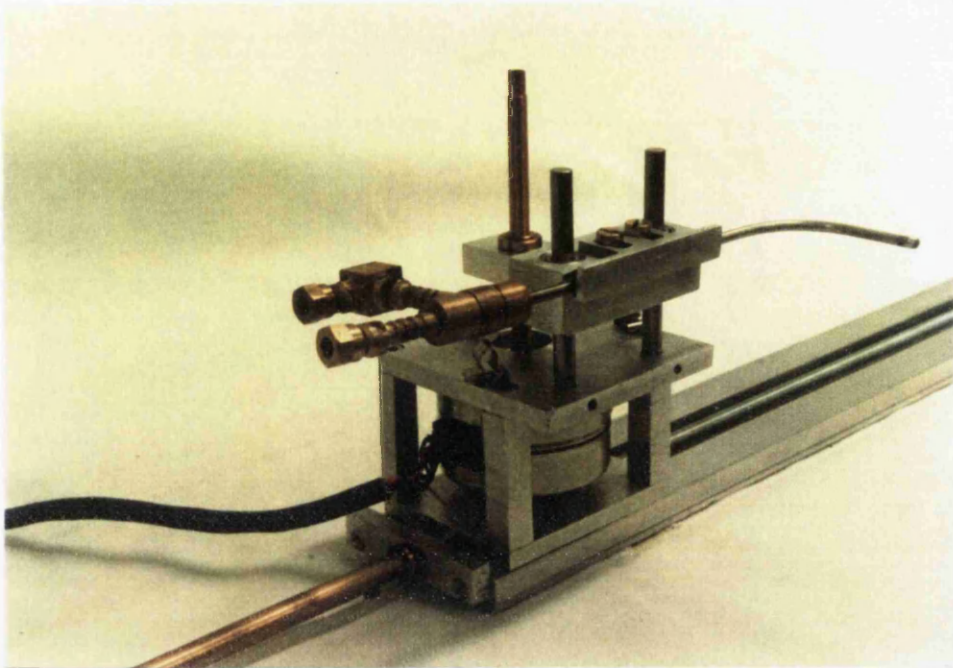


PLATE 3 PITOT-STATIC TUBE AND MOUNT

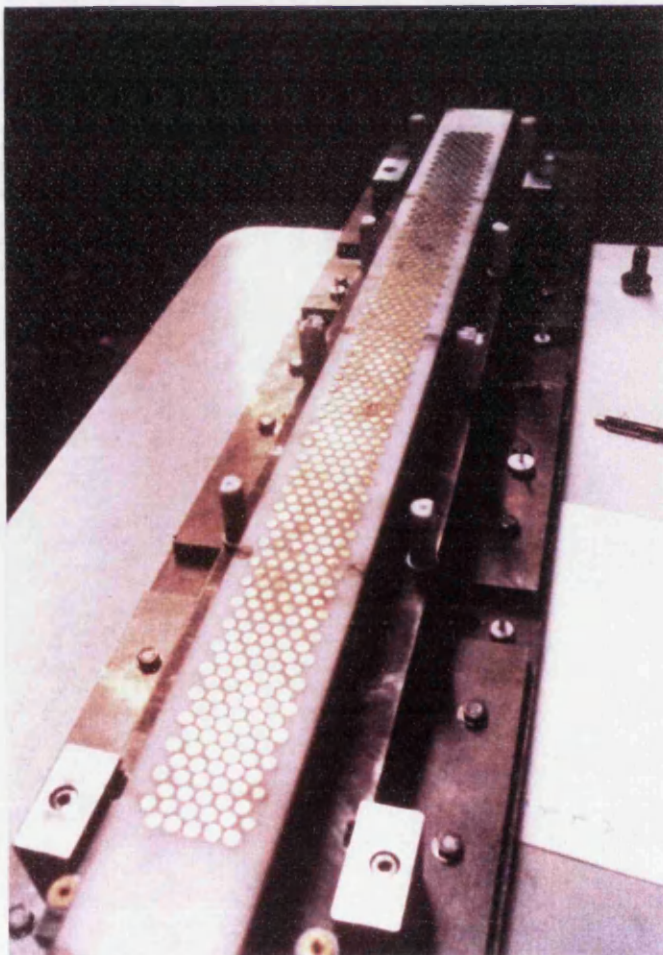


PLATE 4 BALLASTED ELECTRODE

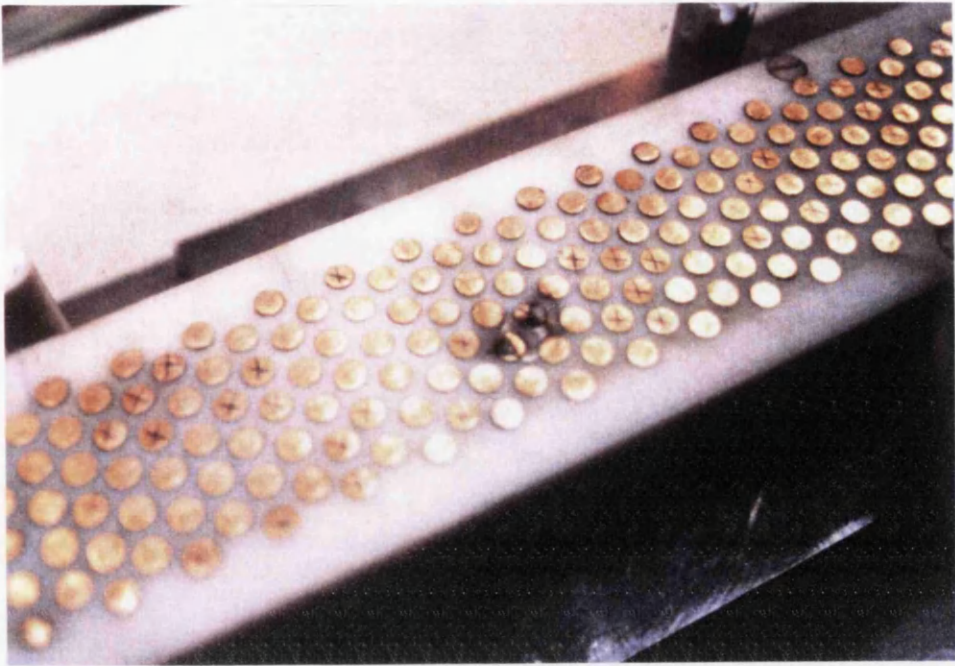


PLATE 5 BALLASTED ELECTRODE

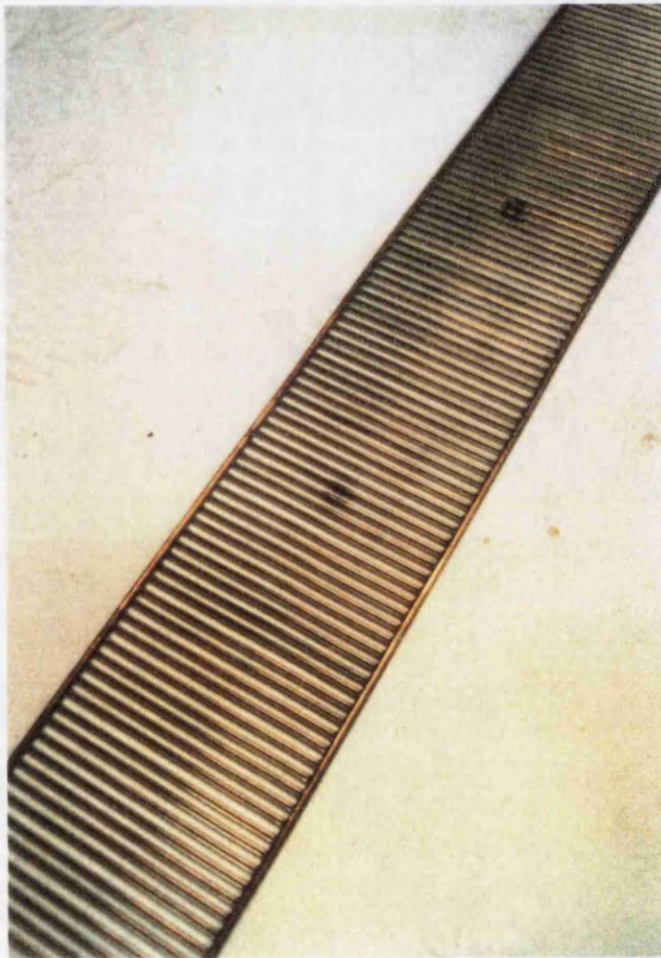


PLATE 6 TRIGGER WIRES

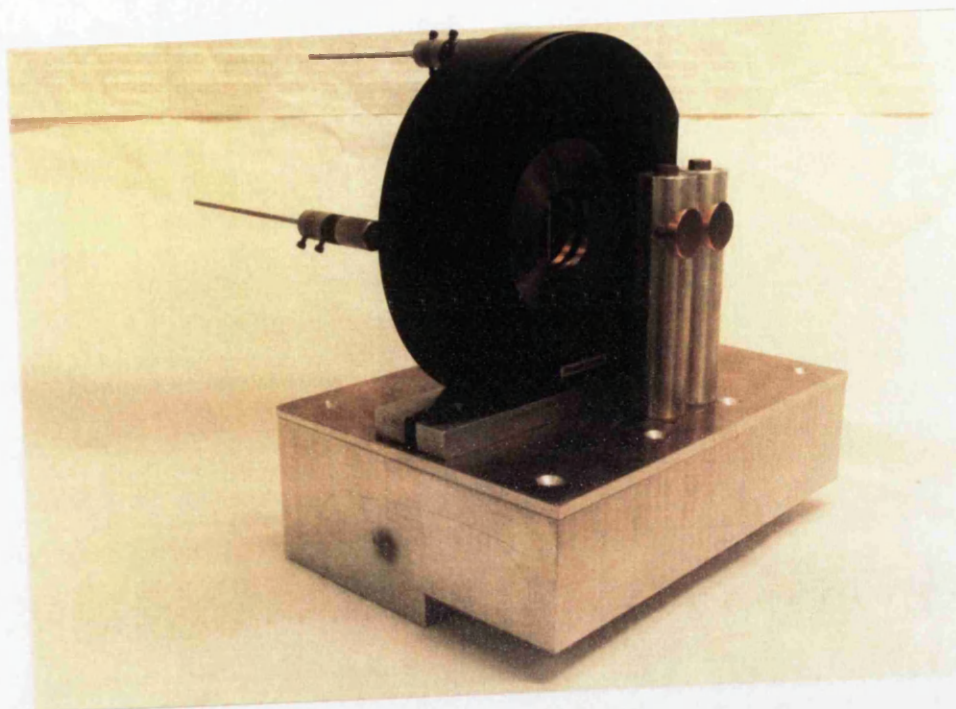


PLATE 7 5 PASS RESONATOR, REAR OPTICS

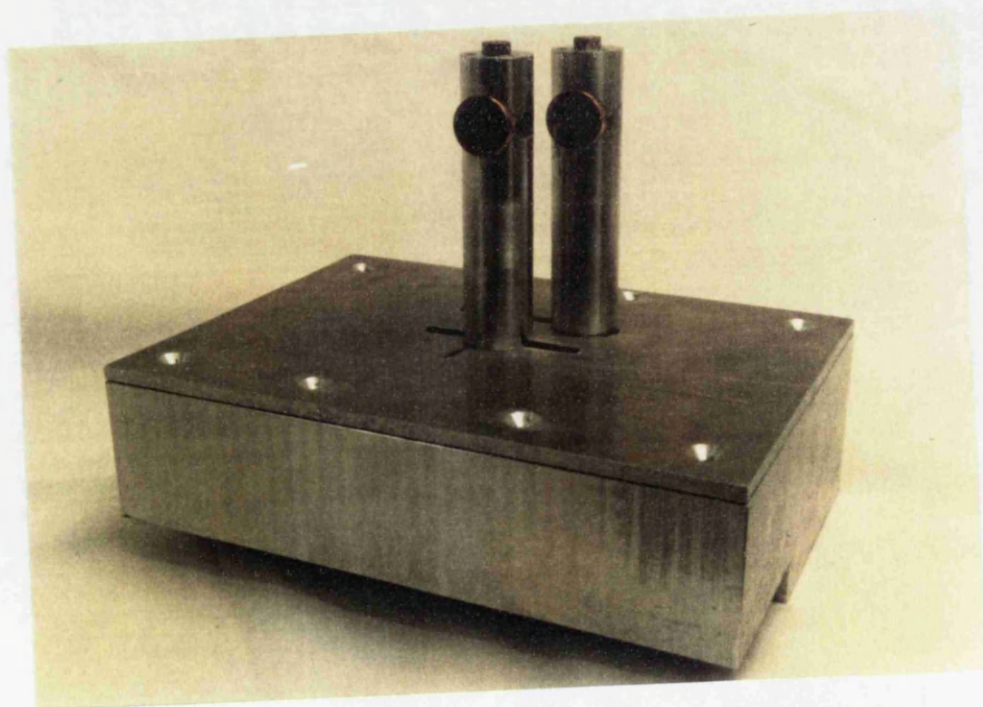


PLATE 8 5 PASS RESONATOR, FRONT FOLD OPTICS

APPENDIX A1 POWER SUPPLY/LASER INITIALISATION PROCESS

Obtain vacuum leak rate $< 1 \text{ mb hr}^{-1}$.

1. Open S3 and turn vacuum pump on. Allow about 20 to 30 minutes for system to evacuate from ambient pressure. Meanwhile, some of the following can be performed.
2. Initiate the control units and auxiliary power
3. Turn on mercury arc rectifiers, i.e. excitation control. Check that MAR's are operating correctly by visually inspecting the discharge. Allow a warm up period of 15 minutes. While waiting perform functions 4 - 9.
4. Initiate power supply for gas recirculators.
5. Turn thyatron heaters on: T1, T2 and if the tailbiter is in operation T3. Allow a warm up period of at least 5 minutes.
6. If a satisfactory vacuum has been obtained: close S3, turn pump off, add required gas mixture.
7. Insert main fuses and turn on.
8. Set the trips.
9. When the warm up periods have elapsed initiate contactor.
10. Turn gas recirculator cooling water pump on and check flow.
11. Initiate blowers.

The time to complete the above initialisation process is approximately 20 minutes. The cavity is now ready for excitation from the pulser.

APPENDIX A2 CX1528 THYRATRON SPECIFICATION

Peak forward anode voltage	35	kV	max
Peak anode current	3500	A	max*
Average anode current	5	A	max
Rate of rise of current	10	kA/ μ s	max
Anode heating factor	70×10^9	V A p.p.s.	max

Cathode heater voltage	$6.3 \pm 7.5 \%$	V	
Cathode heater current	36.0	A	
Reservoir heater voltage	$6.3 \pm 7.5 \%$	V	
Reservoir heater current	5.0	A	
Tube heating time	5.0		min
Cathode flange temperature	150.0	$^{\circ}$ C	max

* For pulse durations t_p longer than $3 \mu\text{s}$ the peak current I_p must be such that

$$I_p < 3000 \left[\frac{3}{t_p} \right]^{0.5} \quad \text{A2.1}$$

Where t_p is in micro-seconds. For $t_p = 10 \mu s$ then $I_p < 1643$ A. However, it should be noted that the maximum rate of rise of current through the thyatron is limited to 10^{10} As^{-1} .

Reference: "Hydrogen thyatron product data". EEV, Chelmsford, Essex, U.K.

APPENDIX A3 SPOT KNOCKING

Ageing thyatrons lose the ability to hold off their specification voltage; this is due to protrusions or troughs on the anode/cathode surface. The resultant of this surface damage is a localised increase in the electric field between the anode and cathode; and consequently, an increased probability of the thyatron breaking down at a lower anode voltage. During a series of experiments investigating the performance of the discharge it was found that T1 (the charging thyatron) was not holding off the required voltage. An effective short circuit existed on the charging side of the network. As soon as the network energy was deposited into the discharge the charging cycle began immediately.

Once the thyatron breaks down electrons drift towards the high potential side, generally the anode, and ions drift toward the low potential side, generally the cathode. The role of the ions is crucial in spot knocking because of their heavy mass. Ion bombardment erodes and smoothes any protrusions or troughs on the cathode surface. However, surface damage may be present on either the cathode or anode surface, for this reason the conventional anode is taken both positive and negative to ensure erosion of both surfaces. This is most easily achieved by employing A.C., although D.C. can be used the physical connections to the anode and cathode have to be reversed, this imposes on the time constraints for, which is in reality, a relatively trivial problem.

The circuit that was used to spot knock the thyatrons is shown in Figure A3.1. The $5 \text{ M}\Omega$ resistor limits the current drawn from the transformer. The thyatron is placed in parallel with a series R-C combination, where the resistor has a value of 10Ω , and is used to damp any ringing in the circuit, the peak current is limited to a maximum of 3500 A (see Appendix A2). The capacitance was $200 \text{ pF} \Rightarrow X_c = 15.9 \text{ M}\Omega$ at 50 Hz . The voltage on the primary side of the transformer is supplied by a $0\text{--}240 \text{ V}$ variac. The H.V. transformer is rated at 20 kV RMS , with a maximum RMS current of 10 mA . The variac output voltage is gradually increased until the thyatron breaks down. A soft crackling sound is heard, this is the sound of arcing in the thyatron, the arcs erode the protrusions and troughs.

After a few seconds the noise stops and the thyatron can now hold off the voltage across the series R-C. The breakdown of T1 occurred at nearly 10 kV. The voltage is increased further until the thyatron holds off the necessary voltage. The voltage was successfully taken to the full rating of the transformer and the maximum peak voltage that was obtained across the thyatron was about 21 kV. It is seen that a considerable fraction of the voltage is dropped across the 5 MΩ resistor. Capacitor C was changed to 100 pF, thus, $X_C = 31.8 \text{ M}\Omega$. The voltage drop across the thyatron was then increased to about 24 kV. The thyatron was tested on the pulser and its performance had improved such that it now functioned correctly. It should be noted that the cathode heater and reservoir connections are all earthed.

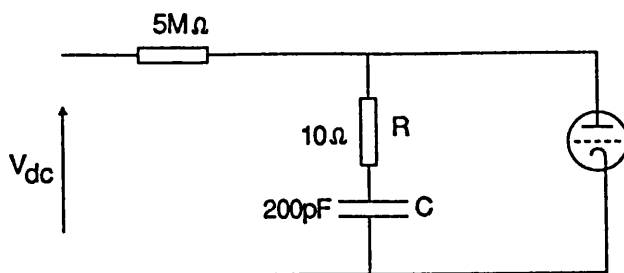


FIGURE A3.1 SPOT KNOCKING THYRATRON CIRCUIT

APPENDIX A4 ROOTS BLOWERS SPECIFICATION

Type: Starvac, Mechanical Booster Pumps, Series EGDB 7 500.

2 off, operating in parallel

Lubrication: Energol ES460, CSS 175/460a (BP)

Direct drive displacement	7418	m ³ /hr
Direct drive	2880	r.p.m.
Normal motor power	18.2	kW

The pulleys that are available and the expected flow through the laser cavity (area $\approx 400 \text{ cm}^2$) are detailed below. The pulleys diameters are denoted by D_i where $i = 1$ or 2 . D_1 corresponds to the pulley which connects to the blower shaft.

D ₁	D ₂	r.p.m of motor shaft	gas velocity (ms ⁻¹)
160	160	2880	103.0
160	190	2453	87.8
190	236	2354	84.2
236	315	2195	78.5
160	236	1972	70.5
315	500	1836	65.7
190	315	1759	62.9
160	315	1482	53.0
236	500	1377	49.3
190	500	1110	39.7
160	500	935	33.4

Reference: Starvac, Mechanical Boosters Instruction manual. Publication No. VPD/EGDB/1083. G.V.E Ltd, Vacuum Engineers, Manchester U.K.

APPENDIX A5 INSTRUMENTATION

DIGITAL OSCILLOSCOPES

LeCroy 9400¹

2 channels
DC-125 MHz
2 ns/div to 100 sec/div
5 mV/div to 5 V/div

Tektronix 468²

2 channels
DC-100 MHz
20 ns/div to 0.5 sec/div
5 mV/div to 5 V/div

Waveform processing options

HIGH VOLTAGE PROBES 2 Off Tektronix P6015³

Attenuation 1000:1
Bandwidth DC - 75 MHz
Rise time 10 ns
Maximum input peak voltage 40 kV
(reference P6015 probe, TEK Instruction Manual)

CURRENT PROBE Pearson 10:1 current transformer⁴

Rise time 2 ns
Bandwidth 100 Mhz

References:

1. "LeCroy model 9400 Digital oscilloscope operators manual". LeCroy, 1987.
2. "Tektronix 468 Digital storage oscilloscope service volume 1". Tektronix, 1981.
3. "P6015 probe, TEK Instruction Manual". Tektronix, 1987.
4. "Pearson current probe manual". Pearson.

APPENDIX A6 DATA ACQUISITION SYSTEM (DAS)

The task of acquiring data from multi-variable systems is alleviated by using computerised, data acquisition systems (DAS). A DAS is developed to collect and analyse the data associated with the laser system.

To quantify the laser performance there are several important system characteristics that have to be found, they fall into three distinct regions. Firstly, those that are associated with the pulser performance, for example: the DC voltage and the PFN voltage. Secondly, those that are due to the discharge, for example: the E/p value, the discharge breakdown time, the peak and plateau values of the discharge voltages and currents. And lastly, those that are associated with the laser output, for example: the laser pulse length, delay time, total pulse energy, peak and plateau pulse powers, and the mean power. A further set can be associated with the material interaction processes, however, this is not currently considered. The performance of the gas recirculator could also be ascertained by monitoring the gas and water cooling temperatures with the DAS.

At the heart of the data acquisition system is a PS/2 IBM computer, and as with any computer based system, it can be divided into its hardware and software components. Figure A6.1 shows the configuration of the hardware side. The oscilloscopes available were the Tektronix 468 and the LeCroy 9400, both are digital and have bandwidths of 100 MHz and 125 MHz respectively. The 468, however, only has a 10 MHz useful storage bandwidth [A6.1] and achieves the 100 MHz resolution for repetitively pulsed waveforms. Because of the higher bandwidth, the LeCroy was used to measure the discharge properties and the laser output pulses, while the Tektronix was relegated to monitor the pulser performance, for example, the PFN voltage. A digital volt meter - type, Keithley 175 - was also used within the system, in particular for the measurement of the gas velocities which is discussed in Chapter 4. These three devices were connected to a PC488 card at the rear of the computer via the GPIB interface. Each device can be accessed individually through a specific device address, for example, the LeCroy was given the address "10". The normal GPIB protocol was used [A6.2]. A MetraByte Dash 16, 16 channel, ADC card [A6.3], with a bandwidth of 16 kHz was used to collect data from the gas recirculator instrumentation, see Section 2.4.5. The interface electronics, consisting of amplifiers and analogue, multiplexed switches were developed, see Plate 1, but the system was not hard wired due to an expected move of the laser structure. A plotter and a printer were attached to the system to provide hard copies of graphs etc. The PS/2 was linked to the departmental computing facilities and the campus 3090 IBM mainframe. This

provided the ability to download the captured experimental data and compare it with theoretical results that were obtained from the suite of software codes developed for assessment of the theoretical laser output performance [A6.4,A6.5,A6.6]

A6.1 DAS Software Development

When data is collected in real time, unforeseen events can occur that were not taken into consideration when the DAS was written. For this reason, the DAS must be flexible so that control can be passed, at any time, to a particular part of the system. Consequently, the DAS was developed so that it was totally user friendly and flexible enough to accommodate unexpected circumstances.

The ASYST programming language [A6.7] was used in developing the DAS. This is a high level language specifically designed for use within a data acquisition and analysis environment. The design structure allows the user to define macro commands – called colon definitions – that are created within a file and can be executed once the file is loaded. The structuring of an ASYST program is naturally hierarchical. A simple colon definition is first defined, which can be used in subsequent colon definitions. Thus, a simple word is capable of executing a complex series of events; for example, triggering the oscilloscope, acquisition of the waveform, processing and analysis. If each colon word is individually tested this reduces the problem of locating software bugs in the complete code. ASYST forces the programmer to write the software code in this procedural format.

As with any software program certain criteria must be established in order to write a concise, easily readable and flexible code. To satisfy this, the system software was developed using a modular approach, several advantages are then apparent. For example, the code is easily debugged and when one module is working it can be used, while other modules are being developed. The data collection method used, for a particular experiment in this thesis; was dependent on the state of development of the DAS software. It was either collected directly from the instrumentation via manually reading the oscilloscope with cursor controls etc. or via the DAS. When the software was being tested both techniques would be used, this provided an efficient method of debugging the software.

Figure A6.2 shows a schematic of the program and highlights the modular structure that was adopted in writing the DAS. When the program is initiated 8 options exist, these are seen at the top of Figure A6.2. To initiate any of these options

the appropriate function key is pressed. Each possible option is briefly described with particular attention given to the option initiated by function key 1 – denoted by F1 – and called Multi data capture. Most of the DAS development concentrated on option F1, enabling data capture pertinent to the discharge experiments and the laser output. Two distinct possibilities were developed for data acquisition, in each case the LeCroy oscilloscope was used. Firstly, the discharge voltage and current were captured, and secondly, the discharge current and the laser output power. These two data sets were classed as V-I or P-I data sets respectively. It was necessary to capture the data in this manner because the LeCroy 9400 only has 2 channels.

The term "waveform" is used to describe the captured signal and is normally quantified to be a voltage, current or laser output power. In practice, the quantity observed by the LeCroy is a voltage due to the transducers characteristics. For example, the current is converted into a voltage by the Pearson current probe and the output laser power into a voltage by the detector: either the photon drag monitor or the CMT detector. A summary of the characteristics of the oscilloscopes and the measuring transducers that were used with the data acquisition system are given in Appendix A5.

A6.2 Pulse Characteristics

The DAS must have the capacity to analyse the captured data, in order to achieve this some fundamental properties of the pulse shapes must be defined. Figure A6.3 shows three typically observed waveforms; i.e., the discharge voltage and current and the laser output power. Several characteristics are defined which are common to all the pulses and can be seen in Figure A6.3. They are: the plateau, the maximum waveform value and the 10 % value. The 90 % level is found for the voltage and current traces. The rise times of the voltage and current traces are found, and defined as the time taken for the pulse to rise from 10 % to 90 % of the peak value of the waveform. The breakdown time for the V-I data set is defined as the time between the 10 % values for the voltage and current trace. The delay time for the P-I data set is defined as the time between the 10 % levels of the current pulse and the laser output pulse. The breakdown and delay times are important quantities in appreciating the performance of the discharge and the laser, they are discussed in depth in Chapters 3 and 5. The total information that is abstracted from the pulses during the analysis is shown in Table A6.1.

Table A6.1 Pulse characteristics for the V-I and P-I data sets

V-I Data Set	
Maximum Voltage	Maximum Current
Plateau Voltage	Plateau Current
Voltage risetime	Current risetime
Rate of rise of voltage dV/dt	Rate of rise of current dI/dt
Breakdown time	
Joules input into the discharge (JIP's)	
E/p value	
P-I Data Set	
Maximum laser Power	Maximum Current
Plateau laser power	Plateau Current
Joules output from the laser (JOP's)	Current risetime
Delay time	Rate of rise of current dI/dt

A6.3 DAS Software Description

The operation of each function key, as shown in Figure A6.2, is briefly described.

F1 MULTI DATA CAPTURE

If the function key F1 is pressed two options exist, namely: collect a number of waveforms (NSTAT) and store the last one or store all of them. If F1 is now pressed again, a statistical analysis can be performed on the captured waveforms and, the last V-I or P-I waveforms and the statistical data from the complete set can be saved to file. This necessitates analysing the data in real time, whereas if F2 is pressed, because all the waveforms are stored, analysis occurs at a later, more convenient time; however, this option was not often used and is not considered further. Assuming that F1 is pressed several options are then available. The number of captured waveforms (NSTAT) can be altered, capture of V-I or P-I data sets can be initiated, one data set can be collected and saved to file or a data set can be saved with no analysis of the plateau characteristics. This last option was introduced because of the difficulty in finding an algorithm suitable for reliably finding the plateau values of the waveforms. If the plateau values are not accurately found errors will occur. For example, the calculation of the plateau voltage is used to calculate the E/p value, which will be incorrect if the plateau voltage is wrong. The E/p value is found by dividing the voltage plateau by the electrode gap distance, d , and the total gas pressure, p . Both d and p are input into the computer as constants, see F5-Change Constants. The way in which the plateau values were eventually determined will be briefly described after discussing how the waveform data is sent to the computer.

The time base on the LeCroy oscilloscope is set at $2 \mu\text{s}/\text{div}$. As there are 10 divisions on the oscilloscope, the total time window is $20 \mu\text{s}$. The $2 \mu\text{s}/\text{div}$ gave the best view of the $10 \mu\text{s}$ voltage and current pulses. The waveforms consisted of 2000 data points, where each point corresponds to a 10 ns interval on the time base. This is the maximum resolution of the oscilloscope that is available without using the internal algorithms and averaging techniques of the LeCroy [A6.8], this resolution was deemed adequate. Once the data acquisition is initiated, the oscilloscope is triggered and the V-I or P-I data set is captured, the data is said to be in a raw format. The raw data is then transferred to the buffer of the PS/2 in three data blocks, see Figure A6.4. The first block, called the data header, contains information on the oscilloscope settings; for example: volts/div and the time base settings. The second block, called the data block, contains the waveform data in a "packed format", which consists of an array of numbers where each number represents 2 integers catenated together to form one number. This raw data requires "unpacking", i.e. separating each number into two integer values, and processing in order to establish the true waveform values. The third data block, called the data trailer, contains information on any processing options that were used within the LeCroy oscilloscope, this facility was not employed as all the processing was performed on the PS/2. The raw, unpacked data is converted into the processed data by using information from the data header, and stored in a single dimensional array with 2000 elements. Each array element is correlative to the waveform value over a 10 ns interval. Once processed, the waveform is ready to analyse and the pulse characteristics, as indicated by Table A6.1, can be found.

The pulse characteristics that are given in Table A6.1 were found in the following manner. Basic search routines were available in ASYST to locate the minimum and maximum values of the processed data arrays, hence, finding the peak values was simple. Search routines were developed to find the 90% and 10 % values which enabled evaluation of: the rise times, discharge breakdown time and the laser output delay time. The plateau region was found by dividing the peak value by 3 and searching the array elements to find the positions corresponding to this value on the increasing and decreasing side of the waveform, these positions are labelled by n and m respectively, see Figure A6.5. The array element given by $p = (m-n)/2$ is in the middle of the waveform. A series of values either side of p are averaged and this is taken as the plateau of the waveform. The plateau values that were evaluated using this algorithm gave excellent agreement with the values that were directly measured from the oscilloscope.

F2 ANALYSE DATA

This option is provided to analyse the data stored in its raw format and is introduced because of the option F2 under multi-data capture.

F3 SCOPE FUNCTIONS

The control of the oscilloscope from the computer is achieved from this menu. When the oscilloscope is controlled from the computer it is said to be in remote, this disables the front panel settings on the oscilloscope. If the settings are adjustable from the front panel of the oscilloscope then it is said to be in local control. As the panel settings of the oscilloscope were known for the V-I and P-I data sets no extensive remote control of the oscilloscope was developed. However, a toggle switch was developed to place the oscilloscope either into local or remote control. This option is available under F6 as Local/Remote toggle. Thus, if the front panel settings had to be changed the oscilloscope can be taken out of the remote setting, and the front panel switches enabled.

The LeCroy can save upto 7 panel settings, i.e. the value of Volts/div, trigger settings, time base etc. Options F7, F8 and F9 enable remote selection of three of these panels. This proved particularly useful when changing from collecting the V-I to the P-I data sets, or vica-versa, as different panel setting are needed.

F4 FILE HANDLING

This section provides the facility to: create raw and processed data files with the names defined by the variable strings called filename1 and filename2 respectively, view the filenames, display a directory listing, read data files, observe the fileshape, or template (i.e. the number of comments and the record format). Control can also be passed to F6 - Output selection menu, this avoids having to pass through the mainmenu, where all the possible options are presented, see Figure A6.2.

F5 CHANGE CONSTANTS

As briefly mentioned, many possible parameters exist for a particular experiment. This option exists to specify and save up to 100 constants with each file, providing

a record with the data of the experimental conditions under which the data was collected. The parameters that could be represented were divided up into subsets of the total data. For example, the subsets included data associated with: the power supply, the gas pressure, roots blowers, discharge dimensions and the resonator. Control could be passed to the output selection menu or the data subsets could be saved as default with control passing to the main menu.

F6 OUTPUT SELECTION

Various options for saving the data sets and constants are given with the ability to convert the data to a file with an ASCII format, which can be transferred to the mainframe, as is indicated by Figure A6.1. The analysed data can be printed or viewed on screen.

F7 GRAPHICS

The captured waveforms can be viewed on screen

F8 GAS

This option provides automatic control of the gas system. The system can be calibrated followed by automatic evacuation of the system. When the pressure has remained at 0 mbar or unchanged for 5 minutes, valve S3 is closed and S2 is opened, the preselected gas mixture is admitted until the required pressure is reached. The pressure can be increased automatically in any desired partial pressure ratio. A purge function was introduced in an attempt to reduce any gas contaminants, for example O₂, which can increase arcing in CO₂ gas discharges [A6.9]. The purge function can be used during the pump down procedure. For example, the system is evacuated down to 0 mbar, N₂ is added to a specified partial pressure, for example 500 mbar, and the system is evacuated again. This process can be repeated if it is felt necessary. Instead of N₂, CO could be used as the purge gas as O₂ attaches quite readily to CO via the reaction [A6.10]



This reduces any excessive O₂ concentration in the gas recirculator. The solenoid valves S₁, S₂ and S₃, and the gas admittance valves are controlled via the

computer and an interface card which was developed to couple to the MetraByte Dash 16 card. Figure A6.6 shows the gas control multiplexer circuit. The digital input on the pins A, B, C and D are derived from the PS/2 and are software controlled, their value can be either 1 or 0. Their combined logic state determines which valves are initiated. LED's on the exterior side of the gas control multiplexer enclosure give a visual indication of the state of the solenoids. The pressure is monitored from the output jack on the rear of the Edwards EMV 251 pressure monitor, the system can be calibrated by selecting F1.

A6.4 Gas Recirculator Instrumentation

As the number of input signals on the Metrabyte Dash was limited to only 16, a multiplexing device was fabricated to increase this to a value appropriate for the acquisition of the data associated with the laser system. For example, the sensors around the recirculator (see Section 2.4.5), the output power measured from the cone calorimeter and the DC voltage on the pulser. Using an addressing system from the computer, a maximum of 256 data channels are available for input of the low bandwidth signals, i.e. 16 kHz. The housing for the electronics can be seen in Plate 1, and is labelled as "acquisition".

REFERENCES:

[A6.1] "Tektronix 468 Digital Storage Oscilloscope Service Volume 1", Tektronix, 1981.

[A6.2] "PC488 Programming and Reference Manual". Capital Equipment Corporation, 1987.

[A6.3] "Metra Byte Dash 16 Data Acquisition and Control Reference Manual". Metrabyte Corporation, 1986.

[A6.4] Kharha J. "Optimisation of the output characteristics of a pulsed CO₂ laser for processing materials". Ph.D. Thesis. Department of Mechanical Engineering, University of Birmingham 1979.

[A6.5] Chatwin C., McDonald D., Scott B. "Design of a high PRF CO₂ laser for processing high damage threshold materials". Selected papers on laser design. SPIE Milestone series, Vol. MS 29, Editor Weichel H. pp 425-433, 1991.

[A6.6] Hasan M. "Thermodynamics of transiently pumped CO₂ gas laser plasmas". Ph.D Thesis. Department of Mechanical Engineering, University of Glasgow, 1989.

[A6.7] "ASYST 2.0 User Manuals: Modules 1, 2, 3 and 4". Macmillan Software Company.

[A6.8] "LeCroy model 9400 Digital Oscilloscope Operators Manual" LeCroy, 1987.

[A6.9] Yamabe C., Matsushita T. et al. "Characteristics of a TEA CO₂ laser preionised by ultraviolet light". Journal Appl. Phys. 51 (3) pp 1345 - 1350, 1980.

[A6.10] Willis C. "Catalytic control of the gas chemistry of sealed TEA CO₂ laser systems". Journal App. Phys. 50 (4), pp 2539-2543, 1979.

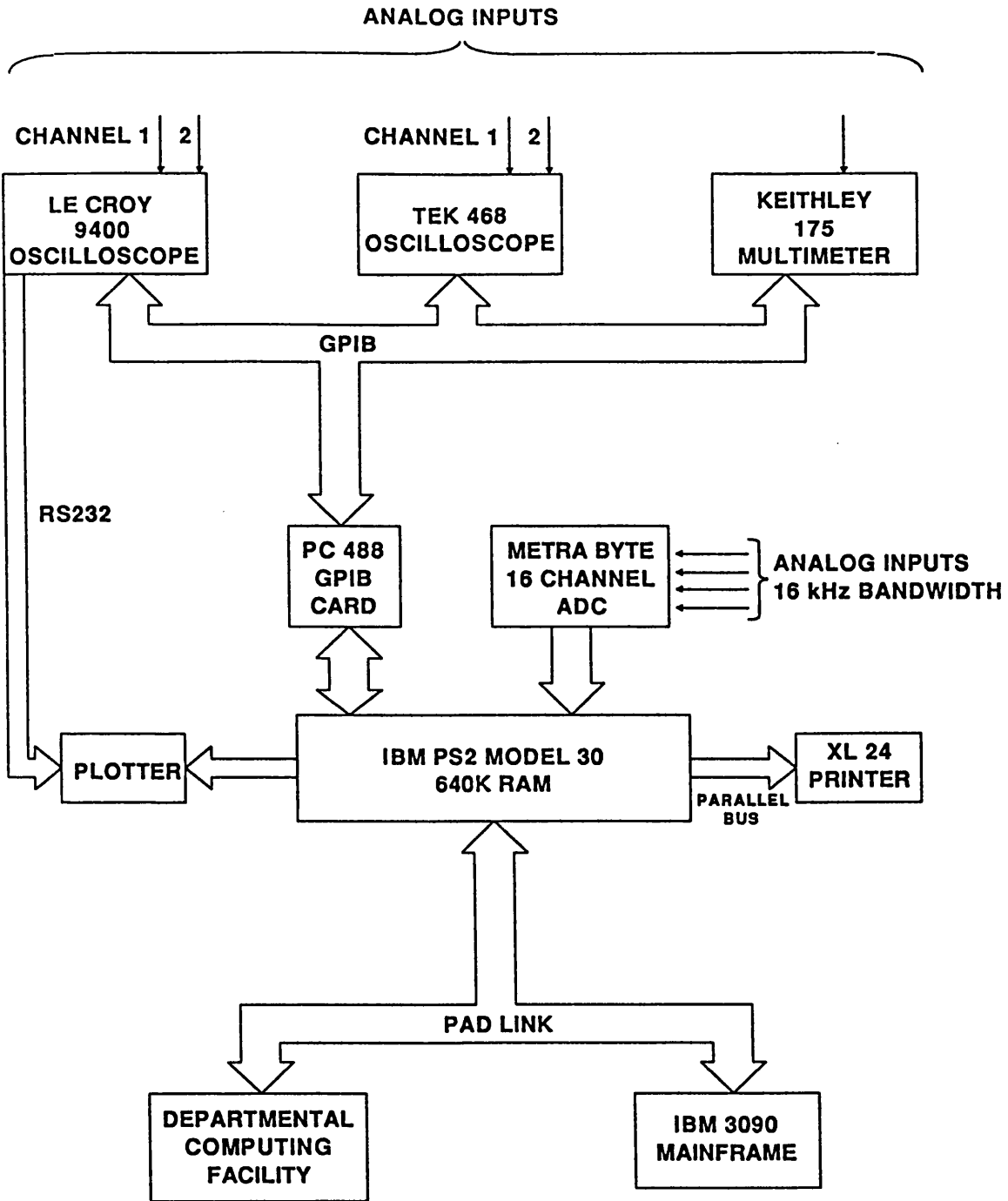


FIGURE A6.1 DATA AQUISITION SYSTEM

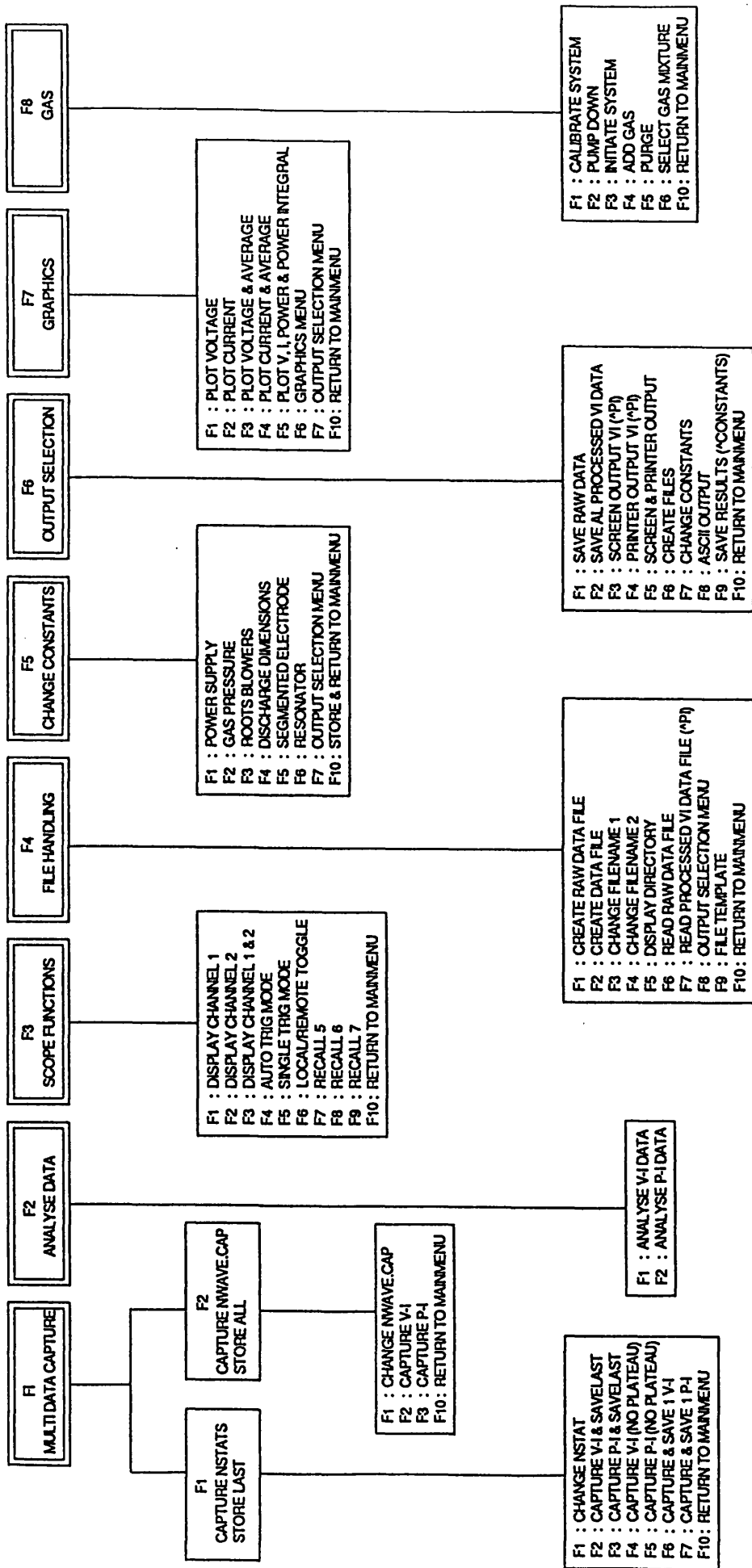


FIGURE A6.2 PROGRAM MENU SELECTION OPTIONS

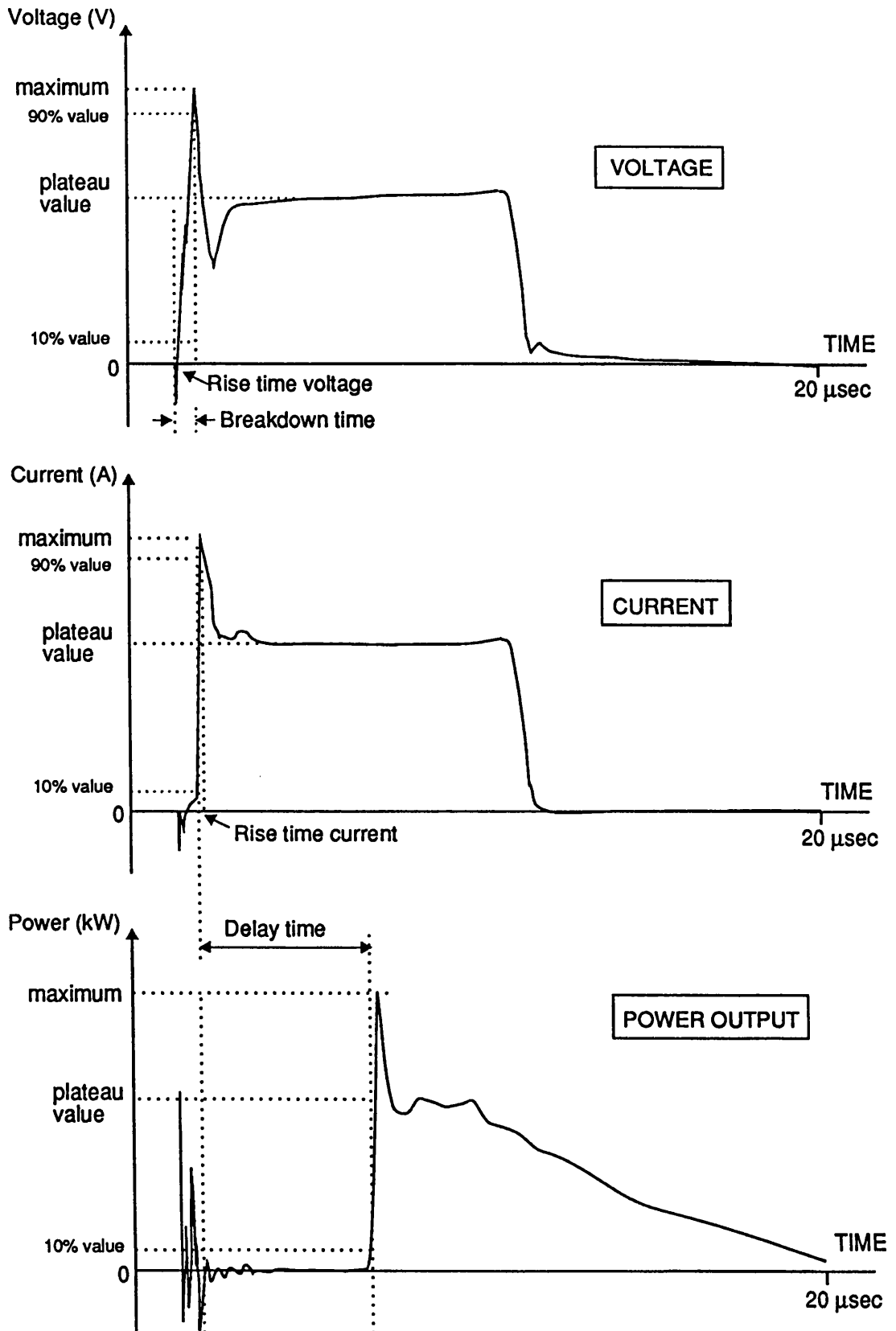


FIGURE A6.3 DISCHARGE VOLTAGE, CURRENT AND LASER OUTPUT PULSE CHARACTERISTICS

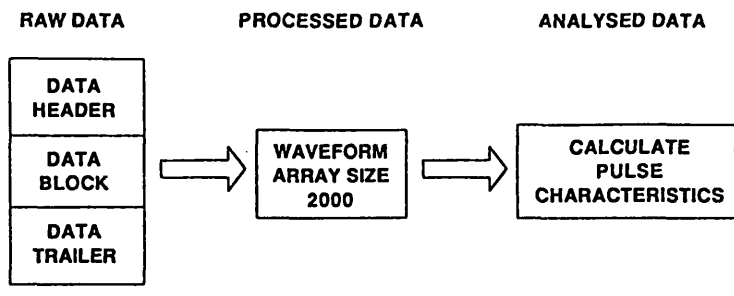


FIGURE A6.4 DATA TRANSFER PROFILE

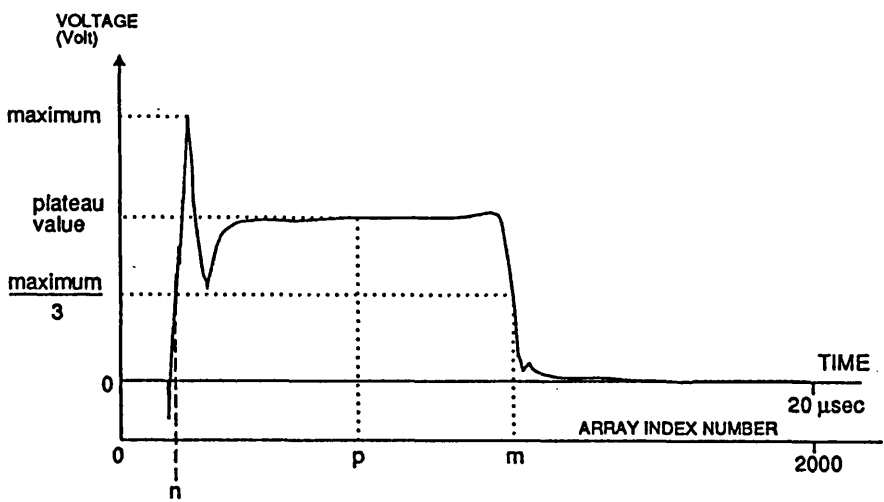


FIGURE A6.5 CALCULATING THE WAVEFORM PLATEAU

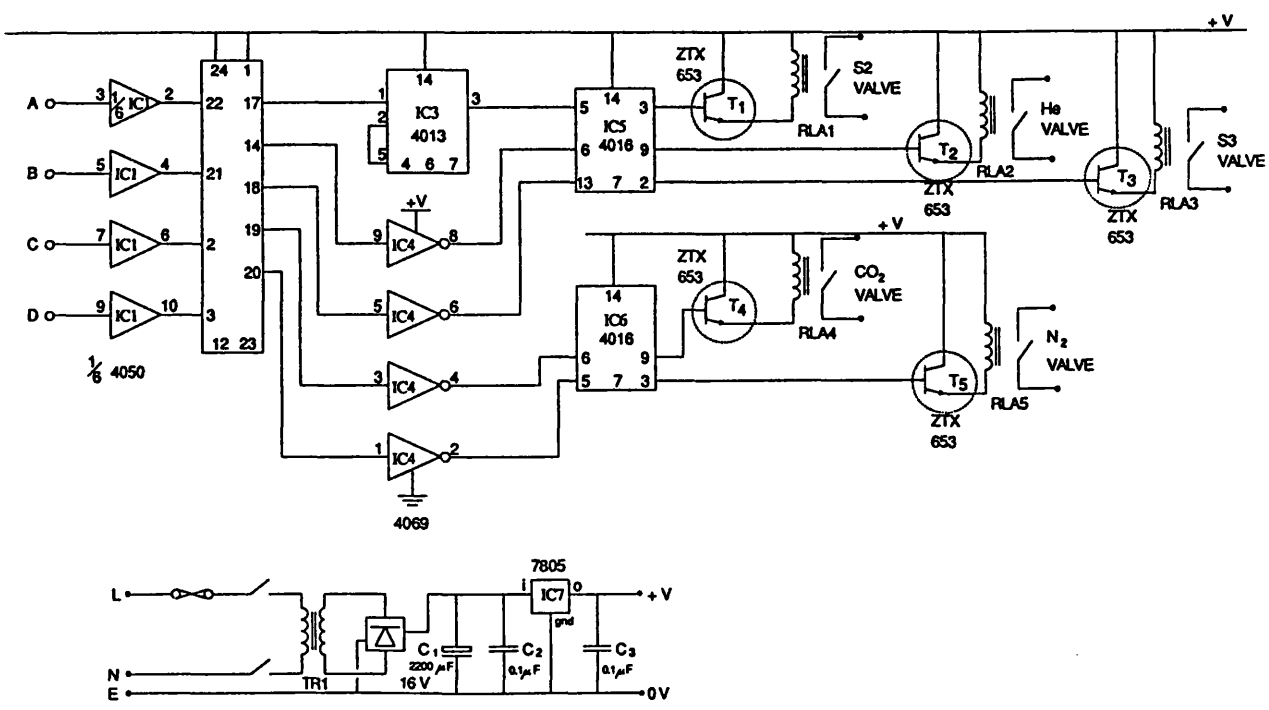


FIGURE A6.6 GAS CONTROL MULTIPLEXER

APPENDIX A7 V-I, P-I AND PFN WAVEFORMS

Some of the experimental waveforms that were collected whilst using the DAS are shown in order to introduce the waveform shapes that are typically observed with the pulsed CO₂ laser and to illustrate the power of the DAS. Waveforms from the collection of V-I and P-I data sets, and the PFN charging cycle are shown.

A7.1 Waveforms from the V-I and P-I Data Sets

Figures A7.1 and A7.2 shows how the numerical values of the calculated pulse characteristics of the V-I and P-I data sets respectively – as shown in Table A6.1 – are displayed. The tapsettings were at 60 %, thus $V_{dc} = 8.4$ kV, the gas mixture was 1:1:8 at a total pressure of 160 mbar. It can be seen that there are 10 values for each parameter, i.e. $NSTAT = 10$, where $NSTAT$ is the variable used to indicate the number of waveforms that are captured. This data set and part thereof is statistically analysed, and the results are shown as two tables for the V-I or P-I data set. The lower table consists of the mean values and the standard error of the mean for all 10 values of the pulse characteristics. Above this is another table, which consists of the mean values and the standard error of the mean of the pulse characteristics with $NSTAT - i$ as the sample size. Where the quantity i is an integer representing the number of data sets that have values in them that lie more than 2 standard deviations from the mean. This was introduced because if the discharge arcs the captured data is erroneous. The voltage collapses and the current increases to the full fault current, which is only limited by the impedance of the network. This results in errors for the plateau characteristics and the E/p values.

Figures A7.3 and A7.4 show the V-I and P-I waveforms respectively. It is seen from Figure A7.3 that the plateau voltage is 3.96 kV, and from Figure A7.4 the plateau current is 93.5 A. If these values are compared to the average values from Figures A7.1 and A7.2, it is seen that the average voltage and current are 3.98 kV and 93.4, there is excellent agreement between the values.

It is apparent that following a transient period the voltage and current collapse to quasi-steady values, these are easily predicted, see Appendix B1. The theoretical calculation of the quasi-steady voltage and current, i.e. the plateau values, generally agree to less than 10 % with the measured values.

A7.2 PFN Waveforms

Figure A7.5 shows the PFN voltage during one cycle. At the moment T1 fires, defined as time $t = 0$, the voltage on the network is resonantly charged. After the charging period, T2 stops conduction and the network voltage V_N is given by equation 2.9, in Chapter 2. After a suitable recovery period has been allowed for T1 ($\approx 20 \mu\text{s}$), the discharge thyatron T2 is fired at time t_1 . In the present case it is seen that $t_1 \approx 130 \mu\text{s}$, allowing ample time for the thyatron recovery period. The voltage collapses to V_1 , given by equation 2.1, in Chapter 2. If a negative mismatch exists, then after the pulse time τ_p , which is governed by the number of meshes on the PFN, the network swings negative and the current reverses as the initial reflected wave reaches the load again – see Chapter 2, Section 2.2.1 – this turns off T2. The PFN now has a negative residual voltage. The negative swing and the subsequent decay of the energy is in part determined by the thyatrons characteristics, the load and the value of the inverse diode stack resistance. It is seen that after time t_2 , the voltage on the network is 0, and the next charging cycle can start again. The value of t_2 dictates the maximum system frequency, F_s , that the laser can run at. From the graph $t_2 \approx 150 \mu\text{s}$, $\Rightarrow F_s = 1/t_2 = 6.6 \text{ kHz}$, which was deemed adequate for the initial experiments investigating the discharge performance. However, F_s can be simply changed by altering the relative firing time of the pulses down the fibre optic cable by adjusting a potentiometer in the Pulser Control Unit.

C:\DATA\11860VI.001 10uF 36uH
data for input into code 16:12:92

C:\DATA\11860PI.001 10uF 36uH
C:\DATA\11860PI.001 10uF 36uH

MAXVOLT	VOLTAV	RISE.TIME.VO	MAXCUR	CURRAV	RISE.TIME.CU
7.012E	3	3.973E	3	4.000E	-1
7.137E	3	3.980E	3	4.000E	-1
7.075E	3	3.981E	3	4.000E	-1
7.137E	3	3.987E	3	4.100E	-1
7.075E	3	3.988E	3	3.900E	-1
7.012E	3	3.982E	3	3.700E	-1
7.075E	3	3.988E	3	3.800E	-1
7.012E	3	4.004E	3	3.700E	-1
7.012E	3	3.989E	3	3.700E	-1
7.325E	3	3.984E	3	2.300E	-1

JIPS	E / P	dV/dt	dI/dt	BREAKDOWN TIME	NUMBER
3.368E	0	8.276E	0	1.938E	4
3.348E	0	8.290E	0	1.625E	4
3.324E	0	8.292E	0	2.575E	4
3.371E	0	8.303E	0	1.829E	4
3.363E	0	8.306E	0	1.827E	4
3.321E	0	8.293E	0	1.655E	4
3.350E	0	8.307E	0	1.530E	4
3.400E	0	8.340E	0	1.841E	4
3.300E	0	8.308E	0	1.622E	4
3.382E	0	8.298E	0	2.989E	4
7.917E	2	4.300E	-1	4.300E	-1
7.708E	2	4.300E	-1	4.300E	-1
8.301E	2	2.800E	-1	2.800E	-1
8.594E	2	4.400E	-1	4.400E	-1
8.301E	2	4.200E	-1	4.200E	-1
8.021E	2	4.100E	-1	4.100E	-1
8.333E	2	4.200E	-1	4.200E	-1
8.340E	2	4.100E	-1	4.100E	-1
7.910E	2	4.100E	-1	4.100E	-1
8.333E	2	2.500E	-1	2.500E	-1

MAXPOWERO	POAV	MAXCUR	CURRAV	RISE.TIME.CU
8.637E	0	3.357E	0	1.574E
7.492E	0	3.298E	0	1.559E
7.387E	0	3.098E	0	1.606E
7.700E	0	3.334E	0	1.559E
8.637E	0	3.245E	0	1.590E
7.908E	0	3.166E	0	1.559E
7.596E	0	3.169E	0	1.574E
8.221E	0	3.205E	0	1.574E
7.804E	0	3.189E	0	1.559E
7.700E	0	3.262E	0	1.543E

JIPS	E / P	dV/dt	dI/dt	BREAKDOWN TIME	NUMBER
8.542E	2	6.810E	0	2.670E	1
8.542E	2	6.550E	0	2.642E	1
8.594E	2	6.470E	0	2.560E	1
8.398E	2	6.720E	0	2.590E	1
8.594E	2	6.820E	0	2.595E	1
8.301E	2	6.540E	0	2.603E	1
8.496E	2	6.540E	0	2.564E	1
8.301E	2	6.750E	0	2.564E	1
8.301E	2	6.610E	0	2.620E	1
8.203E	2	6.930E	0	2.457E	1

MEAN	S.E.M.
(7.075E	3
(3.983E	3
(3.714E	-1
(1.472E	2
(9.329E	1
(1.543E	-1
(3.349E	0
(8.295E	0
(1.854E	4
(8.168E	2
(4.043E	-1

MEAN	S.E.M.
(7.075E	3
(3.983E	3
(3.714E	-1
(1.472E	2
(9.329E	1
(1.543E	-1
(3.349E	0
(8.295E	0
(1.854E	4
(8.168E	2
(4.043E	-1

max power	power average	max current	current average	rise time current	dI/dt	delay time	J O P S
(7.931E	0	(3.227E	0	(1.578E	-1	(6.657E	0
(3.227E	0	(1.573E	2	(9.340E	1	(8.452E	2
(1.573E	2	(9.340E	1	(1.578E	-1	(6.657E	0
(9.340E	1	(1.578E	-1	(1.578E	-1	(6.657E	0
(1.578E	-1	(1.578E	-1	(1.578E	-1	(6.657E	0
(1.578E	-1	(1.578E	-1	(1.578E	-1	(6.657E	0
(1.578E	-1	(1.578E	-1	(1.578E	-1	(6.657E	0
(1.578E	-1	(1.578E	-1	(1.578E	-1	(6.657E	0
(1.578E	-1	(1.578E	-1	(1.578E	-1	(6.657E	0
(1.578E	-1	(1.578E	-1	(1.578E	-1	(6.657E	0

max power	power average	max current	current average	rise time current	dI/dt	delay time	J O P S
(7.908E	0	(3.230E	0	(1.570E	2	(6.684E	0
(3.230E	0	(1.570E	2	(9.338E	1	(8.427E	2
(1.570E	2	(9.338E	1	(1.580E	-1	(6.684E	0
(9.338E	1	(1.580E	-1	(1.580E	-1	(6.684E	0
(1.580E	-1	(1.580E	-1	(1.580E	-1	(6.684E	0
(1.580E	-1	(1.580E	-1	(1.580E	-1	(6.684E	0
(1.580E	-1	(1.580E	-1	(1.580E	-1	(6.684E	0
(1.580E	-1	(1.580E	-1	(1.580E	-1	(6.684E	0
(1.580E	-1	(1.580E	-1	(1.580E	-1	(6.684E	0
(1.580E	-1	(1.580E	-1	(1.580E	-1	(6.684E	0

FIGURE A7.1 V-I PULSE CHARACTERISTICS

FIGURE A7.2 P-I PULSE CHARACTERISTICS

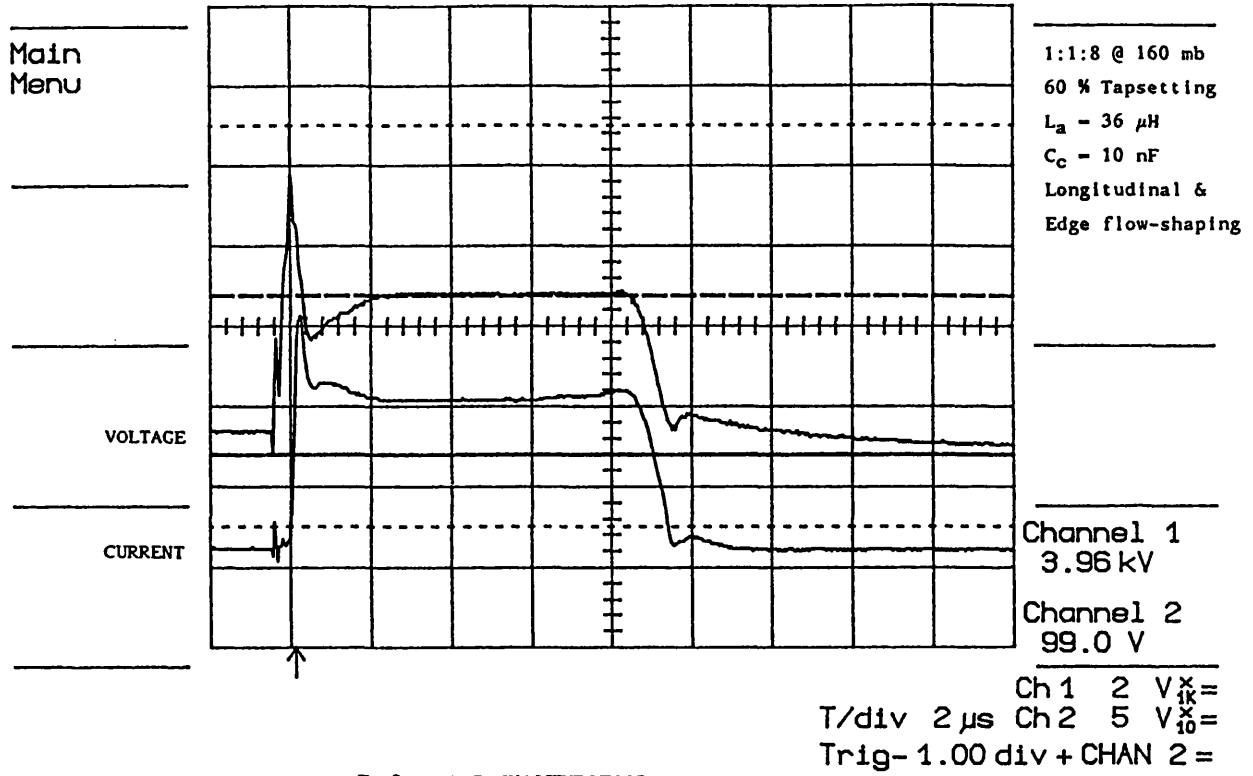


FIGURE A7.3 V-I WAVEFORMS

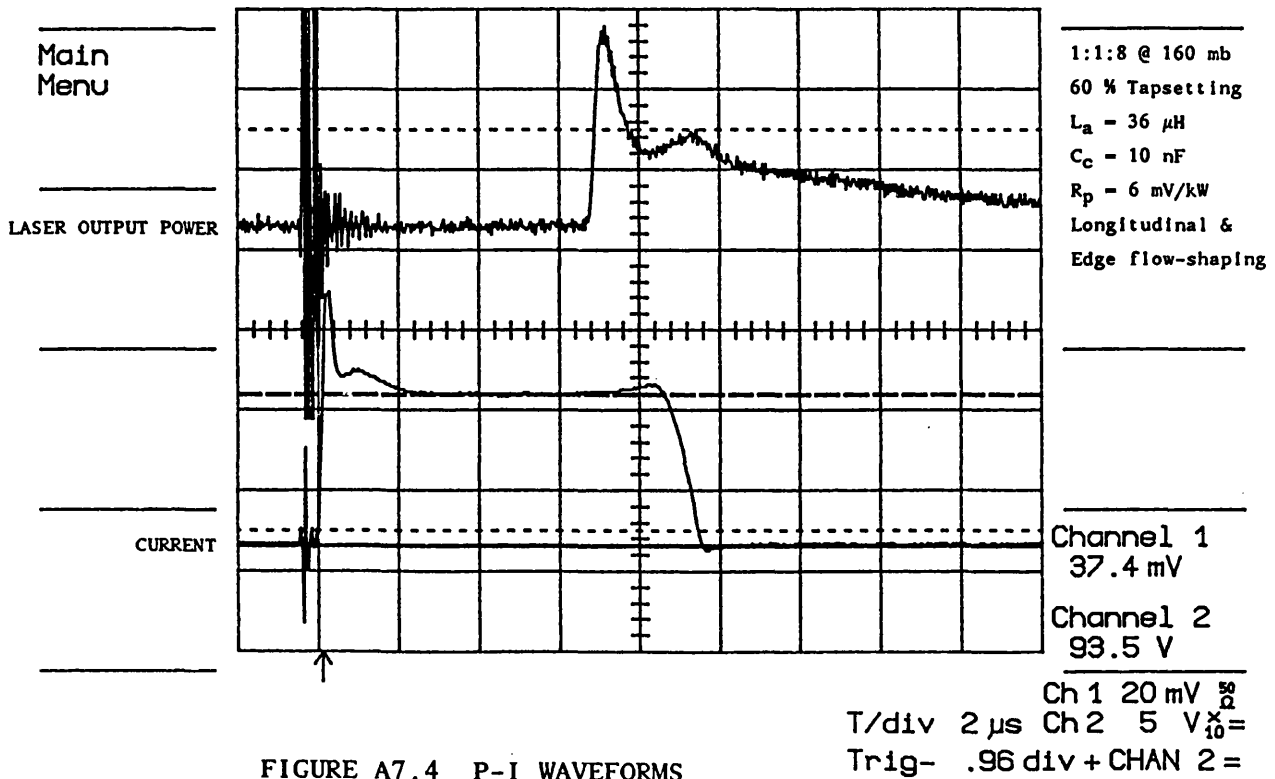


FIGURE A7.4 P-I WAVEFORMS

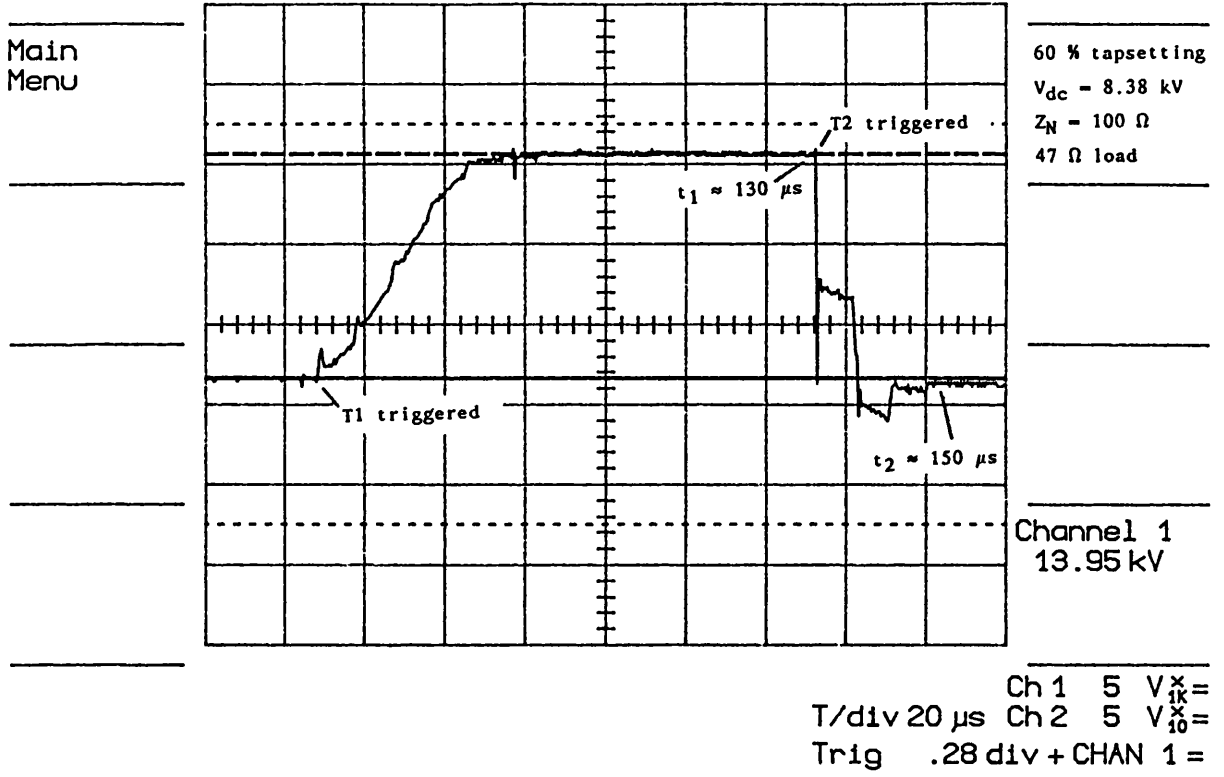


FIGURE A7.5 PFN CYCLE

APPENDIX B1 MODELLING QUASI-STEADY DISCHARGE CHARACTERISTICS

The formation of glow discharges can be modelled in two stages. The first is the discharge formation period, discussed in Chapter 3, and the second a quasi-steady period in which dynamic equilibrium is established in the discharge between electron creation and electron loss processes.

It was mentioned in Chapter 2, Section 2.2.3, that no tailbiter switch was available for the pulser, consequently, the system must not be allowed to run in the positive mismatch regime. In order to assess the operating regime of the discharge, equations are given which can be used to predict the type of load mismatch the system will run at given a particular electrode spacing, gas mixture and operating pressure.

B1.1 Quasi-steady Discharge Voltage and Current

From Figure A7.3, in Appendix A7, which shows the discharge V-I characteristics, it is seen that at the moment T2 fires the discharge voltage begins to rise, this rate of rise is primarily determined by the circuit components. Energy is capacitively coupled into the trigger wires which act as the preionisation source and ensures satisfactory breakdown of the gap and evolution of a stable, glow discharge. After the discharge formation period the discharge voltage and current settle down after $\approx 2.5 \mu\text{s}$, to quasi-steady values which are denoted by V_d and I_d respectively, i.e. the plateau voltage and current values. This implies that the quasi-steady discharge impedance, $Z_d = V_d/I_d$, is approximately constant. The equivalent circuit for the PFN and the discharge during this quasi-steady operating regime can be seen in Figure B1.1. The values of V_d and I_d are simply given by:

$$V_d = \frac{V_N Z_d}{Z_d + Z_N} \quad \text{B1.1}$$

$$I_d = \frac{V_N - V_d}{Z_N} \quad \text{B1.2}$$

Where V_N is the network voltage and Z_N the network impedance.

B1.2 Affect of the Discharge E/N on Discharge Impedance

It is recalled from Section 2.3 that the pulser was ran without the tailbiter, consequently, it is important that the discharge is operated with a negative mismatch. It is convenient at this stage to consider the affect of the gas mixture

on the discharge impedance, and consequently, the maximum pressure that the system can operate at before the positive mismatch regime is encountered.

The discharge E/N is given by

$$\frac{E}{N} = \frac{V_d}{d N} \quad \text{B1.3}$$

E is the electric field between the electrodes, given by the ratio V_d/d , and N is the neutral particle density. The experimental values of E/N for different gas mixtures were investigated and are reported in Chapter 3, Section 3.1. Kharha [B1.1] also performed measurements of E/N for a variety of gas mixtures. It is well known that the value of E/N is approximately: independent of the discharge current and the gas pressure, and only dependent on the gas mixture [B1.2]. If the E/N value is known for a given gas mixture, then the voltage drop V_d across a known discharge gap can be found, as

$$V_d = \left[\frac{E}{N} \right] N d \quad \text{B1.4}$$

Where N is given by

$$N = \frac{p}{k T} \quad \text{B1.5}$$

p is the total pressure of the laser gas mixture at temperature T and k is Boltzmann's constant. E/N is often expressed in units of E/p , i.e. $\text{Vcm}^{-1}\text{torr}^{-1}$ or in $\text{Vcm}^{-1}\text{mbar}^{-1}$.

If $Z_d = Z_N$ then matched conditions exist. For this to occur the voltage on the network, V_N , must be twice the discharge voltage, V_d

$$V_d = \frac{V_N}{2} \quad \text{B1.6}$$

For a given value of V_N , the maximum pressure, P_m , can be found beyond which $Z_d > Z_N$ and positive mismatch conditions will be encountered. If E/p is in units of $\text{Vcm}^{-1}\text{torr}^{-1}$, then P_m in units of mbar – the selected pressure setting for the EMV251 pressure monitor – is given by

$$P_m = \frac{1.333 \times V_N}{2 d \left[\frac{E}{p} \right]} \quad \text{B1.7}$$

B1.3 Energy Transfer Efficiency from PFN to Load

It is informative to examine what fraction of the energy stored on the PFN is transferred to the discharge and how this varies with, for example, the gas pressure. The power transfer efficiency could be examined, however, the power and energy transfer efficiency are numerically equivalent.

The energy stored on the network capacitance C_N , which is charged to a voltage V_N is given by

$$E_N = \frac{1}{2} C_N V_N^2 \quad \text{B1.8}$$

The energy deposited into the discharge is approximately given by

$$E_d \approx V_d I_d \tau_p \quad \text{B1.9}$$

and more exactly by

$$E_d = \int_{t=0}^{t=\tau_p} V(t) I(t) dt \quad \text{B1.10}$$

Where τ_p is the pumping pulse width; and, $V(t)$ and $I(t)$ are the discharge voltage and current respectively as a function of time. The energy transfer efficiency ζ from the network to the gas discharge is found from

$$\zeta = \frac{E_d}{E_N} \approx \frac{2 V_d I_d \tau_p}{C_N V_N^2} = \frac{2 \left[\frac{E}{N} \right] N d I_d \tau_p}{C_N V_N^2} \quad \text{B1.11}$$

Or equivalently E/p values can be used in place of the E/N values, which are multiplied by p instead of N . Figure B1.2 shows the transfer efficiency as a function of V_N using 3 E/p values that were obtained from Kharha [2.1] and are tabulated in Table B1.1, Table B1.2 shows the system parameters. The efficiency transfer is a slowly varying function of the PFN voltage and remains quite high for a large variation in V_N . All curves peak at $\zeta = 1$ when equation B1.6 is satisfied.

To the left of the peak, corresponding to lower values of V_N , a positive mismatch results. To the right of the peak a negative mismatch occurs, because, as V_d is independent of the current, with higher values of V_N the current increases, which reduces the impedance of the discharge. The condition on the network voltage to ensure a negative mismatch is $V_N > 2V_d$.

Figure B1.3 shows ζ with $V_N = 20$ kV as a function of pressure, with the system parameters as defined in Table B1.2. To operate under negative mismatch conditions it is necessary to operate on the lower pressure side of the peak. The gas pressure at which $\zeta = 1$ is given by P_m in equation B1.7. Kharha's E/p results provided an indication of suitable pressures to run the gas discharge at without encountering a positive mismatch.

After establishing these guidelines, the performance of the system was fully investigated. Initially, a series of experiments were undertaken to determine the E/N values for a selection of gas mixtures, these are reported in Chapter 3.

REFERENCES

[B1.1] Kharha J. "Optimisation of the output characteristics of a pulsed CO_2 laser for processing materials". Ph.D. Thesis. Department of Mechanical Engineering, University of Birmingham 1979.

[B1.2] Kline, Denes, Perchersky. "Arc suppression in CO_2 laser discharges". App. Phys. Letts. Volume 29 (9), pp 574-576, 1976.

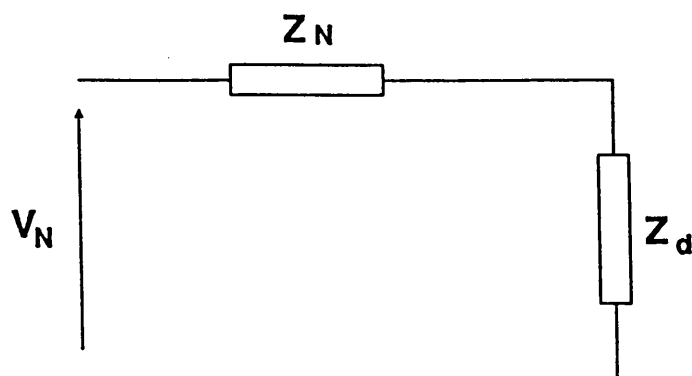


FIGURE B1.1 EQUIVALENT CIRCUIT OF THE QUASI-STEADY DISCHARGE PHASE

Table B1.1 Kharhas' E/p values

Gas Mixture	E/p Vcm ⁻¹ torr ⁻¹
1:1:4	11.0
1:1:2	18.0
1:1:0	29.2

Table B1.2 System Parameters

d = 41.0 mm
C _N = 50 nF
τ = 10 μs
Z _N = 100 Ω

Transfer efficiency

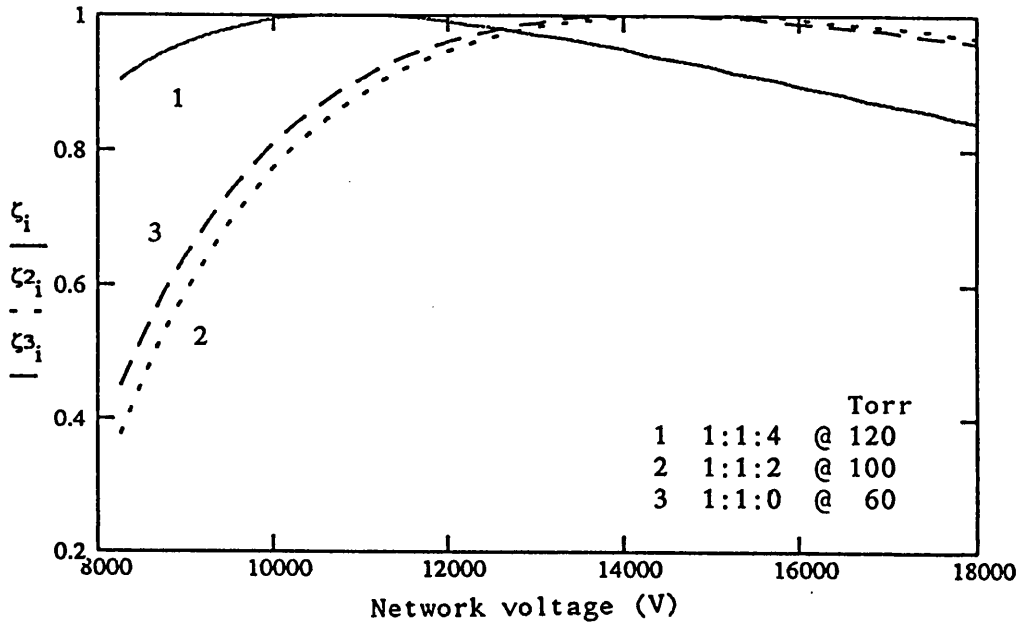


FIGURE B1.2 TRANSFER EFFICIENCY VS PFN VOLTAGE

Transfer efficiency

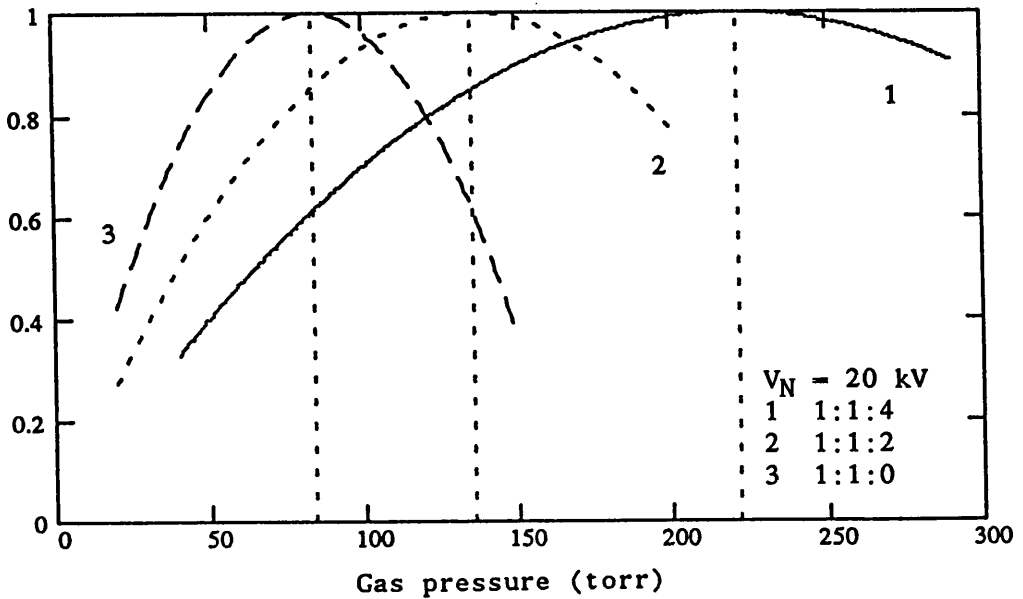


FIGURE B1.3 TRANSFER EFFICIENCY VS GAS PRESSURE

MathCad program to calculate the Townsend sparking voltage for a 1:1:8 gas mixture, as a function of E/N.

Velocity Data

VE :=	<table border="0"> <tr><td>2.00</td><td>49.6</td></tr> <tr><td>3.00</td><td>60.8</td></tr> <tr><td>4.00</td><td>73.4</td></tr> <tr><td>5.00</td><td>84.1</td></tr> <tr><td>6.00</td><td>99</td></tr> <tr><td>7.00</td><td>105</td></tr> <tr><td>8.00</td><td>117</td></tr> <tr><td>9.00</td><td>127</td></tr> <tr><td>10.0</td><td>133</td></tr> <tr><td>20.0</td><td>220</td></tr> </table>	2.00	49.6	3.00	60.8	4.00	73.4	5.00	84.1	6.00	99	7.00	105	8.00	117	9.00	127	10.0	133	20.0	220	$VEL^{<0>} := VE^{<0>} \cdot 10^{-16}$ $VEL^{<1>} := VE^{<1>} \cdot 10^5$	VEL · 10 ²⁰ =	<table border="0"> <tr><td>2 · 10⁴</td><td>4.96 · 10²⁶</td></tr> <tr><td>3 · 10⁴</td><td>6.08 · 10²⁶</td></tr> <tr><td>4 · 10⁴</td><td>7.34 · 10²⁶</td></tr> <tr><td>5 · 10⁴</td><td>8.41 · 10²⁶</td></tr> <tr><td>6 · 10⁴</td><td>9.9 · 10²⁶</td></tr> <tr><td>7 · 10⁴</td><td>1.05 · 10²⁷</td></tr> <tr><td>8 · 10⁴</td><td>1.17 · 10²⁷</td></tr> <tr><td>9 · 10⁴</td><td>1.27 · 10²⁷</td></tr> <tr><td>1 · 10⁵</td><td>1.33 · 10²⁷</td></tr> <tr><td>2 · 10⁵</td><td>2.2 · 10²⁷</td></tr> </table>	2 · 10 ⁴	4.96 · 10 ²⁶	3 · 10 ⁴	6.08 · 10 ²⁶	4 · 10 ⁴	7.34 · 10 ²⁶	5 · 10 ⁴	8.41 · 10 ²⁶	6 · 10 ⁴	9.9 · 10 ²⁶	7 · 10 ⁴	1.05 · 10 ²⁷	8 · 10 ⁴	1.17 · 10 ²⁷	9 · 10 ⁴	1.27 · 10 ²⁷	1 · 10 ⁵	1.33 · 10 ²⁷	2 · 10 ⁵	2.2 · 10 ²⁷
2.00	49.6																																											
3.00	60.8																																											
4.00	73.4																																											
5.00	84.1																																											
6.00	99																																											
7.00	105																																											
8.00	117																																											
9.00	127																																											
10.0	133																																											
20.0	220																																											
2 · 10 ⁴	4.96 · 10 ²⁶																																											
3 · 10 ⁴	6.08 · 10 ²⁶																																											
4 · 10 ⁴	7.34 · 10 ²⁶																																											
5 · 10 ⁴	8.41 · 10 ²⁶																																											
6 · 10 ⁴	9.9 · 10 ²⁶																																											
7 · 10 ⁴	1.05 · 10 ²⁷																																											
8 · 10 ⁴	1.17 · 10 ²⁷																																											
9 · 10 ⁴	1.27 · 10 ²⁷																																											
1 · 10 ⁵	1.33 · 10 ²⁷																																											
2 · 10 ⁵	2.2 · 10 ²⁷																																											

Attachment data

AT :=	<table border="0"> <tr><td>2</td><td>0.989</td></tr> <tr><td>3</td><td>2.94</td></tr> <tr><td>4</td><td>4.211</td></tr> <tr><td>5</td><td>4.819</td></tr> <tr><td>6</td><td>5.272</td></tr> <tr><td>7</td><td>5.272</td></tr> <tr><td>8</td><td>5.04</td></tr> <tr><td>9</td><td>4.819</td></tr> <tr><td>10</td><td>4.405</td></tr> <tr><td>20</td><td>2.146</td></tr> </table>	2	0.989	3	2.94	4	4.211	5	4.819	6	5.272	7	5.272	8	5.04	9	4.819	10	4.405	20	2.146	$ATT^{<0>} := AT^{<0>} \cdot 10^{-16}$ $ATT^{<1>} := AT^{<1>} \cdot 10^{-20}$	ATT · 10 ²⁰ =	<table border="0"> <tr><td>2 · 10⁴</td><td>0.989</td></tr> <tr><td>3 · 10⁴</td><td>2.94</td></tr> <tr><td>4 · 10⁴</td><td>4.211</td></tr> <tr><td>5 · 10⁴</td><td>4.819</td></tr> <tr><td>6 · 10⁴</td><td>5.272</td></tr> <tr><td>7 · 10⁴</td><td>5.272</td></tr> <tr><td>8 · 10⁴</td><td>5.04</td></tr> <tr><td>9 · 10⁴</td><td>4.819</td></tr> <tr><td>1 · 10⁵</td><td>4.405</td></tr> <tr><td>2 · 10⁵</td><td>2.146</td></tr> </table>	2 · 10 ⁴	0.989	3 · 10 ⁴	2.94	4 · 10 ⁴	4.211	5 · 10 ⁴	4.819	6 · 10 ⁴	5.272	7 · 10 ⁴	5.272	8 · 10 ⁴	5.04	9 · 10 ⁴	4.819	1 · 10 ⁵	4.405	2 · 10 ⁵	2.146
2	0.989																																											
3	2.94																																											
4	4.211																																											
5	4.819																																											
6	5.272																																											
7	5.272																																											
8	5.04																																											
9	4.819																																											
10	4.405																																											
20	2.146																																											
2 · 10 ⁴	0.989																																											
3 · 10 ⁴	2.94																																											
4 · 10 ⁴	4.211																																											
5 · 10 ⁴	4.819																																											
6 · 10 ⁴	5.272																																											
7 · 10 ⁴	5.272																																											
8 · 10 ⁴	5.04																																											
9 · 10 ⁴	4.819																																											
1 · 10 ⁵	4.405																																											
2 · 10 ⁵	2.146																																											

Ionisation data

IO :=	<table border="0"> <tr><td>2</td><td>0.163</td></tr> <tr><td>3</td><td>6.703</td></tr> <tr><td>4</td><td>32.246</td></tr> <tr><td>5</td><td>100</td></tr> <tr><td>6</td><td>188.5</td></tr> <tr><td>7</td><td>322.46</td></tr> <tr><td>8</td><td>500.21</td></tr> <tr><td>9</td><td>703.81</td></tr> <tr><td>10</td><td>855.47</td></tr> <tr><td>20</td><td>3733</td></tr> </table>	2	0.163	3	6.703	4	32.246	5	100	6	188.5	7	322.46	8	500.21	9	703.81	10	855.47	20	3733	$ION^{<0>} := IO^{<0>} \cdot 10^{-16}$ $ION^{<1>} := IO^{<1>} \cdot 10^{-20}$	ION · 10 ²⁰ =	<table border="0"> <tr><td>2 · 10⁴</td><td>0.163</td></tr> <tr><td>3 · 10⁴</td><td>6.703</td></tr> <tr><td>4 · 10⁴</td><td>32.246</td></tr> <tr><td>5 · 10⁴</td><td>100</td></tr> <tr><td>6 · 10⁴</td><td>188.5</td></tr> <tr><td>7 · 10⁴</td><td>322.46</td></tr> <tr><td>8 · 10⁴</td><td>500.21</td></tr> <tr><td>9 · 10⁴</td><td>703.81</td></tr> <tr><td>1 · 10⁵</td><td>855.47</td></tr> <tr><td>2 · 10⁵</td><td>3.733 · 10³</td></tr> </table>	2 · 10 ⁴	0.163	3 · 10 ⁴	6.703	4 · 10 ⁴	32.246	5 · 10 ⁴	100	6 · 10 ⁴	188.5	7 · 10 ⁴	322.46	8 · 10 ⁴	500.21	9 · 10 ⁴	703.81	1 · 10 ⁵	855.47	2 · 10 ⁵	3.733 · 10 ³
2	0.163																																											
3	6.703																																											
4	32.246																																											
5	100																																											
6	188.5																																											
7	322.46																																											
8	500.21																																											
9	703.81																																											
10	855.47																																											
20	3733																																											
2 · 10 ⁴	0.163																																											
3 · 10 ⁴	6.703																																											
4 · 10 ⁴	32.246																																											
5 · 10 ⁴	100																																											
6 · 10 ⁴	188.5																																											
7 · 10 ⁴	322.46																																											
8 · 10 ⁴	500.21																																											
9 · 10 ⁴	703.81																																											
1 · 10 ⁵	855.47																																											
2 · 10 ⁵	3.733 · 10 ³																																											

Spline fitting routine to the above data:

$$e_{on_i} := 5 \cdot 10^{-16} + \frac{i \cdot 1 \cdot 10^{-16}}{10} \quad i := 1..150$$

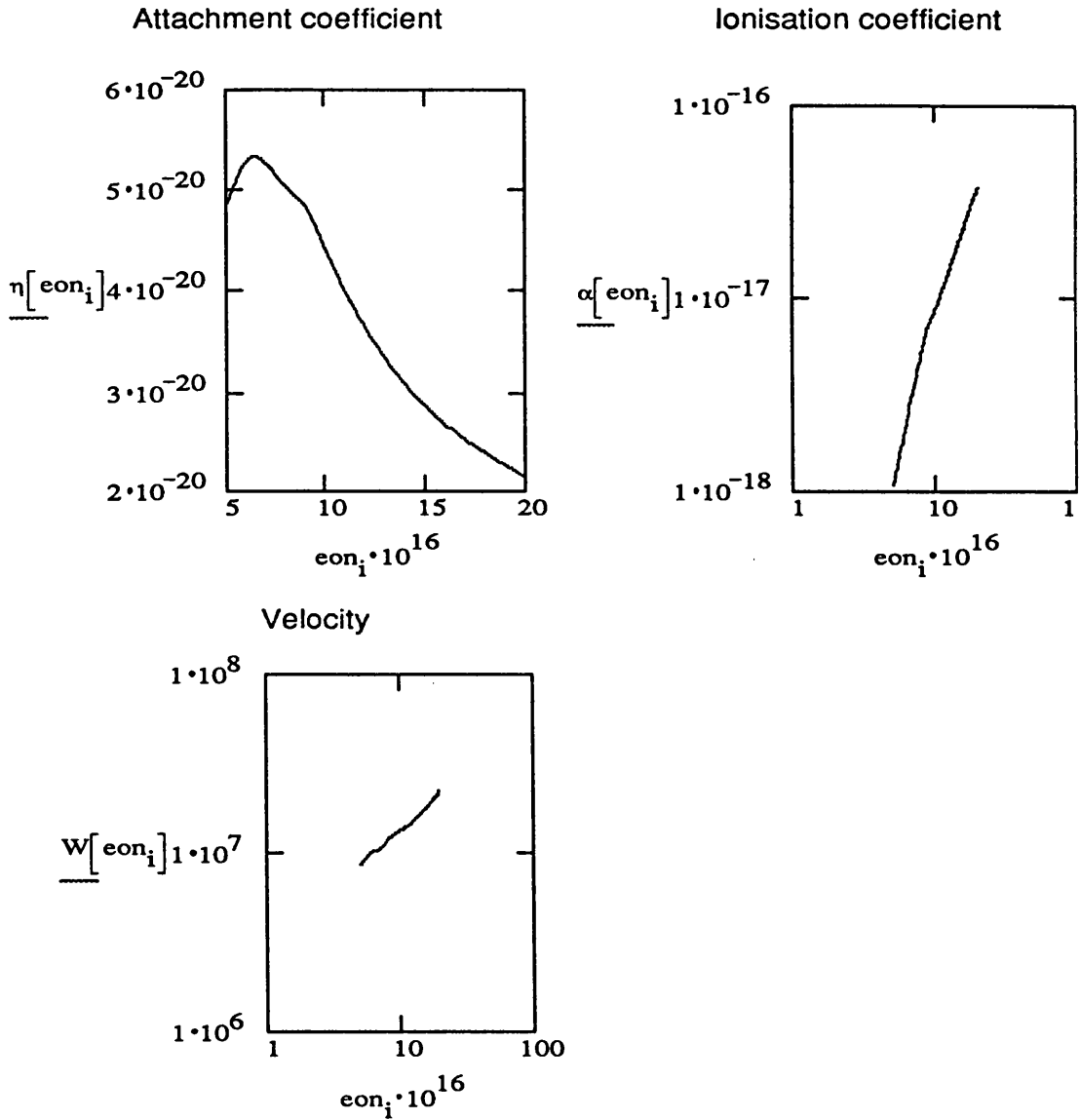
Finding the coefficients

$$ions := lspline[ION^{<0>}, ION^{<1>}] \quad \alpha(e_{on}) := interp[ions, ION^{<0>}, ION^{<1>}, e_{on}]$$

$$atts := lspline[ATT^{<0>}, ATT^{<1>}] \quad \eta(e_{on}) := interp[atts, ATT^{<0>}, ATT^{<1>}, e_{on}]$$

$$vels := lspline[VEL^{<0>}, VEL^{<1>}] \quad W(e_{on}) := interp[vels, VEL^{<0>}, VEL^{<1>}, e_{on}]$$

Plotting the data:



Defining Boltzmann's constant and gas temp $1.3807 \cdot 10^{-23} \quad T := 300$

Defining some other parameters/constants

$i := 1..150$ Counter $E := 2000$ Electric field (Vcm²)

$e_{on_i} := 2 \cdot 10^{-16} + \frac{i \cdot 1 \cdot 10^{-16}}{100}$ E/N range $z := 3.2 \cdot 10^{-16}$ Estimate of E/N i.e. root

$p := 200 \cdot 10^2$ Gas pressure, in mbar

$\gamma := 0.1$ Secondary ionisation coefficient $N := \frac{p}{k \cdot T \cdot 10^6}$ Neutral particle density
 $en := \frac{E}{N}$ E/N value $d := 4.0$ Electrode gap (cm)

Defining the functions:

$$F1(en) := \exp\left[\left[\alpha(en) - \eta(en)\right] \cdot N \cdot d\right] - 1$$

$$F2(en) := \frac{\alpha(en) - \eta(en)}{\alpha(en) \cdot \gamma}$$

Defining the tolerance:

$$TOL := 0.001$$

Finding the roots using the root function:

$$f(en, z) := \text{root}\left[1 - \frac{F1(en)}{F2(en)}, z\right] \quad \text{answer} := \text{root}\left[1 - \frac{F1(en)}{F2(en)}, en\right] \quad \text{answer} \cdot 10^{16} = 3.494$$

$$vs := \text{answer} \cdot N \cdot d \quad vs = 6.748 \cdot 10^3 \quad vd := 2.8942 \cdot 10^{-16} \cdot N \cdot d \quad vd = 5.59 \cdot 10^3$$

$$en \cdot 10^{16} = 4.142$$

$$k := 1$$

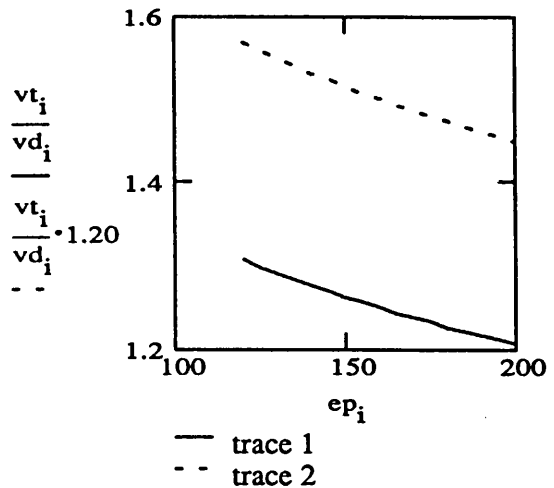
$$TOL := 0.001$$

$$en1_k := 4.2 \cdot 10^{-16} + (-k) \cdot 0.10 \cdot 10^{-16} \quad en1_k \cdot 10^{16} = 4.1 \quad z \cdot 10^{16} = 3.2$$

The collected data is shown below:

$i := 1..17$

$vt_i :=$	$ep_i :=$	$vd_i :=$
4.384	120	3.354
4.538	125	3.494
4.691	130	3.633
4.843	135	3.773
4.993	140	3.913
5.144	145	4.053
5.293	150	4.192
5.442	155	4.332
5.590	160	4.472
5.737	165	4.612
5.883	170	4.751
6.029	175	4.891
6.174	180	5.031
6.318	185	5.171
6.462	190	5.310
6.605	195	5.450
6.748	200	5.590

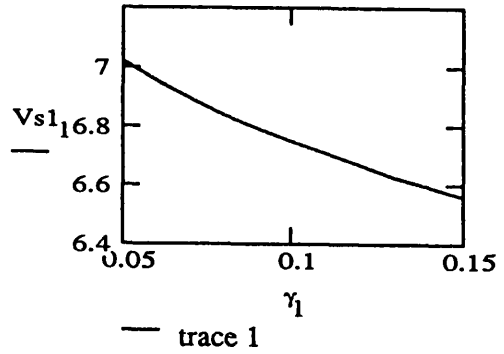
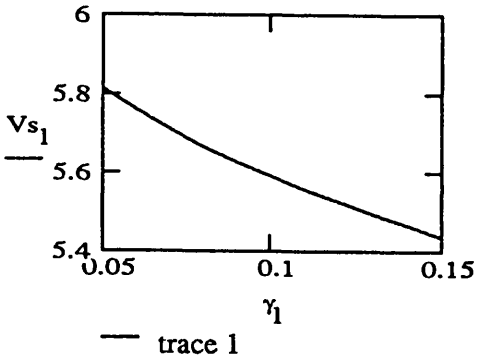
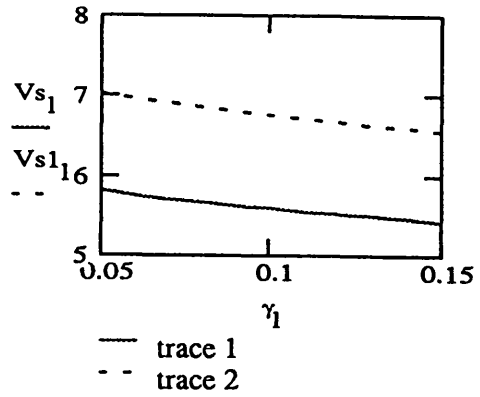


Variation of the Townsend voltage as a function of the secondary ionisation coefficient γ_1 for $E/N=3.883 \cdot 10^{-16}$, and V_{s1} is for $E/N=4.142 \cdot 10^{-16}$.

$i := 1..11$

$\gamma_1 :=$	$V_{s1} :=$	$V_{s1_1} :=$
0.05	5.813	7.022
0.06	5.758	6.955
0.07	5.710	6.896
0.08	5.666	6.842
0.09	5.626	6.793
0.10	5.590	6.748
0.11	5.556	6.706
0.12	5.524	6.667
0.13	5.493	6.629
0.14	5.465	6.593
0.15	5.437	6.560

An error of plus or minus 50% in the value for results in an error of less than 4.0% for the T_0 voltage.



The same data and spline fitting routines were used as for those used in calculation of Townsend sparking voltages.

$\epsilon_0 := 8.8542 \cdot 10^{-12}$ Relative permittivity $i := 1..150$ Counter

$d := 4.0$ Electrode gap $p = 1.2 \cdot 10^4$ Gas pressure $T = 300$ Gas temperature

$E := 1000$ Electric field $N = 2.897 \cdot 10^{18}$ Particles/cc $en := \frac{E}{N}$

$con_i := 5 \cdot 10^{-16} + \frac{i \cdot 1 \cdot 10^{-16}}{10}$ Range of E/N

$\lambda := \frac{4 \cdot k \cdot T \cdot 10^6}{\pi \cdot p \cdot 6.596 \cdot 10^{-16}}$ Electron mean free path

$K := \ln \left[\frac{4 \cdot \pi \cdot \epsilon_0 \cdot E \cdot \lambda}{1.6 \cdot 10^{-19}} \right]$ Log term, see equation 3.9. Chapter 3

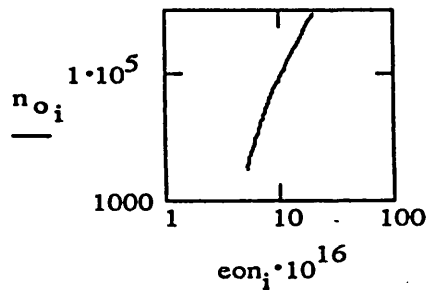
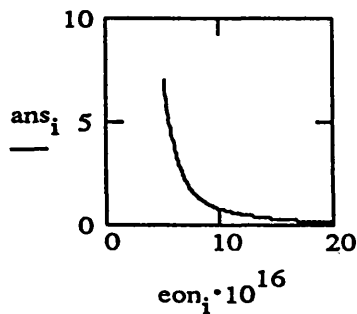
$TOL := 1 \cdot 10^{-6}$ Defining tolerance for calculating root.

$C[en, z_c] := \alpha(en) \cdot N \cdot z_c - \ln[z_c]$

$f[en, z_c] := \text{root}[K - C[en, z_c], z_c]$ Defining equations to solve using the root function

$ans_i := f[con_i, 10]$ Critical distance for streamer to propagate

$n_{o_i} := \frac{1}{[\lambda \cdot ans_i]^{\frac{3}{2}}}$ Initial electron density



APPENDIX C1 RESISTOR POWER RATING REQUIREMENTS

The discharge current I_d is given by

$$I_d = \frac{V_N - V_d}{Z_N + R_T} \quad C1.1$$

Where Z_N is the network impedance, V_N the network voltage, V_d the discharge voltage and R_T the total ballast resistance.

R_T is composed of n_T resistors in parallel. The individual resistance of each element, denoted by R , is given by

$$R = R_T / n_T \quad C1.2$$

The mean power developed in the total ballast resistance can be calculated from

$$P_{RT} = I_d^2 R_T D \quad C1.3$$

Where $D = \tau_p f$. If $\tau_p = 10 \mu s$ and $f = 10 \text{ kHz}$, then $D = 0.1$. The mean power rating W of the resistors can be found by dividing equation C1.3 by the number of segments \rightarrow

$$W = \frac{P_{RT}}{n_T} = \frac{I_d^2 R_T D}{n_T} = \frac{I_d^2 R_T \tau_p f}{n_T} \quad C1.4$$

APPENDIX C2 TRANSFER EFFICIENCY FOR BALLASTED ELECTRODES

Matched conditions occur when the following expression is satisfied:

$$Z_N = Z_d + R_T \quad C2.1$$

Where $Z_d = V_d / I_d$. With $R_T = 0$ and matched conditions, the relationship between the discharge voltage V_d and the network voltage V_N is

$$V_d = \frac{V_N}{2} \quad C2.2$$

It is seen that the discharge voltage is half the voltage on the network, and moreover, the power transfer efficiency $\zeta = 1$; ie, all the energy stored on the PFN is transferred to the discharge when T2 is triggered. The energy transfer efficiency, defined in Appendix B1.3, is numerically equivalent to the power

transfer efficiency. With zero ballast resistance, the power transfer efficiency can be expressed as the ratio of the power available on the network over the pulse period, denoted by P_N , to the power deposited into the discharge, denoted by P_d , and is given by

$$\zeta = \frac{P_d}{P_N} = \frac{E_d \tau_p}{E_N \tau_p} = \frac{E_d}{E_N} \quad \text{C2.3}$$

Where E_N is the energy stored on the PFN.

If the effect of the ballast resistance is taken into account, the power transfer efficiency is given by

$$\epsilon_b = \frac{P_d + P_{RT}}{P_N} \quad \text{C2.4}$$

Where P_{RT} is the power developed in the total ballast resistance.

Under matched conditions and from the principal of conservation of energy, all of the power available on the network is transferred to the ballast resistance and the discharge →

$$P_N = P_D + P_{RT} \quad \text{C2.5}$$

The value of P_N is dependent on the energy available on the network and the pumping pulse width, and is approximately given by

$$P_N = \frac{C_N V_N^2}{2\tau_p} \quad \text{C2.6}$$

Where C_N is the capacitance of the PFN. Assuming that the pumping pulse power can be approximated by a rectangular pulse, the pulse power deposited into the discharge is approximately given by

$$P_d = I_d V_d \quad \text{C2.7}$$

The pulse power developed in the ballast resistance is given by

$$P_{RT} = I_d^2 R_T \quad \text{C2.8}$$

Substituting C2.6, C2.7, C2.8 into C2.5 and rearranging yields

$$V_d = \frac{V_N}{2} - V_{RT} \quad \text{C2.9}$$

Where V_{RT} is the voltage drop across the total ballast resistance ($V_{RT} = I_d R_T$). Matched conditions will occur when equation C2.9 is satisfied.

APPENDIX C3 FAULT CURRENT ANALYSIS

The ballasted electrode consists of n_T elements. If partial breakdown of the discharge occurs then n elements remain conducting the normal discharge current and m conduct the fault current, thus by definition:

$$n_T = n + m \quad \text{C3.1}$$

If the currents passing through each individual n and m elements are labelled i and i_f respectively, the total discharge current I_{dm} is given by

$$I_{dm} = ni + mi_f \quad \text{C3.2}$$

Where if $m = 0 \Rightarrow I_d = I_{dm}$, I_d is given by

$$I_d = \frac{V_N - V_d}{Z_N + R_T} \quad \text{C3.3}$$

If no elements are arcing (i.e. passing the fault current) then substituting $R = R_T$ n_T into C3.3 \Rightarrow

$$I_d = \frac{n_T (V_N - V_d)}{n_T Z_N + R} \quad \text{C3.4}$$

If every segment breaks-down the full fault current I_{df} can be calculated by substituting $V_d = 0$ into expression C3.4, and is given by

$$I_{df} = \frac{V_N}{Z_N + R_T} = \frac{n_T V_N}{n_T Z_N + R} \quad \text{C3.5}$$

The fault current passing through one element, denoted by i_f , is given by

$$i_f = \frac{I_{df}}{n_T} = \frac{V_N}{n_T Z_N + R} \quad \text{C3.6}$$

and, likewise, the normal discharge current i through one element is given by

$$i = \frac{I_d}{n_T} = \frac{V_N - V_d}{n_T Z_N + R} \quad \text{C3.7}$$

Thus substituting from C3.6 and C3.7 into C3.2 gives

$$I_{dm} = \frac{n (V_N - V_d) + m V_N}{(n+m) Z_N + R} \quad \text{C3.8}$$

Substituting for m from C3.1 into C3.8 and rearranging \rightarrow

$$n = \frac{n_T V_N - I_{dm} (n_T Z_N + R)}{V_d} \quad \text{C3.9}$$

Hence m can be found from C3.1.

APPENDIX D1 PULSE CHARACTERISTICS

SPIKE POWER: This is the maximum power of the initial spike and is made dimensionless by referring it to the maximum input power.

SPIKE ENERGY OVER TOTAL OUTPUT ENERGY: Designed to show the proportion of output energy contained in the main pulse.

FLAT PULSE POWER: Devised to show the mean flat pulse power, made dimensionless by referring it to the maximum input power.

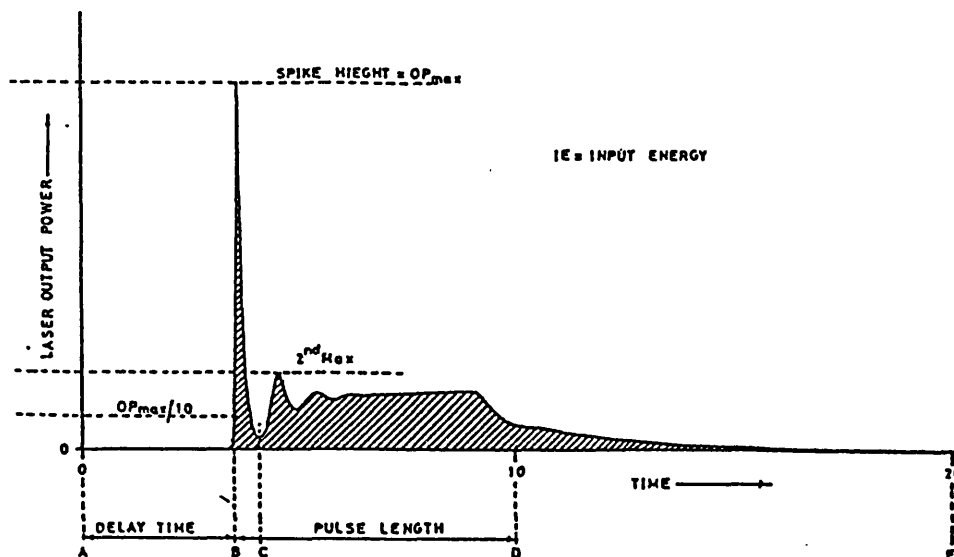
OSCILLATION PARAMETER: Defined in Figure D1.1 and designed to be used with the flat pulse power, which taken in isolation can give deceptively good values.

EFFICIENCY (η_{10}): Efficiency based on 10 μs of output

EFFICIENCY (η_{20}): Efficiency based on 20 μs of output

DELAY TIME: Delay time is defined as the time lag between the start of the current pulse and the laser pulse.

PULSE LENGTH: This is the length of time that the output pulse is of sufficient intensity to be useful for machining.



- (i) SPIKE ENERGY (SE) = INTEGRATE BETWEEN B & C
- (ii) PULSE ENERGY (PE) = INTEGRATE BETWEEN B & D
- (iii) TOTAL OUTPUT ENERGY (TOE) = INTEGRATE BETWEEN B & E
- (iv) FLAT PULSE POWER (FPP) = INTEGRATE BETWEEN C & D AND DIVIDE BY TIME (E-D)
- (v) OSCILLATION PARAMETER (OSC) = $2^{nd}Max / FPP = 100\%$
- (vi) EFFICIENCY $\eta_{10} = PE / IE = 100\%$
- (vii) EFFICIENCY $\eta_{20} = TOE / IE = 100\%$
- (viii) SPIKE ENERGY OVER (TOE) = $SE / TOE = 100\%$
- (ix) PULSE ENERGY OVER (TOE) = $PE / TOE = 100\%$

FIGURE D1.1 PARAMETER DEFINITIONS

REFERENCE: Chatwin C. "Thermodynamics of Pulsed CO₂ laser for Machining Metals". Ph.D. Thesis. Department of Mechanical Engineering, University of Birmingham 1982.

APPENDIX D2 DETECTOR SPECIFICATIONS

Photon Drag Monitor:

Model 7443-05		
Amplifier 7402, gain	100	
Responsivity	6	mV/kW
Minimum power level at 10^8 Hz (S/N = 1)	600	W
Response time	1.8	ns
Fraction of beam absorbed	25	%

Cadmium-mercury-telluride (CMT) detector:

Model	PV 2187	
Type	Photovoltaic	
LN ₂ cooled		
Device area	5.5×10^{-4}	cm ²
Active area	1.0×10^{-4}	cm ²
R _{0A}	0.07	Ω cm ²
Field of view	45°	
D* _{λ}	1.1×10^{10}	cm. $\sqrt{\text{Hz W}^{-1}}$
Bandwidth	150	MHz
Damage threshold	1	W cm ⁻²

Dewer must be pumped to 10^{-4} torr when pressure falls to half the original value. The relative response of the detector as a function of wavelength can be seen in Figure D2.1.

Preamplifier:

Type MPA-1	
Bandwidth	50 kHz - 150 MHz
Output	50 Ω coaxial BNC
Gain	30 dB
Variable bias facility	
Low noise	

Supplier: Laser Monitoring Systems Ltd.

Relative response

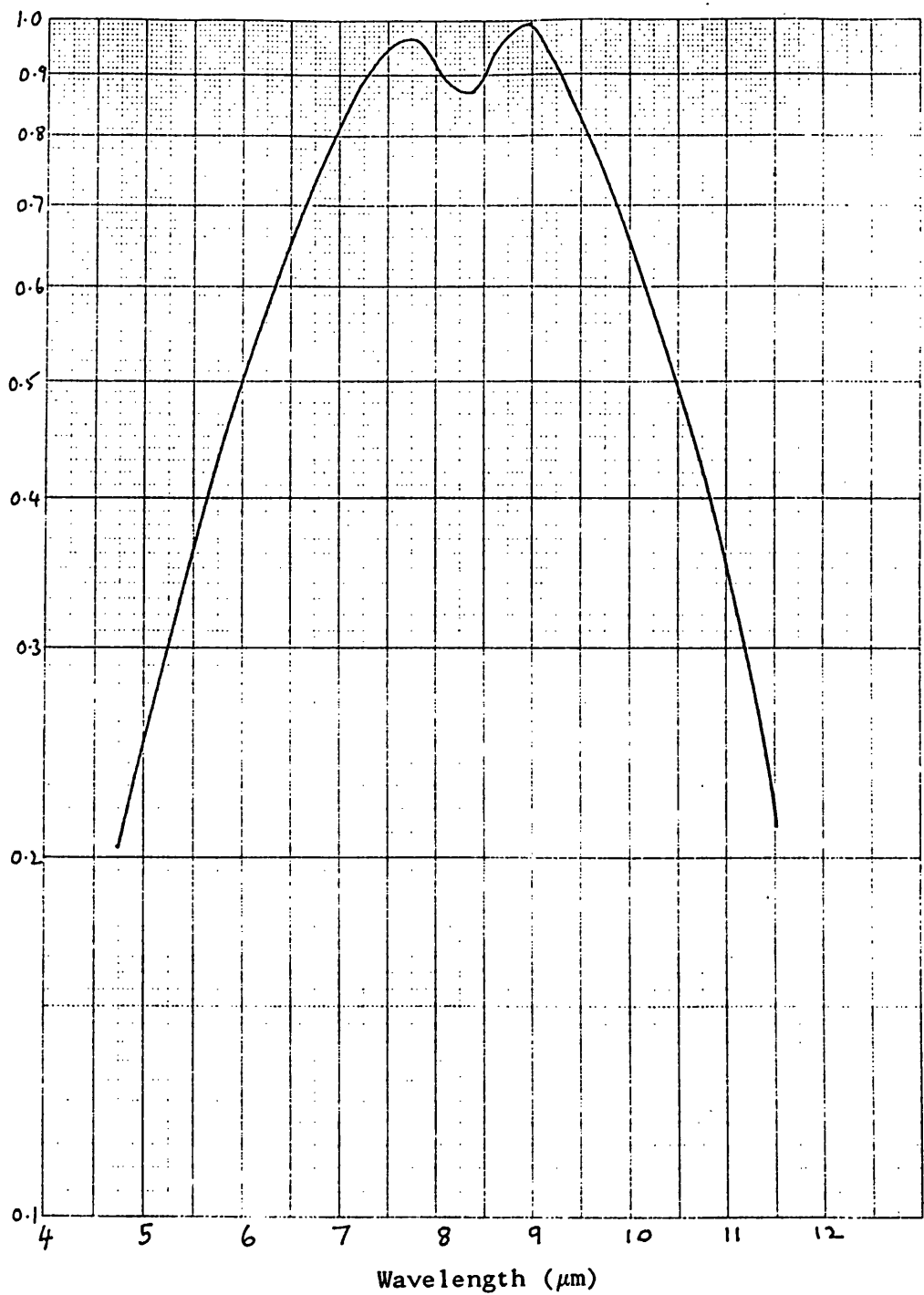


FIGURE D2.2 CMT RELATIVE SPECTRAL RESPONSE

There is a requirement for continuous power and energy measurements of high power cw and pulsed lasers where the measurement technique does not result in any significant degradation of beam quality or power; this is commonly achieved by employing a beam splitter to divert a small fraction of the beam energy to a photodetector.

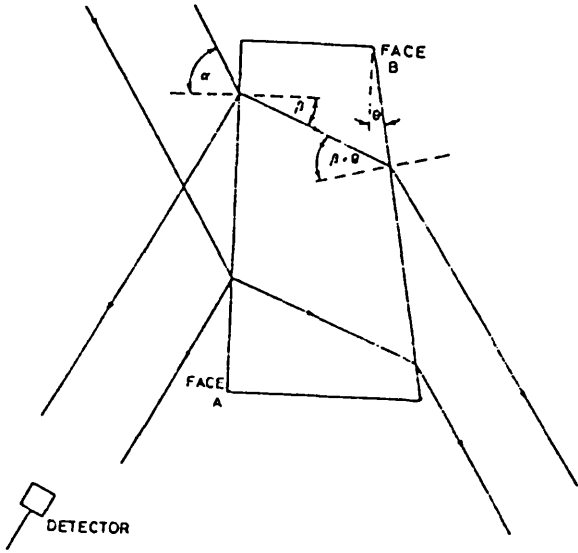


Fig. 1. Experimental arrangement for laser beam power monitoring using a wedge.

A problem in sampling multikilowatt beams is that even 1% of such a beam is sufficient to destroy most photodetectors. For example, cadmium-mercury-telluride (CMT) devices have a damage threshold of only 1 Wcm^{-2} . Thus, to prevent detector damage, beam attenuation to a fraction of a percent is crucial; fortuitously this limitation is complementary to the beam sampling requirements.

A technique is reported which enables sampling of a very small percentage of a linearly polarised incident beam with negligible absorption and very nearly 100% transmission of the unreflected beam. The inherent advantage of this technique is that there is no need for optical coatings, which are expensive for small batch sizes. It can be used across the complete optical spectrum by the appropriate choice of materials and angles. The method exploits the behavior of dielectrics when the incident radiation is at or near the Brewster angle, at which the reflectance component parallel to the plane of incidence is zero or small.

A wedge is used of apex angle θ (see Fig. 1). The reflectance of the front and back face is denoted by R_F and R_B , where F and B refer to the front and back faces, respectively, and the superscript " indicates parallel to the plane of incidence. Face B is arranged so that the internal incident ray is at the Brewster angle χ_B^{int} , allowing for total transmission of the refracted component of the beam, i.e., $R_B = 0$. The condition $R_B = 0$ occurs when $\beta + \theta = \chi_B^{\text{int}}$, where β is the angle of refraction from the face F . The incident ray is slightly displaced from the Brewster angle χ_F^{ext} for face F , resulting in partial reflection of the incident beam.

Table I gives the angle of incidence α and values of θ necessary to ensure $R_B = 0$ for ZnSe (refractive index $n = 2.403$), reflectances R_F are also tabulated. Clearly the percentage reflected is a function of α . The wedge angle θ determines the value of R_F and α for which $R_B = 0$. Conversely, if a desired reflection is specified, angles θ and α can be calculated to yield the chosen value of R_F . It should be emphasized that for any particular θ there is only one α that ensures $R_B = 0$. For different values of R_F with $R_B = 0$ it is

necessary to have more than one wedge. By rotating the incident polarized beam about its optical axis the polarization vector can be made perfectly parallel to the plane of incidence, and theoretically no reflection will occur perpendicular to the plane of incidence.

The accuracy of α is dependent on the positional accuracy of the rotary stage, the accuracy of θ is limited by the manufacturing process; it is worth noting that tight tolerance specification imposes a severe cost penalty. Let the error for α and θ be represented by $\Delta\alpha$ and $\Delta\theta$, respectively. It is apparent that only $\Delta\alpha$ contributes to the uncertainty in R_F , which is designated ΔR_F ; i.e., ΔR_F is independent of $\Delta\theta$. The errors $\Delta\alpha$ and $\Delta\theta$ both contribute to an error in R_B , denoted ΔR_B . Thus it is clear that there may be a reflection off face B .

Typical values of $\Delta\alpha$ were obtained from three commercially available rotary stages; in order of ascending accuracy and cost, these positional accuracies were quoted as 5 min of arc, 30 min of arc, and 0.36 sec of arc. A value of 30 sec of arc was quoted for $\Delta\theta$. For small angles of θ where $\theta \ll 1^\circ$, it would be possible to use an optical flat and rely on the tolerance values of parallelism for wedgelike properties. The wedge angle could be accurately measured by interference techniques.

Table II shows for a particular α and θ the percentage error in R_F for the above quoted $\Delta\alpha$ values, i.e., $\Delta R_F/R_F$ and the error in R_B due to $\Delta\alpha$ and $\Delta\theta$ expressed as a percentage of R_F , i.e., $\Delta R_B/R_F$. The values of α , θ , and R_F were taken as 62.176° , 1.000° , and 0.8742% , respectively. The final column gives the error in R_B when $\Delta\theta = 0$, denoted ΔR_{B0} , expressed as a percentage of R_F , $\Delta R_{B0}/R_F$. The values of ΔR_B are also tabulated where ΔR_B is the reflectance from face

Table I. Wedge Reflectance Behavior*

α	β	θ	R_F (%) ^b
66.406	22.418	0.178	0.0393
65.406	22.234	0.360	0.1500
64.406	22.044	0.551	0.3201
63.406	21.846	0.748	0.5422
62.406	21.642	0.952	0.8077
62.176	21.594	1.000	0.8742

$R_B = 0$ At all angles

* Angle of incidence α , of refraction β , corresponding wedge angle θ to ensure that $(\theta + \beta)$ is equal to the Brewster angle.

^b R_F (%) gives the reflectance as a percentage of the incident beam.

Table II. Reflectivity Errors*

$\Delta\alpha$ $\times 10^4$	$(\Delta R_B/R_F)\%$ $\times 10^4$	$\left(\frac{\Delta R_F}{R_F}\right)\%$ $\times 10^4$	$\left(\frac{\Delta R_B}{R_F}\right)\%$ $\times 10^4$	$\left(\frac{\Delta R_{B0}}{R_F}\right)\%$ $\times 10^4$
833	8.29	27,800	948.0	4.2
83	1.06	2,800	121.8	0.04
1	0.69	34	78.7	0.00001

$R_F = 0.8742$

* This table shows the error in the reflectance off the front and back face (ΔR_F and ΔR_B , respectively) expressed as a percentage of R_F (the reflectance off the front face) for a wedge angle θ of 1° with error $\Delta\theta$ of 30 sec of arc and incident angle α of 62.176° for different errors ($\Delta\alpha$) in α . $(\Delta R_B/R_F)\%$ is the error in the reflectance from the back face (due to errors $\Delta\alpha$ and $\Delta\theta$) expressed as a percentage of the reflectance from the front face. $(\Delta R_{B0}/R_F)\%$ is the error in the reflectance from the back face due to error $\Delta\alpha$ with $\Delta\theta = 0$.

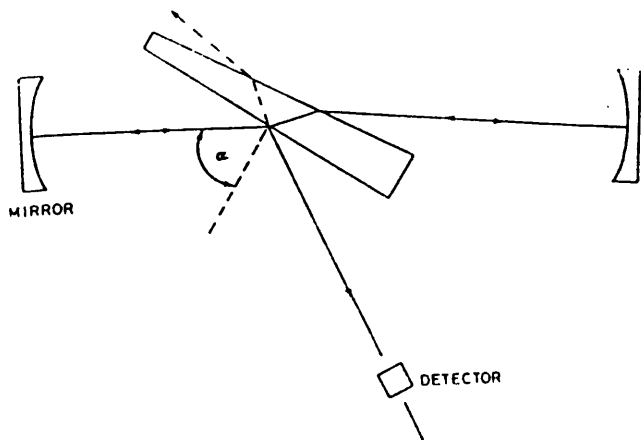


Fig. 2. Power monitoring within the laser resonator.

β expressed as a percentage of the beam incident on face F and due to $\Delta\alpha$ and $\Delta\theta$. It can be seen from Table II that ΔR_H^* is at least 3 orders of magnitude smaller than the incident beam.

$(\Delta R_H^*/R_F^*)\%$ reaches a limiting value as $\Delta\alpha \rightarrow 0$ due to the error $\Delta\theta$. For $\Delta\theta = 8.33 \times 10^{-3}$ and $\Delta\alpha = 0$,

$$\xrightarrow{\Delta\alpha \rightarrow 0} \left(\frac{\Delta R_H^*}{R_F^*} \right) \% \rightarrow 0.00782\%.$$

The error in R_F for the worst case is 3% of R_F . In a laser monitoring system calibration is necessary, so errors in R_F this small can be neglected. However, R_H , if too large, can be minimized by slight adjustment of α .

If a wedge has an antireflection coating on both faces and is placed in an incident beam, more than one reflected beam is obtained, due to reflections from both faces. Consequently any detection system needs to be placed some distance from the wedge to avoid transient interference effects. However, for the technique reported herein there is only one reflection which allows compact and economic design of beam monitoring systems.

By incorporating the wedge in an optical resonator as depicted in Fig. 2, it is possible to construct a power monitoring device that also linearly polarizes the laser output beam. The angle of deviation¹ is corrected for by the repositioning of either the rear mirror or output window.

Summarising, a method has been described to monitor laser output power and energy by use of an uncoated wedge. The advantages are: negligible energy losses, the elimination of the irradiance reflected from the wedge back face, and a specification that does not require expensive optical coatings. The sensitivity of this approach to misalignment and fabrication tolerances has been discussed.

References

1. E. Young, "Deviation of Light Incident at the Brewster Angle on a Wedged Window," *Appl. Opt.* 27, 19 (1988).

APPENDIX D4 GAUSSIAN PROPAGATION

The beam radius as a function of the distance from the beam waist is given by

$$w^2(z) = w_0^2 \left[1 + \left[\frac{\lambda z}{\pi w_0^2} \right]^2 \right] \quad \text{D4.1}$$

and the radius of the curvature of the phase front is given by

$$R(z) = z \left[1 + \left[\frac{\pi w_0^2}{\lambda z} \right]^2 \right] \quad \text{D4.2}$$

Where $w(0) = w_0$ and $R(0) = \infty$, which implies that at the beam waist the radius of curvature of the phase front is plane. An expression for w_0 can be obtained by substituting $R(L) = R_c$ into equation D4.2 and rearranging, R_c is the radius of curvature of the rear mirror and L the distance between the front window and the rear mirror. It can be shown that

$$w_0^2 = \frac{\lambda}{\pi} \left[d (R_c - d) \right] \quad \text{D4.3}$$

The above equations were used to validate the completed code for a number of simple resonator configurations where no internal optics were used to focus or expand the beam.

APPENDIX D5 RAY MATRIX THEORY: DEVELOPMENT OF THE CODE

The code that was developed to predict the development of the beam radius for the TEM_{00} and TEM_{01} modes used the technique of ray matrices. The important parameters to determine were the dead space and active mode volumes, and the beam radius on the optics of the resonator – this allowed an estimation of the diffraction losses for the system. However, it must be remembered that this is only an approximation. The code has full menu facilities to allow interactive running between the user and the computer. The input variables can be changed, for example, those associated with the physical description of the resonator, the discharge dimensions and the optics used for the resonator. The option to make any radii of curvature of the mirrors a variable with values defined by the user was introduced to facilitate parametric analysis. The code was written in ASYST; the main factors leading to this decision were the matrix multiplication techniques

inherent in ASYST and the availability of the software package.

It was decided to include the possibility of using one internal focusing optic within the resonator configuration, with a radius of curvature R_2 . This greatly simplifies programming as the plane folding mirrors are represented by the identity matrix.

Figure D5.1 shows the resonator configuration for a three pass resonator with an internal focusing optic. For the general resonator configuration with n_p passes, the front window is labelled M_1 and the rear mirror as M_{n_p+1} , the other mirrors are labelled in logical sequence from the front to the rear of the cavity. It is seen in Figure D5.1 that the internal focusing optic is at the position indicated by suffix 2 and distance d_1 from the output window, the distance to the rear mirror from the internal focusing optic is d_2 , the length of the cavity is L , thus

$$L = d_1 + d_2 \quad \text{D5.1}$$

A running variable ℓ is used to represent the distance from the front window at which the beam diameter is calculated. For a near, half-symmetric resonator the beam waist and the front window are coincident.

As a specific example, the equivalent lens waveguide is developed for the 3 pass resonator, and is shown in Figure D5.2. The mirrors are represented by convex lenses of focal length f_i , where $f_i = R_i/2$, and R_i is the radius of curvature of mirror i . The plane fold mirrors are represented by the identity matrix and so have no affect on the Guassian propagation of the beam. It is of course assumed that the spatial extent of the mirrors is sufficient to limit the diffraction losses.

The ABCD matrix for the system at the plane A-A, denoted by $[M_T]$, is given by

$$[M_T] = [M_1'] [M_4] [M_3] [M_2] [M_1] \quad \text{D5.2}$$

Where $[M_i]$ corresponds to the positions shown in Figure D5.2 and the plane A-A is a distance ℓ from the front window.

In general, the ray matrix for an optical system consisting of length "u" of free space is simply given by

$$[M_{fs}] = \begin{bmatrix} 1 & u \\ 0 & 1 \end{bmatrix} \quad \text{D5.3}$$

And for a lens with focal length f , the ray matrix is given by

$$[M_1] = \begin{bmatrix} 1 & 0 \\ -\frac{1}{f} & 1 \end{bmatrix} \quad \text{D5.4}$$

If the lens and free space are combined into one system, as shown in Figure D5.3, the system ray matrix is given by:

$$[M_{fS1}] = [M_1][M_{fS}] \quad \text{D5.5}$$

$$\Rightarrow [M_{fS1}] = \begin{bmatrix} 1 & u \\ -\frac{1}{f} & 1 - \frac{u}{f} \end{bmatrix} \quad \text{D5.6}$$

It is seen that matrices $[M_4]$, $[M_3]$, $[M_2]$ and $[M_1]$ are equivalent in form to the ray matrix given in D5.6, with the variable $u = d_1 - \ell$ or $u = d_2$ and $f = f_1$ or $f = f_2$. The matrix $[M_1']$ is equivalent to the matrix given in equation D5.3 with $u = \ell$. Consequently, if $[M_T]$ is evaluated the total ray matrix is found for this equivalent lens waveguide and the elements A, B, C and D are known. The beam radius at ℓ is given by

$$w^2(\ell) = \frac{\lambda B}{\pi n \left[1 - \left[\frac{A + D}{2} \right]^2 \right]^{1/2}} \quad \text{D5.7}$$

Where n is the refractive index of the surrounding space, $n \approx 1$. The radius of curvature of the phase front at ℓ is given by

$$R(\ell) = -\frac{2 B}{A - D} \quad \text{D5.8}$$

It is clear that to find the beam radius throughout the length of the resonator, $[M_T]$ must be evaluated at discrete points. The distance L is divided into a number of equal incremental distances of length δ . $R(\ell)$ and $w(\ell)$ are found from $\ell = 0$ to $\ell = L$.

However, once the beam width is calculated past the internal focusing optic (i.e. $\ell > d_1$) the order of the matrices, as shown by equation D5.2, are changed. The equivalent lens waveguide can be seen in Figure D5.4, where the beam waist is now calculated at the plane B-B. The system ray matrix now becomes

$$[M_T] = [M_2'] [M_1] [M_4] [M_3] [M_2] \quad D5.9$$

This process is repeated until $w(L)$ has been found.

The mode volume is found by calculating each volume element contribution from the element width δ , and summing these contributions from $\ell = 0$ to $\ell = L$. The j^{th} volume element is simply given by

$$\Delta V_j = \pi \delta w(j\delta) \quad D5.10$$

The expression for the total mode volume, V_T is

$$V_T = \sum_{j=1}^{L/\delta} \pi \delta w(j\delta) \quad D5.11$$

The input data set to the code is a description of the distance of the front window and all the other mirrors from the discharge edge, and the length of the discharge. Internal switches in the code are used to identify which volume the value of ΔV_j has to be added to, i.e. the dead space or the active volume.

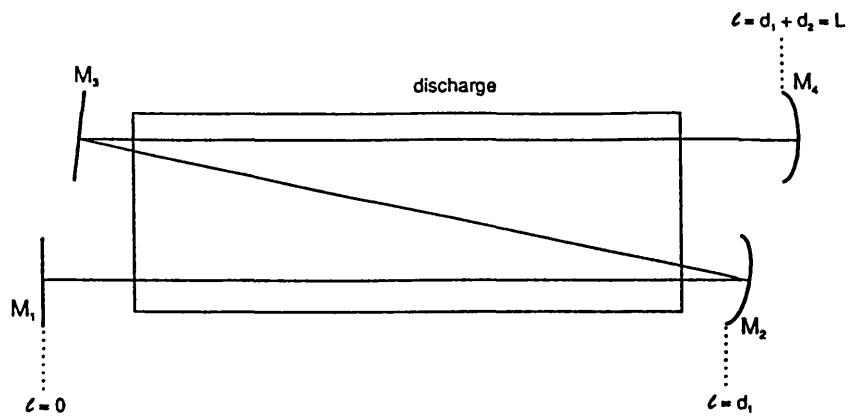


FIGURE D5.1 SCHEMATIC OF 3 PASS RESONATOR

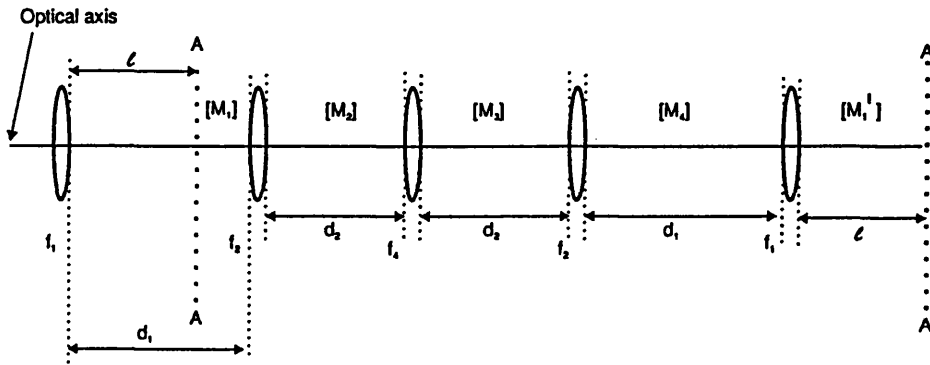


FIGURE D5.2 EQUIVALENT LENS WAVEGUIDE FOR 3 PASS RESONATOR

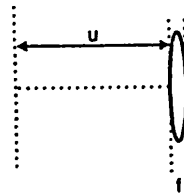


FIGURE D5.3 FREE SPACE AND LENS OPTICAL SYSTEM

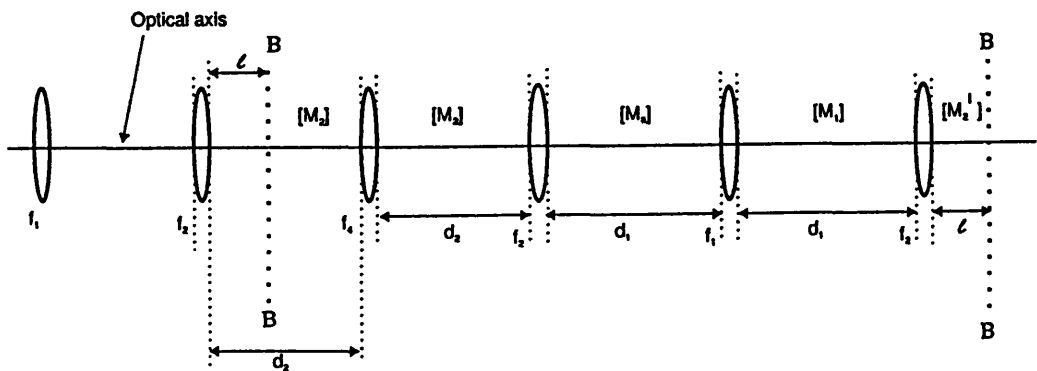


FIGURE D5.4 EQUIVALENT LENS WAVEGUIDE FOR 3 PASS RESONATOR

APPENDIX D6 DIFFRACTION LOSSES: A SIMPLE ESTIMATE

The first order expression for the diffraction loss for the TEM₀₀ mode, incident on mirror i of radius a_i is given by

$$\rho_{00i} = \exp \left[- \frac{2 a_i^2}{w_i^2} \right] \quad \text{D6.1}$$

Where w_i is the radius of the TEM₀₀ mode to the 1/e² point of the beams peak intensity, on mirror i. And for the TEM₀₁ mode, the diffraction loss for mirror i of radius a_i is given by

$$\rho_{01i} = \left[1 + 2 \left[\frac{a_i^2}{w_i^2} \right] \right] \exp \left[- \frac{2 a_i^2}{w_i^2} \right] \quad \text{D6.2}$$

If it is assumed that the right going wave is incident on the front window first, then the fraction of the incident beam diffracted passed the front window is ρ₁, where the subscript used to denote the mode has been dropped. Consequently, 1-ρ₁ is the component of the beam which is reflected towards the second optic. Now, the component of the beam that is diffracted from the second mirror is ρ₂, but this is a fraction of 1-ρ₁. The beam that is reflected towards the third optic now contains the fraction of the original power given by (1-ρ₁).(1-ρ₂). Following in this manner the total diffraction loss for all of the mirrors of the 3 pass resonator, for one complete transit of the right going wave is given by

$$\begin{aligned} DL_R = & \rho_1 + (1-\rho_1)\rho_2 + (1-\rho_1)(1-\rho_2)\rho_3 + (1-\rho_1)(1-\rho_2)(1-\rho_3)\rho_4 + \\ & (1-\rho_1)(1-\rho_2)(1-\rho_3)(1-\rho_4)\rho_3 + (1-\rho_1)(1-\rho_2)(1-\rho_3)(1-\rho_4) \\ & (1-\rho_3)\rho_2 + (1-\rho_1)(1-\rho_2)(1-\rho_3)(1-\rho_4)(1-\rho_3)(1-\rho_2)\rho_1 \end{aligned} \quad \text{D6.3}$$

Collecting like terms and taking the general case of a resonator with n_p passes, it can be shown that an approximate expression for the diffraction loss of the right going wave, assumed incident on the front window first is given by

$$DL_R = \rho_1 + \sum_{n=1}^{n_p} \rho_{n+1} \prod_{i=1}^n (1-\rho_i) + \prod_{i=1}^{n_p} (1-\rho_i) \sum_{n=n_p}^1 \rho_n \prod_{i=n}^{n_p} (1-\rho_{i+1}) \quad \text{D6.4}$$

And, similarly for the left going wave (incident on the rear mirror first) it can be shown that the diffraction loss is given by

$$DL_1 = \rho_{np+1} + \sum_{n=np}^1 \rho_n \prod_{i=1}^{np} (1-\rho_{i+1}) + \prod_{i=1}^{np} (1-\rho_{i+1}) \sum_{n=1}^{np} \rho_{n+1} \prod_{i=n}^1 (1-\rho_i) \quad D6.5$$

The average diffraction losses for the resonator configuration is given by

$$DL = \frac{DL_r + DL_1}{2} \quad D6.6$$

These equations were integrated into the code which has been discussed in Appendix A6. A series of dry runs were used to fully test the results from the code.

APPENDIX D7 COMPARISON OF DIFFRACTION LOSSES WITH NUMERICAL RESULTS

Li [D7.1] calculated the diffraction losses for different resonator configurations by using numerical techniques. These results were abstracted graphically and compared to the values that were obtained with the code described in Appendices D5 and D6. The losses were calculated for a single pass resonator as a function of the Fresnal number. A MathCad code was developed in order to compare the diffraction losses calculated from both techniques. This provided another method to test the output from the code.

For the single pass resonator the Fresnal number is given by

$$N_F = \frac{a_1 a_2}{\lambda L} \quad D7.1$$

Where a_1 is the effective radius of the front window (or aperture if it is smaller), and a_2 the radius of the rear mirror. L is the distance between these optics and λ the transition wavelength of the CO₂ laser.

The graph below shows a comparison of the data calculated from the code and that abstracted from Li for the TEM₀₀. It is seen that there is agreement between the two techniques provided that the Fresnal number is large. For a given Fresnal number, the error increases as the modulus of the stability of the resonator increases towards 1.

Stability parameters g_1 & g_2

given by:

$$g_i = 1 - \frac{L}{R_i}$$

Where $i = 1$ or 2

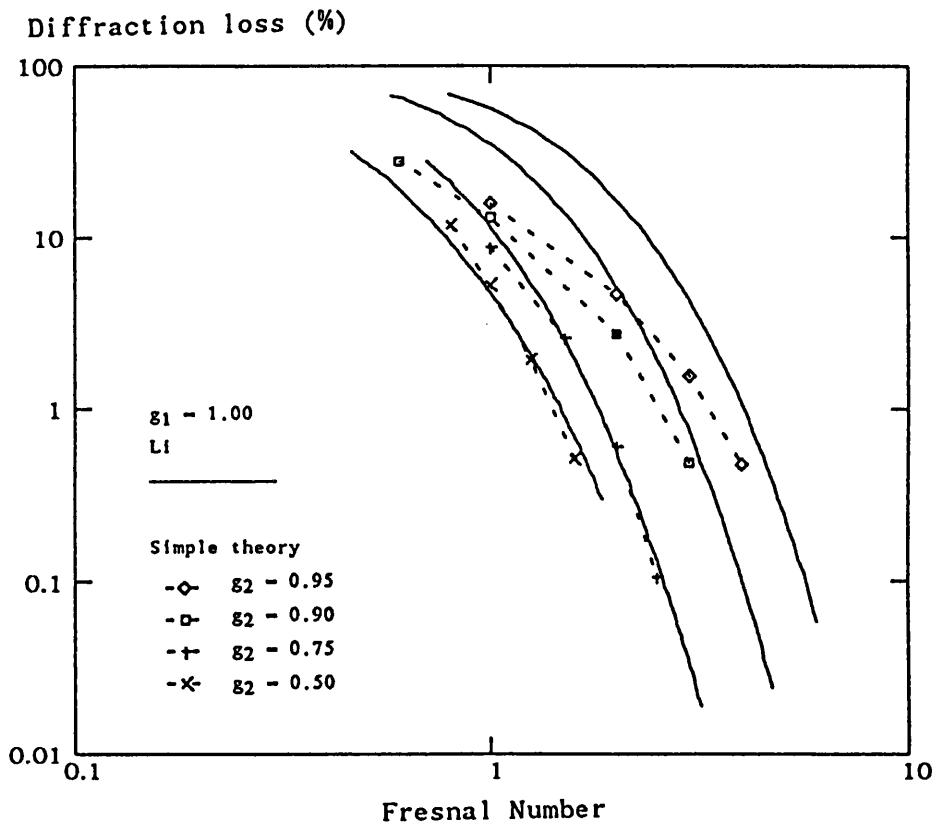


FIGURE D7.1 NUMERICAL AND SIMPLE CALCULATION OF DIFFRACTION LOSSES

REFERENCE [D7.1] Li T. "Diffraction losses and selection of modes in maser resonators with circular mirrors". Bell System Technical Journal, pp 917-932 May 1965.

APPENDIX E1 WORKPIECE INTERACTIONS

The non-conduction limited interaction process has been successfully demonstrated, however, no detailed investigation has been performed into the performance of the laser as a machine tool.

Holes were successfully drilled through 0.046" (1.168 mm) thick aluminium in about 0.2 s for a laser output power of 64.5 W, a discharge frequency of 1.5 kHz, and 1:1:0 gas mixture at 60 mb. Interestingly, for a 1:1:4 gas mixture at a pressure of 60 mb, operating at 2.5 kHz and yielding a mean laser output power of 99.8 W, no holes were drilled. Table E1.1 summarises the laser characteristics.

The 0.8 Ω ballasted electrode and the 5 pass resonator were installed in the laser cavity. The photon drag detector was used to monitor the laser pulse energy E_o at 100 Hz, and the mean laser power was calculated from $P = E_o f$ at frequency f .

Table E1.1 Summary of the laser output characteristics

Gas mixture	P (mb)	E_d (J)	E_o (mJ)	η_5 (%)	f (Hz)	P (W)
1:1:0	60	2.49	43	1.73	1500	64.5
1:1:4	60	2.55	40	1.56	2500	99.8

The values of E_d and E_o are the average of 5 readings to two significant places, taken at $f = 100$ Hz; the standard error of the means for E_d and E_o are typically less than 5 %.

Figures E1.1 and E1.2 show the laser output and current pulses for the 1:1:0 and 1:1:4 gas mixture respectively. It is seen that the pulse characteristics obtained with the 1:1:0 gas mixture are nearer to those defined by Bakewell in order to achieve the non-conduction limited interaction processes. The plateau pulse powers for the 1:1:0 and 1:1:4 gas mixtures were about 8.33 kW and 4.12 kW respectively. The peak powers for the 1:1:0 and 1:1:4 gas mixtures were 23.2 kW and 15.0 kW respectively. It was with the 1:1:0 gas mixture that holes were drilled in the aluminium. It is interesting to note that with the 1:1:4 gas mixture, even with the frequency of 2.5 kHz and a mean laser output power of about 100 W, no holes were drilled for pulse trains of up to 1 s. However, it is possible that the laser output power at this higher frequency was not the estimated 100 W, because of the displacement of the discharge (see Chapter 4); and consequently, this could explain the inability of the laser to drill through aluminium for these conditions. It is recommended that in future experiments the CMT detector system is used to monitor the laser output power while the material is being processed.

Plate E1.1 shows a view of the surface of a hole partially drilled in aluminium. The rectangular shape was attributed to misalignment of the fold optics. The area of the hole is approximately $165 \times 95 \mu\text{m}^2$. The diffraction limited spot size has a diameter given by

$$r_s = \frac{\lambda f_1}{\pi w_1}$$

Where λ is the transition wavelength ($10.6 \mu\text{m}$), f_1 and w_1 are the focal length of the lens (150 mm) and the beam radius at the lens (for the TEM_{00} mode, $w_1 \approx 6.2 \text{ mm}$) respectively. Thus, $r_s \approx 82 \mu\text{m}$ and is comparable to the measured value in one dimension.

The estimated volume of material removed from the aluminium is $1.83 \times 10^{-11} \text{ m}^3$. Thus for 300 pulses (i.e. 1.5 kHz for 0.2 s), the average material removed per pulse is approximately $6.1 \times 10^{-14} \text{ m}^3/\text{pulse}$. If the laser was operating at 10 kHz, assuming that the volume of material removed per pulse was constant; this thickness of aluminium, for these laser pulse characteristics, could be drilled at least 6.6 times faster, i.e. in 30 ms. However, it is likely that for the increased frequency it will be less than this value because the quasi-cw processing regime will be encountered.

Plate E1.2 shows a cross section of a hole.

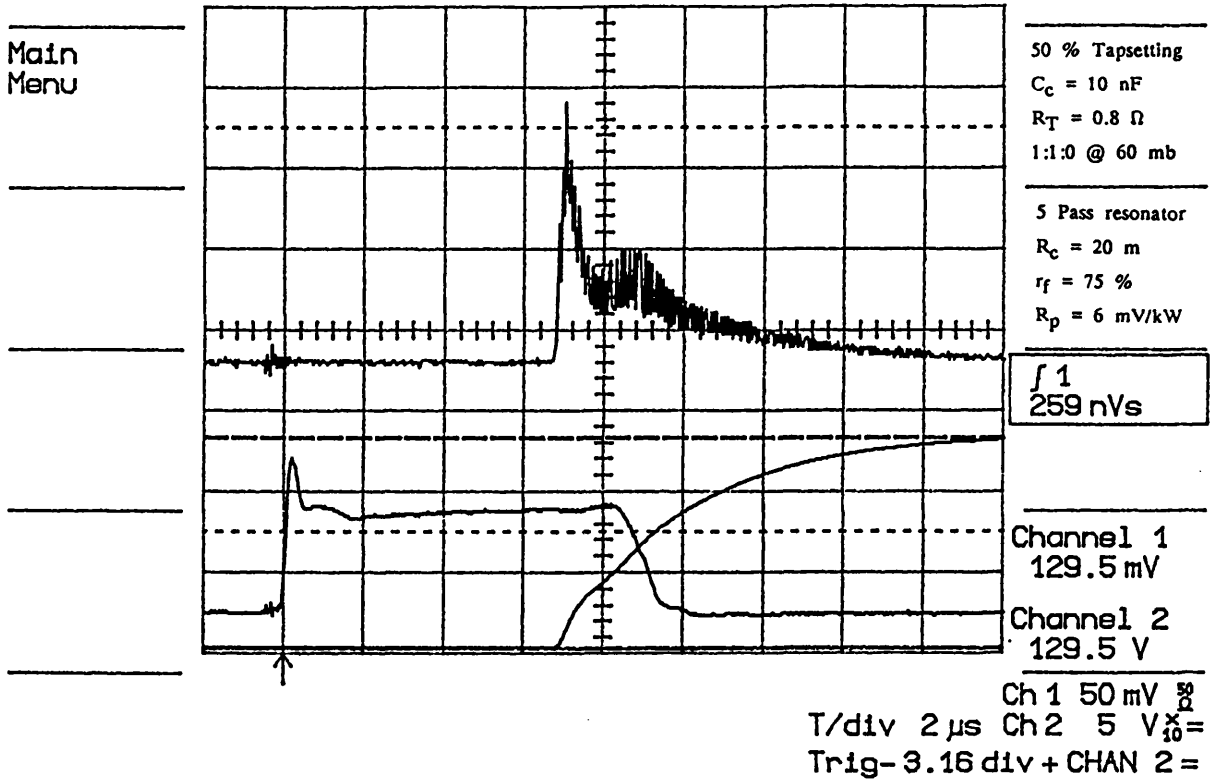


FIGURE E1.1 LASER OUTPUT PULSE AND DISCHARGE CURRENT

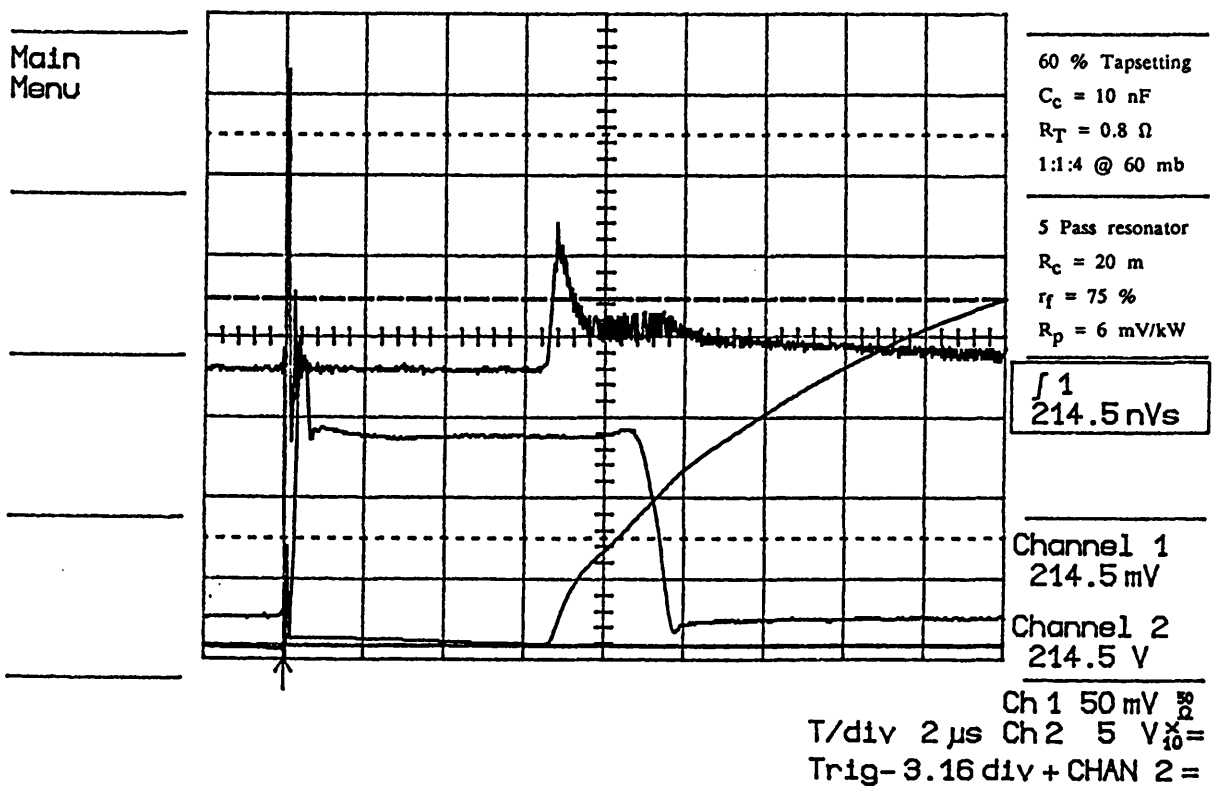


FIGURE E1.2 LASER OUTPUT PULSE AND DISCHARGE CURRENT

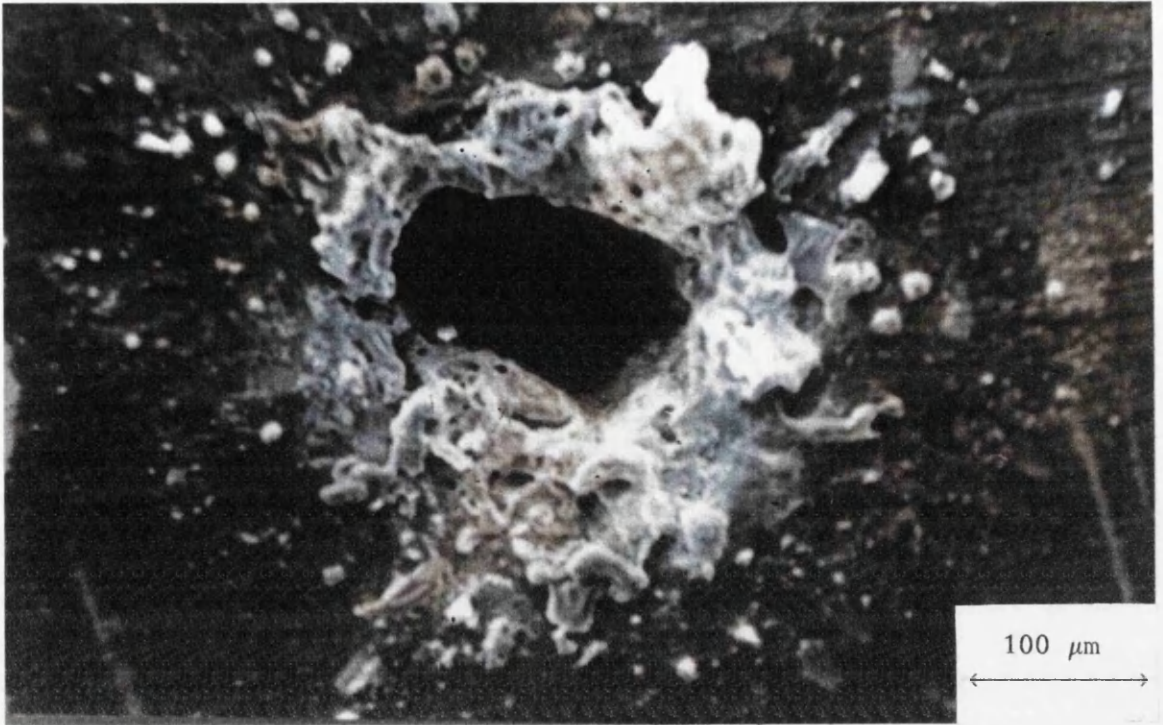


PLATE E1.1 SURFACE VIEW



PLATE E1.2 HOLE CROSS-SECTION